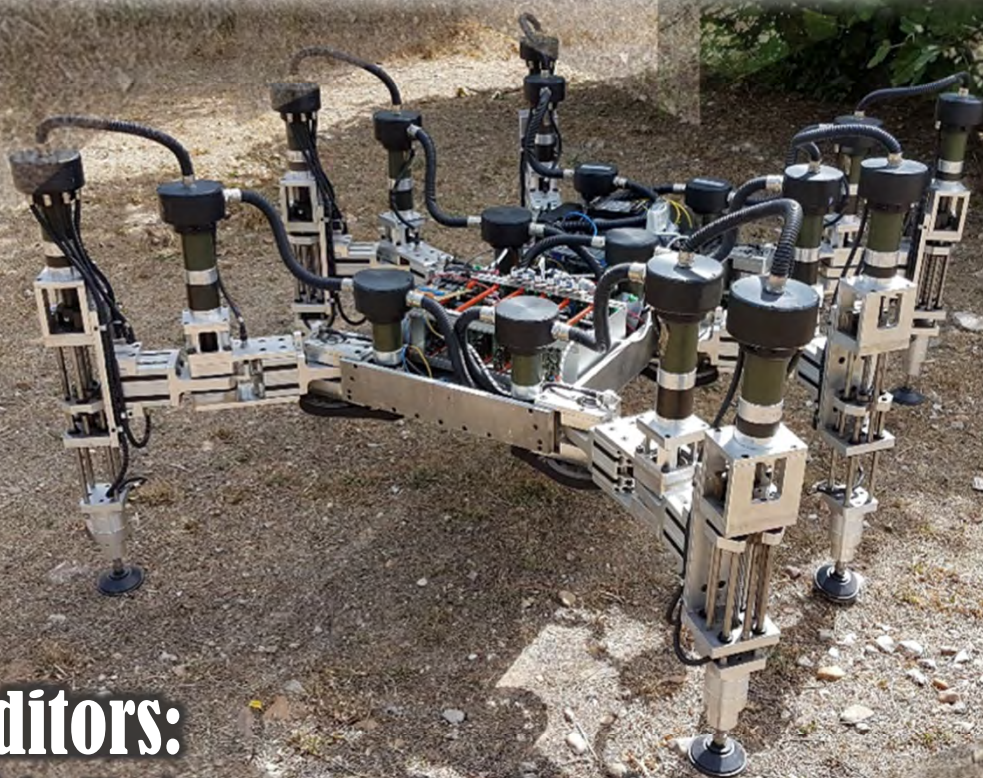# ROBOTICS
TRANSFORMING THE FUTURE

Editors:

Héctor Montes

M. Osman Tokhi

Gurvinder S. Virk

Manuel Armada

Humberto Rodríguez

Roemi Fernández

Pablo González de Santos

Víctor Sánchez

Manuel Silva

CLAWAR
Association Ltd.

Robotics Transforming the Future

Robotics
Transforming the Future

Proceedings of CLAWAR 2018: The 21st International Conference on Climbing and Walking Robots and the Support Technologies for Mobile Machines

Panama City, Panama, 10 – 12 September 2018

Editors:

Hector Montes
Universidad Tecnológica de Panamá, Panama

M Osman Tokhi
London South Bank University, UK

Gurvinder S Virk
CLAWAR Association Ltd, UK

Manuel Armada
CSIC-UPM, Spain

Humberto Rodríguez
Universidad Tecnológica de Panamá, Panama

Roemi Fernandez
CSIC-UPM, Spain

Pablo Gonzalez de Santos
CSIC-UPM, Spain

Victor Sanchez
Universidad Tecnológica de Panamá, Panama

Manuel Silva
Porto Polytechnic, Portugal

ROBOTICS TRANSFORMING THE FUTURE
Proceedings of the 21ˢᵗ International Conference on CLAWAR 2018

PREFACE

CLAWAR 2018 is the twenty-first edition of International Conference series on Climbing and Walking Robots and the Support Technologies for Mobile Machines. The conference is organized by CLAWAR Association in collaboration with the Universidad Tecnológica de Panamá (UTP) within the premises of UTP, Panama City, Panama during 10 – 12 September 2018.

CLAWAR 2018 brings new developments and associated new research findings in robotics technologies for shaping the future. The topics covered include assistive robotics for levels of augmentation to full support for elderly and disabled mobility, rehabilitation and function restoration; services to humans in industrial, public and domestic environments; new locomotion and design strategies to help in climbing on various terrains; navigation and localisation approaches, non-destructive testing and inspection strategies for industrial applications.

The CLAWAR 2018 conference includes a total of 53 articles, including three plenary lectures, from 17 countries. This number has been arrived at through rigorous review of initial submissions, where each paper initially submitted has received on average three reviews.

The editors would like to thank members of the International Scientific Committee and National Organising Committee for their efforts in reviewing the submitted articles, and the authors in addressing the comments and suggestions of the reviewers in their final submissions. It is believed that the CLAWAR 2018 proceedings will be a valuable source of reference for research and development in the rapidly growing area of mobile service robotics.

H. Montes, M. O. Tokhi, G. S. Virk, M. Armada, H. Rodríguez,
R. Fernández, P. González de Santos, V. Sánchez and M. Silva

CONFERENCE ORGANISERS

CLAWAR Association Limited
https://clawar.org/

Technological University of Panama
http://www.utp.ac.pa/

CONFERENCE COMMITTEES AND CHAIRS

Conference Chairs and Managers

Of twenty-first International Conference on Climbing and Walking Robots and the Support Technologies for Mobile Machines

Héctor Montes (General Co-Chair)	− FIE, UTP, Panama
Roemi Fernández (General Co-Chair)	− CAR, CSIC-UPM, Spain
Víctor Sánchez (General Co-Chair)	− SENACYT, Panama
Manuel Armada (General Co-Chair)	− CAR, CSIC-UPM, Spain
M. Osman Tokhi (ISC Chair)	− London South Bank Univ, UK
Humberto Rodríguez (LOC Chair)	− FIM, UTP, Panama
Manuel F. Silva (Publications)	− ISEP & INESCTEC, Portugal
Rony Caballero (Publications)	− FIE, UTP, Panama
Salvador Vargas (Publications)	− FIE, UTP, Panama
Carlos Rovetto (L. Arrangements)	− FISC, UTP, Panama
Gurvinder S. Virk (Special/Workshop)	− Innotech, UK
Deyka García (Special/Workshop)	− FIM, UTP, Panama
Khaled Goher (Special/Workshop)	− University of Lincoln, UK
Iveth Moreno (Competition)	− CR Chiriquí, FIE, UTP, Panama
Abdullah Almeshal (Competition)	− PAAET, Kuwait
Rolando Serracin (Exhibition)	− CR Chiriquí, FIE, UTP, Panama
Giovanni Muscato (Exhibition)	− University of Catania, Italy
Ignacio Chang (Publicity)	− FIE, UTP, Panama
Fareg Aldbrez (Publicity)	− University of Sheffield, UK
Dimitris Chrysostomou (Web-site)	− Aalborg University, Denmark

International Scientific Committee (ISC)

Akin, H. L.	– Turkey	Cruse, H.	– Germany
Alam, Md S.	– Bangladesh	De Almeida, A. T.	– Portugal
Almeshal, A.	– Kuwait	Dehghani, A.	– UK
Amar, F. B.	– France	Dias, A.	– Portugal
Armada, M.	– Spain	Dogramadzi, S.	– UK
Azad, A. K. M.	– USA	Dutra, M. S.	– Brazil
Banfield, I.	– Panama	Eastman, R.	– USA
Belter, D.	– Poland	Fernández, R.	– Spain
Berbey, A.	– Panama	Ferreira, I.	– Portugal
Berns, K.	– Germany	Ferreira, P.	– Portugal
Bidaud, P.	– France	Fortuna, L.	– Italy
Billingsley, J.	– Australia	Fukuda, T.	– Japan
Bonsignorio, F.	– Italy	García, D.	– Panama
Bouazza-Marouf, K.	– UK	Garcia, E.	– Spain
Bridge, B.	– UK	Goher, K. M.	– UK
Caballero, R.	– Panama	Goldman, D.	– USA
Cáceres, D.	– Panama	González de Santos, P.	– Spain
Cameron, S.	– UK	Gradetsky, V.	– Russia
Cardeira, C.	– Portugal	Grand, C.	– France
Carelli, R.	– Argentina	Guedes, P. B.	– Portugal
Chang, I.	– Panama	Heyes, N.	– UK
Chen, W.	– China	Huq, S.	– Malaysia
Chevallerau, C.	– France	Hwang, K-S	– Taiwan
Chew, C-M	– Singapore	Ion, I.	– Romania
Chrysostomou, D.	– Denmark	Jatsun, S. F.	– Russia
Chugo, D.	– Japan	Kadar, E. E.	– UK

Kiriazov, P.	– Bulgaria	Rocha, R.	– Portugal
Kopacek, P.	– Austria	Rodríguez, H.	– Panama
Kozlowski, K.	– Poland	Rovetto, C.	– Panama
Lefeber, D.	– Belgium	Sánchez, V.	– Panama
Leon-Rodriguez, H.	– Colombia	Santibañez, V.	– Mexico
Lewis, M. A.	– USA	Santos, V.	– Portugal
Li, G.	– UK	Sattar, T. P.	– UK
Lima, L.	– Portugal	Sequeira, J. S.	– Portugal
Liu, Y.	– China	Sharma, S. K.	– UK
Malheiro, B.	– Portugal	Silva, F.	– Portugal
Marques, L.	– Portugal	Silva, M.	– Portugal
Massoud, R.	– Syria	Steinicke, L.	– Belgium
Mohamed, Z.	– Malaysia	Su, H.	– China
Molfino, R.	– Italy	Tan, M.	– China
Monje, C.	– Spain	Vajta, L.	– Hungary
Montes, H.	– Panamá	Virk, G. S.	– UK
Moon, S.	– Korea	Vitko, A.	– Slovakia
Muscato, G.	– Italy	Watanabe, K.	– Japan
Nakamura, T.	– Japan	Xie, M.	– Singapore
Park, H.S.	– Korea	Yang, S.	– China
Penders, J.	– UK	Yigit, A.	– Kuwait
Pratihar, D. K.	– India	Zecca, M.	– UK
Preucil, L.	– Czech Republic	Zhao, M.	– China
Qian, J.	– China	Zhong, Z. W.	– Singapore
Rachkov, M.	– Russia	Zielinska, T.	– Poland
Ribeiro, M.	– Portugal		

Local Organising Committee

Of twenty-first International Conference on Climbing and Walking Robots and the Support Technologies for Mobile Machines

Héctor Montes (General Co-Chair)	− FIE, UTP, Panama
Humberto Rodríguez (LOC Chair)	− FIM, UTP, Panama
Carlos Rovetto (L. A. Chair)	− FISC, UTP, Panama
Banfield, Ilka	− FIM, UTP, Panama
Berbey, Aranzazu	− FIE, UTP, Panama
Caballero, Geovanny	− FISC, UTP, Panama
Caballero, Rony	− FIE, UTP, Panama
Cáceres, Danilo	− FIE, UTP, Panama
Chang, Ignacio	− FIE, UTP, Panama
García, Deyka	− FIM, UTP, Panama
Garibaldi, Oscar	− FIM, UTP, Panama
Ho, Ivan	− FISC, UTP, Panama
Moreno, Iveth	− CR Chiriquí, FIE, UTP, Panama
Plazaola, Carlos	− FIM, UTP, Panama
Rodríguez, Samuel	− FISC, UTP, Panama
Saldana, Juan	− CR Chiriqui, FISC, UTP, Panama
Sánchez, Víctor	− SENACYT, Panama
Serracin, Rolando	− CR Chiriqui, FIE, UTP, Panama
Torres, David	− FCyT, UTP, Panama
Tuñón, Andrés	− FISC, UTP, Panama
Vargas, Salvador	− FIE, UTP, Panama

SPONSORS

National Secretariat of Science, Technology and Innovation of Panama (SENACYT)
http://www.senacyt.gob.pa/

Centre for Automation and Robotics (CAR) CSIC-UPM
https://www.car.upm-csic.es/

CONTENTS

Section 1. Plenary Presentations

Section 2. Robotics for Assistance and Rehabilitation

Section 3. Legged Robots and Legged Locomotion

SECTION 1

PLENARY PRESENTATIONS

HUMANOID ROBOT:
A REVIEW OF OUR RESEARCH WORKS

XIE MING

Nanyang Technological University
50 Nanyang Avenue, Singapore 639798

Since 1996, we have embarked into the journey of developing humanoid robots at Nanyang Technological University, Singapore. We have ventured into the various technical aspects of humanoid robot development. In particular, we have placed special emphasis on mechatronics design of humanoid robots, planning and control of biped walking, hand-eye coordination for humanoid robots, cognitive vision for humanoid robots, and cognitive speech for humanoid robots. Since 2006, several teams in Singapore have received a substantial amount of research grants and have developed together two full prototypes of humanoid robots, which are about 1.8 meters in height and weigh about 80 kg each. In addition, each humanoid robot has 42 degrees of freedom with independent actuations. In this plenary talk, I will share some findings and results related to the R&D works of humanoid robot in Singapore.

LOCAL AND GLOBAL ARTIFICIAL POTENTIAL FUNCTIONS IN THE CONTROL OF MOBILE ROBOTS

K. KOZŁOWSKI* and W. KOWALCZYK*

*Faculty of Computing, Poznań University of Technology,
Poznań, 60-965, Poland*
**E-mail: {krzysztof.kozlowski, wojciech.kowalczyk}@put.poznan.pl*
control.put.poznan.pl

The article presents overview of authors' results concerning mobile robot control algorithms that use local artificial potential functions (APF) to avoid collisions and global artificial potential functions, named also navigation functions (NF) used to both collision avoidance and driving robot to a desired goal. All included algorithms assume that the mobile platform is differentially driven mobile robot with nonholonomic constraints. Effectiveness of presented methods is illustrated by simulation and experimental results. Experimental setup used to demonstrate control algorithms is presented.

Keywords: mobile robot; collision avoidance; artificial potential function; navigation function.

1. Introduction

The number of applications in which mobile robots are used to solve some practical problems is rapidly increasing. Collision avoidance is one of the basic problems in this kind of systems. During the task execution robot performs motion to the goal or along the desired trajectory simultaneously avoiding collisions.

In this paper two alternative approaches to collision avoidance are reviewed. The former are APFs originally proposed by[1] in 1986. A large number of methods use this approach. Its main advantages are conceptual simplicity and ease of implementation. On the other hand this methodology has an important limitation. If the obstacles' areas of repulsion overlap local minima may occur.

This problem was solved in the turn of 1980s and 1990s by Rimon and

---

Koditschek,[2],[34] They proposed NF method, called also global potential function that guarantees that local minima will not appear. The proposed method assumed that the robot has no nonholonomic constraints. In 2004 Urakubo proposed an extension to a two-wheeled mobile robot.[5]

This paper presents the overview of the control methods that use APFs and NF to control differentially driven mobile platform. Depending on the method the goal is to track desired trajectory or convergence to the desired fixed position and orientation.

Section 2 presents model of the mobile robot. Section 3 introduces the concept of APF and methods based on it. In Subsection 3.1 the linear control algorithm is described. It uses linearized model of the robot. Subsection 3.2 presents persistent excitation method. Persistent excitation block is responsible for the convergence of the position in the direction transverse to the main axis of the robot. In Subsection 3.3 vector field orientation method is introduced. Section 4 presents two NF control methods. In Subsection 4.1 control algorithm for sphere worlds is described. In Subsection 4.2 its extension to more complex star worlds is presented. Section 5 describes experimental setup used to verify effectiveness of the proposed methods. In the last Section concluding remarks are given.

2. Model of the robot

The kinematic model of the differentially-driven mobile robot is given by the following equation:

$$\dot{q} = \tilde{B}u = \begin{bmatrix} \cos\theta & 0 \\ \sin\theta & 0 \\ 0 & 1 \end{bmatrix} u \tag{1}$$

where x, y, θ are position and orientation coordinates of the robot with respect to a global, fixed coordinate frame; v - linear control velocity, ω - angular control velocity.

3. APF methods

Collision avoidance behavior is based on the artificial potential functions (APF). This concept originally was proposed in.[1] All robots are surrounded by APFs that raise to infinity near objects border r_j ($j = 1, ..., M$, M - number of the obstacles) and decreases to zero at some distance R_j, $R_j > r_j$.

One can introduce the following function:[6]

$$B_{aj}(l_j) = \begin{cases} 0 & for & l_j < r_j \\ e^{\frac{l_j - r_j}{l_j - R_j}} & for \ r_j \le l_j < R_j \\ 0 & for & l_j \ge R_j \end{cases} , \qquad (2)$$

that gives output $B_{aj}(l_j) \in \langle 0, 1 \rangle$. Euclidean distance between the robot and the j-th obstacle is as follows: $l_j = \left\| [x_j \ y_j]^\top - [x \ y]^\top \right\|$. Note that for $l_j < r_j$ an arbitrary value of the function $B_{aj}(l_j)$ can be set assuming that the robot does not get into this area. In the presented algorithms this is guaranteed.

Scaling function (2) within the range $\langle 0, \infty \rangle$ can be obtained as follows:

$$V_{aj}(l_j) = \frac{B_{aj}(l_j)}{1 - B_{aj}(l_j)}, \qquad (3)$$

that is used later to avoid collisions. Note that $V_{aj}(l_j)$ and its spatial derivatives are bounded for $l_j > r_j$.

3.1. *Linear control method*

In this section trajectory tracking controller proposed in[7] is extended by collision avoidance behavior.

The goal of the control is to drive the formation along the desired trajectory avoiding collisions with the static obstacles. The assumption is made that the planner generates desired trajectory that does not intersects APFs of the obstacles. Trajectory tracking is equivalent to bringing the following quantities to zero:

$$\begin{aligned} p_x &= x_d - x \\ p_y &= y_d - y \\ p_\theta &= \theta_d - \theta, \end{aligned} \qquad (4)$$

where x_d and y_d are desired position coordinates and θ_d is desired orientation. The system error expressed with respect to the coordinate frame fixed to the robot is described below:

$$\begin{bmatrix} e_x \\ e_y \\ e_\theta \end{bmatrix} = \begin{bmatrix} \cos(\theta) & \sin(\theta) & 0 \\ -\sin(\theta) & \cos(\theta) & 0 \\ 0 & 0 & 1 \end{bmatrix} \begin{bmatrix} p_x \\ p_y \\ p_\theta \end{bmatrix}. \qquad (5)$$

Using above equations and nonholonomic constraint $\dot{y}\cos(\theta) - \dot{x}\sin(\theta) =$

0 the error dynamics is as follows:

$$\dot{e}_x = e_y\omega - v + v_d\cos e_\theta$$
$$\dot{e}_y = -e_x\omega + v_d\sin e_\theta \quad . \tag{6}$$
$$\dot{e}_\theta = \omega_d - \omega$$

One can introduce the position correction variables that consist of position errors and collision avoidance terms:

$$P_x = p_x - \sum_{j=1}^{M}\frac{\partial V_{aj}}{\partial x}$$
$$P_y = p_y - \sum_{j=1}^{M}\frac{\partial V_{aj}}{\partial y} \quad . \tag{7}$$

V_{aj} depends on x and y according to equation (3). The correction variables can be transformed to the local coordinate frame fixed in the mass center of the robot:

$$\begin{bmatrix} E_x \\ E_y \\ e_\theta \end{bmatrix} = \begin{bmatrix} \cos(\theta) & \sin(\theta) & 0 \\ -\sin(\theta) & \cos(\theta) & 0 \\ 0 & 0 & 1 \end{bmatrix}\begin{bmatrix} P_x \\ P_y \\ p_\theta \end{bmatrix}. \tag{8}$$

Above equation can be transformed to the following form:[8]

$$\begin{bmatrix} \frac{\partial V_{aj}}{\partial e_x} \\ \frac{\partial V_{aj}}{\partial e_y} \end{bmatrix} = \begin{bmatrix} -\cos\theta & -\sin\theta \\ \sin\theta & -\cos\theta \end{bmatrix}\begin{bmatrix} \frac{\partial V_{aj}}{\partial x} \\ \frac{\partial V_{aj}}{\partial y} \end{bmatrix}. \tag{9}$$

Finally, correction variables expressed with respect to the local coordinate frame are as follows:

$$E_x = e_x + \sum_{j=1}^{M}\frac{\partial V_{aj}}{\partial e_x}$$
$$E_y = e_y + \sum_{j=1}^{M}\frac{\partial V_{aj}}{\partial e_y} \quad . \tag{10}$$

For $l_j > R_j$ components of the gradient of the APF vanish: $\frac{\partial V_{aj}}{\partial e_x} = 0$ and $\frac{\partial V_{aj}}{\partial e_y} = 0$. It leads to the conclusion that in this case $E_x = e_x$ and $E_y = e_y$.

The algorithm presented in[7] extended by the collision avoidance functionality is as follows:

$$v = v_d + k_1 E_x$$
$$\omega = \omega_d + k_2\text{sign}(v_r)E_y + k_3 e_\theta \quad . \tag{11}$$

Substituting (11) into (6) one can express error dynamics as follows:

$$\dot{e}_x = e_y\omega - k_1 E_x + v_d(\cos e_\theta - 1)$$
$$\dot{e}_y = -e_x\omega + v_d\sin e_\theta \quad . \tag{12}$$
$$\dot{e}_\theta = -k_2\text{sign}(v_r)E_y - k_3 e_\theta$$

When the robot detects the obstacle its reference trajectory is temporarily frozen, reference signals: v_d and ω_d are set to zero. The tracking process is temporarily suspended because collision avoidance has a higher priority. Once the robot is outside the collision detection region, it updates the reference to the new values.

Error dynamics for $v_d = 0$ and $\omega_d = 0$ becomes:

$$\begin{aligned}
\dot{e}_x &= k_3 e_y e_\theta - k_1 E_x \\
\dot{e}_y &= -k_3 e_\theta e_x \\
\dot{e}_\theta &= -k_3 e_\theta
\end{aligned} \quad . \tag{13}$$

Fig. 1 shows path of the robot in xy-plane. Time graph of position and orientation error is presented in Fig. 2. Notice that despite of the fact that the algorithm is based on the linearization (first Lyapunov method) it ensures quick convergence even if the initial position is far from the equilibrium point.
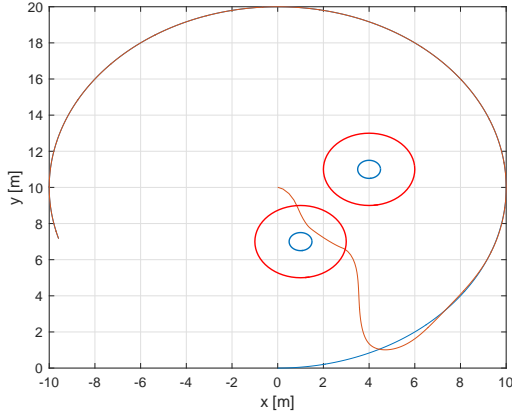
Fig. 1.   Path of the robot in xy-plane (simulation results)

3.2. *Control with persistent excitation*

In this subsection the trajectory tracking control algorithm proposed in[9] is extended by collision avoidance. Equations (4) - (10) introduced in Section 3.1 remain in force in further computations.

Following reference[9] control signals of the robot in the case of collision
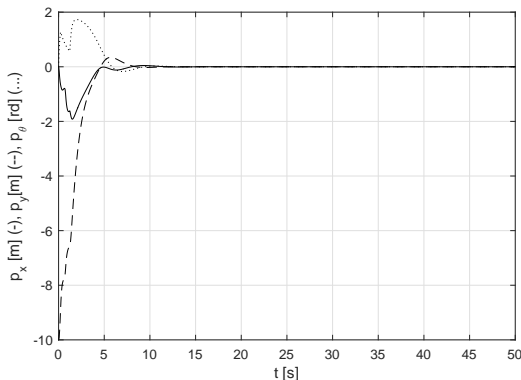
Fig. 2.   Robot position and orientation errors (simulation results)

avoidance are proposed as follows:

$$v = v_d + c_2 E_x$$
$$\omega = \omega_d + h(t, E_y) + c_1 e_\theta \tag{14}$$

where $h(t, E_y)$ is bounded, depends linearly on E_y, and continuously differentiable function. It must be properly chosen to ensure persistent excitation of the reference angular velocity.[10]

Substituting Eq. (14) into Eq. (6) one can express error dynamics as follows:

$$\dot{e}_x = e_y \omega - c_2 E_x + v_d(\cos e_\theta - 1)$$
$$\dot{e}_y = -e_x \omega + v_d \sin e_\theta \qquad . \tag{15}$$
$$\dot{e}_\theta = -h(t, E_y) - c_1 e_\theta$$

When the robot is in the interaction area its reference trajectory is temporarily frozen, reference signals: v_d and ω_d are set to zero.

Error dynamics become:

$$\dot{e}_x = h(t, E_y)e_y + c_1 e_y e_\theta - c_2 E_x$$
$$\dot{e}_y = -h(t, E_y)e_x - c_1 e_\theta e_x \qquad . \tag{16}$$
$$\dot{e}_\theta = -h(t, E_y) - c_1 e_\theta$$

Fig. 3 presents path of the robot in xy-plane. Time graph of position and orientation errors is shown in Fig. 4.

3.3. Vector-Field-Orientation method

This subsection presents VFO trajectory tracking control algorithm[11] extended by the collision avoidance behavior.[12]
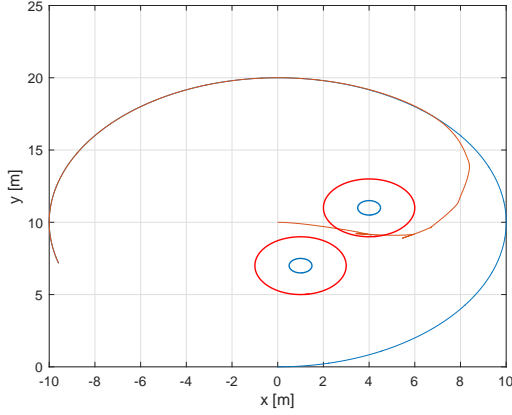
Fig. 3.   Path of the robot in xy-plane (simulation results)
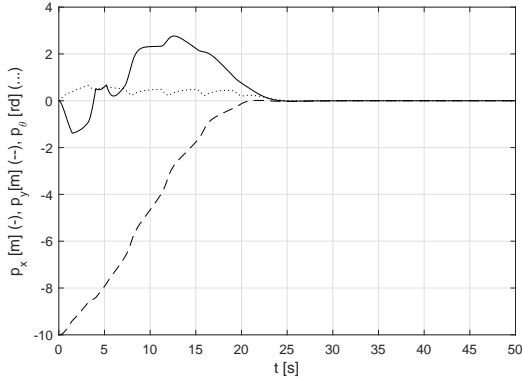
Fig. 4.   Robot position and orientation errors (simulation results)

One can introduce the convergence vector:

$$\mathbf{h} = \begin{bmatrix} h_x \\ h_y \\ h_\theta \end{bmatrix} = \begin{bmatrix} k_p P_x + \dot{x}_d \\ k_p P_y + \dot{y}_d \\ k_\theta e_a + \dot{\theta}_a \end{bmatrix}, \tag{17}$$

where k_p, $k_\theta > 0$ are control gains of position and orientation errors, re-spectively; P_x, P_y are correction variables given by Eq. (4), $e_a = \theta_a - \theta$ is auxiliary orientation error. Auxiliary orientation variable θ_a is defined as follows: $\theta_a = atan2c(h_y, h_x)$ $(atan2c(\cdot, \cdot)$[11] is continuous version of the

function $Atan(\cdot)$). Proposed control law for the robot are the following:

$$u_v = h_x \cos\theta + h_y \sin\theta$$
$$u_\omega = h_\theta \tag{18}$$

The following assumptions are imposed.

Assumption 3.1. *Desired trajectories do not intersect APF areas of obstacles and robots do not interact when tracking is executed perfectly.*

Assumption 3.2. *If robot position is in the repel area then reference trajectory is frozen:*

$$\mathbf{q}_d(t) = \mathbf{q}_d(t^-), \tag{19}$$

where t^- is the time value before robot gets to the repel area. Higher derivatives of $q_d(t)$ are kept zero until robot leaves the repel area.[13]

Assumption 3.3. *When $e_a \in (\frac{\pi}{2} + \pi d - \delta, \frac{\pi}{2} + \pi d + \delta)$, where δ is a small positive value, $d = 0, \pm 1, \pm 2, ...$, then auxiliary orientation variable θ_a is replaced by $\tilde{\theta}_a = \theta_a + sgn\left(e_a - \left(\frac{\pi}{2} + \pi d\right)\right)\varepsilon$, where ε is a small value that fulfills condition $\varepsilon > 0$ and $sgn(\cdot)$ denotes the signum function.*

Assumption 3.4. *When robot reaches a saddle point reference trajectory is disturbed to drive robot out of local equilibrium point. In the saddle point the following condition is fulfilled:*

$$\|\mathbf{h}^*\| = 0, \tag{20}$$

where $\mathbf{h}^* = \begin{bmatrix} h_x & h_y \end{bmatrix}^T$. In this case $\theta_a(t)$ is frozen: $\theta_a(t) = \theta_a(t^-)$.

Fig. 5 presents path of the robot in xy-plane.

4. NF methods

In the turn of 1980s and 1990s Rimon and Koditschek presented concept of the navigation function. At first a sphere world version was introduced[2] that assumes that the obstacles are bounded with spheres in three dimensional space or with circles in planar case. Then the method was expanded to more complex environments,[34] All these algorithms assumed a point-like robot without constraints.

In 2004 Urakubo[5] expanded the method introducing navigation function that takes into account nonholonomic constraints of the mobile robot. In his method the orientation of the robot can reach desired value just as both position coordinates. Convergence proof was included in the paper.
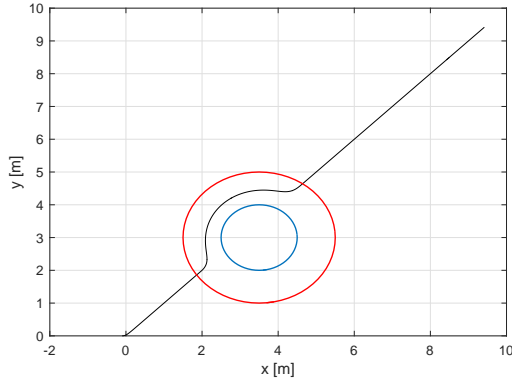
Fig. 5.   Path of the robot in xy-plane (simulation results)

In the papers,[14],[15][16] navigation function was used to control multiple mobile robots. Authors of these publications adress the problem of collision avoidance in multiagent robotic systems. In the first of the mentioned papers extension of the navigation function called multi-robot navigation functions (MRNFs) was applied. Second and third of these papers propose the use of prioritization to solve conflicts in case of concurrent goals of the agents. Examples of navigation function used for collision avoidance in 3D space were presented among others in work[17] and.[16]
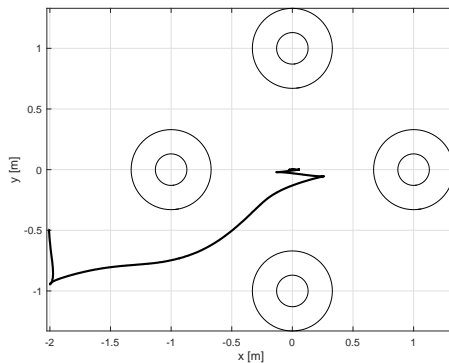
Fig. 6.   Path of the robot in xy-plane (experimental results)
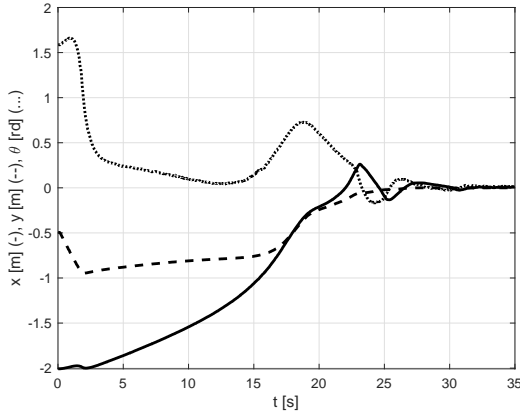
Fig. 7. Time graphs of x, y, θ variables (experimental results)

4.1. *NF for sphere worlds*

The control algorithm requires the robot task space to be bounded by a circle. It is the obstacle number zero described by the following obstacle function:[4]

$$\beta_0 \triangleq \rho_0^2 - ||r - p_0||^2, \tag{21}$$

where ρ_0 is the radius of the task space, $r = [x \ \ y]^\top$ is the current position of the robot and p_0 is the center of the task space. The controller design assumes the obstacles to be circular-shaped objects of radii ρ_i ($i = 1, ..., N$, N being the number of obstacles) with their centers located at positions p_i. The definition of repelling potential function for i-th obstacle is:

$$\beta_i \triangleq ||r - p_i||^2 - \rho_i^2. \tag{22}$$

Given an environment with N obstacles and a task of stabilizing the robot in its origin the total navigation potential is defined as:

$$V \triangleq \frac{C}{(C^\kappa + \beta)^{\frac{1}{\kappa}}}, \tag{23}$$

where κ is a positive, constant design parameter and

$$C \triangleq ||r||^2 + \theta^2 \frac{k_w}{k_w + ||r||^2}. \tag{24}$$

Symbol k_w in (24) denotes a positive, constant design parameter that allows to tune the influence of the orientation term on the navigation function depending on the Euclidean distance to the goal. The aggregation of repelling

potentials happens in term β which is defined as:

$$\beta \triangleq \prod_{i=0}^{N} \beta_i. \tag{25}$$

One must note that the iteration starts from zero, which means the inclusion of task space boundary potential.

The control algorithm proposed in work[18] is defined as:

$$u \triangleq - \left\{ a \begin{bmatrix} 1 & 0 \\ 0 & 1 \end{bmatrix} + b \begin{bmatrix} 0 & 1 \\ -1 & 0 \end{bmatrix} \right\} \tilde{B}^{\top} \nabla V, \tag{26}$$

where a is a positive, constant design parameter and

$$b \triangleq -\bar{b} \frac{L^{\top} \nabla V}{h(g)}. \tag{27}$$

Symbol $\bar{b}$ in (27) denotes another positive, constant design parameter and $L^{\top} \triangleq [\sin\theta \quad -\cos\theta \quad 0]$. Function $h(g)$ is defined as:

$$h(g) \triangleq g^2 + \epsilon\sqrt{g}, \tag{28}$$

where $g \triangleq ||\tilde{B}^{\top}\nabla V||$ and ϵ is a small positive constant. Finally, ∇V denotes the gradient of the navigation function with respect to variables x, y and θ. Regardless of number of obstacles, the gradient can be obtained in analytical form as:

$$\nabla V = \frac{\nabla C (C^\kappa + \beta)^{\frac{1}{\kappa}} - \frac{C}{\kappa}(C^\kappa + \beta)^{(\frac{1}{\kappa}-1)}(\kappa C^{\kappa-1}\nabla C + \nabla\beta)}{(C^\kappa + \beta)^{(\frac{2}{\kappa})}}, \tag{29}$$

where

$$\nabla C = \begin{bmatrix} \frac{\partial C}{\partial x} \\ \frac{\partial C}{\partial y} \\ \frac{\partial C}{\partial \theta} \end{bmatrix} = \begin{bmatrix} 2x(1 - \frac{k_w \theta^2}{(k_w + ||r||^2)^2}) \\ 2y(1 - \frac{k_w \theta^2}{(k_w + ||r||^2)^2}) \\ 2\theta \frac{k_w}{k_w + ||r||^2} \end{bmatrix} \tag{30}$$

and

$$\nabla\beta = \sum_{i=0}^{N} \left\{ \frac{\partial \beta_i}{\partial q} \prod_{j=0, j \neq i}^{N} \beta_j \right\}. \tag{31}$$

As noted in[4] all the undesired local minima of navigation function (23) disappear as the parameter κ increases. An algorithm for automatically tuning analytic navigation functions for sphere worlds was presented in.[19]

The tuning parameter must satisfy a lower bound to ensure convergence to the desired value. In this paper navigation functions have been manually tuned to assure convergence. For the sufficiently high value of the κ parameter navigation function (23) has a critical point associated with each isolated obstacle, the saddle point. V has no other critical point other than these points. Saddle points are unstable equilibrium points. In[18] special control procedure for saddle point avoidance is described. It uses time varying function to push the robot away from the unstable equilibrium point.

4.2. NF for star worlds

NF algorithm for the star world is an extension of the method described in subsection 4.1. In this approach the position of the robot is transformed to auxiliary sphere world:

$$\hat{r} = \left(1 - \sum_{i=1}^{M} s_i(r)\right) r + \sum_{i=1}^{M} s_i(r) T_i(r) \tag{32}$$

where

$$s_i(r) = \frac{||r||^2 \prod_{j=1, j\neq i}^{M} \beta_j(r)}{||r||^2 \prod_{j=1, j\neq i}^{M} \beta_j(r) + \lambda_s \beta_i(r)} \tag{33}$$

and

$$T_i(r) = \frac{\rho_i(1 + \beta_i(r))}{||r - q_i||}(r - q_i) + p_i, \tag{34}$$

$$T_0(r) = \frac{\rho_0(1 - \beta_i(r))}{||r - q_i||}(r - q_i) + p_i. \tag{35}$$

In the above equations p_0 and p_i are centers of the spheres to which original obstacles are transformed, ρ_0 and ρ_i are their radii (they should fall entirely in their original star obstacles), q_0 and q_i are are centers of the stars (points from which all the rays cross the boundary of the obstacle once and only once), β_0 and β_i are star obstacle functions.

Navigation function is given by the following equation:

$$V \triangleq \frac{\hat{C}}{(\hat{C}^\kappa + \hat{\beta})^{\frac{1}{\kappa}}}, \tag{36}$$

where

$$\hat{C} \triangleq ||\hat{r}||^2 + \theta^2 \frac{k_w}{k_w + ||\hat{r}||^2} \tag{37}$$

and

$$\hat{\beta}_0 \triangleq \rho_0^2 - ||\hat{r} - p_0||^2, \qquad (38)$$

$$\hat{\beta}_i \triangleq ||\hat{r} - p_i||^2 - \rho_i^2. \qquad (39)$$

The form of the control law does not change in comparison to the sphere world algorithm (26).

Fig. 8 presents intersection of the potential field for $\theta = 0$. In Fig. 9 path of the robot is shown. Fig. 10 presents time graphs of the robot coordinates.
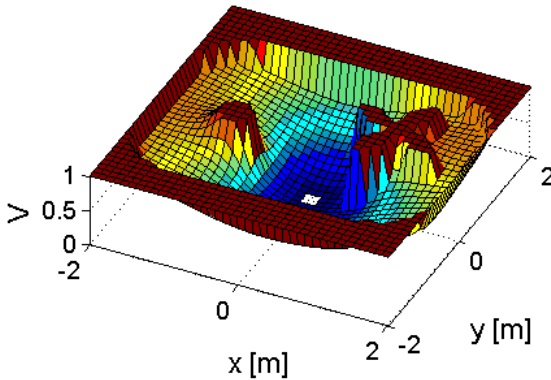
Fig. 8. Intersection of the potential field for $\theta = 0$ (notice that NF is a function of three variables: x, y and θ; it can not be shown on a flat drawing)

5. Experimental setup

The mobile platform that was used in the presented experiments is the differentially driven MTracker robot. It wast designed at Poznan University of Technology, Institute of Automation and Robotics. It is controlled by a two-level hardware controller: the low-level motion controller uses the signal processor TMS320F28335 150MHz and the high-level one is a single-core Intel Atom 1.2GHz board, equipped with WiFi radio used for remote management, task setting and communication with the external localization system. Depending on the requirements the high-level controller works under the Linux Ubuntu or Windows XP operating systems. The MTracker robot is a small platform: its diameter is $0.14m$, its height is $0.13m$, its
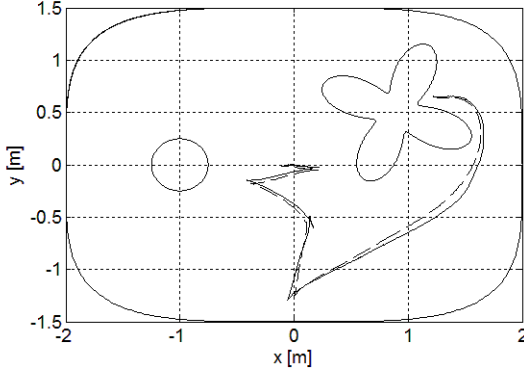
Fig. 9. Path of the robot in xy-plane (solid line - experimental data, dashed line - numerical simulation) (experimental results)
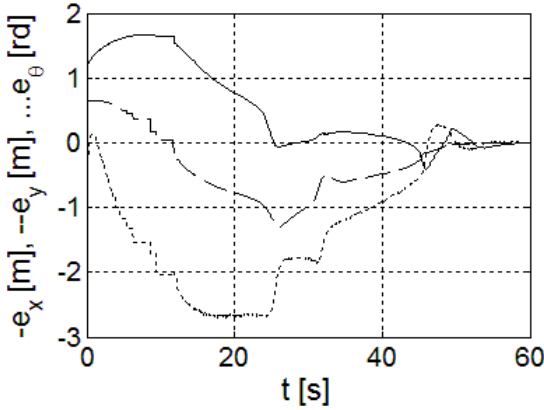
Fig. 10. Time graphs of error variables (experimental results)

weight is $1.4kg$ and its wheels have a diameter of $0.05m$. The on-board power supply is LiIo $3.7Ah$ battery that allows two hour active operation.

During the test the robot is localized by the OptiTrack motion capture system. On the top of the robot four infra-red reflecting markers were mounted.

Wheel velocity control signals were scaled down when their value(s) exceeded the limit. This limit was set to $12rd/s$, while the physical limitation of actuators is $24rd/s$. The lower value of the limit prevented robot wheels from longitudinal slip. The obstacles were known *a priori* to prevent the
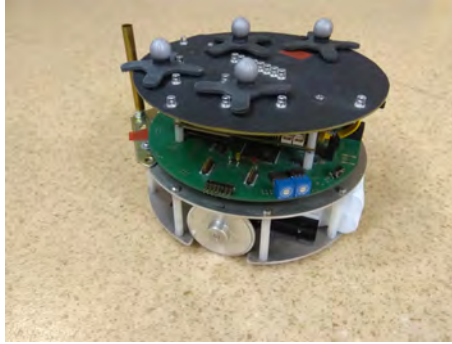
Fig. 11.   MTracker robot (Poznan University of Technology)

influence of measurement inaccuracies on the experimental results.

A special scaling procedure is applied to the wheel controls. The desired wheel velocities are scaled down when at least one of the wheels exceeds the assumed limitation. The scaled control signal $\vec{u}_s$ is calculated as follows:

$$\vec{u}_s = s\vec{u}, \tag{40}$$

where

$$s = \begin{cases} \frac{\omega_{max}}{\omega_o} & \text{if} \quad \omega_o > \omega_{max} \\ 1 & \text{otherwise} \end{cases}, \tag{41}$$

and

$$\omega_o = \max\{|\omega_r|, |\omega_l|\}, \tag{42}$$

where ω_r, ω_l denote right and left wheel angular velocity, ω_{max} is the predefined maximal allowed angular velocity for each wheel. This scaling procedure preserves the direction of motion of the mobile platform.

6. Conclusion

In this article the overview of the control methods that use APFs and NFs is presented. Effectiveness of presented methods was illustrated by simulation results and experiments conducted using MTracker differentially-driven mobile robot. Description of the experimental setup was included.

References

1. O. Khatib, *The International Journal of Robotics Research* **5**, 90 (1986).

2. E. Rimon and D. Koditschek, Exact robot navigation using cost functions: the case of distinct spherical boundaries, in *IEEE International Conference on Robotics and Automation*, 1988.

3. E. Rimon and D. Koditschek, *Transaction of the American Mathematical Society* **327**, 71 (1991).

4. E. Rimon and D. Koditschek, *IEEE Transactions on Robotics and Automation* **8**, 501 (1992).

5. T. Urakubo, K. Okuma and Y. Tada, Feedback control of a two wheeled mobile robot with obstacle avoidance using potential functions, in *IEEE/RSJ International Conference on Intelligent Robots and Systems (IROS)*, 2004.

6. W. Kowalczyk, M. Michałek and K. Kozłowski, *Bulletin of the Polish Academy of Sciences Technical Sciences* **60**, 537 (2012).

7. C. C. de Wit, H. Khennouf, C. Samson and O. J. Sordalen, *Nonlinear Control Design for Mobile Robots* 1994.

8. W. Kowalczyk and K. Kozłowski, Leader-follower control and collision avoidance for the formation of differentially-driven mobile robots, in *23nd International Conference on Methods and Models in Automation and Robotics (MMAR)*, August 2018. accepted for publication in conference proceedings.

9. A. Loria, J. Dasdemir and N. A. Jarquin, *IEEE Transactions on Control Systems Technology* **24**, 727 (2016).

10. A. Loria, E. Panteley and A. Teel, *IEEE Trans. Autom. Control* **46**, 1363 (2001).

11. M. Michałek and K. Kozłowski, *IEEE Transactions on Control Systems Technology* **18**, 45 (2010).

12. W. Kowalczyk, K. Kozłowski and J. Tar, Trajectory tracking for multiple unicycles in the environment with obstacles, in *International Conference on Robotics in Alpe-Adria-Danube Region (RAAD)*, 2010.

13. S. Mastellone, D. Stipanovic, C. Graunke, K. Intlekofer and M. Spong, *The International Journal of Robotics Research* **27**, 107 (2008).

14. D. Dimarogonasa, S. Loizoua, K. Kyriakopoulos and M. Zavlanosb, *Automatica* **42**, 229 (2005).

15. G. Roussos and K. Kyriakopoulos, *Distributed Autonomous Robotic Systems - Springer Tracts in Advanced Robotics* **83**, 189 (2013).

16. G. Roussos and K. Kyriakopoulos, Completely decentralised navigation of multiple unicycle agents with prioritisation and fault tolerance, in *IEEE Conference on Decision and Control (CDC)*, 2010.

17. G. Roussos and K. Kyriakopoulos, *IEEE Transactions on Control Systems Technology* **20**, 1622 (2012).

18. T. Urakubo, *Nonlinear Dynamics* **81**, 1475 (2015).

19. I. Filippidis and K. Kyriakopoulos, Adjustable navigation functions for unknown sphere worlds, in *IEEE Conference on Decision and Control and European Control Conference (CDC-ECC)*, 2011.

CONTROL ARCHITECTURES FOR ROBUST MULTI-ROBOT AUTONOMOUS SYSTEMS

PHILIPPE BIDAUD

French Aerospace Research Center,
Chemin de la Hunière – Palaiseau – France

The control of complex dynamic systems, both in their behaviour and in their mission, goes through the implementation of multi-loop control architectures based on information about the system internal state and from the environment, as well as on the mission plan state. This results in systems that are becoming increasingly autonomous, for which requirements in terms of safety and reliability, as well as expected performance, are increasingly high. Research works developed at ONERA in the field of control for autonomous systems cover all levels of the control architectures, which are basically structured with respect to temporal aspects, as well as the level of abstraction that they entail for the system dynamic.

We will consider them in presentation by increasing level. We will discuss the advances achieved recently in the robust control techniques of uncertain dynamic systems generally implemented at the lower control level and we will discuss their extensions to consider input and output constraints, as well as the hybrid nature of most of the systems considered. To design "task" level control primitives that take place just above the previous control loops, we will introduce sensor-based robust and non-linear control techniques. These are based on information on the environment extracted from exteroceptive sensors, to estimate their state and to adapt system behaviour to uncertainties and perturbations. Multi-sensor and/or multi-objective controls will be discussed in this particular context.

We will also present several recent results in the field of trajectory tracking based on visual navigation techniques in complex environments, which combine objectives and constraints within the same control architecture. We will discuss how model predictive control (MPC) techniques and advanced optimization techniques can be used for solving the resulting control problems. In addition, we will discuss several ongoing developments of these methods by exploiting distributed model predictive control techniques (DMPC) and predictive control of hybrid systems. Finally, integration with the control architectures at the upper

level of reactive, predictive and distributed planning capabilities will be proposed to accommodate time constraints and uncertainties in decision.

SECTION 2

ROBOTICS FOR ASSISTANCE AND REHABILITATION

SYSTEM IDENTIFICATION AND HSDBC-OPTIMIZED PID CONTROL OF A PORTABLE LOWER-LIMB REHABILITATION DEVICE

SULAIMAN O. FADLALLAH[1], KHALED M. GOHER[2]

Auckland University of Technology, NZ, e-mail: sulaiman.fadlallah@aut.ac.nz
University of Lincoln, UK, e-mail: kgoher@lincoln.ac.uk

The present paper introduces a novel portable leg rehabilitation system (PLRS) that is developed to provide the user with the necessary rehabilitation exercises for both the knee and ankle in addition to the portability feature to overcome the hardships associated with both effort and cost of hospitals and rehabilitation clinics' steady sessions. Prior realizing the actual prototype, the proposed configuration was visualized using SolidWorks including its main components. Aiming to control the developed system, and given the fact that tuning controller parameters is not an easy task, Hybrid Spiral-Dynamics Bacteria-Chemotaxis (HSDBC) algorithm has been applied on the proposed control strategy in order to obtain a satisfactory performance. The obtained system performance was satisfactory in terms of desired elevation and settling time.

1. Introduction

Assistive robotic technology for rehabilitation has been and still remains a major field of interest for tremendous amount of research studies over the past years. Rehabilitation devices can be divided into five different categories: stationary gait trainers, treadmill gait trainers, ankle rehabilitation devices, over-ground gait trainers, and foot-plate-based gait trainers [1]. Focusing on lower-limb rehabilitation systems, considerable amount of studies have been conducted in this area. Starting with Hwang and Jeon [2], their research focused on developing a wheelchair integrated lower limb exercise/rehabilitation system. The system consists of a wheelchair, a body lifter, and a lower-limb exoskeleton. The research studies carried out by Banala et al. [3], Agrawal et al. [4] and Banala et al. [5] aimed gradually to design a gravity-balancing exoskeleton with the name ALEX. As for Monaco et al. [6], their study presented a stationary gait trainer (NEUROBike) for bedridden patients that provides them with neuro-rehabilitative treatments. On the other hand, and by utilizing MATLAB®/Simulink software, Zhang and Li [7] proposed a lower-limb rehabilitation mechanism with 4-degrees of freedom. Given the fact that these lower-limb rehabilitation devices must consider the user's physical and health conditions, they require a proper control in order to provide smooth and comfortable operation of the leg movement. Focusing on controlling the cyclical leg movements of paraplegic subjects, Spek et al. [8] developed a control scheme that combines both neural network and fuzzy logic. As for Aguirre-Ollinger et al. [9], their study focused on developing an inertia compensation-based control scheme for a one degree of freedom exoskeleton that assists patients with lower-limb disabilities. Tuning controllers is a difficult problem that remains a field of interest in multiple disciplines. This interest drove

researcher worldwide to provide solutions and techniques for optimizing controller parameters. In nowadays research aspects, bio-inspired and nature-inspired optimization algorithms are significantly gaining attention. Some of these algorithms include genetic algorithm (GA) [10], bacterial foraging optimization algorithm (BFO) [11], spiral dynamics algorithm (SDA) [12], and Hybrid Spiral-Dynamics Bacteria-Chemotaxis (HSDBC) algorithm [13] that represents a fusion between the latter two algorithms. Although the field of lower-limb rehabilitation devices has been provided a lot of interest, up to the authors' knowledge no research addressed the portability feature in developing an affordable portable lower-limb rehabilitation device that gives the user the flexibility needed in performing rehabilitation exercises. In this paper, the authors aim at developing a novel portable leg rehabilitation system (PLRS) that provides the user with the necessary extension/flexion exercises for both the knee and ankle in addition to the portability feature to overcome the hardships associated with both effort and cost of hospitals and rehabilitation clinics' steady sessions. The presented work in this paper is arranged as follows: Section I presents an overview of contributions in the field of lower-limb rehabilitation systems along with their control methods and the potential of optimization algorithms. In Section II, the proposed portable leg rehabilitation system (PLRS) is presented, starting with its concept schematics, moving to the SolidWorks design, and ending with the actual prototype. Section III focuses on the process of estimating the prototype's transfer functions by utilizing System Identification (SI). The design of the control approach including the implementation of HSDBC optimization algorithm is covered in Section IV. Finally, and by highlighting the research findings, the paper is concluded in Section V.

2. Portable Leg Rehabilitation System Description and Design Details

2.1. System Description

Fig. 1 illustrates the developed portable leg rehabilitation system (PLRS) schematics diagram. The proposed two degrees of freedom system consists of two movable links (r_1 and r_2) connected with two revolute joints.
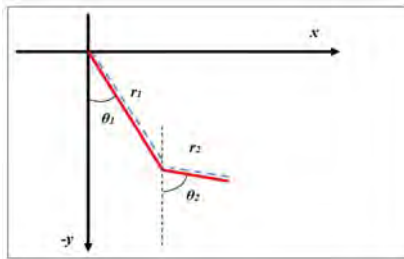
Figure 1.   Schematics diagram of the proposed PLRS

By applying a lifting torque at each joint, the system has the capability to carry out three different rehabilitation exercises by lifting the targeted link to a desired position (θ) (i.e. calf exercise (θ_1), foot exercise (θ_2), both calf and foot exercises (θ_1 and θ_2)).

2.2. Design Details

Taking into account the targeted portability feature, and based on the schematics illustrated in Fig. 1, a SolidWorks conceptual design of the PLRS is demonstrated in Fig. 2. The proposed design main components are calf and foot carriers, thigh covers, and thigh and seat bases. The grooves in both seat and thigh bases simplifies the device adjustments based on the user's requirement. Fig. 3 represents the realized design of the portable device. The system's chassis was manufactured from aluminum to provide a lightweight structure. Two motors are mounted at each joint in order to provide the necessary lifting torque on the calf and foot carriers. These motors are controlled using the circuit shown in Fig.4. The potentiometer's produced analog signal is responsible for controlling the motor's speed and orientation. Given that the speed control's analog voltage range is within 0-5 volts DC, three voltage values are considered, 3.1V (lifting), 2.5 V (zero speed), and 1.9V (descending).
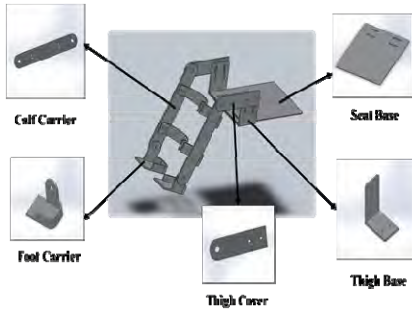
Figure 2.   PLRS SolidWorks design
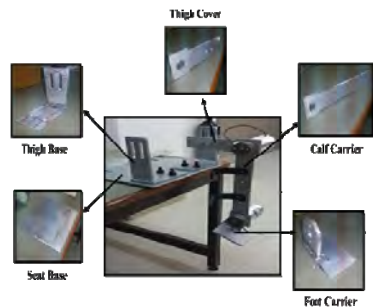
Figure 3.   The developed PLRS.
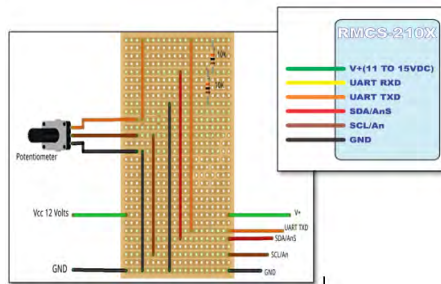
Figure 4.   PLRS motor control circuit

3.   System Identification (SI)

3.1. *Overview of SI*

By utilizing measurements of the device's input and output signals, SI is considered a powerful approach for deriving mathematical representations of dynamic systems. A graphical user interface (GUI) developed by Matlab (Fig. 5) allows the user to simply estimate the system's model by inserting the measured data and adjusting certain parameters until the estimated result becomes closer to the measured output signal. In this part of the study, the PLRS's transfer functions estimation will be carried out based on measured input and output signals extracted from the built experimental setup (Fig. 3).

3.2. *Estimation of Calf and Foot Transfer Functions*

The prototype's system identification process is divided into three major parts: analog input measurements, analog output measurements, and transfer function estimation. For this system, the variation in voltage from the potentiometer is considered as an analog input. The system's outputs are both calf and foot orientations. These orientations are measured using a position sensor and its output is processed using Humosoft MF624 data acquisition card connected to Matlab/Simulink environment.
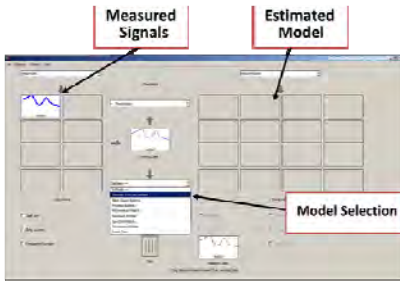
Figure 5.   Matlab's SI toolbox GUI   Figure 6.   PLRS rehabilitation exercises
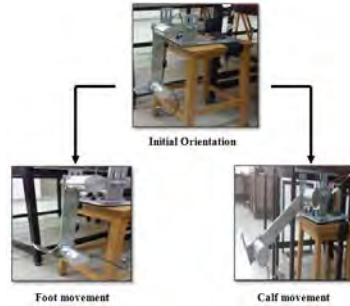
Two rehabilitation exercises are considered and are shown in Fig. 6: calf exercise only (θ_1) and foot exercise only (θ_2). The system considered to orient the calf by 90 degrees ($\theta_1 = 90º$) and the foot by 30 degrees ($\theta_2 = 30º$). Referring to Fig. 7, which represents the calf and foot orientation's measured output, the rehabilitation process is split into three major stages: (1) extension, (2) stability, and (3) flexion. For the calf movement, the actual prototype's maximum measured position was approximately 86 degrees ($\theta_1 = 86º$) and it takes around 12 seconds to reach this position. As for the foot, the maximum measured angular orientation was approximately 32 degrees ($\theta_1 = 32º$) and the system takes approximately 5 seconds to reach this desired position. These measured

outputs and the potentiometer's input are considered as inputs to the Matlab's SI toolbox. In order to estimate the system's appropriate transfer functions, the desired number of poles and zeros are also fed into the toolbox. Two combinations of poles and zeros are considered in order to acquire the best fit from the measured date. A comparison between the measured outputs and the two estimated models for both calf and foot is illustrated in Fig. 8.
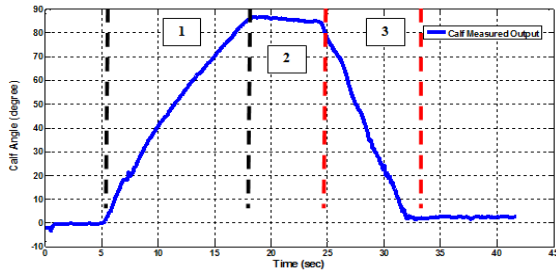
(a) Calf exercise
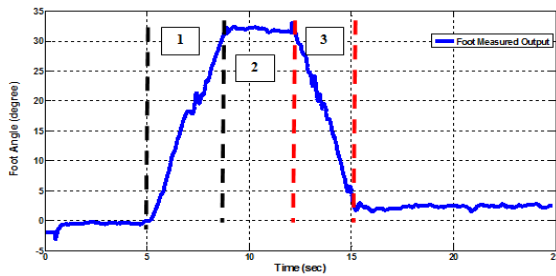
(b) Foot exercise.

Figure 7.   Measured outputs of calf and foot's orientation.

(a) Calf exercise

(b) Foot exercise
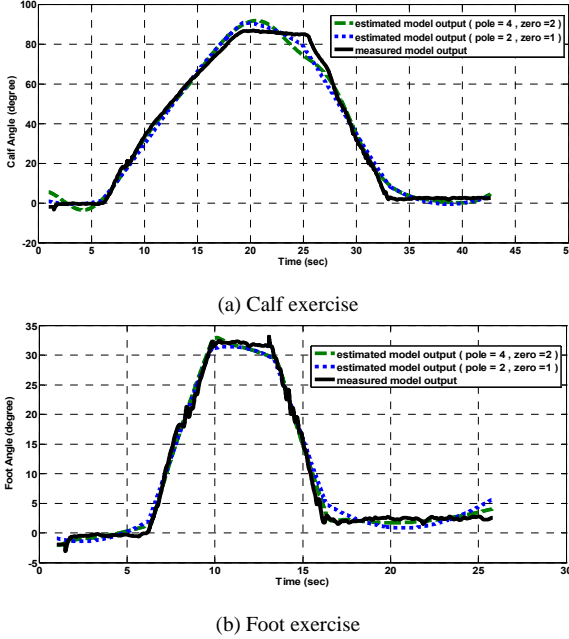
Figure 8.   Measured and estimated model output for calf and foot

Starting with the calf, the combination of two poles and one zero provides better fitting (90.28%) compared to the estimation with the combination of four poles and two zeros (89.89%). As for the foot, on the other hand, the four poles-two zeros model gives better fitting (92.75%) in comparison with the combination of two poles and one zero (88.87%). Based on that, the estimated transfer functions for the calf and foot are represented as the following:

$$\text{Calf Transfer Function} = \frac{1.449s + 0.6824}{s^2 + 0.1549 + 0.02833} \tag{1}$$

$$\text{Foot Transfer Function} = \frac{65.63s^2 + 174s + 0.9918}{s^4 + 5.659s^3 + 13.38s^2 + 0.6049s + 0.2041} \tag{2}$$

4.   Control System Design

For the purpose of obtaining a satisfactory response for the system's transfer functions, this section focuses on proposing a proper control approach by implementing Hybrid Spiral-Dynamics Bacteria-Chemotaxis (HSDBC) algorithm, which is a recently developed optimization algorithm that combines both bacterial foraging and spiral dynamics algorithms. The HSDBC optimization algorithm's main parameters and flowchart are shown in Table 1

and Fig 9. Additional information can be found in [13]. Fig. 10 demonstrates the designed HSDBC-optimized PID control approach for controlling the calf and foot's angular orientation. The optimization process was constrained within specific boundary limits and the performance index has been selected based on the minimum mean squared error (MSE). For each control loop shown in Fig. 10, the MSE can be calculated using the following equations:

$$\text{Objective Function 1} = \min[\frac{1}{N}\sum_{i=1}^{N}(\theta_{1d} - \theta_{1m})^2] \qquad (3)$$

$$\text{Objective Function 2} = \min[\frac{1}{N}\sum_{i=1}^{N}(\theta_{2d} - \theta_{2m})^2] \qquad (4)$$

Based on the total MSE, the PLRS's total objective function can be calculated using the following mathematical representation:

$$J = \sum_{i=1}^{J}(\text{Objective Function i}) \qquad (5)$$

Table 1. Parameters Associated with HSDBC Optimization Algorithm [13]

Parameter	Description
$\theta_{i,j}$	Bacteria angular displacement on x_i - x_j plane around the origin
R	Spiral radius
m	Number of search points
k_{max}	Maximum iteration number
N_s	Maximum number of swim
$x_i(k)$	Bacteria position
R^n	n x n matrix
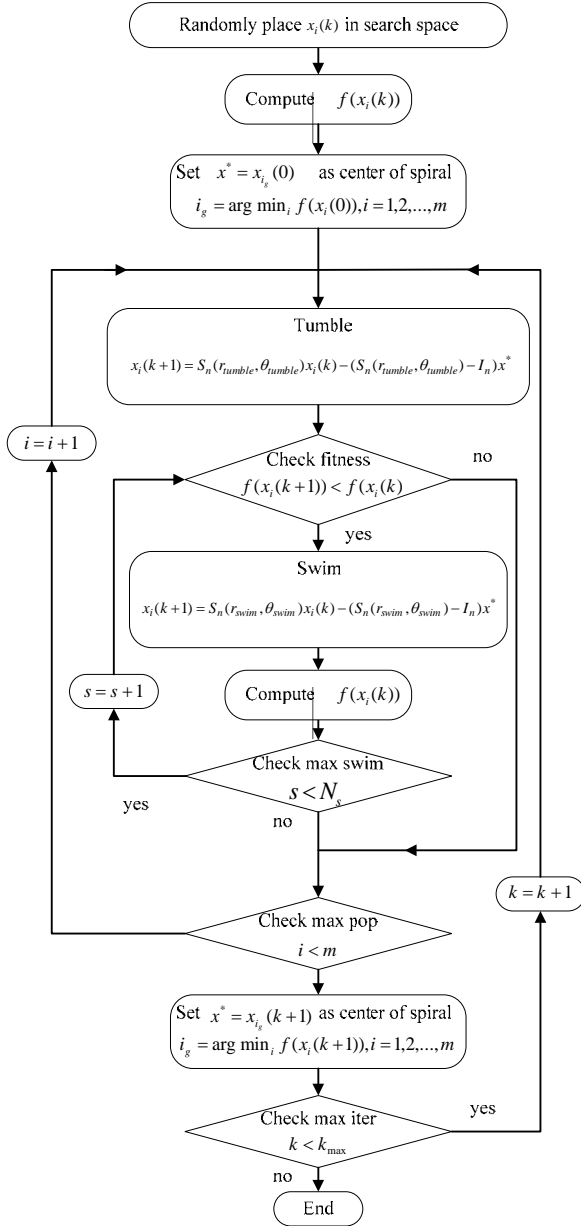
Figure 9.   HSDBC algorithm flowchart
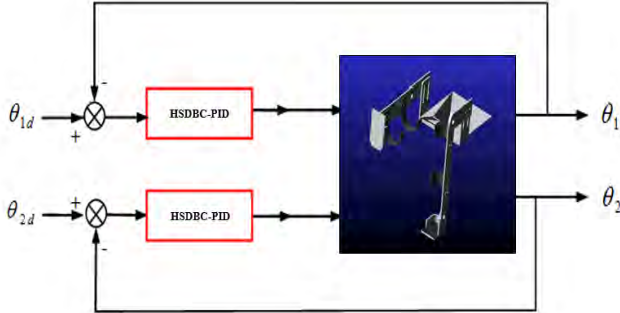
Figure 10. PLRS control scheme.

4.1. Simulation Results

Table 2 lists the calculated optimized controller gain parameters. Fig. 11 illustrates the system response and Table 3 summarizes the performance of the system for both calf and foot using the proposed control scheme. As can be seen, the system reach the desired orientation for both calf and foot. Starting with the results associated with the calf, and with no observable overshoot, the system managed to reach the desired elevation (θ_l = 89.9094º) and it takes around 12 seconds to settle. Moving to the foot's simulation results, the system settles at an angle of 30.017 degrees, which is approximately 0.056% greater than the foot's required orientation. The system's response, with an overshoot of approximately 0.53%, takes approximately 6 seconds to stabilize.

Table 2. HSDBC-PID Controller Gain Parameters

	Gain Parameter	HSDBC-PID
Calf (θ_1)	Kp_1	0.401
	Ki_1	0.010
	Kd_1	1.398
Foot (θ_2)	Kp_2	3.012
	Ki_2	0.010
	Kd_2	5.103
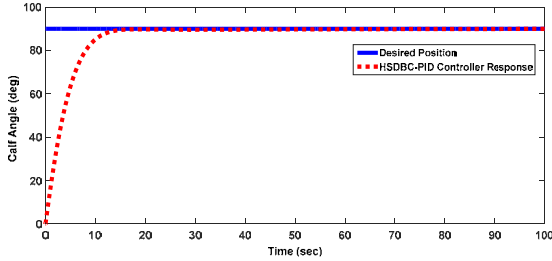
(a) Calf system response.
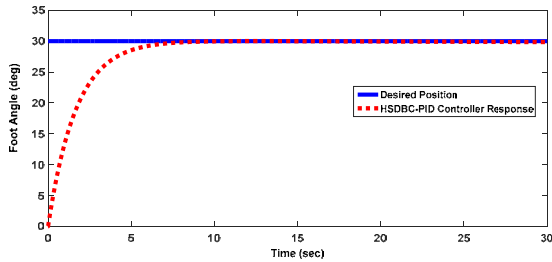
(b) Foot system response

Figure 11. Calf and foot system response using HSDBC-PID controller.

Table 3. System Performance Characteristics

Variable	Parameters	Values	Variable	Parameters	Values
θ_1	Rise Time	7.8159	θ_2	Rise Time	3.5904
	Settling Time	12.3080		Settling Time	6.0497
	Settling, Min	80.9262		Settling, Min	26.8766
	Settling, Max	89.9094		Settling, Max	30.0177
	Overshoot	0		Overshoot	0.5393558
	Undershoot	0		Undershoot	0
	Peak	89.9094		Peak	30.0177
	Peak Time	100.000		Peak Time	12.5039

5. Conclusion

Aiming to provide an affordable portable lower-limb rehabilitation device that gives the user the flexibility needed in performing rehabilitation exercises, this paper presents a novel portable leg rehabilitation system (PLRS) that provides the user with the necessary extension/flexion exercises for both the knee and ankle. The portability feature provided by the device will overcome the hardships associated with both effort and cost of hospitals and rehabilitation clinics' steady sessions. Before actualizing the PLRS, the proposed system has

been described and designed using SolidWorks. The experimental setup has been built for the purpose of estimating its transfer functions using system identification toolbox. For controlling the developed system's transfer functions, HSDBC optimization technique has been implemented on a proposed PID control scheme. Using the proposed control approach, the obtained system performance was satisfactory except for the very small overshoot that the system experienced for the foot movement. Future considerations of this work will include design improvements and developing a mathematical model based on the PLRS's schematics and compare its results with the actual prototype's estimated transfer functions. Future work will consider also implementing other optimization techniques (i.e. bacterial forging (BF), genetic algorithm (GA), spiral dynamics (SD)) and compare between them in order to improve the performance of the system.

References

1. I. Díaz, J. J. Gil, and E. Sánchez, "Lower-Limb robotic rehabilitation: Literature review and challenges," *Journal of Robotics*, pp. 1–11, 2011.
2. B. Hwang and D. Jeon, "A wheelchair integrated lower limb exercise/rehabilitation system: Design and experimental results on the knee joint," *Proceedings of the 2012 IEEE/SICE International Symposium on System Integration* (SII), Kyushu University, Fukuoka, Japan, 2012, pp. 164–169.
3. S. K. Banala, S. K. Agrawal, A. Fattah, V. Krishnamoorthy, W.-L. Hsu, J. Scholz, and K. Rudolph, "Gravity-Balancing leg orthosis and its performance evaluation," *IEEE Transactions on Robotics*, vol. 22, no. 6, pp. 1228–1239, 2006.
4. S. K. Agrawal, S. K. Banala, A. Fattah, V. Sangwan, V. Krishnamoorthy, J. P. Scholz, and W.-L. Hsu, "Assessment of motion of a swing leg and gait rehabilitation with a gravity balancing exoskeleton," *IEEE transactions on neural systems and rehabilitation engineering*, vol. 15, no. 3, pp. 410–20, 2007.
5. S. K. Banala, S. H. Kim, S. K. Agrawal, and J. P. Scholz, "Robot assisted gait training with active leg exoskeleton (ALEX)," *IEEE Transactions on Neural Systems and Rehabilitation Engineering*, vol. 17, no. 1, pp. 2–8, 2009.
6. V. Monaco, G. Galardi, M. Coscia, D. Martelli, and S. Micera, "Design and evaluation of NEUROBike: A neurorehabilitative platform for bedridden post-stroke patients," *IEEE transactions on neural systems and rehabilitation engineering*, vol. 20, no. 6, pp. 845–52, 2012.
7. M. Zhang and X. Li, "A design of the mechanism for lower limbs passive rehabilitation and kinematics analysis," *2010 Fifth International*

Conference on Frontier of Computer Science and Technology, 2010, pp. 603–607.

8. J. H. Van Der Spek, W. J. R. Velthuis, P. H. Veltink, and T. J. A. De Vries, "Neuro fuzzy control of the FES assisted freely," *Proceedings of the 18th Annual International Conference of the IEEE Engineering in Medicine and Biology Society*, 1996, pp. 2234–2235.

9. G. Aguirre-Ollinger, J. E. Colgate, M. Peshkin, and A. Goswami, "Inertia compensation control of a one-degree-of-freedom exoskeleton for lower-limb assistance: Initial experiments," *IEEE Transactions on Neural Systems and Rehabilitation Engineering*, vol. 20, no. 1, pp. 68–77, 2012.

10. D. E. Goldberg, *Genetic algorithms in search, optimization, and machine learning*. Addison-Wesley, Reading, MA, 1989.

11. K. M. Passino, "Biomimicry of bacterial foraging for distributed optimization and control," *Proceedings of the IEEE Control System Magazine*, pp. 52–67, 2002.

12. K. Tamura and K. Yasuda, "Primary study of spiral dynamics inspired optimization," *IEEJ Transactions on Electrical and Electronic Engineering*, vol. 6, pp. 98–100, 2011.

13. A. N. K. Nasir, M. O. Tokhi, N. M. Abd Ghani, and M. A. Ahmad, "A novel hybrid spiral dynamics bacterial-foraging algorithm for global optimization with application to control design," *Proceeding of the 12th Annual Workshop on Computational Intelligence (UKCI2012)*, Edinburgh, UK, 2012, pp. 1–7.

DESIGN OF A SYSTEM TO SUPPORT THE MOBILITY OF VISUALLY IMPAIRED PEOPLE[*]

HECTOR MONTES[1, 2], IGNACIO CHANG[1], GUELDA CARBALLEDA[3], JOSE MUÑOZ[1], ANTONY GARCIA[1], RAFAEL VEJARANO[3], YESSICA SAEZ[1]

[1]Faculty of Electrical Engineering, Universidad Tecnológica de Panamá, Panama;
[2]Field and Service Robotics Group, Centre for Automation and Robotics (CSIC-UPM);
[3]Faculty of Systems Engineering and Computer Science, Universidad Tecnológica de Panamá, Panama, hector.montes1@utp.ac.pa

The autonomous mobility for visually impaired people has been an issue in where several researchers have contributed with proposals in order to solve it. However, there is a lot of work to carry out in the cities in where this kind of technology has been applied, but also in other cities or town where this or other technology not has arrived yet. In this work two different ICT-based systems have been described, which provide helps in the mobility of visually impaired people in the public transport in Panama. One of them consists of the development of new applications for Android-based smartphones, and the second system is based on the development of RF modules into the ISM radio band. These prototypes are used by the visually impaired people and by the bus driver, and one of them is installed at the bus stop.

Keywords: Visually impaired people; autonomous mobility; RF modules; Android-based applications; public transportation system.

1. Introduction

Visual impairment can limit people's ability to perform everyday tasks and can affect their quality of life and ability to interact with the surrounding world [1]. In addition, blindness, the most severe form of visual impairment, can reduce people's ability to perform daily tasks, and move about unaided. Good quality rehabilitation allows people with different degrees of visual impairment to fully profit from life, achieve their goals and be active and productive in today's society [1]. However, in a parallel effort, it is possible to use the technology to support the mobility of these people at indoor and outdoor locations.

H. Montes et al. (eds.), *CLAWAR 2018: 21st International Conference on Climbing and Walking Robots and the Support Technologies for Mobile Machines*,
Robotics Transforming the Future
© ELSEVIER

The World Health Organization (WHO) in the Fact Sheet Updated October 2017 establishes that they count with a global action plan 2014-2019, approved by the World Health Assembly in 2013, with the aim of achieving a measurable reduction of 25% of avoidable visual impairments by 2019 [2]. However, this declaration asserts there is a problem and must be attended.

In [2] is estimated the following: (*i*) 253 million people live with vision impairment: 36 million are blind and 217 million have moderate to severe vision impairment, (*ii*) over 80% of all vision impairment can be prevented or cured. However, most people visually impaired live in low-income settings.

In order to support or help in the mobility of people with visual disability (in several environments), some research groups have carried out different proposals based on technology, e.g., the typical canes with an ultrasound system, laser, or any other similar technology, which informs the user if an obstacle has been detected by means of different types of signs. However, these systems have had few followers, since they frequently required training for the visually impaired people (ViIP) and, besides, they forced to keep more attention on the signals of the device than on the user's own perception of the route they were taking [3].

As mentioned above, there are several works and lines of research based on ICT that are being developed in various universities and research centers, to provide aids in the mobility and orientation of the ViIP. Some works of interest can be reviewed in [4-10]. These works include mobility in public passenger transport, the use of the smartphones, other electronic mobile devices. All of them are currently under development.

In this article, a new design of a dual system to support the mobility of visually impaired people in public transport system in Panama is described. The dual system consists of a low-cost RF system and new applications for smartphone Android-based. In both systems, the main goal is to provide aids based on ICT for that the visually impaired people, in an autonomous way, are able to use the public transport system in Panamá [11-13].

The rest of the article is organised as follow: in Section 2 is described the design of both systems, the apps, and the RF sub-system. Afterward, Section 3 presents some technical evaluations of the system. Finally, conclusions and future works are given in Section 4.

2. Design description of the system

This work has been carried out within the framework of the MOVIDIS project (http://movidis.utp.ac.pa/) [11], funded by the SENACYT of Panama (http://www.senacyt.gob.pa/). This project consists of the design and

development of two different prototypes with the aim to provide assistance for the autonomous mobility of ViIP in public transportation system in Panama. One of the prototypes is related to the design of new apps for Android-based smartphones for ViIP, her/his supervisor (if available), and bus driver. The other prototype consists of a set of RF subsystems that interact among them and localized with the ViIP, the bus, and the bus stop.

2.1. *Design of the Apps*

Three apps with their different modified versions have been designed and developed for the visually impaired people (ViDis app), the bus driver (ViBus app) and the ViIP supervisor (Tutor app). In Figure 1 is presented the functioning scheme of the designed apps with the server, which has a specific database for this project. PHP (Hypertext Pre-processor) is a powerful and widely-used open source server-side scripting language to write dynamically generated web pages.
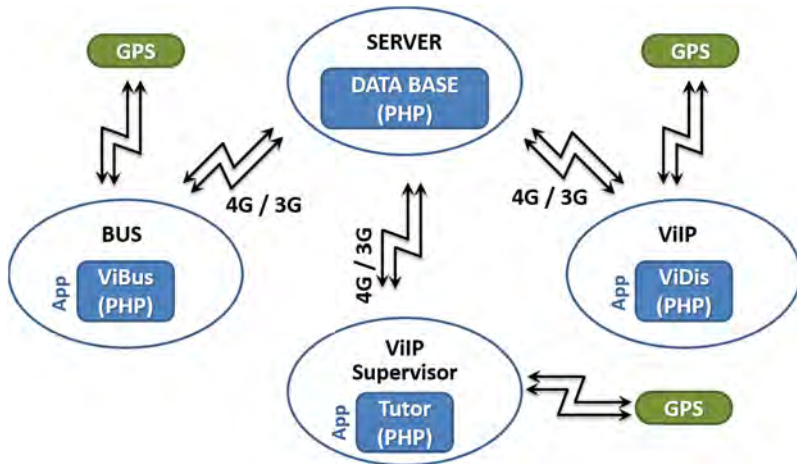
Figure 1. Functioning scheme of the apps.

In this article, the functioning of the system between the ViDis and ViBus apps will be described. The interaction between both apps can be performed when each app is activated in its smartphone. Besides, must be considered the ViIP and bus driver have been trained in the use of each app. The protocol of actuation between the ViIP and the driver, beginning when the ViIP request the bus stop up to him/her get off the bus is described as follow:
  • The bus is on the route and the ViIP is on the bus stop.

- The ViIP is able to know, through the ViDis app, the bus is near to bus stop. Therefore, the ViIP request the bus stop, and he/she is waiting the bus answer.
- The ViBus app detects the bus stop request, and the driver touching the phone screen to send the received message.
- The ViIP receives the bus answer by means of vibration and/or audible message. With this, the first interaction is realized.
- When the ViIP is on the bus, she/he can recognize in advance the different bus stop along the route, by means of the ViDis app. Therefore, the ViIP can request the bus stop at any moment using the app.
- Immediately after request the bus stop to get off on the part of ViIP, the ViBus app receive it. Then, the bus drive send a positive answer to the ViIP touching his phone screen.
- The ViIP receives this answer by means of vibrations and/or audible message. With this, the second protocol interaction is realized.

2.2. *Design of the RF System*

Three RF modules have been designed and developed for the visually impaired people (MOVI-ETA), the bus driver (MOVI-Bus) and the bus stop (MOVI-Stop). These modules transmit their RF signals in the ISM radio band since this radio band is reserved internationally for industrial, scientific and medical purposes other than commercial telecommunications [14] and, besides, it is license-free. In Figure 2 is presented the interaction scheme among the designed RF modules for the MOVIDIS project.
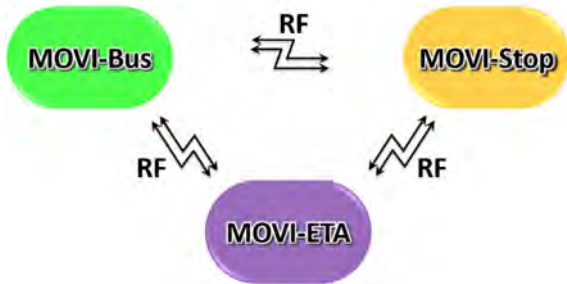
Figure 2. Interaction scheme among the modules of RF system to 433.4-473.0 MHz's

The general functioning of this RF system is as follow:
- A bus is on the route and it is emitting specific RF signal by means of the MOVI-Bus module with the aim to detect the MOVI-Stop modules.
- When the MOVI-Bus detect any MOVI-Stop, the first recognize the bus stop where the second is installed.

- At this moment, if there is a VoIP using MOVI-ETA at that bus stop, the MOVI-Stop detect it and sends a message to the MOVI-ETA of recognizing, and the link is established between them.
- If the ViIP requires stopping the bus, then he/she touch a button of MOVI-ETA and request the bus stop through the MOVI-Stop.
- Afterward, the bus driver send a message to the MOVI-ETA trough the MOVI-Stop indicating that will stop the bus. With this, the first interaction protocol finalise.
- When the ViIP is inside the bus, the MOVI-ETA will connect with the MOVI-Bus. Then, the MOVI-ETA will recognise all bus stop along the route through the MOVI-Bus, since it is will connect with each MOVI-Stop.
- Therefore, the ViIP can request using the MOVI-ETA the bus stop to get off. The bus driver send a message of received. With this, the second interaction protocol finalise.

Both interaction protocols, using apps for smartphones or RF modules using ISM radio band are summarized in this paper (but sufficient for understanding them), since different signals, flags, and process are executed in each moment, however, its description would be the paper extensive.

Why does it necessary to design and developed two different systems to provide help for the ViIP in their mobility in the public transportation of Panama? Because there is no GPS connection and 3G/4G services in several routes in different cities in Panama. Other reasons are that in some zones in Panama City, some places, bus stops, etc., there are not labelled, and neither at other cities of the country. Therefore, the two systems will be very useful in the future. Besides, this problem is not only of Panama, but also of other countries of the region and other towns in developed countries. Consequently, this project can be useful for improve the mobility of the ViIP in the public transport in general.

3. Evaluation of the systems

Firstly, the visually impaired people that collaborate with the MOVIDIS project have been trained with the two systems, the ViDis app, and the MOVI-ETA module. Figure 3 shows the snapshot of the training process. Both collaborators have a full visual disability and the training process have taken a session less than 30 minutes. This demonstrates the phone app and the RF module have user-friendly interface design. In addition, the bus drivers have been trained with the ViBus app and the MOVI-Bus module.

Several experimental tests have been carried out in order to evaluate the designed prototypes in lab conditions and in outdoor conditions using different types of motor vehicles. Figure 4 and Figure 5 show two different scenes when a ViIP is inside the bus and when she is waiting for the bus using the ViDis app. Both experiments have been carried out successfully, shown promising results.

Figure 3. ViIP training process with the MOVI-ETA prototype and the ViDis app.

In the experiment, represented in Figure 4, both app knew the next bus stop, so the ViIP is able to request the bus stop at the respective moment. The bus driver receives this request and sends the response to the ViIP and, subsequently, stop the bus.

Figure 4. ViIP inside the bus using the ViDis app and the ViBus interface, during an experimental test.

In Figure 5 is possible to see the user-friendly interface design of the ViDis app. This interface has big buttons, which send her vibration and audible signals when she touches them. Besides, she receives vibration signals and audible

messages when the bus driver sends some responses to her. Therefore, the ViIP is aware of the interaction with the bus, before and after taking it. The interaction time of the bus driver with de ViBus app is negligible; therefore, it is not compromised road safety.
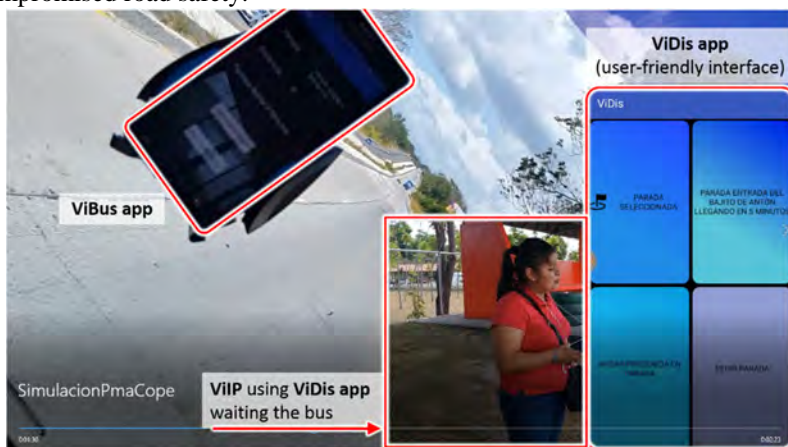
Figure 5. ViIP waiting the bus using the ViDis app and the ViBus interface, during an experimental test.

4. Conclusions and Future works

In this paper has been outlined the conceptualization of the design and implementation of two systems ICT-based, addressed to provide helps to the mobility of visually impaired people in the public transportation in Panama. However, this proposal can be extended to other cities in the world, where technology not has been developed nowadays.

Several experiments have been carried out in outdoor, between bus stops in some transportation routes, given successful and promising results. It should be stressed that have been developed non-commercial prototypes, but they can be innovative products in the future.

Two people with full visually impaired have collaborated with our research group using the ViDis app and the MOVI-ETA module, and they have had a rapid learning using the prototypes and have expressed eagerness.

In future works, the prototypes will be improved, adding new characteristics and broaden their action fields to other outdoor and indoor zones.

References

1. *WHO*, 10 facts about blindness and visual impairment. (August 2014). Available in: http://www.who.int/features/factfiles/blindness/en/.
2. *WHO*, Vision impairment and blindness. (October 2017). Available in: http://www.who.int/mediacentre/factsheets/fs282/en/.
3. J.A. Muñoz, Las TIC y la discapacidad visual. Repositorio *Universidad de la Coruña*, Spain, 293 (2012).
4. E. Fürst, Mobility barriers in urban transport for the sight or hearing impaired: Solutions help all passengers. *Real Corp 2010: Cities for Everyone. Liveable, Healthy, Prosperous*. Vienna, 437 (2010).
5. E. Fürst and C. Vogelauer, Best and bad practices in public transport: approaches to a barrier-free design for the visually and hearing impaired. *Proc. European Transport Conference 2013*, Frankfurt, (2013)
6. G. Baudoin, O. Venard, G. Uzan, A. Rousseau, Y. Benabou, A. Paumier, J. Cesbron, The RAMPE Project: Interactive, Auditive Information System for the Mobility of Blind People in Public Transports. *Proc. the 5th international conference on ITS Telecommunications ITST 2005*, Brest France, (2005).
7. S. Azenkot, S. Prasain, A. Borning, E. Fortuna, R.E. Ladner, and J.O. Wobbrock, Enhancing independence and safety for blind and deaf-blind public transit riders. *Proc. of the SIGCHI conference on Human Factors in computing systems*. Vancouver, Canada, 3247 (2011).
8. M. Markiewicz and M. Skomorowski, Public transport information system for visually impaired and blind people. *Transport Systems Telematics*, 271 (2011).
9. F. Domínguez-Morrondo, Desarrollo de un sistema de guiado para invidentes. *IMSERSO*, Spain, (2005).
10. J.A. Muñoz and C. Blocona, Global Positioning System (GPS) accessibility for people with visual disability: the HaptiMap Project. Integración. *Revista sobre discapacidad visual* **61**, 30 (2011).
11. H. Montes, I. Chang, G. Carballeda, J. Muñoz, A. García, R. Vejarano and M. Armada, Proc. *RoboCity16 Open Conference on Future Trends in Robotics*, **C26**, 211 (2016).
12. G. Carballeda, A. Arcia, R. Pérez, and H. Montes, *Aplicación de Tecnologías de la Inf. y Com. para mejorar la Accesibilidad*, **1**, 93 (2016).
13. A. García, Y. Sáez, J. Muñoz, I. Chang, H. Montes, Proc. *Sixth Eng., Science and Tech. Conf. "Trends and Challenges in Eng., Sci. and Tech.,* 821 (2017).
14. ITU. *Radio Regulations Articles*, (2012).

PROPOSAL OF AIR COMPRESSING DEVICE USING WALKING VIBRATION ENERGY REGENERATION FOR PNEUMATIC DRIVEN ASSISTIVE DEVICE*

MANABU OKUI

Research and development initiative, Chuo university, 1-13-27 Kasuga Bunkoy-ku, Tokyo, 112-8551, Japan

YASUYUKI YAMADA

Faculty of science and engineering, Chuo university, 1-13-27 Kasuga Bunkoy-ku, Tokyo, 112-8551, Japan

TARO NAKAMURA

Faculty of science and engineering, Chuo university, 1-13-27 Kasuga Bunkoy-ku, Tokyo, 112-8551, Japan

Pneumatically driven wearable assistive devices for walking have been developed recently. These devices can achieve flexible assistance without control; however, they require large and heavy air compressors for activation. In this study, a pneumatically driven source using vibration energy regeneration from walking was developed. The aim was to activate the cylinder using vibrations due to walking and compressed air. A mass element, which is connected to a human body via a spring and a cylinder, vibrates along with the human gait cycle. Next, a prototype was developed and tested. In walking experiments, stored pressure was measured at several gait cycles and masses for comparison. Results indicate that the gait cycle period and masses affect the stored pressure; the highest pressure recorded was 0.08 MPa.

1. Introduction

Wearable assistive devices have been developed recently to prolong the health spans of the elderly or to reduce heavy manual labor [1-3]. These devices are required to provide flexible assistance in a safe and natural way. Devices driven by motors and reduction gear are controlled to be flexible by feed back control. In such cases, sensors are required and they cannot adapt to sudden external

forces that are faster than the actuator's performance. In addition, such devices interfere with the wearer's movement because they have low back drivability.

In contrast, pneumatically driven assistive devices that achieve a flexible assistance without control using pneumatic artificial muscles for actuators have been developed [4,5]. These devices can mitigate the problems discussed earlier; however, they require large and heavy air compressors for activation. Therefore, portable pneumatically driven devices have been recently developed [6-9]. However, a mobility comparison of the gas compression methods [10] indicates that the existing methods pose certain limitations.

In this study, a novel air compression method that uses walking vibration energy regeneration is proposed. Additionally, a prototype is developed and tested.

2. Concept and modeling

2.1. *Vibration during walking*

The center of gravity moves vertically during walking. Fig. 1 shows the variation of height and acceleration of the center of gravity for two gait cycles. The center of gravity is low in double-stance phase and high in the single-stance phase. Acceleration is ~180° out of phase with height.
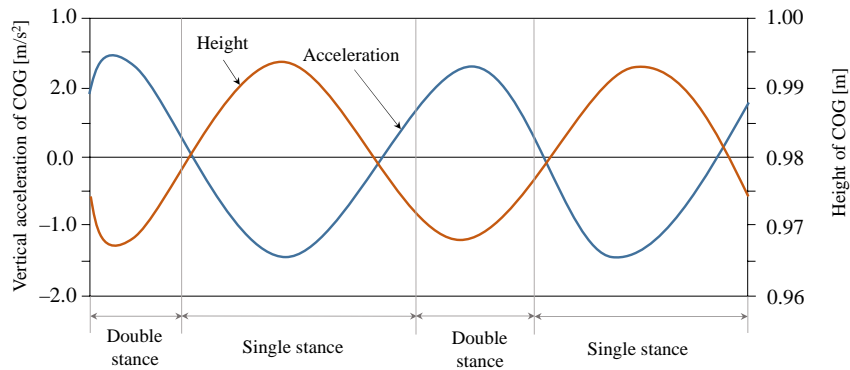
Figure 1. Height and acceleration of the center of gravity during a complete gait cycle.

2.2. *Regeneration of walking energy*

Fig. 2 schematizes the walking energy regeneration device. The regeneration device is fixed to the wearer, and mass elements are connected via a spring and a cylinder. The movement of the mass element is restricted in the vertical direction by a slider. Due to vibrations during walking, the mass element moves up and down and drives the cylinder to compress air. This enables obtaining pneumatic energy from walking energy. The mass element comprises additional systems such as electric valves and a battery.

The inertial force generated by the vibration of the mass element is expected to assist in walking.
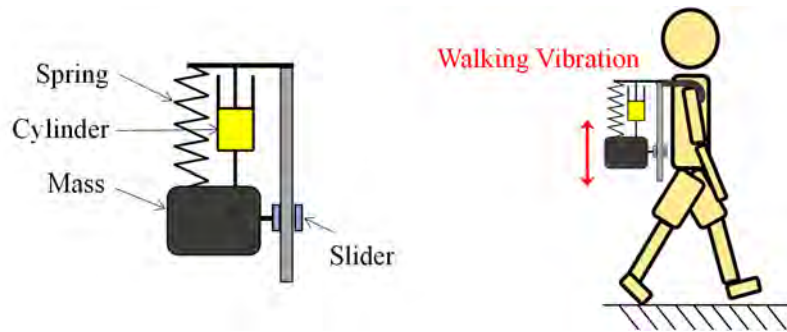
Figure 2. Operation of air compression device using walking vibration energy.

2.3. *Modeling*

The vibration phenomenon of the proposed method can be regarded as the forced displacement vibration of a spring-mass damper system, as shown in Fig. 3. Note that the mass of a human is sufficiently larger than the mass of the device. The impedance elements of the cylinder are regarded as the damper and spring elements. k is the spring constant of the spring, k_c is the spring constant of the cylinder, and d_c is coefficient of viscosity of the cylinder. The resonance frequency of the system can be expressed as $(2\pi)^{-1}\sqrt{km^{-1} - 0.5\, d^2 m^{-2}}$.
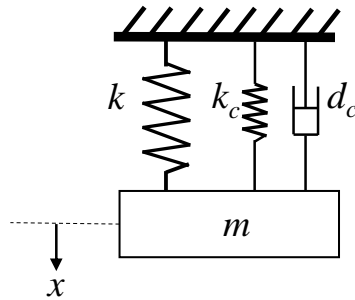
Figure 3. Model of the proposed system.

3. Prototype

3.1. *Design*

The design of the prototype is shown in Fig. 4. The prototype comprises a frame and a plate for loading mass elements. These two parts are connected via a spring, a cylinder for generating compressed air, and a slider that restricts movement of the plate in the vertical direction. Brackets for attaching the shoulder strap are attached to the top and bottom of the frame.
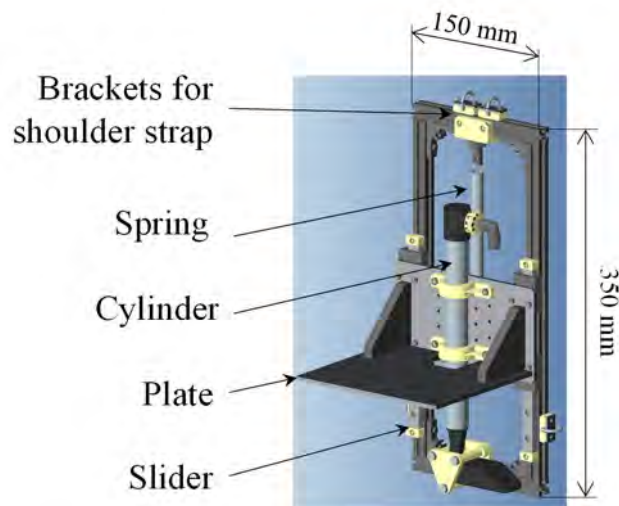
Figure 4. Design of the prototype.

3.2. *Developed prototype*

The developed prototype is shown in Fig. 5, and the specifications are shown in Table 1. The cylinder is composed of a commercially available double-action air pump. The discharge port of the pump is connected to the tank, which is used to store the compressed air. A check valve prevents the backflow of the compressed air, and a pressure sensor is mounted between the tank and the pump.

Table 1. Specifications of the prototype.

Weight of the prototype	1.79 kg
Weight of the plate part	0.570 kg
Size	350 mm × 150 mm × 180 mm
Model number of spring	22-1245 (Samini Co., Ltd.) Spring constant is 0.392 N/mm
Model number of cylinder	D59-35-301
Volume of tank	600 ml
Length of the tube between cylinder and tank	670 mm
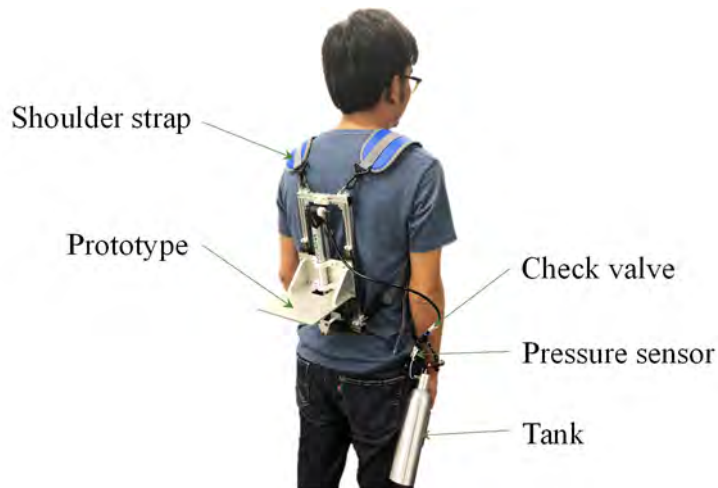
Figure 5. Subject wearing the prototype.

4. Experiment

4.1. *Experimental conditions*

The prototype shown in Fig. 5 was experimentally validated. In each trial, pressure measurements were performed while the subject walked for 120 s with a 700-mm step length. Two parameters were varied: a) the number of weights on the plate [one to four weights (0.85 kg each) were used] and b) the period of the walking cycle (0.9, 1.0, and 1.2 s). The subject is a male with a height of 178 cm and a weight of 68 kg.

4.2. *Results and discussion*

Fig. 6 shows the experimental results, and Table 2 shows the theoretical resonance period, which was calculated assuming that k_c and d_c are 0. Fig. 6 shows the pressure profiles for three different step periods and for different weights. It is evident that short gait cycles yield more amount of compressed air. The highest pressure and fastest compressed air generation were observed for three weights and a 0.9-s gait cycle period. Here, the pressure was ~0.08 MPa, sufficient for activating pneumatic actuators.

Under the two-weight condition, gait cycle periods of 1.0 and 0.9 s showed similar pressure profiles because this experimental condition has a 0.95-s resonance frequency, as shown in Table 2, and is similar to the 1.0- and 0.9-s gait cycles.

However, comparing the results in Fig. 6 with the gait cycle in Table 2, the resonance frequency and experimental results did not correlate with each other were not observed. For example, in the case wherein four weights were used, the compressed air becomes largest at 1.2-s gait period. However, the experimental result showed that 0.9 s period provides the highest pressure.

Therefore, it is necessary to improve accuracy of the model. For example, adjusting the cylinder spring force and coefficient of viscosity according to the cylinder pressure could improve the agreement between model and experiment. Additionally, a more detailed analysis of the model could help determine the optimum values of the spring constant and weight. These proposed adjustments could improve the efficiency of this device to make it practical.
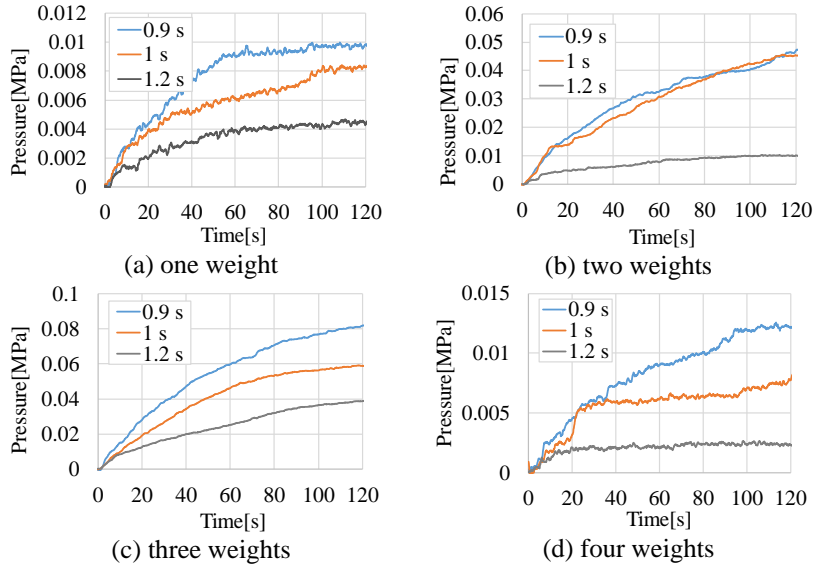
Figure 6. Pressure profiles for various gait cycle periods. Each plot shows the results for a different weight.

Table 2. Resonance period of each condition

Number of weights	Weight [kg]	Resonance period [s]
1	1.42	0.38
2	2.27	0.48
3	3.12	0.56
4	3.97	0.63

5. Conclusion

In this study, an air pressure source using regeneration of energy from walking was proposed and a prototype was constructed and tested. In the walking experiments, pressure profiles during gait cycles were compared at varying gait cycle periods and masses. The highest pressure in the tank was 0.08 MPa for a weight of 3.12 kg and gait cycle period of 0.9 s. Plans for future study include the optimization of the device specifications using a more detailed model.

Acknowledgments

52

References

1. T. Hayashi, H. Kawamoto and Y. Sankai, "Control Method of Robot Suit HAL working as Operator's Muscle using Biological and Dynamical Information," *In Proc. IEEE/RSJ Int. Conf. on Intelligent Robots and Systems (IROS)*, pp.3063–3068. 2005.

2. Y. Lee, S. Roh, M. Lee, B. Choi, J. Lee, J. Kim, H. Choi, Y. Shim and Y. Kim, "A Flexible Exoskeleton for Hip Assistance" *In Proc. IEEE/RSJ Int. Conf. on Intelligent Robots and Systems (IROS)*, pp.1058–1063, 2017.

3. A. Tsukahara and M. Hashimoto, "Pilot Study of Single-Legged Walking Support using Wearable Robot based on Synchronization Control for Stroke Patients", *Proceedings of the 2016 IEEE International Conference on Robotics and Biomimetics*, pp.886-891, Qingdao, China, December 3-7, 2016.

4. A. Ohno, H. Nabae and K. Suzumori, "Static Analysis of Powered Low-Back Orthosis driven by thin pneumatic artificial muscles considering body surface deformation", *In Proc. of 2015 IEEE/SICE International Symposium on System Integration (SII)*, pp.39-44, 2015.

5. M. Okui, S.Iikawa, Y.Yamada and T. Nakamura, "Variable viscoelastic joint system and its application to exoskeleton", *Proc. of The 2017 IEEE/RSJ International Conference on Intelligent Robots and Systems(IROS)*, Vancouver, Canada, pp.3897-3902, 2017.

6. M. Okui, S.Iikawa, Y.Yamada and T. Nakamura, "A pneumatic power source using a sodium bicarbonate and citric acid reaction of for use in mobile devices", *Proc. of The 2017 IEEE/RSJ International Conference on Intelligent Robots and Systems(IROS)*, Vancouver, Canada, pp.1040-1045, 2017.

7. K. Suzumori, A. Wada and S. Wakimoto, "A new mobile pressure control system for pneumatic actuators using reversible chemical reactions of water, *IEEE/ASME International Conference on Advanced Intelligent Mechatronics(AIM)*, pp.122-127, 2013.

8. K.Nakahara, K.Narumi,R.Niiyama, Y.Kawahara, "Electric Phase-change Actuator with Inkjet Printed Flexible Circuit for Printable and Integrated Robot Prototyping", *IEEE International Conference on Robotics and Automation (ICRA)*, pp.1856-1863, 2017.

9. M. Wehner, M. T. Tolley, Y. Menguc¸Y. Park, A. Mozeika, Y. Ding, C. Onal, R. F. Sheperd, G. M. Whitesides, R. J. Wood, "Pneumatic Energy Sources for Autonomous and Wearable Soft Robotics", *Soft robotics*, vol.2, No.00. pp. 1–12, 2012.

10. M. Okui, Y. Nagura, Y. Yamada, T. Nakamura, "Hybrid Pneumatic Source Based on Evaluation of Air Compression Methods for Portability", *IEEE Robotics and Automation Letters.* vol. 3-2, pp. 819-826, 2018

A WALKING ASSISTANT USING BRAKES AND LOW COST SENSORS[*]

LUCIANO CANTELLI, DARIO GUASTELLA, LUCIANO MANGIAMELI,
CARMELO DONATO MELITA, GIOVANNI MUSCATO

Università degli Studi di Catania Dipartimento di Ingegneria Elettrica Elettronica e Informatica, viale A. Doria 6
CATANIA, 95125, ITALY

DOMENICO LONGO

Università degli Studi di Catania, Dipartimento di Agricoltura, Alimentazione e Ambiente - Via S. Sofia 100, 95123 CATANIA Italy

Smart Walkers are a category of robotic assistive devices particularly useful for the elderly. These systems help the users in locomotion and with respect to the classical walkers, reduce the risk of fall. This work presents a new system that has been developed using low-cost time of flight laser sensors in place of the more expensive laser scanners. Control of direction is performed by guiding the user by mean of brakes on the rear wheels. Other sensors include an inertial measurement unit with magnetometer and an interface with an external absolute localization system. Preliminary trials have been performed on a graphical and physical simulator implemented in the V-Rep framework.

1. Introduction

1.1. *Assistive mobility devices*

Nowadays it is well known that the proportion of elderly people in the society is constantly growing. As a consequence, it becomes really important to develop assistive systems to allow a better integration in the society of elderly people in their daily activities. Technology can help and several devices have been developed for the so-called Ambient Assistive Living [1]. The European Commission has also started a specific program for AAL [2] and many countries have developed their specific research plans. Recently the International Standard Organisation has developed the standard ISO 13482:2014 which specifies

requirements and guidelines for the inherently safe design, protective measures, and information for use of personal care robots.

One of the most important activity that is compromised by age or by some disability, is locomotion. As a consequence, an important function of several devices is to guarantee mobility in autonomy of the users. Walkers are important devices, since consent a physical support and stabilizing effect for those persons with reduced mobility and balance problems. These devices allow also to perform rehabilitation exercises and in most cases are more useful and best accepted with respect to wheelchairs [3].

However, several studies report that the adoption of walkers in many situations does not decrease the probability of falls of the users [4]. Walkers sometime can bump or become entangled into obstacles, or tumble into steps or stairs and as a consequence become the main cause of falls.

1.2. *State of the art on Smart walkers*

Several researchers have studied how to improve a classical walkers introducing some sensors, actuators and control strategies. Such devices are usually known as "smart walkers" and in [5] a review of the functionalities implemented on several systems is presented. In particular devices can be classified with respect to their autonomy, shared-control capability, manual guidance, sit-to–stand help, user's state monitoring. In particular, an important distinction is between motorized walkers and passive walkers. Walkers with active motors connected to the wheels help the user in the mobility, by navigating autonomously in the environment. On the other side passive walkers through the adoption of sensors and sometimes brakes in the wheels, guide the users to their desired route leaving them the responsibility of the motion. Previous work concerning the adoption of brakes for guidance of the trajectory have been reported in [6], where expensive servo brakes and laser scanners are used and in [7], where a detailed study of the trajectory control by brakes is described.

It is important to underline that the functions of a smart walker need to be designed specifically for a precise class of users and that universal solutions do not exists.

2. The proposed solution

One of the purpose of the project SUMMIT is to design build and test on real environments an Internet of Things platform based on several smart objects. One of the testing scenario is concerning Smart Health and among the smart objects a smart walker has been selected, to be developed and tested.

The system should have navigation capabilities within a domestic environment. Localization is then performed by interfacing with a specific network in the environment, obstacle avoidance by means of several distance

sensors, while inertial sensors monitor bump into obstacles and are be adopted to predict the risk of fall.

Actuators in the brakes of the rear wheels are installed to guide the users toward desired locations, avoiding obstacles, while a haptic interface in the handlebars sense user's intentions. The main innovative aspect of this work is the adoption of low cost time of flight laser sensors, the integration with an external localization system and the development and implementation of a predictive strategy to prevent the risk of fall.

2.1. *Block diagram of the proposed system*

The draft architecture of the proposed system is reported in Fig. 1. Where all the adopted sensors, actuators and interfaces are reported. In the following sections a short description of the main components is described.

Figure 1. Block diagram of the installed systems on a commercial walker.

2.2. *Time of flight laser sensors*

In order to get a precise obstacle detection without using expensive laser scanner, we decided to adopt some innovative Time-of- Flight (ToF) laser-ranging modules, the VL53L0X by STMicroelectronics. This sensor is housed in a very small package and can measure absolute distances up to 2m with a Field Of View of 25°. This distance is considered more than adequate, considering the typical low speeds and the domestic environments.

These sensors can be adopted into three different modalities: Single ranging, Continuous ranging and Timed ranging with three ranging profiles: High speed, High accuracy and Long range.

In particular, we adopted the three sensors integrated into a microcontroller board X-NUCLEO-53L0A1. The system has been also tested mounted on a servo motor, thus allowing to get a scan of the environment, as it is shown in Fig.2. An example of a scan is reported in Fig. 3. The time needed for a 360° scan is of about 2s, with a resolution of 10°.

(a)   (b)
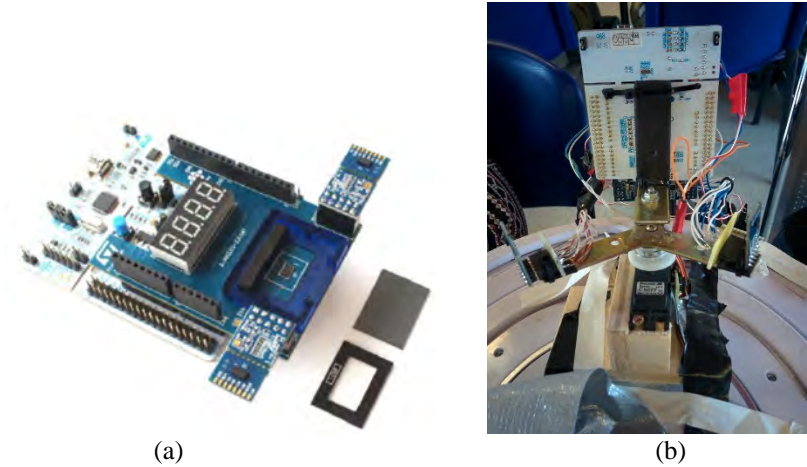
Figure 2. The evaluation board X-NUCLEO-53L0A1 for the VL53L0X sensors (a) and how it was mounted on a servomotor for environment scanning.
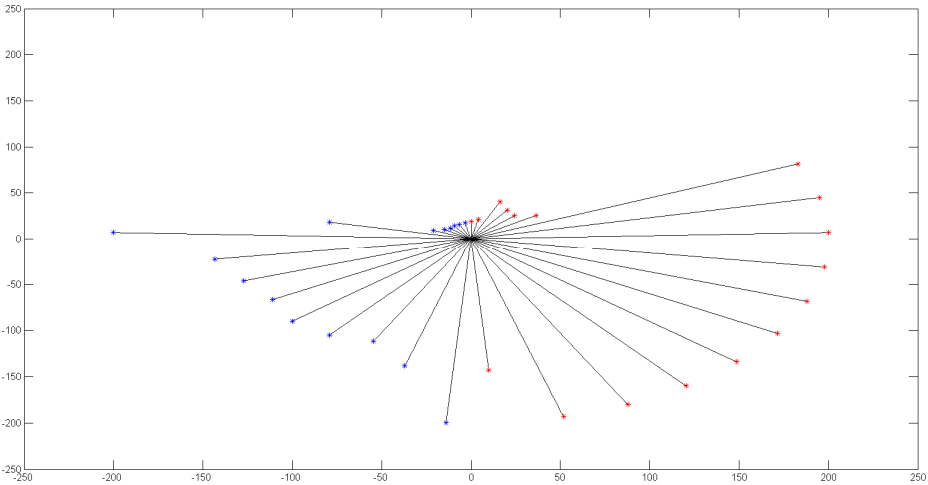
Figure 3. A 360° scan obtained from the fusion of the information from the three sensors (dimensions in cm.).

2.3. *Sensor-Tile IMU*

Information on the accelerations of the system and on its orientation is obtained by using the STLCS01V1 SensorTile system by STMicroelectronics (Fig.4).

 This is a very compact module which includes a 32bit MCU, a 3D accelerometer and 3d gyroscope, a 3D magnetometer, a pressure sensor, a MEMS microphone, a Bluetooth low energy interface and several other external communication interfaces.
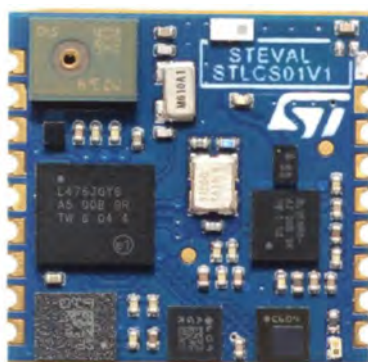
Figure 4. The sensorTile STLCS01V1 board.

 In particular, in our application it is adopted for detecting bumps into obstacles and to obtain the absolute orientation of the system.

2.4. *Absolute Localization System*

In order to get absolute localization of the walker in the environment a smart multisensor assistive system has been developed in our Department [8]. This system performs a data fusion algorithm between a wireless sensor network, based on ultrasound sensors for trilateration, and odometry data, gathered by an Inertial Measurement Unit. The average accuracy of the localization in a typical indoor environment is about 3cm.

2.5. *Obstacle Avoidance Strategy*

As an algorithm to avoid obstacles a potential field approach has been chosen [9]. Data from the map of the environment are fused, by using a Fuzzy Logic algorithm [10], with the Time of Flight sensors to implement a repulsive strategy

on the brakes of the walker. Information from the IMU are also adopted to detect bumps and its magnetometers allow the estimation of the orientation of the user.

3. Results on simulations

As a first step, before implementing the strategies on a real hardware, a simulation environment has been designed by using the V-Rep environment. V-Rep is a tool by Coppelia robotic very useful for graphical and physical simulation of robotic systems and can be easily interfaced with external software. In particular, in our application the control strategy has been written in MATLAB. In this case only three fixed Time of flight sensors have been adopted.

In the Figures 5 and 6 some screenshots of the simulations are reported. In particular, in the Figure 6 the graphs on the left lower part show the minimum distance with an obstacle, while on the right upper part, the views of three virtual cameras, placed on the three laser sensors positions, are shown. The three red cones represent the Field Of View of the ToF sensors.
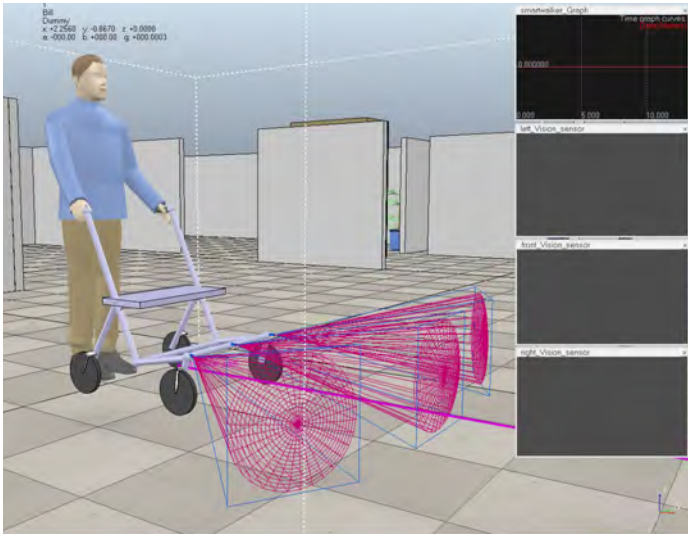
Figure 5. Simulation of the smart walker on a virtual environment in V-Rep.
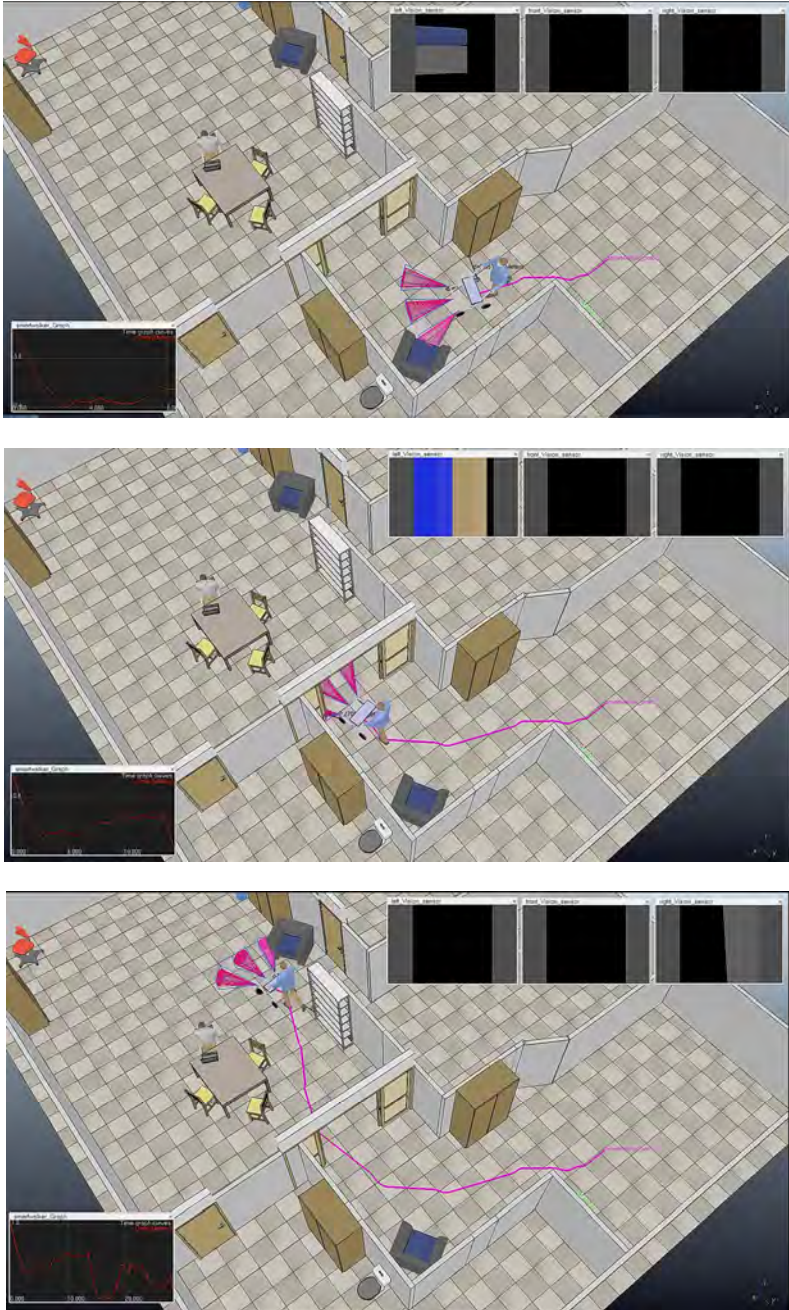
Figure 6. Sequence of a typical path of the smart walker in an indoor domestic environment.

4. Conclusions

This work reported some preliminary results on a new low-cost architecture for a smart walker. The main sensors and the overall strategy has been designed and is under implementation and test on the real hardware. A physical simulator has been implemented and the results are promising. Final implementation and experimental trials on the real system with real users are ongoing.

References

1. Rashidi, P., & Mihailidis, A. (2013). A survey on ambient-assisted living tools for older adults. IEEE journal of biomedical and health informatics, 17(3), 579-590.
2. ACTIVE AND ASSISTED LIVING PROGRAMME http://www.aal-europe.eu/
3. Martins, M. M., Santos, C. P., Frizera-Neto, A., & Ceres, R. (2012). Assistive mobility devices focusing on smart walkers: Classification and review. Robotics and Autonomous Systems, 60(4), 548-562.3.
4. B.A. West, G. Bhat, J. Stevens, G. Bergen, "Assistive devices use and mobility-related factors among adults aged >= 65 years", Journal of Safety Research, Vol.55, pp. 147-150, 2015.
5. Martins, M., Santos, C., Frizera, A., & Ceres, R. (2015). A review of the functionalities of smart walkers. Medical engineering and physics, 37(10), 917-928.
6. Hirata, Y., Hara, A., & Kosuge, K. (2007). Motion control of passive intelligent walker using servo brakes. IEEE Transactions on Robotics, 23(5), 981-990.
7. Fontanelli, D., Giannitrapani, A., Palopoli, L., & Prattichizzo, D. (2015, December). A passive guidance system for a robotic walking assistant using brakes. In Decision and Control (CDC), 2015 IEEE 54th Annual Conference on (pp. 829-834). IEEE.
8. B. Ando', S. Baglio, C.O. Lombardo, RESIMA: an assistive paradigm to support weak people in indoor environment, IEEE Transactions on Instrumentation and Measurement, vol. 63, no. 11, pp.2522-2528, 2014.
9. Khatib, O. (1986). Real-time obstacle avoidance for manipulators and mobile robots. In Autonomous robot vehicles (pp. 396-404). Springer, New York, NY.
10. G Muscato, Fuzzy control of an underactuated robot with a fuzzy microcontroller, Microprocessors and Microsystems 23 (6), 385-391, 1999.

REHABILITATION PROTOTYPE TO IMPROVES MOBILITY OF ACUTE ROTATOR CUFF INJURY

MARIANA TORRENTE ROCHA, LAURA JIMÉNEZ GUZMÁN

El Bosque University, Bioengineering Department
Av. Cra 9 No. 131 A – 02 Bogota, Colombia

HERNANDO LEÓN-RODRÍGUEZ

El Bosque University, Electronics Engineering and Bioengineering Department
Av. Cra 9 No. 131 A – 02 Bogota, Colombia

The deterioration of the components of the rotator cuff is one of the most frequent causes of musculoskeletal pain and disability in the world. The conditions of the rotator cuff increase with the passage of time, since they have a direct relationship with a process of deterioration rather than with a traumatic event. In order to decrease pain and recover shoulder movement, patients are usually treated by regular sessions with a physiotherapist. However, more sessions are required than those stipulated to fully obtain recover mobility. This paper present the development of portable prototype to rehabilitate acute rotator cuff injure, designed from biomechanical analysis and ranges the kinematics and dynamics articulated in the present design determine important requirements in obtaining greater functionality of the prototype and with it, allows the identification of sensors and actuators for executing two types of specific movements: flexion / extension and external / internal rotation by means of a soft rehabilitation robot.

1. Introduction

The component´s deterioration of the rotator cuff is one of the most frequent causes of musculoskeletal pain and disability in the world. The incidence of shoulder pain in the general population is around 11.2 cases per 1,000 patients per year. It is considered to be the most prevalent soft tissue pathology, with an estimated incidence of rotator cuff injuries of 3.7 per 100,000 per year.

The pathology of the rotator cuffs is associated with the overuse of the joint by work, sports, avascularity, mechanical failure located in the supraspinatus tendon, ruptures caused by deterioration or even by the entrapment that the tendon suffers between the humerus and the acromion. There are other risk factors that can lead to a rotator cuff injury, such as obesity, hypercholesterolemia, genetic factors, anatomical variations, scapular dyskinesia and glenohumeral instability. [1]

Currently, the rehabilitation of rotator cuffs starts from the application of conventional therapies, to the use of robotics as alternative mechanisms, which integrate engineering concepts such as compensation of force, motor control at

speeds calibrated according to the motor functions of each individual and sensory contributions that through the repetition of exercises in intensive training programs manage to recover mobility limitations.[2] [10] Some of the referents are Armeo Spring who by providing support for the weight of the arm, allows patients to use any remaining motor function and encourages them to reach a greater number of reach and grip movements based on specific therapeutic objectives, from an arm grab exoskeleton [3]; In-Motion Shoulder-Elbow Robot allows to quantify the control of the motor of the upper extremities and with the recovery of the movement, which allows the doctors to distinguish the real recovery from the compensation of the patient [4]; shoulder exoskeletons; Cable-Robots who have very good kinematic and dynamic characteristics, and also show other properties such as: portability and economy of costs, which also make them suitable for medical applications and rehabilitation even though based on the physical nature of the cables that can only pull and not push [5]; isokinetic force machines such as Humac Norm Testing and Rehabilitation System that allows the diagnosis and treatment of the performance of muscles and joints of orthopaedic patients, starting from the principle of isokinetic force, under the correct anatomical positioning and a positive stabilization to examine the musculature that surrounds the shoulder [6]. Based on the aforementioned developments, the new technologies point to the use of soft materials, which improve the ergonomics of the rehabilitation system like active soft orthotic system [7] [8] [9]

2. Biomechanical evaluation of patient

The biomechanics establishes a specific protocol to certain angles according to each movement as a pattern of healthy patients as example: the flexion motion goes from 0° to 180°, the extension motion from 0° to 60° for the sagittal plane; adduction from 0° to 45°, abduction from 0° to 180° in the frontal plane; the flexion of 130° to 5°, extension of 40° to 50° with respect to the horizontal plane; external rotation from 0 ° to 40° to 60° and internal rotation from 0° to 90°; and external and internal movements, both up to 70°. Although the biomechanical analysis allows limit the total movement angles of the articulation, the functional ranges of mobility are the representatives of movement with minimum balance in the comfortable execution of daily activities. From this conditions, the mechanism of operation of the prototype is designed, being specific in movements of flexo-extension (A), and internal and external rotation of the Shoulder (B).

3. Concepts of prototype design

The figure 1 is showing the design of a portable system driven by two gear-motors. The kinematic and dynamic analyses are based on two of the movements adapted by the articulation: flexion / extension, external / internal rotation which activate two degrees of freedom respectively. The prototype consists of two supports for the arm and the forearm, which will maintain the extremity in the

ranges of joint movements required to perform the different rehabilitation exercises. [11] [12] [13]
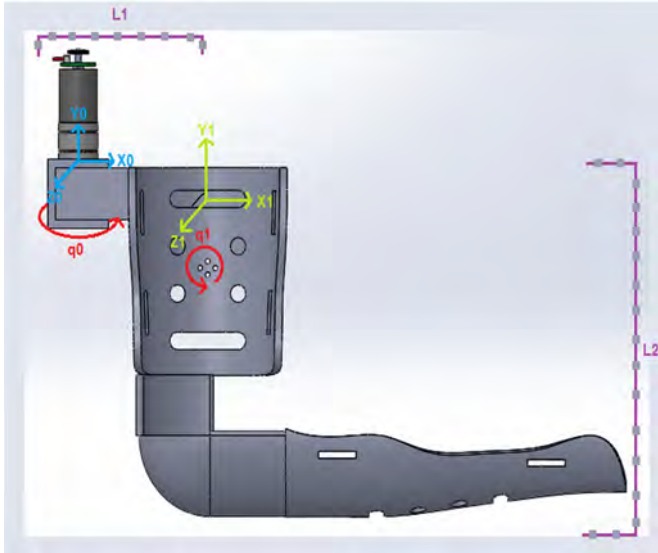
Figure 1: Design of shoulder rehabilitation robot first and second joint.

3.1. *Kinematic Design*

The kinematic system was obtained from a reference axis of the shoulder, which was proposed for the design of the system in the arm. (See figure 1)

$$R_{Y, q0} = \begin{pmatrix} \cos(q0) & 0 & \text{sen}(q0) \\ 0 & 1 & 0 \\ -\text{sen}(q0) & 0 & \cos(q0) \end{pmatrix} \quad Tras_{z,l1} = \begin{bmatrix} 1 & 0 & 0 & 0 \\ 0 & 1 & 0 & 0 \\ 0 & 0 & 1 & l1 \\ 0 & 0 & 0 & 1 \end{bmatrix} \tag{1}$$

The rotation matrix RY, q0 gives the projection of the coordinates in two coordinate systems. the equation 1 is the first rotation matrix it is evident that the system rotates on the Y axis and the articulation that rotates on this axis is the one called q0. In the translation matrix Tras z, we can see which link is transferred for the first system and on which axis the movement is observed. In this case, link 1 moves on the z axis.

$$A_0^1 = \begin{bmatrix} c_{q0} & 0 & s_{q0} & 0 \\ 0 & 1 & 0 & 0 \\ -s_{q0} & 0 & c_{q0} & -l1 * s_{q0} \\ 0 & 0 & 0 & 1 \end{bmatrix} \tag{2}$$

The equation 2 is the homogenous transformation matrix A01, we can see the projection of system 0 in system 1 and we can see the sum or product point

between the matrices of rotation and translation. The breasts and cosines that are evident in the rotation matrix, are the projections of the vectors in both x and y.

$$R_{Z,\,q1} = \begin{pmatrix} \cos(q1) & -sen(q1) & 0 \\ sen(q1) & \cos(q1) & 0 \\ 0 & 0 & 1 \end{pmatrix} \qquad Tras_{x,l2} = \begin{vmatrix} 1 & 0 & 0 & l2 \\ 0 & 1 & 0 & 0 \\ 0 & 0 & 1 & 0 \\ 0 & 0 & 0 & 1 \end{vmatrix} \tag{3}$$

The rotation matrix RZ, q1 gives the projection of the coordinates in two coordinate systems. In the first rotation matrix it is evident that the system rotates on the Z axis and the articulation that rotates on this axis is the one called q1. In the translation matrix Tras $_{x,l2}$ you can see which link is transferred to the second system and on which axis the movement is observed. In this case, link 2 moves on the x-axis.

$$A_1^2 = \begin{bmatrix} c_{q1} & -s_{q1} & 0 & l2*c_{q1} \\ s_{q1} & c_{q1} & 0 & l2*s_{q1} \\ 0 & 0 & 1 & 0 \\ 0 & 0 & 0 & 1 \end{bmatrix} \tag{4}$$

In the homogeneous transformation matrix A12, we can see the projection of system 1 in system 2 and we can see the sum or product point between the matrices of rotation and translation.

$$A_0^2 = \begin{bmatrix} c_{q0}s_{q1} & -c_{q0}s_{q1} & 0 & l2*c_{q1} \\ s_{q1} & c_{q1} & 0 & l2*s_{q1} \\ 0 & 0 & 1 & -l1*s_{q0} \\ 0 & 0 & 0 & 1 \end{bmatrix} \tag{5}$$

After obtaining the homogeneous transformation matrix of the system q1 and q0, multiplication or cross product of both homogeneous matrices is performed to find the position of the end terminal, with respect to the whole system.

$$X = l2*\cos(q1);\ (\tfrac{d}{dt}x) = \tfrac{d}{dt}(l2*\cos(q1)) \Rightarrow Vx = (-\dot{q1}*l2*Sen(q1))$$
$$Y = l2*Sen(q1);\ (\tfrac{d}{dt}y) = \tfrac{d}{dt}(l2*Sen(q1)) \Rightarrow Vy = (\dot{q1}*l2*Cos(q1))$$
$$Z = l1*Sen(q0);\ (\tfrac{d}{dt}z) = \tfrac{d}{dt}(l1*Sen(q0)) \Rightarrow Vz = (\dot{q0}*l1*Cos(q0))$$

$$\begin{bmatrix} \dot{x} \\ \dot{y} \\ \dot{z} \end{bmatrix} = \begin{bmatrix} 0 & -l2*sen(q1) & 0 \\ 0 & l2*cos(q1) & 0 \\ l1*cos(q0) & 0 & 0 \end{bmatrix} \begin{bmatrix} q0 \\ q1 \\ q2 \end{bmatrix} \tag{6}$$

The Jacobian matrix is used to determine the speed of movement in each of the axes and also to determine the kinetic energy, it was necessary to calculate the velocity vector, which is composed of the sum between the vector derivative of r$_{CM}$ center of translational mass plus the angle of rotation, by the cross product of the vector r$_{CM}$ of center of mass. Once the velocity vector is found, the kinetic energy and the potential energy are found.

$$\vec{v} = \dot{\vec{r}}_{CM\ traslacional} + \vec{\omega}_{1\ CM} \times \vec{r}_{1\ CM} \tag{7}$$

$$K=\frac{1}{2}m|\vec{v}|^2 + \frac{1}{2}\omega^T I\omega \tag{8}$$

$$u=mgh=0 \tag{9}$$

The vector r_1 is composed of a medium of link 1 in the direction i0, while the vector w1 is given by the rotation q0 in the opposite direction to the movement - j0, the vector v_1 is given by a means of link1 by the rotation q0 in the address k.

$$\vec{r1} = \frac{l1}{2}(\hat{i}_0)$$

$$\vec{w1} = q_0(-\hat{j}_0) \tag{10}$$

After determining each of the variables ($\vec{r}1$ y $\vec{w}1$), we find the velocity, which gives us as a result, since the derivative of R1 with respect to q0 is 0.

$$\vec{v1}= \frac{l1}{2}q_0(\hat{k}) \tag{11}$$

Once the velocity is found, the value is replaced in the kinetic energy equation, where WT is the transpose of the vector $\vec{k}1$ and I is a matrix of inertia.

$$K1 = \frac{1}{2}m\left(\frac{l1}{2}q_0\right)^2+\frac{1}{2}\begin{bmatrix}0\\q_0\\0\end{bmatrix}I[0 \quad q_0 \quad 0] \tag{12}$$

In addition to this, the potential energy is found where m1 corresponds to the mass of the first link and g to the value of gravity.

$$u = m1g\frac{1}{2} \tag{13}$$

For the second joint articulation of the system showing in figure 1, the same methodology was carried out, with which the energies were obtained in the first articulation. With the difference of the variable $\vec{r}2$.

$$\vec{r2} = l1(-\hat{i}_0) + \frac{l2}{2}(\hat{k}_1)$$

$$\vec{w2} = q_1(\hat{k}_1)$$

$$\vec{v2}= -q_1\frac{l2}{2}(\hat{i}_1) + l1q_1(\hat{j}_1)$$

$$K2 = \frac{1}{2}m2\left(-q_1\frac{l2}{2}\right)^2+(l1q_1)^2+\frac{1}{2}\begin{bmatrix}0\\0\\q_1\end{bmatrix}I[0 \quad 0 \quad q_1]$$

$$u = m2gl1$$

3.2. *Design and operation characteristics.*

The operation of this prototype starts from a 12V power supply that ensures its portability, which replaces the L298N (Bridge H) that will give the control of rotation of two DC motors. Because it is necessary to determine the ranges of extension / flexion movement, external/internal rotation, the angles are sensed by using two encoders, one for each DC motor showing in figure 2. The control of said DC motors, is given by a software system, Raspberry PI3B, controlled by the

Python programming language. A 7805 voltage regulator is required because the software voltage should not exceed 5V.
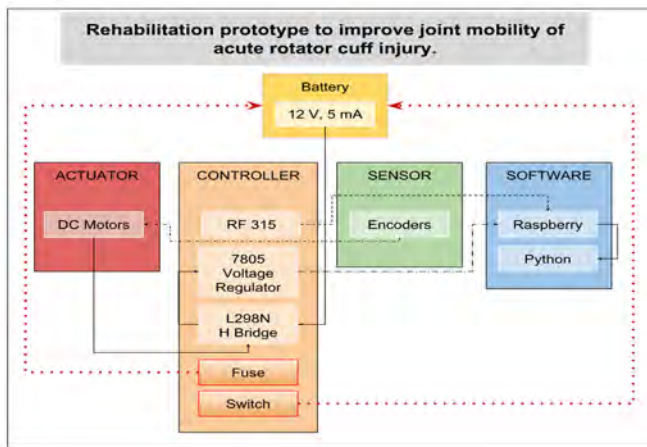
Figure 2: Schematic diagram of control architecture.

3.3. *System Prototype.*

The prototype consists of two stabilizing components showing in figure 3. The first component consists of a piece that supports the forearm and the arm, and has an elongation fabric that allows the user to have mobility in the elbow (1). The second component is an abdominal stabilizer, which brings stability to the back, and so that the therapy is exercised upright, without complications to the spine, in addition, the trellis has two shoulder straps or stabilizers that they allow the weight of the actuators to dissipate through them, in addition, the trellis has a pocket that groups the electronic components, in order to make it easy to access adjustments or even remove the battery to charge it (2). The actuator that exerts the movement of flexion - extension, has a support that is connected directly to the trellis and a connector that intertwines the other actuator, which performs the external and internal rotation movement and is connected to the forearm support by a piece which lengthens as the flexion movement (4) is performed. Then you can see the two pieces coupled (4, 5 and 6).

3.4. *Sensors and actuator to monitor the patient's position.*

In order to control the movements of the patient and emit four types of therapies, in which, each one contemplates the four movements with different repetitions and angular moments. We use two optical encoders to detect direction and rotation by a beam emitted LED that passes through a code disk for each joint. The actuators used for the prototype are RS-545SH-22100, those have an operating range of 12 to 24V, an unloaded speed of 4200 rpm at a current of 0.16

A. One of the most important characteristics are the maximum efficiency, since they have a torque of 19.4 mN-m and a power of 4.36 (W). However, since its main function is to support therapy movements, we needed it to have enough strength to lift a load like the arm, for this we added two reduction boxes or gearbox of 1:500 in each motor, as a result decreased its speed at its maximum efficiency and increased its strength or torque.

Figure 3: Prototype of shoulder rehabilitation robot system; (A): front, (B): posterior sagittal axis of the device, (C): right view, (D): stabilizing components, (E): emergency switch and control access.

4. Discussion result and conclusions

Results are not obtained explicitly related to rotator cuff injury, indispensable parameters are obtained in the operation design of the device, but the functional ranges in which the device responds comfortably and pertinent to a rehabilitation process due to injury, together with the addition of mechanical stops that go to the limits of functional angles.

Once the prototype was built according to the anthropometric measurements, it was possible to demonstrate that it is an ergonomic prototype, since the actuators adapt to the anatomical characteristics of the Glenohumeral joint, because the insertions of the actuators are similar to the anatomical insert that exists between the humerus and the omoplate.

Acknowledgments

References

1. Orth T, Paré J, Froehlich JE; Current concepts on the genetic factors in rotator cuff pathology and future implications for sports physical therapists. International Journal of Sports Physical Therapy. 2017;12 (2):273-285.
2. Chiara Sicuri, Giuseppe Porcellini, Giovanni Merolla; Robotics in shoulder rehabilitation; Muscles, Ligaments and Tendons Journal 2014; 4: 207-213.
3. Domien Gijbels, Ilse Lamers, Lore Kerkhofs, Geert Alders, Els Knippenberg, Peter Feys; The Armeo Spring as training tool to improve upper limb functionality in multiple sclerosis: a pilot study; Journal of Neuro Engineering and Rehabilitation 2011, 8:5
4. James Cannan and Huosheng Hu, Upper Body Rehabilitation A Survey; University of Essex, Colchester CO4 3SQ, U.K; ISSN 1744-8050; 2012
5. W. Nunes, L. Rodriguez and L. Oliveira; Cable based parallel manipulator for rehabilitation of shoulder and elbow movements; IEEE Int Conf Rehabil Robot; 2011.
6. Bas Habets, J. Bart Staal, Marsha Tijssen and Robert van Cingel; Intrarater reliability of the Humac NORM isokinetic dynamometer for strength measurements of the knee and shoulder muscles; Res Notes (2018) 11:15.
7. Kesner, S., Jentof, L., Hammond III, F., Howe, R., & Popovic, M.; Design Considerations for an Active Soft Orthotic System for Shoulder Rehabilitation; 33rd Annual International Conference of the IEEE Engineering in Medicine and Biology Society (EMBC); 2011
8. Ciarán T. O'Neill, Nathan S. Phipps, Leonardo Cappello, Sabrina Paganoni and Conor J. Walsh; A Soft Wearable Robot for the Shoulder: Design, Characterization, and Preliminary Testing; IEEE Int Conf Reh. Robot. 2017.
9. Ignacio Galiana, Frank L. Hammond, Robert D. Howe, and Marko B. Popovic; Wearable Soft Robotic Device for Post-Stroke Shoulder Rehabilitation: Identifying Misalignments; 2012 IEEE/RSJ International Conference on Intelligent Robots and Systems October 7-12, 2012. Vilamoura, Algarve, Portugal.
10. Rodrigo Gonçalves Cerejo Antunes; A Robotic System for Musculoskeletal Rehabilitation of the Shoulder; Biomedical Engineering - U de Lisboa; 2016.
11. Tobias Nef, Marco Guidali and Robert Riener; ARMin III – arm therapy exoskeleton with an ergonomic shoulder actuation; Applied Bionics and Biomechanics Vol. 6, No. 2, June 2009, 127–142.
12. Bongsu Kim and Ashish D Deshpande; An upper-body rehabilitation exoskeleton Harmony with an anatomical shoulder mechanism: Design,

modeling, control, and performance evaluation; The International Journal of Robotics Research; 1–22, 2017.

13. Justin Hunt, Hyunglae Lee, Panagiotis Artemiadis; A Novel Shoulder Exoskeleton Robot Using Parallel Actuation and a Passive Slip Interface; Journal of Mechanisms and Robotics; 2017

ASSISTIVE WHEELCHAIR CASTER UNIT
- IMPROVEMENT OF STEP DETECTION METHOD -

S. YOKOTA*, A. MATSUMOTO*,

*Department of Mechanical Eng., Toyo University,
Kawagoe, Saitama 359-8585, Japan
E-mail: s-yokota@toyo.jp, akihiro@toyo.jp

D. CHUGO** and H. HASHIMOTO***

**Kwansei Gakuin University,
Sanda, Hyogo 669-1337, Japan, E-mail:chugo@kwansei.ac.jp
***Advanced Institute of Industrial Technology,
Shinagawa-ku, Tokyo 140-0011, Japan, E-mail: hashimoto@aiit.ac.jp

The purpose of this research is to develop the assistive caster unit of manual wheelchair for step climbing. This unit is easily replaced with the conventional caster, only a spanner is needed. In addition this caster is simple mechanism, and the power source is only a 006P battery, there is no microcontroller. For realizing this simplicity, The proposed caster unit has two functions to assist the step climbing. One is the assistive plates to enlarge the caster radius imaginarily in the confined front area of the wheelchair, and to enable to climb a higher step. The other is the lock function to fix the caster's swiveling, which realize easy climbing with oblique approach. The lock-function is activated by the detection of the step, and mechanically fixes the caster's swiveling. We have developed some prototypes of this caster unit, so far. However, the problem is still remained in the step detection method being the trigger of activation of the lock function. Therefore, this paper proposes the improved activation method by detecting the step at an instant of touching it.

Keywords: mobility assistance; mechanism; wheelchair; step-climbing

1. Introduction

The purpose of this research is to develop the assistive caster unit of manual wheelchair for step climbing. This caster unit provides easy step-climbing not only frontal approach but also oblique approach by simple mechanism and a small battery 006P without any microcontrollers. In addition, this unit is easily replaced with the conventional caster, only a spanner is needed.

There is uneven terrain as one of the mobility barriers for wheelchair

users, such as steps and stairs. Even a small and slight single step, it becomes a big barrier for mobility of wheelchair users. In order to climb up or passing over a step, the user is required strong arm muscle and technique for wheelie. In addition, in case of oblique step climbing, the more arm muscle is needed. Therefore, the assistive apparatus for step climbing is required.

Based on the above, there are several assistive apparatuses for step climbing[1].[2] Auxiliary step-climbing mechanism[3] being composed by the omnidirectional wheel and auxiliary device were developed. Hinged Caster mechanism[4] was also developed. These systems showed the good results and improved step climbing performance. However, there are remained problem, in terms of the practical use. The mechanism[3] uses omnidirectional wheel, and the hinged caster[4] needs some modifications to the main frame of wheelchair. Moreover, no assistive casters have been developed for oblique step climbing.

On the basis of above, this research develops the assistive caster unit for manual driven wheelchair. This caster unit provides easy step-climbing including oblique approach, namely, driving torque for step climbing can be reduced comparing with conventional caster not only frontal climbing but also oblique climbing. We have developed several prototypes, so far. The first prototype confirmed the effectiveness of above mentioned two functions.[5] The first prototype used the electromagnetic tooth clutch for configuring lock function. As a result, it needed a large battery and was heavy weight. Thus, the 2nd prototype improved this problem.[6] In the 2nd prototype, a solenoid, rack and pinion gear comprised the lock function. Therefore, it could reduce its weight and the battery voltage and capacity. However, the problem is remained in the step detection method which is the trigger of activation of the lock function. Therefore, this paper proposes the improved activation method by detecting the step at an instant of touching it.

2. Outline of the assistive caster unit by reviewing 2nd prototype

The problems in case of step-climbing are following two points.

Problem 1)   The climb-able step height is physically limited by the radius of wheel

Problem 2)   In the oblique step-climbing, the driving force is divided, because the caster swivels when the caster faces the step.

Problem 1) is that: Generally, the climb-able step height is less than 1/3 of a wheel diameter. Thus the large wheel is suited for step-climbing. However, the cater wheel cannot be enlarged, because the attaching portion of it is confined by main frame and footrest of a wheelchair. Thus, diameter of conventional wheelchair is about 100 - 150 mm. As a result, even a small step (30-40 mm height), users need much power, and have to change the center of weight of his/her body to take a wheelie state.
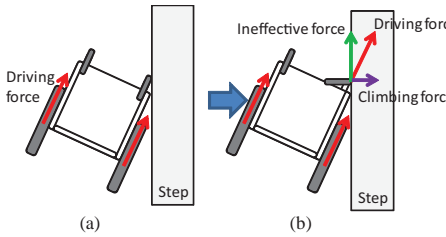
Fig. 1. Driving force in case of oblique approach to a step
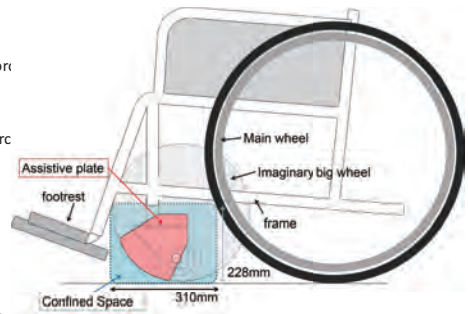
Fig. 2. Assistive plate makes imaginary big caster in the confined space

Problem 2) is that: In case of oblique step climbing (Fig.1(a)), the caster swivels due to the caster dynamics(Fig.1(b)). For this swiveling, driving force being generated by the user is divided into two directions: "moving direction (parallel direction to the step)" and "right direction to the step". The only the force of "right direction" is effective for step climbing. The force "moving direction" is not used, namely the user's force is exhausted. Therefore it is difficult to climb a step obliquely or much power is required(Fig.1(b)).

In order to solve these problems, we have proposed following two functions.

The assistive enlarge the radius of caster wheel as much as possible in the confined space shown in Fig. 2.

Lock-function fix the caster's swiveling in case of oblique step climbing.

Figure 3[6] shows the 2nd prototype having these two functions. The black plates in both sides are the assistive plates. This plate has an equivalent climbing ability to big wheel in confined attachment space. Figure 6 shows
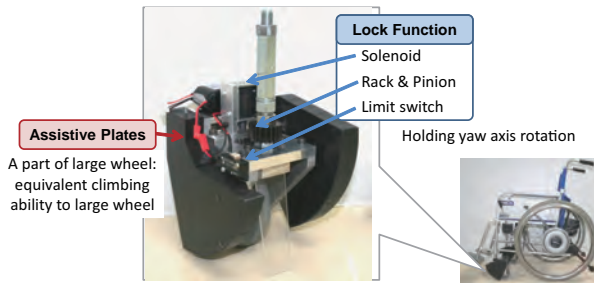
Fig. 3.   Assistive Wheelchair Caster Unit (2nd prototype)

the movement of assistive plates. After the plates touch the step, they rotate, and the caster unit climb the step.
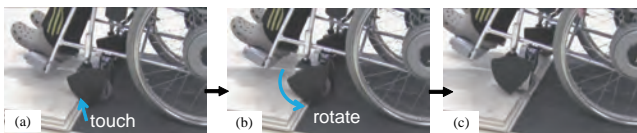
Fig. 4.   Movement of the assistive plates

The lock function is the portion consisting of a solenoid, a limit switch and rack & pinion gears. It holds the caster's swiveling, and assists the oblique step climbing. Figure 5 shows the movement of the lock function. First, (1)After the assistive plates touch the step, they rotates, and step climbing begins. (2) The limit switch detects the rotation of the assistive plates, and (3) current flows into solenoid. (4)The solenoid is activated, and pulls up the rack gear, and then (5) the pinion gear and rack gear are engaged. (6) Finally, the caster's swiveling is fixed.

The performance of this prototype was tested by the experiment.[7] In the experiment, the load cell was sandwiched between main wheel and the hand rim, and the strain was used as the index of user's driving force.

First, the efficiency of assistive plates was tested. The strain at the load cell was measured at the step height of 20, 30, 40 mm in both cases: with assistive plates and without assistive plates. The results are summarized in Table 1. In the table, "X" indicates that the step climbing was failed. The table shows that the asssitive plates could reduce the driving force in all step height.
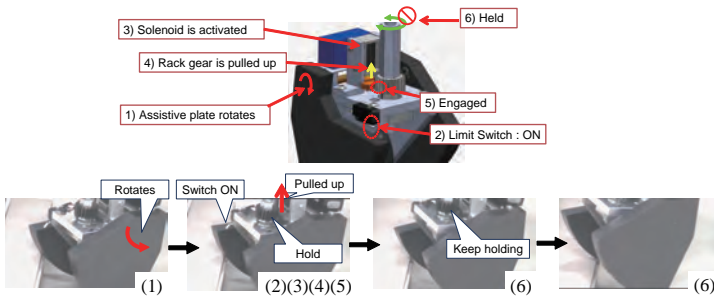
Fig. 5.   Movement of the Lock function

Table 1. Maximum strain [10^{-6}] with/without assistive plates (approach angle = 0 [rad])

Step height [mm]	Without Assistive plates	With Assistive plates
20	73.91	54.13
30	102.38	58.32
40	X	59.88

Table 2. Maximum strain[10^{-6}] with assitive plates, oblieque step climing at $\pi/4$ [rad]

Step height [mm]	Without Lock func.	With Lock func.
20	36.35	34.94
30	56.48	46.27
40	61.30	54.35

Next, the lock function was tested. The strain at the load cell was also measured in the cases: with lock function and without lock function. The result is shown in Table 2. The table shows that the lock function could reduce the users' driving force at the oblique step climbing.

Therefore, it is confirmed that the two functions of our prototype could assist step climbing by the simple mechanism.

3. Problem of 2nd Prototype

Basically the proposed two functions are effective for step climbing. However, in 2nd prototype, occasionally the lock function did not activate properly, and the caster's swiveling occurred when oblique climbing. The cause of this is that the prototype structurally can not instantaneously activate the lock function at the moment the caster unit touches the step. The rotation of the assistive plates were used to detect the step. The limit switch detects this rotation, and activates lock function. Rotating the assistive plates means that step climbing has already been started. Therefore, the problem has been remained that the caster can not be locked at the start

of climbing where the greatest user's force is required.
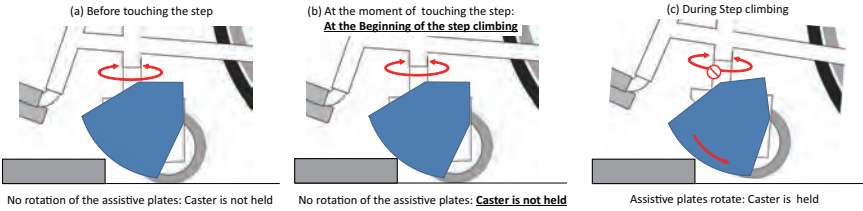
Fig. 6.   Problem of 2nd prototype: Step detection

4. Improvement

In order to solve the above mentioned problem, it is required not to detect the step by rotation of the assistive plate, but to detect the step at the moment the assistive plate touches the step. Therefore, we consider a mechanism for detecting whether or not the arc portion of the assistive plate touches the step. This mechanism realizes instantaneous activation of the lock function at the moment the caster unit touches the step. This detection needs to detect only the contact between the assistive plates and the step, and it is not necessary to detect the contact position on the arc portion of the assistive plates. In order to meet this requirement and easily detect the step, We consider the tape switch (141 - BPH, Tape Switch Japan Co., Ltd.) to be placed on the arc of the assistive plate (Fig. 7).
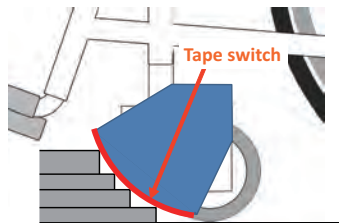
Fig. 7.   Attaching portion of the tape swiche

The 3rd prototypewas made shown in Fig. 8). Parts of the 2nd prototype

were diverted and the tape switch was affixed to the circular arc portion of the assistive plates.

Experiments were conducted to confirm the superiority of step climbing by this new step detection method. In the experiments, the forces required to oblique step climbing were measured by using a force gauge in both cases of 2nd and 3rd prototype. The height of the step was set to 40 mm, and the oblique approach angle was set to $\theta = \pi/3$ [rad]. Under these conditions, the measurements were made ten times using 2nd and 3re prototype, respectively.

The result is shown in Fig. 9. From this result, it can be seen that the proposed new prototype (3re Ver.) has a smaller driving force. Therefore, by locking the caster's swiveling simultaneously with the contact of the step, it can be said that the caster's swiveling was locked before the step climbing and the driving force of user could be reduced.

From the above, by improving the step detection method, the delay of the lock function was gotten rid of, the driving force could be reduced.
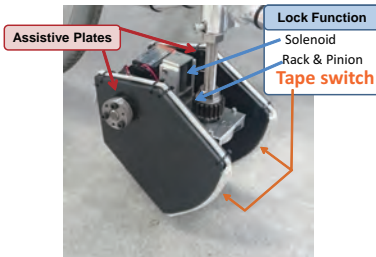
Fig. 8.   Overview of the 3rd prototype
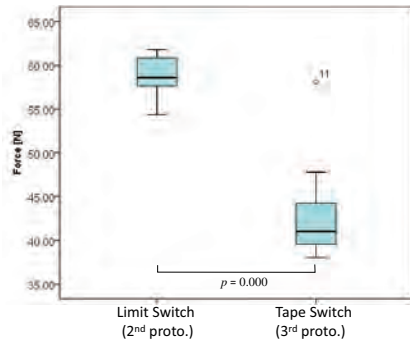
Fig. 9.   Result of the force of step climbing

5. Conclusion

This research develops the assistive caster unit for manual driven wheelchair. This caster unit provides easy step-climbing including oblique approach.This caster unit has two key functions. One is the assistive plates to enlarge the caster radius imaginarily in the confined front area of the wheelchair, and to enable to climb a higher step. The other is the lock-function to fix the swiveling, which realize easy climbing with oblique ap-

proach. The lock-function is activated by the detection of the step, and mechanically fixes the swiveling of the caster. We have developed some prototypes of this caster unit, so far. However, the problem was still remained in the step detection method being the trigger of activation of the lock-function. Therefore, this paper proposed the improved activation method of lock function by detecting the step at the moment of touching it.

The improved method was to attach the tape switch on the circular arc portion of assistive plate as a new step detection method. The experimental result showed that the caster's swiveling was locked before the step climbing and the driving force of user could be reduced by locking the caster's swiveling simultaneously with the contact of the step. Therefore, the delay of the lock function was gotten rid of, the driving force could be reduced by improving the step detection method.

References

1. Y. Sugahara, N. Yonezawa and K. Kosuge, A novel stair-climbing wheelchair with transformable wheeled four-bar linkages, in *Proc. of the 2010 IEEE/RSJ International Conference on Intelligent Robots and Systems (IROS 2010)*, (Taipei, Taiwan, 2010).
2. S. Yu, T. Wang, X. Li, C. Yao, Z. Wang and D. Zhi, Configuration and tip-over stability analysis for stair-climbing of a new-style wheelchair robot, in *Proc. of the 2010 IEEE International Conference on Mechatronics and Automation (ICMA 2010)*, (Xi'an, China, 2010).
3. T. Hayashi, S. Kawakami, H. Matsuo and M. Yuinamochi, A study on a multifunction wheelchair with auxiliary step-climbing mechanism, in *JSME Proceedings of the Welfare Engineering Symposium 2003*, (Tokyo, Japan, 2003).
4. T. Ohmura, T. Iwamoto and K. Shibuya, Step traveling of wheel chair with hinged caster mount, in *Proc. of the 2006 JSME conference on Robotics and Mechatronics*, (Tokyo, Japan, 2006).
5. S. Yokota, T. Ito, T. Yamaguchi, D. Chugo and H. Hashimoto, An assistive wheelchair caster unit for step climbing, in *Proc. of the 37th Annual Conference of the IEEE Industrial Electronics Society (IECON 2011)*, (Beijing, China, 2011).
6. S. Yokota, H. Hashimoto, D. Chugo and K. Kawabata, Improvement of assistive wheelchair caster unit for step climbing, in *Proc. of the 21st IEEE International Symposium on Robot and Human Interactive Communication Ro-Man 2012*, (Paris, France, 2012).
7. S. Yokota, D. Chugo, H. Hashimoto and K. Kawabata, *Journal of Mechanical Engineering and Automation* **3**, 38 (2013).

STANDING ASSISTANCE THAT CONSIDERS USER POSTURE TOLERANCE

M.YOKOTA*, S. KAWAZOE*, D. CHUGO*

*Graduate School of Science and Technology, Kwansei Gakuin University,
Sanda, Hyogo, Japan
E-mail: {yokota, kawazoe, chugo}@chugolab.com
www.chugolab.com

S. YOKOTA** and H. HASHIMOTO***

**Toyo University
Kawagoe, Saitama, Japan
***Advanced Institute of Industrial Technology
Shinagawa, Tokyo, Japan

This paper proposes a novel standing assistance robot, which considers the posture tolerance of its user. In previous studies, conventional assistive robots did not require patients to use their own physical strength to stand, which leads to decreased strength in the elderly. Therefore, an assistive robot that allows patients to maximally use the physical strength they possess is required. To realize this objective, it is important that a robot assists patients according to their body movement and by their intentions. However, in previous studies, general assistive robots helped patients by using a fixed motion reference pathway in spite of their original intention, and as a result, these robots failed to use the physical strength of the patients. Therefore, we propose a novel standing assistance robot, which allows its user to move their body within a prescribed degree of posture tolerance during the process of moving from a sitting to a standing position. Our key findings cover two fundamental research topics. One is the investigation into posture tolerance during a standing motion. The other topic is a novel assistance control algorithm that considers the investigated posture tolerance by combining position control and force control. A prototype assistive robot, based on the proposed idea was fabricated to help patients stand up safely using the maximum of their remaining physical strength.

Keywords: Standing Assistance; Posture Tolerance; Robotic Walker.

1. Introduction

Standing is one of the most serious and important activities in the day-to-day lives of elderly people, as they may lack physical strength and stability[1].[2] In a typically bad case, an elderly person who does not have enough

physical strength will not be able to stand up and may then be restricted to life in a wheelchair life or become bedridden.[3] Furthermore, once an elderly person falls into such lifestyle, the decrease in their physical strength becomes more pronounced due to the lack of exercise and the associated limited use of their own physical strength.[4] Therefore, assistive robots are required to aid patients in the use of their remaining strength during the standing motion in order to maintain their muscular strength.

To realize this objective, assistive robots should be designed to accept some variance in the patient's body motion because human motion does not always fit an established reference path. Despite this, there have been many reports of robots, which assist patients according to a fixed reference path and do not consider the variations in body motion.[56] During standing, these robots interfered with the body motion of the patient, adjusting it to fit the reference path. This external intervention prevents patients from using their own physical strength during the process of standing up and therefore reduces their muscular strength.

Previously, we have developed robotic walkers which have a standing assistance function,[789] and Fig. 1 shows our recent latest prototype.[9] The robotic walker consists of a powered walker and a standing support manipulator with armrests, which moves the patient in an upward direction so as to be lifted. Wheel actuators on the powered walker stabilize the patient, and are also used for lifting the patient up. Our prototype succeeded to assist the patient in a way that enabled them to use their remaining physical strength as seen in Fig.1(b). However, this prototype did not consider the range in movement of the patient's body during standing up, and as a result, if the patient's motion does not fit the designed standing motion pathway, the prototype cannot make use of the remaining physical strength of the patient, as seen in Fig.1(c).

(a) prototype   (b) success to assist   (c) failure to assist
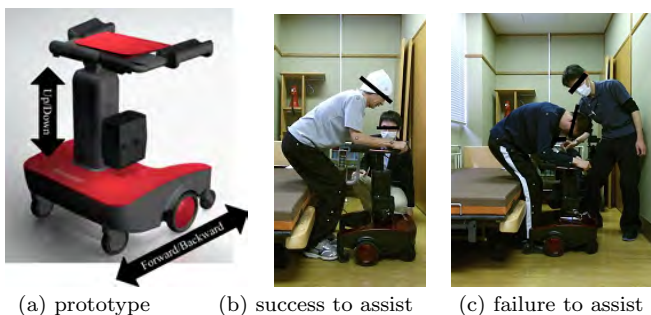
Fig. 1.   Our prototype which assists a patient who requires daily care.

Therefore, in this study, we propose a novel standing assistance robot, which considers the variation in the range of movements of a patient's body when rising from a sitting to a standing position. To achieve this objective, we initially investigated the posture tolerance during the process of standing up. In this range, patients can stand up, stably and safely, using their own physical strength. Secondly, we extend a published assistance algorithm,[8] which combines position control and force control, to adapt to the parameters of the prior investigation into posture tolerance. Using the proposed algorithm, our robotic device only assists them to stand up when necessary; maximizing their muscle exercise.

2. Posture Tolerance

2.1. *Required Condition*

From the viewpoint of body dynamics, the standing posture should be fulfilled by two conditions.

- Stability condition: The patient should be able to keep their body balanced in this posture. This study defines the condition as follows: the position of the center of gravity (COG) should be located within the range of the patients footprint, while keeping the body balanced during standing up.[7]
- Muscle condition: The patient should be able to control their body motion in this posture. In general, the output force generated by muscles, changes according to the human posture because the positional relationship between the muscles and bones changes with the adopted posture.[8] This means an unsuitable posture cannot generate a sufficient upper direction output force for proceeding through with the standing motion. This study defines this condition as follows: the output force of the muscles listed in Fig.2 should not exceed the muscle's maximum output during standing.

This paper investigates the tolerance level, which fulfills these two conditions through computer simulation studies using OpenSim, a human motion dynamics simulator package. In this simulation, we used a 3DGait-Model2392[10] as human model and modified its body parameters to fit a typical Japanese elderly person.[11] The standing motion was based on the references recommended by nursing specialists[8] as shown in Fig.3(b). In Fig.3(b), the Y-axis shows the angular values of the pelvis and trunk, knee and ankle, whereas the X-axis shows the movement pattern,[7] which is the ratio of the standing motion, as shown by (1).

(a) muscles (b) coordination
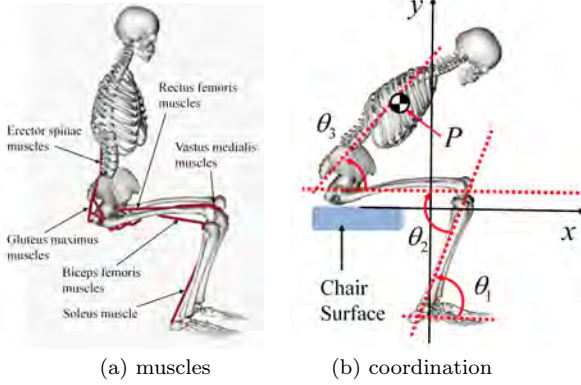
Fig. 2.   Human model

$$\hat{s} = t/t_s \tag{1}$$

In equation 1 (1), t_s is the time required for completion of the standing-up operation and t is the present time. Generally, the standing motion consists of three phases, as shown in Fig.3(a). Thus, we set a variation of $\pm 30[deg]$ range on the reference posture at the end of each phase (Postures (A)-(C)) in the computer simulation. Note posture (D) is the final posture and therefore we did not set a variation on this phase.

(a) standing phases (b) references
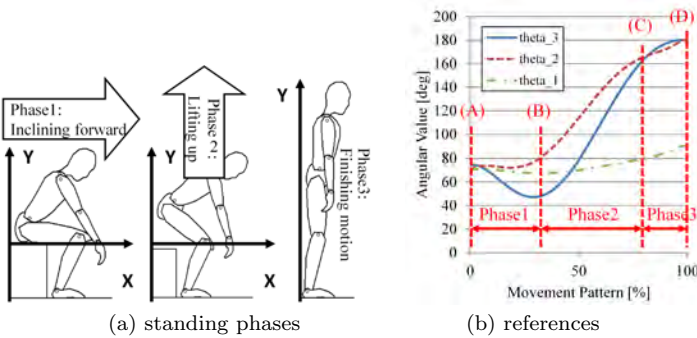
Fig. 3.   Simulation setup

2.2. *Body Motion Tolerance*

Fig.4 shows the acceptable position of point P, identified in Fig.2(b), derived from the computer simulation. The standing motion will be realized within the tolerance shown in Fig.4(a) and in this range of motion, the patient can physically achieve final standing posture.

Fig.4(b) shows the acceptable tolerance at 70[%] movement during the pattern of the standing motion. Muscle condition determines the stability condition in Fig.4(b), and from this result, it is important to consider the patient's capable muscle output force in the standing posture.
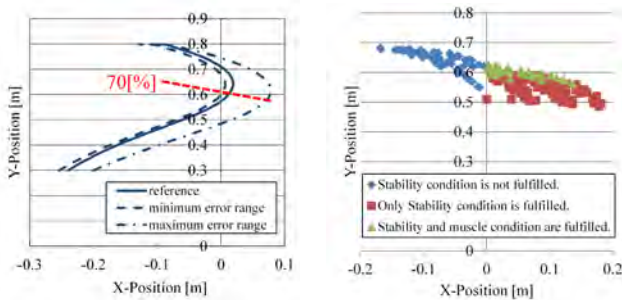
(a) Investigated tolerance   (b) Tolerance at 70[%] movement pattern

Fig. 4. Simulation Results

3. Assistance Control Algorithm

To allow patients to use their remaining physical strength during standing up, our controller uses a combination of damping control and position control. Damping control can change the strength of assistive power, thus, it can determine how strong it applies assistance force to reduce load or use their remaining physical strength. Furthermore it allows for an offset from the reference pathway of motion, allowing the patient to move freely during the standing up process. Considering these characteristics, damping control should be used in the tolerance discussed in section two. By contrast, position control is useful for maintaining body posture, however, its pathway is fixed and so does not consider the physical strength of the patient. Thus, it is useful when the patient's posture exceeds the acceptable range.

In our previous work,[8] we proposed an assistance control algorithm based on the voluntary movement of the patient. We know from previous research[12] that the motion of the human body consists of voluntary movements, which generate the total body motion, and a posture adjustment

action, which keeps the body stable during motion. This means the robot should only provide a force that assists the physical activity in response to the voluntary movement of the patient, and our proposed algorithm only assisted the patient when physical strength was required for doing a voluntary movement. However, the previously reported algorithm did not consider the variation in the range of movements during human motion, so this paper extends this control algorithm as follows:

- First, we defined the body movement vector $\mathbf{P}$ as (2). This shows the velocity direction of point P (Fig.2(b)), which is the COG of the upper body. The position of P $\left(x_p^{ref}, y_p^{ref}\right)$ is a motion reference point based on the standing motion recommended by nursing specialists. Details regarding the generation of this reference point are given in our previous paper.[8]

$$
\begin{aligned}
\mathbf{P} &= \mathbf{v}_p^{ref}\left(\hat{s}\right), \\
\mathbf{v}_p^{ref} &= \left|\begin{array}{c}\dot{\mathbf{x}}_p^{ref} \\ \dot{\mathbf{y}}_p^{ref}\end{array}\right|^T = \left|\begin{array}{c}\dot{x}_p^{ref}(0),\cdots,\dot{x}_p^{ref}(\hat{s}),\cdots,\dot{x}_p^{ref}(1) \\ \dot{y}_p^{ref}(0),\cdots,\dot{y}_p^{ref}(\hat{s}),\cdots,\dot{y}_p^{ref}(1)\end{array}\right|^T
\end{aligned} \quad (2)
$$

Furthermore, our robot has control references for each actuator as detailed in (3), which realize the designed standing motion (2). $\dot{\mathbf{x}}_{rbt}^{ref}$ is the motion reference for a powered walker and $\dot{\mathbf{y}}_{rbt}^{ref}$ is for a standing assistance manipulator.

$$
\mathbf{v}_{rbt}^{ref} = \left|\begin{array}{c}\dot{\mathbf{x}}_{rbt}^{ref} \\ \dot{\mathbf{y}}_{rbt}^{ref}\end{array}\right|^T = \left|\begin{array}{c}\dot{x}_{rbt}^{ref}(0),\cdots,\dot{x}_{rbt}^{ref}(\hat{s}),\cdots,\dot{x}_{rbt}^{ref}(1) \\ \dot{y}_{rbt}^{ref}(0),\cdots,\dot{y}_{rbt}^{ref}(\hat{s}),\cdots,\dot{y}_{rbt}^{ref}(1)\end{array}\right|^T \quad (3)
$$

- Second, we assumed the subject applies all forces $\mathbf{f}_{user}$ at position P because the armrest and the handle of our assistive robot are connected rigidly. We can calculate $\mathbf{f}_{user}$ from the force applied to the armrest $\mathbf{f}_{armrest}$ and the handle $\mathbf{f}_{handle}$ using force sensors in the robot's body (Fig.5(a)) as (4).

$$
\mathbf{f}_{user} = \mathbf{f}_{armrest} + \mathbf{f}_{handle} \quad (4)
$$

- Third, we assumed the patient also applies a force for doing a voluntary movement of their own intention, therefore $\mathbf{f}_{user}$ shows a voluntary component. At the same time, our controller calculates a motion reference $\mathbf{v}_p^{ref}$ at this posture (Fig.4(b)) and refers its investigated tolerance (gray area at Fig.4(b)). Our controller evaluates if $\mathbf{f}_{user}$ is within the tolerance at this posture, the patient's motion fulfills the both conditions as discussed in section two.

- Finally, our robot controls two actuators by (5).

$$
\begin{aligned}
v_{rbt}^{upref} &= \left| \begin{matrix} \dot{x}_{rbt}^{upref} \\ \dot{y}_{rbt}^{upref} \end{matrix} \right|^{T} \\
&= \left| \begin{matrix} \dot{x}_{rbt}^{ref} - \frac{B}{j}\left(f_{handle} - f_{handle0}\right) - K\left(x_{rbt} - x_{rbt}^{ref}\right) \\ \dot{y}_{rbt}^{ref} - B\left(f_{armrest} - f_{armrest0}\right) - K\left(y_{rbt} - y_{rbt}^{ref}\right) \end{matrix} \right|
\end{aligned}
\tag{5}
$$

where $\mathbf{v}_{rbt}^{upref}$ is the updated reference value that our robot actually uses for delivering standing assistance. (x_{rbt}, y_{rbt}) is the actual position of the powered walker and the standing assistance manipulator of our robot. B and K in (5) are constants used to coordinate the ratio between the damping and position controls. j is also a constant which reduces the damping control ratio of the powered walker because it does not reduce the patient's load, and on the other hand, it largely affects the body balance. $f_{handle0}$ and $f_{armrest0}$ are the forces the patient applies to the assistance system before he or she stands.

In order to apply the damping control only when the patient's motion fulfills both the stability condition and the muscle condition, the coefficient B that validates the damping control mode is calculated as (6). B will be larger value if $\mathbf{f}_{user}$ locates on the center of the tolerance and in this situation, it fits $\mathbf{v}_p^{ref}$.

$$
\begin{cases}
B = b\dfrac{\mathbf{v}_p^{ref} \cdot \mathbf{f}_{user}}{|\mathbf{v}_p^{ref}| \cdot |\mathbf{f}_{user}|} & (if\ conditions\ are\ fulfilled) \\
B = 0 & (if\ conditions\ are\ not\ fulfilled)
\end{cases}
\tag{6}
$$

By contrast, the position control is always useful because it helps the patient maintain a stable posture during motion. Therefore, we set the coefficient, K which validates the position control mode, to be constant. The values of b and K were determined experimentally. Using these ideas, our controller sets the ratio of the damping control mode to a larger value if the patient's trajectory fits the expected reference pathway. Thus, the patient can move freely as intended if their posture is not largely different from the reference posture.

4. Experiments

We implemented our proposed idea to the prototype (Fig. 1(a)) and conducted a practical experiment with it. To confirm the efficiency of our pro-
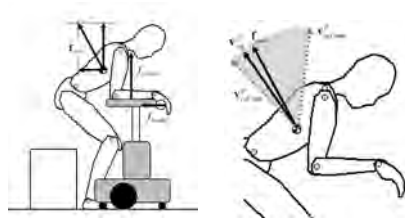
(a) Applied force and body movement vector   (b) Body motion and its range

Fig. 5. Voluntary movement during standing

posed assistance control scheme, we tested three cases.

- Case1: Using only position control, without our proposed idea.
- Case2: Using our proposed idea (Fig. 6(a)).
- Case3: The same as case 2, but in this case, the subject tries to move in a forward direction away from the designed standing motion reference pathway (Fig. 6(b)).

We used five subjects and each subject attempted all three cases, five times each. All subjects were young students who wore special equipment to mimic the experience of the elderly,[13] limiting the testers body motions.

As seen in Fig. 6, our prototype succeeds to assist the standing motion even if the subject does not fit the reference pathway.

(a) Subject A, Case2   (b) Subject B, Case3

Fig. 6. Standing motion achieved using our proposed idea

Fig. 7(a) shows the variation in position of point P of subject A and Fig. 7(b) shows the electromyography (EMG) of the biceps femoris muscle that has been normalized by the maximum voluntary contraction. In case 1, the subject's position fits the reference trajectory and this means our robot does not allow the patient to move freely as intended. As a result, the robot applies all required force for standing up to the subject and the subject is not require to use their own physical strength, as Fig. 7(b).

On the other hand, in case 2, the subject's position does not fit the reference trajectory but is within the investigated tolerance range. This mean our robot evaluates that the patient's motion fulfills both the stability and muscle conditions, and accepts the body motion of the patient even though it does not fit the reference pathway. As the result, the robot does not apply any unnecessary assistive force and succeeds in allowing the subject to use their remaining physical strength during the process of standing up.

In case 3, once again the subject's position does not fit the reference trajectory and the subject tries to exceed the margin of tolerance. At points when the subject moves within the tolerance range, our robot assists the patient in the same manner as in case 2. However, as seen by the dashed circle in Fig. 7(a), when the subject's position exceeds the tolerance trajectory and the patient's motion does not fulfill both the stability and muscle conditions, our robot changes the level of assistance control and as a result, the subject's position is returned to within the tolerance range. Furthermore, even in case 3, our robot allows the subject to use their own physical strength, in contrast to case 1.

According to these results, our robot succeeds to provide assistance to subjects while also allowing them to use their own physical strength. Moreover our robot maintains the body balance during the standing up process and our idea realizes a safe method of robotic assistance.

(a) P position (Subject A)   (b) Maximum EMG during standing
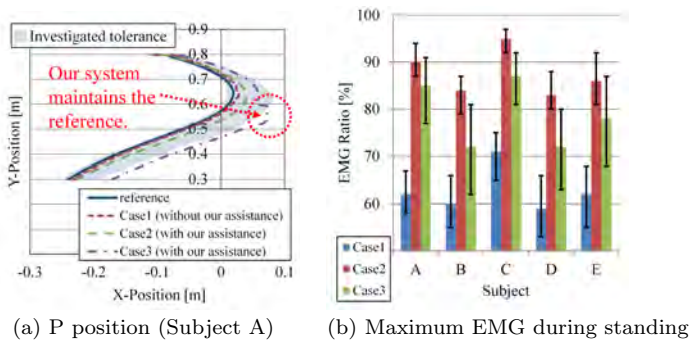
Fig. 7.   Experimental results

5. Conclusion

This paper proposes a novel standing assistance device, which allows patients to maximize the use of their physical strength. To realize this, we investigated the motion tolerance of the standing posture, which fulfills

both body balance and muscle force conditions. Furthermore, we proposed a novel assistance control, which maintains body stability whilst using physical strength. We conducted practical experiments to confirm the efficiency of the proposed idea implemented in our prototype of a robotic standing assistance device.

Acknowledgments

References

1. N. B. Alexander, A. B. Schultz and D. N. Warwick, *J. of Geometry: MEDICAL SCIENCES* **46**, M91 (1991).
2. M. A. Hughes and M. L. Schenkman, *J. of Rehabilitation Research and Development* **133**, 409 (1996).
3. C. Office, *KOUREISHA HAKUSHO (The whitepaper on the aged society, written in Japanese)* (Government of Japan, 2011).
4. M. Hirvensalo, T. Rantanen and E. Heikkinen, *J. of the American Geriatric Society* **48**, 493 (2000).
5. K. Nagai, I. Nakanishi and H. Hanabusa, Assistance of self-transfer of patients using a power-assisting device, in *Proc. IEEE/RAS-EMBS Int. Conf. on Robotics and Automation (ICRA'03)*, (Taipei, Taiwan, 2003).
6. A. Funakubo, H. Tanishiro and Y. Fukui, *J. of the Society of Instrument and Control Engineers* **40**, 391 (2001).
7. T. Yamada, M. Sakaguchi, D. Chugo, S. Yokota and H. Hashimoto, A load estimation of a patient considering with a posture during standing motion, in *Proc. Int. Conf. on Climbing and Walking Robots (CLAWAR'14)*, (Poznan, Poland, 2014).
8. D. Chugo, S. Muramatsu, S. Yokota and H. Hashimoto, A standing assistance for both voluntary movement and postural adjustment, in *Proc. Int. Conf. on Climbing and Walking Robots (CLAWAR'16)*, (London, UK, 2016).
9. S. Kawazoe, D. Chugo, S. Muramatsu, S. Yokota, H. Hashimoto, T. Katayama, Y. Mizuta and A. Koujina, Pattern based standing assistance for a low level of care, in *Proc. Int. Conf. on Climbing and Walking Robots (CLAWAR'17)*, (Porto, Portugal, 2017).
10. Opensim documentation gait 2392 and 2354 models (2018), `https://simtk-confluence.stanford.edu/display/OpenSim/Gait+2392+and+2354+Models`.
11. H. Okada, M. Ae, N. Fujii and Y. Morioka, *Biomechanisms* **13**, 125 (1996).
12. T. Ito, T. Azuma and N. Yamashita, *Europian J. of Applied Physiology* **92**, 186 (2004).
13. K. Takeya, Y. Kanemitsu and Y. Futoyu, *Kawasaki Medical Welfare J.* **11**, 64 (2001).

KINETIC ANALYSIS OF AN ANKLE REHABILITATOR COMPOSED OF TWO PARALLEL DELTA ROBOTS.

MIGUEL PÉREZ BAYAS
Escuela Superior Politécnica de Chimborazo
perezmiguel3877@gmail.com
Riobamba - Ecuador

GEOVANNY NOVILLO ANDRADE
Escuela Superior Politécnica de Chimborazo
gnovillo@espoch.edu.ec
Riobamba – Ecuador

SÓCRATES MIGUEL AQUINO ARROBA
Escuela Superior Politécnica de Chimborazo
saquino@espoch.edu.ec
Riobamba – Ecuador

JAVIER GAVILANES CARRIÓN
Escuela Superior Politécnica de Chimborazo
javier.gavilanes@espoch.edu.ec
Riobamba - Ecuador

The present research shows the kinetic analysis of an ankle rehabilitator, the rehabilitation mechanism consists of a fixed platform in which there are two inverted delta robots linked a mobile platform, actuators are controlled by servomotors which provide six basic movements of ankle rehabilitation like dorsiflexion, plantar flexion, inversion, eversion, abduction and adduction, which was verified through a motion study and singularity analysis. The design of the rehabilitator is based on the establishment of a methodology that allows the development of a machine that achieves all the ergonomic, technological and quality requirements, using tools of computational mechanics that allowed generating a virtual model able to generate the required movements and supporting the mechanical stress generated. The mechanism was modeled in CAD software such as SolidWorks, with the virtual model is possible to analyze the inverse and direct kinematics determining the position and speed of the joints, for the selection of the servomotors the dynamic analysis was made, obtaining the accelerations, forces and torques using the MSC Adams software. For the analysis of deformations, normal stresses and shear forces, the CAE software such as ANSYS was used, which works on the basis of the finite element method, with its

Workbench platform and its structural analysis module. Finally, the machine was built using 3D printing and performance tests were carried out.

1. Robotic rehabilitation

1.1. *Introduction*

The Lower limbs injuries and the ankle injuries are very frequent so they require highly qualified professionals for the rehabilitation process, making it necessary to develop machines that help the rehabilitation processes quickly and without risk to cause harm to the patient.

By designing a system of inverted delta robots we can solve problems such as: efficiency in ankle rehabilitation, prolonged ankle rehabilitation without fatigue of the rehabilitator, suppling the demand of people that need of rehabilitation of the ankle and giving solution to athletes who usually suffer the ankle injuries and they need rehabilitation therapies.

In the rehabilitation of the ankle, unique movements are generated, these movements describe the rehabilitation process of the ankle with mobility ranges, and these movements are described below:

Dorsiflexion, plantar flexion, inversion, eversion, abduction / external rotation, adduction / internal rotation, these rehabilitation movements are shown in Figure 1 [13].
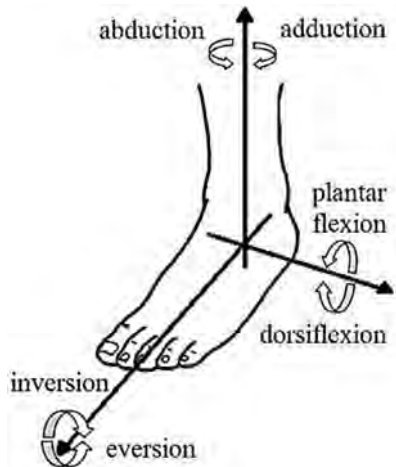
Figure 1. Ankle movements for rehabilitation process.

Figure 1 shows the movements of ankle rehabilitation, these movements have permissible ranges, Table 1 shows the movements with the necessary ranges for

a correct rehabilitation process without causing harm to the patient, and the design of the robot for rehabilitation is based on the permissible ranges shown in Table1.

Table 1. Range of movements for ankle rehabilitation

KIND OF MOVEMENT	MAXIMUM ALLOWABLE MOVEMENT
Dorsiflexion	20,3°-29,8°
Plantar flexion	37,6°-45,8°
Inversion	14,5°-22,0°
Eversion	10,0°-17,0°
Abduction/external rotation	15,4°-25,9°
Adduction/internal rotation	22,0°-36,0°

A parallel robot is composed of a final effector with n degrees of freedom and a fixed base, joined together by at least two independent kinematic chains. The robot is driven by n simple actuators [9]. Currently the development and applications of delta robots has been very different, due to its speed and precision being widely used in selection processes, 3D printers, etc.
.

1.2. *Design*

The design methodology includes the design procedures to get the proposed objective [5], [6], [11] and [12]. Figure 3 shows the following stages to get a robotic rehabilitator prototype: preliminary studies, conceptual design, specification design and materialization design.
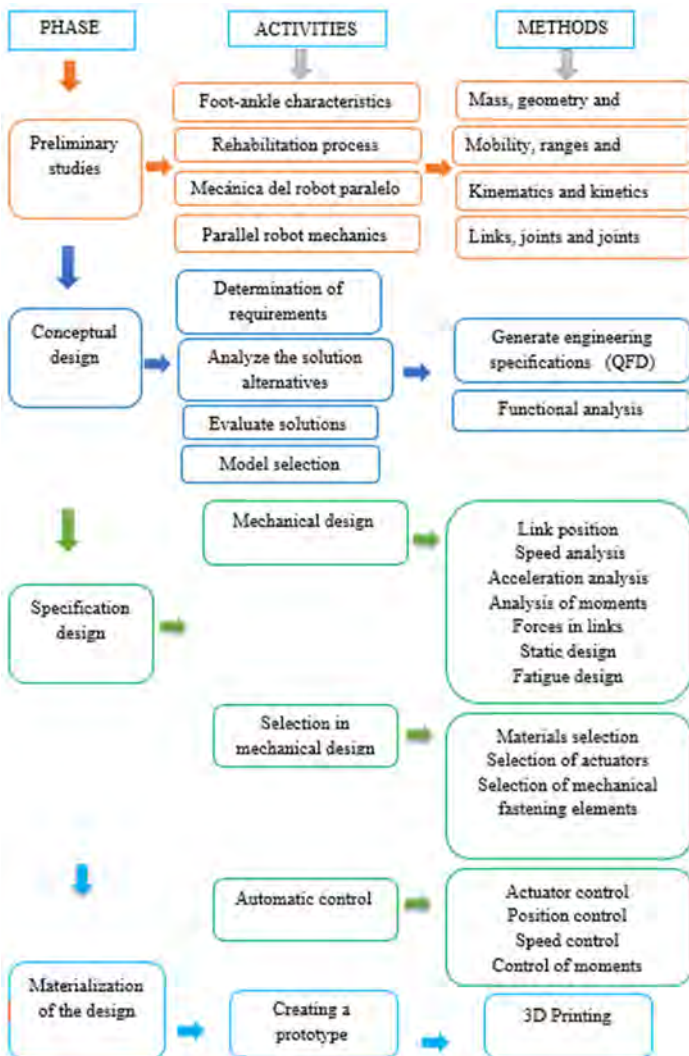
Figure 3. Proposed methodology.

Based in data from Table 1 the prototype allows to reach the movement for ankle rehabilitation.

- The dorsiflexion movement reaches 25º of inclination of the platform.
- The plantar flexion movement reaches 45.8 of inclination of the platform.
- The investment movement reaches 19.5º of inclination of the platform.
- The eversion movement reaches 15º inclination of the platform.
- The abduction movement reaches 22º of inclination of the platform.

- The adduction movement reaches 30.06 ° of inclination of the platform, Figure 4 shows this position.
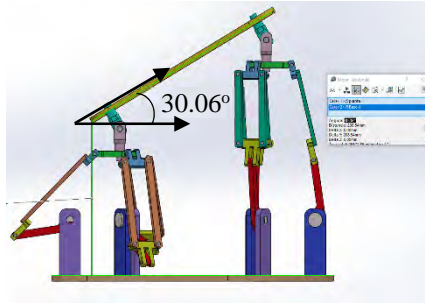
Figure 4. Maximum angle reached in plantar adduction movement by the robot

Cinematic Analysis

The resolution of the direct kinematic problem allows knowing which is the position (x, y, and z) and orientation (θ, $\emptyset$ and φ) adopted by the effector of the robot when each of the variables that limit the orientation of its joints takes determined values, so that to solve a direct kinematic problem it will be given by the relations of position and speed:

$$x = f_x(q_1, q_2, q_3, q_4, q_5, q_6) \quad (1)$$
$$y = f_y(q_1, q_2, q_3, q_4, q_5, q_6) \quad (2)$$

$$z = f_z(q_1, q_2, q_3, q_4, q_5, q_6) \quad (3)$$
$$\emptyset = f_\alpha(q_1, q_2, q_3, q_4, q_5, q_6) \quad (4)$$

$$\theta = f_\beta(q_1, q_2, q_3, q_4, q_5, q_6) \quad (5)$$
$$\varphi = f_\gamma(q_1, q_2, q_3, q_4, q_5, q_6) \quad (6)$$

$$\dot{x} = \sum_1^n \frac{\partial f_x}{\partial q_i} \dot{q}_i \quad (7)$$
$$\dot{y} = \sum_1^n \frac{\partial f_y}{\partial q_i} \dot{q}_i \quad (8)$$

$$\dot{z} = \sum_1^n \frac{\partial f_z}{\partial q_i} \dot{q}_i \quad (9)$$
$$\dot{\emptyset} = \sum_1^n \frac{\partial f_\emptyset}{\partial q_i} \dot{q}_i \quad (10)$$

$$\dot{\theta} = \sum_1^n \frac{\partial f_\theta}{\partial q_i} \dot{q}_i \quad (11)$$
$$\dot{\varphi} = \sum_1^n \frac{\partial f_\varphi}{\partial q_i} \dot{q}_i \quad (12)$$

Based on the equations shown, Figure 5 shows the complete kinematic analysis of all the actuators based on the position of the final effector generated by MSC Adams.
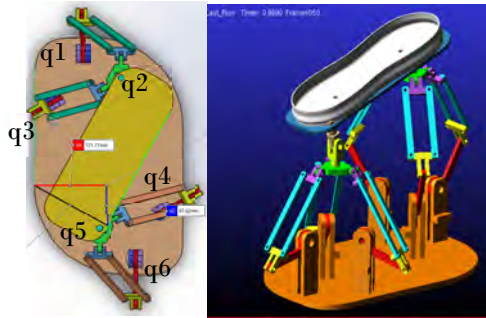
Figure 5. Kinematic analysis based on the position of the final effector generated by MSC Adams.

The kinematic analysis of the delta parallel robot allows demonstrating all the ranges of movement required in the ankle rehabilitation, besides the speeds and accelerations are within the permissible range provided by specialists in ankle rehabilitation.

Dynamic Analysis

The dynamic studies the forces that act on an object and the movement generated in it. (Barrientos, 2007). For the calculation of the dynamic model of a system of articulated links, the Lagrangian formulation established by the equations shown below will be used.

$$L = E_c - E_p \qquad (13)$$

$$\tau_i = \frac{d}{dt}\frac{\partial L}{\partial \dot{q}_i} - \frac{\partial L}{\partial \dot{q}_i} \qquad (14)$$

Where:
L is the Lagrangian function
E_c is the kinetic energy
E_p is the potential energy
q_i corresponds to the coordinates of the joints
τ_i is the torque applied to the degree of freedom q_i

The dynamic simulation of the robot allows knowing what type of actuator is required to achieve the movements in the rehabilitation process. In the simulation, a static load of 100 N is considered as a reference value. Figure 6 shows the Torque-Speed curves of the different actuators of the robot, the curves allow to select the motors for the control.
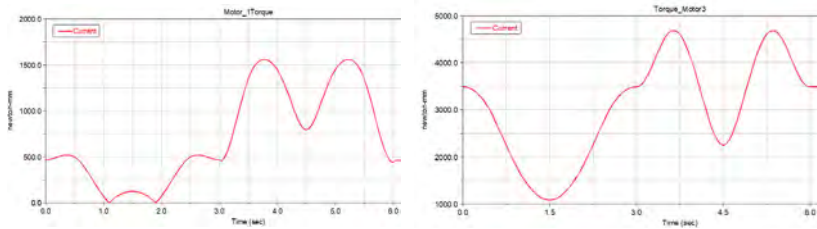
Figure 6. Dynamic analysis generated by MSC Adams.

Mechanical strength analysis

Finite element method (MEF) is a numerical method for the approach of solutions of complicated partial differential equations used in various engineering problems. Figure 7 shows the deformation due to the load of 100N, the simulation was generated in the ANSYS software where the deformation ranges can be verified due to the load.
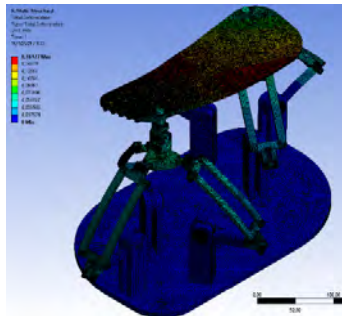
Figure 7. Deformation of the robot due to the static load of 100N.

2. Results

Results of kinematic analysis:

- The results obtained from the kinematic analysis are as follows: The maximum angular velocity of the actuator_1 is 63.15 deg. / s, the maximum angular velocity of the actuator_2 is 58.58 deg. / s, the maximum angular velocity of the actuator_3 is 53.46 deg. / s, depending on the position of the effector_1 which is 407.342 mm.
- The maximum speed of the actuator_4 is 34.0488 mm. / s, the maximum speed of the actuator_6 is 23.7753 mm. / s depending on the position of the effector_2 which is 174.029 mm. the maximum speed of the actuator_5 is

24.5336 deg. / s, depending on the position of the effector_2 which is 181.4925 mm.

Dynamic analysis results:

- The results of the dynamic analysis are described below: The maximum torque reached by motor_01 is 1559.7509 N mm. The maximum torque reached by the motor_02 is 2633.2061 N mm. The maximum torque reached by the motor_03 is 4689.27 N mm the maximum torque reached by the motor_04 is 3595.1272 N mm. The maximum torque reached by the motor_05 is 2594.1011 N mm. These values are given as a function of time, the maximum value being that of motor_03, this value helps us to select the actuators for the robot.

Results of resistance analysis:

- The analysis of mechanical resistance of the delta robot, where the maximum deformation is 0.16177 mm with a load of 100N and the composition of Aluminum with density = 2770 kg / m3 shows that the structure will work properly without suffering damage and the equivalent effort von Mises: 21,912Mpa MAX - 1,2083 x 10-8Mpa MIN.

Tests on the prototype

- The tests in the prototype show that the generated simulations were adequate for the design, obtaining that the prototype generates the necessary movements for the rehabilitation of the ankle.

Figure 8. Prototype of ankle rehabilitator generated by 3d impression.

References

1. Aracil, Rafael, Y Otros. 2006. Robots paralelos: Máquinas con un pasado para una robótica del futuro. págs. 16-28.
2. Barrientos A., Peñin F. L., Balaguer C., Aracil R., (2007) "Fundamentos De Robótica" España editorial McGraw.Hill. Segunda edición.
3. Benjamin, C. 2015. Esguince de tobillo. [En línea]. http://arh.adam.com/content.aspx?productId=102&pid=7&gid=100209.
4. Beer P. Ferdinand & JOHNSTON E. Russell, (2013) "Mecánica de Materiales" editorial McGraw. Hill. Sexta edición.
5. Budynas Richard G., & Nisbett J. Keith, (2008) "Diseño en ingeniería mecánica de Shigley" editorial McGraw. Hill. Octava edicion.
6. Hamrock J. Bernard, Jacobson B.O, Schmid Steven, (2000) "Diseño de elementos de máquinas" editorial McGraw. Hill.
7. Kumar Saha S., (2010) "Introducción a la robótica" México editorial McGraw.Hill. Segunda edición.
8. Kelly R., Santibáñez V., (2003) "Control de Movimiento de Robots Manipuladores" España Editorial PEARSON educación, S.A. Primera edición.
9. Merlet, J P. 2006. Parallel Robots. Second. Dordrecht: Springer.
10. Moore, Keith L, Dalley, Arthur F Y Agur, Anne M. 2010. Anatomía con orientación clínica. Sexta. Barcelona: Wolters Kluwer.
11. Norton L. Robert, (2009) "Diseño de maquinaria" Editorial McGraw. Hill. Cuarta edición.
12. Peña C; Martínez E; Cárdenas P. (2011) "Optimización dimensional de un robot paralelo tipo delta basado en el menor consumo de energía" Bogota.
13. Saladin, Kennerh. 2013. Anatomía y Fisiología. La Unidad entre Forma y Función. Sexta. México: Mc Graw Hill.
14. Silva, Luis Ángel. 2005. Control visual de robots paralelos. Análisis, desarrollo y aplicación a la plataforma robotenis. Madrid: s.n.

SECTION 3

LEGGED ROBOTS AND LEGGED LOCOMOTION

BODY DESIGN OF TENDON-DRIVEN JUMPING ROBOT USING SINGLE ACTUATOR AND WIRE SET

T. TAKUMA*, K. TAKAI*, Y. IWAKIRI* and W. KASE*

*Osaka Institute of Technology,
Osaka 5358585, Japan
E-mail: takashi.takuma@oit.ac.jp

Although a mechanism in which a single actuator and a wire passing through pulleys drive the joints is a strong candidate for realizing the dynamic behavior because of its appropriate weight and simple mechanism, the problem arises that the position of the pulley influences the dynamic behavior. This paper is focused on vertical jumping. In our research, we searched an appropriate set of positions of a pulley considering the practical development of the robot and derived the relationship between the position of the pulley and the force on the tips of the robot's foot for jumping. Simulation results suggest the possibility that some sets of positions allow an error in the attachment of the pulley, and the derived relationship indicates that the ratio of the pulling force of wire and vertical force on the ground strongly constrain the position of the pulley.

Keywords: Tendon-driven robot, vertical jumping, body design

1. Introduction

One of the challenging issues presented by the design of legged robots is the realization of dynamic motion, such as jumping and running. In order to lift a heavy robot body, in conventional approaches, an electric servo motor drives each joint. However, a motor that generates relatively high force is heavy and further increases the robot's weight, which causes its joints or motor to break. One of the key mechanisms for achieving such a motion is a body design in which the robot is equipped with a minimal number of an actuator. For realizing a robot driven by minimal number of actautor, Günter and Iida proposed a unique monopod hopper equipped with a large curved foot driven by only one motor.[1] In many studies, an interlock mechanism using light weight elastic materials was adopted[2,3] A tendon-driven system in which a wire to drive the joint(s) is pulled by an actuator is a suitable mechanism for achieving a light weight robot. In such a tendon-driven mechanism, the wire passes through pulleys attached on the links, and torques to rotate the joints are generated, depending on three

factors: the amount of pulling force, the length of the moment arm between the joint and the pulley, and the angle between the moment arm and the direction of the pulling force. Therefore, it is very important to examine the position of the pulley, which determines the angle between the moment arm and the pulling force.

By utilizing a tendon-driven mechanism, we aim to achieve successful vertical jumping. In this study, we investigated two issues related to the design of the tendon-driven robot, in particular to the position of the pulley: searching the position of the pulley for realizing the vertical jumping, and the formulation of a relationship between the position of the pulley and the force added on the toe for determining candidates of the pulley position. To examine the former issue, a simulation was conducted. In the simulation, an appropriate set of the possible positions of the pulley was searched, and the area in which the appropriate pulley positions were gathered was then extracted considering the practical development of the robot. To address the latter issue, we determined the condition of the position of the pulley required to realize vertical jumping by utilizing a mathematical model of the position of the pulley and the reaction force at the working point.

2. Model configuration

2.1. *Frame model*

Figure 1(a) shows the frame of the robot and the driving mechanism consisting of a single actuator and a wire set. The model has four links: the trunk, thigh, shank, and foot. It has three joints: the hip, knee, and ankle. The lengths of the links are denoted by $l_1 - l_4$, respectively, and torques of the hip, knee, and ankle are denoted by τ_1, τ_2, and τ_3, respectively. The angle is denoted by θ_i. For further simulation and derivation of the relationship between the positions of the pulley and a reaction force, we set the coordinate system Σ_0: the origin is set on the tips of the trunk, the Y_0 axis is set along the trunk link, and the X_0 axis is perpendicular to the Y_0 axis, as shown in Figure 1(b). The positions of the pulley and end point of the wire are labeled P_i^a (i = 0, 1, 2, 3) and the joints are labeled P_j (j = 1, 2, 3). Note that the point where the wire is attached to the actuator is P_0^a and the other endpoint of the wire is P_3^a. P_1^a is attached to the thigh and P_2^a is attached to the shank link. In this paper, the position of the attaching point P_0^a did not move when the actuator pulled the wire, although the actual linear actuator does move while pulling the wire. P_1, P_2, and P_3 correspond to the hip, knee, and ankle joint, respectively. The coordinate of

P_i^a is defined based on Σ_0 when the model stands vertical to the ground as $(x_t, y_t)^T$, $(x_h, y_h)^T$, $(x_k, y_k)^T$, and $(x_a, y_a)^T$ [mm], respectively. The coordinate of P_j is also defined based on Σ_0 as $(x_1, y_1)^T$, $(x_2, y_2)^T$, and $(x_3, y_3)^T$ [mm], respectively. As shown in the figure, the pulley or endpoint is set at the front side when $x_*(* = t, h, k, a) > 0$. y_* is negative when the pulley or endpoint is set below the origin of Σ_0. $\mathbf{e}_k$ $(k = 1, 2, 3)$ is a unit vector of tensional force on the pulley P_i^a and T is the magnitude of pulling force of the actuator.

(a) Joint configuration, position of pulley, joint angle, and torque

(b) Definition of coordinate system
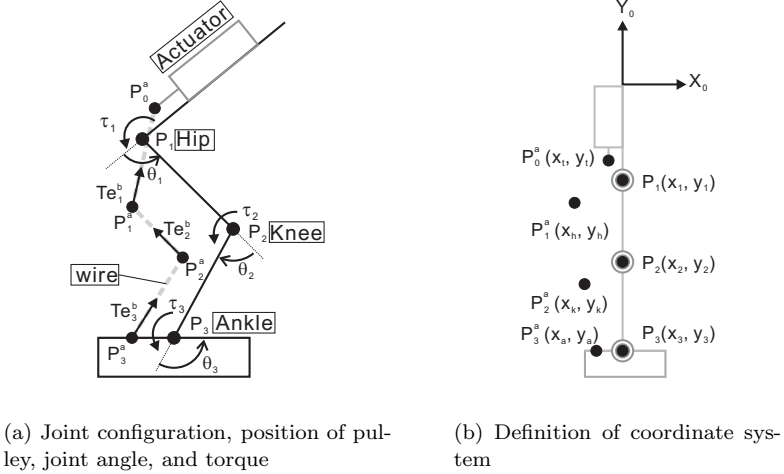
Fig. 1. Tendon-driven jumping robot using single set of actuator and wire

2.2. *Relationship between joint angles and joint torques*

The joints are driven by the force applied on the pulley. The joint torque is determined by the amount of pulling force T, the length of moment arm between the joint and the pulley, and the angle between the moment arm and the direction of pulling force. Higashimori et al. derived the torques for such a tendon-driven mechanism[4] with a single wire and actuator. In their study, the radius of the pulley is assumed to be non-zero, that is, the pulley was assumed to have a certain volume. For simple expression, in this paper, it was assumes that the radius of the pulley is infinitely small. Following this assumption, the relationship between the position of pulley and torques are expressed by modifying Higashimori's equation as

$$\begin{pmatrix} \tau_1 \\ \tau_2 \\ \tau_3 \end{pmatrix} = -T \begin{pmatrix} (\boldsymbol{p_1^a} - \boldsymbol{p_1}) \otimes \boldsymbol{e_1^b} - (\boldsymbol{p_2^a} - \boldsymbol{p_2}) \otimes \boldsymbol{e_2^b} \\ (\boldsymbol{p_2^a} - \boldsymbol{p_2}) \otimes \boldsymbol{e_2^b} - (\boldsymbol{p_3^a} - \boldsymbol{p_3}) \otimes \boldsymbol{e_3^b} \\ (\boldsymbol{p_3^a} - \boldsymbol{p_3}) \otimes \boldsymbol{e_3^b} \end{pmatrix}, \qquad (1)$$

where p_i^a is the position vector of P_i^a, and p_j is that of P_j. e_i^b is a unit vector from P_i^a to P_{i-1}^a. $\otimes$ is the operator as

$$(x_1, y_1)^T \otimes (x_2, y_2)^T = x_1 y_2 - y_1 x_2$$

We assume that the weights of pulley and wire are zero, and the model is constructed on a sagittal plane.

2.3. *Simulation model*

To search an appropriate set of the position of the pulley, a simulation using the Open Dynamics Engine[5] was conducted. In the simulation, the size and mass of each link were determined, as in Table 1, supposing that the link is made of ABS, the density of which is lower than that of metal. The joint torque was calculated by following Equation (1). Figure 2 shows an illustration of the simulation. We supposed that a physical pneumatic actuator (SMC CDUJ6-30DM) is adopted as the linear actuator in the frame shown in Figure 1(a), and we set the tensional force T as 10 N by referring to the data sheet of the actuator.

Fig. 2. Snap shot of the simulation

Table 1. Link size (width $\times$ depth $\times$ height) [mm] and weight [g]

Link	Size [mm]	Weight [g]
Actuator	$13.0 \times 20.0 \times 48.0$	28
Trunk	$10.0 \times 20.0 \times 125.0$	17
Thigh	$30.0 \times 20.0 \times 113.75$	25
Shank	$20.0 \times 20.0 \times 81.25$	15
Foot	$60.0 \times 20.0 \times 15.0$	17

3. Simulation

3.1. *Simulation setup*

In the simulation, the positions of the pulley P_1^a and P_2^a were changed within a certain area, and we observed whether the model successfully achieves a jumping motion. The results of the test trials showed that the robot achieved the jumping motion successfully when the parameters were set within a certain range. Therefore, the parameters were searched for $0 \leq x_h \leq 30$, $-125 \leq y_h \leq -95$, $-15 \leq x_k \leq 15$, and $-238.75 \leq y_k \leq -208.75$ mm at 1.5 mm intervals. The height of a jump was determined as $min(max(z_p(t)), max(z_t(t)))$, where $z_p(t)$ is the height of the heel (pastern)

from the ground and $z_t(t)$ is that of the toe, $min(a, b)$ is smaller value of a and b, and $max(c(t))$ is highest value of c during the jump; that is, the height is defined as the smaller of the values of the highest position of the heel and toe. The position of P_0^a, the origin of pulling force, was fixed at (-11.5, -78.0). The position of the endpoint of the wire P_3^a was also fixed at (-15.0, -320.0). We observed whether the robot achieves successful jumping, i.e., it lifts off and lands without falling down, and whether the height of the jump is over 200 mm. Before its lift off, the angles of the robot's joints were set as $\theta_1 = 120°$, $\theta_2 = -100°$, and $\theta_3 = 140°$. In order to ready the robot for landing after lifting off, the joints were controlled with a small actuation as

$$\widehat{\tau_i} = -Kp_l(\theta_m - \theta_{dm}) - Kd_l\dot{\theta}_m,$$

where $\theta_m(m = 1, 2, 3)$ is the joint angle and θ_{dm} is the initial angle of the joints, that is, $\theta_{d1} = 120°$, $\theta_{d2} = -100°$, and $\theta_{d3} = 140°$. The gains Kp_l and Kd_l are sufficiently small not to hinder the torque generated by the pulling wire (Equation (1)), 0.01 Nm/rad and 0.001 Nm/(rad/s), respectively. Note that the torque $\widehat{\tau_i}$ and the torque τ_i explained in Equation(1) are added when the foot contacts on the ground, and only $\widehat{\tau_i}$ is added after the foot leaves the ground. We assumed that the mass of pulley is zero.

3.2. *Simulation results*

In the simulation, the parameters x_h, y_h, x_k, and y_k were varied, and the results showed that 658 sets of parameters allow the robot to jump successfully; that is, there exist 658 solutions in the 4 dimensional x_h, y_h, x_k, and y_k space. In the practical installation of the pulleys, a position error because of technical problems such as the radius of the hole to attach the pulley should be allowed. Therefore, among the 658 solutions in the four dimensions, we searched a group of solutions in which the distance between the neighbor solutions is very small, i.e., the position error is allowed. In order to search such an area, we adopted cluster analysis using Ward's method and Euclidean distance, and we did not perform normalization. Table 2 shows the means (M) and standard deviations (SD) of four larger clusters. The largest, and the second, third and fourth largest clusters contain 273, 165, 126, and 93 solutions, respectively. Those clusters are labeled as Cluster 1 to 4, respectively. The results indicate two points. One is that the areas that allow a position error are distributed. Considering that the position of the hip joint is $(0, -125)$ and that of the knee joint is $(0, -238.75)$, the distances of P_1^a from the hip joint in Cluster 1 and 3 are longer than

those in 2 and 4. The positions of P_k^a in Cluster 1 and 2 are set at the rear of the knee joint, and those in Cluster 3 and 4 are set at the front of the knee joint. The variation in the SD explains the allowance of each parameter. For example, in Cluster 3, the SD of x_k is larger than that of y_k. This means that the position error in this cluster is allowed along the horizontal direction and is not allowed to some degree along the vertical direction.

Table 2.   Means and standard deviations of parameters

	x_h[mm] M(SD)	y_h[mm] M(SD)	x_k[mm] M(SD)	y_k[mm] M(SD)
Cluster 1	25.7(3.2)	-102.5(4.6)	-5.6(4.8)	-217.85(4.3)
Cluster 2	13.4(4.5)	-97.2(2.9)	-5.5(3.5)	-220.85(2.2)
Cluster 3	24.3(3.6)	-97.3(2.5)	8.6(4.3)	-223.75(2.3)
Cluster 4	14.0(5.9)	-100.4(4.6)	11.7(3.0)	-215.25(5.9)

4. Mathematical model

In the last section, we checked whether the proposed mechanism achieves successful jumping by utilizing the dynamics simulation. However, in order to investigate an appropriate set of pulley positions, it is important to derive a numerical model. In order to derive the numerical model, we have some assumption. On is that the model is constrained on the sagittal plane. The other is that the interaction between the robot and the ground is occurred instantly and the joint angles are not changed. We also have an assumption that the link moments are ignored. In order to derive a mathematical model of jumping, we applied an assumption that the joint angles are not changed during the lifting off motion and the reaction force is added at the toe because the interaction between the robot and the ground occurs instantaneously. We also applied the condition that the reaction force on the toe should be vertical and the projection of the center of mass (CoM) on the ground should correspond to the toe; otherwise, the robot tumbles while in the air. Based on this condition, the joint angles are strongly constrained, and we examined the position of the pulley that provides a vertical reaction force without a horizontal force being exerted on the toe following the assumption. Figure 3(a) shows the relationship between the joint torques and the force on the toe. The horizontal and vertical forces generated by the joint torque are expressed as F_x and F_y, respectively. Following the principle of virtual work, the relationship between the joint torque $(\tau_1, \tau_2, \tau_3)^T$ and $(F_x, F_y)^T$ is expressed as

$$\begin{pmatrix} \tau_1 \\ \tau_2 \\ \tau_3 \end{pmatrix} = \tau = \mathbf{J}_\omega{}^T \mathbf{R} \begin{pmatrix} F_x \\ F_y \end{pmatrix} . \ J_\omega = \begin{pmatrix} \frac{\partial x}{\partial \theta_1} & \frac{\partial x}{\partial \theta_2} & \frac{\partial x}{\partial \theta_3} \\ \frac{\partial y}{\partial \theta_1} & \frac{\partial y}{\partial \theta_2} & \frac{\partial y}{\partial \theta_3} \end{pmatrix}, \tag{2}$$

where (x, y) is the position of the toe. The elements of matrix J_ω are expressed from

$$x = l_2 \sin \theta_1 + l_3 \sin(\theta_1 + \theta_2) + l_4 \sin(\theta_1 + \theta_2 + \theta_3),$$
$$y = -l_1 - l_2 \cos \theta_1 - l_3 \cos(\theta_1 + \theta_2) - l_4 \cos(\theta_1 + \theta_2 + \theta_3)$$

$\mathbf{R}$ is the rotation matrix from the force based on Σ_0 to $(F_x, F_y)^T$,

$$\mathbf{R} = \begin{pmatrix} \sin \Theta & \cos \Theta \\ -\cos \Theta & \sin \Theta \end{pmatrix}, \quad \Theta = \theta_1 + \theta_2 + \theta_3.$$

(a) Force applied on the toe $(F_x, F_y)^T$

(b) Distance from joint to the line between P_i^a and P_{i-1}^a
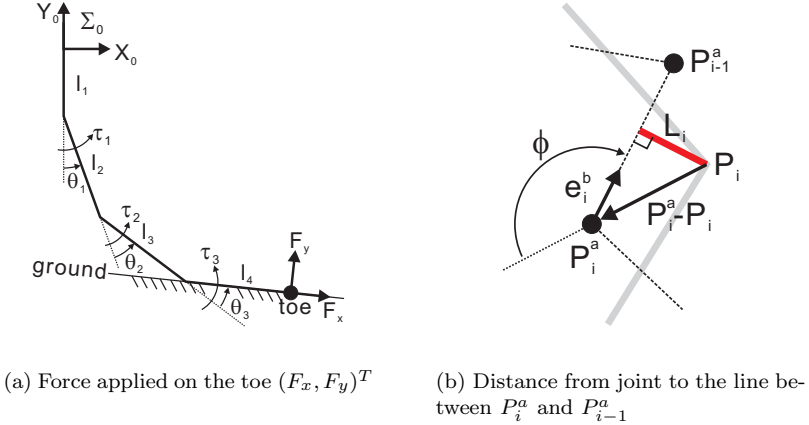
Fig. 3.   Posture of the model and distance between the joint and the wire

Considering that the vector $\mathbf{e}_i^b$ in Equation (1) is the unit vector, the term of $(\mathbf{p}_i^a - \mathbf{p}_i) \otimes \mathbf{e}_i^b (i = 1, 2, 3)$ is deformed as

$$(\mathbf{p}_i^a - \mathbf{p}_i) \otimes \mathbf{e}_i^b = |\mathbf{p}_i^a - \mathbf{p}_i| \sin \phi \overset{\text{def}}{=} L_i, \tag{3}$$

where ϕ is the angle between $\mathbf{p}_i^a - \mathbf{p}_i$ and $\mathbf{e}_i$ (see Figure 3(b)). Therefore, the term L_u is expressed by the length between the line of P_{i-1}^a and P_i^a and the joint P_i. By substituting $F_x = 0$, in which the horizontal force does not occur, the length of L_i is expressed as

$$\begin{pmatrix} L_1 - L_2 \\ L_2 - L_3 \\ L_3 \end{pmatrix} = K \begin{pmatrix} l_2 \cos(\theta_2 + \theta_3) + l_3 \cos \theta_3 + l_4 \\ l_3 \cos \theta_3 + l_4 \\ l_4 \end{pmatrix}, \tag{4}$$

where $K = -F_y/T > 0$ is the ratio of the force of pulling wire T and the reaction force from the ground $-F_y$. From the third row, the length L_3 is obtained when K is determined. From the second row, L_2 is automatically

obtained when the joint angles that satisfy the condition of the CoM are determined. From the first row, L_3 is also obtained. Because the positions of end points P_0^a and P_3^a are fixed, the positions of P_1^a and P_2^a are strongly constrained by the condition of L_1, L_2, and L_3. For example, position P_2^a should be set so that the distance between the line of P_3^a and P_2^a and the joint P_3 is L_3. Therefore, we conclude that the candidate positions of the pulley that generates vertical force are limited when the value of K is set.

5. Conclusion

This paper addressed a legged jumping robot, the joints of which are driven by a single wire and actuator. The wire passes through pulleys attached on each link and the joints are driven by pulling the wire. Although the weight of this mechanism is appropriate and the mechanism is simple and compact, the positions of pulley influence the dynamic behavior. This paper suggested a design principle for a tendon-driven joint mechanism considering of a single wire and actuator set for vertical jumping. A simulation utilizing a physical engine showed that there are some areas that allow an error in the position of the pulleys, which will facilitate the practical development of the robot. We also found that the area is not isotropic and an error is allowed along a certain direction and is not allowed in some extent along the other direction. We also derived a procedure for determining the appropriate pulley positions. In order to verify the validity of the simulation results and mathematical models, we intend to develop a physical robot in the future.

References

1. F. Günther, F. Giardina, and F. Iida. Self-stable one-legged hopping using a curved foot. In *Proceedings of 2014 IEEE International Conference on Robotics and Automation*, pages 5133–5138, 2014.
2. S. Kitano, S. Hirose, G. Endo, and E. F. Fukushima. Development of lightweight sprawling-type quadruped robot TITAN-XIII and its dynamic walking. In *Proceedings of 2013 IEEE/RSJ International Conference on Intelligent Robots and Systems*, pages 6025–6030, November 2013.
3. S. Cotton, I. M. C. Olaru, M. Bellman, T. van. der. Ven, J. Godowski, and J. Pratt. FastRunner: A fast, efficient and robust bipedal robot. concept and planar simulation. In *Proceedings of 2012 IEEE International Conference on Robotics and Automation*, pages 2358–2364, 2012.
4. M. Higashimori, M. Kaneko, A. Namiki, and M. Ishikawa. Design of the 100G capturing robot based on dynamic preshaping. *International Journal of Robotics Research*, 24(9):743–753, 2005.
5. *ODE Home Page*. http://www.ode.org/.

SLIDER: A BIPEDAL ROBOT WITH KNEE-LESS LEGS AND VERTICAL HIP SLIDING MOTION

KE WANG, AKSAT SHAH and PETAR KORMUSHEV

Robot Intelligence Lab, Dyson School of Design Engineering,
Imperial College London, UK
E-mail: {k.wang17, aksat.shah09, p.kormushev}@imperial.ac.uk
www.imperial.ac.uk/robot-intelligence

This paper introduces SLIDER, a new bipedal robot featuring knee-less legs and vertical hip sliding motion. Its non-anthropomorphic design has several advantages over the conventional anthropomorphic leg design. The lack of knees reduces the overall leg weight to only 3 kg and also reduces the moment of inertia of the leg rotation. SLIDER's ultra-lightweight legs make it suitable for agile locomotion. To test the design, we created a dynamic model of SLIDER in Gazebo and implemented a two-stage walking pattern generator, achieving a walking speed of 0.18 m/s in simulation. A physical prototype of SLIDER is currently under construction for real-world testing.

Keywords: Bipedal Walking, Legged Robot Design, Gait Pattern Generation

1. Introduction

Legged robots have advantage over wheeled ones because they can operate on rough terrain. In recent years legged robots have attracted a lot of attention and the research on legged robots has significantly intensified with a number of advanced robots being produced, including Atlas (2), Cassie (3), and TORO (5). However, most of the current legged robots still use the conventional anthropomorphic design, in which the knee actuator is mounted somewhere on the thigh, making the leg relatively heavy. This design either limits the robot's ability to perform agile locomotion (jumping, hopping, fast stepping etc.) or needs powerful motors to accomplish these motions (2) (6). We introduce our bipedal robot SLIDER, which has knee-less legs and vertical hip sliding motion. This new and non-anthropomorphic design enables SLIDER to have very lightweight legs and to perform agile loco-motion with relatively small power. Hodgins et.al (7) made a simple planar biped utilizing the idea of straight legs, but that robot only has three de-
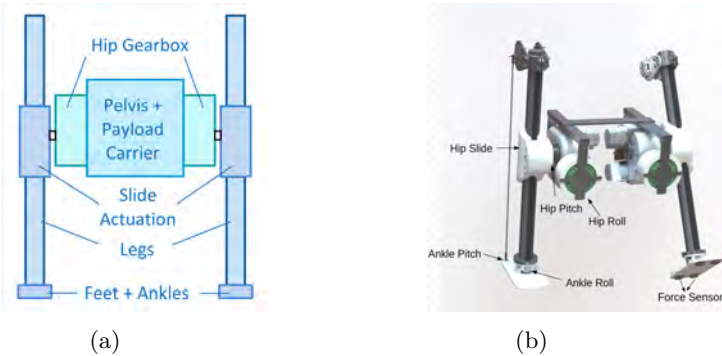
Fig. 1: An overview of SLIDER (a) Diagram of the SLIDER concept. (b) A rendering CAD model of SLIDER, showing all degrees of freedom

grees of freedom (DOF) and lacks the hip roll and also the ankle actuation. Schaft (4) released a video with a knee-less leg design, however the design details are unknown. To the best of our knowledge, there is no existing bipedal robot design similar to SLIDER in the published research.

The purpose of building SLIDER is to explore novel designs as well as novel actuation mechanisms for bipedal robots. A second motivation is that SLIDER can serve as an experimental platform for developing control and machine learning algorithms for agile locomotion. To validate SLIDER's design, we created a dynamics model in Gazebo and implemented a two-stage walking pattern generator developed by Przemyslaw et. al (9), making SLIDER walk very stably at 0.18 m/s in simulation.

This paper is organized as follows: Section 2 gives an overview on SLIDER's mechanical design, also this section compares SLIDER's design with the anthropomorphic leg design. In Section 3, we briefly outline the gait pattern generation used for SLIDER walking and describe the result in simulation. In Section 4 we conclude the paper and give the future work.

2. Overview of SLIDER's Design

SLIDER is a bipedal walking robot with ultra-lightweight legs. It has a height of 96 cm and a width of 50 cm, with a total weight of only 18 kg, an overview of the robot is shown in Fig 1a. Currently each leg has 4 DOF: hip pitch, hip roll, vertical hip slide and ankle pitch, resulting in 8 DOF in total, as shown in Fig 1b. Compared with the conventional anthropomorphic leg, SLIDER's leg doesn't have knees and has a vertical hip sliding motion.

2.1. *Mechanical Design*

Table 1: SLIDER joint specifications

Joint	Gear Ratio	Gearbox Type
Hip Pitch	1:24	Spur gear
Hip Slide	1:4	Spur gear and belt
Hip Roll	1:36	2 stage cycloid
Ankle Pitch	1:16	1 stage cycloid

The pelvis is located at the center, holds the electronics and carries the payload. The hip gearbox is connected with the pelvis and the leg, which houses the motors and transmissions for the hip pitch joint and the vertical hip slide joint. The hip slide joint has a gear ratio of 1:6 and is actuated using a pulley and tensioned belt. The hip pitch joint is achieved with a gear ratio of 1:24 using a second, concentric shaft, bolted onto the side of the leg. Figure 2a shows the inner view of the gearbox and illustrates the transmission of hip slide and hip pitch. To make the design of SLIDER compact and to directly drive and swing the gearbox, we placed the hip roll on the st side of the gearbox, as is shown in Figure 2b and Figure 1b. A stationary bracket holds the hip roll motor and the transmission in place. A direct cycloidal drive with a ratio of 1:36 is employed in the hip roll transmission, chosen for shock handling and to minimize the bracket length. Furthermore, this hip roll design is also easily adaptable to integrate hip yaw, which will be potentially added.

To minimize the weight of the robot we use carbon fibre rods for the whole leg, which weights only 3 kg. The robot's hip sliding mechanism is inspired by the pulley based linear actuator: two timing belts are adhered at two sides of each leg, turning the leg into a two-sided rack in configuration with several pinions on either side. A 3D printed casing houses three pinions used for moving along the belt and the casing is connected with the inner shaft from the hip gearbox, as is shown in Figure 3a. Using a timing belt is more lightweight and the three-pinion configuration lets pinions get more contact with the belt and avoid the skipping of belt teeth.

The ankle pitch actuation is implemented by a parallel rod driven mechanism which is similar to the ankle pitch design of ASIMO (6). One rod is attached to the back of the foot. By moving the rod the ankle pitch angle can be adjusted, as is shown in Figure 3b. The feet are 3D printed and have
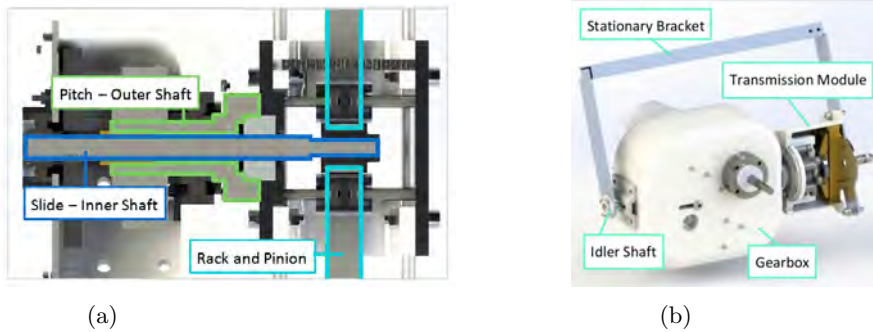
Fig. 2: (a) The inner view of the hip gearbox, it shows the transmission of vertical hip slide and hip pitch. (b) A side view of the gear motorbox and the hip roll transmission.
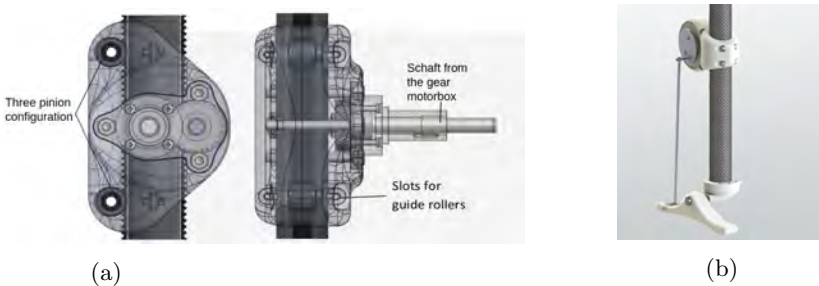
Fig. 3: (a) The pulley belt vertical hip slide design which has a three pinion configuration. (b) The rendering of the 1 DOF ankle.

an elongated shape with a length of 20cm. See Table 1 for a summary of all joint specifications.

2.2. *Comparison of SLIDER's design with conventional anthropomorphic bipedal robot design*

The novel mechanical design of SLIDER, which has knee-less legs and vertical sliding motion, has several advantages over the conventional anthropomorphic leg design. In the SLIDER design we put both hip pitch joint and vertical hip slide joint off the leg and in the pelvis, and straight legs are used instead of the anthropomorphic legs which have knees. With this design we reduce 1 DOF of the leg and remove the need for having the motor and the

Table 2: Comparison of the SLIDER design with the anthropomorphic bipedal robot design

	Anthropomorphic Design	SLIDER Design
DOFs on the leg	2 (1 on the knee and 1 on the ankle)	1 (1 on the ankle)
Vertical Compliance with Straight Legs	No	Yes
Occurrence of Singularity	When legs are straight	None
Required joint range of ankle pitch	Large	Small
Compactness of the Hip	More compact	Less compact
Social Acceptance	Easier	Harder

transmission for the knee, thus making the leg more lightweight. Moreover, while the knees on anthropomorphic legs require a compact transmission design which is expensive, the cost can be reduced. Another major advantage of SLIDER is that it has vertical compliance even if the leg is straight. This is not possible with conventional anthropomorphic bipedal robot design. Even if passive compliance is used (e.g. springs in the knee joints (11) (12)) when the leg is straight the impact force is transmitted directly to the hip, bypassing the knee springs. This means that the cushioning effect of the springs is lost when the leg is straight. In comparison, by adding a spring on the vertical hip slide joint of SLIDER, the robot can have the vertical compliance at any configurations of the leg. Furthermore, the straight leg of SLIDER also avoids the problem of singularity which happens to the conventional anthropomorphic bipedal robots when they stretch their legs fully.

There are more benefits of using the novel mechanical design: the required joint range of SLIDER's ankle pitch motion during walking is smaller than that of the anthropomorphic robots. The geometric compactness of SLIDER's straight legs makes SLIDER less prone to hit stairs than the anthropomorphic robots in the task of stair climbing.

We have to mention that there are drawbacks of the new design of SLIDER. There may be a problem with the social acceptance of the robot, because it is less human-like. Furthermore, while the design of SLIDER simplifies the structure of the leg, it makes the structure of the hip more complex by adding the vertical hip sliding joint. In addition, the straight legs of SLIDER have no knees to bend, making SLIDER harder to stand up after falling. Nevertheless, the knee-less leg design enables SLIDER to

(a) (b)
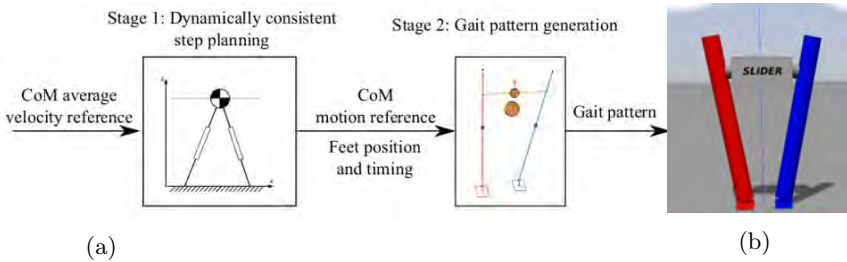
Fig. 4: (a) Overview of the flow of the two-stage pattern generation. The input to the system is an average CoM velocity during individual steps. The first stage uses Linear Inverted Pendulum model to plan the position of feet in sagittal and frontal plane, as well as step time. The second stage based on these information and uses more accurate Multi-Body System model to generate the final gait pattern. (b) the SLIDER simulation in Gazebo.

have lighter legs, making it better equipped to agile locomotion. Table 2 summarizes the difference between the SLIDER design and the conventional anthropomorphic bipedal robot design.

3. Control Strategy and Simulation Result

This section introduces the walking controller implemented for SLIDER. For generating walking gaits we used a two-stage dynamically consistent procedure (9) which is shown in Fig 4a.

At the first stage, given the average velocity of Center of Mass (CoM) as input, a simplified Linear Inverted Pendulum (LIP) model is used for step planning of foot position in frontal and sagittal plane as well as for tuning the step time.

The location of foot in time and the CoM trajectory generated from the first stage is then passed to the second stage which generates reference joint trajectories of SLIDER. At the second stage we used the Multi-Body System (MBS) model which approximates the system more accurate than the LIP model. Firstly the Zero Moment Point (ZMP) is calculated by the following equation:

$$ZMP_x^{ref} = x - \frac{z}{g}\ddot{x}$$

where ZMP_x^{ref} is the reference ZMP at x direction. Then a preview controller developed by Kajita et.al (8) (10) is used to compensate the discrepancies between the simplified LIP model and MBS model. The reference

trajectories computed from the preview controller are used as an input to the inverse kinematics which eventually calculates the individual reference joint position. A PD controller is used in each joint to follow the reference trajectory.

To validate the walking capability of SLIDER, we simulated the dynamics of SLIDER in MATLAB. Results show that SLIDER's ZMP has little difference with the referenced ZMP, indicating the chosen control method working well for SLIDER. Moreover, we created a model in Gazebo which has the same kinematic and dynamic properties as the physical version of SLIDER, see Figure 4b. By employing the same control strategy mentioned above, the robot can walk stably with a speed of 0.18 m/s in Gazebo simulation. A video of this walk is available at (1).

4. Conclusion

This paper introduces our ongoing work on SLIDER: a new bipedal walking robot with knee-less legs and vertical hip sliding motion. Its mechanical design is described and a comparison with the conventional anthropomorphic design shows that SLIDER has much lighter legs which is suitable for agile locomotion. Moreover, we also show that by using a two-stage gait pattern generator SLIDER can walk stably in simulation.

In the future, we will continue building the physical robot prototype and test it in the real world. Also, we plan to add an additional degree of freedom in the ankle (roll) and in the hip (yaw). Furthermore, force sensors will be added on the bottom of the feet for calculating the center of pressure. ZMP feedback will be added to the control loop for online gait generation and the controller will be implemented on the physical robot.

References

1. The SLIDER robot walking in a Gazebo simulation.
   `http://www.imperial.ac.uk/robot-intelligence/robots/slider/`
2. Boston Dynamics: Atlas, The next generation. `https://www.youtube.com/watch?v=rVlhMGQgDkY&t=9s`
3. Cassie, next generation robot. `https://www.youtube.com/watch?v=Is4JZqhAy-M&t=99s`
4. The Schaft robot. `https://www.youtube.com/watch?v=iyZE0psQsX0`
5. Johannes Englsberger, Alexander Werner, Christian Ott, Bernd Henze, Maximo A. Roa, Gianluca Garofalo, Robert Burger et al. "Overview of the torque-controlled humanoid robot TORO." In Humanoid Robots

(Humanoids), 2014 14th IEEE-RAS International Conference on, pp. 916-923. IEEE, 2014.

6. Kamioka, T., Kaneko, H., Kuroda, M., Tanaka, C., Shirokura, S., Takeda, M., Yoshiike, T. "Dynamic gait transition between walking, running and hopping for push recovery." Humanoid Robotics (Humanoids), 2017 IEEE-RAS 17th International Conference on. IEEE, 2017.

7. Jessica Hodgins. "Legged robots on rough terrain: experiments in adjusting step length." Robotics and Automation, 1988. Proceedings., 1988 IEEE International Conference on. IEEE, 1988.

8. Kajita, S., Kanehiro, F., Kaneko, K., Fujiwara, K., Harada, K., Yokoi, K., Hirukawa, H. "Biped walking pattern generation by using preview control of zero-moment point." Robotics and Automation, 2003. Proceedings. ICRA'03. IEEE International Conference on. Vol. 2. IEEE, 2003.

9. Przemyslaw Kryczka, Petar Kormushev, Nikos Tsagarakis, Darwin G. Caldwell. "Online Regeneration of Bipedal Walking Gait Optimizing Footstep Placement and Timing". In Proc. IEEE/RSJ Intl Conf. on Intelligent Robots and Systems (IROS 2015), Hamburg, Germany, 2015.

10. Kajita, S., Kanehiro, F., Kaneko, K., Yokoi, K., Hirukawa, H. "The 3D Linear Inverted Pendulum Mode: A simple modeling for a biped walking pattern generation." Intelligent Robots and Systems, 2001. Proceedings. 2001 IEEE/RSJ International Conference on. Vol. 1. IEEE, 2001.

11. Petar Kormushev, Barkan Ugurlu, Darwin G. Caldwell, Nikos Tsagarakis. "Learning to exploit passive compliance for energy-efficient gait generation on a compliant humanoid." Autonomous Robots (2018): 1-17.

12. Petar Kormushev, Barkan Ugurlu, Luca Colasanto, Nikos Tsagarakis, Darwin G. Caldwell. "The anatomy of a fall: Automated real-time analysis of raw force sensor data from bipedal walking robots and humans." Intelligent Robots and Systems (IROS), 2012 IEEE/RSJ International Conference on, IEEE, 2012.

OPTIMIZATION OF FEEDBACK CONTROL INPUTS FOR POSTURE CONTROL OF A SIX-LEGGED ROBOT

HIROAKI UCHIDA

Department of Mechanical Engineering, National Institute of Technology, Kisarazu College, 2-11-1 Kiyomidai-higashi, Kisarazu, Chiba 292-0041, Japan

In this study, an optimization method of feedback control inputs for a posture control of a six-legged robot was developed. The authors had proposed a method to control using an optimum servo system as a posture control method of a six-legged robot. As a problem of this method, because the feedback (FB) gain was switched at the time of switching the swing leg, the control inputs becomes discontinuous and there was a problem that the posture variation increases. After that, FB inputs of the thigh link obtained by optimum servo system were optimized. Then, we design a control system that suppressed the posture variation that occurs during swing leg switching. The effectiveness of the proposed control method was confirmed using a 3D model of a six-legged robot.

Keywords : Six-legged robot; Posture control; Optimization; Optimum servo control

1. Introduction

Multi-legged robots can operate under extreme conditions where it is difficult for humans to work. Walking robots are considered to be active on uneven terrain, and posture control is important for walking. In terms of posture control, there are studies that examined the subject from the perspective of control methods that consider robot dynamics [1][2]. In one such study [2], the authors used a six-legged robot with a leg mechanism proposed by Hirose et al. [3] to investigate a posture control method. The body height, pitching angle, and rolling angle were controlled by the thigh link during walking with support legs, and a 3D simulation was used to demonstrate the method's effectiveness. As a problem of this method, because the feedback (FB) gain is switched at the time of switching the swing leg, the control inputs becomes discontinuous and there is a problem that the posture variation increases. In this study, we construct an optimal servo system using a mathematical model considering the dynamics of the thigh link proposed by the authors. Moreover, FB inputs of the thigh link obtained by optimum servo system are optimized. Then, we design a control system that reduces the posture variation that occurs during swing leg switching. The effectiveness of the proposed control method is confirmed using a 3D model of a six-legged robot.

2. Six-Legged Robot

Figure 1 shows the six-legged robot used in this study. Each leg of the six-legged robot consists of three joints, a rotating part, a thigh part, and a shank part. Table 1 shows the dimensions of the six-legged robot.
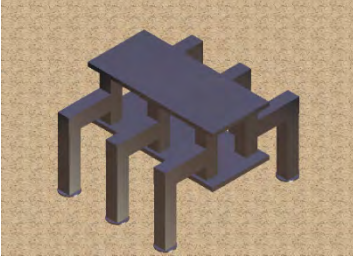
Fig. 1 3D CAD model of a 6-legged robot

Table 1 Robot dimensions

Height	500 mm	Length of Thigh	168 mm
Length	666 mm	Length of Shank	312 mm
Width	710 mm	Moment of Inertia I_z	1.966 kgm^2
Weight	24.9 kg		

3. Walking Planning

The effectiveness of the proposed control method is verified by the walking pattern of five support legs and one swinging leg. Walking period is 9 sec. Figure 2 shows Leg number and Figure 3 shows walking pattern.
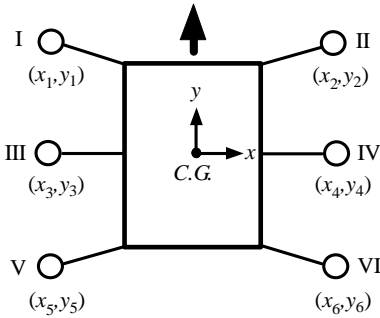
Fig.2 Leg number and position
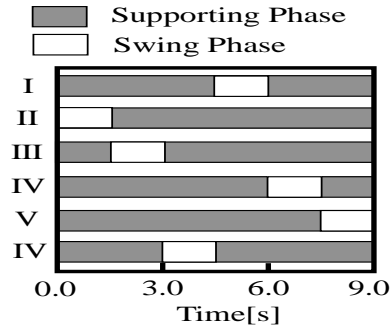
Fig.3 Walking pattern

4. Posture Control Method [4]

4.1. *Mathematical Model of the Thigh Link*

The thigh links are driven by the DC motor in this study, and the DC motor is controlled by the current. The equilibrium equation of the torque becomes the next equation for the thigh link shown in Figure 4.

$$T_i = Ki_a = J\frac{d^2\theta_{2i}}{dt^2} + c\frac{d\theta_{2i}}{dt} + F_i l_{ti}cos\theta_{2i} \qquad (1)$$

4.2. Mathematical Model from the Input of the Thigh Link to the Posture of the Body

The force F_i in the perpendicular direction of the supporting leg is given by the following equation:

$$F_i = K_e l_{ti}\{sin\theta_{2i} - sin(\Delta\theta_{2eqi})\} + C_e \dot{\theta}_{2i} l_{ti} cos\theta_{2i} \qquad (2)$$
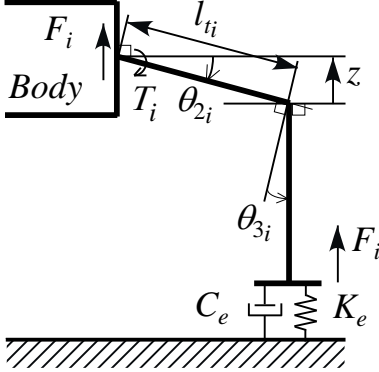
Fig.4 Relationship between the angle of thigh
and the force in the perpendicular direction
of the supporting leg
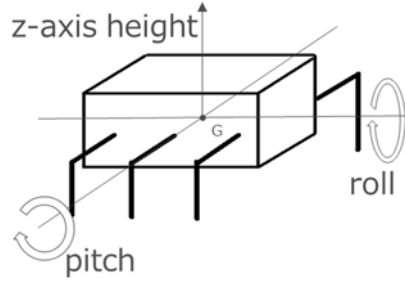
Fig.5 Three parameters of a six-legged robot for
posture control

Moreover, the height, and the pitching and rolling angles of the body are controlled by controlling the force in the vertical direction of the support leg. The motion equations of the force and the moment equilibrium in the vertical direction and the pitching and rolling axes in the case of support by six legs are given by Eq. (3) [2][4]. Fig.5 shows the controlling parameters of the body posture.

$$\begin{cases} M\ddot{z} = F_1 + F_2 + F_3 + F_4 + F_5 + F_6 - Mg \\ I_p \ddot{\theta}_p = y_1 F_1 + y_2 F_2 + y_3 F_3 + y_4 F_4 + y_5 F_5 + y_6 F_6 \\ I_r \ddot{\theta}_r = x_1 F_1 + x_2 F_2 + x_3 F_3 + x_4 F_4 + x_5 F_5 + x_6 F_6 \end{cases} \qquad (3)$$

Here, it should be noted that the thigh link range of movement used in this study is –30° to +30°, θ_{2i} is linearized at zero degrees. Substituting Eq. (1) and (2) for Eq.(3), and, by defining the 18th order state value $x = [x_{11}, x_{12}, \cdots, x_{61}, x_{62}, z, \theta_p, \theta_r, \dot{z}, \dot{\theta}_p, \dot{\theta}_r]$ which consist of the state values of each thigh link, pitching and rolling angles, the height of the body and their velocity, the following state equation is obtained. In Eq.(4), explanations of A, B, C, d and f are omitted.

$$\dot{x}(t) = Ax(t) + Bu(t) + dg + f \qquad (4\text{-}a)$$

$$y(t) = Cx(t) \qquad (4\text{-}b)$$

4.3. *Posture Control Method*

The servo system that the system shown by Eq. (4) follows to the desired value is designed.

$$\begin{cases} \dot{z}(t) = r(t) - Cx(t) \\ \dot{x}(t) = Ax(t) + Bu(t) + dg + f \end{cases} \tag{5}$$

Equation (5) is described in equation form as follows:

$$\dot{x}_g(t) = A_g x_g + B_g u + d_g g + f_g + e_g r \tag{6}$$

The control input to the actuator driving the thigh link is obtained to minimize the following equitation.

$$J = \int_0^\infty \left(x_g(t)^T Q x_g(t) + u(t)^T R u(t) \right) dt \tag{7}$$

Here, $Q(n \times n)$ and $R(m \times m)$ are the weighting matrix given by the design specification, and $Q \geq 0, R > 0$. The control input u_b^o to minimize Equation (7) is shown as following:

$$u_b^o = -R^{-1} B_g^T P x_g \tag{8}$$

Here, $P(n \times n)$ is the solution of the following Ricatti equation.

$$P A_g + A_g^T P - P B_g R^{-1} B_g^T P + Q = 0 \tag{9}$$

The feature of the proposed control method is that angles of the thigh links controlling the body posture are estimated by the detection of the pitching, rolling and the height of the body. In this study, in order to examine the walking pattern of the five support legs, six sets of FB controller are switched and applied each time the swing leg changes. Therefore, there is a case that the inputs of the support legs greatly change at the moment when the control system switches.

5. Optimization of Control Input

In this chapter, we consider a method to further optimize the control inputs obtained by the optimum servo system designed in Chapter 4. An evaluation function is necessary for optimization. Here, we consider the relation between vertical forces generated by the FB inputs obtained in Chapter 4 and the ideal forces in the support legs. We consider the squares of the difference between the ideal force, ideal moments (F^*, M^*_x, M^*_y) and the actual force, actual moments (F, M_x, M_y), and the weight values $(\alpha_F, \alpha_x, \alpha_y, \alpha_\angle)$ are set. Then, the evaluation function is set as follows:

$$J = \frac{1}{2} \alpha_F (F - F^*)^2 + \frac{1}{2} \alpha_x (M_x - M_x^*)^2 + \frac{1}{2} \alpha_y \left(M_y - M_y^* \right)^2$$

$$+\frac{1}{2}\alpha_\Delta \sum_{i=1}^{N}\left(f_i - \frac{F}{N}\right)^2 \tag{10}$$

Equation (10) is an evaluation function. The outputs are the forces in the vertical direction of the support legs. The inputs are constructed by the three components, first one is the body force in the vertical direction and second and third one are the rotational moments in the x- and y-axis. The first term on the right side of the Eq. (10) is the error sum of squares with respect to the force in the z-axis direction, and the second term and the third term on the right side are error sums of squares with respect to the moment about the x-axis and y-axis. The fourth term on the right side is the error sum of squares with respect to the average generating force of all the actuators and the generated force of each actuator. In this study, to minimize the value of J, we use "fminsearch" function which is a solver of MATLAB 's Optimization Toolbox. This solver uses the Nelder-Mead algorithm [5], which searches for function minimization without using a derivative function. The ideal force and moments (F^*, M^*_x, M^*_y) expressed by Eq.(10) are defined by following equations.

$$F^* = M_{\text{height}} * (z_r - z) - C_{\text{height}} * \dot{z} + M \tag{11-a}$$

$$M^*_x = -M_{pitch} * \theta_p - C_{pitch} * \dot{\theta}_p \tag{11-b}$$

$$M^*_y = -M_{roll} * \theta_r - C_{roll} * \dot{\theta}_r \tag{11-c}$$

$M_{\text{height}}, M_{\text{pitch}}, M_{\text{roll}}, C_{\text{height}}, C_{\text{pitch}}, C_{\text{roll}}$ are the virtual spring constants and the virtual damping coefficients about the position of the z-axis, the roll angle and pitch angle. z_r is the target value of the body in z-axis.

Figure 6 shows the block diagram with the optimization part shown in this chapter added to the optimum servo system shown in Chapter 4. The control input u of the support legs obtained by the optimum servo system is corrected to u^* by the optimization method and it is used as the control inputs of the thigh links.
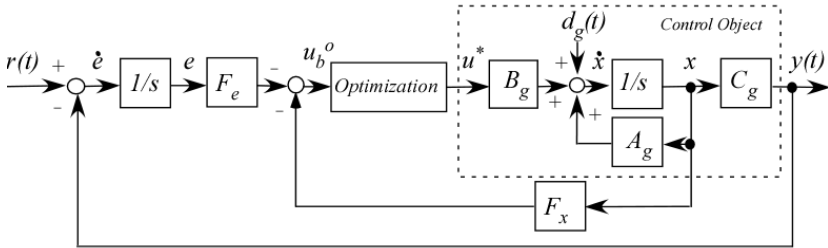
Fig.6 Block diagram of optimal servo with optimization

6. 3D Simulation

The 3D simulation results are shown in Figure 7. Since the Nelder-Mead method is an iteration method, we performed a simulation with the maximum iteration

number as 200 in this study. $Q = \mathrm{diag}(10^3, 10^3, 10^3, 0, \cdots, 0)$, $R = \mathrm{diag}(1,1,1)$ in Eq.(7). Also, $(\alpha_F, \alpha_x, \alpha_y, \alpha_\angle)$ in Eq.(10) were set to (1, 1, 1, 1). $(M_{\mathrm{height}}, M_{\mathrm{pitc}}, M_{\mathrm{roll}})$ are $(10^3, 10^3, 10^3)$ in Eq.(11), $(C_{\mathrm{height}}, C_{\mathrm{pitc}}, C_{\mathrm{roll}})$ are $(10^1, 10^1, 10^1)$. These parameters were determined by trial and error. Fig.7 (a) is time response of the height of the body, Fig.7 (b) is the pitching angle, Fig.7 (c) is the rolling angle, respectively. In the figure, the red solid line and the green dash-and-dotted line show the cases with optimization where iteration number is 200 and 50, the blue dashed line shows the case without optimization where posture control is performed with the FB input obtained by the optimum servo system shown in Chapter 4, and the black dotted line shows the target trajectory. In Fig. 7 (a) - (c), in the case of controlling the support legs with the FB gain obtained by
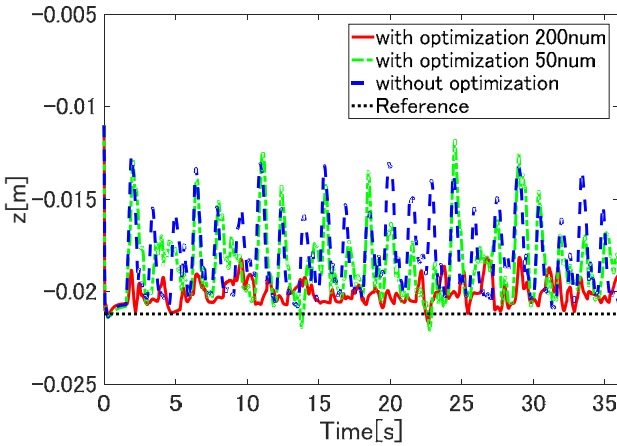
(a) Height of the body
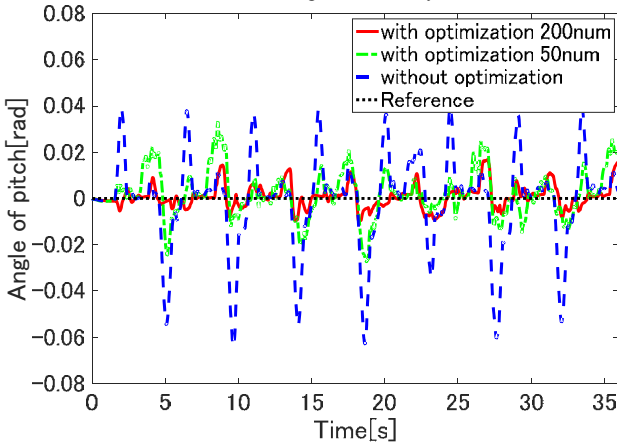
(b) Pitching angle of the body

Fig.7. Simulation results on even terrain

(c) Rolling angle of the body

Fig.7. Simulation results on even terrain

(a) Thigh of Leg I

(b) Thigh of Leg II

(c) Thigh of Leg III

(d) Thigh of Leg IV

(e) Thigh of Leg V

(f) Thigh of Leg VI
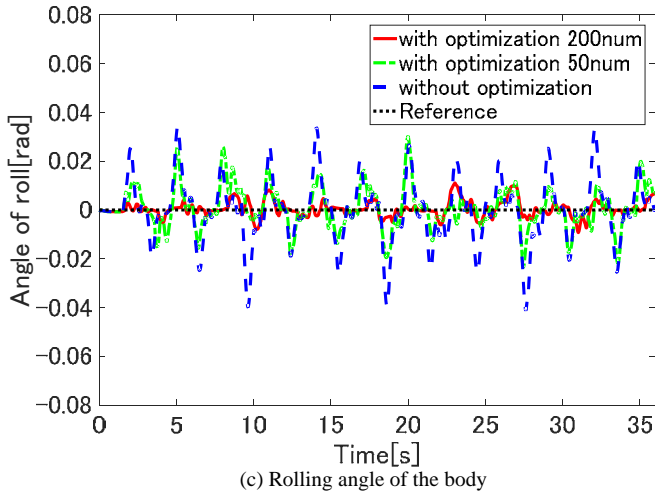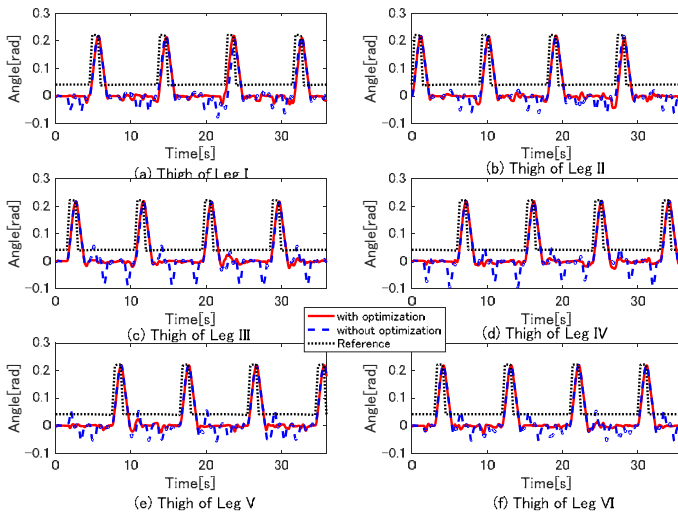
Fig.8 Time response of thigh angle

the optimum servo system without optimization, posture variation occurs because the FB control system switches at the time of changing the swing leg. However, when applying the optimization method, it can be seen that large variation occurring at the time of switching the swing legs are reduced in all control amounts of the body height, the pitching angle, and the rolling angle. Especially, with pitching angle and rolling angle, the maximum deflection width is reduced to less than half, and improvement in control performance can be seen. The

deflection width is suppressed to about half in the pitch angle where iteration number is 50. We can see the effectiveness of the proposed control method. Figure 8 shows the time response of the thigh angle in the case of the posture control shown in Fig.7. In the case that the optimization is not performed, the thigh angle variation becomes large at the time of switching the swing leg, but the case that the optimization is performed, it can be seen that this large variation is reduced. From these results, it was shown that by applying the optimization method proposed in this study to the posture control of the 6-legged robot, it is possible to reduce the variation of the input due to switching of the control system generated at the time of switching the swing leg.

7. Conclusion

In this study, we examined a control method to optimize the control input obtained by the optimum servo system as a posture control method of a six-legged robot and verified the effectiveness of the proposed method by 3D simulation of a six-legged robot.

1. The design procedure of the optimum servo system as the posture control method of the six-legged robot and the method to optimize the FB control input obtained by the optimum servo system are shown.
2. The effectiveness of the proposed control method was confirmed by 3D simulation using the 3D CAD model of the six-legged robot. Specifically, in the case of walking with five support legs, when the optimization is not performed, a large variation occurs in the height of the body, the pitching angle, and the rolling angle at the time of switching the swing leg. However, when the optimization method is applied, the variation was reduced.

References

1. Q. Huang, Y. Fukuhara and X. Chen, Posture and Vibration Control Based on Virtual Suspension Model Using Sliding Mode Control for Six-Legged Walking Robot, *Jour. of System Design and Dynamics,* **1**, 2(2007), pp.180-191.
2. H. Uchida and K. Nonami, Attitude Control of a Six-legged Robot in Consideration of Actuator Dynamics by Optimal Servo Control System, Climbing & Walking Robots Towards New Application, I-Tech, 2007, pp 299-312.
3. S. Hirose, and K. Arikawa, Development of quadruped walking robot TITAN-VIII, *Proc. of the 1996 IEEE/RSJ International Conference on Intelligent Robots and Systems*, vol.1(1996), pp.208-214.
4. H.Uchida, Six-degree-of-freedom Control by Posture Control and Walking Directional Control for Six-legged Robot, *Journal of Mechanical Engineering and Automation*, **7**, 2(2017), pp.30-45.
5. Nelder, John A., R. Mead., A simplex method for function minimization, *Computer Journal*, **7**, 1965, pp.308–313.

INTERACTIVE CO-DESIGN OF FORM AND FUNCTION FOR LEGGED ROBOTS USING THE ADJOINT METHOD

RUTA DESAI*, BEICHEN LI, YE YUAN and STELIAN COROS

Carnegie Mellon University, 5000 Forbes Ave., Pittsburgh, PA-15213, USA.
* Email: rutad@cmu.edu

Our goal is to make robotics more accessible to casual users by reducing the domain knowledge required in designing and building robots. Towards this goal, we present an interactive computational design system that enables users to design legged robots with desired morphologies and behaviors by specifying higher level descriptions. The core of our method is a design optimization technique that reasons about the structure and motion of a robot in a coupled manner to achieve user-specified robot behavior and performance. We are inspired by the recent works that also aim to jointly optimize robot's form and function. However, through efficient computation of necessary design changes, our approach enables us to keep user-in-the-loop for interactive applications. We evaluate our system in simulation by starting with initial user designs that are physically infeasible or inadequate to perform the user-desired task. We then show optimized designs that achieve user-specifications, all while ensuring an interactive design flow.

Keywords: Legged robots, Automatic robot design, Design optimization

1. Introduction

Even from a cursory inspection, it is clear that the morphological features of living creatures are intimately related to their motor capabilities. For e.g., the long limbs and flexible spine of a cheetah lead to extreme speeds. Therefore, roboticists often look to nature for inspiration.[1–3] However, rather than copying the designs that we see in nature, we are interested in beginning to address the question: can we develop mathematically-rigorous models with the predictive power to inform the design of effective legged robots? Furthermore, we are interested in integrating such computational models into interactive design tools that make robotics accessible to casual users.

Towards this goal, we develop a computationally efficient interactive design system that allows users to create legged robots with diverse functionalities, without requiring any domain-specific knowledge. Our system automatically suggests required changes in order to achieve a specified be-

havior or task performance. In particular, we focus on periodic locomotion tasks characterized by footfall patterns, motion speed and direction. The core of our system consists of a mathematical model that maps the morphological parameters of a robot to its motor capabilities. Equipped with this model, we present an automatic design framework to co-optimize robot's structure and motion in a hierarchical manner. To deal with the computational complexity for user-interactivity, we leverage the Adjoint method.[4]

Our long term goal is to make the process of creating customized robots highly accessible.[5] In our prior work, we developed an interactive design system for rapid, and on-demand generation of custom robotic devices.[6] A major limitation of our system was that it did not provide any feedback about design improvements. To overcome this limitation, we take inspiration from past work.[7–9] However, instead of directly weaving in the robot's physical parameters within motion optimization, we establish a mapping between them using the implicit function theorem.[10] Our approach is also complementary to evolutionary approaches.[11] Rather than synthesizing designs from scratch, we adopt a user-in-the-loop approach to allow the users to guide the design process as they desire – thereby converging onto their needed outcome much faster. Further, unlike evolutionary approaches that provide no guarantees, our gradient-based optimization is locally optimal.

Finally, we validate our system in a physics-based simulation, through various task-based robot design scenarios that are challenging for casual users. We demonstrate how our system aids users in issues ranging from physical in-feasibility of the design, to sub-optimality in task performance.

2. Interactive Design

Our interactive design system is rooted in a design abstraction that allows us to combine off-the-shelf and 3D printed parts for designing robots.[6] As figure 1(a) illustrates, our graphical user interface (GUI) consists of a design workspace for designing (left) and a simulation workspace for design testing (right). The users can browse through various modules from a menu (top) in the design workspace, and drag-and-drop them into the scene to construct or modify a robot design. We assume that all parts of a robot's articulated structure (other than motors for joints) are 3D printed. We automatically create these 3D printable connecting structures between actuated joints. These structure geometries are updated with every manual user operation or automatic design update that changes the robot morphology.

To enable this, we define a parameterized 3D printable connector module (see fig. 1(b)) whose position and orientation can be updated interactively with changes in the design. Each connector module has 'virtual' attachment
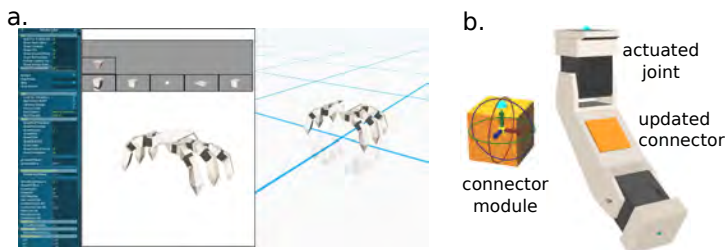
Figure 1. (a) GUI. (b) A parameterized 3D printable connector (orange) dynamically updates to connect actuated joints. Our system's capabilities are highlighted in our video.

points on its face that get updated based on the positions of the connector and the motors. These attachment points are used to update the shape and size of the connector's convex hull structure as needed. The users can also pause and restart the optimization at any point, to update the structure manually in between for achieving desired aesthetics.

Although our interactive design interface is a powerful approach for forward design, modifying designs to achieve a desired task requires domain knowledge. We next present our design optimization framework, which automatically optimizes the robot's form and behavior for a desired task.

3. Automatic Design Optimization

Designing robots with task-specific behaviors is highly skill-intensive and time-consuming. One must decide the robot's structure – physical dimensions of its body, and its articulated parts, as well as the placement of motors. One must then define how to control the motors for a co-ordinated movement that achieves a task. The robot's structure has a huge effect on the tasks it can perform. Therefore, designers typically iterate back and forth between physical and behavior design to create a task-specific robot. To capture this coupling between the robot's form and function, we parameterize a robot with a set of structure parameters $\mathbf{s}$, and motion parameters $\mathbf{m}$. However, instead of treating $\mathbf{m}$ and $\mathbf{s}$ independently, our goal is to represent robot motions as a function of its structure $\mathbf{m}(\mathbf{s})$. Apart from being intuitive, such a representation allows us to solve for an optimal task-specific behavior and design hierarchically, in a computationally efficient manner enabling interactivity during design.

3.1. Parameterization

A larger variety of robots including manipulators, and walking robots are composed of articulated chain like structures, in particular, of serially connected and actuated links. Such robot morphologies can be well described as kinematic trees starting at the root of the robot. The design parameters

s is used to specify such robot morphology, which is given by:

$$\mathbf{s} = (l_1, \ldots, l_g, \mathbf{a}_1, \ldots, \mathbf{a}_n, b_w, b_l) \ , \tag{1}$$

where g is the number of links, $l_i \in \mathbb{R}$ is the length of each link, n is the number of actuators, and $\mathbf{a}_i \in \mathbb{R}^3$ is the actuator parameters. For linear actuators, $\mathbf{a}_i$ defines the 3D attachment points, while for rotary actuators, it corresponds to orientation of axis of rotation. Apart from these parameters that represent the kinematic tree morphology of the robot, we use two additional parameters b_w and b_l to represent the physical dimensions of the robot's body (width and length respectively). Likewise, the motion parameters $\mathbf{m} = (\mathbf{P}_1, \ldots, \mathbf{P}_T)$ are defined by a time-indexed sequence of vectors $\mathbf{P}_i$, where T denotes the time for each gait cycle. $\mathbf{P}_i$ is defined as:

$$\mathbf{P}_i = \left(\mathbf{q}_i, \mathbf{x}_i, \mathbf{e}_i^1, \ldots, \mathbf{e}_i^k, \mathbf{f}_i^1, \ldots, \mathbf{f}_i^k, c_i^1, \ldots, c_i^k, \right) \ , \tag{2}$$

where $\mathbf{q}_i$ defines the pose of the robot, i.e., the position, and orientation of the root as well as joint information such as angle values, $\mathbf{x}_i \in \mathbb{R}^3$ is the position of the robot's center of mass (COM), and k is the number of end-effectors. For each end-effector j, we use $\mathbf{e}_i^j \in \mathbb{R}^3$ to represent its position and $\mathbf{f}_i^j \in \mathbb{R}^3$ to denote the ground reaction force acting on it. We also use a contact flag c_i^j to indicate whether it should be grounded ($c_i^j = 1$) or not.

3.2. *Method Overview*

Given an initial robot design and a task specification, our goal is to change **s** and **m** (eq. 1, 2) to obtain a design better suited for the task. Users typically define the initial design using our GUI. Various task descriptions such as preferred motion direction, speed, motion styles (walking, trotting, turning) etc. can also be specified with the GUI. These task specifications can then be encoded into a cost function $F(\mathbf{s}, \mathbf{m})$. Assuming **p** to be the parameter vector containing both structure and motion parameters $\mathbf{p} = [\mathbf{s}, \mathbf{m}]$, one can search for an optimal **p** along the direction of $F(\mathbf{p})$'s gradient $\frac{\partial F}{\partial \mathbf{p}}$. However, **s** and **m** are inherently coupled. Hence, instead of searching **s** and **m** independently, we first update **s**, and then update **m** within a constrained manifold that ensures the validity and optimality of **m**'s update, given **s**. By constructing a manifold of structure and motion parameters of a robot design, we can explore the sensitivity of robot's motion **m** to its structure **s**. Starting with an initial design $(\mathbf{s_0}, \mathbf{m_0})$ on the manifold, one can search for **s**, and corresponding $\mathbf{m}(\mathbf{s})$ on this manifold, such that $F(\mathbf{s}, \mathbf{m})$ is minimized. This dependency of **m** on **s** is captured by the Jacobian $\frac{d\mathbf{m}}{d\mathbf{s}}$ (see Sec. 3.3). This Jacobian is used to compute the search direction $\frac{dF}{d\mathbf{s}}$ for updating **s**

within the manifold. However, $\frac{d\mathbf{m}}{d\mathbf{s}}$ is expensive to compute. Therefore, we further simplify this computation by using the Adjoint method (Sec. 3.4).

At each iteration i, an update $\mathbf{s}'$ is proposed along the gradient direction $\frac{dF}{d\mathbf{s}}$ with step $\delta_{\mathbf{s}}$. For each such update of $\mathbf{s}$, multiple updates of $\mathbf{m}$ are executed to obtain the corresponding optimal $\mathbf{m}'$. Specifically, $\mathbf{m}$ is updated in the search direction defined by Newton's method $\left(\frac{\partial^2 F}{\partial \mathbf{m}^2}^{-1} \frac{\partial F}{\partial \mathbf{m}}\right)$ by $\delta_{\mathbf{m}}$ step obtained using line-search.[12] Note that $\frac{\partial^2 F}{\partial \mathbf{m}^2}$ and $\frac{\partial F}{\partial \mathbf{m}}$ represent the Hessian and gradient of F with respect to $\mathbf{m}$ respectively. If $F(\mathbf{s}', \mathbf{m}') < F(\mathbf{s}_i, \mathbf{m}_i)$, the updates are accepted, else a new $\mathbf{s}'$ is proposed along $\frac{dF}{d\mathbf{s}}$ with smaller step size $(\frac{\delta_{\mathbf{s}}}{2})$. We iterate over this procedure till $F(\mathbf{s}_i, \mathbf{m}_i) < threshold$ implying that $\mathbf{s}_i$ and $\mathbf{m}_i$ are optimal. A more detailed overview of this algorithm can be found in the extended version of our paper on <u>arXiv</u>.

3.3. *Coupling form and function for robot design*

It is hard to analytically represent the dependency of robot's motion on its structure. Instead, we assume a manifold that relates robot's structure and behavior capabilities, given a specific task: $\mathbf{G}(\mathbf{s}, \mathbf{m}) = 0$, where $\mathbf{G}(\mathbf{s}, \mathbf{m}) : \mathbb{R}^{n_s} \times \mathbb{R}^{n_m} \rightarrow \mathbb{R}^{n_m}$. Such an implicit manifold between structure and function can be converted into an explicit relation between the two within a small region around a point $P_0(\mathbf{s_0}, \mathbf{m_0})$ on the manifold, using the implicit function theorem.[10] The theorem states that when we change $\mathbf{s_0}$ and $\mathbf{m_0}$ by $\Delta\mathbf{s}$ and $\Delta\mathbf{m}$, the change in the function $\Delta\mathbf{G}$ should be zero to remain on the manifold. Using chain rule to compute $\Delta\mathbf{G}$, we obtain the following explicit relation between $\Delta\mathbf{s}$ and $\Delta\mathbf{m}$:

$$\Delta\mathbf{G} = \frac{\partial\mathbf{G}}{\partial\mathbf{s}}\Delta\mathbf{s} + \frac{\partial\mathbf{G}}{\partial\mathbf{m}}\Delta\mathbf{m} = 0 \implies \Delta\mathbf{m} = -\left(\frac{\partial\mathbf{G}}{\partial\mathbf{m}}\right)^{-1}\frac{\partial\mathbf{G}}{\partial\mathbf{s}}\Delta\mathbf{s} \qquad (3)$$

where $\left(\frac{\partial\mathbf{G}}{\partial\mathbf{m}}\right)$ and $\left(\frac{\partial\mathbf{G}}{\partial\mathbf{s}}\right)$ represents the Jacobian of $\mathbf{G}(\mathbf{s}, \mathbf{m})$ with respect to $\mathbf{m}$ and $\mathbf{s}$ respectively.

To compute such a manifold, we start with a task-specific cost function $F(\mathbf{s}, \mathbf{m})$. For each robot morphology $\mathbf{s}$, there exists an optimal $\mathbf{m}^*$ that minimizes $F(\mathbf{s}, \mathbf{m})$. Hence, the gradient of F with respect to $\mathbf{m}$ at point $(\mathbf{s}, \mathbf{m}^*)$ should be zero. One can then search for an optimal $\mathbf{s}^*$ along the manifold defined by this gradient $\mathbf{G}(\mathbf{s}, \mathbf{m}) = \frac{\partial F(\mathbf{s}, \mathbf{m})}{\partial \mathbf{m}}$. An optimal $\mathbf{s}^*$ on such a $\mathbf{G}(\mathbf{s}, \mathbf{m})$ would automatically ensure a corresponding valid and optimal $\mathbf{m}^*$ for the task. For searching such an optimal $\mathbf{s}^*$, we thus need to solve the following optimization problem:

$$\min_s F(\mathbf{s}, \mathbf{m}) \qquad s.t. \quad \mathbf{G}(\mathbf{s}, \mathbf{m}) = 0 \qquad (4)$$

where $F(\mathbf{s}, \mathbf{m})$ is the cost function; $\mathbf{G}(\mathbf{s}, \mathbf{m})$ denotes the gradient of $F(\mathbf{s}, \mathbf{m})$ with respect to motion parameters $\mathbf{m}$. Empowered by the Jacobian $\frac{d\mathbf{m}}{d\mathbf{s}}$ that essentially encodes $\mathbf{m}(\mathbf{s})$ (eq. 3), we can define the search direction for $\mathbf{s}$ as:

$$\frac{dF}{d\mathbf{s}} = \frac{\partial F}{\partial \mathbf{m}} \frac{d\mathbf{m}}{d\mathbf{s}} + \frac{\partial F}{\partial \mathbf{s}} \implies \frac{dF}{d\mathbf{s}} = -\frac{\partial F}{\partial \mathbf{m}} \left(\frac{\partial \mathbf{G}}{\partial \mathbf{m}}\right)^{-1} \frac{\partial \mathbf{G}}{\partial \mathbf{s}} + \frac{\partial F}{\partial \mathbf{s}}. \quad (5)$$

3.4. *The Adjoint method*

Computing $\frac{dF}{d\mathbf{s}}$ requires the calculation of the Jacobian $\frac{d\mathbf{m}}{d\mathbf{s}}$ which is computationally very expensive. It requires solving n_s linear equations (for each column in Jacobian matrix $\frac{\partial \mathbf{G}}{\partial \mathbf{s}}$), and the procedure gets very costly for large n_s. Instead, we use the Adjoint method to efficiently compute the gradient $\frac{dF}{d\mathbf{s}}$. This method formulates the computation of gradient as constrained optimization problem, and then uses the dual form of this optimization problem for faster computation.[4] Other applications have also sought out the Adjoint method for similar purposes in the past.[13] In particular, $\frac{dF}{d\mathbf{s}}$ takes on the following form using the adjoint method:

$$\frac{dF}{d\mathbf{s}} = \lambda^{\intercal} \frac{\partial \mathbf{G}}{\partial \mathbf{s}} + \frac{\partial F}{\partial \mathbf{s}}, \quad (6)$$

where λ is called the vector of *adjoint variables*. Such a computation of $\frac{dF}{d\mathbf{s}}$ now involves solving only one linear equation to obtain λ, followed by one matrix-vector multiplication and one vector addition (eq. 6). This is more efficient as compared to solving n_s linear equations for $\frac{d\mathbf{m}}{d\mathbf{s}}$ earlier.

4. Results

We explore three simulated examples to study the utility and effectiveness of our approach. Although, we only show our current results in simulation, we have confirmed that the simulation matches physical results previously.[6]

When novices design robots, it can be hard for them to decide where the actuators should be located and how they should be oriented for achieving a specific behavior. Fig. 2(a) shows one such example of a 'puppy' robot with three motors per leg. Even with enough number of actuators, the robot can only walk in one direction (forward) owing to its actuator placements. Parameterization of the actuator orientations $\mathbf{a_i}$ in eq. 1 enables design optimization to change them for equipping the robot to walk in any specific direction. Without the optimization of such structural parameters, it may be impossible to achieve such tasks (see fig. 2(b)).

Even when a design can theoretically achieve the desired behavior, it may be rendered infeasible due to real world constraints such as collisions. Fig. 3(a) shows a robot that can walk in the user-specified direction at
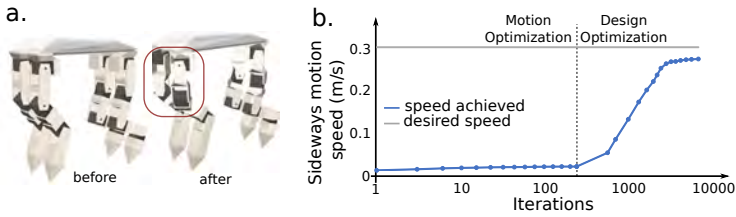
Figure 2. (a) The initial design of 'puppy' robot can only walk forward. Our design optimization enables the robot to walk sideways. (b) Optimizing motion parameters is not sufficient and optimization of the structure parameters is essential in this example.
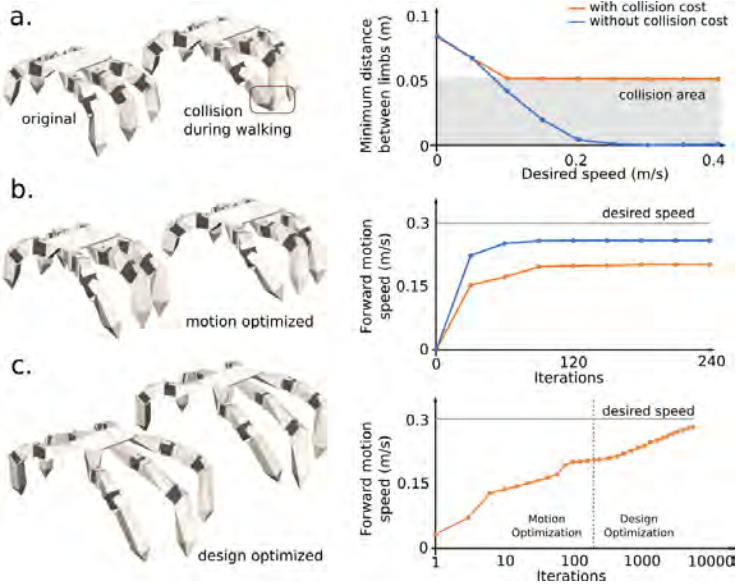
Figure 3. (a) Collision in a hexapod's limbs at high speeds. (b) Accounting for collisions in motion optimization prevents this, but also restricts the robot from walking faster. (c) Instead, design optimization increases spacing between limbs and their lengths.

desired speeds. However, when walking speeds increase above $0.1\ ms^{-1}$, the robot's limbs start colliding. It is hard to anticipate such issues *a priori*. Along with helping the user to test such scenarios in simulation, our system can also automatically prevent them by using feasibility constraints during motion optimization. However, these constraints prevent the required range of limb motions needed for fast walking, limiting the ability of the robot to walk at desired speed (fig. 3(b)). Instead, design optimization changes the design to achieve both these contradicting requirements (see fig. 3(c)).

Finally, designing robots for multiple tasks is also highly challenging, especially if the tasks demand opposing design characteristics. Consider the task of walking and pacing for a quadruped robot shown in fig. 4(a).
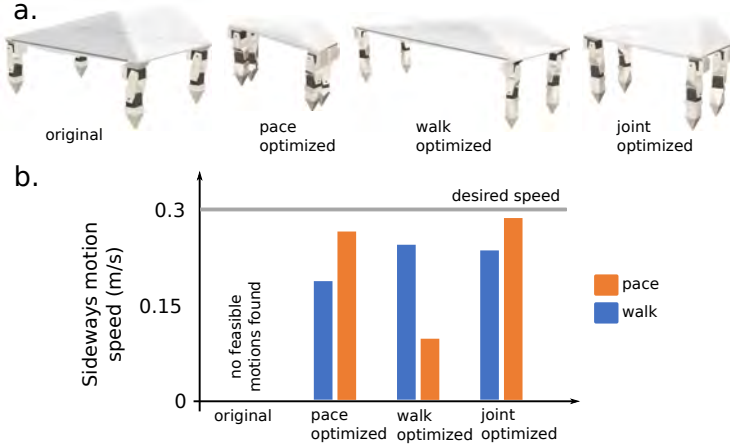
Figure 4.   (a) A quadruped robot design that can only walk forward, is optimized for pace, sideways walking, and jointly optimized for both these behaviors. (b) Jointly optimized design achieves a reasonable trade-off between the performance of both tasks.

The original design can only walk forward owing to its actuator placements (similar to the 'puppy' robot in fig. 2(a)). Its wider body and shorter limbs prevent it from pacing in stable manner. Individually optimizing the design for pacing and walking may not be sufficient for enabling the robot to perform both tasks. Pace-based design optimization generates a slim bodied robot, while walk-based design optimization produces a wider body size to increase stability during fast walking (see fig. 4(a)). Such a wider body in turn, negatively affects the pacing behavior (fig. 4(b)). To achieve reasonable performance for both these tasks, a trade-off is thus required. The individual requirements for each task $F_i(\mathbf{s}, \mathbf{m_i})$ can be combined in weighted manner into $F_{joint}(\mathbf{s}, \mathbf{m}) = \sum w_i F_i(\mathbf{s}, \mathbf{m_i})$. Weights w_i representing the importance of each task can be set by the users. Such joint optimization of walking and pacing (with $w_1 = w_2 = 0.5$) for quadruped in fig. 4(a) succeeds in achieving the necessary trade-off as illustrated in the resultant medium bodied optimized design, and the corresponding task performance.

Table 1. Design optimization statistics for example robots

Robot	Number of Parameters	Motion Opt. Iterations	Design Opt. Iterations	Time (s)
Puppy (Fig. 2)	614	6207	32	107.66
Hexapod (Fig. 3)	1044	5013	53	97.47
Quadruped (Fig. 4)	1050	14873	100	124.47

Table 1 shows the design times for optimizing the designs of robots in fig. 2, 3, 4. For quadruped in fig. 4 these statistics are reported for the joint optimization scenario. Note that, even when its number of optimization pa-

rameters are roughly similar to that of the hexapod, there is a significant difference in the number of optimization iterations, and the time required. This is because of the contradicting requirements that the two tasks demand, making the problem more challenging. Also note that for each iteration of design optimization, multiple iterations of motion optimization are executed. However, as shown in the statistics, the large number of these iterations are executed in minutes. Such computational efficiency is at the core of interactivity in our system. Apart from an efficient implementation in C++, a scalable approach using the Adjoint method enables the same.

5. Discussion and Future Works

We introduced an interactive robot design and optimization system that allows casual users to create customized robotic creatures for specific tasks. Apart from generating feasible behaviors, our system improves the performance of robot through an automatic design optimization process. In the future we plan to extend our design optimization technique for a broader class of motions and behaviors, including climbing, carrying weights or avoiding obstacles. Further, to find the right balance between automation and user control during design, we plan to perform an extensive user study as well.

References

1. A. Crespi, K. Karakasiliotis, A. Guignard and A. J. Ijspeert, *TRO* **29** (2013).
2. K. Graichen, S. Hentzelt, A. Hildebrandt, N. Kärcher, N. Gaißert and E. Knubben, *Control Engineering Practice* **42**, 106 (2015).
3. M. Spenko, G. C. Haynes, J. Saunders, M. R. Cutkosky, A. A. Rizzi, R. J. Full and D. E. Koditschek, *Journal of Field Robotics* **25**, 223 (2008).
4. M. B. Giles and N. A. Pierce, *Flow, turbulence and combustion* **65**, 393 (2000).
5. N. Bezzo, A. Mehta, C. D. Onal and M. T. Tolley, *IEEE Magazine* **22** (2015).
6. R. Desai, Y. Yuan and S. Coros, Computational abstractions for interactive design of robotic devices, in *IEEE International Conference on Robotics and Automation*, 2017.
7. B. Canaday, S. Zapolsky and E. Drumwright, Interactive, iterative robot design, in *ICRA*, 2017.
8. S. Ha, S. Coros, A. Alspach, J. Kim and K. Yamane, Joint optimization of robot design and motion using implicit function theorem, in *RSS*, 2017.
9. A. Spielberg, B. Araki, C. Sung, R. Tedrake and D. Rus, Functional co-optimization of articulated robots, in *ICRA*, 2017.
10. K. Jittorntrum, *An implicit function theorem, JOTA* **25**, 575 (1978).
11. N. Cheney, J. Bongard, V. SunSpiral and H. Lipson, On the difficulty of co-optimizing morphology and control in evolved virtual creatures, in *Proceedings of the Artificial Life Conference*, 2016.
12. J. Nocedal and S. Wright, *Springer, New York, USA, 2006* (2006).
13. A. McNamara, A. Treuille, Z. Popović and J. Stam, Fluid control using the adjoint method, in *ACM Transactions On Graphics (TOG)*, (3)2004.

STABLE WALKING DYNAMICS IN A SEMI-PASSIVE BIPED

CARLOS F. RODRIGUEZ HERRERA

Department of Mechanical Engineering, Universidad de Los Andes, Carrera 1 Este No. 19A – 40 Bogotá, DC, Colombia

JUAN CAMILO MARTINEZ FRANCO

Department of Mechanical Engineering, Universidad de Los Andes, Carrera 1 Este No. 19A – 40 Bogotá, DC, Colombia

SEBASTIAN MURILLO HERRERA

Department of Mechanical Engineering, Universidad de Los Andes, Carrera 1 Este No. 19A – 40 Bogotá, DC, Colombia

Semi-passive biped robots have been proposed to achieve efficient and robust bipedal locomotion, based on their natural dynamics. In this work, a compass biped with arc shape feet, actuated by a rocker mechanism on the hip is presented and studied. Initially, the effects of the variation of the excitation frequency and amplitude on the stability of the walking cycle are determined. Both, simulation results and experimental tests, suggest that, for a given range of excitation frequencies, the robot exhibits attractive equilibrium as well as entrainment. In addition, strategies for startup, turning and stopping were explored, obtaining promising results. This work supports the possibility of developing controllable, energy efficient, semi-passive, low cost bipeds.

1. Introduction

Bipedal robots are of interest because of their similarity to humans, but compared with robots on wheels, or even robots with four or more legs, bipedal robots seem to have few practical uses nowadays. Some of their drawbacks include low efficiencies and difficulty to control. However, bipedal robots have numerous potential applications in several fields: their locomotion can help understand human gait; traverse through irregular terrain, and they are the base for developing humanoid robots that can operate infrastructure designed for people.

Regarding energy efficiency, it has been suggested that by taking advantage of the natural dynamics of a system, it is possible to produce locomotion with a low cost of transport. Such ideas where demonstrated by the passive dynamic walker, developed by McGreer [1]. Passive dynamic walkers do not have any

actuation and depend on the conversion of potential energy to maintain a stable walking cycle, as friction and partially elastic collisions drain energy from the system. In this paper, we study a simple semi-passive biped developed as a passive dynamic walker equipped with a servo-actuated rocker mechanism on the hip, following the proposals of Collins et al. [2], in which the gravitational power is substituted by a simple actuation. The biped, initially developed by Botero et al. [3], was designed after a reviewing several passive compass gait robots with arc-shaped feet.

The mathematical model for passive dynamic walking is non-linear in nature, more so if actuation is to be added. Instead of addressing this non-linear model, we propose a series of dynamic simulations to gain insight of the robot's behavior. The software used for both modelling and simulation is Autodesk Inventor, that includes a variable-step dynamic simulation environment with a solver using a five-order Runge-Kutta integration scheme [4]. Different simulations were run to evaluate the stability and estimate the degree to which the robot can be controlled. A prototype was constructed and tested to validate the simulations.

The paper is presented as follows: section 2 contains the physical description of the robot as well as the assumptions made during modelling. Simulation parameters and trajectories are described on section 3. The results of the simulations and experiments with the prototype are presented and discussed on section 4. Conclusions and future work can be found on section 5.

2. Semi-passive biped description

The semi-passive biped (SPB) developed for this study is based on a knee-less passive dynamic walker: a compass biped with arc-shape feet. This is one of the simplest passive walkers since it is statically stable and only has two rotational joints in the hips. The actuation power is a rocker mechanism attached to the hip of the passive walker. Roughly, this mechanism provides swinging motion in a coronal plane allowing the biped to walk with a controlled gait on a flat surface. The proposed SPB results in a low cost prototype, with potential to study dynamic characteristics and control of the gait in robots or humans.

2.1. *Passive walker*

The base of the SPB is a passive walker (figure 1). It is a biped without actuation consisting of a 500 mm long steel shaft (hip) and two 400 mm long aluminum square profile (legs) ending in a spherical section wooden assembly (feet) with a radius of 120 mm.

This walker has a weight of 950g. It can maintain a repeating gait in ramps with slope angles ranging from 1.5 to 8 degrees, exhibiting a synchronized lateral swinging which allows each leg to oscillate alternately to produce the gait.
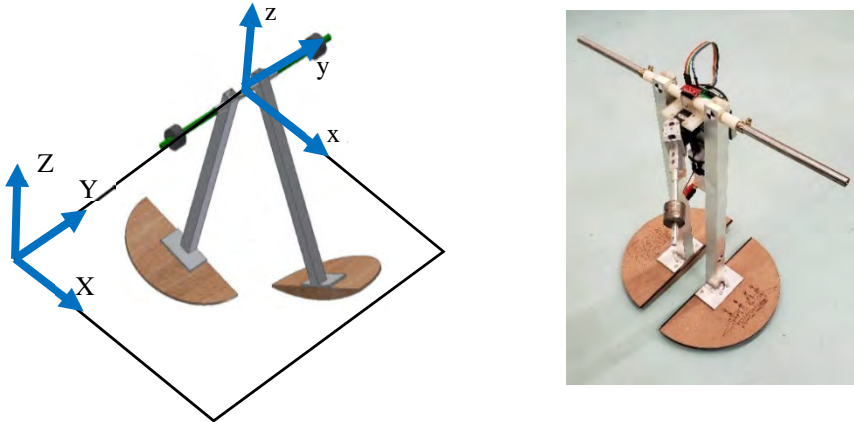
Figure 1. a) 3D Walker model. B)SPB

2.2. *Actuation mechanism*

Once a passive walker has an initial impulse, it needs additional energy to move on a flat surface. Enough power must be provided to produce the walking motion, while compensate the energy dissipated because of friction and impact damping. In this SPB, the actuation is a rocker mechanism on the hip, which generates the following effects: preserves its lateral swinging (roll), produces inclination in the forward direction (pitch), and generates inertial moment in coronal plane (yaw).

Figure 1 shows the SPB with the actuation mechanism. The rocker consists of an 80g mass attached to a 150 mm rod, coupled to a Dynamixel AX-12A servomotor. The mass rotates around the shaft of the motor, in the plane x-y (figure 1). This motor can deliver a rated torque of 1.5 Nm at 59 rpm, enough to produce the required operation oscillation frequency. A Raspberry Pi 3 controls the servomotor.

Garcia et al. [5] proposed a system of equations that describe the walker without actuation. While it is possible to extend this methodology to formulate a similar system for the SPB, it would result in a non-linear model, requiring some mathematical manipulation to become useful for control purposes. Instead, we propose to explore the behavior of the SPB via simulation and testing on a prototype, to gain some insight of its control possibilities.

3. Simulation parameters

The SPB was modelled in Autodesk Inventor® using the geometry and mass properties previously described. The settings for the motion of the rocker mechanism are the following: amplitude from 40 to 60 degrees, frequency between 0.8 and 1.2 Hz, and offset from -15 to 15 degrees. These testing conditions were selected after some experimentation on the passive walker prototype and some initial simulations.

3.1. *Cyclic stable gait and entrainment*

A system can be forced to oscillate to a given frequency with little energy input if the selected frequency is close to the system's natural frequency. This phenomenon is called entrainment and it is necessary for the control of the SPB.

Since the gait cycle frequency of the passive walker prototype in a ramp with a slope of 1.5 degrees was of 1.05 Hz, the rocker mechanism was actuated for the first set of simulations following a sinewave trajectory with frequencies between 0.8 Hz and 1.2 Hz.

3.2. *Contact and damping*

Impact is modelled in the Autodesk Inventor dynamic simulation environment as a series of elastic collisions with a damping coefficient. Marin [6] conducted an experimental estimation of these parameters for the passive walker prototype on a wooden ramp. For the simulations, we used the values obtained by Marin [6] (rigidity K=10 N/mm, dampening coefficient C=5.142 Ns/mm and coefficient of friction μ=0.3572), as nominal values with variations of 5% and 10%, in order to consider the influence of possible variations in a real level-ground.

4. Simulation and experimental results

4.1. *Cyclic stable gait*

To determine the operational conditions for a cyclic stable gait of the SPB, the conditions of simulation were simplified setting the offset to zero. Input frequency varied from 0.8 Hz to 1.2 Hz in steps of 0.1 Hz and amplitude varied between 40º and 60º in steps of 5º. The initial condition was set to a roll angle of 8° and zero initial velocity.

The SPB shows a cyclic stable gait for a range of input frequencies depending on the contact conditions (figure 2). As was expected, the gait is stable for frequencies up to the natural frequency of the UBR (1.05 Hz).
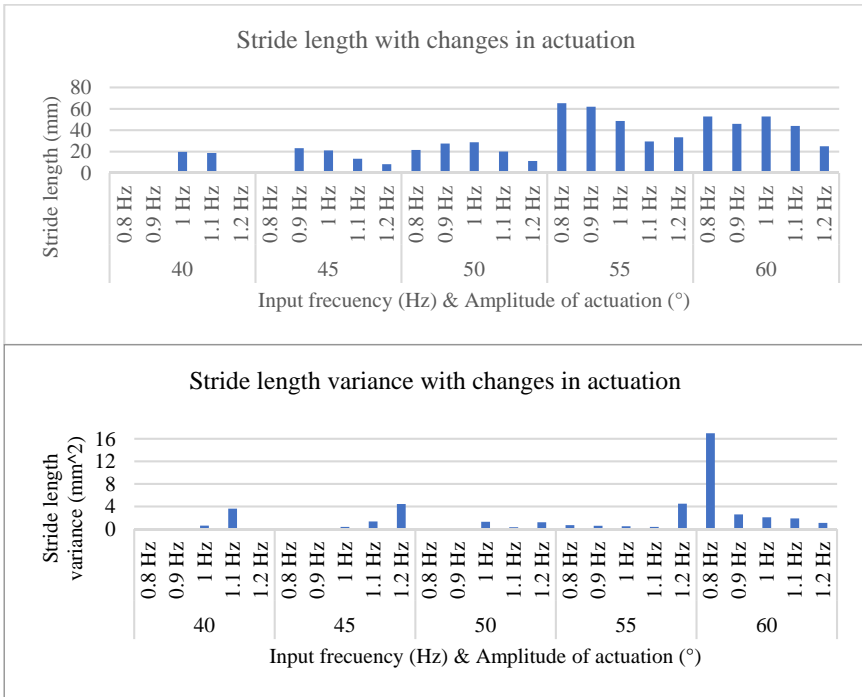
Figure 2. Cyclic stable gait

Figure 3 shows the horizontal view of the evolution of the trajectory of the center of mass of the hip for a set of input conditions (frequency of 1 Hz, zero offset and proposed contact conditions).
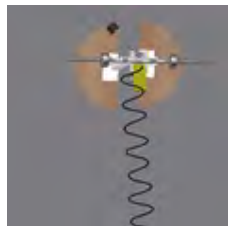
Figure 3. Trajectory of the center of mass of the hip.

The operating conditions were defined as K=10N/mm, C=5.172Ns/mm and μ=0.3571 with marginal variations. The interval of operating frequencies depends on the contact settings. Simulation results are shown on Figure 4. The marginal changes in K doesn't produce important effects in the gait cycle.
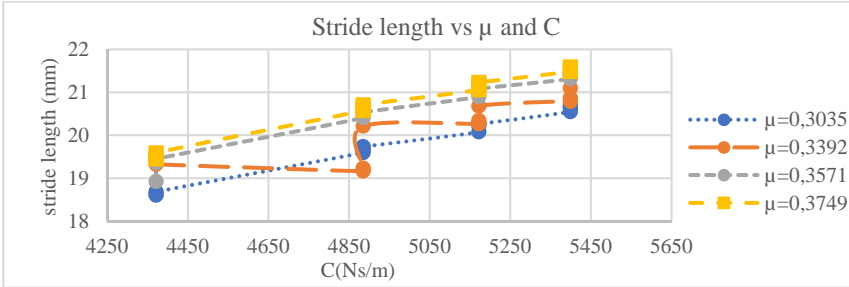
Figure 4. Marginal changes in contact conditions

In all cases, frequency entrainment was observed, to various degrees, although many of them do not produce gait. If the rocker is actuated in phase with the roll oscillation, the later will stop to a halt. This effect of the phase of the input with respect to the roll angle of the SPB is shown in Figure 5.
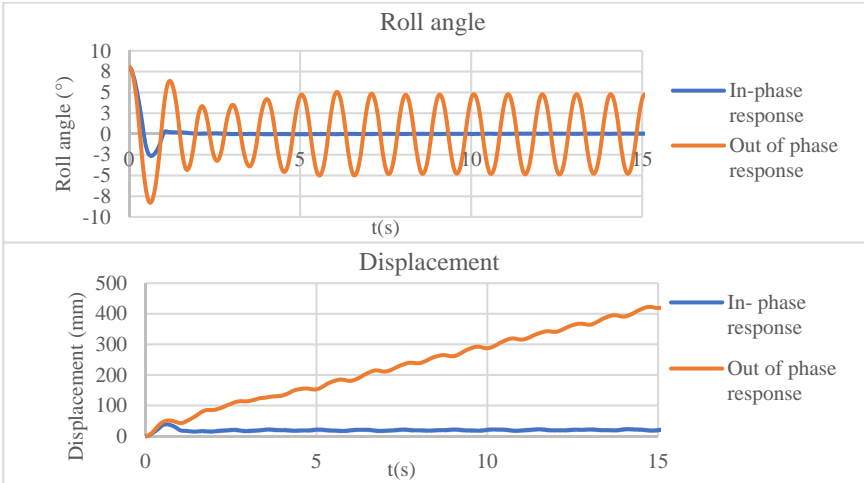
Figure 5. Rocker oscillation phase response in phase and out of phase (half a period).

4.2. *Starting and stopping*

Simply rocking the mass in the frequency that produces the best results (1 Hz) will produce an entrainment in approximately the same phase, which, as it was explained above, won't result in a gait cycle.

In this regard, a "startup trajectory" was proposed, where the rocker is actuated too rapidly for the SPB to respond with entrainment. Instead, the SPB is slowly forced out of its stable stationary state, until conditions approximating the

ones presented in the previous section are reached. In the same way, actuating the walker in-phase will cause it to stop walking.

4.3. *Turning*

Up to this point, the input function of the rocker mechanism had no offset around the x-axis of the SPB. This condition produces the SPB gait to be straightforward. When the input function has an offset, the SPB gait follows a curved trajectory. Table 1 shows the trajectory of the center of mass of the SPB when the amplitude of the input function is displaced 15 degrees towards the right (a) and to the left (b).

Table 1. SPB turning radius response to amplitude displacement, measured on the transverse plane.

Offset angle (°)	Turn radius (m)
0	-
2,5	11,9
5	7,8
7,5	12,4
10	2,5
12,5	2,0
15	1,5

The amplitude displacement results in a change of direction as expected, albeit at the cost of a relatively unstable gait. This opens the possibility partial control of one additional degree of freedom with the same actuator.

4.4. **Experimental results.**

The most reasonable dynamic parameters, found in simulation work, where replicated with the physical SPB. The prototype exhibited a cyclic gait very similar to the one observed in simulation. Acceleration and orientation data were collected with an inertial measurement unit (IMU), with the acceleration on the SBP's x axis integrated to observe the travelled distance, as seen on figure 6.
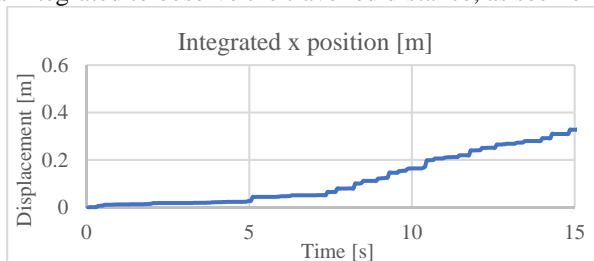
Figure 6. Position response on the physical SBP during experimental tests at 1Hz and 45° of amplitude in actuation

5. Conclusions

This paper presents an underactuated biped robot based on a passive dynamic walker with a simple hip rocker mechanism. The proposed system was studied using dynamic simulation to establish general parameters of the actuation conditions for controlling its gait. Three gaits were studied: stable cyclic gait, starting and stopping, and turning.

Simulation and experimental results shows that it is possible to achieve entrainment between certain input frequencies and the gait frequency, when the input is half a period out of phase form the gait. A strategy for stopping the gait is also derived from the behavior of the gait with an input in phase with the gait. An excitation with a frequency higher than the natural frequency of the system can provide a starting condition. Finally, turning can be achieved by adding offset to the input signal.

This work shows a promising development direction for simple biped robots, especially considering the low cost of the prototype. Further simulation and experimental work could be useful to understand the effects of external conditions on the walking cycle of the robot. However, after this exploratory phase, mathematical modelling of the system is also necessary.

References

1. T. McGreer, *Passive Dynamic Walking*, The International Journal of Robotics Research, Vol. 9, Issue 2, pp. 62-82 (1990).
2. S. Collins, A. Ruina, R. Tedrake, M. Wisse, *Efficient Bipedal Robots Based on Passive-Dynamic Walkers*, Science, Vol 307, pp. 1082-1085 (2005).
3. C. Botero, J. Montoya, N. Sánchez, F. Vergara, *Development of a passive dynamic walker prototype*, Intermediate project report, Universidad de los Andes (2012).
4. W. Younis, Up and Running with Autodesk Inventor Simulation 2011, Elsevier, 2nd ed., Burlington (2010).
5. M. Garcia, A. Chatterjee, A. Ruina, M. Coleman, *The Simplest Walking Model: Stability, Complexity, and Scaling,* Journal of Biomechanical Engineering, Vol. 120, Issue 2, pp. 281-288 (1998).
6. D. Marín, *3D Dynamic Modeling and Observer Design for a Passive Biped Walker*, MSc. Thesis, Universidad de los Andes (2017).

A scalable, modular leg design for
multi-legged stair climbing robots

T. BUETTNER* and D. WILKE and A. ROENNAU and G. HEPPNER
and R. DILLMANN

Intelligent Systems and Production Engineering (ISPE),
FZI Research Center for Information Technology,
Karlsruhe, 76131, Germany
*E-mail: timothee.buettner@fzi.de

Improving robustness of walking robots has always been problematic. Their complex kinematics and locomotion has always been prone to damage: a broken cable, an unstable foothold or a wrong set of parameters has been an everlasting source of frustration. Nature developed an extraordinary robustness through redundancy and fast adaptation. Theories about decentralized nervous systems has inspired this paper with a novel approach. The presented solution aims at relocating low-level walking behaviours to a network of computers and, more exactly, into the robots individual legs. This paper will not cover the full scope of the software implementation (this is a field found especially in modular robotics), but presents how such an encapsulated leg with all necessary hardware is built and focuses on the mechanical and kinematic aspect of such legs. It highlights how a robotic leg needs to be designed to tackle structured environments serves as explanatory guide through the design process of legs with integrated PCU and sensors.

Keywords: Mechanical Design; Legged Locomotion; Assistive Robots; Walking Robots; Modular Robots.

1. Introduction

Insects and spiders have developed remarkable abilities of the course of their evolutionary history. Abilities that many researchers in the field of walking robots try to adapt and apply to their own systems. The most extreme behaviour such animals express is the voluntary amputation of endangered limbs. This autonomy is triggered in various situations and ranges from preventing venom to afflict the rest of the body[1] to freeing itself from a fatal grip.[2] This skill became necessary due to the size of their bodies compared to their predators or dangers in their surroundings. The most remarkable skill though can be observed in the aftermath: the complete adaptation to

the missing limb. Both represent inspiring qualities for robotics and are objective to many papers in the domain. The have been efforts in finding faster ways to recover from damage by exploring parameter spaces and avoiding diverging behaviours[3] or make use of artificial neural networks to learn new walking strategies.[4] The presented approach will more closely adapt the idea of decentralized behaviours. More exactly: it will propose a way of designing legs which house a decentralized computational unit for redundancy. A well known animal with such motion redundancy is the octopus. The behavioural and control hierarchy offers the capability to move limbs individually but overwrite signals to coordinate multi-limb movements (many controlled by individual brain lobes).[5] Walking robots can't be compared

Fig. 1.   Examples for different monolithic robot systems: (f.l.t.r.) LAURON V,[6] HEC-TOR,[7] BigDog.[8]

to this structure since their natural inspirations come from the domain of vertebrates or insects with different topologies (see Fig. 1). On the other hand, there has been efforts to recreate decentralized systems in walking robots by connecting different central pattern generators and recreating a motion control close to the intra-spinal neural network real animals[9].[10] This paper takes a mechanical approach to the problem. It will explain a way to design the basic leg kinematics for a walking robot to overcome obstacles met in daily life and also house enough internal computing power to be used as decentralized unit. Modularity, meaning the decoupling of the legs, will not be part of this work since this would cover another field and topic. The proposed design method will focus on the overarching development of a leg and the early assessment of possible obstacles. This is a more detailed design step and can be seen as a subroutine of more overarching design strategies as proposed by Tedeschi[11] for example. The order in which each aspect of the robotic leg is presented also serves as possible procedure for other robotic leg designs.

2. Kinematic Restrictions

Kinematic restrictions represent the minimum or maximum requirements a robotic leg has to meet to fulfil certain purposes. This can on one side be the workspace, length, carrying weight or the total mass for example. Each aspect defines the final shape of the robot. This section will take apart the design process and introduce a more accurate way of designing robotic legs by highlighting several pitfalls in this process. The leg was designed for a small walking robot with a minimum of six legs attached. The minimum weight to be carried was set to be approximately 2kg with three degrees of freedom per leg (for a small demonstrator). The need for a smaller testing platform and the interest in decentralized walking is the driving factor for this small, intelligent leg. Using four DoF would allow the use of low energy walking strategies and intelligent posture control[12] found in bigger robots such as LAURON V.[6]

2.1. *Robots and Environments*

The first step in defining the kinematic restrictions of a robot is assessment. The environment represents the biggest design factor right after the payload and motion type. Knowing the environment the robot will meet helps defining obstacles in its future path. As an example: The small decentralized demonstrator will be designed for indoor use. The ground is flat,solid and no dynamic changes occur. Nevertheless, there can be 2 more challenging obstacles involved: **slopes and stairs**. Other robotic systems will have to identify such obstacles in different environments, such as rocks, holes or bodies of water. With slopes being in place for wheelchair access and stairs as a general means of changing level within the building, this work will mainly focus on how to design the robot to climb these obstacles successfully. The following sections will explain, how these obstacles alter the shape of robots and require beforehand design decisions to render the robot capable of climbing successfully.

2.2. *Defining Proportions*

Starting top-down in design, the first decision is the number of joints per leg. These were set to be three, as explained beforehand, since redundancy or energy efficiency won't be part of this research. Starting from the joints, it is possible to define basic proportions of the leg without knowing the final length of it. Coming from an analogy to robotic manipulators, the work of Yoshikawa[13] has shown a way of optimizing segment proportions by improv-

ing its theoretical manipulability. This manipulability can be represented for non-redundant systems through (1).

$$w = ||det J(\Theta)|| \tag{1}$$

with (2) representing the vector of joint angles

$$\Theta = [\Theta_1, \Theta_2, \Theta_3, ..., \Theta_m]^T \tag{2}$$

and (3) its Jacobian.

$$J(\theta) \in R^{m \times n} \tag{3}$$

By decomposition of the Jacobian into its singularities $\sigma_1, \sigma_2, \sigma_3, ...\sigma_m$, the manipulability becomes

$$w = \sigma_1 \cdot \sigma_2 \cdot \sigma_3 \cdot ... \cdot \sigma_m \tag{4}$$

Expressed in the terms of a 3DOF Robot with L_1, L_2, L_3 being its segment lengths and $\Theta_1, \Theta_2, \Theta_3$ being its joint angles, formula (4) becomes

$$w = L_2 \cdot L_3 \cdot |(L_2 \cdot sin(\Theta_2) + L_3 \cdot sin(\Theta_2 + \Theta_3)) \cdot sin(\Theta_3)| \tag{5}$$

This formula has its maximum for $L_2 = L_3$ and $\Theta_3 = \pm 90°$. The manipulability can be described as the capacity of the manipulator to change the orientation and position of its end-effector at a given joint state. But since the robotic leg moves freely, the 90° angles can't be maintained. Still, it is possible to use the proportions $L_2 = L_3$ as design restrictions for the two longest segments: lower and upper leg. Even though climbing is not considered a manipulation task, applying this rule leads to a larger manipulation volume, allowing more variety in footpoints.

2.3. *Minimum Length*

Returning to the environmental restrictions, there are several leg parameters that can be calculated from known obstacle sizes. The stairs have been identified as the most challenging obstacles in an indoor environment as many multi-legged robots will fail if their legs are not scaled correctly. The more prominent examples for stair climbing robots are BigDog from Boston Dynamics or ANYmal from ETH Zurich.[14] Six and more legged examples have only vaguely shown success. One example being the modular robot Snake Monster from Carnegie Mellon. The comparison of both climbing styles shows how four legged approaches exceed their six legged competitors: The leg constellation is rotated in a way, that most of the

workspace covers the stair area (similar to mammalian topologies). In comparison, insect-like arrangements allow a better foothold but under-perform if bodies have to be pushed upwards and forwards. For the next step, we will assume the robotic legs will be placed parallel to the sagittal plane. *Selecting the body pose* - Even though most stairs have regulatory obligations to remain within a certain range of height (this also counts for slopes) no works have been made to link the design process directly to these rule sets to define robotic lengths. We are looking at the case with the least favourable body orientation: The robot body is in direct contact with the stairs. This orientation can either be parallel to the stair inclination or horizontal (as sketched in Fig. 2).

Fig. 2.   Two possible body poses for stair climbing robots with sagittal leg constellations. The simplified image shows the closest positions in contact with the stair outline. The tilted approach is found more often than a constant horizontal position (r.).

Maximum and minimum inclination - Stairs have strict regulations which allows the estimation of possible obstacles for indoor environments. There are several international rules that differ slightly. The regulation for this example is drawn from the German *DIN 18065*. The indoor riser height lies between 140 and $200mm$ and the tread depth between 230 to $370mm$. As an example, the *International Residential Code for Stair treads and risers R311.5.3* has a maximum riser height of $196mm$ and minimum tread depth of $254mm$. These numbers describe the majority of stairs in buildings. The maximum and minimum slope a robot can encounter are calculated by combining the highest rise with the shortest tread (and vice versa). The resulting slopes can be seen in Fig. 3.The maximum slope will be taken as design reference since it highlights the steepest obstacle for an indoor robot. As a result. All calculations will be made with the **inclination** of $41°$, a **riser height** of $200mm$ and a **tread depth** of $230mm$.
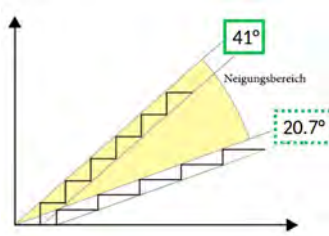
Fig. 3. Relative comparison of the highest and lowest slope angle. Both are drawn from the values found in DIN 18065.

Minimum length - Next would be the calculation of the minimum leg length through geometrical approximation. This is done by selecting the closest possible distance a horizontally oriented robot would take while it is climbing stairs. This minimum distance is sketched in Fig. 4: The robot has its front and bottom pressed against the stairs and is therefore closest to the stairs. Any other position would require longer legs. To move the robot forward, the following order of movement is required:

(1) The robot in Fig. 4 is currently at the beginning of the step. The hind legs are extended and the front legs are pushed against the stair.
(2) The robot needs to move its hind legs one step up to push its body upwards alongside the stair.
(3) The hind leg then pushes the robot forward to maintain minimum distance with the stair.
(4) The new position is one stair further but in the same constellation.

Fig. 4 also shows, that any downward movement of the extended hind leg is impossible since it would collide with the edge of the stairs. This occurrence also represents the geometric connection between the shortest robotic leg and the size of the stairs: It is impossible for robots with a body length shorter than the stair tread (in this example $230mm$) to shorten their leg any further. The robot wouldn't be able to lift its body to the next step in a single movement. This minimum length necessary to lift the robot up one stair at the time represents a measure that is independent from any speed or gait since it maintains the smallest possible distance between robot and stairs. Using the two tread depths of $460mm$, riser heights of $400mm$ and the $41°$ slope, the length results to $l_{total} = 609mm$ from shoulder joint to foot.

Longer robots - Surely it is possible to apply this to longer robots, in which case legs become shorter as the robot grows in length. The greyed out sketch

in Fig. 4 shows the effect of an extended body length: The robot is able to move the leg lower (compared to the short version), thus allowing him to push itself to the next step while having its footpoints move inwards. A robot with $400mm$ body length would only require $l_{total} = 418mm$ in total length at its hind legs. The absolute minimum would be reached with a robot length of twice the tread with the shortest distance to the step being twice the step $(l_{min} = 400mm)$.
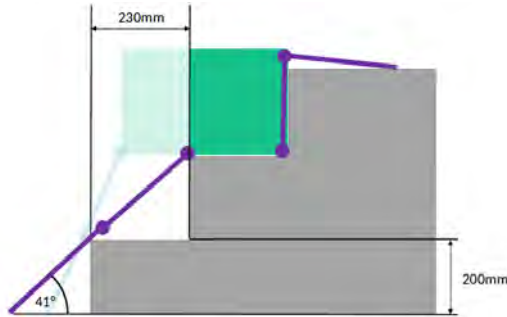
Fig. 4.   Relative comparison of the highest and lowest slope angle. Both are drawn from the values found in DIN 18065.

3. Mechanical Design

The mechanical design was derived from the beforehand explained kinematic restrictions (proportions and length). The subsequent step would be the theoretical load cases for such a climbing robot. Working with the extreme load-cases for walking robots, one would assume that extending the robots legs away from its body is the classic maximum: the distance between footpoints and centre of mass is a full leg-length apart which causes the maximum torque in the beta joint. To take a different approach and because it is unlikely the robot might get into this situation, a different, more probable load-case was selected. Fig. 5 shows the case for stair climbing: The robots CoM is vertically aligned with one row of footpoints. This result the entire load being carried by only these legs. Placing the legs orthogonally to the gravitational force results in the largest possible torque (in this case for joint β)

The resulting torque (with the center of mass placed above one leg as in Fig. 5) can be expressed as follows:

$$T_{max} = m_{total} \cdot g \cdot L_{segment} \tag{6}$$

Fig. 5. A highly unfavourable pose: the centre of mass is aligned directly above the footpoints while the lower limb itself is arranged orthogonally.

Having finished the theoretical part of the calculations, one would need to add a first estimate of the robots mass to the equation (6). This is necessary and part of every design process: later calculations or materials will most like (and as in our case) change the final numbers the torque values. We have picked an estimated mass of $m_{total} = 15kg$ as initial guess from experience. This step may vary depending on the planned robotic setup, payload and material. Adding this to the equation results in $T_{max} = 32.373Nm$ (for our segment length of 0.22m).

3.1. *Structure*

The structure was conceived to be capable of housing an IMU, and gyroscope in its shoulder as well as the motors with their corresponding transmission. The theoretical proportions were integrated with both β and γ shafts being 0.22m apart and both leg segments being equidistant. The casing as seen in Fig. 6 was designed to be milled from aluminium. Extensive load calculations and computer aided analysis have lead to the decision to manufacture both drive shafts of β and γ separately since aluminium was unfit for most load-cases.

4. Conclusion and Future Works

A new concept for an decentralized robotic leg was presented in detail. With focus on the theoretical proportions of the leg, all steps of the design process were highlighted. Starting with the definition of proportions, which were calculated via the Yoshikawa ellipsoids, the leg was designed to be biologically inspired. The length was derived from the robots environmental restrictions and planned stair climbing. A novel method of calculating the

Fig. 6. A complete view of the robotic leg. The blue motors represent MX-106 model actuators. The dark red part is an integrated Raspberry Pi 3 for decentralized task handling.

minimum required leg length was proposed as well. The method links the robots legs length to the geometric values of stairs and can be applied for any robot with such climbing tasks. *Future works* can mainly be seen in the development of a more detailed formula for stair climbing. The presented use-case only covers a part of the robots possibilities and needs further elaboration. Using this concept on rocky terrain is planned in the future but requires geometric abstraction of the terrain. Such design formula would allow the calculation of the optimum length of legs with the knowledge of the terrain characteristics. Tests are planned with the first leg design (shown in Fig.7).

References

1. T. Eisner and S. Camazine, Spider leg autotomy induced by prey venom injection: An adaptive response to 'pain'? (1983).
2. P. A. Fleming and P. W. Bateman, Just drop it and run: the effect of limb autotomy on running distance and locomotion energetics of field crickets (gryllus bimaculatus) (2007).
3. S. Koos, A. Cully and J.-B. Mouret, Fast damage recovery in robotics with the t-resilience algorithm (2013).
4. D. Berenson, N. Estevez and H. Lipson, Hardware evolution of analog circuits for in-situ robotic fault-recovery, in *2005 NASA/DoD Conference on Evolvable Hardware (EH'05)*, June 2005.
5. L. Zullo, G. Sumbre, C. Agnisola, T. Flash and B. Hochner, Nonsomatotopic organization of the higher motor centers in octopus (2009).

152

Fig. 7. The final manufactured leg.The initial aluminium parts were manufactured in FDM (PLA base) to reduce weight furthermore.

6. A. Roennau, G. Heppner, M. Nowicki and R. Dillmann, Lauron v: A versatile six-legged walking robot with advanced maneuverability(07 2014).
7. A. Schneider, J. Paskarbeit, M. Schaeffersmann and J. Schmitz, Hector, a new hexapod robot platform with increased mobility - control approach, design and communication, in *Advances in Autonomous Mini Robots*, eds. U. Rückert, S. Joaquin and W. Felix (Springer Berlin Heidelberg, Berlin, Heidelberg, 2012).
8. D. Wooden, M. Malchano, K. Blankespoor, A. Howardy, A. A. Rizzi and M. Raibert, Autonomous navigation for bigdog, in *2010 IEEE International Conference on Robotics and Automation*, 2010.
9. D. Owaki, T. Kano, K. Nagasawa, A. Tero and A. Ishiguro, Simple robot suggests physical interlimb communication is essential for quadruped walking(10 2012).
10. E. Berg, S. Hooper, J. Schmidt and A. Bschges, A leg-local neural mechanism mediates the decision to search in stick insects(07 2015).
11. F. Tedeschi and G. Carbone, **3**, 181(06 2014).
12. A. Roennau, G. Heppner, M. Nowicki, J. Zoellner and R. Dillmann, Reactive posture behaviors for stable legged locomotion over steep inclines and large obstacles(09 2014).
13. T. Yoshikawa, Manipulability and redundancy control of robotic mechanisms, in *Proceedings. 1985 IEEE International Conference on Robotics and Automation*, Mar 1985.
14. T. Takuma and W. Kase, Robust and directive quadruped locomotion on rough terrain without requiring sensing and actuation, in *2016 IEEE International Conference on Robotics and Biomimetics (ROBIO)*, Dec 2016.
15. S. Kalouche, Snake monster stair ascent https://www.youtube.com/watch?v=urjp3wb3vsy.

SECTION 4

PERCEPTION AND MANIPULATION

REAL TIME CAMERA HOMOGRAPHY ERROR MODELLING FOR SENSORIAL DATA FUSION[*]

RONY CABALLERO[†]

Faculty of Electrical Engineering, Universidad Tecnológica de Panamá, Campus Dr. Victor Levi Sasso, P.O.Box 0819-07289, Panama, Republic of Panama

ARANZAZU BERBEY

Faculty of Electrical Engineering, Universidad Tecnológica de Panamá, Campus Dr. Victor Levi Sasso, P.O.Box 0819-07289, Panama, Republic of Panama

The camera homography estimation involves using complex algorithms. They provide good results after some interactions, however the error model provided for such algorithm seems to be no appropriate for sensorial data fusion in real time. In this work a new methodology is proposed for camera homography and IMU data fusion. The experiment consists in rotate the camera. The experiment is done for frames. Here it is presented results about the error in homography estimation with and without bias compensation. The last section concerns about the experimental results and conclusions about this approach.

Keywords: camera homography estimation, IMU data fusion, bias compensation.

1. Introduction

In the last decades there has been remarkable progress in new robotics applications [1]–[4]. Among the design requirements for such kind of robots, there has been an important effort in using low cost sensor technologies. Now days it is possible to acquire IMUs and cameras for a few dollars. Nevertheless, such kind of Microelectromechanical Systems demands, drift, nonlinear or thermal compensation.

There are several approaches for inertial sensors drift and thermal compensation. However, a more effective one implementation applies first a bias, scale and misalignment effects compensation offline in addition with a real time

drift correction. Drift correction could be realized by using additional measurement systems [5], [6].

Cameras are very useful sensors in many robotics applications. However, in order to obtain accurate measurement most of the cheaper ones, not only need calibration but also distortion compensation [7]–[9]. In addition, in order to track correctly image features, it is necessary to estimate the homography between consecutive images.

Camera homography estimation involves using complex algorithms [9-10]. Even though, these algorithms provide good results after some interactions, the error model provided for such algorithm seems to be no appropriate for sensorial data fusion in real time.

Therefore, it is necessary to estimate an appropriate homography error in real time for data fusion. In this work a new methodology is proposed for camera homography and IMU data fusion.

2. IMU and Camera Modelling

2.1. *Inertial Measurement Unit Error Modelling*

Inertial Measurement Units are usually formed by an array of three gyrorates and three accelerometers. Such kind of sensors present bias drift, scale and misalignment errors. These errors could be characterized approximately by the following equations [6],

$$\xi_\omega = B_\omega + N_\omega \alpha + M_\omega \omega + v_\omega \qquad (1)$$

$$\xi_\alpha = B_\alpha + M_\alpha \alpha + v_\alpha \qquad (2)$$

Where, $\alpha = \begin{bmatrix} \alpha_x & \alpha_y & \alpha_z \end{bmatrix}^T$ are the accelerations in IMU frame,

$\omega = \begin{bmatrix} \omega_x & \omega_y & \omega_z \end{bmatrix}^T$ are the rotational velocities in IMU frame,

$B_\omega = \begin{bmatrix} B_{\omega x} & B_{\omega y} & B_{\omega z} \end{bmatrix}^T$ are the gyrotates bias,

$B_\alpha = \begin{bmatrix} B_{\alpha x} & B_{\alpha y} & B_{\alpha z} \end{bmatrix}^T$ are the accelerometers bias,

$v_\omega = \begin{bmatrix} v_{\omega x} & v_{\omega y} & v_{\omega z} \end{bmatrix}^T$ are gyrorates white noise,

$v_\alpha = \begin{bmatrix} v_{\alpha x} & v_{\alpha y} & v_{\alpha z} \end{bmatrix}^T$ are accelerometers white noise,

$\xi_\omega = \begin{bmatrix} \xi_{\omega x} & \xi_{\omega y} & \xi_{\omega z} \end{bmatrix}^T$ and $\xi_\alpha = \begin{bmatrix} \xi_{\alpha x} & \xi_{\alpha y} & \xi_{\alpha z} \end{bmatrix}^T$ represent the gyrorates and accelerometers errors in IMU frame respectively. Additionally,

N_ω is a matrix that considers the acceleration effects in gyrorates outputs,

M_ω and M_α are matrices that consider scale and misalignment errors in IMU unit.

There are some calibration algorithms that consider bias, scale and misalignment compensation offline. Nevertheless, it will be very useful if a real time drift correction is implemented. Such kind of correction could be realized by using GPS, electronic compass, active ranging sensors or cameras.

2.2. Camera Model

There are several image camera models that could be applied. However, this work will be limited for such applications where scene depth is small compared to average distance to camera. Therefore, the pinhole camera model is chosen to map any visible point in the fixed reference frame (x,y,z) to image plane (u,v).

2.2.1. Pinhole Camera Model

In this approximation, the origin of camera reference frame matches with optical center and z axis matches with camera optical axis. In addition, the image plane (u,v) is not only parallel to (x,y) plane, but also u and v axis are parallel to x and y axis respectively.
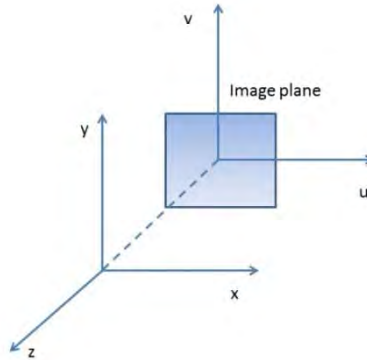
Figure 1. Pinhole Camera Model. Coordinates reference frames.

Any point in reference frame (x,y,z) could be mapped to image plane (u,v) by the following approximation,

$$u \approx \frac{k_x}{z} x \left(1 + \varepsilon \left(x^2 + y^2\right)\right) \tag{3}$$

$$v \approx \frac{k_y}{z} y \left(1 + \varepsilon \left(x^2 + y^2\right)\right) \tag{4}$$

Where, k_x and k_y are the effective focal lengths of the camera. ε is a parameter that approximates radial optical distortion. If ε parameter is positive the image suffers a pincushion effect, but, if it is negative the image suffers a barrel effect. The parameters k_x and k_y could be obtained using an appropriate calibration. Then, radial distortion could be compensated by using Fitzgibbons approach [6],

$$u_{CF} = \frac{u}{1 + \varepsilon_{CF}\left(u^2 + v^2\right)} \tag{5}$$

$$v_{CF} = \frac{v}{1 + \varepsilon_{CF}\left(u^2 + v^2\right)} \tag{6}$$

Where, ε_{CF} is an appropriate chosen parameter that compensates radial optical distortion.

2.2.2. *Affine Transformation*

In order to fusion IMU and camera data is necessary to track image features in video frames. Therefore, it is necessary to analyze how two consecutive frames changes. This relation between two images could be modeled with affine transformation,

$$\begin{bmatrix} u_2 \\ v_2 \\ 1 \end{bmatrix} = H \begin{bmatrix} u_1 \\ v_1 \\ 1 \end{bmatrix} \tag{7}$$

Where, (u_1, v_1) corresponds to pixel coordinates from first image, (u_2, v_2) corresponds to pixel coordinates from second image and H is the homography matrix. The affine transformation homography matrix has the following form,

$$H = \begin{bmatrix} a & b & c \\ d & e & f \\ 0 & 0 & 1 \end{bmatrix} \tag{8}$$

Where, c and f reflect u and v translations respectively. In other hand, a, b, d and e are used to model rotation, shear and scale changes.

2.2.3. *Homography Matrix Estimation*

The homography matrix estimation is a complex process. Various algorithms have been proposed in order to estimate the homograpy matrix between two images. However, must of them consider the following steps: feature detection, feature matching and fitting matrix parameters [10]. The most effective image features for feature matching are corners and SIFTs (Scale Invariant Features Transform).

The feature matching could be implemented with the Scott and Higgins Features Association Algorithm [11]. On the other hand, the matrix parameters could be fitted with RANSAC algorithm (Random Sampling and Consensus Algorithm)[12].

Even though, the RANSAC algorithm is a powerful tool to estimate homography matrix, it does not ensure an unbiased solution. In addition, it does not provide any information about the variances of matrix parameters. Such information could be very useful for sensorial data fusion.

3. Homography Matrix Statistics

The uncertainty around homography matrix parameters could be obtained with the help of feature matching matrix. Even though, this matrix was used by RANSAC algorithm to find homography matrix parameters, it contains outliers data points. These outliers could be produced by low contrast, non-uniform lighting and blurring effects.

3.1. *Homography Error Model Estimation.*

3.1.1. *Bias and Variance Estimation of parameter c and f*

For n samples, c and f bias could be estimated with,

$$\begin{bmatrix} \delta c_k \\ \delta f_k \end{bmatrix} = \frac{1}{n} \sum_{k=1}^{n} \begin{bmatrix} u_{2k} \\ v_{2k} \end{bmatrix} - \begin{bmatrix} \hat{a} & \hat{b} \\ \hat{d} & \hat{e} \end{bmatrix} \begin{bmatrix} u_{1k} \\ v_{1k} \end{bmatrix} - \begin{bmatrix} \hat{c} \\ \hat{f} \end{bmatrix} \tag{9}$$

And variances are estimated with,

$$\begin{bmatrix} \sigma_{ck}^2 \\ \sigma_{fk}^2 \end{bmatrix} = \frac{1}{n-1} \sum_{k=1}^{n} \begin{bmatrix} \left(u_{2k} - \hat{a}u_{1k} - \hat{b}v_{1k} - \hat{c} - \delta c \right)^2 \\ \left(v_{2k} - \hat{d}u_{1k} - \hat{e}v_{1k} - \hat{f} - \delta f \right)^2 \end{bmatrix} \tag{10}$$

3.1.2. *Bias and Variance Estimation of parameter a and d*

For n samples, a and d bias could be estimated with,

$$\begin{bmatrix} \delta a_k \\ \delta d_k \end{bmatrix} = \frac{1}{n} \sum_{k=1}^{n} \begin{bmatrix} \dfrac{u_{2k} - \hat{b}v_{1k} - \hat{c} - \delta c}{u_{1k}} - \hat{a} \\ \dfrac{v_{2k} - \hat{e}v_{1k} - \hat{f} - \delta f}{u_{1k}} - \hat{d} \end{bmatrix} \tag{11}$$

And variances are estimated with,

$$\begin{bmatrix} \sigma_{ak}^2 \\ \sigma_{dk}^2 \end{bmatrix} = \frac{1}{n-1} \sum_{k=1}^{n} \begin{bmatrix} \left(\dfrac{u_{2k} - \hat{b}v_{1k} - \hat{c} - \delta c}{u_{1k}} - \hat{a} - \delta a \right)^2 \\ \left(\dfrac{v_{2k} - \hat{e}v_{1k} - \hat{f} - \delta f}{u_{1k}} - \hat{d} - \delta d \right)^2 \end{bmatrix} \tag{12}$$

3.1.3. *Bias and Variance Estimation of parameter b and e*

For n samples, b and e bias could be estimated with,

$$\begin{bmatrix} \delta b_k \\ \delta e_k \end{bmatrix} = \frac{1}{n} \sum_{k=1}^{n} \begin{bmatrix} \dfrac{u_{2k} - (\hat{a} + \delta a) u_{1k} - \hat{c} - \delta c}{v_{1k}} - \hat{b} \\ \dfrac{v_{2k} - (\hat{d} + \delta d) u_{1k} - \hat{f} - \delta f}{v_{1k}} - \hat{e} \end{bmatrix} \tag{13}$$

And variances are estimated with,

$$\begin{bmatrix} \sigma_{bk}^2 \\ \sigma_{ek}^2 \end{bmatrix} = \frac{1}{n-1} \sum_{k=1}^{n} \begin{bmatrix} \left(\dfrac{u_{2k} - (\hat{a} + \delta a) u_{1k} - \hat{c} - \delta c}{v_{1k}} - \hat{b} - \delta b \right)^2 \\ \left(\dfrac{v_{2k} - (\hat{d} + \delta d) u_{1k} - \hat{f} - \delta f}{v_{1k}} - \hat{e} - \delta e \right)^2 \end{bmatrix} \tag{14}$$

3.2. *Translation, Rotation and Scale Estimation.*

The parameters and variances calculated before could be used to estimate any change in translation, rotation or scale. This information could be used for sensor fusion.

3.2.1. *Translation Estimation*

A change in image translation is directly related with c and f parameters,

$$\begin{bmatrix} \Delta u \\ \Delta v \end{bmatrix} = \begin{bmatrix} c \\ f \end{bmatrix} \tag{15}$$

The variance could be approximated as follows,

$$\begin{bmatrix} \sigma_u^2 \\ \sigma_v^2 \end{bmatrix} = \begin{bmatrix} \sigma_c^2 \\ \sigma_f^2 \end{bmatrix}$$
(16)

3.2.2. *Rotation Estimation*

A change in image rotation could be calculated with a and b parameters,

$$\Delta\theta_z = \text{atan}\left(\frac{\hat{b} + \delta b}{\hat{a} + \delta a}\right)$$
(17)

Meanwhile, if rotation is small, the variance could be approximated as follows,

$$\sigma_{\theta z}^2 \approx \left(\frac{1}{\hat{a}^2}\right)\sigma_b^2 + \left(\frac{\hat{b}^2}{\hat{a}^4}\right)\sigma_a^2$$
(18)

3.2.3. *Scale Estimation*

Any change in image scale could be calculated with,

$$s_u = \sqrt{\hat{a}^2 + \hat{b}^2}$$
(19)

variance could be approximated as follows,

$$\sigma_{su}^2 = \left(\frac{4\hat{a}^2}{\hat{a}^2 + \hat{b}^2}\right)\sigma_a^2 + \left(\frac{4\hat{b}^2}{\hat{a}^2 + \hat{b}^2}\right)\sigma_b^2$$
(20)

4. Data Fusion Methodology

It is important to stablish a relationship between IMU and camera data. The camera homography could be useful to calculate inertial sensors bias if the IMU and camera reference frame are the same. Therefore, any change in the image plane is related with changes in IMU frame,

$$\begin{bmatrix} \Delta u \\ \Delta v \\ \Delta\theta_z \end{bmatrix} = \begin{bmatrix} \dfrac{k_x}{z} & 0 & 0 & \dfrac{k_x l_z}{z} & 0 \\ 0 & \dfrac{k_y}{z} & -\dfrac{k_y l_z}{z} & 0 & 0 \\ 0 & 0 & 0 & 0 & 1 \end{bmatrix} \begin{bmatrix} \Delta x \\ \Delta y \\ \Delta\theta_x \\ \Delta\theta_y \\ \Delta\theta_z \end{bmatrix}$$
(21)

Where, l_z is the average distance from camera reference frame origin to scene plane. This last equation (21) could be used for data fusion. However, accelerometers and gyrates bias drift correction needs additional measurement systems to be estimated simultaneously.

One possible solution is based that in some applications translations and rotations movements are done separately. Therefore, bias correction to accelerometers or gyrates could be applied independently.

4.1. *Accelerometer Bias Correction.*

The accelerometer bias correction could be estimated as follows,

$$
\begin{bmatrix} b_{axk} \\ b_{ayk} \end{bmatrix} = \begin{bmatrix} \dfrac{1}{n-m} \displaystyle\sum_{i=m+1}^{n} \dfrac{z_i c_i}{m\,T^2 k_x} - \dfrac{z_{i-m} c_{i-m}}{m\,T^2 k_x} - a_{xi} \\ \dfrac{1}{n-m} \displaystyle\sum_{i=m+1}^{n} \dfrac{z_i f_i}{m\,T^2 k_y} - \dfrac{z_{i-m} f_{i-m}}{m\,T^2 k_y} - a_{yi} \end{bmatrix} \tag{22}
$$

Where, a_{xi} and a_{yi} are accelerometers outputs, m is a parameter that adjusts acceleration estimation average.

4.2. *Gyrorate Bias Correction.*

The gyrate bias correction could be estimated as follows,

$$
\begin{bmatrix} b_{\omega xk} \\ b_{\omega yk} \\ b_{\omega zk} \end{bmatrix} = \begin{bmatrix} \dfrac{1}{n} \displaystyle\sum_{i=1}^{n} - \dfrac{z_i f_i}{T k_y l_{zi}} - \Omega_{xi} \\ \dfrac{1}{n} \displaystyle\sum_{i=1}^{n} \dfrac{z_i c_i}{T k_x l_{zi}} - \Omega_{yi} \\ \dfrac{1}{n} \displaystyle\sum_{i=1}^{n} \dfrac{\Delta\theta_{zi}}{T} - \Omega_{zi} \end{bmatrix} \tag{23}
$$

Where, Ω_{xi}, Ω_{yi} and Ω_{zi} are gyrates outputs.

5. Experimental Results

The proposed methodology approach is tested for estimating the heading angle of camera. The algorithm uses the Scott and Higgins Features Association, RANSAC and a Kalman filter algorithms to fuse camera and IMU data.

5.1. *Experimental Setup.*

The utilized hardware consist in a color video camera 240x320 and a IMU MPU6050 connected to a Pentium i5 using a frame grabber and a Raspberry PI 3

respectively. The sampling rates are chosen to operate the camera at to 2 images per second and the IMU to 20 samples per second.

5.2. *Kalman Filtering.*

The Kalman filter (please see figure 2) is tuned with the following parameters,

$$x_k = \begin{bmatrix} \theta_k & \dot{\theta}_k & b_k \end{bmatrix}^T, \qquad u_k = 0, \ \Gamma_k = 0, \ \Lambda_k = 1,$$

$$y_k = \begin{bmatrix} \Omega_k - b_{\omega yk} & \dfrac{z_k c_k}{l_z k_x} \end{bmatrix}^T, \qquad \dfrac{z_k}{l_z k_x} \approx 0.2026,$$

$$\Phi_k = \begin{bmatrix} 1 & T & 0 \\ 0 & 1 & 0 \\ 0 & 0 & 1 \end{bmatrix}, \qquad Q_k = \begin{bmatrix} 0.0031 & 0 & 0 \\ 0 & 0.0627 & 0 \\ 0 & 0 & 0.0003 \end{bmatrix},$$

$$H_k = \begin{cases} \begin{bmatrix} 0 & 1 & 1 \\ 1 & 0 & 0 \end{bmatrix} & \text{for } k = 10, 20, 30, 40, 50, \ldots \\ \begin{bmatrix} 0 & 1 & 1 \\ 0 & 0 & 0 \end{bmatrix} & \text{for } k \neq 10, 20, 30, 40, 50, \ldots \end{cases}, \qquad R_k = \begin{bmatrix} 0.33 & 0 \\ 0 & \sigma_{ck}^2 \end{bmatrix}$$

Where, θ is heading angle, $\dot{\theta}$ is the heading angle rate, b is gyrorate bias and Ω_k is the gyrorate output.
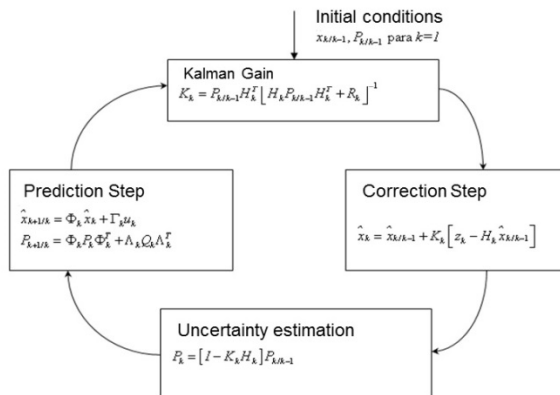
Figure 2. Kalman Filter Algorithm.

5.3. *Result Analysis.*

The experiment consists in rotate de camera 30 degrees. The experiment is done for 14 frames (See figure 3). The homography is first calculated for each pair of frames. Then, homography bias is corrected with help of equation (9). The root mean square error homography is shown in the table 1 for uncompensated and compensated homography. It is clear that camera provides more accurate estimation, however it is slower than gyrorates. Now, the Kalman filter is used for fuse camera and gyrorate information (figure 4). Here, gyrorate data is available for each filter correction step, but camera data is only available each ten steps.
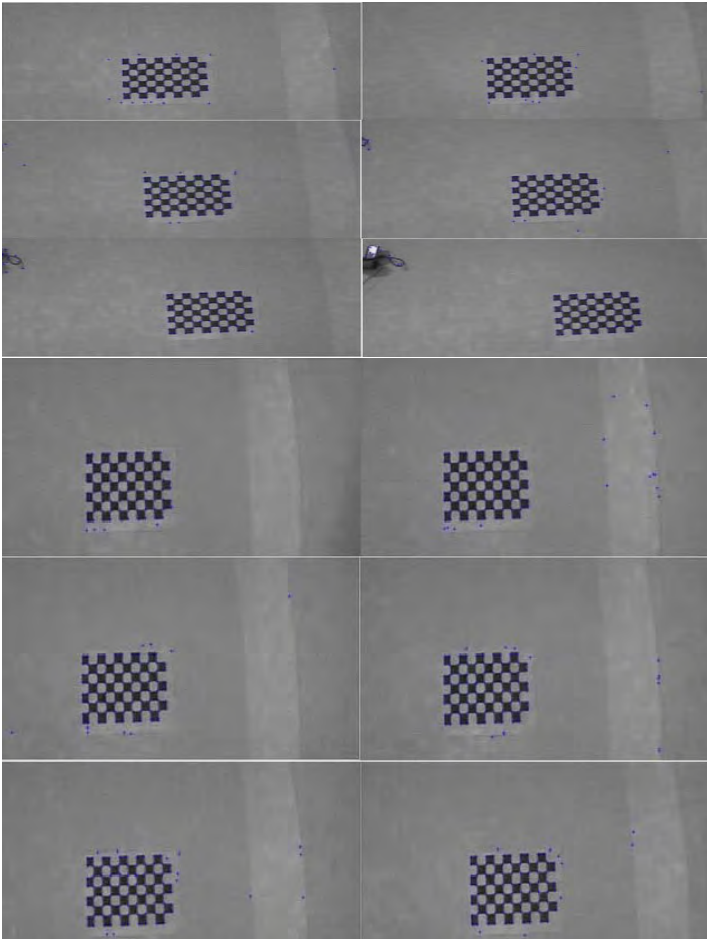
Figure 3. Frames with corners detection.
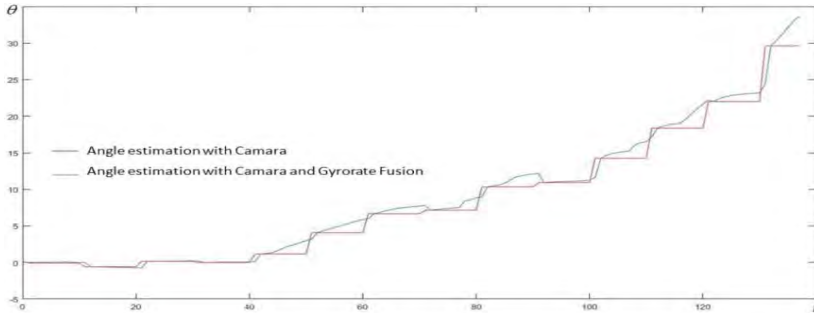
Figure 4. Heading angle estimation.

Table 1: Root mean square error in homography estimation for 800 interactions RANSAC with and without bias compensation.

	Frames 0 to 1	Frames 1 to 2	Frames 2 to 3	Frames 3 to 4	Frames 4 to 5	Frames 4 to 6	Frames 6 to 7
without compensation	1.1551	0.9389	4.3063	0.2882	2.7688	2.8641	4.0229
with compensation	0.9295	0.5755	0.9494	0.2877	0.9075	0.5464	2.5672
	Frames 7 to 8	Frames 8 to 9	Frames 9 to 10	Frames 10 to 11	Frames 11 to 12	Frames 12 to 13	Frames 13 to 14
without compensation	1.8736	0.7202	0.4909	0.7146	2.0290	2.8287	4.3092
with compensation	1.5800	0.3466	0.1091	0.4921	2.0158	2.4149	3.1275

6. Conclusions

The homography error model estimation was not only a useful tool for data fusion, but also for improving homography. The bias compensation improves system velocity, since RANSAC interaction could be diminished. However, in this aspect, more research must be done in order to obtain an appropriate value of interactions. Also, lot of further work is necessary in order to improve data fusion methodology. It is interesting, to analyze fusion with two or more cameras, other sensors technologies or applying artificial intelligence algorithm approaches.

References

1. M. Quan, S. Piao, M. Tan, and S.-S. Huang, "Accurate Monocular Visual-inertial SLAM using a Map-assisted EKF Approach," pp. 1–12, 2017.
2. F. M. Mirzaei and S. I. Roumeliotis, "A Kalman Filter-Based Algorithm for IMU-Camera Calibration: Observability Analysis and Performance Evaluation," *IEEE Trans. Robot.*, vol. 24, no. 5, pp. 1143–1156, 2008.
3. K. Nirmal, A. G. Sreejith, J. Mathew, M. Sarpotdar, A. Suresh, A. Prakash, M. Safonova, and J. Murthy, "Noise modeling and analysis of an IMU-based attitude sensor: improvement of performance by filtering and sensor fusion," 2016.
4. M. Alatise and G. Hancke, "Pose Estimation of a Mobile Robot Based on Fusion of IMU Data and Vision Data Using an Extended Kalman Filter," *Sensors*, vol. 17, no. 10, p. 2164, 2017.
5. S. Romaniuk and Z. Gosiewski, "Kalman filter realization for orientation and position estimation on dedicated processor," *Acta Mech. Autom.*, vol. 8, no. 2, pp. 88–94, 2014.
6. E. H. Shin and N. El-Sheimy, "A new calibration method for strapdown inertial navigation systems," *Zeitschrift für Vermessungswes.*, vol. 127, no. 1, pp. 41–50, 2002.
7. J.Y.Weng, P.Cohen, and M.Herniou, "Camera calibration with distortion model and accuracy evaluation," *IEEE Trans. Pattern Anal. Mach. Intell*, vol. 14, no. 10, pp. 965–980, 1992.
8. J. H. Brito, R. Angst, K. Koser, and M. Pollefeys, "Radial distortion self-calibration," *Proc. IEEE Comput. Soc. Conf. Comput. Vis. Pattern Recognit.*, pp. 1368–1375, 2013.
9. L. Ma, Y. Chen, and K. L. Moore, "A Family of Simplified Geometric Distortion Models for Camera Calibration," vol. 1, no. 2, pp. 1–14, 2003.
10. R. Hartley and A. Zisserman, "Multiple View Geometry in Computer Vision Second Edition," *CEUR Workshop Proc.*, vol. 1542, no. 9, pp. 33–36, 2015.
11. G. L. Scott and H. C. Longuet-Higgins, "An Algorithm for Associating the Features of Two Images," *Proc. R. Soc. B Biol. Sci.*, vol. 244, no. 1309, pp. 21–26, 1991.
12. I. Austvoll and B. Kwolek, "39.Region covariance matrix-based object tracking with occlusions handling.pdf," pp. 1–8.

CUCUMBER DETECTION FOR PRECISION AGRICULTURE APPLICATIONS[*]

ROEMI FERNÁNDEZ[†], VICTOR ALIENDE, PABLO GONZALEZ-DE-SANTOS, MANUEL ARMADA

Centre for Automation and Robotics CAR CSIC-UPM
Ctra.Campo Real, km 0.2, La Poveda, Arganda del Rey 28500, Madrid, Spain

JELENA SURDILOVIC

Leibniz-Institut für Agrartechnik und Bioökonomie e.V. ATB
Max-Eyth-Alle 100, D-14469, Potsdam, Germany

DRAGOLJUB SURDILOVIC

Fraunhofer-Institut für Produktionsanlagen und Konstruktionstechnik IPK
Palcalstraße 8-9, 10587 Berlin, Germany

The objective of this research was to explore the feasibility of detecting cucumber fruits in field conditions for autonomous robotic harvesting applications. A high resolution colour camera and a time-of-flight camera are proposed as primary sensors for the design of the sensory system. The preliminary detection algorithm includes a pixel-based classifier that labels areas of interest that belong to cucumber fruits and a registration procedure that combines the results of the aforementioned classifier with the range data provided by the time-of-flight camera. The detection algorithm is extremely simple and efficient, and provides a satisfactory discrimination of the cucumbers fruits with respect to the rest of the

elements of the scene. Several experimental tests have been carried out in outdoor conditions in order to evaluate and demonstrate the capabilities of the proposed approach.

1. Introduction

Over the past two decades, several studies have been conducted to provide automatic detection and measurement systems for different features of cucumbers crops. For instance, van Henten et al. [1] proposed a combination of two CCD cameras, one equipped with an 850 nm filter and the other with a 970 nm filter for detecting cucumber fruits grown in greenhouses using a high-wire cultivation system, in which every plant is attached to a wire. Experimental tests showed that the designed system was able to detect more than 95% of the fruits in a dataset of 106 cucumbers. A segmentation algorithm based on rough set theory was presented in [2] for solving the problem of cucumber identification in greenhouses. However, no quantitative results derived from the proposed algorithm were presented. In [3], a three-layer back-propagation neural network combined with a texture analysis was established to detect greenhouse cucumber fruits. The algorithm was tested on 40 cucumber plant images, and a detection rate of approximately 76% was achieved considering only backlighting conditions. A multi-template matching method was utilized by Bao et al. [4] to recognize matured Radit cucumbers grown vertically in a greenhouse. Proportional scaling and rotation operations were applied to a standard cucumber image to build a multi-template matching library, whereas the multi-template matching method was developed by using the normalized correlation coefficients algorithm.

This paper presents the first steps carried out for the design, implementation and validation of an efficient, adaptable and robust sensing system for the detection of cucumbers fruits in field conditions. The proposed solution differs from all previous approaches found in the literature, which mainly focus on the detection of cucumbers grown in greenhouses by using wire cultivation systems.

The manuscript is organized as follows. Section 2 describes the sensory rig that has been designed and manufactured for the acquisition of images. Section 3 presents the algorithm proposed for the detection of cucumbers fruits in outdoor conditions. In Section 4, results of this study are discussed. Finally, major conclusions and lines of future extensions are summarised in Section 5.

2. Description of the sensory system

The proposed multisensory system consists of an AVT Prosilica GC2450 high resolution CCD colour camera and a Mesa SwissRanger SR-400011 TOF (Time-Of-Flight) 3D camera. The 5-megapixel GC2450 has a frame rate of up to 15 fps

at 2448×2050 pixels resolution. Meanwhile, the TOF camera provides a depth map and an amplitude image at the resolution of 176×144 pixels with 16 bit floating-point precision and a maximum frame rate of 54fps, as well as x, y and z coordinates to each pixel in the depth map. The detection range (radial distances) of this device goes from 0.1 m to 5.0 m, and its field of view is $69°$ (h) $\times 56°$ (v). The proposed multisensory system is shown in Figure 1.

Intrinsic and extrinsic calibration parameters of both cameras (RGB and TOF) were estimated by using the Matlab camera calibration toolbox [5]. A distance measurement calibration was also carried out in Matlab (http://www.mathworks.com/products/matlab/) for the TOF camera by following the method proposed in [6].

Figure 1. Proposed multisensory system.

3. Detection algorithm

Taking into consideration the configuration described in the previous Section, two complementary procedures are proposed for the detection algorithm: a pixel-based classification procedure that labels areas of interest that are candidates for belonging to cucumber fruits and a registration procedure that combines the results of the aforementioned classifier with the data provided by the TOF camera for the 3D reconstruction of the desired regions. These procedures are described below.

The first procedure, based on Support Vector Machines (SVMs), is capable of labelling each pixel of the image into three classes that are: cucumber, leaves and background. SVM is a supervised learning method utilized for classifying set of samples into two disjoint classes, which are separated by a hyperplane defined on the basis of the information contained in a training set [7-10]. In the case at

hand, three SVMs are utilized sequentially, each one for detecting a class against the rest. Therefore, after the first SVM is applied, pixels identified as belonging to cucumber class are labelled and a mask is generated in such a way that only the remaining pixels are considered for the following SVMs. This step is then repeated for the leaves class and the background class. The SVM classifiers are trained by selecting a random subset of samples from the RGB images and manually labelling the regions of interest from these images into the three semantic classes mentioned above.

Once regions of interest have been detected in the scene, it is necessary to locate them spatially. The TOF camera included in the proposed multisensory system provides amplitude, depth and confidence data simultaneously for each pixel of the captured image. The amplitude represents the greyscale information, the depth is the distance value calculated within the camera and the confidence is the strength of the reflected signal, which means the quality of the depth measurements. Although TOF data is fundamental for localisation purposes, it is still necessary to automatically match this information with the classification map obtained from the previous step in a common reference frame [11]. For accomplishing this procedure it should be taken into account that TOF images and resulting classification maps come from sensors that exhibit different field of view and different pixel array size. Thus, data will only depict the same content partially, and the pixel correspondence will not be direct. To overcome this problem, the random sample consensus (RANSAC) algorithm is adopted for the multisensory registration [11, 12]. RANSAC is one of the most robust algorithms for model fitting to data containing a significant percentage of errors [13]. This iterative method estimates parameters of a mathematical model from a set of observed data which contains outliers. As the multisensory system has been designed in an enclosure that prevents the relative movements between the different elements that compose it, the idea is to use the RANSAC method to find the rotation and translation (R, T) that enable the transformation of the TOF data into the reference frame of the classification map. In this way, the transformation given by (R, T) may be applied to any image acquired with the TOF camera, obtaining quickly and efficiently the registered data and it won't be necessary to recalculate this transformation as long as the multisensory rig is not modified.

4. Experimental results

In order to validate the proposed approach, several experimental campaigns for acquiring training and ground truth data were carried out in the summer of 2017.

The experimental field was planted with Liszt cucumbers from the seed producer Ryk Zwaan GmBH.

Figure 2(a, b) shows the RGB image for one scene, together with the classification map resulting after applying the first part of the detection algorithm. In the classification map, yellow, green and white colours are utilised to visualize pixels classified as cucumbers, leaves and background, respectively. In addition, the blobs extracted from the classification map are displayed on Figure 3. For each blob, the centroid and the area are calculated.

(a)   (b)

Figure 2. (a) Original RGB image. (b) Resulting classification map.

Figure 3. Resulting blobs provided by the first part of the detection algorithm.

Computation of the registration procedure required a significant collection of ground truth correspondences (about 300 pairs of points), trying to cover the entire field of view of the cameras [11, 12]. Registration procedure was tested indoors and outdoors, in order to evaluate possible interferences due to natural light (direct sun light), as well as the response to objects exhibiting different geometries. For this purpose, several landmarks were located in a scene with known objects, in order to measure the deviations. Table 1 summarizes not only the minimum and maximum errors but also the mean errors in each axis for indoor conditions. Table 2 gathers the obtained results for outdoor conditions. Figure 4 shows two close-up views of a registered region of interest extracted from the scene displayed on Figure 2(a).
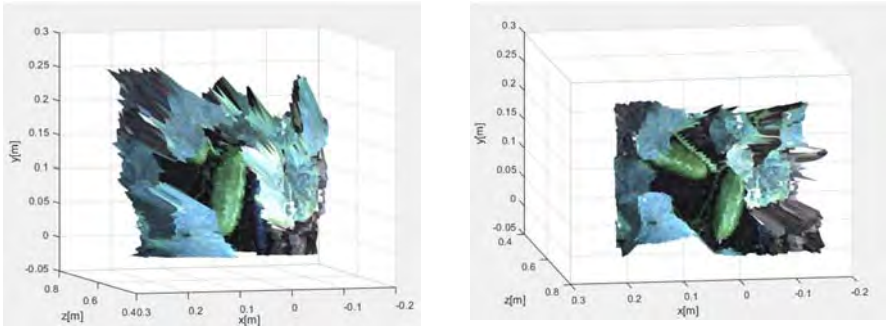
Figure 4. Close-up views of a registered region of interest extracted from the scene displayed on Figure 2(a).

Table 1. Position errors from the TOF registered data in indoor conditions.

Axis	Minimum error [cm]	Maximum error [cm]	Mean absolute error [cm]
X	0.2	1.3	0.8
Y	0.3	1.6	1.1
Z	0.1	2.2	1.0

Table 2. Position errors from the TOF registered data in outdoor conditions.

Axis	Minimum error [cm]	Maximum error [cm]	Mean absolute error [cm]
X	0.5	1.9	1.4
Y	1.0	2.3	1.7
Z	0.4	3.0	1.5

Assuming that cucumbers are always lying on the ground, it is possible to use resulting registered data for improving detection algorithms. The idea is to discard all the blobs that are located above a predefined height (false positive detections). Figure 5 shows results of this procedure for the scene displayed previously on Figures 1-3. In this way, only blobs that correspond with the cucumbers are preserved.

<table>
<tr><td>(a)</td><td>(b)</td></tr>
</table>

Figure 5. (a) Original RGB image. (b) Detection result after discarding blobs located above a predefined height.

5. Conclusions

This paper proposes a multisensory approach for the detection of cucumbers in natural scenarios. The solution includes a high resolution colour camera, a TOF camera, and a detection algorithm composed of a pixel classifier based on SVMs and a registration procedure that combines the resulting classification map with the data provided by the TOF camera, in such a way that the range data can be associated to the image pixels identified as cucumbers.

Preliminary experimental results demonstrate the feasibility of the proposed approach and highlight the advantages of the solution. The simplicity of the sensory rig in comparison with other multispectral approaches decreases the total cost of the system and makes the future harvesting robot in which it is incorporated more competitive in the market.

Future work will be directed to reduce the detection and localization errors in order to achieve a more robust application.

References

1. van Henten, E.J., et al., *An Autonomous Robot for Harvesting Cucumbers in Greenhouses.* Autonomous Robots, 2002. **13**(3): p. 241-258.
2. Qing-Hua, Y., et al., *Cucumber image segmentation algorithm based on rough set theory.* New Zealand Journal of Agricultural Research, 2007. **50**(5): p. 989-996.
3. Zhang, L., et al., *Recognition of greenhouse cucumber fruit using computer vision.* New Zealand Journal of Agricultural Research, 2007. **50**(5): p. 1293-1298.
4. Bao, G., et al., *Multi-template matching algorithm for cucumber recognition in natural environment.* Computers and Electronics in Agriculture, 2016. **127**: p. 754-762.
5. Bouguet, J.-Y., *Camera calibration toolbox for MATLAB*. 2010.
6. Chiabrando, F., et al., *Sensors for 3D Imaging: Metric Evaluation and Calibration of a CCD/CMOS Time-of-Flight Camera.* Sensors, 2009. **9**(12): p. 10080.
7. Fernández, R., H. Montes, and C. Salinas, *VIS-NIR, SWIR and LWIR Imagery for Estimation of Ground Bearing Capacity.* Sensors, 2015. **15**(6): p. 13994.
8. Fernández, R., et al., *Combination of RGB and Multispectral Imagery for Discrimination of Cabernet Sauvignon Grapevine Elements.* Sensors, 2013. **13**(6): p. 7838.
9. Fernández, R., et al., *Multisensory System for Fruit Harvesting Robots. Experimental Testing in Natural Scenarios and with Different Kinds of Crops.* Sensors, 2014. **14**(12): p. 23885.
10. Mucherino, A., P.J. Papajorgji, and P.M. Pardalos, *Data Mining in Agriculture*. 2009: Springer New York.
11. Salinas, C., et al., *A New Approach for Combining Time-of-Flight and RGB Cameras Based on Depth-Dependent Planar Projective Transformations.* Sensors, 2015. **15**(9): p. 24615.
12. Salinas, C., *A non-feature based method for automatic image registration relying on depth-dependent planar projective transformations. Ph.D. Thesis*, in *Departamento de Arquitectura de Computadores y Automática*. 2015, Universidad Complutense de Madrid.
13. Fischler, M.A. and R.C. Bolles, *Random sample consensus: a paradigm for model fitting with applications to image analysis and automated cartography.* Commun. ACM, 1981. **24**(6): p. 381-395.

VISUAL CONTROL OF A ROBOTIC ARM

GEORGE CARTER, M. OSMAN TOKHI AND OUSMANE A. OUMAR

School of Engineering, London South Bank University, London, UK.

Abstract. Integration of robot control with computer vision is an emerging technology. The ability to capture a real world scenario, filter out a specific object, and then localise it with respect to a specific point opens up many avenues for future technologies. In this paper, computer vision is integrated with a 6-DOF robotic arm. The aim is to develop a methodology for controlling a robotic arm through visual interaction. The investigations carried out include mathematical and geometrical representation of the physical manipulator, object detection utilising a colour segmentation approach, establishing communications from the command line of the visual recognition program with an Arduino and development of a user orientated software package that integrates the two key objectives.

Keywords: Robotic arm, computer vision, object localisation.

1. Introduction

The aim for most robotic designs is to alleviate the need for human intervention; that is, for robots to perform tasks with more efficiency, accuracy and precision over a more sustained period. For a robot to execute a task in this manner, it needs to be equipped with human-like senses; somatosensation, audition, vision, balance and local body orientation. With the advancement of digital cameras, machine vision has become an interesting field of discovery. One of the key tools developed is OpenCV, which is an open-source computer vision library [1]. Scenarios utilising computer vision use a digital camera attached to the end-effector [2], a fixed [3] or a mobile robot [4]. The fixed approach has proved more accurate with its detection compared to mounting the camera on the end-effector and to the mobile robot due to error caused by vibration through their movement. To overcome this, stereovision has become a viable option, with algorithms developed to achieve synchronised vision using two cameras [5].

Two main image-processing routes are widely used due to their accuracy rates and amount of relevant literature available. The first technique utilises colour detection within the Hue, Saturation and Value (HSV) scale [6]. The HSV

parameters are varied to single out a specific colour before morphological operations are performed on the image to increase the accuracy of detection. The alternative to this is to use grayscale, which is a binary image equating the light intensity of each pixel with a particular shade of gray [7]. Similar to HSV, the BGR/RGB image is converted to grayscale in order to be processed. Once in this binary form an algorithm called canny edge detection is used to single out particular objects [8]. The detected object will have a white line around its edges, signifying the location. The major issue coming out of these two approaches are the accuracy of detection due to lighting and camera quality.

The work presented in this paper focuses on the control a 6 degree of freedom (DOF) robotic arm. In order to orientate the end-effector of a manipulator to a particular Cartesian coordinate, the inverse-kinematics approach is adopted, where the Cartesian space is transformed into joint variable space. There are several approaches available for solving the inverse-kinematics problem for a six-joint manipulator. These include inverse transform, screw algebra, dual matrices, dual quaternion, iterative and geometric approaches [9]. The possibility of extensive modelling of the approach chosen is imperative. The geometric approach was selected in this study as it enables modelling of all six joints individually and concurrently, providing extensive understanding of response of each joint. The work presented forms the basis of integrating machine vision with robot control. The concept could be extended for implementation in areas such as hazardous environments, exploration or explosive ordnance disposal.

2. Control Algorithm

Figure 1 shows the physical and mathematical representations of joint 1 of the manipulator. An external camera with a limited field of vision; 60°, is used, and to allow maximum coverage of the manipulator's workspace, the camera is mounted, at a 45° angle and located approximately 38cm to the left of the base of the robot.

(a)   (b)
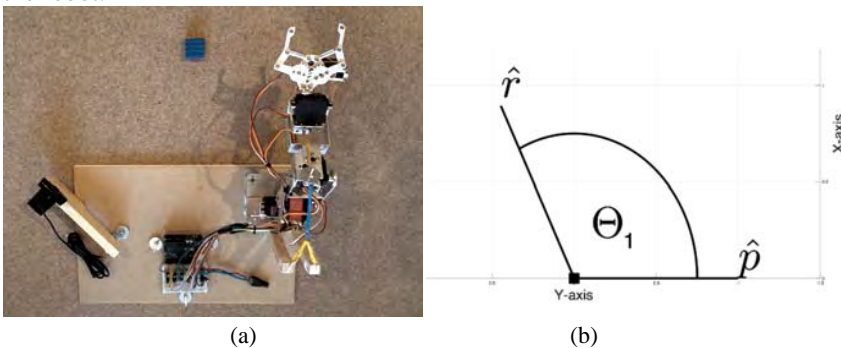
Figure 1: (a) Physical representation of joint 1. (b) Mathematical representation of joint 1.

The geometric approach to solving the inverse kinematics problem for a six-joint manipulator produces several solutions depending on the desired orientation of the arm. In order to minimise the number of solutions available, enabling full robot autonomy, the six joints are broken down into sections. Each section, in turn, is then analysed and an algorithm for its control is generated, along with a visual representation of the joint.

The purpose of joint 1 is to orientate the robot arm in the direction of the object. For the servomotor to move to a desired location, a joint angle must be specified. If the servomotor is already stationed at 90° and a new angle is specified, the servomotor would move from 90° to the new angle. This functionality means that the displacement angle of the object needs to be referenced to a fixed point, $\hat{p}$.
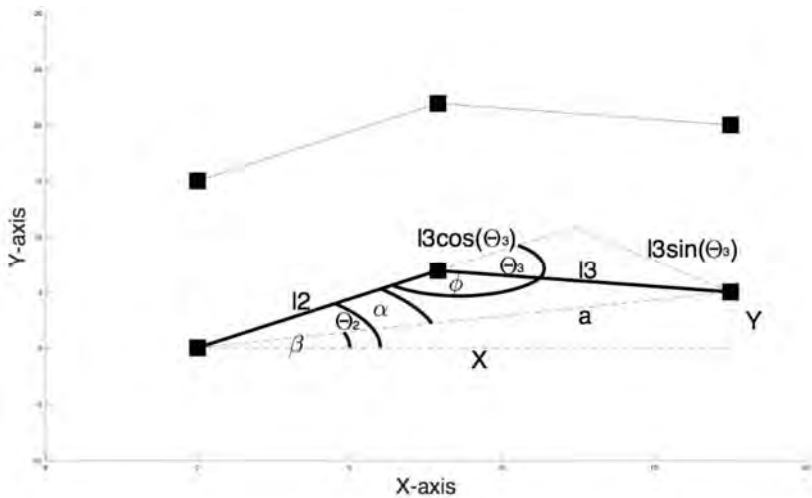
Figure 2: Mathematical & geometrical representation of joints 2 & 3

The final three joints would orientate the end-effector so that it is perpendicular to the face of the object it is grabbing. With this operation joints 2 and 3 would position the arm so that joint 4 is able to rotate the final joints to this objective. Figure 2 shows a geometric representation of joint orientations, where x and y are the desired coordinates of joint 4, $l2$ and $l3$ are the lengths of link 2 and link 3 respectively, a is the magnitude of x and y , θ_2 is the displacement angle of joint 2 from the x -axis, θ_3 is the displacement angle from the continuation of link 2 and link 3, ϕ is $\pi - \theta_3$, α is the difference of $\theta_2 - \beta$, where β is the displacement angle of a from the x -axis. The calculation for each parameter is as follows:

$$\phi = atan2(cos(\phi), sin(\phi)) \tag{1}$$

where,

$$cos(\phi) = \frac{l2^2 + l3^2 - a^2}{2 \cdot l2 \cdot l3} \tag{2}$$

$$sin(\phi) = \pm\sqrt{1 - cos^2(\phi)} \tag{3}$$

$$\theta_3 = 180 - \phi \tag{4}$$

$$\beta = atan2(x, y) \tag{5}$$

$$\alpha = atan2(l2 + (l3 \cdot cos(\theta_3)), l3 \cdot sin(\theta_3)) \tag{6}$$

$$\theta_2 = \alpha + \beta \tag{7}$$

Therefore, the resultant servo joint angles are given as

$$Joint2 = 90^o + \theta_2 \tag{8}$$

$$Joint3 = 90^o + \theta_3 \tag{9}$$

3. Pinhole Camera Model

The pinhole camera model depicted in Figure 3 shows the approach for real world mapping onto an image plane for a calibrated camera at a single instance of an objects depth from the camera. F_c is the optical centre, from which all of the information from the real world is passed to the image plane. The distance from the optical centre to the principal point changes depending upon the real world value of the objects distance from camera, known as the focal length. Calibrating this enables rudimentary calculation of the objects distance from the focal point.

Figure 4 shows measured values of focal length as function of distance from optical centre. The blue line in Figure 5 illustrates how the focal length changed with respect to the distance of the object. As the object moved further away, the focal length increased, insinuating that it was increasing the distance from the optical centre to the principal point allowing more information from the real world to be captured. The line of best fit generated a function for the focal length as

$$f(z) = (0.2537 \cdot z) + 658.7 \tag{10}$$
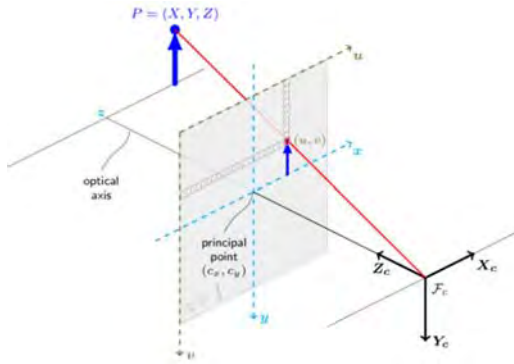
Figure 3: Pinhole camera model [10].
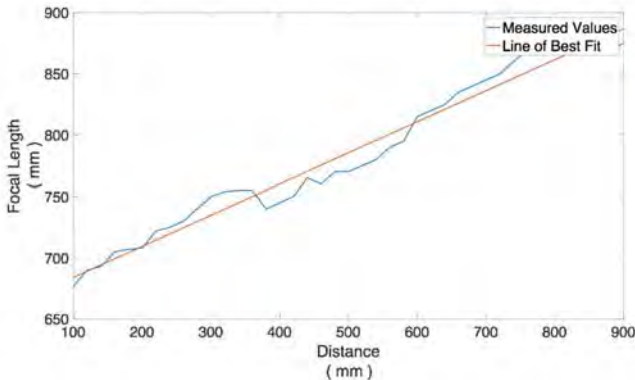
Figure 4: Focal length with respect to distance of object from optical centre.

4. Object Detection and Localisation

Figure 5 illustrates the procedure undertaken within the visual recognition algorithm. Utilising the colour segmentation approach, understanding the HSV scale was imperative. Hue defines the colour type; saturation defines the brightness and value the intensity of the colour. OpenCV enables user interactivity through graphical user interfaces. In this case, a trackbar was used to vary the values of HSV to visualise the filtering. Once filtering has taken place the threshold image undergoes morphological operations; erosion, dilation and Guassian blur, removing any unwanted noise in the frame. After the object has been correctly filtered its contours and centre of mass are detected, with a bounding box and centre circle displayed to the user on the camera frame. The focal length is updated on each frame, increasing its precision, from which the x, y & z coordinates with respect to the camera frame are generated. These are then

rotated and translated with respect to the robot base in order for the joint angles to be calculated.

Convert BGR to HSV		Calculate Joint Angles
Filter HSV		Calculate X, Y & Z w.r.t. Robot Frame
Morphological Operations		Calculate X, Y & Z w.r.t. Camera Frame
Contour Detection		Update Focal Length
Centre of Mass		
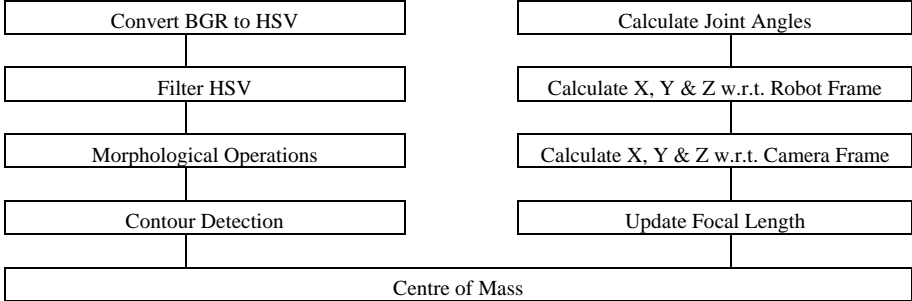
Figure 5: Visual recognition algorithm

Figure 6 demonstrates the visual recognition program detecting the yellow object; drawing a bounding box around it as well as its centre of mass, displaying its dimensions in pix-els and millimetres and its location in pixels as well as with respect to the robot base in millimetres. The left hand frame is the camera feed, the right hand frame is the threshold image, and the two lower trackbar boxes are used to vary the hue, satura-tion and value parameters and the object's dimensions in millimetres.
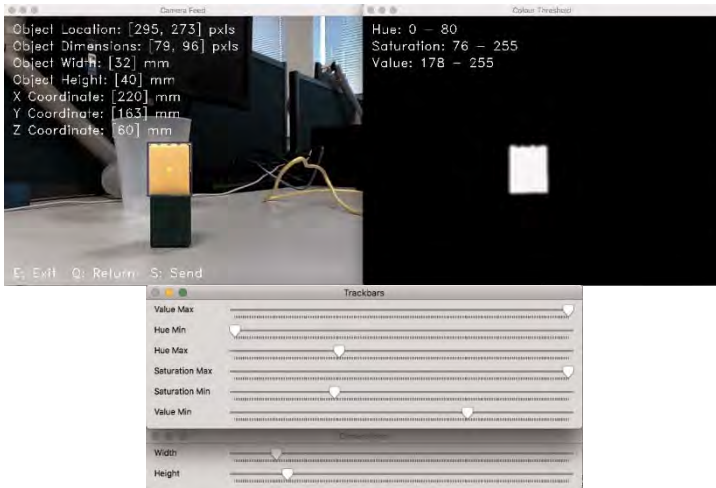
Figure 6: Visual recognition program detecting and localising object with respect to robot base.

5. Communication

The communications platform CoolTerm was chosen as the means of communication [11]. This piece of software accesses the USB port and sends a string of characters in ASCII format via TTL logic. At first, the TX-RX cables of the TTL were connected to the Arduino. With some manipulation of the SoftwareSerial library within the Arduino, the ASCII characters were converted back to decimal integer format, allowing a more complete design to digest and disseminate data effectively and efficiently ensuring the robot autonomously orientates itself to grab an object.

6. Results and Analysis

Object detection and localisation was achieved, yet with some error. The curvature of the lens assumed the object was closer to the centre than it actually was. However, as the curvature was uniform it could be modelled and an error reduction algorithm was generated to compensate for this undershoot. Implementing the error reduction algorithm the visual recognition program correctly detected and localised a block coloured object with respect to the robot base. The servomotor controlling the first joint produced some error due to the loading of the successive joints and object. The servomotor was undershooting from 45° - 135° and overshooting from 0° - 45° and 135° - 180°. An algorithm was written to compensate for this under and overshooting. A communications platform was established utilising the software program CoolTerm. Data was sent and received as ASCII characters between the Arduino and the program correctly.

7. Conclusion

A visual approach for control of a 6DOF manipulator has been presented. The robot arm and camera have been mounted on one solid base with the camera positioned to maximise its field of vision. Although low quality, the camera has still correctly detected and localised the object on each trial. Reasonable accuracy in object detection and localisation has been achieved, and any errors caused by the quality of the camera have been mitigated by introduction of an error reduction algorithm. The visual recognition program has been shown to correctly detect and localise a block coloured object. The work presented provides a framework for further research into object detection and localisation, as well as precise robot control.

References

1. OpenCV Team. (2018). OpenCV Library [Online]. Available: https://opencv.org/

2. A. De Luca, M. Ferri, G Oriolo, "Visual servoing with exploitation of redundancy: An experimental study," International Conference on Robotics and Automation (ICRA 2008), 2008, pp. 3231-3237. doi: 10.1109/ROBOT.2008.4543703

3. Mussabayev RR. "Colour-based object detection, inverse kinematics algorithms and pinhole camera model for controlling robotic arm movement system," International Conference on Electronics Computer and Computation, 2015, pp. 1-9. doi: 10.1109/ICECCO.2015.7416879

4. J. Cernohorsky, P. Jandura, O. Mach. "Mobile robot localization and object description," 18th International Carpathian Control Conference, 2017, pp. 1-4. doi: 10.1109/CarpathianCC.2017.7970452

5. A. Tse, J. Saegnwipharat, K. Supayanant, "Controlling children-toy tank by using image processing technique," ICT International Student Project Conference (ICT-ISPC), 2016, pp. 73-76. doi: 10.1109/ICT-ISPC.2016.7519239

6. P. Khelbude, S. Shelke, "Real time iris controlled robot," Online International Conference on Green Engineering and Technologies (IC-GET), 2016, pp. 1-4. doi: 10.1109/GET.2016.7916648

7. M. Dragusu, A. N. Mihalache, R. Solea, "Practical applications for robotic arms using image processing," 16th International Conference on System Theory, Control and Computing (ICSTCC), 2012, pp. 1-6. [Online] Available: http://ieeexplore.ieee.org/document/6379295/

8. K. S. Fu, R. C. Gonzalez, C. S. G. Lee, Robotics: Control, Sensing, Vision, and Intelligence, International Edition, Book, Singapore: McGraw-Hill Book Co, 1987. ISBN 0-07-100421-1.

9. OpenCV Team. (2014). Camera Calibration and 3D Reconstruction [Online]. Available: https://docs.opencv.org/2.4/modules/calib3d/doc/camera_calibration_and_3d_reconstruction.html.

10. Roger Meier. (2018). Roger Meier's Freeware [Online]. Available: http://freeware.the-meiers.org/.

A NOVEL HOLONOMIC MOBILE MANIPULATOR ROBOT FOR CONSTRUCTION SITES

A. J. Gmerek, A. Plastropoulos, M. Kimball, A. Sain, K. Shah, A. Wheatley,
P. Collins, P. T. Karfakis, J. Liu, J. Carroll and G. S. Virk*

*Innovative Technology and Science Ltd,
Cambridge, United Kingdom
E-mail: gurvinder.virk@innotecuk.com

This article describes a novel mobile manipulator robot designed to work at height on construction sites. The robot comprises a mobile platform and a scissor lifter on which an ABB 6 dof manipulator is mounted. The mobile base is characterised by holonomic kinematics, provided by a novel designed omnidirectional wheel system that can travel directly and autonomously to desired poses. The robot was successfully tested in a construction site scenario to perform drilling tasks.

Keywords: Construction site; Mobile manipulation; Holonomic, omni-wheel, ROS.

1. Introduction

Construction work involves a variety of challenging and hazardous scenarios which cannot be easily automated. The main issues that need to be addressed are the dynamic and relatively unstructured environment and the complexity of the tasks that need to be carried out. Hence, the industry has traditionally relied heavily on manual processes and has not made major productivity gains found in other sectors; in addition, it is suffering from widespread labour shortages.

Given these issues, efforts are being made to introduce innovations such as automation and robotics to improve worker safety and increase productivity levels in line with other domains, as it is well known that robotics and automated systems have the potential to address revolutionise the field. In many applications, robots are more efficient and more precise than humans and can perform dangerous and physically demanding tasks, thereby reducing the risk to workers and allowing them to focus on more cognitive tasks. As robotics continues to advance, construction firms are becoming

more receptive to adopting automated processes. Many diverse applications within the industry can be enhanced using robotic technology, e.g. traditional activities such as welding, cutting, material handling, and drilling.

Variations of robotic construction platforms have been developed since the 1970s, with on-site operations beginning in the 1980s.[1] The specialisation of construction robots in bricklaying, welding, demolition, and surveying sectors have been advanced, due to the repetitive and monotonous nature of the work. Anlinker et al.,[2] Lehtinen et al.,[3] and Slocum et al.[4] developed some of the earliest bricklaying and welding robots, utilising robotic grippers on a moveable platform. Dharmawan[5] outlines the development of an agile robotic arm mountable on scaffold structures (used for in situ large-scale construction), highlighting the need to reach elevated heights on construction sites. Since 2012, nLink from Norway[6] has been developing a mobile scissor lifter fitted with a robotic arm, providing on-site assistance for overhead drilling with autonomous control. However, until recently, manufacturing and assembly robots have been confined to the regulated workcells in industrial environments. With the advent of innovative localisation and detection systems, other types of service robots have recently been emerging because they can operate more readily in wider rugged environments such as construction sites.[5,7]

Precise control of construction robots is vital in compliance with safety regulations to ensure safety and effectiveness, especially as there are many possible hazards present on building sites. Efficient collision-free path planning is particularly important and has been explored in[8] to achieve obstacle avoidance in an unknown environment with static and dynamic obstacles. Different levels of autonomy have also been explored for construction robots, mainly fully autonomous robots and teleoperated robots.

The objective of this paper is to introduce a mobile robot that was developed to carrying out a variety of tasks in construction sites. The remainder of the paper is as follows. Section 2 describes the methodology used to select the robot's kinematics and Section 3 presents details of the robot developed in a systematic manner starting from system design, mechanical design, and ending with software and control. Section 4 presents results of experiments carried out to test the robot and section 5 presents conclusions from the research.

2. Methodology of selecting robot's kinematics

The most important part of work was to select a kinematic configuration of a robot that can provide high manoeuvrability, good obstacle crossing ca-

pabilities, good stability during all operations and high positional accuracy while being relatively easy to develop and manufacture. The main purpose of the mobile platform is to carry the robotic arm while it performs manipulation tasks. Thus, the platform must have good stability when stationary otherwise extrinsic motion errors may be introduced in the robotic arm system, affecting the accuracy of the arm's end effector position. The platform must also have precise and stable control to enable the above criteria to be met.

The desired manner of motion determines the type of drivetrain system used for the mobile platform. Typical drivetrain configurations include Ackermann steering, differential drive, and omnidirectional drive. Ackermann steering is the least manoeuvrable of the three as the turning circle is greatly limited, and zero radius turns cannot be accomplished. Differential drive is more manoeuvrable, although estimating the orientation is more difficult. It also requires greater power, and it is difficult to find tyres that can withstand differential drive turning for a long time. Swedish or Mecanum wheels have greater manoeuvrability and do not require high power to turn, although these types of wheel require a clean surface to operate.

To confirm the drive system selection, two small pre-prototype robots were designed and built. One was designed with an omni wheel configuration using four Swedish wheels connected to individual drive motors. The second was built using four classic wheels, each with its own drive and steering motor stack, in an omni steering arrangement. Both robots were developed with similar control architectures. Through experimentation and trials of the two systems, it was found that the omni steering was the optimal design for our application.

3. Mobile platform

The developed mobile platform is a semi-autonomous scissor lifter with four novel omni wheels. The maximum height of the scissor lifter is 2 metres. The lifting mechanism is a hydraulic cylinder what can lift payloads of up to 150 kg. The driving system consists of four omnidirectional wheels, where each wheel is powered by two actuators: the first is responsible for yaw motion (turning), and the second is responsible for normal rolling to drive the robot. The second wheel, which is responsible for moving the robot, is attached to a passive suspension system. The omni wheel is controlled by a custom lower-level controller that regulates desired roll speed and yaw actuator position. The mobile platform is also equipped with a mobile camera, allowing visual
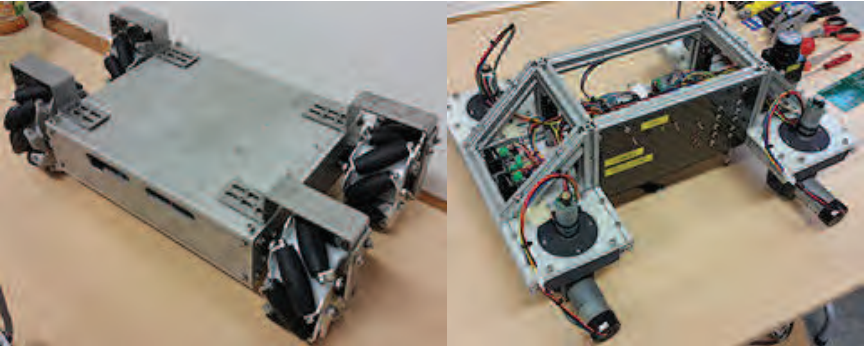
Fig. 1. The preprototypes developed to compare properties of kinematic configuration. *Left* - a robot with Swedish wheels, *Right* - a robot with omnidirectional wheel.

observation on an external computer. The main controller of the platform runs on Robot Operating System, which allows easy adaptation and quick development of future components. In the current version, the robot can autonomously travel to the desired pose via a series of waypoints, and stops if obstacles are detected. The platform has been designed to allow easy transportation to various construction sites (the footprint is like a car, and a winch is fitted to the front of the chassis).
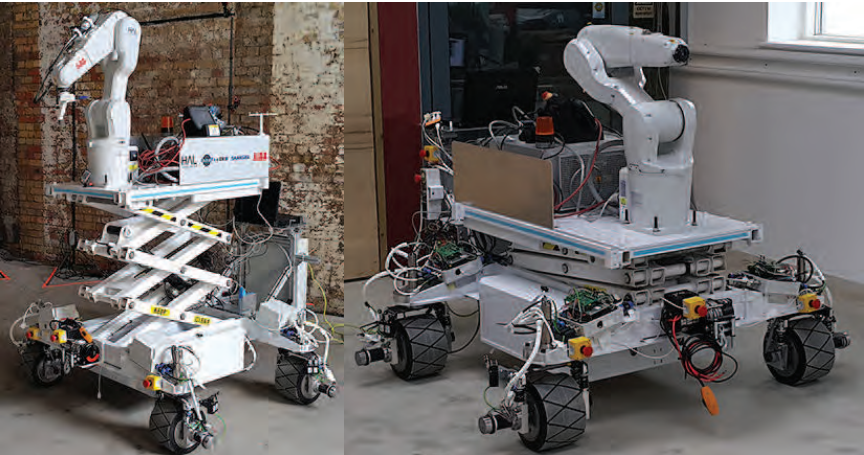
Fig. 2. The final robot developed within the project.

3.1. *Safety*

While there are currently no standards specifically for "construction robots", the developed robot would be covered by the following safety and risk assessment standards:

- ISO 10218:2011: Robots and robotic devices Safety requirements for industrial robots (Part 1: Robots[9] & Part 2: Robot systems and integration[10])
- ISO TS 15066:2016: Robots and robotic devices Collaborative robots[11]
- ISO 13482:2014: Robots and robotic devices Safety requirements for personal care robots[12]
- ISO 12100:2010 Safety of Machinery General Principles for design Risk assessment and risk reduction[13]

To comply with these standards, a number of safety features were implemented at different levels of the robot system:

High-level software

   (a) Functional safety-related control - an immediate Emergency STOP command can be sent by E-stops initiated manually to take the robot to a safe state and shut down the system.

   (b) Obstacle detection system - the system can identify and avoid obstructions at ground level.

   (c) Constant monitoring of robot's inclination - the scissor lifter will automatically retract if the platform is in danger of tipping.

Lower-level hardware

   (a) Motor protection - the controllers have over-current, over-voltage and short-circuit protection sub-systems.

   (b) Limit switches - safety switches on the wheel stack prevent yaw motors from exceeding their rotation limits.

Electrical safety-related features

   (a) Use of safe voltage - Extra-low voltage (ELV) of 48 VDC and 12 VDC are used (except for the ABB robot arm), which minimises the risk of electric shock.

   (b) Isolation of ABB power supply from the mobile platform - power supplies are separated in accordance with separated extra-low voltage (SELV) describe in IEE Wiring Regulation BS 7671.[14]

   (c) 4 Emergency STOP buttons around the robot - in the event of software failure, relays can physically cut power to the motors.

    (d) 1 Emergency STOP button tethered to robot - a button that is not fixed to the chassis can be activated at a distance from the robot platform.

    (e) Toggle power switch

    (f) Optimally selected motor torque

Mechanical safety-related features

    (a) Minimal number of sharp corners, pinching, crushing point, etc

    (b) Partially enclosed rotating and hydraulic equipment

    (c) Intrinsically stable static design.

3.2. *Mechanical design*

The base of the robot is built around a scissor lifter to which four omni wheels are attached. The key element of the design is an omni wheel that allows the robot to travel in any direction without re-orienting the robot chassis. The base of the wheel stack consists of a fork element that holds a driving wheel. The wheel is actuated from the side by a BLDC motor, while a DC motor rotates the fork element. The fork is supported by two bearings that can support axial and radial loads. The whole stack must withstand high stresses due to the considerable mass of the overall robot (550 kg); hence, stress and fatigue analysis was an important element of the design process.

3.3. *Hardware architecture*

The omni wheel motors are directly controlled by MaxonMotor controllers, which amplify the signal from embedded computers using a custom-developed control framework. Each omni wheel's computer regulates the yaw position and roll speed. This sort of structure is compatible with a standard kinematics model of a mobile robot; thus, it was easy to implement the kinematic-based controller. That omni wheel computer communicates with the main controller (laptop with ROS installed) via UART protocol.

3.4. *Software and control*

The software architecture for the robot is based on ROS (Robot Operating System)[15] as middleware, installed on a computer running Linux. The majority of code is developed using Python except for critical performance parts, where C++ is used. The JSON-ROS bridge server is developed at the top of the architecture to accept requests from a server that controlled a

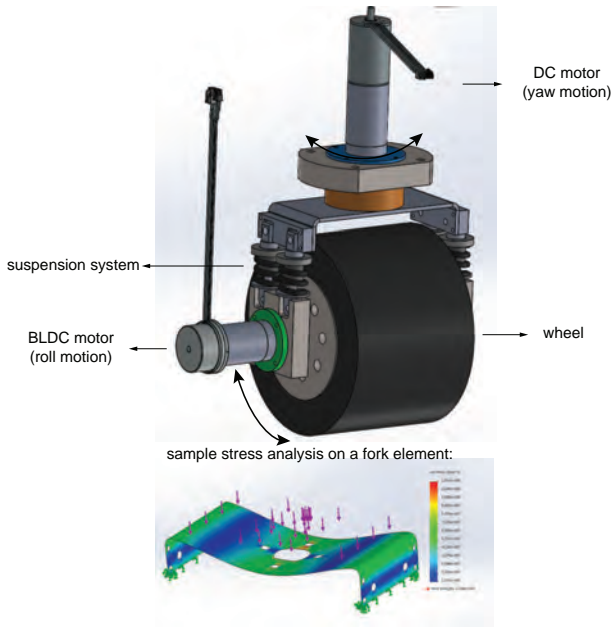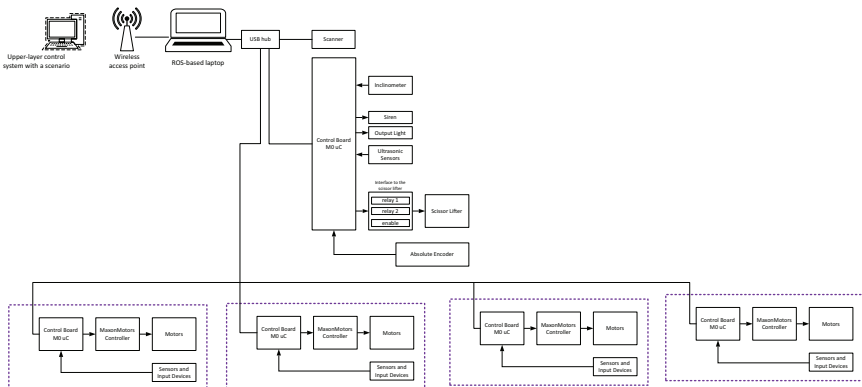Fig. 3.   The omni-directional wheel - a key element of a robot

Fig. 4.   The general overview of a system design

high-level construction site scenario. The JSON server translates incoming strings to ROS service requests and topic data, and converts ROS service responses to JSON string feedback and sends this back to the scenario server. The heart of the system is the autonomous controller module which

processes localisation and obstacle avoidance data and publishes motion commands to drive each wheel individually. For the lower level control, two custom hardware interface modules were developed to communicate with the omni wheels via serial connections.

4. Experiments

The developed mobile platform allows for controlling the robot by using a variety of kinematic strategies; three strategies have been explored; namely, Ackermann steering, modified Ackermann steering in which the rear wheels rotate in the opposite direction to the front wheels, and holonomic motion that exploits omni wheel motion features. In the first series of experiments, the robot was moved to a specific pose with the selected kinematics. During the experiments the pose of the robot was estimated only based on encoder odometry; thus, the positional accuracy in the tested system depended on many factors, such as the path travelled, obstacles, and wheel slip. When moving in a square of approximate area 10x10 metres, the platform was able to position itself with approximate accuracy of 30 cm, which was sufficient for a mobile manipulator base to reach the desired drilling locations so that the manipulator can carry out the drilling task to the desired level of accuracy.

In the final series of experiments, a scenario was tested where the robot task was to drill at precise locations in a construction site environment. The scenario involved mobile robot platform navigation to the required location, raising the scissor lifter to ensure the point of interest is within the workspace of the robot arm, and finally arm movement control and evaluate the performance of drilling tasks. To drill precisely, the ABB manipulator was localised with an OptiTrack camera system. This allowed successful task completion.

5. Conclusions

This paper describes the development of a novel mobile platform for use in the construction industry to perform mobile manipulation at height. The robot can move autonomously to a specific pose by exploiting three different kinematics. The omni wheel design has permitted a satisfactory improvement in robot manoeuvrability, stability, and ability to overcome obstacles when compared to pre-existing similar robots. The platform can be used for a variety of novel applications within the industrial construction site and beyond.

6. Acknowledgements

References

1. T. Bock, *Autonomous Robots* **22**, 201(Apr 2007).
2. F. Anlinker, M. Anlinker and K. Rothenbacher, Automation of design and construction of single-family made of brickwork, in *Proceedings of the 8th ISARC*, (Stuttgart, Germany, 1991).
3. H. Lehtinen, E. Salo and H. Aatlo, Outlines of two masonry robot systems, in *Proceedings of the 6th ISARC*, (San Francisco, USA, 1989).
4. A. Slocum, L. Demsetz, D. Levy, B. Schena and A. Ziegler, Construction automation research at the massachusetts institute of technology, in *Proceedings of the 4th ISARC*, (Haifa, Israel, 1987).
5. A. G. Dharmawan, B. W. C. Sedore, S. Foong and G. S. Soh, *Construction Robotics* **1**, 15(Dec 2017).
6. www.nlink.no, nlink - mobile robot for construction sites (2017).
7. V. Helm, J. Willmann, F. Gramazio and M. Kohler, In-situ robotic fabrication: Advanced digital manufacturing beyond the laboratory, in *Gearing up and accelerating crossfertilization between academic and industrial robotics research in Europe:*, eds. F. Röhrbein, G. Veiga and C. Natale (Springer International Publishing, Cham, 2014).
8. S.-K. Kim, J. Russell and K.-J. Koo, *Journal of Computing in Civil Engineering* **17**, 97(April 2003).
9. ISO 10218-1: 2011: Robots and robotic devices–safety requirements for industrial robots–part 1: Robots (2011).
10. ISO 10218-2: 2011: Robots and robotic devices–safety requirements for industrial robots–part 2: Robot systems and integration (2011).
11. ISO TS 15066:2016: Robots and robotic devices collaborative robots (2016).
12. ISO EN 13482:2014: Robots and robotic devices safety requirements for personal care robots (2014).
13. ISO EN 12100: Safety of machinery–general principles for design–risk assessment and risk reduction (iso 12100: 2010) (2010).
14. D. Locke, *Guide to the Wiring Regulations: IEE Wiring Regulations (BS 7671: 2008)* (John Wiley & Sons, 2008).
15. M. Quigley, K. Conley, B. P. Gerkey, J. Faust, T. Foote, J. Leibs, R. Wheeler and A. Y. Ng, ROS: an open-source robot operating system(April 2009).

INVERSE KINEMATIC MULTIOBJECTIVE OPTIMIZATION FOR A VEHICLE-ARM ROBOT SYSTEM USING EVOLUTIONARY ALGORITHMS

HUMBERTO RODRÍGUEZ,

ILKA BANFIELD

Mechanical Engineering Department, Universidad Tecnologica de Panama, Panama City, Panama

This work is aimed at discussing the solution of the inverse kinematic problem using Multi-Objective Evolutionary Algorithms (MOEA) for a vehicle-arm redundant robot. A simplified 5 DoF model was used to simulate the problem and the objective functions were properly selected assuming underwater operation. In addition, we present a review of the most important techniques used for solving the inverse kinematic problem, focusing at the end on the application of a Non-Dominated, Sorting, Elitist MOEA with nonlinear constraints.

1. Introduction

Currently, robotics plays an important role in increasingly complex engineering applications, with high demands in terms of dexterity, such as the performance of underwater robots; which in most cases are redundant [1-4]. In this work, we are interested in the case of redundant systems composed of a mobile platform and a manipulator arm, that could be used for ship's hull cleaning and maintenance.

The buildup of organisms on the side of boat hulls, propellers, and other infrastructure in marine environments increases fuel consumption and ecosystem's problems of invasive species. Many ship owners periodically deploy divers to inspect ship hulls and remove the buildup of organism, known as Biofouling [5]. Hull cleaners are autonomous or semi-autonomous underwater robot used to scrub hull clean while still in the water. The use of Robot cleaners can result in fuel savings and reduce the risk of the task itself.

There are several functional prototypes and patents developed for the inspection and cleaning of underwater surfaces. We can classify the different cleaning systems as, fastening methods to the hull surface and maneuverability mechanisms [6-9]. The results of this work will be applied to development of a manipulator on a free-floating submarine vehicle for inspection and cleaning of the target. Cui and others [10] reviewed the different challenges in terms of navigation of a mobile base and manipulation in conjunction with a robotic arm from four important aspects: positioning of the mobile robot by means of (GNSS), navigation based on vision and visual servo, robotic manipulation, planning and control of trajectories.

The present development analyzes the implementation of a method for the control of a redundant robot performing multiple prioritized tasks in the presence of limits in the joint range, speed and acceleration / torque efficiently.

The redundancy problem is described such that, given a desired trajectory, $r_d(t) \in R^m$, defined in a coordinate system for the end effector of a manipulator, it requires the corresponding displacements in the joint space of the robot, the sets of vectors $\theta(t) \in R^n$, where $m < n$, using the definition: $r_d(t) = f(\theta(t))$, where $f(\cdot)$ is the direct kinematics, which is nonlinear and differentiable with a structure and known parameters, for a given manipulator robot.

Several methods have been proposed as resolutions for the redundancy problem, and to characterize multiple approaches, two general methods have been proposed [11], indirect methods and direct methods. Indirect methods, such as the Pseudoinverse method, the Extended Jacobian method, kinematic optimization methods and the Lyapunov method or gradient method, are differential methods that are computationally intensive, so they are developed offline under previously specified optimization criteria. The main disadvantages with this type of methods are that solution of the optimization problem only guarantees to be locally optimal and that the algorithms used exhibit numerical difficulties when the manipulator is close to kinematic singularities [12-14]. Differential control algorithms must be initialized with some joint configuration, θ, from the set of possible solution. Then the manipulator is kinematically controlled by the desired trajectory while remaining within the set of solutions [15].

On the other hand, there are direct methods based on the approach of solving the inverse function of $f(\cdot)$ in a closed form or approximate form. Direct methods seek the explicit resolution of redundant degrees of freedom. These tend to be fast, but generally require strong assumptions regarding the structure of the set of possible solutions [11]. Generally, task dependent constrains need to be specified to accommodate the redundancy.

The inverse functions are local and cyclical and because their evaluation is frequently rapid, when these can be determined, they are computationally suitable for real time control [16]. It must be considered that expressions in closed form for inverse kinematics are difficult if not impossible to determine, however it is possible to adapt approximate forms of these using neural networks or other approximation methods for nonlinear functions.

Traditionally, three models have been used to solve the inverse kinematic problem: geometric models, algebraic models and iterative models [17]. The use of geometric models is limited by the complexity of the structure, while algebraic models do not guarantee a closed form solution [18]. In iterative methods, convergence depends on the initial point of evaluation and are computationally prohibitive, which is why many researchers have focused their work on solving inverse kinematics using Artificial Neural Networks (ANN).

The application of Neural Networks to construct self-organized maps of the inverse kinematic problem, are well referenced [18-20]. In those works, the kinematics of non-redundant and redundant robots is solved after training the ANN for a period, yielding a unique solution corresponding to the desired position in the workspace. Recently, the work of hybrid approaches based on Neural

Networks has allowed the training of ANN with variable optimization criteria over time, which was not possible on earlier works [10]. As example, Jin, L. and Li, S [21], use a Dynamic Neural Network to solve a problem of optimization of the manipulability of a redundant robot, transforming it into the resolution of a set time variants non-linear equations. However, the major drawback of using ANN are still the difficulty of how to collect training sets, and that the training process when gradient-based learning algorithms is very slow, especially for a complex configuration, or a large set of training data.

2. Genetic Algorithms and Multi-Objective Evolutionary Algorithms

When formulating the redundancy problem, as a case of optimization, the techniques based on Genetic Algorithms (GAs), take relevance. The GAs are methods that solve constrained and unconstrained optimization problems and the popularity of their use is because they are naturally appropriate, with some modifications, for cases of multi-objective optimization. GA allows a population composed of many individuals to evolve under specific rules of selection towards a state that maximizes fitness (function aptitude) or cost function. The GA subsequently modifies the population of individuals, which represent the possible solutions. On successive generations, the population evolves towards an optimal solution. This method solves a variety of optimization problems such as discontinuous, non-differentiable, stochastic or highly non-linear functions, which are intractable under other optimization techniques [22].

Non-dominated Sorting Genetic Algorithm (NSGA) [22], was one of the first MOEAs, and from its use the following disadvantages have been highlighted [23]: a high computational cost, lacks elitism, and finally must specify the exchange parameter, which is a parameter that ensures diversity and equivalence in the solutions. From here on, various modifications and new MOEAs algorithms have been developed [23, 24].

2.1. MOEAs Constraints Management

This work involved the optimization of multiple cost functions to solve the kinematic redundancy of a robot manipulator, subject to several constrains equations, which are related to the task and the robot configuration itself. In general, an optimization problem can be defined as,

$$
\begin{aligned}
\min o \max \quad & f_m(x), & m &= 1,2,\ldots,M; \\
subject\ to \quad & g_i(x) \geq 0, & i &= 1,2,\ldots I; \\
& h_j(x) = 0, & j &= 1,2,\ldots J; \\
& x_k^{inf} \leq x_k \leq x_k^{sup}, & k &= 1,2,\ldots,K;
\end{aligned}
\tag{1}
$$

where $f_m(x)$ are the fitness or cost functions and $g_i(x) \geq 0$ and $h_j(x) = 0$ are inequalities and equalities constraints, respectively. The constrained optimization divides the search space into two regions; feasible (those solutions that comply with the constrains) and not feasible. It's clear that the set of optimal solution, Pareto-optimal, must belong to the feasible region. A possible solution would be for the MOEA to assign more pressure to the group that violates the constraints to a lesser degree, so in this way the algorithm is provided with a direction in the search for a feasible region [22].

Another popular technique for handling constraints is the penalty function approach, in which, the objective and the normalized constraints are added and multiplied by a factor that penalizes them based on a minimization process. A drawback is that this factor needs to be updated according to some strategy. In the literature we can find several works [17-27], which present static and dynamic strategies for updating the penalty factor according to the objectives. The quality of the solution obtained depends on factor's quality. Recently, in the works of Fan, Z. *et al*. and Chehouri, A. *et al*. [27, 28], the authors claim that the penalization approach deviates from the philosophy of evolution of the algorithms and propose a technique that preserves the main concept of the GAs, developing rules that include the value variations of the constraints for the selection and generation of new individuals. In this work, the last approach was used for handling the nonlinear equality constraints.

3. Inverse Kinematic Solution of a Vehicle-Arm Robot

In this section we present the solution of the inverse kinematic problem of a vehicle-arm robot model using a Non-Dominated, Sorting, Elitist Algorithm MOEA II, developed by Deb, K. [23]. The fitness functions were selected to maximized manipulability and minimized joint angle average displacement when moving to consecutive points of the trajectory.

For the application of the MOEA II, the individuals of a population are defined as configurations, q, of the vehicle-arm, which will be used to evaluate two fitness (objective) function. Figure 1 shows the 5 DoF planar model and the generalized coordinates used.

In the context of evolutionary multi-objective minimization problems, the term dominance refers to the case when the evaluation of a fitness functions, g_i, for an individual q_1 gives smaller values than for other individual q_2:

$$g_i(\boldsymbol{q_1}) \leq g_i(\boldsymbol{q_2}) \quad \forall\, i \tag{2}$$

$$g_j(\boldsymbol{q_1}) < g_j(\boldsymbol{q_2}) \quad for\ some\ j$$

Thus, q_1 dominates q_2. The group of individuals that have noninferior fitness function values are non- dominated by any other individual and its set is called a *pareto front*. Therefore, for each individual on the Pareto front, one fitness function can only be improved by degrading another.
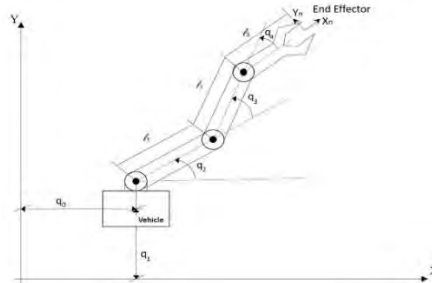
Figure 1. Vehicle – Manipulator Schematic: The generalized coordinates of the robot, q, are shown.

3.1. The *MOEA II algorithm*

The MOEA II was implemented in MATLAB. The first step in the algorithm is creating an initial population (200 in our case) which is feasible with respect to the nonlinear constraints and the joint angles bounds. In this algorithm both, the objective function and constraints values are used to obtain scores for the population.

After each next generation is created from selected parents, the children are obtained by mutation and crossover. Afterward, all infeasible individuals are assigned a lower rank than any feasible individual. Within the infeasible population, the individuals are sorted by an infeasibility measure, which we take as the value of the constraints function. For the new generation, the current population is combined with the children.

For a controlled elitist GA, it is important to maintain the diversity of population for convergence to an optimal Pareto front (23). The diversity is increase by keeping some of those individuals of the current population that are relatively far away of the pareto front. In addition, the number of individuals on the Pareto front (elite members) is limited using a fix fraction.

3.2. The Model and Simulation Results of the Vehicle-Arm system

The direct kinematic function $f(q)$, in equation 3, defines the position and orientation of the end effector (x, y, θ) in terms of the generalized coordinates q_o, q_1, q_2, q_3, q_4, as shown in figure 1.

$$f(\boldsymbol{q}) = \begin{bmatrix} q0 + l1 * cos(q2) + l2 * cos(q2 + q3) + l3 * cos(q2 + q3 + q4) \\ q1 + l1 * sin(q2) + l2 * sin(q2 + q3) + l3 * sin(q2 + q3 + q4) \\ q2 + q3 + q4 \end{bmatrix} \quad (3)$$

For the intended application, it is important to assure a manipulability as high as possible to exert the require forces while following the desired trajectories on the vessel surface. Thus, Yoshikawa's manipulability index was used as the first

Fitness Function. A second function, the square root of the difference between consecutive configurations, $\hat{q}_i{}^t - \hat{q}_i{}^{t-1}$, is used to assure that the optimal configuration of two consecutive points in the trajectory are close.   In addition, since it is easier to control the joint angles than the vehicle position in the water, a reducing gain, K_i, is used for the first two coordinates in the second fitness function to reduce as much as possible the motion of the vehicle or platform. Thus, the optimization problem is stated as:

$$g = \frac{1}{Y(\boldsymbol{q}) + 1}; \quad \text{where } Y(\boldsymbol{q}) = \sqrt{J(\boldsymbol{q})J^T(\boldsymbol{q})}$$

$$\min \qquad S(\hat{q}) = \sqrt{\sum_i K_i(\hat{q}_i{}^t - \hat{q}_i{}^{t-1})^2} \qquad\qquad (5)$$

Subject to: $f(\boldsymbol{q}) = \hat{\mathbf{x}}_d$; $\boldsymbol{q}^{inf} \leq \boldsymbol{q} \leq \boldsymbol{q}^{sup}$.

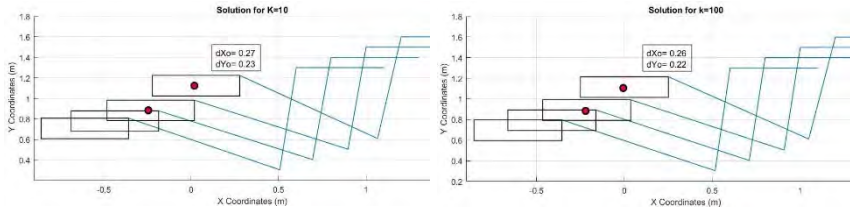Figure 2. Effect of applying different gains to q_0 and q_1. with K=10 (left) and K=100 (right),

Where $\hat{\mathbf{x}}_d$, is the desired position and orientation of the end effector, $\boldsymbol{q}^{inf}$ and $\boldsymbol{q}^{sup}$ are the lower and upper bound of the joint angles, and $J(\boldsymbol{q})$ is the Jacobian matrix, which obtained by direct differentiation of equation. Figure 2, shows some of the typical results obtained when a series of positions of the end effector are given and a fixed orientation pointing in the positive x direction is asked. The effect of the gain K can be appreciated, since the consecutive vehicle/platform positions stay closer when we increase its value. When only K_1 and K_2 are increased, the relative displacement of the vehicle between successive configurations is reduced (shown in the text box for last two), as expected.

With these results we have shown that a non-dominated elitist sorting evolutionary algorithm can be used to solved effectively the inverse kinematic problem of a redundant manipulator using multi-objective optimization.   The fitness/objective functions have been selected bearing in mind the characteristics of the task and still need to be validated in actual operational conditions.

4. Conclusions and Future Work

The final individuals or joint coordinates were effectively selected out of the pareto front by choosing the best solution for the smoothness cost function, since the values of the manipulability does not vary much for the different solutions of

the front. It is worth to mention that, to generate populations that expand into feasible and not feasible regions the number of initial individuals was increased up to 200. The next step in this research is to simulate the complete 12 DoF system (6 DoF for the vehicle and 6 DoF on the arm) and implement an Impedance Control System on a ground vehicle + arm manipulator, having the kinematic optimization technique presented in this work as an offline process.

References

1. Rui Y., Benoit C., Ali M., Ming L., Nailong W., Modeling of a complex-shaped underwater vehicle for robust control scheme. J Intell Robot Syst. 2015; 80:491-506.
2. Azorin-Lopez J., Saval-Calvo M., Fuster-Guillo A., Oliver A., A predictive model for recognizing human behavior based on trajectory representation. In 2014 International Joint Conference on Neural Networks (IJCNN), pages 1494-1501. IEEE, July 2014.
3. Calinon S., Sardellitti I., Caldwell D. G. Learning-based control strategy for safe human-robot interaction exploiting task and robot redundancies. In Proceedings of IROS pages 249-254. IEEE, October 2010.
4. Cambon S., Alami R., Gravot F., A Hybrid Approach to Intricate Motion Manipulation and Task Planning. The International Journal of Robotics Research, 28(1);104-126, January 2009.
5. Coutts AD, Valentine JP, Edgar GJ, Davey A, Burgess-Wilson B., Removing vessels from the water for biofouling treatment has the potential to introduce mobile nonindigenous marine species. Marine pollution bulletin, 60(9):1533–1540, (2010).
6. Michael J Maloney & Ronald C Pennock. Boat hull cleaning apparatus. US Patent 5,222,452, June 29 1993.
7. William George Ecklund. "Ship hull cleaning apparatus and method of use", March 10 2004. US Patent App. 10/798,528.
8. Goldberg, D. "Huxley: a flexible robot control architecture for autonomous underwater vehicles". OCEANS, 2011 IEEE-Spain, pages 1–10. IEEE, 2011.
9. Muelling, K., Venkatraman, A., Valois, J-S., Downey, J. y Weiss, J., Autonomy Infused Teleoperation with Application to BCI Manipulation. Auton Robot, 41: 1401-1422, 2017.
10. Cui L, Tan T, Duc Do K y Teunissen P. Challenges and Solutions for Autonomous Robotic Mobile Manipulation for Outdoor Sample Collection. Journal of Electrical and Electronic Engineering. 3(5): 156-164 (2015).
11. DeMers D. Kreutz-Delgado K. Inverse Kinematics of Dextrous Manipulator, Neural Systems for Robotics Academic Press, pp. 75-116 (1997).
12. P. Kinematic singularities of Robot Manipulators. 5772/9548. (2010).

13. Lara-Molina, F.A., Rosario, J.M., Dummur, D., Multi-Objetive Design of Parallel Manipulator Using Global Indices, The Open Mechanical Engineering Journal, 4, 37-47 (2010).

14. Taghirad H., Nahon M., Kinematic Analysis of a Macro-Micro Redundantly Actuated Parallel Manipulator, Advanced Robotics 22, 657-687 (2008).

15. Zhang, T., An, H., Ma, H., Joint torque and velocity optimization for a redundant leg of quadruped robot, International Journal of Advanced Robotic Systems, pp 1-12, (2017).

16. DeMers D. Kreutz-Delgado K, Canonically Parameterized families of Iinverse Kinematic Functions for Redundant Manipulators, Robotics and Automation, pp. 1881-1886, (1994).

17. Korein, J., Balder N., Techniques for generating he goal-directed motion of articulated structures, IEEE Computer Graphics and Applications, 2(9), 71-81, (1982).

18. Alavandar, S., Nigam, M., Inverse Kinematics Solutions of 3DOF Planar Robot using ANFIS, Int. Journal of Computers, Communications and Control, (3)150-155, (2008).

19. Ding, H., Wang, J., Recurrent Neural Network for Minimum Infinity-Norm Kinematic Control of Redundant Manipulators, IEEE Trans Syst Man Cybern 29(3)269-276, (1999).

20. Mao, Z., Hsia, T., Obstacle Avoidance Inverse Kinematics Solution of Redundant Robots by Neural Networks. Robotica 15(1)3-10, (1997).

21. Jin, L., Li, S., Manipulability Optimization of Redundant Manipulators Using Dynamics Neural Networks, IEEE Transactions of Industrial Electronics, (2016).

22. Deb, K., Multi-Objetive Optimization using Evolutionary Algorithms, John Wiley and Sons, Inc. New York, NY, USA, (2001).

23. Deb, Kalyanmoy, A Fast and Elitist Multiobjetive Genetic Algorithm: NSGA II. IEEE Transactions on Evolutionary Computation 6(2) 182-197, (2002).

24. Deb, Kalyanmoy, An Evolutionary Many-Objective Optimization Algorithm Using Reference-Point-Based Nondominated Sorting Approach, Part I: Solving Problems with Box Constraints. IEEE Transactions on Evolutionary Computation 18(4) 577-601, (2014).

25. Coello, C., Use of a Self-adaptive penalty approach for engineering Optimization Problems. Computation Industrial 41 133-127.

26. Yeniay, O., Penalty Function Methods for Constrained Optimization with Genetic Algorithms. Mathematics Computing Applic. 10 45-56 (2005).

27. Fan, Z., Li, W., Cai, X., Li, H., Wei, C., Zhang, Q., Push and Pull Search for Solving Constrained Mutli-objective Optimization Problems. Neural and Evolutionary Computing, (2017).

28. Chehouri, A., Younes, R., Perron, J., Ilinca, A., A Constraint-Handling Technique for Genetic Algoritms using a Violation Factor. Journal of Artificial Intelligence of Computer Sciences. 12(7) 350-362. (2016).

USING COLLABORATIVE ROBOTS AS A TOOL FOR EASIER PROGRAMMING OF INDUSTRIAL ROBOTS

I. M. Sarivan, A. Batuev, A. E. Ciontos, Ø. Holtskog, E. N. Sivertsen and C. Schou

Materials and Production, Aalborg University,
Aalborg, 9220, Denmark
E-mail: cs@mp.aau.dk

Programming industrial robots using traditional jogging via teach pendant is a time-consuming task that requires extensive training. More intuitive and faster task programming is often possible using kinesthetic teaching. Although this feature is available on many commercial collaborative robots, it is rarely available on traditional industrial robots. In this paper we propose a framework for allowing tasks to be instructed using a collaborative robot via kinesthetic teaching, and afterwards deployed to a traditional industrial robot. The framework consists of a physical modular concept for robot exchange, and a online programming software tool called Universal Industrial Interface. To assess the framework, a feasibility study is conducted where an industrial relevant task is first programmed using a collaborative manipulator, and afterwards deployed on an industrial manipulator.

Keywords: Robot programming, industrial manipulator, collaborative robot, kinesthetic teaching, cross-vendor compatibility, flexible production.

1. Introduction

Robotic manipulators are the backbone of modern industry and one of the main tools to have in an automated industrial environment. However, programming traditional industrial robots is both time-consuming and requires special training. Nowadays due to numerous factors such as dynamic market demands, shorter product-cycles and an ever increasing demand for customization, manufacturing equipment need not only to be efficient, but also flexible and reusable. Within robotics, one answer to this need is the introduction of collaborative robots which provide more intuitive instruction methods such as kinesthetic teaching. Several have shown that this enables non-robotics experts to engage in task programming.[1–3] This is considered desirable in a dynamic environment with frequent task adjustments and new product introductions since it empowers the on-site shop floor person-

nel to manage the robots with less dependency on experts and engineers. However, in most existing manufacturing industries, it would not be practical to simply exchange the majority of the installed traditional industrial robots for collaborative robots only to gain the ability to do kinesthetic teaching. Additionally, traditional robots may also hold certain features or performance metrics which cannot be met by a collaborative robot.

Since the development of collaborative robots, one of the key benefits of kinesthetic teaching is the eased instruction, therefore we propose in this paper a framework utilizing collaborative robots as an instruction tool for tasks which can later be deployed to a traditional industrial robot. Thus, a collaborative robot is installed and used to intuitively instruct a given task through a cross-vendor robot programming tool. Enabled by a modular mechanical concept, the collaborative robot is afterwards exchanged with a traditional industrial robot which performs the task execution.

The proposed framework consist of a modular mechanical concept enabling quick and precise exchange of robot manipulators, and a custom software tool called Universal Industrial Interface (UII) providing a cross-vendor graphical user interface (GUI) for robot programming.

Further on, this paper is structured as follows: Section 2 presents related work, Section 3 presents the design and user experience of UII and Section 4 describes the modular mechanical concept used for efficient exchange of robots. These are followed by a preliminary feasibility study and the conclusion in section 5 and 6 respectively.

2. Related Research

With the introduction of the *collaborative robot*,[4] robots are now moving into the dynamic environment of the human workers with more frequent task changeover, several ad-hoc tasks and less structure. A key challenge here is the need for more frequent changeovers, resulting in an increased need to reprogram the robot. In this context, faster and easier programming approaches are needed as opposed to traditional online programming using teach pendants.[5]

Biggs and MacDonald[6] present a survey on robot programming methods and find two overall approaches; manual and automatic programming of robots. In the latter, cognitive methods are used to make the robot more autonomous and thus less dependent on instruction details. It often relies on planning algorithms based on sensor inputs and a comprehensive world model. Contrary to reducing human intervention, recent research on manual programming instead focuses on making online robot programming easier

and faster.[3,7–11] This decreases the need for high-wage engineering hours and allows the shop floor operators to channel valuable process knowledge and experience into the instruction.

A common approach to ease online instruction of collaborative robots is to use kinesthetic teaching. Several researchers have already demonstrated the potential of using kinesthetic teaching for eased instruction of collaboration robots,[2,8,12] and the technology is also featured on several of the commercially available collaborative robots; e.g. Universal Robots, KUKA iiWA and Rethink Robotics Baxster.

Although several commercial collaborative robots offer kinesthetic teaching, they also exhibit vendor-specific user interfaces and programming languages. This increases the complexity in allowing shop floor operators to program robots in a company with multiple robot vendors. It furthermore prohibits the transfer of an already instructed robot task from one robot to another robot of a different vendor.

To overcome this issue, several has proposed third-party robot programming tools with cross-vendor capabilities.[10,11,13] Schou et al.[11] present a comprehensive tool for easy instruction of collaborative robots. The tool uses robot skills to allow robot instruction using task-level operations rather than device level commands. The tool also features cross-vendor compatibility achieved using the Robot Operating System (ROS).[14] Paxton et al.[10] also present a comprehensive tool for creating tasks for collaborative robots based on ROS. The tool combines kinesthetic teaching with explicit, object-centered instruction arranged in behaviour trees.

Compared to the tools presented above, we propose a light-weight, cross-vendor tool providing robot programming for both collaborative and traditional industrial robots. Our tool allows tasks instructed using kinesthetic teaching on a collaborative robot to be deployed on a traditional industrial robot. The programming is done on the same abstraction level as current teach pendants. Thus, the need to learn and adapt to various vendor-specific teach pendants is removed, however, the familiarity of traditional online programming is preserved. Furthermore, our tool is designed to be light-weight with the potential of being deployed to low-cost, small-scale computational units, e.g. Raspberry Pi.

3. Universal Industrial Interface

Central to the proposed framework is the software, Universal Industrial Interface (UII), developed by the authors. This tool is a cross-vendor robot operating tool with options to both program and execute industrial

robot tasks. It supports both kinesthetic teaching and traditional jogging. As such, UII supports programming of both industrial and collaborative robots. However, in this paper we focus on the exploitation of kinesthetic teaching on a collaborative robot and deploying it on an industrial robot. UII is designed to be applicable to the majority of commercial industrial robots and grippers. It is designed to provide task programming using interaction on the same level as traditional online programming. As such, the same motion commands as found on most traditional industrial robots and grippers are available; e.g., move linear, move joint, open gripper and close gripper.

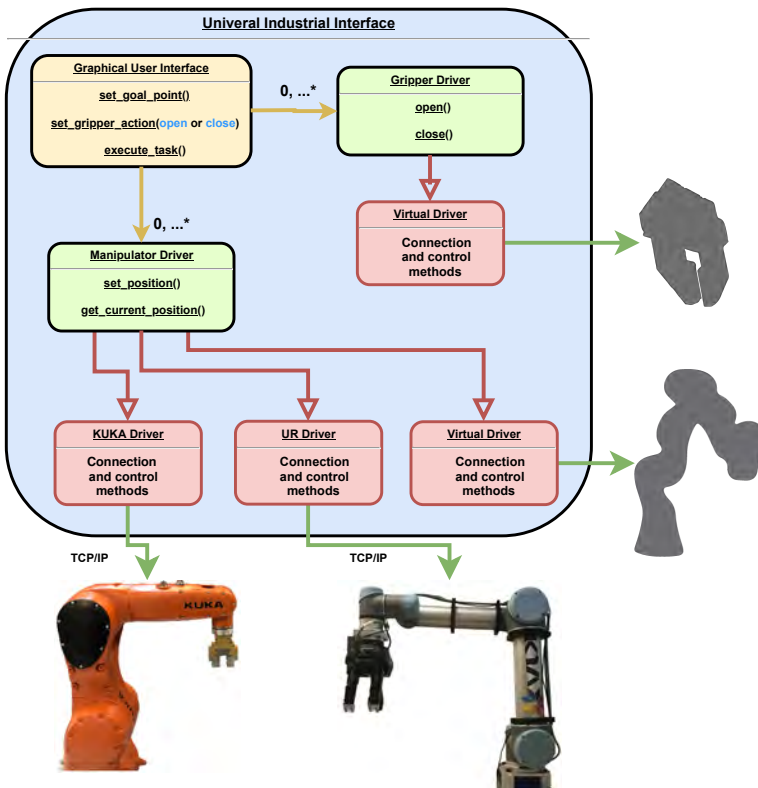### 3.1. *System Architecture and Implementation*

Fig. 1.   Simplified UML class diagram of UII architecture.

UII is designed to be light weight and cross-platform. It is written in Python and will run on both Windows and Linux computers. It supports connection to robot manipulators and grippers using TCP/IP connections through the local area network (LAN). Figure 1 shows the overall architecture of UII.

3.1.1. *UII GUI*

The GUI provides a high level, intuitive interaction between the operator and the manipulators. The GUI enables the operator to set a sequence of goal points and gripper actions which can later be executed on a collaborative or industrial manipulator. The GUI is directly integrated inside UII without the need of a special API, as this component will stay unchanged regardless of the device connected to UII.

3.1.2. *UII Core*

This element contains the core functions of UII. This includes engines for task programming and task execution, task file management and system state monitoring. The UII core is implemented as a number of classes.

3.1.3. *UII Drivers*

The driver layer of UII provides connectivity to the devices utilized by UII. Thus, any specific driver provides the means to control and communicate with a specific robot manipulator or gripper. This is done by using the devices own protocol of sending and receiving data using a TCP/IP connection. To ensure the possibility of adding more manipulators and grippers in UII, an application programming interface (API) was designed which has to be implemented when building a driver. This API is implemented as a generic driver for a robot manipulator and a generic driver for a gripper. As seen on figure 1, the specific drivers (red boxes) all inherit from either a generic robot manipulator driver or gripper driver (green boxes). Figure 1 contains a simplified UML diagram of UII. The generic drivers provide a set of generic device functions for manipulators and grippers in a generic syntax. The generic device functions are used by the programming and execution engines in the UII core. When a generic device function is invoked by either the programming or execution engine in UII core, the specific device driver instantiated will translate the generic device function into the specific syntax and format of a particular device. This translation includes

converting between different units, angle representations and parameter sequences.

3.2. *Task programming and execution*

The UII GUI is designed to be as simple and intuitive as possible while still providing the essential features to program and execute tasks. It provides the necessary means for the operator to program a task by using both kinesthetic teaching and jogging. During programming, the operator can quickly guide the robot kinesthetically to any desired position. Afterwards, that position can be fine tuned using the jogging buttons of the GUI. When the desired position is reached, the set goal point button stores the point. Gripper actions can be added in between the robot motions by pressing the assigned button on the GUI. The UII GUI is shown in Figure 2.
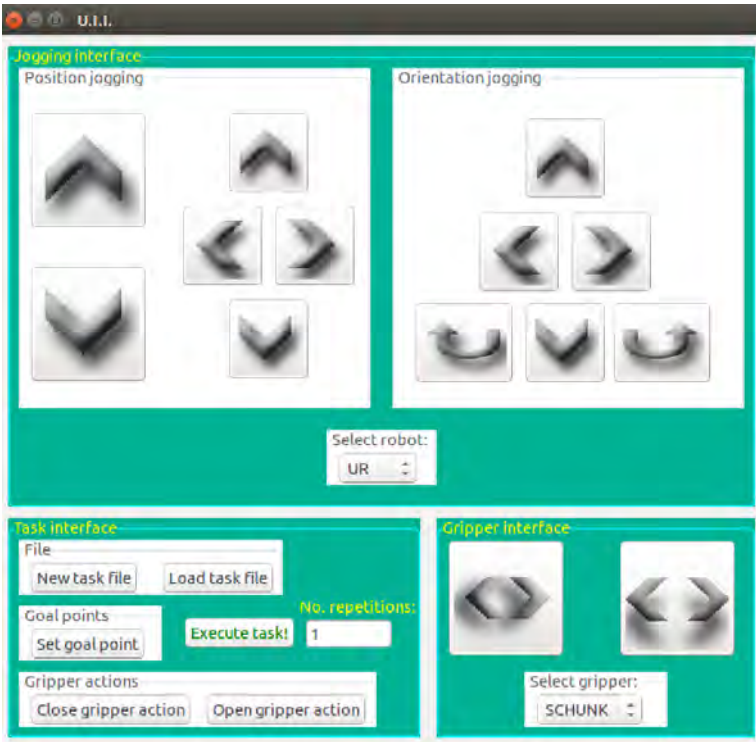

Fig. 2.   UII Graphical User Interface

Once the programming is completed, the obtained robot program is stored in a UII-specific file format. It can now be executed again by loading the task and pressing the execute task button on the GUI. Given the cross-vendor capability of UII, the obtained task can be executed on any connected hardware. Thus, the option to use collaborative robot for task programming and a traditional industrial robot for execution arise. However, it only makes sense to execute the task on a different setup if the robot is installed in the same work-space in which the task was programmed. This also requires accurate positioning of the robot to ensure correct task execution.

4. Modular Mechanical Interface

To allow a task programmed using a collaborative robot to be executed on an industrial robot, it is essential that the two robots can be exchanged efficiently and accurately. To achieve this, our proposed framework adopts a modular hardware concept proposed by Schou and Madsen.[15] This concept is build around a modular table-top with standardized pallets for mounting robots, fixtures, feeders and other equipment, see Figure 3.

With this concept, each robot manipulator is mounted to a pallet providing it with the interface defined on the table-top concept. A similar "adapter" flange is used between the tool and the robot manipulator, see Figure 4. As a result, only four M8 bolts are to be removed in order to exchange a robot manipulator with another. It should be noted, that only manipulators with a weight and size suitable for table-top applications are applicable in this hardware concept.

5. Preliminary Feasibility Study

A feasibility study is conducted in order to examine the presented framework and demonstrate the procedure of programming a task using a collaborative robot and afterwards deploying the task on a traditional industrial robot. Thus, the purpose of the feasibility study is to prove that kinesthetic teaching can be used as an alternative programming tool for traditional industrial manipulators.

The task used in the feasibility study is inspired from a real industrial task described by Madsen et al.,[16] where parts exiting a processing machine on a conveyor must be picked up and placed into a container. In our simulated setup, the parts (cups) are to be picked from a mock-up conveyor and placed into a cardboard box, see Figure 5.
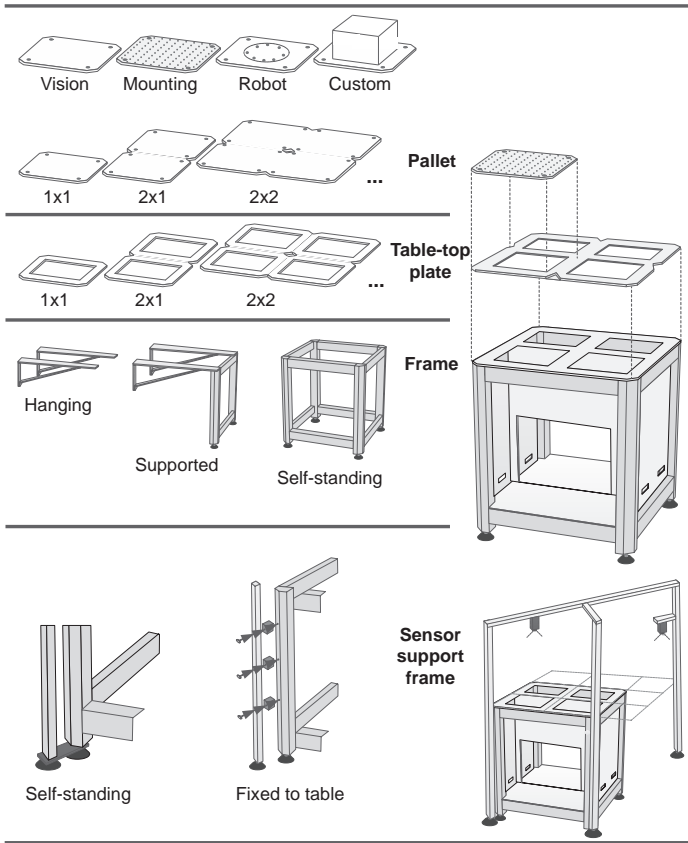
Fig. 3.   Modular table-top concept used for quick exchange of robots. Concept proposed by by Schou and Madsen.[15]

The task was first programmed on a Universal Robots UR5 collaborative robot equipped with a Robotiq 3-finger electric gripper. Once programmed and verified, the UR5 was dismounted from the table-top, and replaced with a KUKA Agilus KR6 R700 sixx industrial robot. The generated program was then without further refinement or system adaptation executed on a KUKA Agilus KR6 R700 sixx. It is important to note, that the UII software does not need reconfiguration or rebooting.

As part of the examination of the framework, the programming time, the exchange time and the execution time was recorded, see Table 1.

It should be noted, that the exchange time is measured for exchanging the Universal Robots UR5 with the KUKA Agilus KR6 R700 sixx. However,

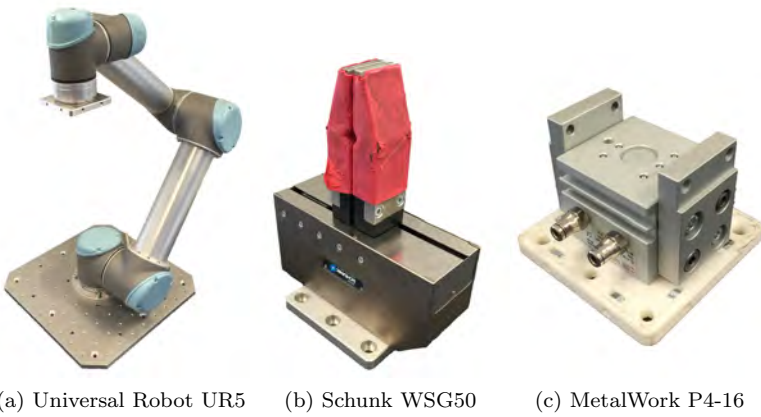(a) Universal Robot UR5   (b) Schunk WSG50   (c) MetalWork P4-16

Fig. 4.   Examples of robots and grippers adapted to fit the modular hardware concept.
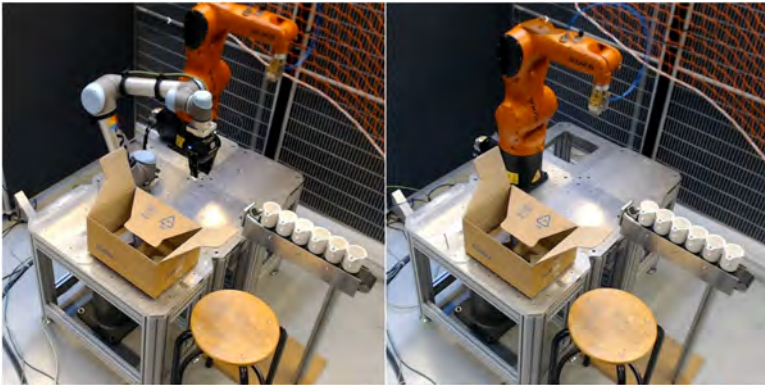
Fig. 5.   The test setup before and after the exchange of robots.

Table 1.   Test parameters used for evaluating the feasibility of the system.

Timing of programming:	1min 20sec
Timing of exchange:	2min 13sec
Timing of execution on Universal Robots:	12sec
Timing of execution on KUKA:	8sec

in cases where an existing robot cell has to be reprogrammed, an exchange of the traditional robot with the collaborative one prior to programming must be considered as well. Here, the exchange time is estimated to be the

same. For timing of execution, only one repetition was measured for both robots. As expected, the industrial manipulator is faster.

6. Conclusion

This paper presents a framework for using a collaborative robot as a programming tool for industrial robot tasks with the purpose of reducing programming time and effort.

The framework features a cross-vendor robot operating tool called UII. This software provides an intuitive, simple GUI for programming tasks of both collaborative and industrial robots. In the case of collaborative robots, it support kinesthetic teaching, which several has concluded to be reduce the required skill-level in robot programming. The framework also includes a modular hardware concept enabling quick and accurate exchange of robots and grippers. The concept is designed as a table-top robot cell, and thus only support robotic manipulators of a certain size and weight. However, the majority of collaborative robots are also found in this "small" segment of robots.

To examine the proposed framework, a preliminary feasibility study was conducted. A simple pick and place task was instructed using kinesthetic teaching and UII, and afterwards executed using an industrial robot. The feasibility study demonstrates how the proposed framework successfully allows a collaborative robots to be used as programming tool. In conclusion, we find the framework feasible, but further assessment and development is needed.

In future work, we will conduct a series of user studies in order to assess the skill-level required to use the framework. This will include users with different background and robotic experience. Furthermore, we will also verify the framework on more complex and diverse tasks. This includes the integration of additional devices, as well as improving cross platform compatibility. The integration of vision could allow for object-recognition and possibly improved grasping techniques. A throughout safety study would also be beneficial for a system such as UII.

UII is currently running of a PC, either laptop or desktop. However, deploying UII on a portable device (tablet, phone, etc.) could ease the use within a robot cell with little free space. We intend to develop a UII into a portable user interface, and a back-end running of a micro-computer, e.g. a Raspberry Pi.

References

1. C. Schou, J. Damgaard, S. Bøgh and O. Madsen, Human-robot interface for instructing industrial tasks using kinesthetic teaching, in *44th International Symposium on Robotics (ISR)*, (IEEE, 2013).

2. S. Wrede, C. Emmerich, R. Grünberg, A. Nordmann, A. Swadzba and J. Steil, *Journal of Human-Robot Interaction* **2**, 56 (2013).

3. K. R. Guerin, C. Lea, C. Paxton and G. D. Hager, A framework for end-user instruction of a robot assistant for manufacturing, in *2015 IEEE International Conference on Robotics and Automation (ICRA)*, 2015.

4. J. E. Colgate, W. Wannasuphoprasit and M. A. Peshkin, Cobots: Robots for collaboration with human operators, in *Proceedings of the 1996 ASME International Mechanical Engineering Congress and Exposition - Atlanta, GA, USA*, 1996.

5. T. Owen, *Assembly with robots* (Prentice Hall, Inc.,Old Tappan, NJ, Jan 1985).

6. G. Biggs and B. MacDonald, A survey of robot programming systems, in *Proceedings of the Australasian conference on robotics and automation*, 2003.

7. Y. Maeda, T. Ushioda and S. Makita, Easy robot programming for industrial manipulators by manual volume sweeping, in *2008 IEEE International Conference on Robotics and Automation*, 2008.

8. A. Muxfeldt, J.-H. Kluth and D. Kubus, Kinesthetic teaching in assembly operations – a user study, in *Simulation, Modeling, and Programming for Autonomous Robots*, eds. D. Brugali, J. F. Broenink, T. Kroeger and B. A. MacDonald (Springer International Publishing, 2014).

9. M. Stenmark and J. Malec, *Robotics and Computer-Integrated Manufacturing* **33**, 56 (2015), Special Issue on Knowledge Driven Robotics and Manufacturing.

10. C. Paxton, A. Hundt, F. Jonathan, K. Guerin and G. D. Hager, Costar: Instructing collaborative robots with behavior trees and vision, in *2017 IEEE International Conference on Robotics and Automation (ICRA)*, 2017.

11. C. Schou, R. S. Andersen, D. Chrysostomou, S. Bgh and O. Madsen, *Robotics and Computer-Integrated Manufacturing* **53**, 72 (2018).

12. R. Caccavale, M. Saveriano, A. Finzi and D. Lee, *Autonomous Robots* (2018).

13. R. H. Andersen, L. Dalgaard, A. B. Beck and J. Hallam, An architecture for efficient reuse in flexible production scenarios, in *Automation Science and Engineering (CASE), 2015 IEEE International Conference on*, 2015.

14. M. Quigley, K. Conley, B. Gerkey, J. Faust, T. Foote, J. Leibs, R. Wheeler and A. Y. Ng, Ros: an open-source robot operating system, in *ICRA workshop on open source software*, (3.2)2009.

15. C. Schou and O. Madsen, Towards shop floor hardware reconfiguration for industrial collaborative robots, in *In proceedings of the 19th International Conference on Climbing and Walking Robots and Support Technologies for Mobile Machines (CLAWAR 2016), London, United Kingdom*, 2016.

16. O. Madsen, S. Bøgh, C. Schou, R. S. Andersen, J. S. Damgaard, M. R. Pedersen and V. Krüger, *Industrial Robot: An International Journal* **42**, 11 (2015).

SECTION 5

SPECIAL SESSION ON ROBOTICS IN EDUCATION AND EDUCATION IN ROBOTICS

EDUCATIONAL MOBILE ROBOTS IN CLOUD-BASED FRAMEWORK FOR LABORATORY ENVIRONMENT

NM FONSECA FERREIRA

Institute of Engineering of Coimbra / Polytechnic of Coimbra
Rua Pedro Nunes, 3030-199, Coimbra, Portugal
Knowledge Research Group on Intelligent Engineering and Computing for Advanced
Innovation and Development (GECAD) of the ISEP/IPP, Porto, Portugal
INESC TEC Porto, Portugal
nunomig@isec.pt

ATEF A. ATA

Department of Engineering Mathematics and Physics, Faculty of Engineering,
Alexandria University, Alexandria, Egypt
atefa@alexu.edu.eg

YURY KOROBOV

Ural Federal University, Welding Technology department, Russian Federation
yukorobov@gmail.com

This article describes the development of architecture cloud-based for control different robotic platform to be used as an interdisciplinary teaching tool integrated in the curriculum. The results obtained with this educational approach for control robotic platform shown that a practical-learning approach usage in conjunction with highly motivating topics and promotes academic success and improves theoretical concepts comprehension. Students increased knowledge and skills during the problem resolution and achieved a real solution according their options. Moreover, this approach provides students an extensive learning experience on current technologies, architectures, modules and programming languages.

PROPOSAL OF A LOW COST HIGH PERFORMANCE EDUCATIONAL MOBILE ROBOT: AN RPI AND ARDUINO APPROACH

JOSÉ GONÇALVES *

Research Centre in Digitalization and Intelligent Robotics (CeDRI), Instituto Politécnico de Bragança, Campus de Santa Apolónia, 5300-253 Bragança, Portugal & INESC-TEC
* E-mail: goncalves@ipb.pt

ANDRÉ F. PINTO, VITOR H. PINTO, PAULO COSTA

Faculty of Engineering of the University of Porto & INESC-TEC
E-mail: {ee12007,vitorpinto,paco}@fe.up.pt

In this paper the proposal of a low cost high performance educational mobile robot is described. The robot is based on an Arduino, applied in the low level control, while the high level control loop is carried out by an RPI running an object pascal application. The described robot was prototyped in order to have a competitive participation in the Robotic Day Line Follower 2017 competition, taking advantage of the RPI capabilities. The RPI allows the use of higher performance sensors, when compared with the most common standard approaches based on a single 8 bit RISC micro-controller, having as disadvantage the inevitable robot size increase, which compromises in certain situations the robot maneuverability and increases the power consumption. The robot is equipped with DC Motors, the chosen line follower sensor is the picamera and for the obstacle detection sonar sensors are used.

Keywords: Robotics, Education, Prototyping

1. Introduction

Robotic Day is a very successful international robot competition, that is held annually in Prague. This robot competition has been active during the last 14 years and still continues to grown in number of participants, teams, visitants and competitions[1] . In this paper it is described the proposal of a low cost high performance educational mobile robot, that was prototyped in order to have a competitive participation in the Robotic Day Line Follower 2017 competition. The Line Follower Robotic Competition can be

seen in Figure 1 and the proposed robot in Figure 2. The robotic competitions present standard problems that can be used as a benchmark, in order to evaluate and to compare the performances of different approaches. Although there are many robotic competitions , there is the need to create new ones, in order to solve new challenges[2][3][4][5][6] . The robot prototyping and programming, in a competition context, can play an important role in education due to its inherent multidisciplinary approach, which can motivate students to bridge different technological areas. It can also play an important role in research and development, because it is expected that its outcomes will later be transferred to real-world problems in manufacturing or service robots.

The proposed robot is based on an Arduino, applied in the low level control, while the high level control loop is carried out by an RPI running an object pascal application. The RPI allows the use of higher performance sensors, when compared with the most common standard approaches based on a single 8 bit RISC micro-controller, having as disadvantage the inevitable robot size increase, which compromises in certain situations the robot maneuverability and increases the power consumption.
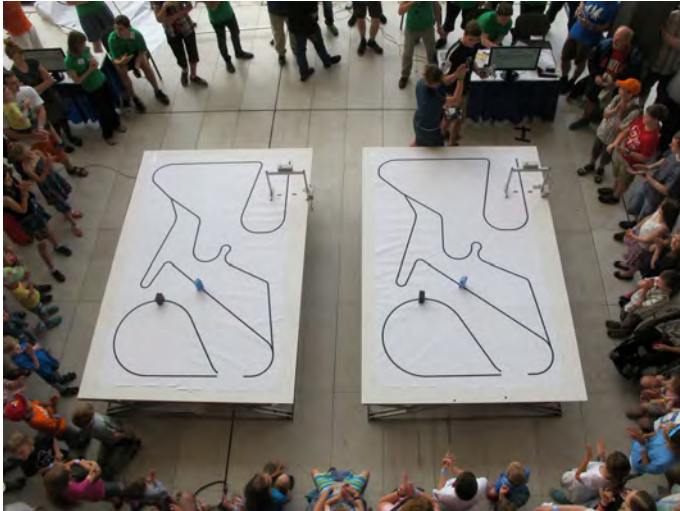

Fig. 1: Line Follower Robotic Competition

The robot has to run over the course and follow black line. During the qualifications robots proceed to next round if they successfully pass all obstacles and finish the run. Robots with the best time in the last

qualification round qualify for the finales. In the finale part, the races will be held on a knock-out basis. In case of a tie, a repeated race may be ordered by the organizers. There may be some obstacles on the track:

- An object: There could be an object laid on the track. The robot may touch it but it must not move it.
- Line cut-off: The line may be discontinued at any place for max. 20 cm.
- Line split and join: Situation like line split and join could exist.

The described robot was qualified for the finals of the Robotic Day 2017 edition, it were qualified 8 robots, from a total of 53 participants, the robot performance can be observed in the video available in[7] .
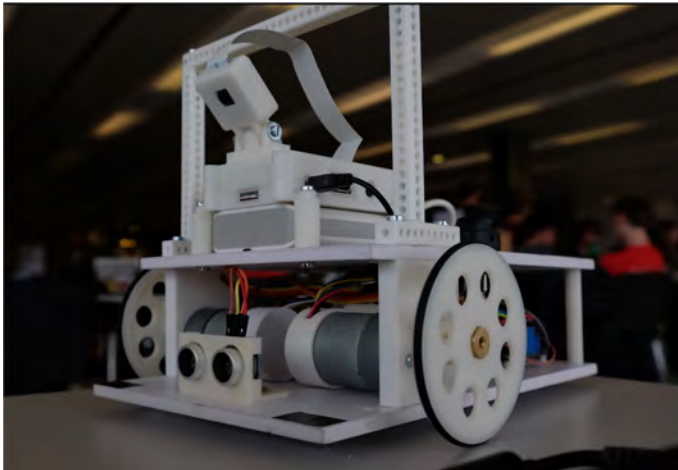

Fig. 2: Robot Prototype

2. Robot Prototype Description

The prototyped mobile robot consists in a 3D printed small prototype, that uses inexpensive hardware, such as DC motors, an Arduino, an RPI3, sonars and a picamera to sense the line, the robot prototype components are shown in Figure 3. The 3D printer models, that were developed in order to prototype the robot, are presented in Figure 4, where it can be seen the 3D models for the robot chassis, wheels, RPI case and picamera support and hinge 3D models.
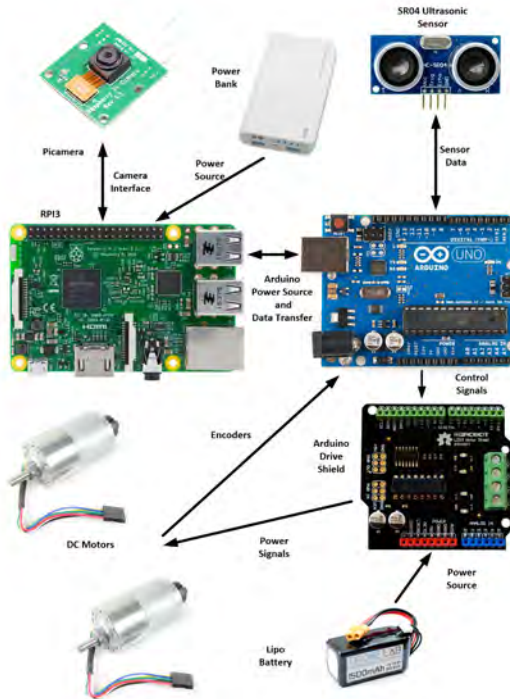
Fig. 3: Robot Prototype Components

Fig. 4: Robot Prototype 3D Printer Models.

2.1. Sensors

In this section are presented the sensors that are applied in the robot. Initially is presented the computer vision sensor, which is a common sensor

in mobile robotics, and it is also presented the sonar being used for obstacle detection[8] .

2.1.1. *Computer Vision*

A Raspberry Pi camera was used to detect the line that must be followed. While the standard approach is to use an array of IR sensors, it is very inflexible and its resolution is limited. By implementing a virtual line sensor from the image pixels, an higher resolution can be achieved and multiple virtual sensors can easily be implemented.

The current setup has a resolution of 320 x 240 with a frame rate of 30 frames per second. The acquired image covers an area in front of the robot with an width of 25 cm and a length of 35 cm. The virtual line sensors can be placed anywhere inside that area. A dedicate application handles the image acquisition, that can be seen in Figure 5, the virtual line sampling and processing. For each virtual sensor the line position is calculated and its width is used to access the measure confidence. There is some degree of adaptability on the luminance thresholds to deal with different light conditions.
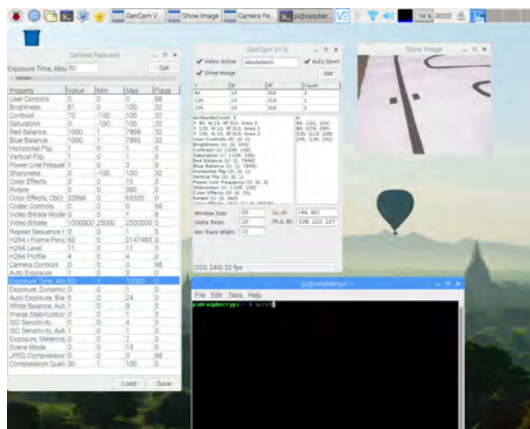

Fig. 5: Virtual Line Sensor Software

2.1.2. *Sonar*

The chosen sensor used to detect the obstacles is the Ultrasonic ranging module HC - SR04, shown in Figure 3, which provides 2 cm - 400 cm

measurement function, with a ranging accuracy that can reach to 3 mm. The modules include ultrasonic transmitters, receiver and control circuit.

2.2. *Actuators*

The applied DC motors have built in encoders which are very important in mobile robots in order to obtain the closed loop Velocity Control and also to estimate the robot odometry calculation and the applied drive is the DFRobot L293 Arduino Shield.

3. Controller description

Following a line with a robot based on the differential kinematics is a classical introductory experiment that allows students to be introduced to the challenges of mobile robotics[10][11] . Understanding the concepts of sensor, actuator and locomotion are the primary goals of this challenge based on the control of a reactive robot[9] . In this section it will be described the developed prototype controller.

3.0.1. *Line Following*

The goal of the robot is to follow a line as fast as possible, for that purpose it is necessary to maintain the highest possible linear velocity, with an angular velocity that is proportional to the path curvature. With the picamera, applied as line sensor, it is possible to know at each sample time the robot posture in relation to the line. A detailed description of the applied line following controller algorithm can be found in[12] .

3.0.2. *Obstacle avoidance*

In order to the robot avoid and contour an obstacle the state machine observed in Figure 6 was used. Initially the robot, when an obstacle is detected, rotates with a null linear velocity and then, using odometry, the robot performs a smooth trajectory without using the camera data to navigate, finally the camera data is used and if a line is detected the robot will navigate using the standard line following controller, as described in in[12] .

3.0.3. *Line Interruption*

Each virtual sensor can detect the line presence or absence, by analyzing the line total dynamic range. The line absence can be detected by testing if
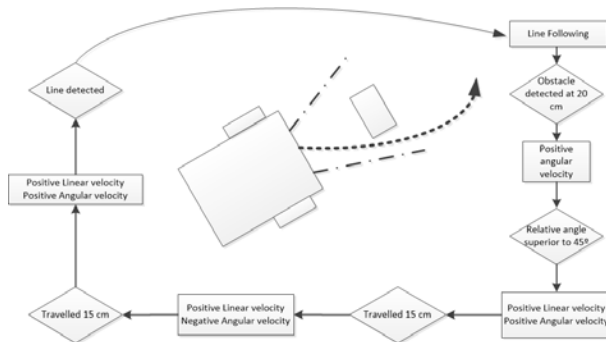
Fig. 6: Obstacle avoidance State Machine

the minimum sampled value is above a certain threshold, that means there isn't a black zone on the line. If the condition is met for a few samples the line interruption event is triggered and the current direction is frozen, that allows the robot to travel until it meets the line again.

4. Conclusions and Future Work

In this paper it is described the proposal of a low cost high performance educational mobile robot. The robot is based on an Arduino, applied in the low level control, while the high level control loop is carried out by an RPI running an object pascal application.

The described robot was prototyped in order to have a competitive participation in the Robotic Day Line Follower 2017 competition. The RPI apply allows the use of higher performance sensors, when compared with the applied in the most common standard approaches based on a single 8 bit RISC micro-controller, having as disadvantage the inevitable robot size increase, which compromises in certain situations the robot maneuverability and increases the power consumption.

The robot is equipped with DC Motors with built in encoders, which allows the apply of velocity closed loop control and the necessary data to the odometry calculation. The ability to calculate the robot odometry was very important, because the robot had, in some situations, to perform trajectories without sensing the line. The chosen line follower sensor is the picamera, providing a very flexible sensor based on image processing.

The authors intend to evolve the software robustness of the proposed robot in order to participate in the 2018 Robotic Day Line Follower Competition edition.

Aknowledgements

References

1. Richard Balogh , Grzegorz Granosik , Valery Kasyanik , David Obdrzalek. Experiences from the Series of International Robotics Workshops. Computer Science and Information Technology, 4 , 126 - 133. doi: 10.13189/csit.2016.040304, 2016.
2. A. Eguchi *RoboCupJunior for promoting STEM education, 21st century skills, and technological advancement through robotics competition,* Robotics and Autonomous Systems, 2016.
3. E. Pagello and E. Menegatti and A. Bredenfeld and P. Costa and T. Christaller and A. Jacoff and D. Polani and M. Riedmiller and A. Saffiotti and E. Sklar and T. Tomoichi, Robotic Competition Based Education in Engineering,AI Magazin, 2004
4. F. Ribeiro and I. Moutinho and P. Silva and C. Fraga and N. Pereira, Controlling Omni-Directional Wheels of a Robocup MSL Autonomous Mobile robot, Scientific Meeting of the Portuguese Robotics Open, 2004
5. B. Browning and J. Bruce and M. Bowling and M. Veloso, USTP: Skills, tactics and plays for multi-robot control in adversarial environments, IEEE Journal of Control and Systems Engineering, 2005
6. R. Nakanishi and J. Bruce and K. Murakami and T. Naruse, and M. Veloso, Cooperative 3-robot passing and shooting in the RoboCup Small Size League, Proceedings of the RoboCup Symposium, 2006
7. Gonçalves, J., Robotic Day 2017, Robot: LF@RD17, TEAM: PT@RDLF17, ORGANIZATION: IPB/FEUP, 2017, https://www.youtube.com/watch?v=6qnDiBPg2Ms
8. Borenstein, J., Everett, H., Feng, J. 'Where am I?' Sensors and Methods for Mobile Robot Positioning Technical Report, The University of Michigan 1996
9. Pakdaman, M. Design and Implementation of Line Follower Robot Second International Conference on Computer and Electrical Engineering 2009
10. Gregory Dudek and Michael Jenkin Computational Principles of Mobile Robotics Cambridge University Press 2000
11. H. Choset, K. Lynch, S. Hutchinson, G. Kantor, W. Burgard, L. Kavraki, S. Thrun, *Principles of Robot Motion : Theory, Algorithms, and Implementations,* MIT Press, 2005.
12. Gonçalves, J and Costa, P *Differential mobile robot controller study: A low cost experiment based on a small arduino based prototype,* 25th Mediterranean Conference on Control and Automation, 2017

EDUCATIONAL HUMANOID ROBOT USING A SENSORING FUSION THROUGH ARDUINO

JESSICA P. M. VITAL

INESC TEC-INESC Technology and Science and
University of Tras-os-Montes and Alto Douro, Vila Real, Portugal
Email:Jessicavital_hotmail.com
ORCID: 0000-0002-1660-7718

N. M. FONSECA FERREIRA

INESC TEC - INESC Technology and Science and
Institute of Engineering Of Coimbra, Polytechnic Institute of Coimbra, and
Knowledge Research Group on Intelligent Engineering and Computing for Advanced
Innovation and Development (GECAD) of the ISEP/IPP, Portugal.

Email: nunomig@isec.pt
ORCID: 0000-0002-2204-6339

ANTONIO VALENTE

INESC TEC-INESC Technology and Science and
University of Tras-os-Montes and Alto Douro, Vila Real, Portugal
Email: avalente@utad.pt

ORCID: 0000-0002-5798-1298

This paper describes the use of NAO robot, a humanoid robot and the use of Arduino in education for final engineering projects in the area of engineering. This learning approach was implemented in the final project of the Biomedical Engineering degree. The objective this project is the sensorial extension of the NAO platform, integrating a set of sensors that allow not only to analyze multiple vital parameters in a passive way but also to obtain a more precise contextual information.

Keywords: NAO robot, Arduino, Humanoid robots, Education, Sensory Fusion

1. Introduction

Over the years robotics has made great progress and nowadays robots begin to be part of the life of any person, designated social robotics [1]. For this reason, robotics has become a common subject in engineering courses, such as biomedical, computer, electrical, mechanical and electromechanical. Humanoid

robots are fascinating and have several advantages, such as they can work in places where there is a risk of contamination, risk of health, danger of life, places that are difficult to access [2]. They also are able to access different types of terrain and to climb stairs [3].

The behavior of humanoid robots produces feelings that facilitate the communication between machine and man. There are many cases where you need a machine similar to the man to be able to replace it in your work environment [4].

Robotics courses embrace diverse areas such as, kinematics, programming, sensors, and artificial intelligence. However, in recent years, social robotic has seen the emergence of sophisticated humanoid robots, which makes it impossible to obtain funding for the latest and most developed robots on the market. For this, the use of the NAO robot was chosen.

NAO that is currently the humanoid platform with high sensory capacity that it has lower costs in the market. This robot is similar to the human in order to have a more real and natural interaction with society. NAO is a good platform for software development because it is easy to learn how to program and it has a high sensory ability.

Students during the degree acquired a lot of knowledge in electronics, which makes it easier to use different sensors and their integration into Arduino. Students also learned different programming language, such as C language, C ++ language, MATLAB, LabView, among others, which makes it easier for students to program the NAO robot. However, students will work in a more motivated, fast and effective way because they will be working with a humanoid robot, capable of walking, communicating with people, and being able to be programmed by the students to do any task like a human. Students will not only learn theoretically and with a simple robot, but with a humanoid robot currently used in research in the field of robotics.

NAO robot is only a tool in which educational theory can be applied and developed, learned during the course that will make all the difference in the development of the project using the robot.

This paper analyzes the educational approach adopted for the final project of Biomedical Engineering course. This paper is organized as follows. Section 2 shows objectives of this project and the work plan during 9 months. Section 3 presents NAO robot has a humanoid robot that will be used in this project and it different applications. Section 4 will be described the different programming tool that it is useful in this project. Finally, section 5 presents the evaluation of the course.

2. NAO robot and a sensorial fusion

The content of the curricular unit of the final project, of the Biomedical Engineering Degree of the Engineering Institute of Coimbra (ISEC), is organized according to the area of interest of the students, and what is currently being developed in the world of scientific investigation.

The objective of this project is the sensorial extension of the NAO platform, integrating a set of sensors that allow not only to analyze multiple vital parameters in a passive way but also to obtain a more precise contextual information, thus accomplishing the fusion of all this information.

The project is aimed at a group of 3 students, so that they can interact. The project is multidisciplinary, which may include students interested in the area of programming and electronics which makes it possible to complement during this project.

The final course project lasts 9 months. The work plan will be divided as follows:

- Familiarization with the NAO platform and first tests with the hardware (1 month);
- Acquisition and development of sensors for passive monitoring of vital signs (e.g., heart rate, body temperature) (2 months);
- Acquisition and development of sensors to monitor contextual quantities (e.g., surrounding temperature, humidity, among others) (2 months);
- Sensory integration (e.g., using Bayesian networks) (2 months);
- Tests, tests and possible system improvements (1 month);
- Writing of the project work report (1 month).

3. NAO robot – a humanoid robot

In recent years, social robotic has seen the emergence of sophisticated humanoid robots, as Honda, Asimo and NAO [5]. NAO robot (figure1) is currently the humanoid platform with high sensory capacity that it has lower costs in the market. This robot is similar to the human in order to have a more real and natural interaction with society.

NAO is a good platform for software development because it is easy to learn how to program and it has a high sensory ability. It has been used in different applications, such as: sports and interaction with humans [6].

It can help people in rehabilitation. By cameras robot can see the movement of patients and avoid them if the movement are correct or no [7]. NAO is able to replicate the movement of humans, so it can explain to patient how to the correct

movement [8, 9]. NAO robot has been used to help autistic children in improving their behavior [10, 11]. The studied cases show that children suppress the autistic behavior during human-robot interaction and they can maintain visual contact with NAO [12]. NAO robot participate in RoboCup (the World Championship of Robotics) as a soccer playing NAO robot. It has been the star of the Standard Platform League where robots are expected to operate fully autonomously [13, 14].

Figure 1- NAO robot

It is important for students to understand that this robot is a tool of great interaction potential with humans. This robot is able to walk, speak and act as a human if it is programmed. At the end of the project students should be able to develop various programs for the robot in order to perform different tasks with humans.

The main objectives of the final course project are based on a deep understanding of the fundamental principles of the use and programming of humanoid robots. Another objective is to develop students' practical and autonomous sense, in which the teacher will simply have the purpose of guiding only the students. The work carried out by the students promotes different autonomous and team research, leading to greater learning, as the students devote more time and have greater involvement in it.

4. Programming Tools

The university has an NAO robot that is available in the laboratory so that the students can do experiments and get to know the robot better, in order to implement the project more efficiently.

The program used to program the robot NAO is called Choregraphe. The figure 2 shows the virtual robot and the graphical environment of the software simulator, a software very intuitive and identical to the real system. This simulator allows the students to develop all the work in the place that they want without the use of the robot, not having to be constantly in the laboratory of robotics.
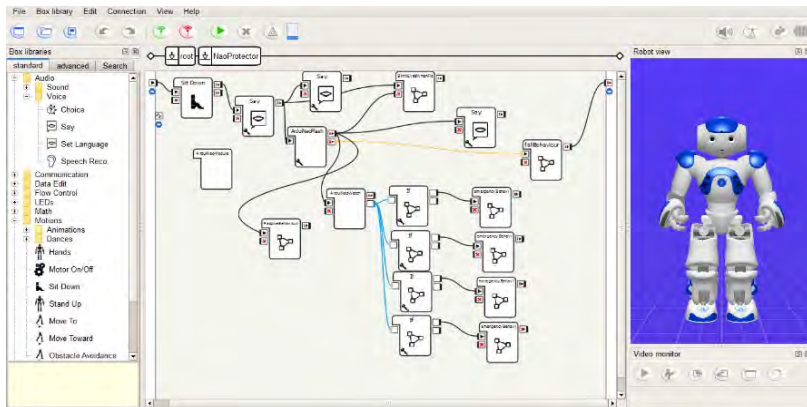

Figure 2- Choregraphe program

Arduino, Wireless Proto Shield and several sensors, such as a light sensor, a temp sensor and a gas sensor are available to students. If students need other materials or other types of sensors, it will be made available to them. Students will not have difficulty in using / programming the Arduino, since they already have some notions of programming seized during the course. The programming language used in Arduino is C ++ (with small modifications), which is a very traditional and familiar language. In the internet there are different forums in which are made available several programs and libraries already made for Arduino in which students will have easy access and quick learning in the use of it. With the use of Coreographe and Arduino programming students will see that programming is simple and they will be more motivated because they get faster results. Despite this, students find it simpler, more intuitive and more interactive the programming in the Choregraphe.

The sensors are integrated into the Arduino, it is receiving the values of the sensors continuously, it reads and analyzes the values that the sensors transmit and sends an alert to the robot via Wifi, if it justifies, and if there is in the presence of a situation of danger. The robot must find people to communicate the programmed alert.
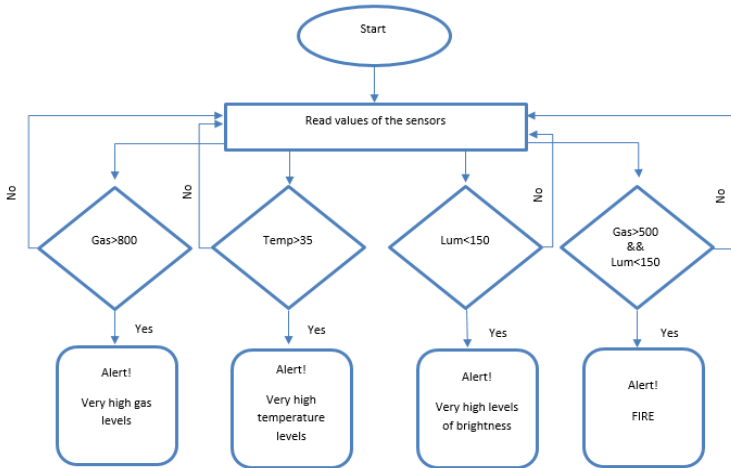
Figure 3- Flowchart of Operation

The figure 3 shows a flowchart, that is, a diagram of how the sensors work and how they are programmed to issue the alert. The robot must find people to communicate the programmed alert. For example, if the temperature sensor measures more than 35 ° C, the robot is programmed to raise an alert because the temperature level is too high.

5. Course Evaluation

Students have all the help of the guiding teacher, meeting with the same every week. These meetings have the purpose of the students to show weekly the work developed, to ask questions, and so that the teacher can guide them in the best way. Students will be able to attend the robotics lab whenever they request and put questions with the teacher outside the meetings, through the email. Students are required to take at least 15 hours per week to make the project robust and recognized by the scientific community.

The final year project is projected with 14 ECTS (European System of Transfer and Accumulation of Credits). It is through the evaluation of the results of the final project that one can recognize the benefits of the humanoid robotics approach and all the content taught during the course. Through evaluation, the teacher should be able to evaluate the student's attitudes regarding the ability to investigate, develop and implement each proposed task during the development of the project autonomously.

There are different approaches to evaluating students' learning outcomes, using the following methods:

- Project report, where the student report includes the written designation of the state of the art, the work done, the conclusions and the future work;
- Writing an article at a conference about the project developed;
- Oral presentation, where a jury composed of 5 teachers will be present.

This oral presentation is divided in two phases, the first phase: the students present the project developed through a Power Point presentation and present the development prototype, with a duration of 20 min; the second phase: the different members of the jury ask the students several questions about the project developed and what they think is operative in relation to the humanoid robots. The members of the jury are composed of the teacher of the students, a professor from another university who is related to the area and by three other teachers, one from the electronic area, another from the programming area and another from the robotics area. The final course project offers students an opportunity to interact with humanoid robots, thus allowing them a greater motivational dimension. Students demonstrated that using this type of robot learned faster and more efficiently the knowledge acquired during the course and that are able to integrate new technologies. Students demonstrated that this is a developing area and of interest in the area to continue in the master's degree.

Acknowledgments

References

1. T. Fong, I. Nourbakhsh and K. Dautenhahn, "A survey of socially interactive robots," *Robotics and Autonomous Systems,* pp. 143-166, 2003.
2. R. Calo, "Robots and privacy," 2010.
3. A. Hornung, K. M. Wurm and M. Bennewitz, "Humanoid Robot Localization in Complex Indoor Environments," in *Intelligent Robots and Systems (IROS)*, 2010.

4. L. Takayama, W. Ju and C. Nass, "Beyond Dirty, Dangerous and Dull: What Everyday People Think Robots Should Do," in *Proceedings of the 3rd ACM/IEEE international conference on Human robot interaction* , 2008.

5. I. Rodriguez, A. Astigarraga, E. Jauregi, T. Ruiz and E. Lazkano, "Humanizing NAO robot teleoperation using ROS," in *14th IEEE-RAS International Conference on Humanoid Robots (Humanoids)*, 2014.

6. J. P. M. Vital, N. M. M. Rodrigues, M. S. Couceiro, C. M. Figueiredo and N. M. F. Ferreira, "Fostering the NAO platform as an elderly care robot," in *Serious Games and Applications for Health (SeGAH)*, 2013.

7. D. L. Recio, E. M. Segura, L. M. Segura and A. Waern, "The NAO models for the elderly," in *Proceedings of the 8th ACM/IEEE international conference on Human-robot interaction*, 2013.

8. C. Stanton, A. Bogdanovych and E. Ratanasena, "Teleoperation of a humanoid robot using full-body motion capture, example movements, and machine learning," in *Proceedings of Australasian Conference on Robotics and Automation*, 2012.

9. J. Lei, M. Song, Z.-N. Li and C. Chen, "Whole-body humanoid robot imitation with pose similarity evalution," *Signal Processing,* vol. 108, pp. 136-146, 2015.

10. S. Shamsuddin, H. Yussof, L. I. Ismail, S. Mohamed, F. A. Hanapiah and N. I. Zahari, "Initial Response in HRI- a Case Study on Evaluation of Child with Autism Spectrum Disorders Interacting with a Humanoid Robot NAO," *International Symposium on Robotics and Intelligent Sensors ,* pp. 1448-1455, 2012.

11. S. Shamsuddin, H. Yussof, L. I. Ismail, S. Mohamed, F. A. Hanapiah and N. I. Zahari, "Humanoid Robot NAO Interacting with Autistic Children of Moderately Impaired Intelligence to Augment Communication Skills," *International Symposium on Robotics and Intelligent Sensors,* pp. 1533-1538, 2012.

12. A. Tapus, A. Peca, A. Aly, C. Pop, L. Jisa, S. Pintea, A. Rusu and D. David, "Children with autism social engagement in interaction with Nao, an imitative robot : A series of single case experiments.," *Interaction studies,* pp. 315-347, 2012.

13. T. Niemuller, A. Ferrein , G. Eckel, D. Pirro, P. Podbregar, T. Kellner, C. Rath and G. Steinbauer, "Providing Ground-truth Data for the NAO Robot Paltform," *RoboCup,* pp. 133-144, 2010.

14. L. M. Cruz, Humanoid Robot NAO: Developing Behaviors for Soccer Humanoid Robots, LAP Lambert Academic Publishing, 2013.

NAO ROBOT AS A DOMESTIC ROBOT

JESSICA P. M. VITAL

INESC TEC-INESC Technology and Science and
University of Tras-os-Montes and Alto Douro, Vila Real, Portugal
Email:Jessicavital_hotmail.com
ORCID: 0000-0002-1660-7718

N. M. FONSECA FERREIRA

INESC TEC - INESC Technology and Science and
Institute of Engineering Of Coimbra, Polytechnic Institute of Coimbra, and
Knowledge Research Group on Intelligent Engineering and Computing for Advanced
Innovation and Development (GECAD) of the ISEP/IPP, Portugal.

Email: nunomig@isec.pt
ORCID: 0000-0002-2204-6339

ANTONIO VALENTE

INESC TEC-INESC Technology and Science and
University of Tras-os-Montes and Alto Douro, Vila Real, Portugal
Email: avalente@utad.pt
ORCID: 0000-0002-5798-1298

Over the years robotics has made great progress. Nowadays, robots begin to be part of the life of any person, designated social robotic. Humanoid robots are fascinating and have several advantages, such as they can work in places where there is a risk of contamination, risk of health, danger of life, places that are difficult to access. They also are able to access different types of terrain and to climb stairs. NAO robot is currently the humanoid platform with high sensory capacity that it has lower costs in the market. This robot is similar to human in order to have a more real and natural with society. Using the capabilities of the robot and adding other sensors, we can have a more powerful machine in our society. NAO robot is presented in this paper as a domestic robot.

Keywords: NAO robot, wireless sensors, Humanoid robots, Domestic robots, object recognition

1. Introduction

Over the years robotics has made great progress, nowadays robots begin to be part of the life of any person, designated social robotics [1].

Humanoid robots are fascinating and have several advantages, such as they can work in places where there is a risk of contamination, risk of health, danger of life, places that are difficult to access [2]. They also are able to access different types of terrain and to climb stairs [3]. The behavior of humanoid robots produces feelings that facilitate the communication between machine and man.

There are many cases where you need a machine similar to the man to be able to replace it in your work environment [4].

In recent years, social robotic has seen the emergence of sophisticated humanoid robots, as Honda Asimo and NAO [5].

We chose the platform NAO that is currently the humanoid platform with high sensory capacity that it has lower costs in the market. This robot is similar to the human in order to have a more real and natural interaction with society. NAO is a good platform for software development because it is easy to learn how to program and it has a high sensory ability.

This paper is divided into four sections. The first section gives a brief introduction of different domestic robots. The second section presents NAO robot. An extension of platform NAO using sensors and an architecture of recognize objects using NAO robot is described in third section. Our conclusions are drawn in the final section.

2. Domestic Robots

Domestic Robots can help you carry out all kinds of tasks at home, such as cooking, cleaning, company, babysitting or answering questions. Science fiction has come to fruition, and they are available to make people's lives easier by dismissing people from household chores and giving them the opportunity to do other leisurely things [6].

Nowadays all people use domestic robots in their homes, such as:
- Roomba Vacuum: can vacuum the floor of the house alone [7];
- Bimby: can cook alone meals, sweets or whatever the person wants;
- Winbot: robot that clean the glass;
- Husqvarna automower: robot that mows the lawn very efficiently.

The area of robots has been an area of great evolution appearing also robots as: Zenbo, Kuri. The use of humanoid robots as domestic robots were appeared, as, Pepper [8], Honda Asimo and NAO robot [5]. These robots are more developed able to do different household tasks, thus becoming much more expensive when compared with the simpler robots and that only perform one task. To combat this situation we present the NAO robot, as a domestic robot.

3. NAO robot

NAO robot (figure 1) is humanoid robot developed by Aldebaran Robotics, a French company. It has 58 cm in height and it weighs 5.4 kg which make it easy to transport [9]. With twenty five degrees-of- freedom (DOF) and more than 50 sensors, NAO is a robust robot to develop a wide range of applications.
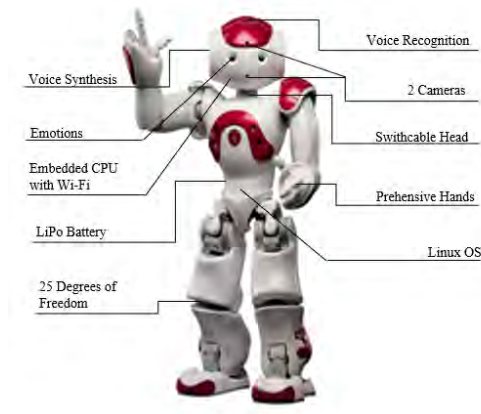

Figure 1- NAO robot

NAO is specially used as a social robot. NAO robot has a similar appearance when compared with a human. NAO allows to perform several basic actions, such as sitting, walking, picking up objects with your hands, among others.

NAO robot has a disadvantage, its autonomy. In normal use NAO just has 90 minutes of autonomy which makes this robot only used as proof of concept and not as a daily instinctive use robot. On the other hand we can conclude that the robot has several advantages, as it is easy to carry, because it is small and it is light. It has equipped with two cameras, like human eyes and can speak and can recognize the most popular languages in world [10]. Are so many applications that NAO robot has been used, such as: sports and interaction with humans.

A. Rehabilitation

By cameras robot can see the movement of patients and avoid them if the movement are correct or no [11]. NAO is able to replicate the movement of humans, so it can explain to patient how to the correct movement [12, 13].

B. Autism Children

NAO robot has been used to help autistic children in improving their behavior [15, 16]. The studied cases show that children suppress the autistic behavior during human-robot interaction and they can maintain visual contact with NAO [17].

C. Traditional Robotic Soccer

NAO robot participate in RoboCup (the World Championship of Robotics) as a soccer playing NAO robot has been the star of the Standard Platform League where robots are expected to operate fully autonomously [17, 18].

4. Nao robot as a domestic robot

In this section we present different architectures that can reach NAO robot as a domestic robot. Firstly is presented an extension of NAO robot using sensors and after is presented an architecture to recognize objects.

4.1. Platform using sensors

This architecture present the integration of three sensors to NAO robot (figure 2). To integrate the sensory network were chosen the following sensors:

- Temperature sensor: LM35 sensor 545753 YWrobot.
- Photoresistor Light sensor: 531289 ywrobot;
- Gas sensor: MQ Series Gas Sensor Module L1te v1.0 sandbox electronics
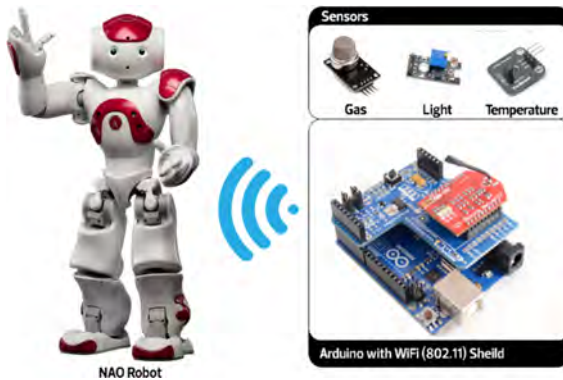

Figure 2- Architecture integrating three sensors to NAO robot

When integrating three sensors in Arduino, a set of collections is provided in order to validate their operation against the accuracy and precision.

The Arduino is equipped with the Wireless Proto Shield by using SPI Communication. This allows pairing both NAO and sensorial array using WIFI 802.11 [19]. Using Choreographe, the tool used to program the NAO, it is possible to elaborate a set of tasks for the interaction with the general public.

An Arduino library called CoGasSensorShield was used. This library allowed to receive a value (e.g., gas sensor) via Wifi from an Arduino board and thus issue an alert when desired. Given the limitations of the library, it was extended in order to access the three sensors previously chosen, and with the respective intervals that had previously been analyzed. After this work of adaptation, a project was developed in Choregraphe that allowed to execute a set of movements and dialogues associated to the output of the program in Arduino in order to promote the human-machine interaction.

Intervals of values for the presence of gas, high temperature and luminosity were analyzed and elaborated. In the Arduino, an alert was sent via Wifi when values outside these ranges were registered. It reads and analyzes the values that the sensors transmit and throws an alert, if it justifies, and if it has in the presence of a dangerous situation. So that the alert is given correctly, different parameters have been stipulated. The Arduino continuously reads all sensor values and processes this information and whenever there is a state change it alerts the robot.

NAO robot will transmit alerts in different situations that was predefined, in situations of danger to people, taking into account the ambient temperature, gas levels and brightness. If the sensors detect that ambient has a high level of temperature and the light is less, the robot will transmit a fire alert. In case of an alert, NAO tells people to evacuate and explains to them what is happening. The alert is also given by sending a message directly to the responsible. In case of fire the message will be sent directly to the firemen, with the address, in order to solve the problem effectively and quickly.

4.2. Recognition Objects

Choregraphe Software is the tool used to program the NAO, it is possible to elaborate a set of tasks for interaction with the general public. Through this program that we used to program NAO robot can learn the different objects so that later it can identify them. As proof of concept we used five types of object to recognize, such as, a banana, a bottle of water, a mobile phone and a medicine. Objects of different areas that are essential in ambient assisting living.

First we used robot to capture different images with different objects. We selected different objects in different positions and at different distances, in order to create a dataset, so that the robot could distinguish the different objects. Then the images were segmented. The contour of the object was made so that the robot could distinguish it when the object is surrounded by other objects. After the outline of each object, we indicate the name of the object and the position in which it is.

All the information is sent to the robot so that it can memorize the different images, the name of the different objects and their position so that the robot can later distinguish the different objects in different circumstances.

Finally, the vision recognition module belonging to the Choreographe program was used. We was used this module robot acquire an image in real time and analyze, if him recognize they tell what it is.

One of the limitations of NAO robot is the memory, so as future work will be created a cloud computing service. It is through the cloud computing service that the robot can recognize objects more quickly and accurately. Cloud will have a wide set of images of many objects in different positions so that the robot can recognize all the existing objects in a more viable and faster way of processing. Despite being connected to the cloud will always have the ability to recognize a set of predefined objects, essences of that environment so that in case there is some failure of connection to the cloud the robot with him in the same way do their activities. In a house we may have one robot but we can have more than one.
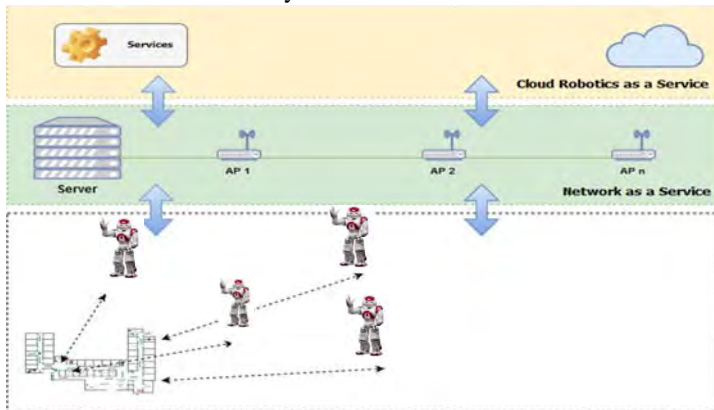

Figure 3- Cloud Operating Diagram

In figure 3 we can observe a cloud operating diagram. There we see robots in different places of the house communicating each other and communication with the server. The server communicating with the cloud to obtain the information and give it back to the robot.

5. Conclusion

NAO robot can perform different domestic tasks. NAO robot can walk, talk, see and grab objects. Despite its basic functions, through cameras the robot can recognize objects and people. Adding sensors to the robot, it is able to send

environmental alerts in dangerous situations. We can conclude that the robot is a domestic robot capable of doing not only domestic tasks, but also doing company or having a dialogue. Having a humanoid aspect and an affordable cost is a key point in the acceptance of the robot by our society.

Acknowledgments

References

1. T. Fong, I. Nourbakhsh and K. Dautenhahn, "A survey of socially interactive robots," *Robotics and Autonomous Systems,* pp. 143-166, 2003.

2. R. Calo, "Robots and privacy," 2010.

3. A. Hornung, K. M. Wurm and M. Bennewitz, "Humanoid Robot Localization in Complex Indoor Environments," in *Intelligent Robots and Systems (IROS)*, 2010.

4. L. Takayama, W. Ju and C. Nass, "Beyond Dirty, Dangerous and Dull: What Everyday People Think Robots Should Do," in *Proceedings of the 3rd ACM/IEEE international conference on Human robot interaction* , 2008.

5. I. Rodriguez, A. Astigarraga, E. Jauregi, T. Ruiz and E. Lazkano, "Humanizing NAO robot teleoperation using ROS," in *14th IEEE-RAS International Conference on Humanoid Robots (Humanoids)*, 2014.

6. J. Carpenter, J. M. Davis, N. Erwin-Stewart, T. R. Lee, J. D. Bransford and N. Vye, "Gender Representation and Humanoid Robots Designed," *International Journal of Social Robotics,* vol. 1, pp. 261-265, 2009.

7. J. Forlizzi and C. DiSalvo, "Service robots in the domestic environment: a study of the roomba vacuum in the home," in *Proceedings of the 1st ACM SIGCHI/SIGART conference on Human-robot interaction*, 2006.

8. J. Lafaye, D. Gouaillier and P.-. B. Wieber, "Linear Model Predictive Control of the locomotion of Pepper,a humanoid robot with omnideirection wheels," in *Humanoid Robots (Humanoids), 2014 14th IEEE-RAS International Conference on*, 2014.

9. D. Gouaillier, V. Hugel and P. Blazevic, "Mechatronic design of NAO humanoid," in *Robotics and Automation*, 2009.

10. S. Fojtu, M. Bresler and D. Prusa, "Nao Robot Navigation Based on a Single VGA Camera," in *17th Computer Vision Winter Workshop*, 2012.

11. D. L. Recio, E. M. Segura, L. M. Segura and A. Waern, "The NAO models for the elderly," in *Proceedings of the 8th ACM/IEEE international conference on Human-robot interaction*, 2013.

12. C. Stanton, A. Bogdanovych and E. Ratanasena, "Teleoperation of a humanoid robot using full-body motion capture, example movements, and machine learning," in *Proceedings of Australasian Conference on Robotics and Automation*, 2012.

13. J. Lei, M. Song, Z.-N. Li and C. Chen, "Whole-body humanoid robot imitation with pose similarity evalution," *Signal Processing,* vol. 108, pp. 136-146, 2015.

14. S. Shamsuddin, H. Yussof, L. I. Ismail, S. Mohamed, F. A. Hanapiah and N. I. Zahari, "Initial Response in HRI- a Case Study on Evaluation of Child with Autism Spectrum Disorders Interacting with a Humanoid Robot NAO," *International Symposium on Robotics and Intelligent Sensors ,* pp. 1448-1455, 2012.

15. S. Shamsuddin, H. Yussof, L. I. Ismail, S. Mohamed, F. A. Hanapiah and N. I. Zahari, "Humanoid Robot NAO Interacting with Autistic Children of Moderately Impaired Intelligence to Augment Communication Skills," *International Symposium on Robotics and Intelligent Sensors,* pp. 1533-1538, 2012.

16. A. Tapus, A. Peca, A. Aly, C. Pop, L. Jisa, S. Pintea, A. Rusu and D. David, "Children with autism social engagement in interaction with Nao, an imitative robot : A series of single case experiments.," *Interaction studies,* pp. 315-347, 2012.

17. T. Niemuller, A. Ferrein , G. Eckel, D. Pirro, P. Podbregar, T. Kellner, C. Rath and G. Steinbauer, "Providing Ground-truth Data for the NAO Robot Paltform," *RoboCup,* pp. 133-144, 2010.

18. L. M. Cruz, Humanoid Robot NAO: Developing Behaviors for Soccer Humanoid Robots, LAP Lambert Academic Publishing, 2013.

19. J. P. M. Vital, N. M. M. Rodrigues, M. S. Couceiro, C. M. Figueiredo and N. M. F. Ferreira, "Fostering the NAO platform as an elderly care robot," in *Serious Games and Applications for Health (SeGAH)*, 2013.

EDUCATIONAL BANDWIDTH TRAFFIC PREDICTION USING NON-LINEAR AUTOREGRESSIVE NEURAL NETWORKS

SHWAN DYLLON

School of Engineering, London South Bank University, 103 Borough Road, London, SE1 0AA, UK

TIMOTHY HONG

School of Engineering, London South Bank University, 103 Borough Road, London, SE1 0AA, UK

OUSMANE ABDOULAYE OUMAR

School of Engineering, London South Bank University, 103 Borough Road, London, SE1 0AA, UK

PERRY XIAO

School of Engineering, London South Bank University, 103 Borough Road, London, SE1 0AA, UK

Time series network traffic analysis and forecasting are important for fundamental to many decision-making processes, also to understand network performance, reliability and security, as well as to identify potential problems. This paper provides the latest work on London South Bank University (LSBU) network data traffic analysis by adapting nonlinear autoregressive exogenous model (NARX) based on Levenberg-Marquardt backpropagation algorithm. This technique can analyse and predict data usage in its current and future states, as well as visualise the hourly, daily, weekly, monthly, and quarterly activities with less computation requirement. Results and analysis proved the accuracy of the prediction techniques.

1. Introduction

Prediction of time series network traffic analysis is important for many decision-making processes, also to understand network performance, reliability and security, as well as to identify potential problems. Many types of research have been carried out such as statistical analysis, machine learning, neural networks, Fast Fourier transforms (FFT) wavelets, Continuous wavelet transform (CWT),

fuzzy set, chaos theory for that purpose to deal with the different characteristics of time series.

Artificial neural network (ANN) is an excellent tool for machine learning in terms of performance, classification and regression problems, which is very useful for time series and forecasting. Neural network techniques used comprehensively in many organisational applications such as financial, economic, energy systems, media (weather) to predict and forecasting their time series information

With network traffic analysis, network security staff would be able to identify any malicious or suspicious packets within the traffic, whilst network administrators could monitor the download/upload speeds, throughput etc., and therefore to have a sounder understanding of web operations.

Many techniques have been used in the network data traffic analysis. The neural network (NN), likewise known as the ANN, has been applied for prediction, as easily as to identify the presence of anomalies [1 -3]. Pattern recognition has been utilized for traffic data classification [4, 5], and chaos theory has been employed for the correlation and the prediction of time series data, and to identify the nonlinear dynamical behaviour of real-time traffic data [6, 7].

Applied back-propagation algorithm and feed-forward neural net models (FNNs) parameterized for nonlinear time series [8]. ANN forecasting has been compared with an autoregressive integrated moving average with exogenous variables (ARIMAX) model to predict the future [9], this mainly limited use in ANN for capturing the first-order non-stationarity in a time series data. Recurrent neural networks, recurrent neural networks (RNN) model has been evaluating the performance to identify and forecast in order to discover the presence of anomalies [10].

Different forecasting models were able to capture different aspects of the data available for prediction. Bates and Granger showed that a linear combination of forecasts would give a smaller error variance than any of the individual methods [11]. The basic idea of the model combination in forecasting is to use each models unique feature to capture different patterns in the data. With the ensemble model, the problem of model selection can be eased with little additional exertion. In summation, the ensemble method is potential to produce stable forecasts and less potential to make catastrophic predictions than any single network used in isolation [12]. Combining several models to improve the forecasting accuracy has been extensively analysed in the traditional forecasting literature. The question is how to combine these different forecasts into a single forecast, which is assumed a more accurate forecast. A simple approach to combining network outputs is to simply average them together. The NNE provides a prediction based on the norm of the MLPNN, RNN and RBFNN outputs [13]. A model based on the simple

average of neural networks, Gaussian process regression, and linear models for the NN5 time series forecasting competition [14].

Recently, several mathematical programming approaches have been proposed to determine the weights in combined forecasts. Several types of objective concerning accuracy to be used in forecast combinations [15] and considered to minimize mean absolute percentage error and the maximum absolute percentage error independently [16]. However, most previous focus on minimizing squared errors or absolute errors, they should be considered at the same time. An ensemble-forecasting model integrating ARIMA with ANN based on combined objectives, the combined objectives are composed of sum squares errors (SSE) and MAXAE, the MAXAE achieved by an ensemble model based on minimizing SSE, and then 0.618 criteria are used in deciding the weight of two objectives. This method is examined by using the data of Canadian Lynx data series. The empirical results show that the prediction using the proposed ensemble model is generally safer than other examples introduced in this field in terms of the same evaluation measurements.

2. Methodology

Data capture: In order to capture the data, we needed permission to access the LSBU network. This was easily acquired, as the researcher was working as a senior network engineer on the infrastructure team.

Once access was acquired, it was time to capture traffic data on the network. There are many tools available to capture network traffic. At the bottom end of the market, there are tools such as Wireshark and network analyser; in the mid-range, there is the SolarWinds network-monitoring tool; and at the upper end of the market, we have For this study, LSBU network traffic raw data were first captured using the Paessler Router Traffic Grapher (PRTG) network monitoring tool, which has been selected for this study.

The PRTG network-monitoring tool is equipped with SNMP, sFlow and port utilisation in order to provide the necessary data that is then used to analyse the network.

Many vendors use sFlow protocol to collect IP traffic information. Today, sFlow has become an industry standard for traffic monitoring. This protocol exports network flow data from routing devices. The sFlow analysis provides the results of network traffic from the two main links for LSBU for traffic modelling, traffic engineering, capacity planning and forecasting, and anomaly and attack detection. This analysis allows us to find approximate average traffic on both core switches and their main link to the outside world. Other studies have been carried out

investigating SNMP statistics and the methodology for network bandwidth expansion. The methodology investigates trends and changes that have an effect on providing good IP backbone prediction and upgrades to the backbone infrastructure.

In this research, we studied the traffic of the LSBU network to see the efficiency of the entire infrastructure and to identify and manage the traffic both inbound and outbound at the gateway.

Data analysis tools: The process of inspecting, cleaning, transforming, and modelling data with the goal to discover useful information is data analysis. Network traffic analysis is primarily done to get in-depth insight into what type of traffic/network packets or data is flowing through a network. Typically, network traffic analysis is done through a network monitoring or network bandwidth monitoring software/application. In our case, monitoring download/upload speeds, throughput, content, etc. to understand network operations.

The PRTG tool provides some functionality in order to analyse network traffic

Model design and code: The program used the latest technique for analyzing and predicting the future trends on LSBU's network data, based on nonlinear autoregressive exogenous model (NARX) based on Levenberg-Marquardt backpropagation algorithm to solve an autoregression problem with external input with NARX neural network is proposed in [17]. NARX predict time series $y(t)$ given p past values of series y and another external series $x(t)$.

The following NARX equation shows the time series prediction behavior

$$y(t) = h(x(t-1), x(t-2), ..., x(t-k), y(t-1), y(t-2), ..., y(t-p)) + \in (t) \quad (1)$$

The program will normalise the attributes to reach the target accuracy by dividing the entries into 90-10 percent ratio for training and testing also training parameters such as training function, learning rate etc. Then generate the date for ahead number of days for which predicting the output by using the previously trained neural network with the ahead number of days for 24 hours.

The results of the analysis will provide the accuracy of the prediction techniques with less computation. Also, plot the predicted data usage in its current and future states, as well as visualise the hourly, daily, weekly, monthly, and quarterly activities.

Figure 1 describes each processing step in the program for the proposed admission control algorithms. Moreover, there are different scenarios with different steps in this project, which are related to the simulation. The simulation's approach includes the simulation methodology, which demonstrates the simulation design including different algorithms.
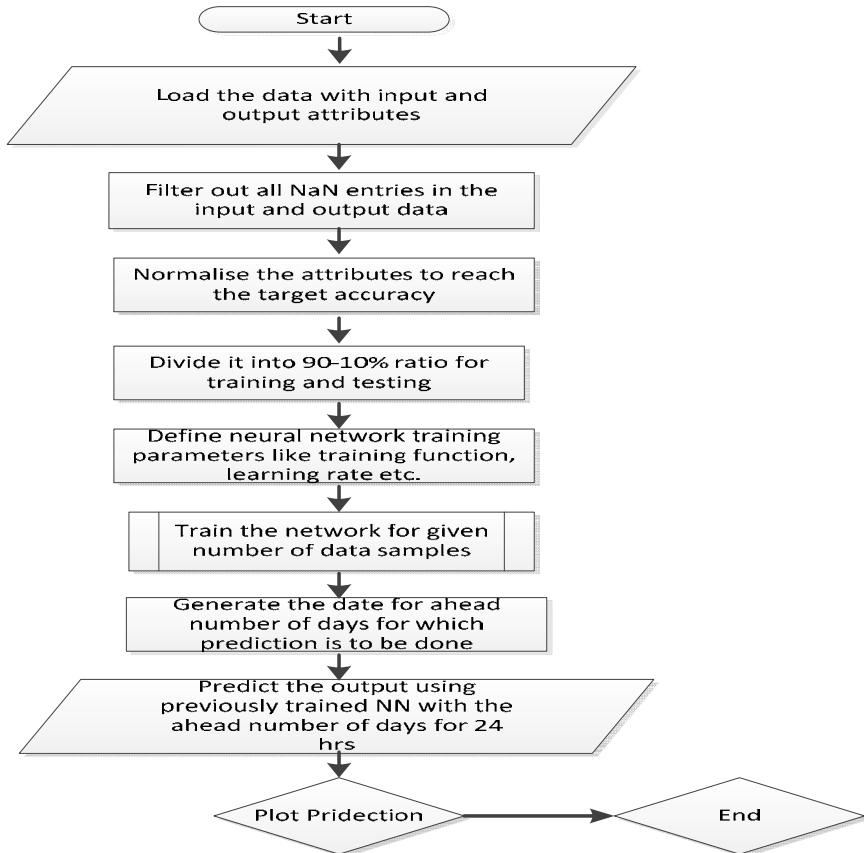
Figure 1: Flowchart of MATLAB code.

3. Analysis Results

In this study, we have recorded over two years of WWW (World Wide Web) traffic data from the 1st of January 2016 to the 1st of February 2018. Within this data, exactly two years of data, from the 1st of January 2016 to the 1st of January 2018, has been selected for training and testing the neural networks. We will predict the network traffic for the period between the 1st of January 2018 to the 1st of February 2018. The predicted traffic will be then compared with the real traffic during this period. Figure 1 shows the two year total WWW traffic data, from the 1st of January 2016 to the 1st of January 2018. The data was recorded at a rate of once per hour. Figure 2 shows the randomly selected 70% of the total WWW traffic data, used for training the neural networks. Figure 3 shows the randomly

selected 30% of the total WWW traffic data, used for testing the neural networks. This 30% includes a 15% validation ratio and another 15% testing ratio.
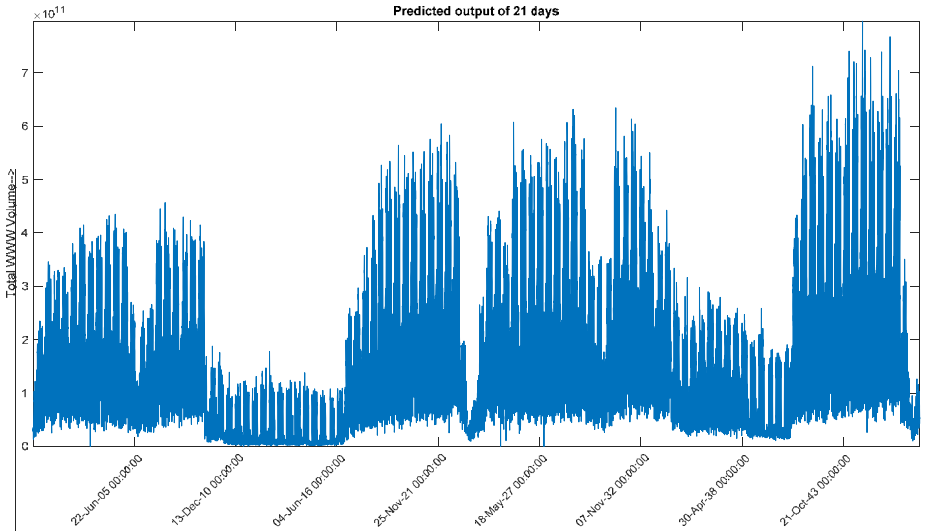

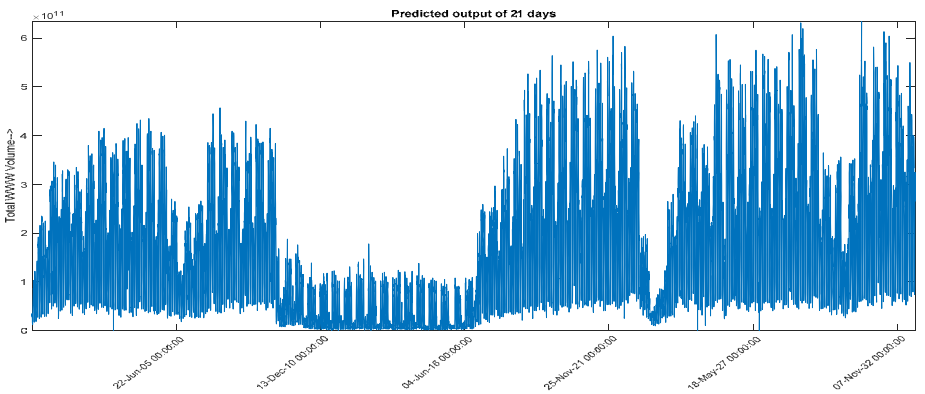Figure 2: Total WWW traffic from 1st Jan 2016 to 1st Jan 2018.

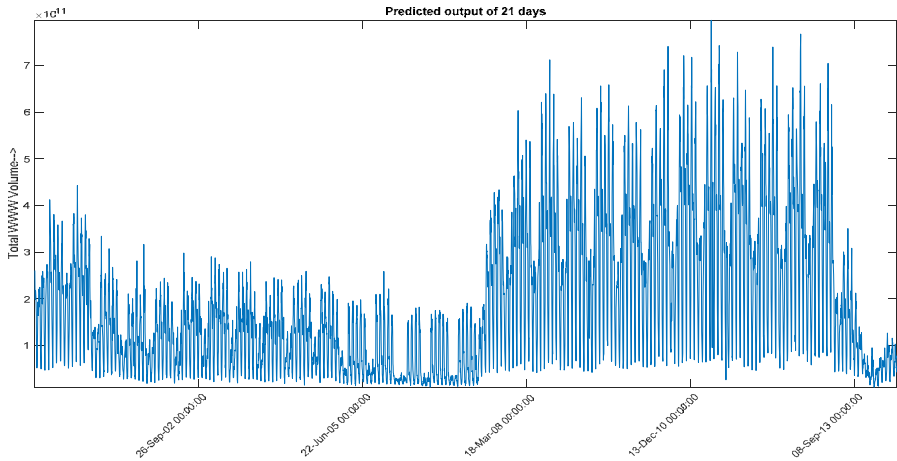Figure 3: 70% of the total WWW traffic used for training.
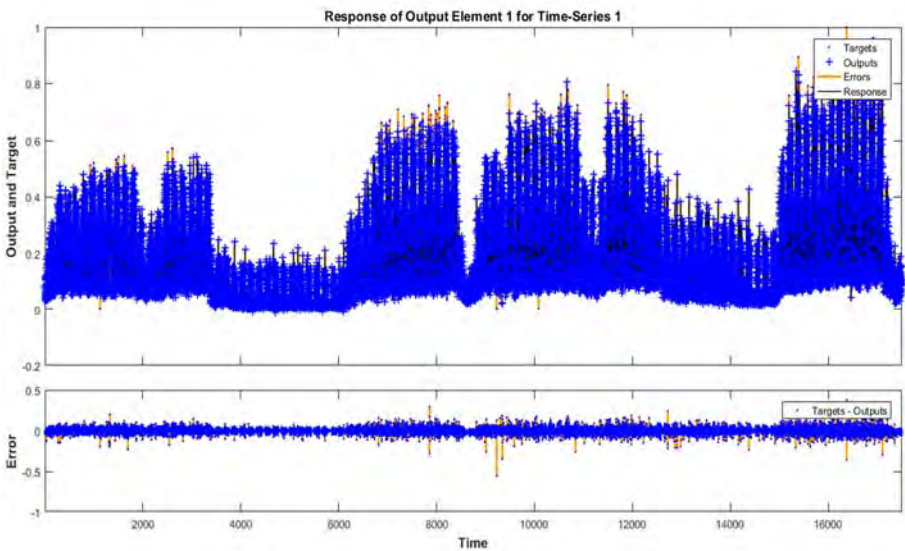
Figure 4: 30% of the total WWW traffic used for testing.

Figure 5: Add the time series response plot, something similar to above.

Figure 5 shows the one week predicted WWW traffic from 1st Jan 2018 to 8th Jan 2018. The predicted traffic data can clearly show the day and night effect over the week. Figure 6 & 8 shows the regression plot of one week predicted traffic data,

which can prove the accuracy of the model by showing how close the output is to the actual values.
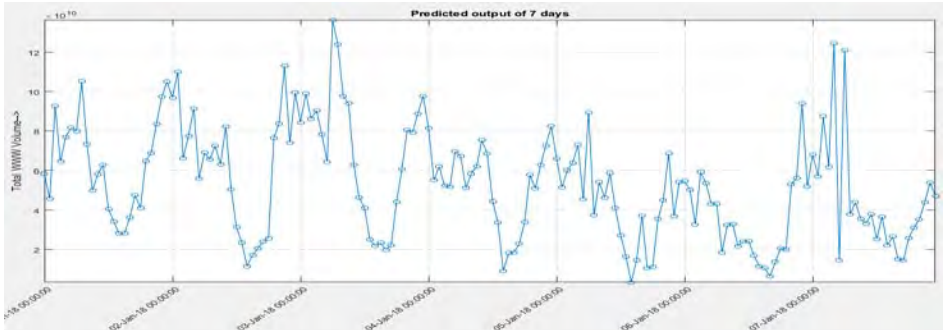

Figure 6: One-week predicted WWW traffic from 1st Jan 2018 to 8th Jan 2018.
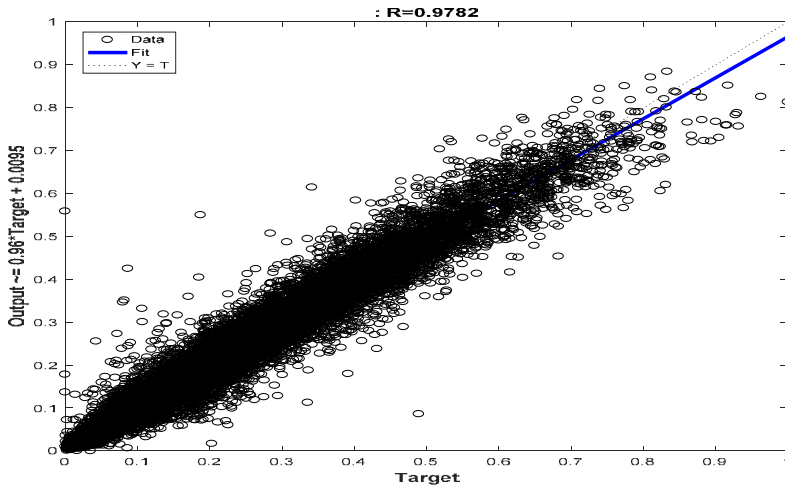

Figure 7: Regression plot of one week.

Figure 7 shows the four weeks predicted WWW traffic from 1st Jan 2018 to 29th Jan 2018. The predicted traffic data shows that in the first week, total traffic is relative low, this is likely due to the fact that university is still within the three weeks Christmas and New Year break. In the second week, traffic starts to pick, as the university re-open again. In the third and fourth week, the traffic reaches maximum, which not only show the day and night effect, but also the weekday and weekend effect.
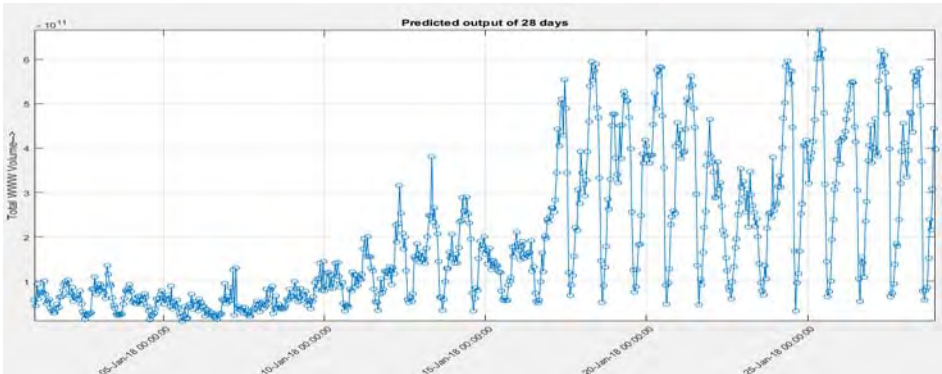
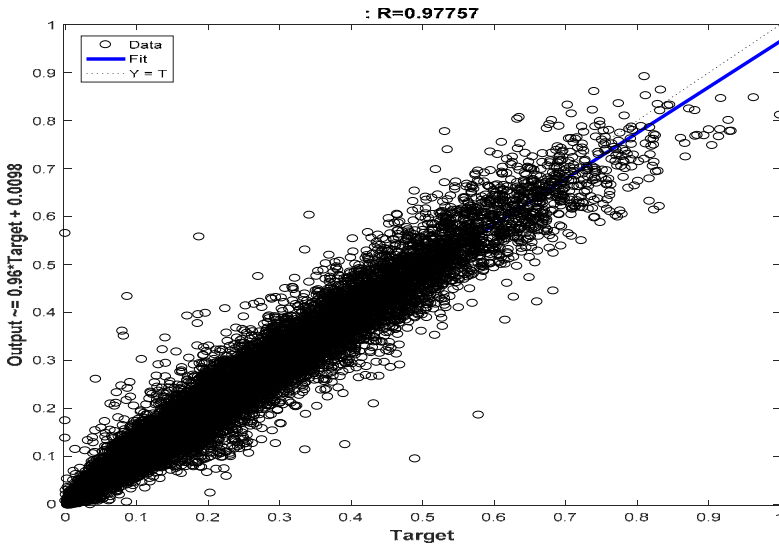Figure 8: Four weeks predicted WWW traffic from 1st Jan 2018 – 29th Jan 2018.

Figure 9: Regression plot of four weeks

4. Conclusion

We have developed a nonlinear autoregressive exogenous neural network model (NARX) based on Levenberg-Marquardt backpropagation algorithm for time series network traffic analysis. This study has implemented the methodology by developing a neural network model to predict the future trends of the LSBU bandwidth data traffic. It helped reasonably predict what traffic could be similar, given anomalies and outcomes. It has also proven that applying NARX neural

network can identify fundamental network usage and provide more accuracy on the prediction.

Furthermore, the prediction allowed us to focus on specific time in order to analyse the actual readings taken from the PRTG tool. This will allow us to predict user-driven network usage much more accurately in the future, as an efficient and effective way for decision-making process. The result shows that NARX neural network is a good method for predicting time series data.

References

1. Zhang, J., Song, C., Hu, Y., Yu, B., 2012. Improving robustness of robotic grasping by fusing multi-sensor. IEEE International Conference on Multisensor Fusion and Integration for Intelligent Systems, pp.126–131.
2. Pablo, B.J. et al., 2016. Artificial Neural Network and Monte Carlo Simulation in a hybrid method for time series forecasting with generation of L-scenarios. (1), pp.665–670.
3. Guo, T., Xu, Z., Yao, X., Chen, X., Aberer, K., and Funaya, K., 2016. Robust Online Time Series Prediction with Recurrent Neural Networks. 2016 IEEE International Conference on Data Science and Advanced Analytics (DSAA), pp.816–825. Available at: http://ieeexplore.ieee.org/ document/7796970/.
4. Rocha, E., Salvador, P. and Nogueira, A., 2011. A real-time traffic classification approach. 2011 International Conference for Internet Technology and Secured Transactions (ICITST), (December), 620–626.
5. Han, L., Huang, L., Hu, Q., Han, X., Shi, J., 2012. Fast fourier transform based IP traffic classification system for SIPTO at H(e)NB. 7th International Conference on Communications and Networking in China, pp.430–435. Available at: http://ieeexplore.ieee.org/lpdocs/epic03/wrapper.htm?arnumber=6417521.
6. Shang, P., Li, X., Kamae, S., 2005. Chaotic analysis of traffic time series, 25, 121–128. http://doi.org/10.1016/j.chaos.2004.09.104
7. Feng, H., Shu, Y. and Yang, O.W.W., 2009. Nonlinear analysis of wireless LAN traffic. Nonlinear Analysis: Real World Applications, 10(2), pp.1021–1028. Available at: http://www.sciencedirect.com/science/article/pii/S1468121807002386.
8. Zhang, J. et al., 2012. Improving robustness of robotic grasping by fusing multi sensor. IEEE International Conference on Multisensor Fusion and Integration for Intelligent Systems, pp.126–131.
9. Pablo, B.J. et al., 2016. Artificial Neural Network and Monte Carlo Simulation in a hybrid method for time series forecasting with generation of L-scenarios. (1), pp.665–670.
10. Guo, T. et al., 2016. Robust Online Time Series Prediction with Recurrent Neural Networks. 2016 IEEE International Conference on Data Science and Advanced Analytics(DSAA),pp.816–825.Availableat: http://ieeexplore.ieee.org/ document/7796970/.
11. J. M. Bates,and C. W. J. Granger, "The Combination of Forecasts," Operations Research Quarterly, vol. 20, no. 4, pp. 45l-468,1969.

12. G. P. Zhang and V. L. Berardi, "Time series forecasting with neural network nsembles: an application for exchange rate prediction," Journal of the Operational Research Society, vol. 52, pp. 652-664, 2001.
13. A. Chaouachi, R. M. Kamel, R. Ichikawa, H. Hayashi, and K. Nagasaka, "Neural Network Ensemble-based Solar Power Generation Short-Term Forecasting. International," Journal of Information and Mathematical Sciences, vol. 5, no. 4, pp. 332-337, 2009.
14. R. R. Andrawis, A. F. Atiya, H. El-Shishiny, "Forecast Combinations of Comptioal Intelligence and Linear Models for the NN5 Time Series Forecasting competition. International Journal of Forecasting," International Journal of Forecasting, vol. 27, no. 3, pp.672-688,2011.1883–1887, 2002.
15. G. R. Reeves, K. D. Lawrence, "Combining forecasts given different types of objectives," European Journal of Operational Research, vol. 51, pp.65-72,1991.
16. K. F. Lam,H. W. Mui, H. K. Yuen, "A note on minimizing absolute percentage error in combined forecasts," Computers & Operations Research, vol. 28, pp.1141-1147,2001.

SECTION 6

CLEANING AND INSPECTION ROBOTS

Prospects and possibilities of using thermomechanical microrobots for solving technological tasks in space

N. N. Bolotnik*, V. G. Chashchukhin V. G. Gradetsky, D.V. Kozlov, I.P. Smirnov and
A.A. Zhukov

*Institute for Problems in Mechanics of the Russian Academy of Sciences
Moscow, Russia*
* E-mail: bolotnik@ipmnet.ru
www.ipmnet.ru

The possibilities of microrobots for inspection and technological operations on spacecraft board and in open space are analyzed. Utilization of such robots for operations on outer hulls of spacecraft and on internal units and aggregates is discussed.

Keywords: microrobot, space, spacecraft, utilization.

1. Introduction

Research and development of mini- and microrobots designed for operations in space are performed in industrially developed countries, mainly in Japan, USA, Germany, France, and Russia [1–5]. Among the prospective applications of microrobots in space are inspection and monitoring operations. To be able to perform such operations the robots should be equipped with appropriate sensors. The action of the microrobots can be based on various physical principles. Depending on the types of actuators, the robots can be classified into electromagnetic, piezoelectric, electroadhesive, thermomechanical, pneumatic, electromechanical, etc. robots [2,4]. We suggest an analysis of application areas of space microrobots that takes into account the requirements of inspection and fault detection systems for spacecraft on-board equipment [5,6]. The inspection crawling microrobot with a miniature optical sensor for detecting cracks on the spacecraft body (Fig.1) produced by Company SRI International [1] provides an example of a prospective robotic system for using in space.
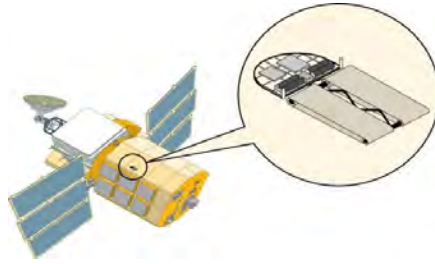
Fig. 1. Inspection crawling microrobot with a sensor for detection of cracks on the spacecraft body [1]

2. Specific design features of inspection microrobots

The microrobots must satisfy all requirements related to resistance of the robots to the influence of the external factors of space; the respective factors are discussed, e.g., in [6–10]. These requirements, in particular, are met by thermomechanical microrobots [11,12]. A justification for using such robots in space is given in the next section. Depending on the tasks to be performed, microrobots can be used separately or they can be combined into chains. The table below illustrates the correspondence between the structure of the robotic system and the tasks to be implemented.

| Type of the system	Motion in narrow holes, slots, and space between cables
Separate walking microrobots	Motion in narrow holes, slots, and space between cables
Chains of microrobots connected by flexible couplers (snake-like robots)	Motion in gaps
Chains of crawling microrobots	Inspection of inner surfaces of pipes
Chains of walking microrobots	Inspection of spacecraft outer surfaces

To be able to form chains, separate walking microrobots should have flexible coupling devices on their end faces. In addition, the microrobots should be autonomous and have an on-board power supply.

3. Justification of using a thermomechanical microrobot for operations in space

We have developed a microrobotic walking platform shown in Fig. 2 (a,b). This platform could be a prototype for developing advanced autonomous microrobotic devices for inspection of hard-to-access areas on the surface and in internal compartments of spacecraft. In addition, this platform can be used for positioning various microdevices inside spacecraft [11, 12]. A unique technology for manufacturing the microrobotic platform has been developed in Russia [5]. The walking motion of the microrobot is performed due to controlled deformation of its legs. The leg unbends when is heating and bends when is cooling. Having a mass of 70 mg, the platform can keep a load that is 20 times as large as its proper mass and move a load that 5 times exceeds the mass of the platform. The velocity of the platform with such a load is about 14 mm/min, which is rather high for mobile devices of such a type and size. For its motion the microrobot engages at least 8 legs covered with a special adhesive material, which enables the microrobot to adhere to the surface of motion in weightlessness. In a more complex design, an array of smaller legs is formed on the foot of each leg. The platform is manufactured as an integral microelectronic unit from silicon and polyimide. On one silicon plate (Fig. 2 (b)), several microrobotrs can be manufactured simultaneously by means of photolithography, sputtering, and anisotropic etching. The microrobot described is designed for operations both inside and outside of a spacecraft. The robot can operate within a temperature range of -200 to +200 C, in the presence or absence of an atmosphere, and at low gravity. The device should also be resistant to the influence of atomic oxygen. A prototype of the walking platform of a microrobot with thermomechanical actuators [12] is shown in Fig. 3.

4. Possible applications of microrobots for inspection of spacecraft in space

Currently, microrobots have not found broad applications for solving various tasks on board of spacecraft, in open space or on the surfaces of other planets. This can be accounted for by both the difficulties in the creation of microrobots for solving tasks in space and the lack of justification for using such robots in space flights. Analysis of feasible applications of space microrobots suggests the following areas for them: inspection and fault detection in internal compartments of spacecraft; inspection and fault detection on outer units and surfaces of spacecraft and other structures in open space;
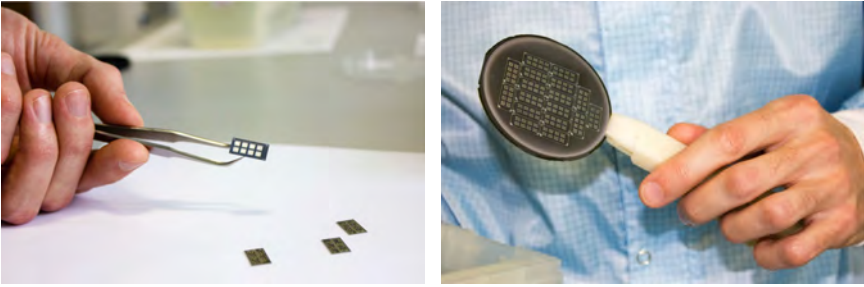
(a)   (b)

Fig. 2. (a)A microchip for a bimorph thermomechanical microrobot. (b) A silicon plate for fabricating several microrobots.
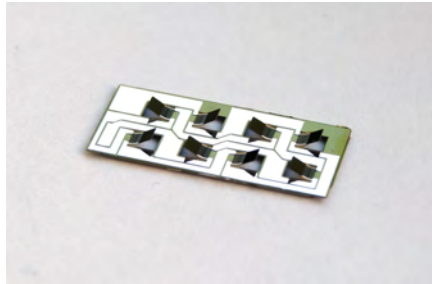

Fig. 3. A prototype of the thermomechanical walking platform [12]

operations on the surfaces of celestial bodies, including planets and large asteroids. As an example of an outer element of the structure we can consider the body of a spacecraft. The main compartments and units of a spacecraft are shown in Fig. 4. The figures indicate the areas of possible applications of microrobots. The units located in these areas are most responsible for the spacecraft and must have elevated reliability and provide a quick access for an inspection microrobot equipped with appropriate microsensors.

These areas, in particular, involve:

- Docking unit and its components (1); this unit can be inspected by a microrobot with an optical sensor.;
- Outer surface of the body of the spacecraft (2); a microrobot can be used for nondestructive inspection of the surface for detecting cracks and other damages.;
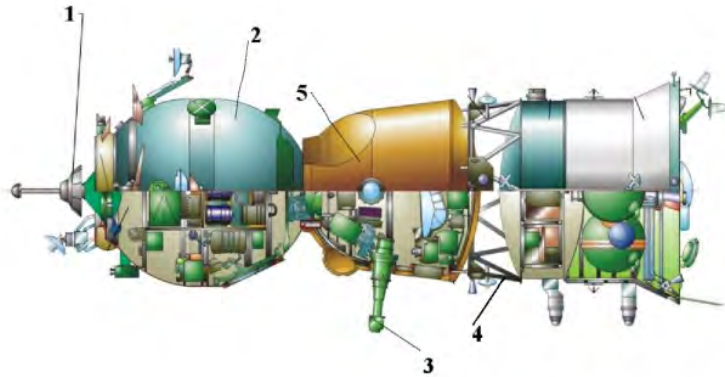
Fig. 4. Areas of possible applications of inspection microrobots on external units of a spacecraft [13]

- Optical viewfinders and other sensors of external information (3).;
- Outer components of the transfer compartment (4);
- Docking unit of the descent module (5).

5. Utilization of microrobots in internal compartments of spacecraft

The interior of spacecraft involves a number of structural components the inspection of which can be performed by mobile microrobots:

- ducts for laying electric cables;
- bundles of various cables;
- pipelines;
- corner compartments;
- distribution boxes;
- slits and gaps in the structure.

Operations that can be performed by microrobots involve:

- inspection of the space between cables;
- inspection of the technical state of internal compartments;
- transmission of visual information about dirt, dust, mildew, etc.;
- transmission of visual information about possible places that require a repair, about technical state of the distribution boxes,

pipelines, cable bundles, etc.;
- cleaning;
- penetration into the slits in the inner lining;

In addition, microrobots can be used for fault detection on surfaces and coverings, as well as for inspection of solar panels.

Acknowledgments

References

1. https://www.nasa.gov/pdf/626527main_3B-5_Pelrine.pdf.
2. W. Driesen, *Concept, Modeling and Experimental Characterization of the Modulated Friction Inertial Drive (MFID). Locomotion Principle: Application to Mobile Microrobots*, Computing Science Technical Report 4108, École polytechnique fédérale de Lausanne (CE 3 316 (Centre Est), Station 1, CH-1015 Lausanne, 2008).
3. P. Kladitis and V. Bright, *Sensors and Actuators* **80**, 132 (2000).
4. R. D'Souza, S. Sharma, A. Pereira and A. Hashimi, *AJER* **5**, 32 (2016).
5. I. Smirnov, D. Kozlov, A. Zhukov, V. Chashchukhin, V. Gradetsky and N. Bolotnik, Microsystem space inspector robot (versions)(October 2015), RU Patent 2566454.
6. M. Panasyuk and L. Novikova (eds.), *Space Model: Physical Conditions in Space* (KDU, Moscow, 2007).
7. M. Panasyuk and L. Novikova (eds.), *Space Model: The Influence of the Space Environment on Materials and Equipment of Spacecraft* (KDU, Moscow, 2007).
8. http://www.gctc.ru/main.php?id=940.
9. A. Baranovsky and A. Privalov, *Journal of Instrument Engineering* **52**, 51 (2009).
10. https://en.wikipedia.org/wiki/Outer_space.
11. N. Bolotnik, V. Gradetsky, A. Zhukov, D. Kozlov, I. Smirnov and V. Chashchukhin, Mobile microrobotics for space exploration: the state-of-the-art and prospects, in *Advances in Cooperative Robotics. Proc. of the 19th Int. Conf. of Climbing and Walking Robots*, (London, UK, 2016).
12. N. Bolotnik, V. Chashchukhin, V. Gradetsky, D. Kozlov, I. Smirnov, A. Sukhanov and A. Zhukov, Design of mobile microrobots with thermomechanical actuators, in *Proceed. 12th Intern. Conf. on Informatics in Control, Automation and Robotics (ICINCO-2015)*, (Colmar, France, 2015).
13. https://www.energia.ru/en/iss/soyuz-tma-m/soyuz-tma-m.html.

DEVELOPMENT OF A PERISTALTIC CRAWLING MOTION TYPE DUCT CLEANING ROBOT COMPATIBLE WITH CLEANING EFFICIENCY AND RUNNING SPEED BY CLEANING JOINT

T. KAWAGUCHI *, Y. TANISE, M. KAMATA, Y. YAMADA, AND T. NAKAMURA

Faculty of Science and Engineering, Chuo University,
1-13-27 Kasuga, Bunkyo-Word, Tokyo 112-8551, Japan
*E-mail: t_kawaguchi@bio.mech.chuo-u.ac.jp

Air conditioning equipment using duct piping is used to ventilate residences. If this residential ducting is used in a dirty environment, it will lead to adverse effects on human health. Therefore, a method to clean the ducts is required. However, with existing duct cleaning tools, it is difficult to clean the duct perfectly. Therefore, a duct cleaning robot is required. In previous research, we focused on a peristaltic crawling motion type robot, and developed a type of drive brush mounting. Cleaning and driving experiments confirmed a cleaning efficiency of 97.2%; however, the speed fell below the target value of 4.6 mm/s. In this paper, we propose a cleaning joint that strives for both cleaning efficiency and driving speed. We aim to realize an optimal duct cleaning robot by comparing the drive brush mounting types with a robot equipped with the proposed method.

Keywords: Duct cleaning, Peristaltic crawling motion, In-pipe inspection robot.

1. Introduction

Air conditioning equipment that uses ducting plays a key role in keeping the indoor air of various types of buildings clean. However, if dust in the duct is sent inside the building, together with the ventilation air, it causes a decrease in cleanliness and leads to health damage, such as sick house syndrome [1]. Therefore, duct cleaning is necessary.

The outline of the conventional cleaning method is shown in Fig. 1. The duct of a large building, such as a factory, has a large cross sectional area and has few curved parts, so cleaning in this way is relatively easy. cleaning agency use a propeller-attached brush and an Air lance (Nihon Winton, Tokyo, Japan), on a pneumatically driven cleaning device, as a cleaning tool for large building ducts [2]. A pneumatically driven cleaning tool has a cleaning portion at the tip of an air tube. This is pushed into the duct, and a cleaning portion at the tip removes the dust, by applying air pressure. On the other hand, the ducts in domestic housing, which are generally 75 mm inside diameter, have a relatively small duct diameter

and many curved parts. In a housing duct, even if the cleaning tool is pushed inside, it cannot move deeply into the duct due to the friction at curved portions of the ducting. Hence, it is difficult to clean the housing duct completely. Therefore, the development of a duct cleaning robot capable of cleaning housing ducts is required. There are three requirements for a duct cleaning robot: being able to move while negotiating a number of curved parts in the duct, be capable of rapid cleaning, and to remove the dust from the duct. Existing in-pipe traveling robots include snake types, wheel types, cilia vibration types, and peristaltic crawling motion types. However, each of these has problems. Since the snake type robot meanders, it requires a large driving space. The wheel type of robot is difficult to miniaturize, because it is equipped with a motor. the cilia vibration type robot is unable to drive in reverse [3]-[7]. On the other hand, the peristaltic crawling movement type is a movement method that propagates through the expansion and contraction of the body segment in the axial direction, imitating the peristaltic crawling motion of the earthworm. Because of this, it is possible to drive with stability in a thin tube. Existing peristaltic crawling motion robots have been used as inspection devices for both sewer pipes, and gas pipes. They have a high traction force, and can break through right angle pipes [8][9]. The peristaltic crawling motion type of robot can be expected to satisfy the driving performance required, for a duct cleaning robot.

The authors considered a peristaltic crawling motion type duct cleaning robot, and devised a cleaning unit and a cleaning joint. In the previous study, we developed a type of drive brush mounting (type-A) with cleaning unit, and confirmed it had a cleaning efficiency of 97.2 %, and a speed of 4.3 mm/s, in a cleaning experiment using simulated dust [10]. However, we have not yet investigated the cleaning efficiency and speed performance of a robot equipped with a cleaning joint which is the other cleaning tool. Therefore, in this paper, we discuss the development of a robot equipped with a cleaning joint, and investigate the cleaning efficiency and driving speed. Based on the experimental results, we attempted to balance the cleaning efficiency and driving speed of the peristaltic crawling motion type duct cleaning robot.
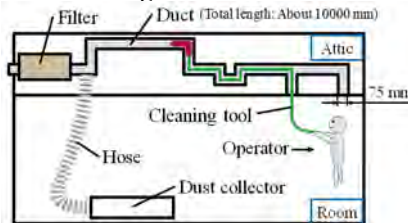

Fig. 1 Existing cleaning method

2. Duct cleaning and the need for a duct cleaning robot

We explain the procedure of cleaning a duct in a house. Firstly, ventilation is stopped in the whole house. Next, the operator takes one end of the duct installed

in the attic, inserts a cleaning tool, and peels off dust adhering to the inside of the duct (Fig. 2). Finally, the operator applies suction to the peeling dust, using a dust collector attached to the other end. The time needed to clean the ducting in a house is about six hours. The duct used in houses (Fig. 3) has an inner diameter of 75 mm, a radius of curvature of 1000 mm, and a length of about 10 m. One house would require between 8–10 m of ducting. This ducting easily bends and stretches, and has many curved parts.

The requirements for a duct cleaning robot are as follows. The first is driving performance: it is necessary to be able to insert the robot into the duct and it must adapt to many bends. The second is speed performance: in order to clean 10 ducts within 6 hours, the target speed is 4.6 mm/s. The third is cleaning performance: it is necessary to be able to peel the dust from the inner wall of the duct, and to make it possible to use suction to remove it with the dust collector.

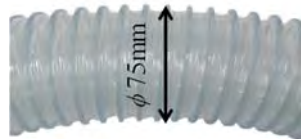Fig. 2 Dust adhered in the duct   Fig. 3 Appearance of duct

3. Peristaltic crawling motion type duct cleaning robot

In this chapter, we discuss the movement and cleaning methods that satisfy the requirements described in Chapter 2.

First, we describe the movement methods. Existing in-pipe driving robots cannot be used as a cleaning robot, because they are difficult to make small enough, and do not operate in reverse. Therefore, we focused on a peristaltic crawling motion type robot, which is excellent in traction, and can be miniaturized.

The peristaltic-crawling-motion-type-robot consists of a driving unit responsible for movement, and a joint connecting the constituent parts. The driving unit uses a straight-fiber-type artificial muscle. This artificial muscle is a structure in which natural rubber, containing carbon fibers arranged in a single direction, is molded into a tube shape. Therefore, the expansion of the driving unit in the axial direction is restricted. Hence, when air pressure is applied, it expands in the radial direction and contracts in the axial direction, as shown in Fig. 5 (b). By propagating this movement from the head to the back, it moves as shown in Fig. 6. In a previous study, a peristaltic crawling robot with the same diameter as the duct (type-N) confirmed that it had a running speed of 9.8 mm/s [10]. This performance satisfies the requirements of the driving speed, which is 4.6 mm/s.

Next, we describe the cleaning method. Candidates for the cleaning methods are two existing cleaning tools: the Air lance, and a brush. The Air lance is a cleaning tool for large-sized ducts, and cannot clean inside a narrow duct. When

a brush is used, it can be classified into three different types of robots: drive brush mounting type (type-A), top brush mounting type (type-B), and joint brush mounting type (type-C), as shown in Fig. 4.

Type-A is a robot equipped with a cleaning unit comprising a type-N driving unit wrapped around a brush. Type-A robots move while pressing the brush against the inner wall of the duct, ensuring it can be cleaned reliably.

Type-B is a robot with a cleaning joint comprising a type-N joint wrapped around a brush. Type-B robots peel off the dust by pushing out the brush while simultaneously advancing through the duct. However, the speed decreases due to the friction between the brush and the inner wall of the duct.

Type-C is a robot with a cleaning joint on the top, between the driving units. Cleaning can be performed reliably by increasing the number of cleaning points. However, since the friction between the brush and the inner wall of the duct also increases, it is predicted that the speed reduction is larger than type-B.

In the previous study, a type-A robot was examined. The type-A robot was confirmed to have a cleaning efficiency of 97.2 %, and a speed of 4.3 mm/s. Although the cleaning performance was sufficient, the speed fell below the target speed of 4.6 mm/s. That is, the type-A robot is inappropriate as a cleaning tool. Therefore, after considering the cleaning joint, we compared robots of types A, B and C.
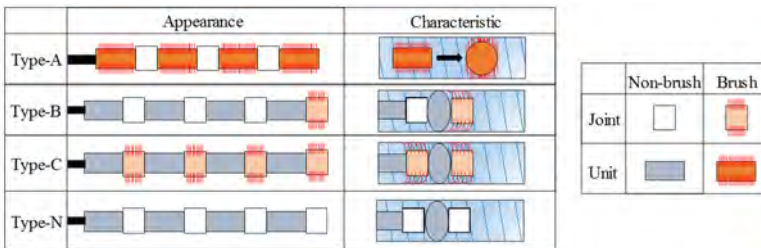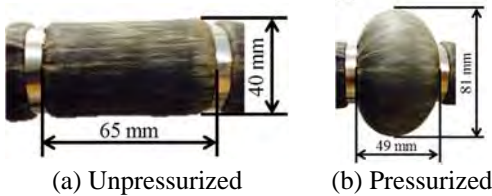

Fig. 4 Types of robot structure

(a) Unpressurized   (b) Pressurized
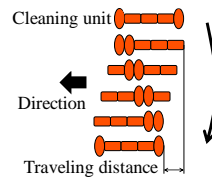
Fig. 5 Appearance of a driving unit

Fig. 6 Operation progress of the air duct cleaning robot

4. Drive brush mounting type (type-A) robot

Figure 7 and Fig. 8 show the drive brush mounting type robot (type-A) and cleaning unit, developed in the previous research. Type-A is a robot with a brush seat wound around the driving unit of a peristaltic crawling motion type robot,

without a cleaning function (type-N). When air pressure is applied to the type-A robot, the brush is pressed against the inner wall of the duct due to expansion of the driving unit in the radial direction, thereby removing the dust. The brush uses nylon bristles, with a hair length of 11 mm. A cleaning efficiency 97.2 %, and speed 4.3 mm/s were confirmed by a cleaning experiment.
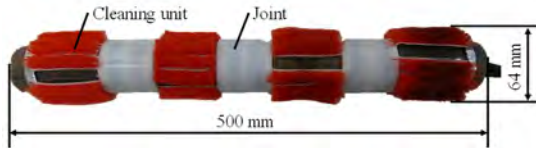
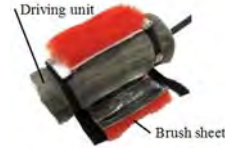Fig. 7 Appearance of the drive brush mounting type (type-A)

Fig. 8 Appearance of the cleaning unit

5. The peristaltic motion type duct cleaning robot using a cleaning joint

In Chapter 5, we propose a cleaning joint as a cleaning method, which works by attaching brushes to places other than the driving unit. Further, we considered the optimum shape of the brush.

5.1. *Cleaning unit*

The cleaning joint shown in Fig. 9 has a structure in which a sheet of nylon brush material (Fig. 10), is wrapped around the joint of the duct cleaning robot (type-N). The cleaning joints can be mounted at both ends of the type-N robot, or between the driving units. Since it drives while also rubbing the brush against the inner wall of the duct, it can be expected that the duct would be cleaned thoroughly.

Fig. 9 Appearance of the cleaning joint

Fig. 10 Appearance of the brush sheet

5.2. *Consideration of the cleaning joint*

We estimate that the diameter of the cleaning joint, and the area of the brush, will both affect the cleaning efficiency and speed of the robot. However, it is difficult to determine how the interaction of all the different design parameters can affect the performance of the robot. Therefore, we limited the range of parameters to be investigated to the diameter of the cleaning joint, and conducted an experiment where we considered the influence of the diameter of the cleaning joint on both cleaning efficiency and speed. We conducted experiments with two patterns of

top brush mounting type (type-B), and joint brush mounting type (type-C), as shown in Fig. 11. We investigated the optimum diameter for each type. Furthermore, by comparing the experiment results of type-B and type-C robots, with the experimental results of a drive brush mounting type (type-A) and peristaltic crawling motion type robot without cleaning function (type-N), we decided on a practical peristaltic crawling motion type duct cleaning robot. The diameter of the cleaning joint used in the experiment was equal to, greater than, and less than the inner diameter of the duct. Specifically, a cleaning joint with three outer diameters of 73 mm, 75 mm, and 77 mm were prototyped. They were each mounted in both a type-B and a type-C robot. Hereinafter, these are referred to as type: B-1, B-2, B-3, C-1, C-2 and C-3.
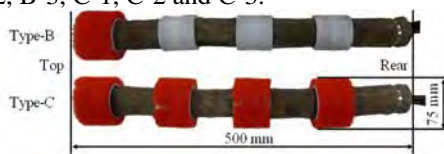
Fig. 11 Appearance of duct cleaning robots equipped with a cleaning joint.

6. Driving experiment of top brush mounting type (type-B) and joint brush mounting type (type-C) robots

In this chapter, we perform driving experiments with all six types of brush format mentioned in section 5.2. The robot was driven into the duct, then the time taken to travel through a 500 mm section was measured, from which the speed was calculated.

6.1. *Experimental environment of the driving experiment*

The experimental environment is shown in Fig. 12. The pressure applied to the driving unit was set to 0.1 MPa, and the contraction and extension time were set to 0.6 s.
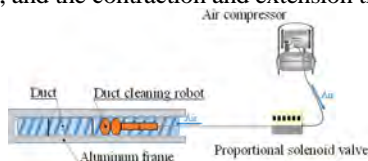
Fig. 12 Environment of the driving experiment

6.2. *Experimental results of the driving experiment*

The experimental results are shown in Fig. 13. We confirmed that all six robots of type B and type C exceeded the target speed of 4.6 mm/s. In addition, we confirmed that type B-1, B-2, and C-1 speeds were equivalent to a type-N speed. We considered that the type-C robot speed is lower than the type-B robot speed because the movement of the driving unit was hindered. The movement of the driving unit was hindered by the expansion and contraction of the duct, caused by the friction of the multiple brushes.
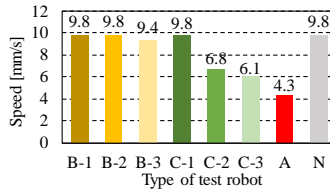
Fig. 13 Speed of robot

7. Cleaning experiment of top brush mounting type (type-B) and joint brush mounting type (type-C) robots

In this chapter, we perform cleaning experiments with all the six types mentioned in section 5.2. Evaluation of the cleaning experiment was conducted using the parameter of cleaning efficiency E (%). The cleaning efficiency (E) is shown in equation (1):

$$E = (1 - \frac{m}{M}) \times 100 \tag{1}$$

where m is the mass of the object to be cleaned (after cleaning), and M is the mass of the object to be cleaned (before cleaning).

7.1. *Experimental environment of the cleaning experiment*

The experimental environment is shown in Fig. 12. The object to be cleaned (50 g of silica sand) was fixed to the 500 mm section of the inner wall of the duct.

7.2. *Experimental results of the cleaning experiment*

The experimental results are shown in Fig. 14. It was confirmed that the cleaning efficiency increased as the diameter of the cleaning joint increased, and that the cleaning efficiency of type C-3 robot was higher than that of type A robot. The reason why the cleaning efficiency increases as the diameter of the cleaning joint increases, is because the friction increases between the brush of the cleaning joint and the inner wall of the duct. From the experimental results in Sections 6.2 and 7.2, it can be confirmed that type C-3 exceeds a type-A robot in both cleaning efficiency and speed. Therefore, we consider that the optimum cleaning tool for the duct cleaning robot is a cleaning joint, with a diameter of 77 mm.
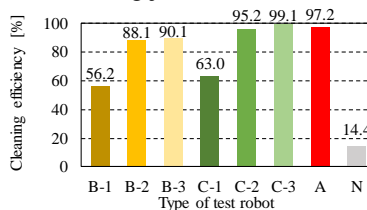

Fig. 14 Cleaning performance of the robot

8. Conclusion

A cleaning joint was proposed to achieve both the required cleaning efficiency and speed. In order to explore the optimum diameter of the cleaning joint, a trial production of three different diameter cleaning joints were made. The cleaning efficiency and speed of both a top brush mounting type (type-B), and joint brush mounting type (type-C) were measured, using three different diameters of cleaning joints. From the results, it was confirmed that the type-B robot, equipped with the 77 mm diameter cleaning joint, had a cleaning efficiency of 99.1%, and a speed of 6.1 mm/s. Therefore, we consider that a type-B robot equipped with a 77 mm diameter cleaning joint is best suited as a peristaltic crawling motion type duct cleaning robot.

References

1. B. Zhou, B. Zhao and Z. Ta, *How Particle Resuspension from Inner Surfaces of Ventilation Ducts Affects Indoor Air Quality – A Modeling Analysis*, Aerosol Science and Technology 45:8, 2011, pp. 996-1009
2. Osaka Winton Co., Ltd. Home Page. 16 Jan. 2017. Osaka Winton Co. Ltd. http://www.osaka-winton.co.jp/en/air_conditioning/
3. A. Kuwada, K. Tsujino, K. Suzumori, and T. Kanda, *Intelligent actuators realizing snake–like small robot for pipe inspection*, in Proc. International Symposium on Micro-nano Mechatronics and Human Science, 2006, pp.1–6
4. P. Li, S. Ma, B. Li, and Y. Wang, *Development of an adaptive mobile robot for in-pipe inspection task*, in Proc. ICMA International Conference on Mechatronics and Automation, 2007, pp. 3622–3627
5. S. W. Jeon, W. Jeong, D. Park, and S. Kwon, *Design of an Intelligent Duct Cleaning Robot with Force Compliant Brush*, in Proc. 12th International Conference on Control, Automation and Systems, 2012, pp. 2033-2037
6. A. H. Heidari, M. Mehrandezh, R. Paranjape, and H. Najjaran, *Dynamic analysis and human analogous control of a pipe crawling robot*, in Proc. International Conference on Intelligent Robots and Systems, 2009, pp. 733–740
7. M. Konyo, K. Hatazaki, K. Isaki, and S. Tadokoro, *Development of an Active Scopecamera Driven by Ciliary Vibration Mechanism*, in Proc. 12th Robot. Symposia, 2007, pp. 460–465
8. R. Ishikawa, T. Tomita, Y. Yamada, and T. Nakamura, *Development of a peristaltic crawling robot for long-distance complex line sewer pipe inspections*, 2013, pp. 413-418
9. M. Kamata, S. Yamazaki, Y. Tanise, Y. Yamada, and T. Nakamura, *Development of pneumatically driven peristaltic-type robot for long distance inspection in half-inch pipes*, Advanced Intelligent Mechatronics, 2017, pp. 309–314
10. Y. Tanise, K. Taniguchi, S. Yamazaki, M. Kamata, Y. Yamada, and T. Nakamura, *Development of an air duct cleaning robot for housing based on peristaltic crawling motion*, Advanced Intelligent Mechatronics, 2017, pp. 1267-1272

TOWARDS SAFE INSPECTION OF LONG WELD LINES ON SHIP HULLS USING AN AUTONOMOUS ROBOT [*]

GABRIELA GALLEGOS GARRIDO, TARIQ SATTAR, MICHAEL CORSAR[†]

London South Bank University, London South Bank Innovation Centre, Granta Park Great Abington, Cambridge CB21 6AL, UK.

RICHARD JAMES

InnotecUK, R&D department, Hildersham Road Cambridge, Cambridgeshire CB21 6DR, UK.

DJELLOUL SEGHIER

NDT Consultants LTD, R&D department, Siskin drive MiddleMarch House, Coventry CV3 4FJ, UK.

Inspection of ship-hull welds must be carried out in accordance with classification society guidelines during manufacture and when in service. Failure of ship-hull welds can result in the loss of a vessel, loss of life and pollution of the environment. Typically weld lines are inspected using ultrasound NDT techniques which are labour intensive, expensive and often hazardous to operators. To remain competitive shipbuilders and inspection companies need to reduce costs while maintaining or improving inspection quality. Automated inspection can achieve this, but current systems are complex, expensive and not suited to shipyard operation. AWI is a novel robotic autonomous system (RAS) that uses magnetic adhesion to climb ship hulls and autonomously track weld lines while performing ultrasonic scans of the welds. Communication of the inspection data is transmitted wirelessly to the inspector sited remotely. This addresses a key challenge in overcoming the payload limitations of current climbing robots. Therefore, AWI is equipped with rugged, fast and secure wireless communications, which robustly integrates with the robot hardware for industrial service [§].

H. Montes et al. (eds.), *CLAWAR 2018: 21st International Conference on Climbing and Walking Robots and the Support Technologies for Mobile Machines*,
Robotics Transforming the Future
© ELSEVIER

1. Introduction

1.1. *Objectives of the research*

All ship hull welds must be inspected prior to a vessel entering service and at periodic intervals during its service life as per guidelines issued by the classification societies [8]. Ultrasound based methods are widely accepted as standard means for non-destructive inspection of welds. For each ship hull many 100s of metres of weld may require inspection. Due to the nature of the hull and the ship yard environment inspections can be hazardous, often requiring rope access and scaffolding to reach the weld lines. Safety and productivity can be greatly enhanced throw automation of the hull inspection. Therefore, the present work outlines the development of a new climbing robot designed to carry out phased array ultrasound inspection on ship hulls.

1.2. *Outline of robot requirements*

AWI is a climbing robot, using magnetic adhesion, designed specifically to inspect weld lines. Its primary operating environment is the external hull of newly manufactured ships, focussing particularly on areas which are difficult to access by humans. The aim is to remove the requirement for inspection by rope access and scaffolding which will improve safety for the inspector and greatly reduce the cost of inspection.

In order to move the state of the art forward and to be attractive to industry the robot and inspection system must be able to autonomously follow weld lines while carrying out ultrasound inspection. When defects are identified they must be marked so that intervention can be carried out. The robot must travel at high speed between inspection areas but also be able to travel at a lower rate determined by the inspection system.

2. Industrial climbing robots

The design of a climbing robot for industrial applications depends on several factors influenced by its operating environment and the task it must carry out. Research activities on wall climbing robot has been carried out for several years now [1][3][4], but inspection of weld lines on large ship hulls remains a challenge. Payload capacity, mobility, adhesion safety and energy consumption are the primary factors influencing design choices [5]. For climbing on non-ferrous surfaces, systems tend to employ either energy intensive suction or dynamic vortex adhesion methods. For ferrous structures, the choice is permanent magnets

or electromagnetic adhesion. Electromagnets offer the ability to control the magnetic on command but require constant energy consumption to maintain their magnetic field [6]. To overcome payload limitations and power consumption problems, it was necessary to use permanent magnets mounted in the robot wheels. This will also prevent the robot from falling in the case of a power failure. The robot must be capable of climbing on both steeply sloped and vertical surfaces and be able to transition across different planes. Therefore, a force analysis has been carried out to ensure stability of the robot across all climbing modes to avoid sliding and roll-over failure. Figure 1 shows a free body diagram of the robot operating on a vertical plane, where the robot weight is **G**, the pitch between the centre of the front and rear wheels is **L**, and the centre of gravity from the climbing surface is **h.** The robot acceleration is **a,** and the coefficient of surface friction **μ** (wheels-surface). To avoid slipping, the total adhesion force **F_t**, must satisfy Equation (1):

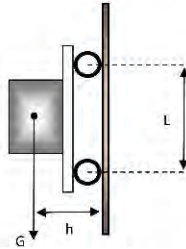$$F_t \geq \frac{(G + ma)}{\mu} \tag{1}$$

Figure 1. Free body diagram of a robot climbing a vertical plane.

According to [2], by taking the moment about point G from Figure 1, the required force can be found. Therefore,

$$F_t \geq \frac{Gxh}{L} \tag{2}$$

To prevent roll-over, the centre of gravity of the robot should be designed to be as close to the wall as possible and the wheel base should be as long as possible.

3. Magnetic adhesion system

The adhesion force for AWI is generated by four magnetic wheels. In order to ensure that the target adhesion force is achieved numerical simulations were carried out using COMSOL Multiphysics software. Each wheel is composed of four segments of N35 neodymium magnet of 20mm thickness. The outer diameter of the wheel is 100mm and the inner diameter is 35.70mm.

The magnets are surrounded by a 10mm thickness stainless steel on both sides to keep the magnets aligned, plus 4mm of rubber for protection. The ship hull has been simulated as 20mm steel plate. The key properties of the materials used in the simulation are listed in Table 1. The adhesion force achieved per wheel is 82.485N, which corresponds to 8.4Kg of pull. The distance (L) between wheels is 150mm and horizontally the distance is 430mm. Hence, the total adhesion force is computed as 330.70N, i.e. 33.72Kg pull.

Table 1. Values used for FEA simulations with N35 and N42 magnets.

Properties	N35	N42
Magnetic induction intensity of magnets $B_r(T)$	1.13	1.31
Magnetic Coercive force H_{cb} (KA/m)	868	915
Intrinsic Coercive force Hci (KA/m)	955	955
Magnetic energy product HB (KJ/m^3)	263	318
Relative permeability of magnets (μ_r)	1.05	1.05
Relative permeability of wheels steel enclosure	1	1
Relative permeability of steel climbing surface	1500	1500

In further simulations the grade of the magnets was changed to higher intensity N42 magnets. This achieves an adhesion force of 110.50N (11.26Kg) per wheel. Therefore, with four wheels the total adhesion force of AWI is 444.44N (45.32Kg).
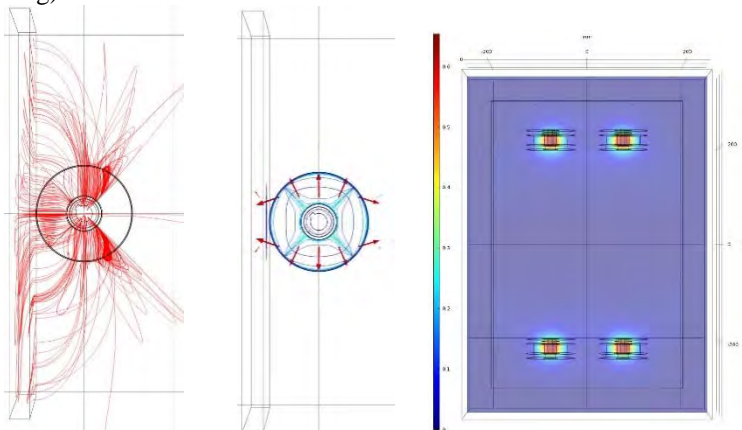

Figure 2. Results on COMSOL: a) Magnetic flux streamlines. b) Direction of the magnetic flux of the four magnets (polarisation of magnets). c) Magnetic flux density norm (four wheels).

4. Design of the climbing robot

4.1. *Mechanical hardware*

The main chassis of AWI is constructed from folded and welded 316 stainless steel with a sealed marine grade anodised aluminium lid. The drive shafts are all fitted with double acting lip seals made of Therban HNBR, which when combined with IP67+ electrical connectors ensure that AWI remains watertight.

- Dimensions of AWI are L: 410mm x W: 472mm x D: 210mm
- Weight 25kg   - Wheelbase of 150mm - Track of 430mm
- Powered by 40V DC from control box

4.2. *Electronics hardware*

Autonomous robots commonly use embedded software to operate, but AWI was designed to function using a custom made desktop application written in C#. The main advantage of this approach is that loosely-bound code allows for future features or modifications to be made without impacting other areas of code. This is possible via a device server, which is connected to a USB hub and Ethernet switch. Some of the components on AWI work on RS485 and RS232 protocols, which are converted to USB to allow a desktop computer to identify the components as COM ports. The Ethernet switch is connected to an industrial wireless card, which has a 3 channel rugged antenna operating on 2.4-5GHz frequency. Figure 3 illustrates the overall hardware connections within the AWI robot.
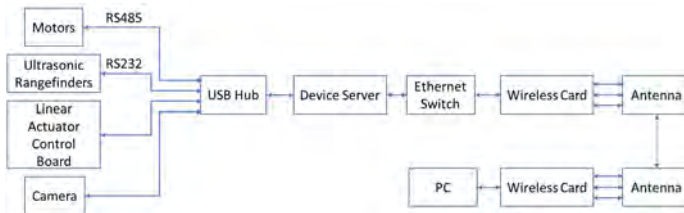

Figure 3. Diagram of hardware connections within the AWI robot.

The optical sensing of the weld lines is achieved using a green 2D laser line generator and an HD USB camera mounted in adjustable holders. The information required by the weld following algorithm is a frame captured by the camera, which applies a colour filter to the image given user selectable RGB values and then pixel detection to highlight weld area.

The NDT inspection equipment is mounted at the front of the robot. This includes an ultrasound phased array probe and a Hengstler optical encoder (more details of the inspection system is provided in section 5). Position data from the

encoder is fed directly to the NDT system rather than using the motor driven encoders in order to minimise the problem of the driven wheels slipping.
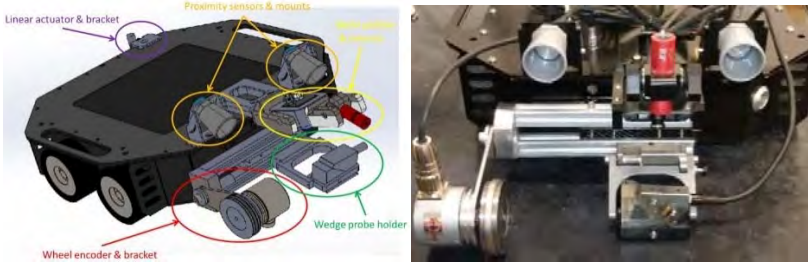

Figure 4. AWI's NDT payload.

4.3. *Robot software and control*

The purpose of AWI is to automatically follow long welds while carrying out inspection, however, the user interface also allows operators to manually drive the robot. Image frames from the front mounted camera are displayed in bitmap format.

Weld line detection is achieved by processing each camera frame using the AForge.Net framework. The image is first filtered to remove RGB colour outside the desired threshold. The resulting monochromatic image is shown in Figure 6. The raw bitmap data is then scanned, and the peak *y* pixel is selected to identify the centre point of the weld.
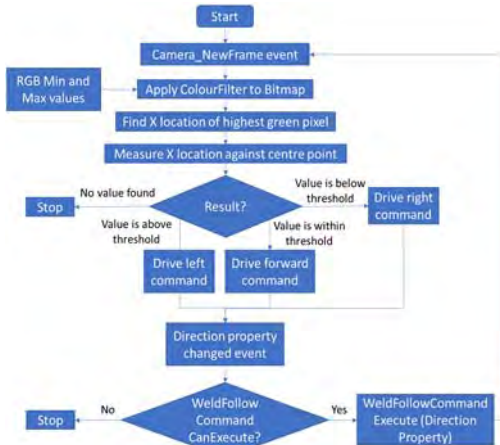

Figure 5. Weld following algorithm flow chart.

The weld centre is then compared to the centre point of the camera resolution. The difference between the two is then used as the feedback error to correct the

robot direction. The weld following algorithm is described in the flowchart in Figure 5.

5. Experimental results

5.1. *Performance of the climbing robot*

After assembly was completed (see fig. 4) a full system test of the robot performance was carried out on a horizontal and vertical test wall (see fig. 6a) at InnoTecUK. The wall features around 36 different defects embedded in the weld, such as cracks, lack of penetration, and discontinuities. The wireless communication was robustly established and data could successfully be retrieved including visual information of the weld and the laser profiler (see fig. 6b). During inspection AWI's speed was set at less than 50mm/sec, which is suitable for weld inspection. AWI's maximum speed achieved when not inspecting the weld and by teleoperation using a remote control was around 150mm/sec.
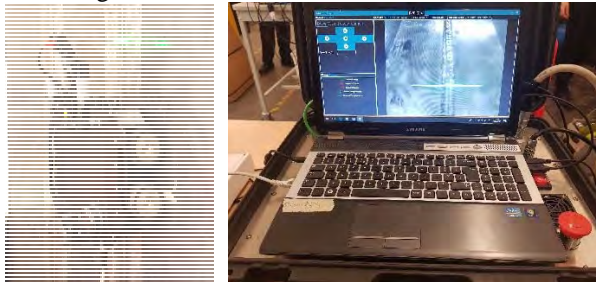

Figure 6. AWI's Trials.

AWI was able to localise itself along the weld based on the feedback provided from the wheel encoder. The emergency stop button feature allows the operator to cut the power of the whole system and stop the robot if safety related problems are encountered. Despite being powered down, the robot will maintain its position due to its magnetic wheels, which do not require any power to work. Furthermore, AWI was shown to be able to physically mark the position of the defects as they were encountered.

5.2. *Defect detection using the on-board inspection system*

The inspection system used during the trials was a conventional phased array ultrasound system. Calculations were made to determine the wedge angle and the full and half skip distances required for full inspection of the weld line, taking into account the weld thickness (fig. 7a).
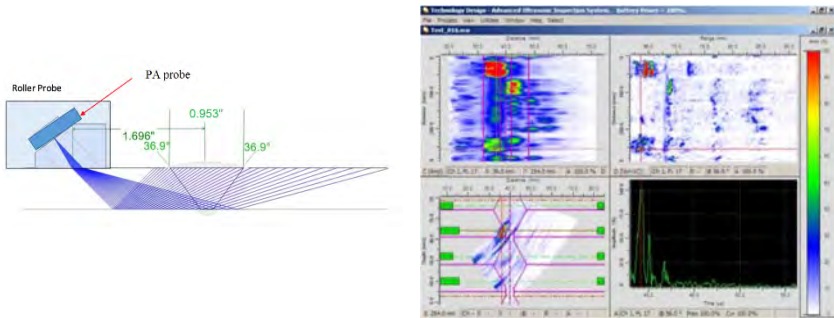
Figure 7. a) PA probe is mounted in the roller probe at 19°. b) Example of c-scan measured from the weld showing identification of defects.

With such an angled wedge and distance from the weld line inspection of the weld was possible and all the defects were correctly identified (fig. 7b).

6. Conclusions and future work

We presented a successful integration of a phased array ultrasound inspection system on a climbing robot and demonstrated that our method could effectively detect defects in welds. Communication between the robot and the remote computer is completely wireless. As future work, we intend to reduce the chassis weight to mount a high capacity battery for at least five hours of autonomy. Our initial demonstration uses also an umbilical to provide the couplant for the inspection system. Removing the umbilical using a dry couplant as in [7] will allow AWI to operate fully wireless, so further work will be carried out to find a suitable substitute for the couplant. Finally, we will trial AWI under realistic conditions on real ship hull at several meters from the remote computer, in a range of light conditions and poor weather.

References

1. Howlader, O.F. & Sattar, Tariq. (2015). "Development of magnetic adhesion based climbing robot for non-destructive testing", **CEEC**2015.
2. Howlader, O.F. & Sattar, Tariq. (2015). "Novel Adhesion Mechanism and Design Parameters for Concrete Wall-Climbing Robot", **IntelliSys**2015.

3. S. Nansai, R. Elara Mohan (2016). "A Survey of Wall climbing robots: Recent Advances and challenges", **Robotics**2016, 5,14.
4. M. Armada, P. Santos, M. Jimenez & M. Prieto (2003). "Application of Clawar Machines", **International Journal of Robotics Research**, vol. 22, no. 3, pp. 251-259, 2003.
5. F. Manuel & J. Tenreiro (2010). "A Survey of Technologies and Applications for Climbing Robots Locomotion and Adhesion", **INTECH**.
6. H. Prahlad, R. Pelrine, S. Stanford, J. Marlo & R. Kornbluh (2008). "Electroadhesive robots wall climbing robots enabled by a novel, robust, and electrically controllable adhesion technology". **IEEE ICRA**: 3028-3033.
7. S.C. Mondal, T.P.Sattar & T. Pattel (2010). "Remote mobile vehicle and its suitable non-destructive testing (NDT) inspection methods for the melt Weld inspection", **CLAWAR2010**.
8. 'Non-destructive testing of ship hull steel welds', International Association of Classification Societies, IACS Rec. 1988/Rev. 1 2007

MINIATURE MAGNETIC ROBOTS FOR IN-PIPE LOCOMOTION

GEORGE H MILLS[†]

*Department of Mechanical Engineering, University of Leeds,
Leeds, LS2 9JT, United Kingdom*

DR. JASON H W LIU, DR. BILAL Y KADDOUH, DR. ANDREW E JACKSON,
PROF. ROBERT C RICHARDSON

*Institute of Design Robotics and Optimisation, Lab G.54,
Leeds, LS2 9JT, United Kingdom*

Abstract— Inspection of both small and large diameter bore pipelines for pipe integrity and defect identification with a single system has previously been impractical; especially using wall-press locomotion methods with low adaptive range. A miniature magnetic wall-climbing robot has been developed as a robotic solution for the inspection of 50mm bore diameter pipelines which can scale in-pipe geometry obstacles to access larger connected pipelines. Using magnetic arrays directed through steel flux plates within the wheels, the robot uses magnetic forces to adhere to the pipe. The system is 3D printed and includes soft printed material rubber wheels. The robot prototype is wirelessly driven, controlled remotely through serial Bluetooth communication radio at 2.4 GHz rated up to 100m. The robot's unique compact geometry and magnetic design allows it to scale concave right-angle wall cases in just a 50mm diameter bore. By entering pipe networks through these small existing access points the robot removes the need for expensive drilling procedures required to fit launch vessels.

Index Terms—In-Pipe Robot; 3D Printed Robot; Magnetic Robot; Pipe Inspection

1. Introduction

The field of in-pipe robotics is rapidly growing as pipeline networks around the world begin to reach the end of their initial design lives. Maintenance and repair of these networks can be costly and damaging to the environment due to the unnecessary excavation of healthy pipelines. Inspection robots can be used to investigate sections of pipe flagged for replacement and can

determine the true interior condition. Types of in-pipe robotic locomotion can be categorized using basic elements, the elements presented in Figure 1 expand on the types of locomotion discussed in previous in-pipe hybrid literature reviews [1]. Modern in-pipe robots combine basic locomotion elements to form hybrid in-pipe systems with the ability to traverse a wide range of pipe obstacles and diameters [2]. The simplest of these being wheeled and caterpillar type robots (B & D). Specialized in-pipe methods of movement include, screwing, wall-press, and inchworm systems (C, E, & F). These locomotion methods are often combined with the more advanced methods, snake, walking, and magnetic (G, H, & J). The most widely used hybrid is wheeled wall-press systems due to their ability to use the pipe walls for traction. Adaptable Quad Arm Mechanism (AQAM) is a hybrid wheeled wall-pressing robot for 260mm – 300mm pipes, consisting of four arm mounted wheels in a single plane. The robot has impressive maneuverability due to its four independently controllable arms and swivel mechanism [3]. Multifunction Robot for INSPECTion of pipeline (MRINSPECT) is a wheeled wall-press hybrid in-pipe robot series designed at Sungkyunkwan University. The robot can perform all types of in-pipe geometry problems shown in Figure 2. MRINSPECT uses a multi-axial differential gear system to control each of its four wheeled legs angles through active bevel drive connections [4].

Figure 1: Basic in-pipe robotic locomotion types A – I.

Hanyang University developed a single-plane wheeled system. The problem faced with single plane contact is stability, any loss of wall contact in these designs will de-centralize the robot and make recovery extremely difficult [5]. Heli-Pipe is a series of wall-press systems that have a diametric adaptive ability of 10mm, as a result four different prototypes were made, ranging from 170mm to 40mm [6]. Caterpillar wall-press robots are also popular as a higher traction alternative to wheeled hybrid systems. Kanagawa University developed a hybrid of caterpillar and wall-press components, built from modular units each containing a driving caterpillar track. Connecting three or more units allows the robot to drive in-pipe, should a larger diameter need to be traversed the number of driving units can be increased [7]. Pipe Adaptive Robot of YonSei University (PAROYS-II) uses an actively controlled pantograph mechanism with a partially passive spring mechanism, this allows large changes to be controlled and small obstacles to be ignored. Its use of a second set of articulated caterpillar tracks allows a huge adaptive range of 400mm – 700mm [6]. SPRING is a screw type wall-press robot developed at Osaka University, although it relies on full wall traction it is unlike traditional full-bore wall-press systems which keep their chassis centralized in the pipe [9]. Snake robots are popular in industry pipe applications, they maximize space available and can be easily made to be modular in design allowing them to be flexibly suited to different tasks. PIRATE snake-like, and modular in nature featuring articulated clamping modules that can actively change the height of the robot to adapt to changes in pipe diameter [10]. The PipeTron series developed by HiBot, Tokyo is a multitude of robotic in-pipe exploration snake robots. Predominantly designed for tight bend systems such as refineries and chemical plants, the system is tethered for instant retrieval and consists of passively articulated wheels connected in a series [11]. The Explorer series is a multitude of industrial snake robots designed for the inspection of live gas networks under operating conditions, however it requires a full bore to operate with little adaptability ranging from just 150mm – 200mm [12].
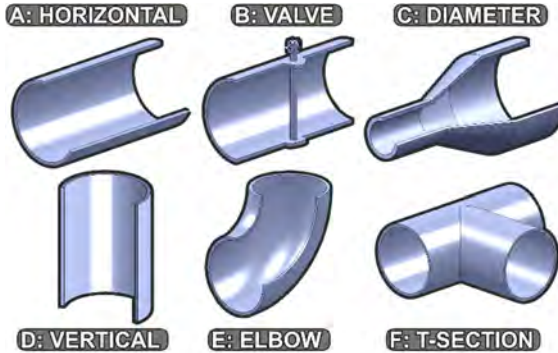
Figure 2: Common in-pipe obstacles A-F.

In ferrous pipelines, magnetic systems have all the locomotive advantages of wall-press without the need for adaptive diameter mechanisms. The first magnetic in-pipe robot was developed by the Osaka Gas Company in 1995, the system was a dual wheeled magnetic concept for the inspection 150mm - 600mm iron pipelines [13]. An advanced example of a magnetic wheeled in-pipe robot would be MagneBike. It can steer in a large range of in-pipe diameters, and can make obstacles such as T-Sections become trivial [14]. Synthotech [15] is making innovative progress towards complete pipe inspection with two robotic platforms targeting different challenges. The first; the Tier One Replacement System (TORS), a snake pipe robot focusing on lower diameter consumer pipeline replacement. Project Gas, Robotic Agile Inspection Device (GRAID) [16], will inspect the National Grid Gas Network under live operating conditions using a magnetically adhered caterpillar system. Magnetic robots are also used in out-pipe cases to traverse walls, ship hulls, and ferrous structures such as the boiler tube inspection prototype robot [17]. Omni-directional wheels used in conjunction with magnetics can lead to extremely maneuverable out-pipe robots such as Omni—Climber [18].

2. In-pipe robot design

The proposed in-pipe robot is intended to travel from small diameter pipelines to larger bores. The target inspection network consists of ferrous pipelines in the diameter range of 50mm – 1250mm. Magnetic adhesion is a suitable method in this case, performing the function of adhesion without the need for a full-bore wall-pressing system. As seen in other wall-pressing designs a full-bore adaption mechanism severely limits the range of pipelines that can be inspected by a single robot, even in the best case: the robot called PAROYS-II has a full adaption range

of 300mm [8]. The proposed robot will be specified to enter a 50mm inner diameter pipe and be able to overcome obstacles present in the network. For miniature wall-climbing robots, obstacles in Figure 2 can be simplified to distinct cases shown in Figure 3 in which a bend is either concave, or convex. Completion of both convex and concave geometries using magnetic systems is challenging without the use of articulated systems or many actuators allowing multiple degrees of freedom. Driving directly up to a convex case with magnetic wheels causes them to lock in place as the magnets act with equal force to each wall in contact.
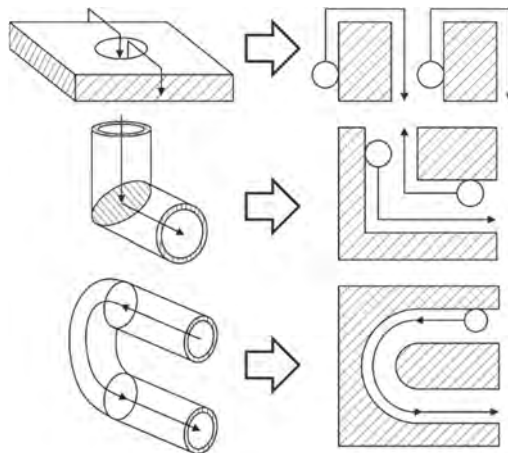

Figure 3: Simplified in-pipe geometry.

The concave case is equally challenging, as the wheels reach the right angle, magnetic force drops dramatically as the total potential magnetic flux transferred into the steel decreases causing slip at the wheels. The design challenge is to overcome these types of obstacle using a robot that stays within the tight space constraints of a 50mm pipeline. For this to be possible the robot profile must be below the given diameter with a clearance of the magnetic wheels such that they do not attract or lock with the top side of the inner pipe.

2.1. *Robot Design Overview*

The magnetic pipe robot, shown in Figure 5 was designed to enter 50mm internal diameter ferrous pipelines. The robot is equipped with magnetic wheels, a wireless control system, and two motors, it is 3D printed, including soft rubber wheels printed in-situ using soft printed material. Many basic vehicle designs were considered to save space within the pipe. The planar wheel (bike like)

configuration as used in MagneBike [14] Figure 4 (a), allows for efficient placement of magnetic wheels however it requires stabilisers to remain laterally stable (b). In a 50mm pipe, space is paramount and so a two-wheel vehicle (d) has been designed which grants efficient motor placement along the length of the pipe, this reduces the length and complexity vs both a 4 wheeled magnetic vehicle (c), and caterpillar system (e).
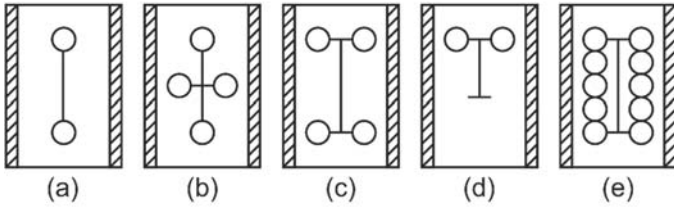

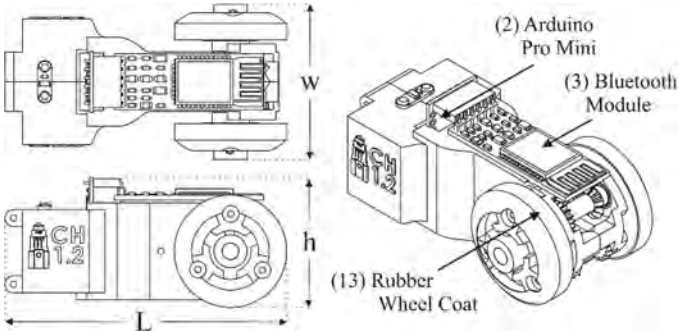Figure 4: Magnetic robot skeleton base designs (a – e).

Figure 5: (a) Geometry of the magnetic robot.

$$L \times w \times h = 85.10mm \times 46.88mm \times 38.65mm$$

The main body of the robot is printed as two separate halves and screwed together after the addition of motors, electronics and battery. The wireless Bluetooth radio transceiver is mounted on top of the chassis directly with the Arduino FTDI. This allows reprogramming later by detaching the radio.

2.2. *Transmission System*

Due to the size constraints when designing a robot for a 50mm diameter pipe, the motors are mounted perpendicular to driveshaft and the wheels. The motors sit parallel one on top of the other, each drive one gear train with transmission through a bevel gear, shown in Figure 6. The driveshaft then transmits power through the spur gear on the opposite side to drive the wheel with a transmission

ratio of 1.2:1. These sections are 3D printed, they are assembled with 5mm I.D. 8mm O.D. bearings which are push fit into the chassis during assembly. These allow smooth rotation and locating the centers for transmission assembly, keeping meshing distance of the gears constant. Although the motors are interchangeable depending on the desired gear ratio the current 250:1 motors allow a max wheel speed of 80 RPM.
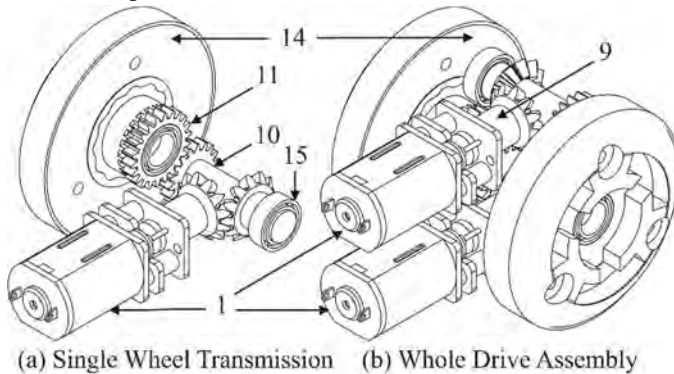

Figure 6: Transmission system, & Motor Layout, with part No. 1: Motor, 9: Gear, 10: Driving Shaft, 11: Wheel Gear, 14: Magnetic Wheels.

The prototype was formed using Objet material VeroWhite (60g) and Tango+ (4g) as well as breakaway support (186g) to form a complete model. The total build time for one robot is 2hrs:45min and requires an hour of support cleaning from surrounding material due to the delicacy and small size of the robot parts. Shown in the Table 1 is the bill of materials required to assemble the robot. The price is quoted as £171 to produce one unit, however the printing costs for the chassis account for 66% of this price. This price is based on the production of one robot, charged at a £25 hourly rate for use of the Objet 1000 printer and a printing time of 3 hours. These costs could be reduced if the robot were to be printed in batches.

2.3. Wireless Driving System

The robot is controlled using a 3.3V version of the Arduino Pro Mini which interfaces wirelessly over serial using the SparkFun Bluetooth Mate Silver. The 3.3V level logic voltage uses less power than 5V version of the pro mini at the cost of processing speed (8MHz vs 16MHz) however it is directly compatible with all secondary components and does not require a voltage regulator. Bluetooth radio was chosen for the same reason, when idle it draws much less current than

Wi-Fi options such as the ESP8266 (50mA vs 170mA during communication). As this robot is designed to operate in 50mm -1250mm diameter pipes, the Bluetooth 2.4 GHz module will only be effectively operational in 80mm - 1250mm diameter pipes. We are currently investigating the use of a 5.8GHz module for smaller diameter pipes (50mm - 80mm) in future versions. For the purpose of this proof of concept, the Bluetooth module achieves the desired outcomes. A SparkFun dual motor driver breakout board is used to control direction of the two motors and hence steering, and a 3.3V LED is used as a power indicator. The whole system runs on a 260mah 7.4V Lithium Polymer (LiPo) rechargeable battery which supplies logic voltage to the Arduino, and raw voltage to the dual motor driver board. Commands are given to the Pro Mini via serial sent from a master computer running LabVIEW. The additional circuitry required increases assembly time in terms of the time it takes to solder, estimated at half an hour. The circuit boards and LED's simply slide into the printed grooves and are held in place by frictional forces. A summary of the electronic materials used in the production of one unit, including price and weight can be found in Table 1.

2.4. *Magnetic Wheel System*

The magnetic wheels were designed to increase the strength of the magnets by redirecting the flux of the magnets to focus it into the tracks. Instead of having magnets directly in contact with the inner surface of the pipe, they are housed between two steel plates, Figure 7. This has two benefits; redirection of the magnetic flux into the steel plates, and protection of the neodymium magnets. Corrosion and shock impact can cause degradation and fracturing of the magnets, by encapsulating them rather than placing them in direct contact with the pipe wall they are significantly safer. The magnets used in the wheel assembly are N42 6x4x2mm rectangular magnets with a pull strength of 0.75kg. These magnets have their north and south faces on opposite sides of the 6mm x 4mm faces, which are in contact with the plates. The evenly spaced circular array of 9 magnets shown in Figure 7 is held within the wheel using a 3D printed spacing layer, this smooths out the flux dissipation to maintain an even distribution of tractive force as the wheel rotates.
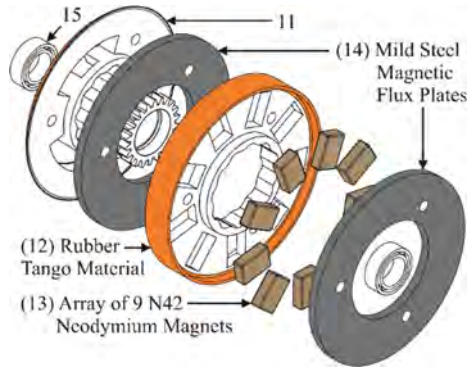
Figure 7: Exploded view of the 34mm diameter wheel assembly.

The wheel is connected using three screws which locate the entire assembly ensuring the wheel lines up optimally as intended in the CAD model. The through holes are seen in Figure 7. The flux lines run from one side the plate back, through the 1.5mm steel, into the pipe wall, and back through the second plate with the opposite face. By focusing the flux through the pipe wall in this way the magnetic absorption force increases, and a higher traction is generated at the wheel. Figure 8 presents a close up of a central wheel cross-section and shows the wheel in contact with a flat steel surface. The distance between the magnetic flux plates and the steel contact surface are seen to be offset by the rubber tango material. The distance between these two surfaces is 0.5mm on a flat plate and up to 3.5mm in a 50mm diameter pipe section.
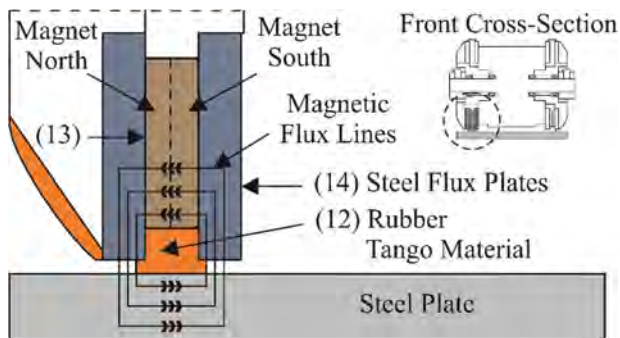

Figure 8: Magnetic wheel cross-section flux diagram.

3.   Robot Performance

The robot was printed, wheel flux plates laser cut, and assembled. The complete system was then analyzed in terms of locomotive capabilities, magnetic force, and maneuverability, the finished robot is shown in a 50mm pipe Figure 9.
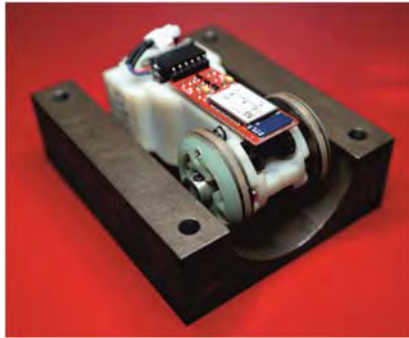
Figure 9: Assembled robot in a 50mm I.D. half-pipe.

The magnetic force generated by the wheels was tested on mild steel plates of varying diameter. The plates were fastened to a testing rig using 3D printed spacers, seen in orange, the robot was clamped to the 10 Newton load cell of the Emperor Force measurement device, Figure 10, and then pull force tests were undertaken. The tests followed the same method; initially the load cell was zeroed and the robot lowered down into contact with the plate until the load was at zero again. The robot was then pulled off the plate at a rate of 0.5mm/sec until a height was reached where the magnetic field no longer has influence (30mm). The experiment was repeated 5 times for each plate size. The setup for this experiment shown in Figure 10, the results; Figure 11. It should be noted that the robot was first placed in a compression pre-loaded state to reach equilibrium with the magnetic force. This pre-loaded state is highlighted before each peak force point in Figure 11.

Figure 11 shows that the pull force case for flat plate produces significantly stronger force (almost triple) when compared to the 50mm case. The uneven contact of the robot wheels in the 50mm diameter pipe case results in sub-optimal transfer of magnetic flux through the steel. The inner flux plates are a minimum of 3mm from the pipe walls making a complete flux flow through the two sides difficult.
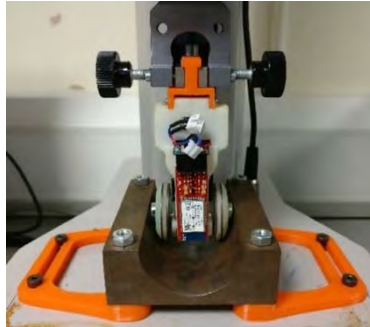
Figure 10: Single column linear force tester with a 10N load cell.
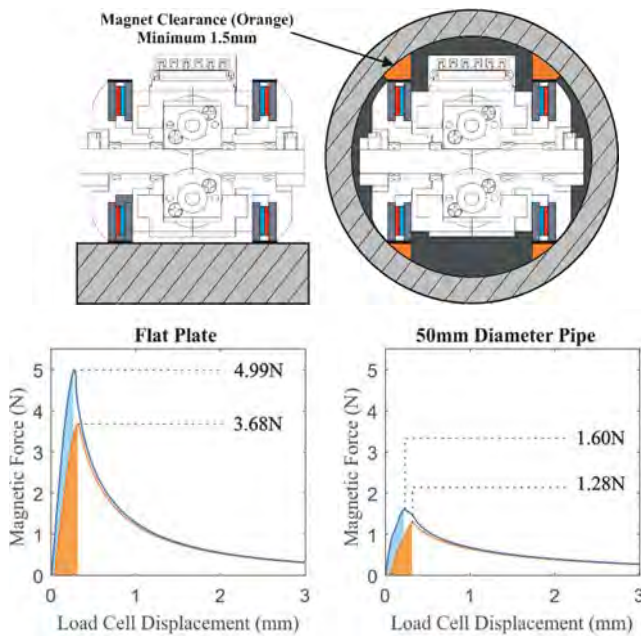
Figure 11: Magnetic pull force experiment result, pull force (blue), connection force (orange).

In Figure 11, the peak pull force required to remove both wheel is highlighted in blue, whereas the re-attachment force is shown in orange. The shaded areas of the graphs indicate that the robot is in a compressed state.

Table 1: Standard deviation of 5 experiment samples.

	Flat Plate Pull	Flat Plate Push	50mm Pull	50mm Push
Standard Deviation	0.017	0.002	0.114	0.009

Magnetic wheels can encounter problems in cases where one wheel has more than one point in contact with a ferrous surface. The wheel can become stuck as to move in either direction it first has to overcome the unwanted magnetic force produced. The forces involved in this situation are described in Figure 12, where the robot is driving up a wall at a 90-degree concave angle. The robot is capable of completing the case presented in Figure 12 in a pipe, where traction is minimum. The robot has been designed with this worst case scenario in mind; travelling vertically in-pipe in the lowest diameter where magnetic force is minimum. This scenario results in lowest traction case, designing to complete this ensures the robot can perform any other section with a wider inner diameter or preferable orientations where magnetic or traction force applied is higher.
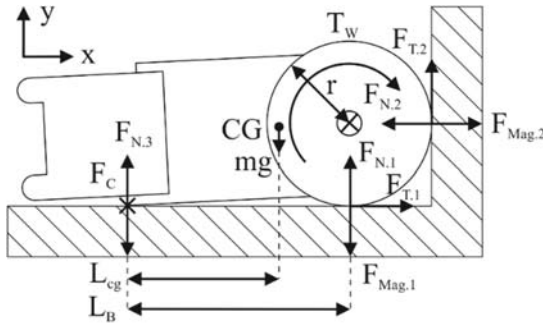
Figure 12: Forces acting at point of 90-degree wall contact.

For the wheel to drive up the wall from this position, the traction force $F_{T.2}$ must overcome the wheels magnetic pull $F_{Mag.1}$. In this scenario the weight of the vehicle must also be overcome making this the most difficult case in terms of tractive effort. Balancing the forces around the point of contact and assuming the wheel is at the point just before accelerating up the wall, traction $F_{T.2}$ will equal $F_{Mag.1}$ plus the weight component, equation (1).

$$F_{T.2} * (L_B + r)_c = F_{Mag.1} * (L_B) - mg(L_B - 2L_{cg}) \quad (1)$$

The magnetic forces required to allow this robot to provide enough traction to overcome weight means that the mg component is comparatively low (2).

$$-0.144 * 9.81 * (0.047 - 0.066) = 0.0276N \quad (2)$$

Balancing forces in terms of $F_{T.2}$ the total force that the wheel traction must overcome to climb the wall can be determined by equations (3), and (4).

$$F_{T.2} = \frac{F_{Mag.1} * (L_B)}{(L_B + r)} + 0.0276 \quad (3)$$

$$F_{T.2} = 2.89 + 0.0276 = 2.91N \quad (4)$$

To accelerate up the wall at this equilibrium point the traction force must satisfy the equation (5). Maximum tractive force that can be applied at $F_{T.2.MAX}$ is governed by equation (6):

$$F_{T.2} > \frac{F_{Mag.1}*(L_B)}{(L_B+r)} + mg\sin(\emptyset) \qquad (5)$$

$$F_{T.2.MAX} = \mu_s F_{N.2} \qquad (6)$$

$Where: \mu_s =$ Static coefficient of friction of wheels

To satisfy the traction requirements, the static coefficient of friction, μ_s must be maximized. In the scenario outlined in Figure 12 $F_{N.2}$ is equal to the magnetic force from Figure 11; 4.99N (lowest recorded force), and $F_{T.2}$ is equal to 2.91N from equation (4). When entered into (7) the minimum required static friction co-efficient can be obtained:

$$\mu_s > \frac{F_{T.2}}{F_{N.2}} \qquad \mu_s > 0.58 \qquad (7)$$

In Figure 13 the robot is shown driving on a steel floor directly up to a 90-degree steel wall in replica of the case outlined in Figure 12.
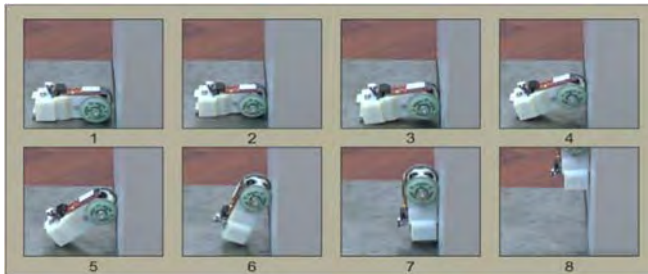
Figure 13: Magnetic robot climbing 90-degree from steel to steel.

The robot is optimized for high magnetic force on flat plate travel, this is due to the decreased risk in lower diameter pipelines. In large pipelines gas flow will likely be at the highest rate, hence a larger normal force will be required to maintain friction levels necessary to remove wheel slip. The robot can move at a top speed of 90mm/sec on a flat steel plate (Maximum magnetic attraction case) and can currently drive from any orientation. The robot is capable of completing a 180° pipe bend with minimum radius of 25mm within a 50mm pipeline. Driving straight around the inside of a pipeline is possible as when the robot reaches wall angles greater than 90 degree's the chassis simply hangs upside-down. This version requires that you turn around at the top of the pipe as the Bluetooth mate module blocks wheel contact. Removing additional actuators to climb step cases greatly reduced the size of the robot however currently the robot is incapable of

convex right-angle cases due to the limited step space between the wheel and the chassis; currently 2.4mm.

4. Conclusion

A wheeled-magnetic in-pipe robot has been designed to enter small 50mm pipelines found within larger pipe networks. These small entrances of 50mm will allow the robot to enter the larger connected network pipes which range from 50mm – 1250mm. By using a magnetic robot that does not rely on wall-pressing for traction the obstacles usually encountered in-pipe can be simplified and focus can be narrowed to just two cases. The robot has proven effective at 90-degree wall climbing cases where two magnetic forces are active at once and can generate tractive forces necessary to overcome the unwanted magnetic force. Further work will be done on the optimization of the circular magnetic array, such as testing N52 neodymium and reducing the rubber thickness. Smaller magnetic wheels are to be added to stabilize the rear of the chassis, and the electronic component stack will be integrated within the frame of the robot to allow it to drive on either side of the chassis.

Acknowledgments

References

1. Roslin, N. S., Anuar, A., Jalal, M. F. A., & Sahari, K. S. M. (2012). A review: hybrid locomotion of in-pipe inspection robot. *Procedia Engineering*, *41*, 1456-1462.
2. Mills, G. H., Jackson, A. E., & Richardson, R. C. (2017). Advances in the Inspection of Unpiggable Pipelines. *Robotics*, *6*(4), 36.
3. Lee, D., Park, J., Hyun, D., Yook, G. and Yang, H.-s. Novel Mechanisms and Simple Locomotion Strategies for an In-Pipe Robot that can Inspect Various Pipe Types. Mechanims and Machine Theory. 2012, 56, pp.52 - 68.
4. Yang, S.U., Kim, H.M., Suh, J.S., Choi, Y.S., Mun, H.M., Park, C.M., Moon, H. and Choi, H.R. Novel Robot Mechanism Capable of 3D Differential Driving Inside Pipelines. In: International Conference on Intelligent Robots and Systems, 14-18 Sept. 2014, Chicago, IL. IEEE, 2014, pp.1944-1949.
5. Kwon, Y.-S., lee, B., Whang, I.-C., Kim, W.-k. and Yi, B.-J. A Flat Pipeline Inspection Robot with Two Wheel Chains. In: International Conference on Robotics and Automation (ICRA), 9-13 May 2011, Shanghai. IEEE, 2011, pp.5141-5146Will

6. Horodonica, M., Preumont, A., Burda, I. and Mignon, E. The Heli-Pipe Inspection Robots Architecture for Curved Pipes. In: International Conference of Manufacturing Systems. 2003.

7. Sato, K., Ohki, T. and Lim, H.-o. Development of In-Pipe Robot Capable of Coping with Various Diameters. In: 11th International Conference on Control, Automation and Systems, 26-29 Oct. 2011, Gyeonggi-do, Korea. IEEE, 2011, pp.1076-1081

8. Park, J., Hyun, D., Cho, W.-H., Kim, T.-H. and Yang, H.-S. Normal-Force Control for an In-Pipe Robot According to the Inclination of Pipelines. In: Transactions on Industrial Electronics, Dec. 2011. IEEE, 2011, pp.5304 - 5310.

9. Nishihara, T., Osuka, K. and Tamura, I. Development of a Simulation Model for Inner-Gas-Pipe Inspection Robot: SPRING. In: Society of Instrument and Control Engineers of Japan, 18-21 Aug, Taiwan 2010.

10. Dertien, E., Stramigioli, S. and Pulles, K. Development of an Inspection Robot for Small Diameter Gas Distribution Mains. In: International Conference on Robotics and Automation (ICRA), 9-13 May 2011, Shanghai, China. IEEE, 2011, pp.3447-3448.

11. Debenest, P., Guarnieri, M. and Hirose, S. PipeTron Series - Robots for Pipe Inspection. In: 3rd International Conference on Applied Robotics for the Power Industry, 14-16 Oct, Foz do Iguassu. IEEE, 2014, pp.1-6.

12. Schempf, H., Mutschler, E., Gavaert, A., Skoptsov, G. and Crowley, W. Visual and Nondestructive Evaluation Inspection of Live Gas Mains Using the Explorer Family of Pipe Robots. Journal of Field Robotics. 2010, 27(3), pp.217-249.

13. Kawaguchi, Y., Yoshida, I., Kikuta, T. and Yamada, Y. Internal Pipe Inspection Robot. In: International Conference on Robotics and Automation, 21-27 May 1995, Nagoya. IEEE, 1995, pp.857-862.

14. Tache, F., Fischer, W., Caprari, G. and Siegwart, R. MagneBike: A Magnetic Wheeled Robot with High Mobility for Inspecting Complex-Shaped Structures. Journal of Field Robotics. 2009, 26(5), pp.453-476.

15. Synthotech Limited. [Online]. 2018. [Accessed: 16/04/2018.] Available from: http://www.synthotech.com/

16. National Grid 2018. Project GRAID. [Online]. 2018. [Accessed: 16/04/2018.]. Available from: http://projectgraid.com/

17. Boonyaprapasorn, A., Maneewarn, T., & Thung-Od, K. (2014, October). A prototype of inspection robot for water wall tubes in boiler. In *Applied Robotics for the Power Industry (CARPI), 2014 3rd International Conference on* (pp. 1-6). IEEE.

18. Tavakoli, M., Viegas, C., Marques, L., Pires, J. N., & De Almeida, A. T. (2013). Omniclimbers: Omni-directional magnetic wheeled climbing robots for inspection of ferromagnetic structures. *Robotics and Autonomous Systems*, *61*(9), 997-1007.

DEVELOP A SENSOR BASED ROBOT FOR RAILWAY INSPECTION

Nathan Western; Shyamal Mondal

Department of Engineering, London South Bank, 103 Borough Road London, SE1 0AA, England

This project produced a sensor based robot capable of testing a section of railway track, using both magnetic flux and visual inspection. Surface quality inspection is performed by a probe consisting of a number of Hall effect sensors. Visual inspection is performed by a camera connected to the robot. A replica rail section was also created for the purposes of calibrating and demonstrating the robot. The hardware and software developed successfully collected video data and magnetic flux readings. The output of the hall effect sensor array was processed in MATLAB producing a heat-map. The shape and depth of artificially induced defects were successfully displayed.

1. Introduction

In this project a robot was created to provide non-destructive testing (NDT) for rail. It aimed to provide a service comparable to a fully staffed test. It is hoped this will be a step towards more regular testing by being convenient and cheap to use, resulting in a safer railway service. A variety of NDT methods were considered and evaluated, and two were selected and incorporated into a functional testing robot that can detect common flaws in rail track.

Rail testing and maintenance is essential to keeping Britain's extensive network of train track operational. 1.7 billion journeys were made in 2016 accounting for 8% of all passenger travel and over 10% of all freight moved [1]. Maintenance costs Network Rail £1.3 billion a year according to latest available figures from 2016-2017 [2]. It is still primarily carried out by technicians and engineers on site. Not only is this costly, it also limits the time at which maintenance can be performed to ensure the safe working conditions of the engineers. This creates problematic scheduling conflicts.

Considering this, the project aimed to determine whether automation could reduce the costs of routine rail inspection or increase the effectiveness of NDT for

rail. This should be achieved using a mobile testing platform capable of utilising multiple testing methods.

2. Rail Inspection Robot Design

The platform was designed to enable movement across the rail and contact between the rail and the sensor array. A single rail crawler design was selected.
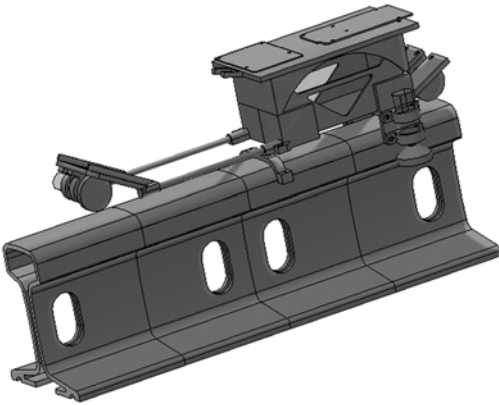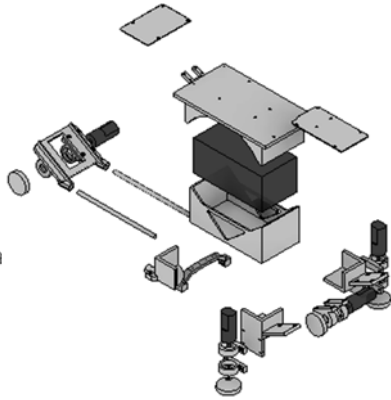
Figure 1a. Assembly of Robot and Track	Figure 1b. Exploded View of Robot

This used wheels on the top and sides of the rail to travel across one rail and perform an inspection. This design supported visual and magnetic flux inspection with the optimal cost, time and materials usage.

The robot was initially designed to move at a speed of 0.1m/s to ensure the sensors could take accurate readings. It would be hoped that the speed could be increased in future developments, but at this feasibility stage it was more important to achieve accuracy to prove the concept.

The sensor array consisted of seven Hall effect sensors. The Arduino Mega board powered the sensors and collected the output signal. This was sent via serial out to the Raspberry Pi for storage. Neodymium magnets were used to magnetise the rail, and the sensors then measured any change in flux caused by defects. The sensors were positioned an equal distance from each other and the magnets.

The robot comprises of two sub-assemblies. The lower part of the chassis holds the motors, battery and sensor array. The upper chassis, which sits on top of the lower, contains the microprocessors, power supply for the boards and the

camera. The chassis was printed in PLA plastic using Fused Filament Fabrication techniques.

Figure 2a. A robot carried out inspection on the rail track. Figure 2b. Disassembled Robot.
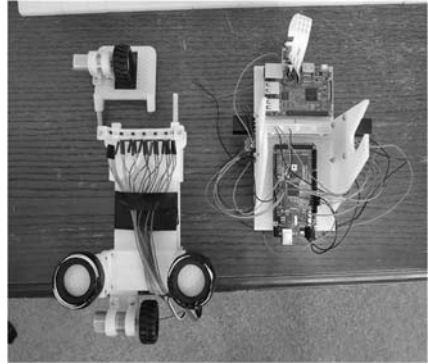
3. Robot Controller Software Design

The Arduino takes readings from the sensor array at an interval of 1ms. This data is then sent via Serial.print to the Raspberry Pi for logging as a .csv file. The Arduino was also responsible for managing the movement of the robot. An infrared sensor detects the presence of obstacles in the path of the robot and sends a signal to the motors, only if the path is clear.

The Raspberry Pi was instructed to collect video and serial data using the command line over SSH. The video was collected using the raspivid command. The serial data was collected using the grabserial library.

4. Data Processing Method

The Hall effect sensor data was analysed using MATLAB. A program was produced to calculate the average gauss reading for each sensor, and then construct a matrix of the difference between the average values and the results. A contour plot was chosen to represent this data because it displays the change in Gauss readings visually. Higher difference in Gauss values was shown as a darker colour, indicating a deeper defect.
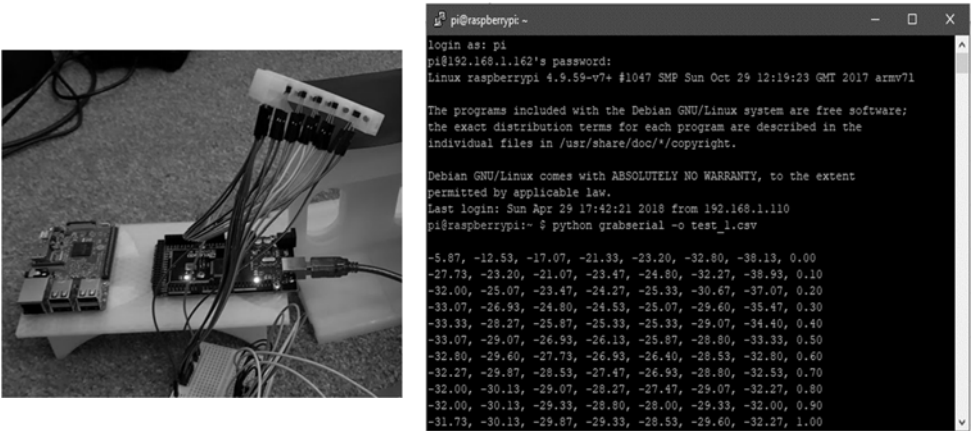
Figure 3. Using the Grabserial Command to Collect Data from the Arduino

5.   Results and Discussion

The robot collected data from the Hall effect sensors and camera as it travelled the length of the rail section. The rail contained 5 defects of various size and depth. These represented common rail faults; severe detail fracture (at 590mm), spalling as a result of rolling contact fatigue (515mm), two small head checking defects (380mm and 435mm), and finally a gauge corner crack with divergence (212mm). Multiple tests were conducted to determine the ideal distance between the Hall effect sensor array and the track.

5.1.   *Test 1 – 0.5mm Sensor Height from Rail Surface*

The initial test results are shown in Figure 4 after being processed by the MATLAB program. The readings were taken with the sensor a distance of approximately 0.5mm from the rail surface. Although there is some interference caused by the uneven surface all the defects are shown. Especially clear is the spalling type defect visible at reading 60. The sensor array was raised to a height of 1.5mm for the next test to try to remove some of the interference.

Figure 4. Test 1 Results for 0.5mm Sensor Height.   Figure 5. Test 2 Results for 1.5mm Sensor Height

5.2. *Test 2 - 1.5mm Sensor Height from Rail Surface*

During test 2 the sensor array was raised too far and did not make proper contact with the rail. This lead to the results being harder to interpret. The robot also slipped towards the end of the test, causing the jagged pattern visible from reading 70 onwards in Figure 5. The sensor was lowered to 1mm for the next test.

5.3. *Test 3 - 0.7mm Sensor Height from Rail Surface*

Test 3 produced a clearer image of the test rail than test 2, as shown in Figure 6. The divergent crack at 212mm is more clearly shown from readings 5-15. The deepest crack at 590mm is now very clear between readings 60-70. This did cause some distortion in the area by readings 50-60, making the spalling defect harder to see. The sensor was raised just 0.2mm for test 4 to compensate for this.
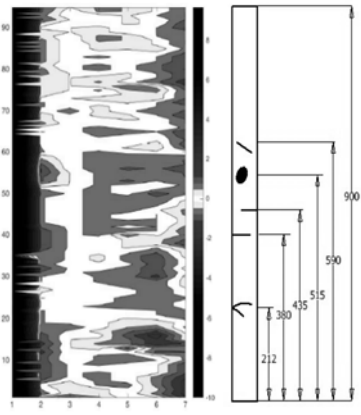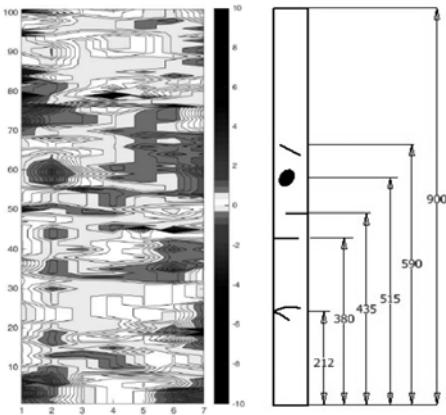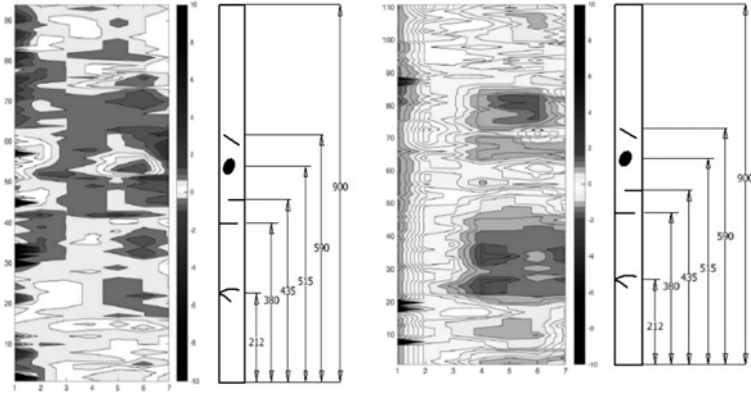
Figure 6. Test 3 Results for 0.7mm Sensor Height   Figure 7. Test 4 Results for 0.9mm Sensor Height

5.4. *Test 4 - 0.9mm Sensor Height from Rail Surface*

Figure 7 shows the results taken during test 4. The dark orange shape at readings 10-15 show a change in Gauss of 1.75. This was caused by the gauge corner crack at 212mm, and the shape of the defect is represented. The two cracks at 380 mm and 435 mm are clearly shown at reading 25 and 35, with an indication of the shape and depth of the cracks. The spalling defect is less clear, but still visible in the readings at position 65-70. Finally, the deep crack at 590mm is shown at reading 80, with indication of depth.

5.5. *Video Inspection Data*

Visual data was also collected by the robot using the Raspberry Pi camera. Stills from the video are shown in figures 8 & 9 below. This is the ferromagnetic top surface of the PLA replica rail section. When a defect is detected by the sensor array the video can be examined to further determine the nature of the faults. This also reduces erroneous readings, for example the sensor array travelling over organic debris such as leaves.
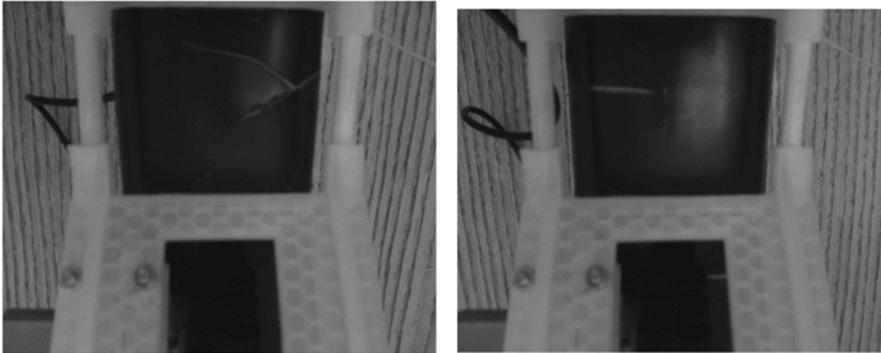
Figures 8 & 9. Images of Cracks in the Gauge and Head Region

6. Conclusions and Recommendations for Future Work

6.1. *Recommendations for future work*

The slow speed of the robot was identified as a weakness during the project. If the speed could not be increased this could be compensated for by scheduling tests for small parts of the rail at one time. A study of railway maintenance [3] stated that a busy European railway might have inspection intervals of 4 months. Assuming testing being conducted solely during the working week, one robot could be scheduled to test each 115.2km of rail in a 4-month period.

The distance the sensor is operating from the rail has a large impact on the results. The design would benefit from the addition of a thumb screw system to make sensor height adjustments easier. The addition of small wheels or rollers to the bottom of the sensor would also increase sensor stability.

6.2. *Conclusions*

A robot capable of traversing railway track was developed, using a sensor array to conduct non-destructive testing of the rail. Additionally, the robot uses visual inspection to conduct a test of a section of track. This ensures a greater degree of accuracy and more conclusions about any defects can be drawn. The digital data was suitably interpreted, producing an image of the rail condition. Achieving this level of inspection using an automated, sensor based robot suggests that the costs of manual inspection can be reduced using automation.

Whilst the exact location and shape of defects was not always clearly displayed, the sensor array did detect all the defects in the replica rail section. It

also gives a good indication of depth. At a sensor height of approximately 0.6mm from the rail surface the processed data is easy to interpret and indicates where further maintenance is needed.

The project has successfully built on the paper "Sensor Development and Application on the oil-gas pipeline Magnetic Flux Leakage Detection" [4], making a Hall effect sensors for NDT application. The optimising of the sensor systems explored in their paper have been successfully modified for use testing railway track. Additionally, the work has included the development of software to visualise the sensor data.

References

1. M. Shaw, "Rail Trends Factsheet 2016," *Gov.uk*, 2017.
2. Office of Rail and Road, "UK rail industry financial information 2016-17," 2018.
3. D. F. Cannon, K.-O. Edel, S. L. Grassie, and K. Sawley, "Rail defects: an overview," *Fatigue Fract. Eng. Mater. Struct.*, vol. 26, no. 10, pp. 865–887, 2003.
4. P. Lad and M. Pawar, "Evolution of Railway Track Crack Detection System," in *2nd IEEE International Symposium on Robotics and Manufacturing Automation*, 2016.
5. Lidén, T. and Joborn, M. (2016) 'Dimensioning windows for railway infrastructuremaintenance: Cost efficiency versus traffic impact', *Journal of Rail Transport Planning & Management*, 6(1), pp. 32–47.
6. Lijian, Y. *et al.* (2009) 'Sensor Development and Application on the oil-gas pipeline Magnetic FluxLeakage Detection', *The Ninth International Conference on Electronic Measurement & Instruments*. doi: 10.1109/ICEMI.2009.5274410.
7. Mahfuz, N. *et al.* (2017) 'Autonomous Railway Crack Detector Robot for Bangladesh', in *2017 IEEE Region 10 Humanitarian Technology Conference*. American International University – Bangladesh. doi: 10.1109/R10-HTC.2017.8289014.
8. Misron, N. *et al.* (2011) 'A Mobile Ferromagnetic Shape Detection Sensor Using a Hall Sensor Array and Magnetic Imaging', *Sensors*, 11, pp. 10474–10489. doi: 10.3390/s111110474.

SECTION 7

CLIMBING AND INSPECTION ROBOTS

TRAVELING-WAVE-TYPE WALL-CLIMBING ROBOT FOR AIRPLANE SURFACE INSPECTION

D. HAGIWARA*, N. TADAMI, T. AMAKAWA, Y. YAMADA, T. NAKAMURA

Department of Precision Mechanics, Chuo University,
1-13-27 Kasuga, Bunkyo-Word, Tokyo 112-8551, Japan
*E-mail: d_hagiwara@bio.mech.chuo-u.ac.jp

Robots are expected to substitute for humans for work performed in locations at a height, such as the inspection of an airplane surface. The authors propose a traveling-wave-type wall-climbing robot simulating a snail movement. To this end, in this study, the negative pressure adsorption method was employed to develop a wall-climbing robot that could move on curved surfaces for high-altitude work.

Keywords: Wall-climbing robot; Airplane inspection; Traveling wave.

1. Introduction

High-altitude work includes the inspection of airplane surface, maintenance of high-rise buildings, maintenance of storage tanks, and operation of petrochemical product facilities at nuclear power plants, among others. These operations are performed regularly, wherein the assembling and footing of a tower wagon are necessary each time, thus affecting the time and cost. Furthermore, it is a problem to ensure the safety of workers performing work at high altitudes [1]. Therefore, to reduce time and cost and ensure worker safety, the development of a robot capable of performing these tasks is required.

The application of multicotters and the development of a wall-climbing robot can help realize high-altitude work robots. [2]-[6]. Multicotters have the advantages of light weight, easy transportation, and fast running speed of the robot. However, the robot is not robust against the weather and has low loading capacity, among other issues. [2]. Nevertheless, the wall-climbing robot is less influenced by weather and rain compared with the multicotter, and the load carrying capacity is higher [3]-[6]. In addition, the existing wall-climbing robot has adopted vacuum suction using a suction cup to obtain high adsorption power [3]. However, in vacuum adsorption, objects cannot adhere well to a rough surface or a surface with irregularities, and suction cup wear is a problem. Negative pressure

adsorption by a fan, however, always discharges air to generate and maintain adsorption force. Therefore, adsorption to a rough surface or a surface with irregularities is possible. As such, in recent years, a negative pressure adsorption-type wall-surface climbing robot has been proposed as a high-altitude work robot having high versatility [4]-[6]. The existing robot was confirmed to be adsorptive, and it could move on a rough surface. However, owing to the reduction in the adsorption power on the uneven surface, the robot cannot obtain sufficient grip and stacks [4] [5]. In order to solve this problem, a robot having a plurality of adsorption parts has been proposed; however, a passive joint and correspondence to a curved surface have not been realized to help increase the robot size [6].

To this end, the authors propose a traveling-wave-type mobile robot simulating a snail traveling [7]-[9]. In this robot, several adsorption units are respectively connected by a universal joint, and the robot progresses by the propagation of expansion and contraction between the units. At this time, the moving unit slides on the wall surface, and the unit that does not move is fixed with a strong force, such that each unit switches the frictional force [7] [8]. Consequently, the robot has a wide ground contact surface, thus maintaining a high adsorption force and stable traveling. Further, even if some of the units become insufficient owing to disturbance, they can be supported without being dropped by other units. Furthermore, the curved wall surface can also be traversed [9]. However, this robot can move only on magnetic surfaces to satisfy the properties of adsorption and friction switching with magnets.

In this study, we adopt the negative pressure adsorption method for the traveling-wave-type mobile robot and aim for the development of a wall-climbing robot to be used for high-altitude work. We propose a negative pressure adsorption unit and evaluate the traveling of the mobile robot composed of that unit, as well as examine the application to the work robot.

2. Outline of High-altitude Work in Airplane Surface Inspection

The surface of an airplane can be damaged by hail, bird collision, and lightning. Further, small scratches and dents are generated on the surface of the airplane during operation. Large damages are visually observed [10] and damages that are difficult to confirm visually are inspected using nondestructive inspection techniques such as penetrant inspection, magnetic particle inspection, X-ray inspection, and ultrasonic inspection.

The radius of curvature of the airplane surface is approximately 1 m or more [11]. In addition, gaps and steps of approximately 5 mm exist at locations of door installation and other installations. [12].

3. Proposal of Wall-climbing Robot

3.1. *Required performance for robots*

The inspection robot requires adsorption while traversing the airplane body surface, which is made of nonmagnetic duralumin, and it must be able to inspect equipment. Furthermore, the robot is required to traverse the doors, window gaps, and oversteps. Therefore, the robot must satisfy the following performance requirements:

- Adsorption movement on the wall surface and curved surface of nonmagnetic metal surface.
- High adsorption power capable of mounting nondestructive inspection equipment and other equipment.
- Ability to move on a surface with steps and gaps.

3.2. *Proposal of a robot for airplane surface inspection*

The outline of the proposed robot is shown in Fig. 1, and the method of operation of the robot is shown in Fig. 2. The robot consists of four units that adsorb negative pressure using a centrifugal fan. Each unit is connected by a universal joint and can be adsorbed to a curved surface (Fig.1 (b)). In addition, each unit changes its frictional force simultaneously with expansion and contraction (called high-friction unit during high friction, and low-friction unit during low friction). By this friction-force switching, the expansion and contraction of the unit facilitates the propagation, as shown in Fig. 2. Therefore, even during movement, a high adsorptive power can be maintained constantly and running stability can be secured. Furthermore, the lower part of the unit is a detachable part, and the friction material and seal material can be changed against the suction surface, as shown in Fig. 3. Consequently, the friction material and the sealing material can be changed with respect to the shape and material of the attracting surface.
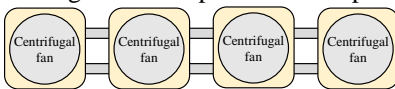
(a) Top view of a traveling-wave-type wall-climbing robot

(b) Traveling-wave-type wall-climbing robot on a curved surface

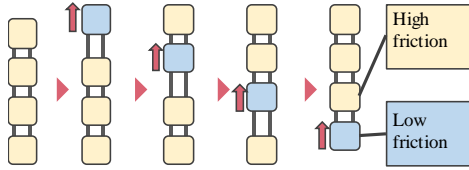Fig. 1 Overview of a traveling-wave-type wall-climbing robot

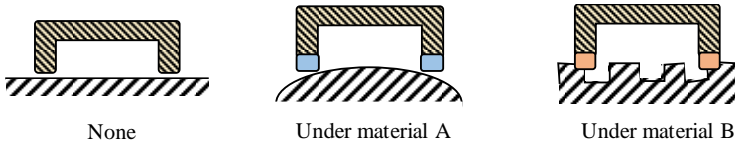Fig. 2 Movement of a traveling-wave-type wall-climbing robot

None   Under material A   Under material B

Fig. 3 Under material of a traveling-wave-type wall-climbing robot

3.3. *Calculation of frictional force and attractive force required for robot*

We calculate the frictional force and attractive force required for the adsorption at an angle θ made by the proposed robot to the wall surface. The dynamic equilibrium model of the robot is shown in Fig. 4, and the parameters are listed in Table 1. Because the unit changes the frictional force simultaneously with expansion and contraction, at the time of movement, a maximum of two low friction units are generated. Therefore, in the dynamic equilibrium model of the robot, these two are set as low friction units. Furthermore, the weight of the proposed unit is assumed to be 0.70 kg, and the weight of the model unit including the weight of the loaded equipment is set to 1.5 kg. The height of the center of gravity of the model unit is 70 mm, which is the proposed unit height. Further, the robot is a rigid body, and the attraction force and friction force are concentrated loads acting on the center of the face. Here, Equation (1) represents the sum of the necessary attraction forces obtained from the force components perpendicular to the attracting surface. Equation (2) indicates the required attraction force obtained from the moment around the lower part of the unit. When the robot is regarded as a rigid body, the center of rotation of the moment is the point that is the most difficult to support (Fig. 4, point A), and the two low-friction units are located as the unit with the weakest supporting force. Equation (3) shows the necessary friction coefficient obtained from the force component horizontal to the attracting surface.

$$(A_{\mathrm{h}} + A_{\mathrm{l}}) \geqq 2mg\cos\theta \tag{1}$$

$$A_{\mathrm{h}}(2a + l) + A_{\mathrm{l}}(2a + 5l) \geqq (4a + 6l)mg\cos\theta + H_{\mathrm{G}}mg\sin\theta \tag{2}$$

$$\mu \geqq 2mg\sin\theta / (A_{\mathrm{h}} + A_{\mathrm{l}} - 2mg\cos\theta) \tag{3}$$

To calculate the maximum required adsorption force and friction coefficient, we calculate θ that maximizes the value of each right side. From the differential function of Equations (1)–(3), the right-hand side is maximum when $\theta = 0°$, 87°, and 8.8°, respectively. Equations (4)–(6) show the expressions in which the numerical values of θ, and the values listed in Table 1, are substituted into the respective expressions.

$$A_h + A_l \geqq 29 \tag{4}$$

$$2A_h + 7A_l \geqq 1.3 \times 10^2 \tag{5}$$

$$\mu \geqq \frac{39.2 \sin\left\{\cos^{-1}\left(\frac{39.2}{A_h + A_l}\right)\right\}}{A_h + A_l - 39.2\cos\left\{\cos^{-1}\left(\frac{39.2}{A_h + A_l}\right)\right\}} \tag{6}$$
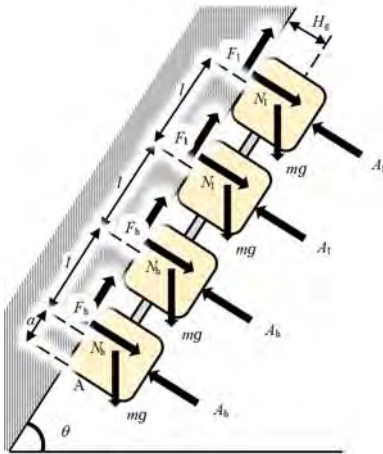
Fig. 4 Equilibrium model

Table 1 Parameters

	Parameter	Value
θ	Angle of an adhered surface	$0 \geqq \theta \geqq 2\pi$
A	Half length of a unit [m]	9.0×10^{-2}
Hg	Height of the center of gravity[m]	8.0×10^{-2}
M	Mass of a unit [kg]	2.0
G	Acceleration of gravity [m/s^2]	9.8
L	Distance between each center point of a unit [m]	0.30
A_l	Adhesion force of a low-friction unit [N]	-
A_h	Adhesion force of a high-friction unit [N]	-
N_l	Normal force of a low-friction unit [N]	-
N_h	Normal force of a high-friction unit [N]	-
F_l	Frictional force of a low-friction unit [N]	-
F_h	Frictional force of a high-friction unit [N]	-

4. Running Experiment

4.1. *Running experiment on a horizontal plane*

The developed robot is shown in Fig. 5, and the robot parameters are listed in Table 2. The moving speed of the robot was measured with a horizontal metal surface. In addition, the unit of this robot adopted a sponge rubber having a large

friction coefficient to the airplane fuselage surface and a sealing effect to the material of the lower part of the unit [11]. Table 3 lists the adsorption force and friction coefficient of this unit during high adsorption and low adsorption. These values satisfy Equations (4)–(6). Therefore, the robot can be adsorbed on the wall surface at an arbitrary angle.

After the beginning of expansion and contraction, the robot requires 25 s until one extension and contraction has been propagated to all the units and advanced (hereinafter referred to as a stroke), and the robot advances by 20 mm with one stroke. The time and moving distance necessary for the stroke depend on the performance of the linear motion servomotor.
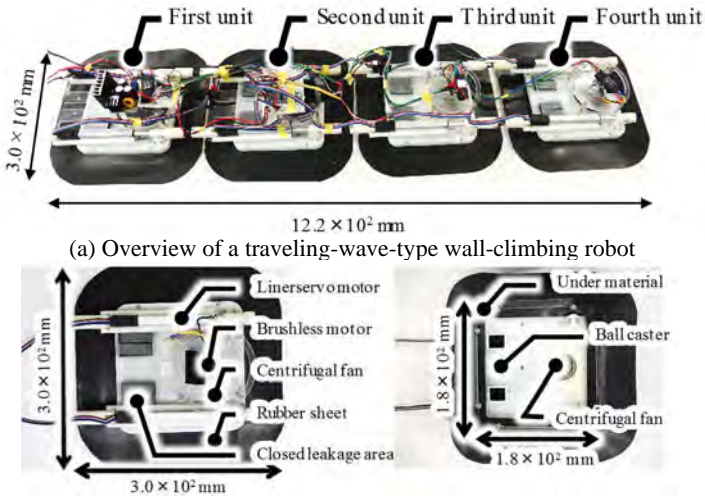
(a) Overview of a traveling-wave-type wall-climbing robot

(b) Negative pressure suction unit

Fig. 5 Traveling-wave-type wall-climbing robot

Table 2 Specifications of the traveling-wave-type wall-climbing robot

Parameter	Value
Weight [kg]	3.0
Length [mm]	1.2×10^3
Width [mm]	3.0×10^2
Height [mm]	80
Speed [mm/s]	0.80
Time required for a stroke [s]	25
Distance travelled in a stroke [mm]	20

Table 3 Measured values

Parameter	Value
Adhesion force of high-friction unit[N]	61
Adhesion force of low-friction unit [N]	30
Coefficient of friction	1.2

4.2. *Wall climbing and slip of robot*

The developed robot can climb on a metal wall, as shown in Fig. 6. The trajectory of each unit of the robot at this time is shown in Fig. 7, and the running state is shown in Fig. 8. Figure 7 shows that each unit slips immediately after it is extruded into a linear servomotor. Further, the differences in the feed speeds of the linear servomotor that pushes the unit from the bottom at the time of expansion and contraction propagation, and the linear motion servo motor that draws from above were visually confirmed. This may be attributed to the difference in load applied by its own weight. Furthermore, from this difference in feed speed, the motor pulling the unit from the above stops first. Therefore, force is applied temporarily to the unit in the direction opposite to the climbing direction, and as shown in Fig. 7, slip occurs immediately after the extension of the unit.
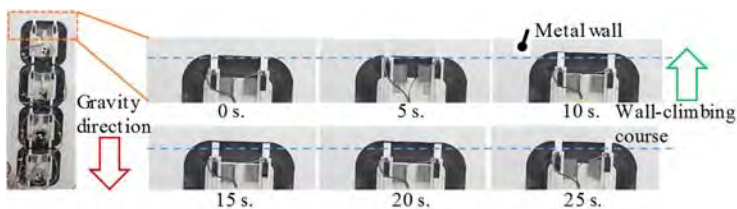

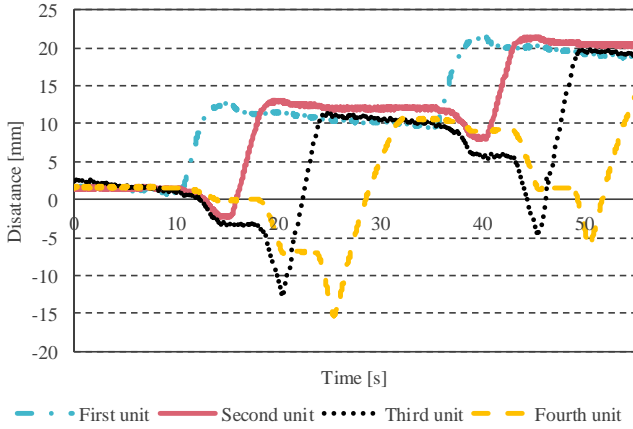Fig. 6 Example of wall-climbing experiment

Fig. 7 Trajectory of the units

5. Conclusion

In this study, we developed a traveling-wave-type wall-climbing robot for high-altitude work such as inspection of an airplane surface. The main conclusions obtained from the study are as follows:

1. A new negative pressure absorption-wall-type mobile robot was proposed.
2. The frictional force and adsorption force necessary for the robot to traverse the surface were calculated.
3. A running experiment was conducted considering a horizontal surface and a vertical wall surface. We confirmed that the robot satisfied the performance requirements considered to be necessary for airplane inspection.

In the future, we will perform a running experiment on a ceiling surface, a curved surface, a step within 5 mm, and on a gap. We will devise an inspection method suitable for this robot and perform mounting of the inspection equipment. In addition, if necessary, we will reconsider the used actuator and improve the running speed of the robot.

References

1. DEATH ON THE JOB, *AFL-CIO Safety and Health Department* (April 2017).
2. Al Habsi, S., Shehada, M., Abdoon, M., Mashood, A., and Noura, H., *Integration of a Vicon Camera System for Indoor Flight of a Parrot AR Drone*, International Symposium on Mechatronics and its Applications (ISMA) (07 January 2016).

3. Zhiwei, X., Muhua, C., and Qingji, G., *The structure and defects recognition algorithm of an airplane surface defects inspection robot*, IEEE International Conference on Information and Automation (June 22 -25, 2009).

4. Zhou, Q., and Li, X., *Design of Wall-climbing Robot Using Electrically Activated Rotational-flow Adsorption Unit*, IEEE/RSJ International Conference on Intelligent Robots and Systems (IROS) (October 9-14, 2016).

5. T. Amakawa, T. Yamaguchi, N. Tadami, Y. Yamada and T. Nakamura, *DEVELOPMENT OF OMNIDIRECTIONAL WALL-CLIMBING ROBOT FOR AIRPLANE INSPECTION*, International Conference on Climbing and Walking Robots and the Support Technologies for Mobile Machines (September 11-13, 2017).

6. Wang, K., Liu, R., and Qu, Y., *Development of a Double-Cavity Climbing Robot for On-Site Inspection of Glass-Curtain-Walls,* IEEE International Conference on Information and Automation Yinchuan (August 2013).

7. K. Satoh and T. Nakamura, *Development of an omni-directional mobile robot based on snail locomotion,* in Proc. 7th Int. Conf. Climbing and Walking Robots and Support Technologies for Mobile Machines, pp. 144-152 (2007).

8. T. Ogawa, M. Yamoto, and T. Nakamura, *Proposed omnidirectional locomotion strategy for traversing-wave-type mobile robot*, in Proc. 14th Int. Conf. on Climbing and Walking Robots and the Support Technologies for Mobile Machines, pp. 127–134, (2011).

9. T. Go, T. Osawa, T. Ogawa, and T. Nakamura, *Development of Traveling Wave Type Omnidirectional Wall Climbing Robot using Permanent Magnetic Adhesion Mechanism and Proposal of Locomotion Strategy for the Robot*, in Proc. 2014 IEEE/ASME Int Conf. Adv. Intel. Mechatron., pp.1000–1010, (2014).

10. T. Amakawa, T. Yamaguchi, Y. Yamada and T. Nakamura, *Proposing an adhesion unit for an traveling-wave-type, omnidirectional wall-climbing robot in airplane body inspection applications*, IEEE International Conference on Mechatronics, (Feb. 2017).

11. T. Amakawa, T. Yamaguchi, Y. Yamada, T. Nakamura, *Development of an Adhesion Unit for a Traveling-wave-type, Omnidirectional Wall-climbing Robot in Airplane Body Inspection*, EEE International Conference on Advanced Intelligent Mechatronics, (July 3-7, 2017).

12. T. Ymaguchi, T. Go, T. Amakawa, Y. Yamada and T. Nakamura, *Development of Negative Pressure Suction Mechanism in Omnidirectional Wall-climbing Robot for Inspect of Airplanes*, International Conference on Climbing and Walking Robots and the Support Technologies for Mobile Machines, pp.106-114 (2016).

STABLE CLIFF CLIMBING FOR HEXAPOD ROBOT WITH ARTICULATED BODY

A. V. PANCHENKO

Faculty of Mechanics and Mathematics, Lomonosov Moscow State University, Moscow, 119991, Russia
E-mail: PanchenkoAV@vap.ru

V. E. PAVLOVSKY

Faculty of Mechanics and Mathematics, Lomonosov Moscow State University, Moscow, 119991, Russia
E-mail: vlpavl@mail.ru

The paper describes kinematic control for hexapod robot with three–segment articulated body. Forward and inverse kinematics for articulated body described. Static stability studied in case of climbing the so–called cliff obstacle. Conditions for static stability during climbing sequence provided.

Keywords: Multi–legged robot; obstacle climbing; articulated body; simulation.

1. Introduction

Study of walking machines is a rather old question. Starting from Ancient China mechanical designs[1] and ending with state of the art reinforcement learning[2] and model predictive control approaches.[3] Multi–legged walking robots are complicated systems in terms of control and planning due to significant number of degrees of freedom (d.o.f.) and actuators, complexity of the environment and etc. Nowadays the most complex and robust walking machines are made by Boston Dynamics company.[4] Its robots are capable of working in human environment and outdoors. The basis of their approach is model predictive control and non-linear optimization.

The main subject of article is to find simple approaches for building control algorithms for multi–legged walking robots with articulated body. It is clear that robots with flexible body can overcome obstacles that are more complex.

For that purpose, a hexapod robot with three–segment body was studied

in task of overcoming a cliff obstacle using Coulomb forces with coefficient of static friction less than 1.

Static stability equations were resolved for robot in different configurations with additional assumptions of symmetry. Motion sequence for climbing on a cliff with static stability preservation was build and verified in computer simulation.

The designed approach for static stability study can be further used for other types of obstacles, such as narrow passage, sharp ditch, windrow and so on. Besides of that, the approach can be applied for different models of robot's body without any modifications.

2. Robot Kinematics

Let us consider robot depicted on figure Fig. 1. It has six so-called insectomorphic legs, i.e. insect-like leg kinematics. Each leg has three degrees of freedom. Body consists of three rigid segments connected with hinges to each other. Body that consists of several segments connected to each other with controllable joints and can change its geometry is called articulated.
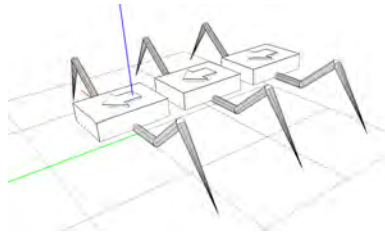
Fig. 1.   Hexapod robot with articulated body.

The total number of degrees of freedom (d.o.f.) for specified robot is 26:

- 3 d.o.f. for each leg, i.e. 18 d.o.f. for all legs;
- 2 d.o.f. for body segments;
- 6 d.o.f. for the whole system as one single body.

Overall it's 26 d.o.f. and 20 of them can be controlled with actuators installed in corresponding rotational joints. Leg kinematics is well–known and was already studied in all details.

3. Cliff Obstacle

Cliff obstacle consists of three planes two of which are horizontal and one is vertical as depicted on Fig. 2.
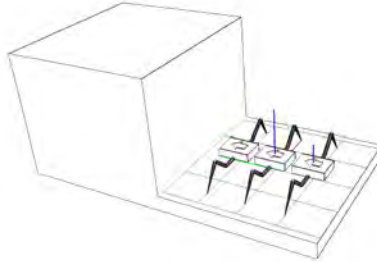

Fig. 2.   Cliff obstacle.

The distance between two horizontal planes is equal to H. Robot starts from the lower horizontal plane and his goal is to climb up the higher horizontal plane using only the Coulomb friction. To overcome cliff obstacle robot moves using so-called gallop gait when a pair of symmetrical legs from left and right sides of the robot are in transition state and the others are in support state, i.e. in every moment of time there are four legs in contact with obstacle. Body kinematics will be considered in next section.

4. Body Kinematics

Robot's body consists of three equal rigid segments connected to each other with rotational joints with axes aligned in lateral direction of the body. Each segment has a pair of legs connected. Additional joints with angles δ_1 and δ_2 in the robots body allow to bend body and follow the surface shape, shift legs mounting points towards to supporting surface. To find body joint angles the following procedure is defined.

Initial and goal poses for middle segment are connected with a cubic spline curve, which represents target trajectory for middle segment. If segments and their trajectory are known, then the task is solved through simple linear approximation as depicted on Fig. 3.

To keep the contact points on the goal trajectory all joints should act in a coordinated way. At every moment of time all joint coordinates must be
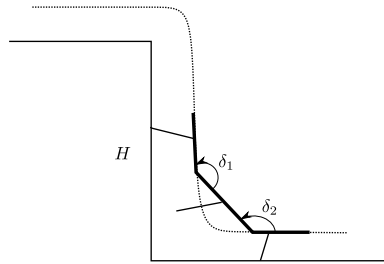
Fig. 3.   Body inverse kinematics through simple linear approximation.

updated to keep the end effectors at the goal position. Additional mobility inside the robots body should be taken into account because all legs are connected to the different segments. Target point $\overline{R}_i$ for i-th leg is given in global reference frame. To obtain leg joint angles the inverse kinematic equations are used, point $\overline{R}_i$ must be translated into legs reference frame. To manage all relative coordinate transformations of shifts and rotations between body segments, legs and joints, homogeneous coordinates are used. Calculation of all coordinate transformation for each leg at every moment of time can be easily done automatically through well-known kinematics of robot. The main differences between articulated body and single segment body are:

- Higher ability to overcome obstacles – segments follow the surface;
- Articulated body is able to shift mounting points of its legs – service region is not a constant, i.e. in some conditions robot can reach contact surface and put legs on it;
- Center of gravity is shifted in a wider range with all else parameters being equal – critical parameter in static stability preservation in extreme conditions.

5. Cliff Climbing Stability

The system is stable when sums of all external forces and all momentums are equal to zero.

$$
\begin{cases}
\sum\limits_{i=1}^{N} \overline{R}_i + \overline{P} = 0 \\
\sum\limits_{i=1}^{N} [\overline{r}_i \times \overline{R}_i] + [\overline{r}_c \times \overline{R}_c] = 0
\end{cases}
\tag{1}
$$

The following configurations of supporting legs displacement should be studied for static stability:

- All legs on some horizontal plane. This case is already well studied;
- Front legs lean against the vertical plane and rear legs stand on the lower horizontal plane. Let us refer to this configuration as Number One.
- Front legs are placed at the upper horizontal plane, while the rear legs stand on the vertical plane. Let us refer to this configuration as Number Two.
- All legs stand on the upper horizontal plane – this case is similar to the initial one.

Considering the robot as a slow moving system at every moment of time let us find conditions for static stability. Reference frame Oxyz is defined as depicted on Fig. 4.

5.1. *First Configuration*
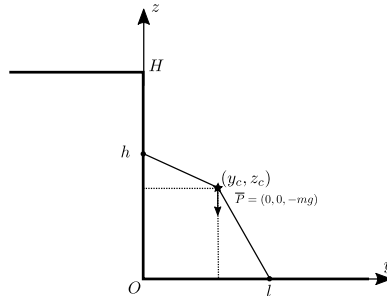
Fig. 4. First static configuration.

Contact points of the legs for first configuration are as follows:

$$\bar{r}_1 = (d, 0, h), \bar{r}_2 = (-d, 0, h), \bar{r}_3 = (d, l, 0), \bar{r}_4 = (-d, l, 0). \qquad (2)$$

There is a reaction $\overline{R}_i$ acting on the robots legs at each contact point:

$$\overline{R}_i = N_i \cdot \bar{n}_i + F_\tau^i \cdot \bar{\tau}_i + F_\nu^i \cdot \bar{\nu}_i \qquad (3)$$

The $\bar{\tau}_i$ and $\overline{nu}_i$ vectors have the following coordinates:

$$\begin{aligned}
\bar{n}_1 &= (0,1,0),\ \bar{\tau}_1 = (0,0,1),\ \bar{\nu}_1 = (1,0,0),\\
\bar{n}_2 &= (0,1,0),\ \bar{\tau}_2 = (0,0,1),\ \bar{\nu}_2 = (1,0,0),\\
\bar{n}_3 &= (0,0,1),\ \bar{\tau}_3 = (0,1,0),\ \bar{\nu}_3 = (1,0,0),\\
\bar{n}_4 &= (0,0,1),\ \bar{\tau}_4 = (0,1,0),\ \bar{\nu}_4 = (1,0,0).
\end{aligned} \tag{4}$$

The center of gravity has coordinates:

$$\bar{r}_c = (0, y_c, z_c) \tag{5}$$

The gravity force $\overline{P}$ acts on the center of gravity of the robot:

$$\overline{P} = (0, 0, -P) \tag{6}$$

The equations of static stability for first configuration are as follows:

$$\begin{cases}
F_\nu^1 + F_\nu^2 + F_\nu^3 + F_\nu^4 = 0,\\
N_1 + N_2 + F_\tau^3 + F_\tau^4 = 0,\\
F_\tau^1 + F_\tau^2 + N_3 + N_4 = P,\\
\quad N_1 h + N_2 h + P y_c = l(N_3 + N_4),\\
\qquad d(F_\tau^1 + N_3) = F_\tau^2 d + F_\nu^1 h + F_\nu^2 h + N_4 d,\\
\qquad d(F_\tau^3 + N_1) = F_\tau^4 d + N_2 d + F_\nu^3 l + F_\nu^4 l.
\end{cases} \tag{7}$$

The total number of equation is six. The number of unknown variables is twelve. Let us assume that the friction forces are modelled with Coulomb mathematical model:

$F_j^i = k_j^i \cdot N_i$, where k_j^i is coefficient of friction for i-th leg in j-th direction.

After substitution of the Coulomb friction model, the Eq. (7) will transform into the following system:

$$\begin{cases}
N_1 k_\nu^1 + N_2 k_\nu^2 + N_3 k_\nu^3 + N_4 k_\nu^4 = 0,\\
\quad N_1 + N_2 + N_3 k_\tau^3 + N_4 k_\tau^4 = 0,\\
\quad N_3 + N_4 + N_1 k_\tau^1 + N_2 k_\tau^2 = P,\\
\quad N_1 h + N_2 h + P y_c = l(N_3 + N_4),\\
\qquad d(N_3 + N_1 k_\tau^1) = dN_4 + dN_2 k_\tau^2 + hN_1 k_\nu^1 + hN_2 k_\nu^2,\\
\qquad d(N_1 + N_3 k_\tau^3) = dN_2 + dN_4 k_\tau^4 + lN_3 k_\nu^3 + lN_4 k_\nu^4
\end{cases} \tag{8}$$

The number of unknowns variables remains the same, and besides $N_i > 0$. Let us introduce additional assumptions that the left and the right side of the robot are loaded equally and coefficients of friction are the same between left and right legs:

$$\begin{cases} k_\nu^1 = -k_\nu^2 = k_\nu, \\ k_\nu^3 = -k_\nu^4 = k_\nu, \\ k_\tau^1 = k_\tau^2 = k_\tau^u, \\ k_\tau^3 = k_\tau^4 = k_\tau^d, \\ N_1 = N_3 = N_u, \\ N_2 = N_4 = N_d. \end{cases} \tag{9}$$

The system of three equations and four variables obtained:

$$\begin{cases} N_u + N_d k_\tau^d = 0, \\ 2N_d + 2N_u k_\tau^u = P, \\ 2hN_u + Py_c = 2lN_d. \end{cases} \tag{10}$$

Number of unknowns is still greater than number of equations. One more assumption must be introduced:

$$k_\tau^u = k_\tau^d = k_\tau > 0 \tag{11}$$

Finally, the system of three equations and three unknowns is obtained:

$$\begin{cases} N_u = N_d k_\tau, \\ 2N_d + 2N_u k_\tau = P, \\ 2hN_u + Py_c = 2lN_d. \end{cases} \tag{12}$$

Let us find unknown reactions N_u, N_d and k_τ. From first and second equations of Eq. (12) follows:

$$N^u = N^d k_\tau, \\ N^d = \frac{P}{2(1 + k_\tau^2)}. \tag{13}$$

After substituting Eq. (13) to the third equation of Eq. (12) we have quadratic equation relative to k_τ:

$$y_c k_\tau^2 + h k_\tau + (y_c - l) = 0 \tag{14}$$

There are two solutions for quadratic Eq. (14), but only one satisfies condition $0 < k_\tau < 1$:

$$0 < k_\tau = -\frac{h - \sqrt{h^2 - 4y_c^2 + 4ly_c}}{2y_c} < 1 \tag{15}$$

5.1.1. *Dimensionless parameters*

It is easy to see that the Eq. (15) for k_τ depends on l, h and y_c parameters that are measured in meters they all have the same physical dimension. Let us use this circumstance and define the following dimensionless parameters:

$$p_1 := \frac{h}{y_c}, \; p_2 := \frac{l}{y_c}, \; \text{where } y_c \neq 0. \tag{16}$$

After solving Eq. (15) with substituted Eq. (16), the solution of Eq. (15) is depicted on Fig. 5.
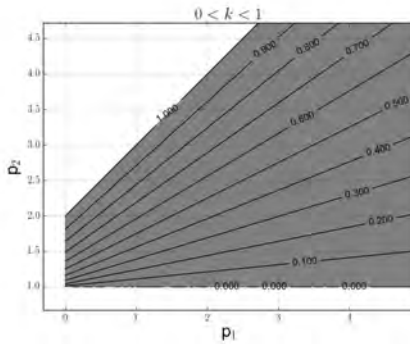
Fig. 5.   Solution of Eq. (15) with labeled contour lines for k_τ as a function of (p_1, p_2).

From Fig. 5 it becomes clear that if there is lack of friction in contact points the robot should:

- move its center of gravity closer to the rear legs;
- choose contact points higher on the vertical plane for front legs;
- choose contact points closer to vertical plane for rear legs.

5.2. *Second Configuration*

Leg contact points for the second configuration are:

$$\begin{aligned} \bar{r}_1 = (d, l, H), \; \bar{r}_2 = (-d, l, H) \\ \bar{r}_3 = (d, 0, h), \; \bar{r}_4 = (-d, 0, h) \end{aligned}, \text{where } l < 0, H > h, y_c > l. \tag{17}$$

Similarly, for the second configuration we get the following system of three equations:

$$\begin{cases} N_u - N_d k_\tau = 0, \\ 2N_u + 2N_d k_\tau = P, \\ 2N_d h + P y_c = 2N_u(l + H k_\tau) \end{cases} \tag{18}$$

There are two possible solutions for k_τ, but only one meets requirement $0 < k_\tau < 1$:

$$0 < k_\tau = \frac{(H - h) - \sqrt{(H - h)^2 - 4y_c^2 + 4ly_c}}{2y_c} < 1 \tag{19}$$

5.2.1. *Dimensionless parameters*

Let us find solution of inequality $0 < k_\tau < 1$ using the following dimensionless parameters:

$$p_1 := \frac{(H - h)}{y_c}, p_2 := \frac{l}{y_c}, where \ y_c \neq 0. \tag{20}$$

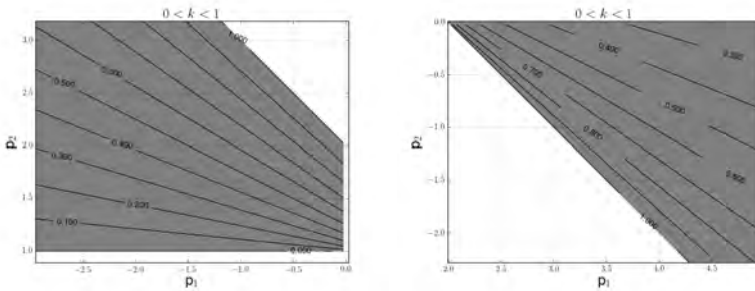The solution of Eq. (19) is depicted on Fig. 6.

Fig. 6.   Solution of Eq. (19). Left - $y_c < 0$, right - $y_c > 0$.

From Fig. 6 it can be shown that for case when $y_c > 0$ to reduce the value of k_τ robot should:

- keep its center of gravity far from front legs;
- keep rear legs as low as possible;
- keep front legs closer to cliff edge.

From Fig. 6 it can be shown that for case when $y_c < 0$ to reduce the value of k_τ robot should:

- keep its center of gravity closer to front legs;
- keep rear legs as low as possible;
- keep front legs closer to cliff edge.

In Eq. (20) we have considered substitution in assumption that $y_c \neq 0$. Let us see what happens when center of gravity is right above the cliffs edge in second configuration.

5.2.2. *Second configuration. y_c equals to zero*

If the $y_c = 0$ the equations of static stability Eq. (18) will transform into the following system:

$$\begin{cases} N_d - N_u k_\tau & = 0 \\ 2N_u + 2N_d k_\tau = P \\ N_d h - N_u l & = H N_u k_\tau \end{cases} \tag{21}$$

There is only one solution for k_τ, N_u and N_d for Eq. (21):

$$\begin{cases} k_\tau & = -\dfrac{l}{H-h}, \\ N_u & = \dfrac{P(H-h)^2}{2((H-h)^2 + l^2)} \\ N_d & = \dfrac{-Pl(H-h)}{2((H-h)^2 + l^2)} \end{cases} \tag{22}$$

Due to Eq. (17) the Eq. (22) for k_τ is always greater than zero. From the other side, the requirement $k_\tau < 1$ is equivalent to the following inequality:

$$0 < -l < (H-h), \, where \, l < 0 \tag{23}$$

Equation (23) means that to provide stable configuration in case when $y_c = 0$ the contact points should be chosen in a way, that the front legs should be closer to cliff edge than the rear legs.

6. Hexapod simulation for cliff climbing

To verify the static stability conditions the computer simulation of articulated hexapod was made. The "Universal Mechanism"[5] software package

was used to provide dynamical model of the articulated hexapod robot and the cliff obstacle. All robot's legs have so called viscous elastic point contact models with the cliff obstacle.
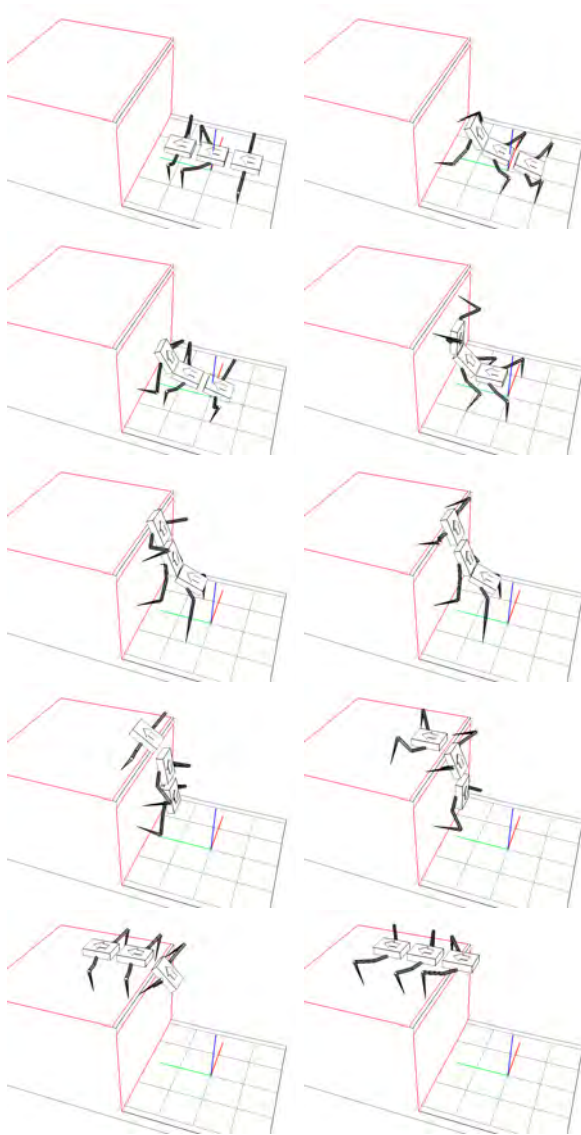

Fig. 7.   Climbing motion sequence (left-to-right, top-to-bottom).

The desired robot motion was manually scripted as list of scheduled commands for leg's positions and body configuration along with position and orientation. Robot's climbing motion sequence during simulation is depicted on Fig. 7. The resulting time of climbing maneuver in quasi static regime of motion takes about 50 seconds to climb up the cliff. The ratio between real and simulation time is approximately equal to 1 on computer with Core-i7 CPU and GTX950M GPU.

7. Conclusion

The analysis of robot's configurations in different poses on the cliff proved that stable quasi static motion is possible for all steps, i.e. the robot is capable of climbing the cliff with static stability preservation using only Coulomb friction forces. Articulated three segment body has shown advantages in comparison with similar rigid body in context of extreme obstacle overcoming. On the other hand, increased passability requires more complex motion planning and control. Conditions for statics stability for all main climbing configurations obtained.

Acknowledgements

References

1. H.-S. Yan, *Journal of the Chinese Society of Mechanical Engineers* **26**, 133 (2005).
2. X. B. Peng, G. Berseth, K. Yin and M. Van De Panne, *ACM Transactions on Graphics (TOG)* **36**, p. 41 (2017).
3. H. Diedam, D. Dimitrov, P.-B. Wieber, K. Mombaur and M. Diehl, On-line walking gait generation with adaptive foot positioning through linear model predictive control, in *Intelligent Robots and Systems, 2008. IROS 2008. IEEE/RSJ International Conference on*, (Nice, France, 2008).
4. M. Raibert, K. Blankespoor, G. Nelson and R. Playter, *IFAC Proceedings Volumes* **41**, 10822 (2008).
5. Universal mechanism `http://www.umlab.ru/en`.
6. Y. F. Golubev and V. Koryanov, *Journal of Computer and Systems Sciences International* **47**, 139 (2008).
7. Y. F. Golubev and V. Koryanov, *Journal of Computer and Systems Sciences International* **48**, p. 801 (2009).
8. A. V. Panchenko, I. A. Orlov and V. E. Pavlovsky, Control algorithm for walking robot with mosaic body, in *ASSISTIVE ROBOTICS: Proceedings*

of the 18th International Conference on CLAWAR 2015, (Hangzhou, China, 2016).

9. Y. F. Golubev, V. V. Korianov, V. E. Pavlovsky and A. V. Panchenko, Motion control for the 6-legged robot in extreme conditions, in *Nature-Inspired Mobile Robotics*, (Sydney, Australia, 2013).

MOORING CHAIN CLIMBING ROBOT FOR NDT INSPECTION APPLICATIONS

MATTHEW KIMBALL, AMIT SAIN, ARTUR GMEREK, PETER COLLINS, ANDREW WHEATLEY, KIRAN SHAH, JIANWEI LIU, MAHESH DISSANAYAKE[1], JESSICA CAROLL, ANGELOS PLASTROPOULOS, PANAGIOTIS KARFAKIS, GURVINDER S VIRK AND TARIQ SATTAR[1]

InnotecUK, Hildersham Road, Cambridge, CB21 6DR, UK

[1] *London South Bank Innovation Centre,103 Borough Road, London SE1 0AA, UK*

Inspection of mooring chains is a dangerous and costly procedure covering inspection above and below the waterline. The paper presents initial results from the RIMCAW project which was aimed at designing and building an inspection robot able to climb mooring chains and deploy NDT technologies for scanning individual links thereby to detecting critical defects. The paper focuses on the design and realisation of the inch worm type novel crawler developed and tested in the TWI Middlesbrough water tank.

1. Introduction

1.1. *Background*

With increasing global energy demand, the number of floating oil and gas production systems have increased dramatically since the 1990s. It is not possible to move most floating oil production systems for inspection or repair. Moreover, mooring systems which are used to attach the floating platforms to the seabed often experience high tidal waves, storms and other harsh environmental conditions. Therefore, ensuring integrity of mooring chains is crucial, because single mooring line failure can cost approximately £2-10.5M [1]. There were 21 accidents due to mooring failures between 2001 and 2011 including 8 multiple mooring chain breaking incidents [2]. Mooring chain breakage can cause vessel drift, riser rupture, production shutdown and hydrocarbon release. For example, "Gryphon Alpha" had to spend $1.8 billion to resume operations after its mooring failure [3]. Replacing mooring chains to inspect the original is expensive and there is a high probability of causing damage. In view of these issues, the RIMCAW project was formulated to develop a mobile crawler robot able to climb on mooring chains while in service and be able to perform in-situ inspection in both air and water.

1.2. *Review of mooring chain inspection systems*

Attempts to establish effective climbing robot mechanisms have been made but due to the mechanical complexity mooring chains as climbing structures, research has not progressed beyond initial experimental stages. The "MoorInspect" inchworm climbing robot [4] was huge and weighed 450 kg in air and carried NDT equipment to give a total weight of 750 kg. The ICARE platform is another heavy climbing robot for subsea cleaning and inspection of anchor lines [5] which uses a human-like climbing method with two paws. Such heavy robots are not easily deployable in offshore environments, nor do they have sufficient manoeuvrable capabilities to climb over the chain links in realistic scenarios when there is chain link mis-alignment and catenary curves in the chain structures. These robots are deployed manually by using divers and boats. Therefore, it is not practically possible to handle heavy large platforms in small boats with divers without major lifting equipment.

A novel automated ultrasonic inspection system to inspect mooring chains during the manufacturing process [6] where the welded joints on chain links are inspected during manufacture. The main aim of the project "ChainTest" was to develop a system which can be operated without bringing the chain on board [7]. A mechanism was developed but during final tests, the robot was unable to perform the inspected as designed.

1.3. *Design requirements*

Mooring chains are often subjected to high environmental changes due to tidal waves, wind, etc. Therefore, it is required to design an automated/robotic system that can tolerate real-world in situ conditions. The mooring chain link structures are curved and mostly rusted with uneven surfaces, so the inspection system should be able to handle the physical nature of mooring chains. Following detailed analysis, it was concluded that a compact climbing robot able to work in subsea environments needed to be developed for the solution to have any commercial viability. Furthermore, it was clear that the robot must be able to handle climbing on a range of chain scenarios and sizes as shown in Figure 1.

a. Taut-leg scenario in deep water b. Catenary chains in shallow water   c. Mooring chains range
Figure 1 - Mooring chain scenarios and range of sizes

The robot should be easily deployed and retrieved. Therefore, it is necessary to make the system lightweight while still able to carry a payload of ≈ 12kg. The adhesion mechanism for vertical climbing should be sufficient to keep the robot attached to the chain during motion. Moreover, due to the amphibious nature of mooring chains, the developed robot must be marinized to operate in real-world normal and abnormal conditions.

2. Design methodology

2.1. *Deployment plan*

Methods to deploy the robot were studied in detail to identify all procedural requirements as testing of the developed platform was planned to take place in a 7m deep test tank at TWI Middlesbrough with a 10-link chain suspended from an overhead gantry system into the water. The dimensions of the chain are outlined in the Figure 2.

a. CAD model of test mooring chain with dimensions   b. Picture of the testing chain
Figure 2 – Details of test sample mooring chain

It was important that the prototype RIMCAW system realised was able to satisfy all the testing requirements planned and of a real deployment scenario as presented in Figure 3.
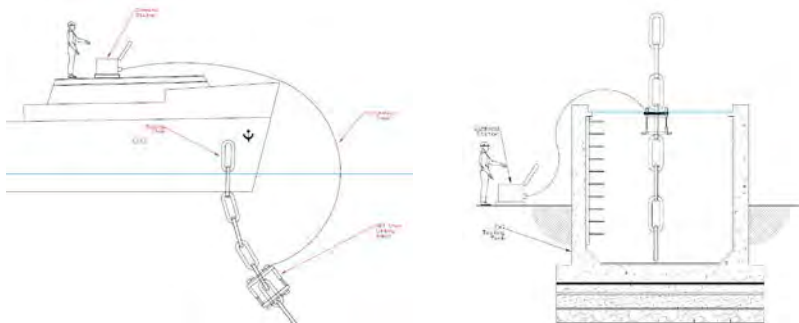
a. Real-world subsea RIMCAW scenario   b. Tank facility testing scenario at TWI
Figure 3 - Deployment RIMCAW scenarios

2.2. *Concept design and analysis*

Five different design concepts were developed, as presented in 4 with different locomotion and adhesion/gripping mechanism configurations being explored from which different crawler ideas emerged. Each design was analysed and investigated with respect to the outlined crawler criteria and the associated engineering challenges. The final design, Figure 5e, concept was selected after a detailed Delphi study involving the full technical team revealing that it was best suited to meet all the technical, fiscal and time requirements.

a) Concept 1   b) Concept 2   c) Concept 3   d) Concept 4   e) Concept 5
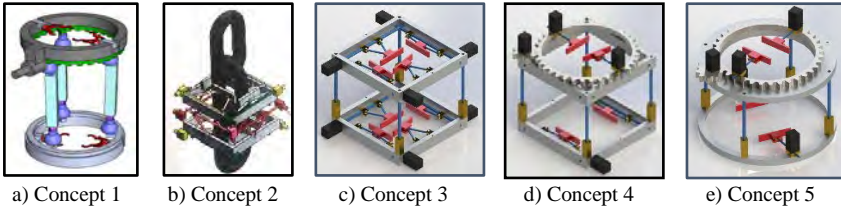
Figure 4 – RIMCAW concept designs developed and investigated

3. RIMCAW robotic platform

3.1. *Mechanical design*

The final RIMCAW robot design and actual robot is shown in Figure 5; this was based on a standard Stewart platform, comprising six prismatic actuators attached in pairs to three positions on the platform's baseplate, crossing over to three mounting points on the top plate. This design allows the robot to control the pitch, roll and yaw of the top and bottom baseplates. This controllability of the platform's crawling orientation is crucial as it needs the robot to traverse the various catenary curves of mooring chains likely to be found in real scenarios. In addition, this configuration allows the robot to contract and expand allowing it to crawl by inch worming along the chain links. The method of positioning and securing the robot onto the mooring chain structure had been extensively studied and a latch/ hinge system was incorporated into the design to allow simple opening of the simplify the deployment process for end user.

a) Final detailed CAD model   b) Actual RIMCAW robot   c) Command station and umbilical

**Figure 5 - Detailed Mechanical Design**

3.2. *Electrical design*

For testing and trials, a custom designed command and control box was required to supply power to the RIMCAW robot as shown in Figure 6. After researching British Standards for safe operating electrical power supplies in a submerged water environment, it was found that the 30V DC was the permissible SELV (Safety Extra Low Voltage) for 'Swimming Pools and Basins' outlined in BS EN 7671:2008, Regulation 702.410.3.4.1. Four IP68 enclosures with dimensions 260x160x120 mm were used to house all electronics. To minimise cables and entries, the electronics were divided into sub-sections of the electrical system. Box 1 housed the electronics required for the Stewart platform, Box 2 housed the electronics required for the gripping function, Box 3 housed the power electronics, and Box 4 housed the communications systems.

3.3. *Software design*

The control of the low-level systems (actuators and sensors) was accomplished via local specialised controllers. The mid-level systems (Raspberry Pi and Arduinos) were used to coordinate the control functions specified by the top-level interface. The top-level system (GUI) provides operators with a simple means of controlling the chain crawling functionality using visual feedback from the onboard cameras.

As development progressed, the software architecture evolved, and the messaging protocol and variable details were finalised. The robot's roll, pitch, yaw, crawling motion, upper and lower grippers and gripper rotation could all be controlled via one message sent from either the keyboard, joystick or GUI interfacing devices. A ROS switch node was developed to provide an easy means of switching between the different forms of top level control.
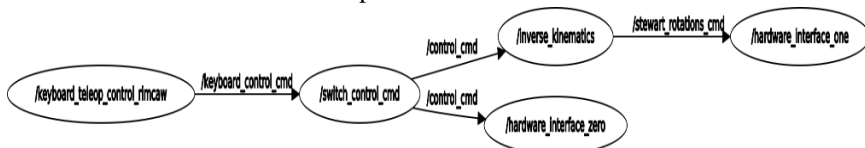
Figure 6 - ROS node/ topic network

Figure 6 shows the ROS node and topic communication structure with keyboard control outlined. The kinematics of the Stewart platform is a well-documented

problem and used to control the 6 actuators as required. In robotics, singularities can pose serious problems to the overall operation and hence proximity to such singularity points needs to be monitored and avoided. To mitigate this issue, precautions had to be built into the control system where the inverse kinematics node, motions and orientations were restricted. The desired roll, pitch and yaw angles were limited to ±10° range and the x, y positions were locked to zero, allowing only movement in the z axis for performing the climbing function. For the chain climbing function, movement outside this constraint is not felt to be necessary at the initial stages. If the inverse kinematic solver derived any extension outside of its defined boundaries, the move request would be ignored, and the previous orientation would not change.

4. Experimental testing

4.1. *Procedure*

A structured approach was formulated to perform testing and demonstration of the realised RIMCAW climbing robot. Three tests were planned to verify the integrity of key aspects of the design; if there was failure of one, the remaining tests could not proceed. These tests are as follows:

- Test 1 to assess the neutral buoyancy. This was performed by slowly winching the robot into the tank and verifying that the weight of the platform was cancelled out in water via the attached floatation foam
- Test 2 was to assess the water ingress integrity of the robot; after complete submersion of the platform, all the electronic components and devices had to be confirmed to be fully functioning, and
- Test 3 was to assess the functionality of the mobile robot, verifying the crawler's ability to climb the test chain.

The command station was set up next to the test tank at TWI Middlesbrough and a split screen display was set up to view the video from Figure 7. Compressed air was connected to the enclosures via a regulator, set to 0.3 Bar. Using winch straps connected to the eyebolts of the platform, the TWI staff picked up and slowly lowered the platform into the tank.

a. Command station   b. Testing and preparation area

Figure 7 - Testing area and command station deployed at TWI Middlesbrough

### 4.2. *Test 1 – Neutral buoyancy*

For this test the robot was slowly submerged using a gantry system over the tank. The operators of the gantry were instructed not to provide too much slack or move the robot too quickly. At a certain point during the lowering process, the winch straps became slack as the buoyancy was confirmed. The buoyancy was able to counteract the weight of the robot. However, it was noted that part of the platform remained slightly above the water line, indicating that the robot had positive buoyancy. This was deemed to be acceptable as the buoyancy could be adjusted during the testing process if it was found to affect the climbing functionality.

4.3. *Test 2 – Water ingress integrity*

The robot was submerged for ≈15 minutes, to allow for all trapped air bubbles to escape. Air leaks are indicated by a visible streams of air bubbles, which were then searched for. The seals on all the enclosure lids were found to be satisfactory. Minor leaks were found to be coming from the cable glands on the gripper control box indicating it was not tightened properly. Proceeding with Test 2 was deemed to be satisfactory provided that compressed air was connected to maintain the positive pressure in the enclosures for maintaining water ingress integrity. While still in the water, the functionality of sensors and actuators was checked. The Stewart platform and manipulators were moved and were verified to be functioning correctly.

4.4. *Test 3 – Chain climbing functionality*

The mooring chain was introduced into the tank before the robot was lowered next to it. Two overhead gantry systems could not bring their end effectors together, requiring the platform to be lowered into the tank, with sufficient slack on the winch to allow the diver to move the robot onto the mooring the chain, Figure 8.
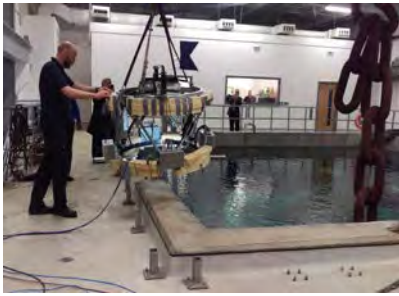
Step 1: Robot raised off ground for moving to water tank

Step 2: Robot lowered into water tank

Step 3: Robot moved onto chain by diver

Figure 8 - Deployment of RIMCAW robot prototype platform

This was executed without any problems, the one diver was able to successfully manoeuvre the robot around the chain, close it and lock the latches, Figure 9. However, when it came to grasping the mooring chain, the grippers could not reach the chain. This was found to be an electrical limitation preventing the actuators from achieving full extension.

a) Submerged robot

b) Diver opening latch

c) Robot placed onto chain

Figure 9 - On-board camera view of the attachment to the mooring chain

5. Conclusions

There were several technical challenges and problems that were experienced during the design and testing phases. Minor software and electronic problems, prevented completion of the final functionality tests. Although NDT inspection testing of mooring chains was not completed, the developed RIMCAW robot met the initial design specifications for mobility and is able to operate underwater on mooring chains as required. The robot is being considered for further improvement to meet different underwater inspections applications. The aim is to make improvements to facilitate developments and testing so that commercially viable means of inspecting underwater assets is possible.

Acknowledgments

References

1. N. D. E. Limited, "*Floating production system -JIP FPS mooring integrity*," Health and Safety Executive, Aberdeen, 2016.
2. M. Kai-tung, A. Duggal, P. Smedley, D. L'Hostis and S. Hongbo, "*A Historical review on Integrity issues of permanent mooring systems*," in *Houston, Texas*, Offshore Technology Conference, 2013.
3. P. Elman, . J. Bramande, . E. Elletson and K. Pinheiro, "*Reducing Uncertainty Through the Use of Mooring Line Monitoring*," in Offshore Technology Conference, Rio de Janeiro, Brazil, 2013.
4. T.P. Sattar, A.Ruiz Garcia, M. Sanz Correa, M., & B.S. Filloy Rodriguez , *Inspection of floating platform mooring chains with a climbing robot*. 17th International Conference on Climbing and Walking Robots and the Support Technologies for Mobile Machines (CLAWAR 2014), Poland.
5. P. Weiss, F. Andritsos, F. Schom and A. Fidani, "*Innovative Robotic Solutions for the Survey and Certification of Ships and Mobile Offshore Units*," in *COMPIT*, Siguenza, Spain, 2004.
6. J. L. García, E. García, C. M. Suárez, D. Blanco and N. Beltrán, "*Automated Offshore studless chain inspection system*," in 16th WCNDT - World Conference on NDT, Montreal, Canada, 2004.
7. S. Williams, "cordis.europa.eu," 14 March 2008. [Online]. Available: http://cordis.europa.eu/docs/publications/1216/121625181-6_en.pdf. [Accessed 10 Dec 2015].

MAGNETO STATIC ANALYSIS OF ADHESION FORCE FOR THE WALL CLIMBING ROBOT

SHYAMAL C. MONDAL and ZOLJARGAL FALLOWS

London South Bank University
School of Engineering
Mechanical and Design
103 Borough Road, London SE1 0AA

This paper describes the analysis and results of the magneto static adhesion force which required for the climbing robot to climb the high walls when additional loads are need to be carried such as scanning devices for the non-destructive testing inspection of nuclear plants or high rise wind towers. Magneto-static simulations and experiments have been carried out for the investigation of the parameters of magnetic adhesion system and the static analysis of a climbing robot is performed with regard to anti-slipping forces and anti-overturning moments. The results from both simulations and experiments show that the adhesion mechanism with just two N52 magnets has enough adhesion capacity to carry a payload exceeding 300N. The prototype wheeled locomotion robot is built and magnetic adhesion mechanism has been mounted on the belly of a robot. The simulation and experimental results are compared. The experiment has been carried out in the robotic laboratory on the vertical surface and the result from the prototype show that the adhesion mechanism provides enough adhesion force for the prototype designed robot.

1. Introduction

A Permanent magnetic contact or non-contact with the surface system design for wall climbing robot is common. Basically, the robot consists of framework, two servo motors and tracked wheels. Each track has two sprockets, roller chain and evenly spaced permanent magnetic units. Two independent motors are used to drive the tracks on each side of the robot allowing it have good manoeuvrability and rotate about its own axis. Furthermore, when the robot in motion there are always set number of magnetic units in contact with the surface resulting in more reliable attachment to surface. The magnetic wheel mechanism can move on vertical surface and good turning capability. However, the adsorption area is limited and there is a fixed air-gap, thus the energy ratio limited to minimal [1, 4, 6].

Symmetrically centralised magnetic wheel unit for wall climbing robots have been proposed by Kang Liu and the others. The unit consists of wheel, permanent magnetic blocks and connecting parts. The unit has a fixed number of permanent magnets symmetrically arranged around the wheel and there is always a certain air-gap between the magnet blocks and the surface. The characteristics of the design provides stable adsorption for between the magnetic blocks and the surface with different curvature radius. The tracked type mechanism has large adsorption area and great adhesion force due to the small gap between the track magnets and the ferromagnetic surface when active. Even though, it can rotate about its axel; it is not really flexible as the wheeled type thus making it harder to turn [2 5].

Minghui Wu and the others have proposed a non-contact adjustable permanent magnetic adhesion mechanism for a wall climbing welding robot [3 6]. The magnets are mounted under the mobile a platform and there is an air-gap between the permanent magnets and the ferromagnetic surface. The layout of the magnets offer enough adsorption area to generate enough adhesion force for the robot to carry heavy payload and pass obstacles. The non-contact adjustable permanent magnetic adhesion mechanism can overcome these disadvantages by utilising a large absorption area with certain air-gap and lifting mechanism for passing obstacles.

For turbine inspection robot, the obstacles does not have to be considered but a large adsorption area and high adhesion force is essential as it is required to carry heavy payload. Thus, the non-contact adjustable permanent magnetic adhesion mechanism has most compatible system principle for the robot. However, the weight of this design is the main concern; mainly due to its lifting mechanism. In conclusion, embedded magnetic adhesion mechanism can be implemented for in this project and subsequent simulations or experiments can be carried out in order to investigate the permanent magnetic adhesion force. Furthermore, lifting mechanism is not needed as there is no obstacle for the robot to tackle.

This paper investigates an analysis of forces and moments required in order to achieve the minimal sliding force and overturning moment that oppose adhesion forces when a robot is attached to a vertical surface.

2. Static analysis of a climbing robot

When the robot stays static on a vertical surface, the forces acting on it are gravitational force, the adhesion force generated by the permanent magnetic unit, the supporting force of the surface and the frictional force between the drive member and the surface it moves on, which are denoted as G, F_m, N and F_f,

respectively. The adhesion force is the most critical part for the climbing robot as it keeps the robot attached to the surface.

2.1. Sliding and Slipping analysis of a climbing robot

For a climbing robot, it is ideal to avoid sliding and slipping during transition or moving on an inclined surfaces. To understand the forces, we must consider the static forces that acting on a robot, where a robot is resting on a inclined surface with angle, θ, as shown in Fig.1.

This allows us to determine the minimum adhesion force for a robot to keep stay static on a vertical surface without slipping or slipping. Furthermore, by tapering the angle of the wall, the friction force will have bigger impact, thus the adhesion force it needs to keep stay on the surfaces reduced proportionally to the angle.
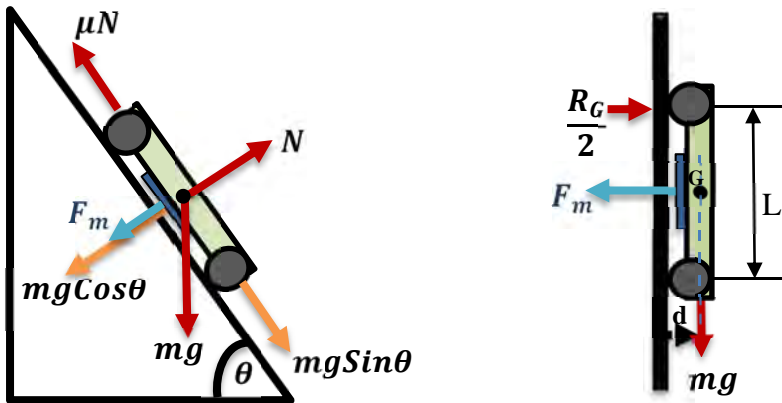
Figure 1. Robot on inclined surface.

For a robot stay under the condition of static equilibrium, it must obey:

$$\uparrow^+ \Sigma F_y = 0 \quad \gg \quad -mgCos\theta - F_m + N = 0 \; ; \; N = mgCos\theta + F_m$$

$$\rightarrow^+ \Sigma F_x = 0 \quad \gg \quad mgSin\theta - \mu N = 0 \; ; \; N = \frac{mgSin\theta}{\mu} \quad \text{and} \quad mgCos\theta + F_m = \frac{mgSin\theta}{\mu}$$

Thus, for the robot to avoid slipping: $\quad F_m > \frac{mgSin\theta}{\mu} - mgCos\theta$

In the case of the robot to climb on a pure vertical surface where the angle, $\theta = 90$, the magnetic adhesion force becomes: $\quad F_m > \dfrac{mg}{\mu}$

The calculations suggest that the minimum magnetic adhesion force that needed to avoid slipping must be greater than mg/μ . The Fig.2 states that the performance of the robot can be improved by decreasing the weight of the robot or increasing the friction coefficient between the drive member mechanism and the surface it moves on. Furthermore, high friction is desirable for a wheeled climbing robot as the motion can only be provided from friction. However, the friction coefficient might change depending on the environment and aerodynamic resistance, where weather condition has major impact on the performance of the robot
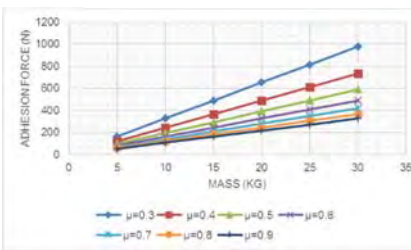
Figure 2. Minimum adhesion at different friction coefficient, μ.
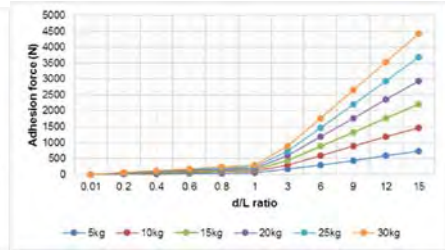
Figure 3. Effect of d/L on Adhesion force.

2.2. Overturning analysis of a climbing robot

Avoidance of overturning is a very subject for climbing robot, which subsequently keeps it attached to a vertical surface during operation. The sum of the moments at centre point G is M_g, R_G – reaction force. At equilibrium, it obeys:

$$\Sigma M_G = 0 \quad ; \quad mg \times d + \frac{R_G}{2} \times L = 0 \quad \text{and} \quad R_G = -\frac{2mgd}{L}$$

For a wheeled climbing robot, magnetic adhesion force is shared equally among the wheels. Thus, magnetic adhesion force can be considered: $\quad F_m = \dfrac{R_G}{4}$ or $\quad 4F_m = R_G$

For the robot to avoid overturning, the magnetic adhesion force must satisfy following equation: $\quad F_m > \dfrac{mgd}{2L}$

The calculations state that by decreasing the ratio d/L, (where L- distance between front and rear wheel, d – the distance between the surface and centre of gravity line) the overturning of the robot can be avoided. Which means that the centre of the gravity of robot should be as close as possible to the surface and the distance between the front and rear wheels, where taking L large as possible. However, this this increase the overall weight of the robot, subsequently the adhesion force that needed to avoid overturning also increases, therefore it should be optimised.

In conclusion, the following criteria determines the minimum magnetic adhesion for a robot to stay statically equilibrium on a vertical, without slipping and overturning: $\quad \mathbf{F_m} > \left\{ \frac{\mathbf{mg}}{\mathbf{\mu}}; \frac{\mathbf{mgd}}{\mathbf{2L}} \right\}$

The calculated results from the static analysis determine that overturning can be avoided as long as slipping of the robot overcome with sufficient friction and adhesion force. Moreover, the friction force generated should be greater than the robot weight in order to any slippage, thus a higher friction coefficient will improve the stability of the robot.

3. Magneto-static simulation

Permanent magnetic adhesion system mainly depends upon the magnetic field distribution and the structural size of the device, which has been optimized through the Finite Element Analysis (FEA). For the simulation, rear earth Neodymium magnet (N52) is used. The characteristics of the magnet used for the simulation is shown in Table 1.

3.1. Distance between magnets on Adhesion Force

When two magnets set on a yoke, the distance between magnets has effect on the magnetic flux density which would affect the total force. For this simulation, two pieces N52 magnets with 10mm thickness, 25mm length and 50mm width, are placed on iron bar (flat) with 10mm thickness, and steel plate with 5mm thickness. The air-gap between the magnets and the steel plate is kept constant at 5mm for this simulation. By varying the distance between the magnets, magnetic field and flux density were observed.
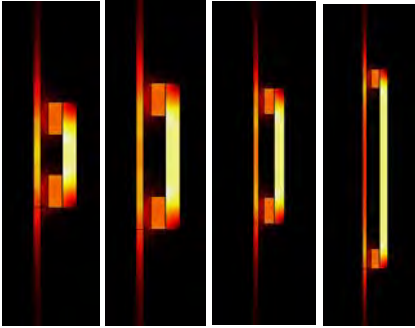
Figure 4. Magnetic flux density at distance of 30mm, 60mm, 80mm and 200mm between two magnets.
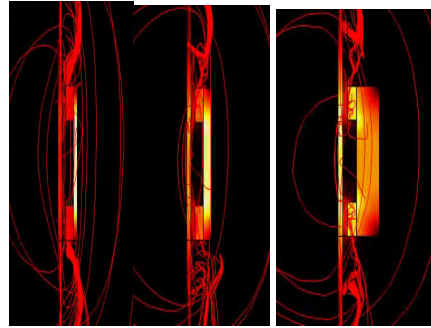
Figure 6. Magnetic field and flux density with yoke thickness of 5mm, 10mm and 25mm.

Simulation results states that the magnetic flux density in the steel plate increases with the distance between magnets but it starts to decrease significantly after the distance between the magnets gets bigger than 60 to 80mm. The hotspot shows that when the distance between the magnets is kept at 200mm, the magnetic flux concentration become much less, compared to 60mm, which means that the flux lines take much longer to reach one magnet to other (north to south), as shown in Fig.4.

3.2. Thickness of Yoke on Adhesion force

Previuos simulations for distance between magnerts show that the most optimum distance between the magnets is 60mm for 10mm thick yoke. To observe the effect of the thickness of the yoke on adhesion force, other parameter kept same as first simulation. The magnetic flux concentration increases with thickness of yoke as well as the magnetic flux leackages is been reduced respectively, as shown in fig.6. Therefore, increase in thickness of yoke induces higher adhesion force. However, the magnetic flux concentration in steel plate is significcally resduced and the adhesion force starts to fall when yoke thickness bigger than 25mm, as shown in Fig.7. Furtheremore, By varying the thickness of the yoke shows that the maximum adhesion force is induced when thickness of yoke between 10 to 25mm. However, thicker yoke is not ideal for a climbing robot as it adhesion force to wieght ratio would decrease significantly, which is not diserable. Therefore, most optimum yoke thickness is most likely 10mm.
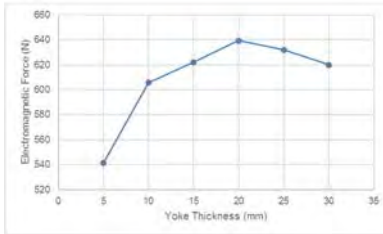
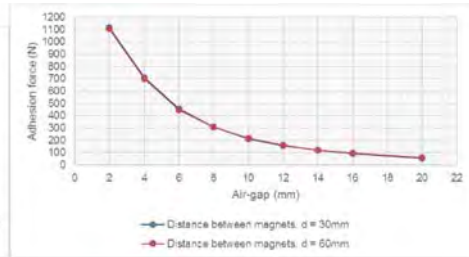Figure 7. Yoke thickness on adhesion
 Force.

Figure 8. Air-gap between member of magnets
and surface of steel plate on Adhesion Force.

3.3. Air-gap on Adhesion force

To understand the effect of air-gap between the member of magnets and the surface of steel plate on the adhesion, the simulations were carried out accordingly.

Fig.8 states that the adhesion force falls exponentially with increase in air-gap, so in order to get high adhesion force air-gap has to small as possible. Even though, a small air-gap is desirable, the design criteria limits air-gap for climbing robot. Moreover, the magnetic flux concentrations in steel plate are almost identical when air-gap is at 2 to 5mm, for both cases. The optimum air-gap for the project is at 2mm, where magnetic flux leakage slightly more than 3mm air-gap and with similar magnetic flux concentration.

Furthermore, the comparison of two different distances between the magnets are shown in Fig.8. The yellow bar represents the adhesion forces for 30mm and the blue bar is for 60mm. When air-gap gets smaller than 8mm, adhesion force for d=30mm is slightly higher than d=60mm and slightly less when the air-gap gets bigger than 8mm. However, the behaviour of the both curves are almost identical. On the other hand, weight to adhesion force ratio of 60mm is smaller than 30mm, which is due to the increase in yoke size for bigger d.

This results are supported by the experiment. As expected, the Fig. 10 states the adhesion force drops exponentially with increase in air gap. However, adhesion force drops significantly at 2 to 8mm of air-gap. On the other hand, the rate of drop in adhesion force much smaller at 8 to 10mm. This is mainly due to the magnetic flux concentration in the steel plate is reduced significantly for which flux leakage much greater at this point.

4. Magneto-static experimental setup

The experiment was carried out to validate the simulation results. In this experiment, two weighing scales are used to measure the adhesion force that generated from the magnets at different parameters. In this experiment, only 2

different magnet arrangements are explored. The picture shown in Fig.9 was taken during the experiment, to demonstrate the experiment approach.
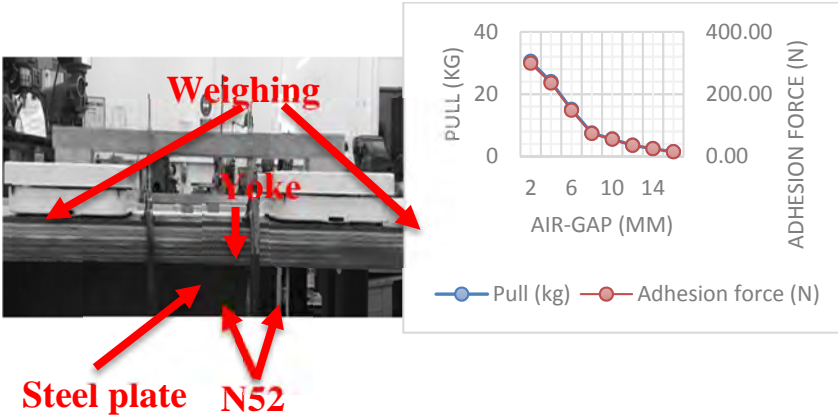

Figure 9. Experimental set-up.   Figure 10. Effect of air-gap on adhesion force.

4.1. Prototype design and implementation

The prototype robot was designed based on the simulations results and calculations that has been carried out. The hardware of the robot consists of two different types of parts, electronic and mechanical. The mechanical components are consists of four 65mm rubber wheels, upper and lower platforms, four DC motors and magnetic adhesion device. Upper platform is implemented to accommodate the electronic components, which offset from the lower platform by 30mm, in order to protect the electronic components from magnetic flux leakages from which induced from the magnetic adhesion device. Moreover, the upper and lower platforms are made out of 6mm and 3mm acrylic, respectively in order to minimise the weight of the robot.

Four wheel drive is implemented for better friction force from the wheels. Rubber wheels with diameter of 65mm is chosen for the prototype to increase the traction between the drive member and the surface which it climbs. DC motors has torque of 0.49Nm at maximum rotational speed of 37rpm. Total weight of the prototype is 1.54kg (15.1N). Static analysis suggests that the overturning and slipping can be avoided as long as the adhesion force is sufficient enough to keep the prototype attached to a wall. According to the experimental results, the air-gap between the adhesion mechanism and ferromagnetic surface must be less than 15mm, in order to provide keep the prototype robot attached to a vertical wall. On the other hand, the simulation analysis showing that the air-gap can be increased to as high as 20mm. However, when the robot attached to a wall, the payload increases significantly due to the adhesion force.

For testing the climbing capability of the prototype robot, it was carried out on a vertical steel wall in robotic lab as shown in Fig. 11 (a & b). The robot was placed on a vertical surface with 10mm of air-gap to check its adhesive force. According to the experiment results, it is assumed to be the minimum air-gap the motors could operate at although the simulation results suggested a slightly bigger air-gap in order to move the robot on the vertical surface. Furthermore, the torque required from each wheel has to be bigger than 1.72Nm at 10mm air-gap for simulations, however it is much bigger than the maximum torque of the chosen motor.

Results showed, adhesive force was sufficient enough to keep the robot attached to the wall and produced a good friction at 10mm air-gap. However, the robot was unable to climb up the wall when an additional 5N payload was added and started to make whizzing noise, which meant that the chosen motors were incapable of carrying that payload and any further increase in speed beyond 60 percent was too risky as it could cause permanent damage to the motors due high current from the power supplier. On the other hand, moving down and stopping was demonstrated by the robot with no difficulty. Thus, the correlation between the technical results and practical work show that the main issue was mostly with chosen motor.
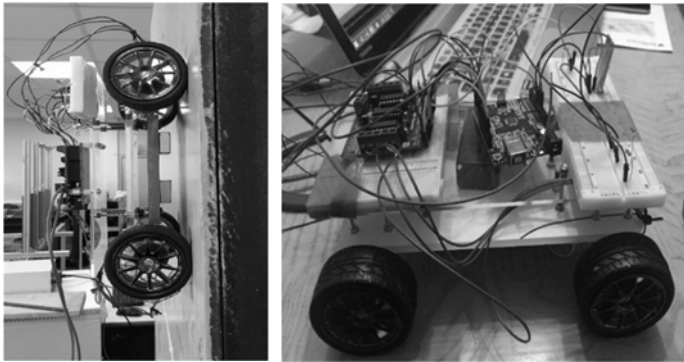
Figure 11. Prototype climbing robot: (a) Testing on the vertical surface; (b) Testing with the hardware.

5. Conclusion

A prototype wall climbing robot with magnetic adhesion mechanism is constructed to demonstrate the theory and analysed results for a wall vertical surface. Based on the investigation carried out on the working environment, a permanent magnetic adhesion mechanism was used for this application. However, there was one main issue with the robot as the torque required for the robot to climb is much higher than anticipated, for which higher torque motors were needed. On the hand, the robot seems have no difficulty of scaling down and

stopping; thus, the overall performance of the robot was achieved and was able to induce enough adhesive force at 10mm air-gap.

The experimental results states that the adhesion mechanism has a maximum payload capacity of 75N at 10mm air-gap. Furthermore, both simulation and experiment results show that adhesion force can be increased by introducing more magnets into the adhesion mechanism, which subsequently will increase the absorption area. In terms of magnetic adhesion, further research has been carried out in order to investigate the magnetic flux density in the steel plate with different thicknesses and carbon contents, and observed its effects on adhesion force. In extension, static and dynamic analysis of a climbing robot will need to be investigated further with respect to its change in orientation of the centre of mass, as well as real life testing.

There are some improvements that has to be made in order to transform the robot to real industrial use. A differential drive can be implement by introducing a tracked locomotion to the robot for better manoeuvrability and traction and an embedded pressure sensor can be implemented into the electrical system in order to monitor the payload during real life operation, which is essential as the payload increases greatly due to aerodynamic resistance.

References

1. Anne Jungert "Damage Detection in Wind Turbine Blades using two Different Acoustic Techniques", The e-Journal of Nondestructive Testing (December, 2008)
2. Raju D.Dethe ,Dr. S.B. Jaju, "Developments in Wall Climbing Robots: A Review", International Journal of Engineering Research and General Science Volume 2, Issue 3, (April-May 2014)
3. Joseph L. Jones, Anita M. Flynn, Mechanics, Mobile Robots, Inspiration to Implementation, p139,
4. Weimin Shen, Jason Gu, "Permanent Magnetic System Design for the Wall-climbing Robot", Proceedings of the IEEE International Conference on Mechatronics & Automation Niagara Falls, Canada, (July 2005)
5. Kang Liu, Wenzeng Zhang, "Symmetrically centralized magnetic-wheel unit for wall-climbing robots", Proceedings of the 13th IASTED International Conference ROBOTICS AND APPLICATIONS, (August 29-31, 2007)
6. Minghui Wu, Gen Pan, Tao Zhang, Shanben Chen, Fu Zhuang, Zhao Yan-zheng, "Design and Optimal Research of a Non-Contact Adjustable Magnetic Adhesion Mechanism for a Wall-Climbing Welding Robot", International Journal of Advanced Robotic Systems, (October, 2012)
7. MD Omar faruq Howlader, (IJACSA) International Journal of Advanced Computer Science and Applications, Vol. 6, No. 8, 2015

SECTION 8

BIOLOGICALLY-INSPIRED SYSTEMS AND SOLUTIONS

DISTRIBUTED DRIVING SYSTEM FOR THE EXCAVATION UNIT OF A LUNAR EARTHWARM-TYPE "LEAVO" EXCAVATION ROBOT

AMI FUJIWARA, TOYOHARU NAKATAKE, NAOAKI TADAMI, KEITA ISAKA, YASUYUKI YAMADA AND TARO NAKAMURA

Faculty of Science and Engineering, Chuo University,
1-13-27 Kasuga, Tokyo 112-8551, Japan

HIROTAKA SAWADA AND TAKASHI KUBOTA

Japan Aerospace Exploration Agency (JAXA), 3-1-1 Chuo-ku,
Sagamihara-shi, Kanagawa 252-5210, Japan

The authors have developed a small excavation robot called the "LEAVO" for lunar exploration, and they have confirmed its usefulness as an excavation robot. They then attempted to add a curved excavation function in order for the LEAVO to increase its exploration field. To achieve this goal, it was necessary for the LEAVO's excavation unit to transmit the motor output torque to the excavation head without any losses. In this paper, therefore, the authors proposed a new driving system called the "distributed driving system," which reduced the transmission losses by distributing the actuators and arranging them in the frontal part of the robot. Moreover, the authors developed the prototype of this system and measured its output torque as an operational check.

1. Introduction

In recent years, many lunar explorations have been initiated. However, there has not been enough exploration of the underground of the moon. An analysis of the components and internal construction of the underground is needed to understand the origin of the planets. Therefore, the Japan Exploration Agency (JAXA) is considering lunar exploration missions that collect environmental data from buried sensors and analyze some underground regolith samples.[1] For these planetary underground exploration missions, considering the transportation costs and safety issues, small excavation robots will be required.

Some small excavation robots have already been developed. For example, a mole-type robot was developed by Watanabe et al.[2], and a screw-type buried robot was developed by Nagaoka et al.[3] However, those robots are unsuitable

for practical use because they are susceptible to earth pressure and have difficulty discharging soil.

Therefore, in this research, the authors focused on the peristaltic crawling motion of an earthworm, which is not susceptible to earth pressure, and they developed a small excavation robot called the "LEAVO."[4] The LEAVO achieved a vertical excavation depth of 938 mm. In that test, there was no decrease in the robot's excavation speed, and it was confirmed that the LEAVO was not susceptible to earth pressure. Therefore, the LEAVO proved its usefulness as a small excavation robot.[5] However, the LEAVO could only excavate a straight direction at that time, and there was a limit to its exploration range. To increase the exploration range and improve the LEAVO's usefulness, it was necessary to add a curved excavation function. To achieve this function, it was necessary to transmit the motor power to the excavation heads efficiently. Therefore, in this paper, the authors propose a new driving system called the "distributed driving system" with distributed actuators, which can be set in the frontal part of the LEAVO. Moreover, the authors developed the distributed driving system and measured its maximum output torque as an operational check.

2. Concept of the "LEAVO" Planetary Excavation Robot

Figure 1 provides an overview of the LEAVO. As the figure shows, the LEAVO contains three basic units: propulsion, excavating, and discharging. The propulsion unit consists of a further three propulsion subunits. A propulsion subunit produces a peristaltic crawling motion by making itself expand and extend, which propels it in the hole and supports the reaction force during excavation. The excavation unit consists of an "earth auger," which is an excavation instrument, and a "casing pipe," which covers the earth auger. The earth auger not only excavates the soil in front of the LEAVO but also transports it to the back of the LEAVO. This is accomplished by screws at the back of the excavation head. The discharging unit clears the soil out of the
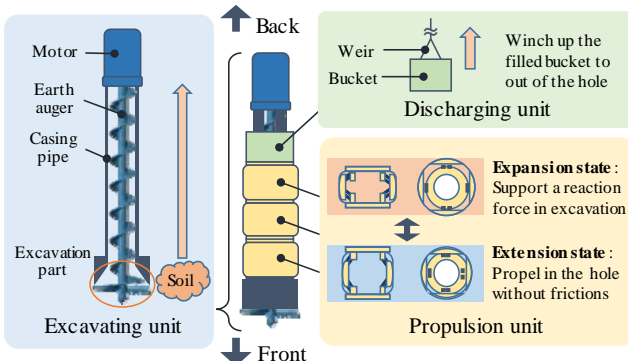

Figure 1. Overview of the LEAVO.

borehole.

3.   Curving excavation for spread of exploration ranges

The usefulness of the LEAVO as a practicable excavation robot was confirmed in the excavation test. However, the LEAVO could excavate only in a linear direction and was limited in its exploration range. Therefore, the authors proposed to add a curved excavation function to the LEAVO. In this section, the authors describe the concept of curved excavation and bendable excavation instruments called the "flexible auger" and "both-ends-supported flexible auger", which the author developed to achieve curved excavation.

3.1.   *Overview of curved excavation*

Figure 2 shows the concept of curved excavation. As the figure indicates, for this excavation method, authors decided to use the LEAVO Mk.5, which had bendable joint units between its propulsion subunits. In this excavation method: 1) the LEAVO excavates vertically to a certain depth; 2) the front bendable joint unit bends to change the excavation direction; 3) the excavation continues, and the propulsion maintains this posture. Using this excavation method, the LEAVO Mk.5 could excavate in a curved path.
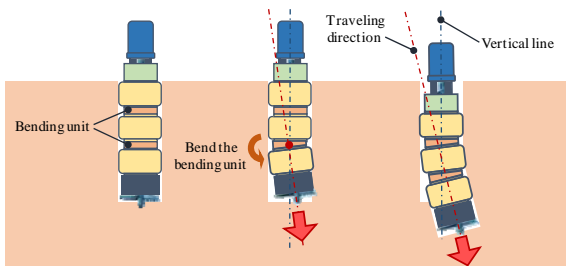
Figure 2. Overview of curved excavation.

3.2.   *Flexible auger and both-ends-supported earth auger*

Figure 3 shows an overview of the flexible auger. This excavation instrument can bend passively because it has two universal joints between its earth auger parts. The flexible auger excavated a curved borehole in the excavation test owing to its curved casing pipe. However, it was supported only at its back end, and the axis of rotation of the excavation head was unstable.

  Figure 4 shows an overview of the both-ends-supported flexible auger, which was developed to address the problems of the flexible auger. As this

figure indicates, the both-ends-supported flexible auger has its rotation supported by a disk on its frontal part, which makes its axis of rotation stable.

However, both the flexible auger and both-ends-supported flexible auger had some parts that inhibited the power transmissions between the motor and excavation head (e.g., universal joints and disk). Therefore, the authors proposed the "distributed driving system," which can be set on frontal part of the LEAVO, made its prototype, and measured its maximum output torque.
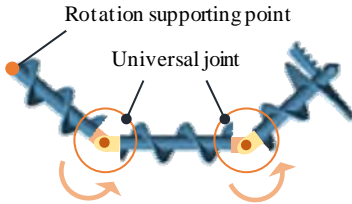
Figure 3. Flexible auger.
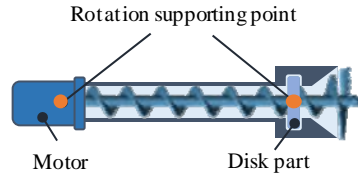
Figure 4. Both-ends-supported flexible auger.

4. Distributed Driving System

In this section, the authors describe the distributed driving system.

4.1. *Concept of the Distributed driving system*

Figure 5 shows the concept of the distributed driving system. As this figure indicates, in this system, a hollow gear was installed on the disk of the both-ends-supported flexible auger. It is driven by small pinions, which are arranged around the disk. This system allows the motors to be set on or near the excavation head and can efficiently convert the motors' power to excavation torque. Moreover, with this system, the flexible auger is driven by several motors, which decreases the load on an individual motor. This is expected to easily allow the driving system to be made smaller.
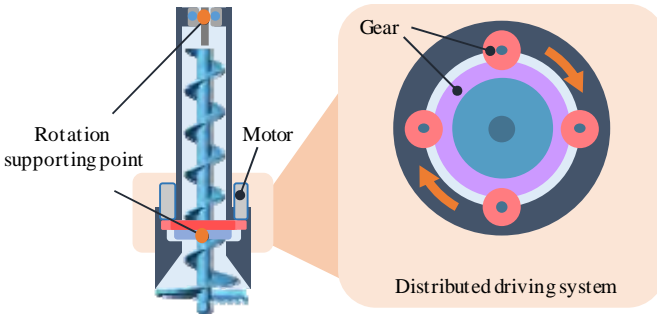
Figure 5. Concept of the distributed driving system.

4.2. *Design of the distributed driving system*

Figure 6 shows an overview of the prototype of the distributed driving system, and Table 1 shows its theoretical specifications. In this system, four geared motors (reduction ratio = 172:1, Pololu Co.) are used. The reduction ratio of the overall system was determined by considering the excavation torque and speed of the LEAVO. The rotational speed was about 5 rpm at an idling state, and the stall torque was about 27.5 Nm.

Moreover, a hollow-shaft gear was added to the construction of the disk to bear the burden of the excavation. Therefore, the disk was supported in its rotation by a radial bearing to accurately maintain the distance between the gear axes.
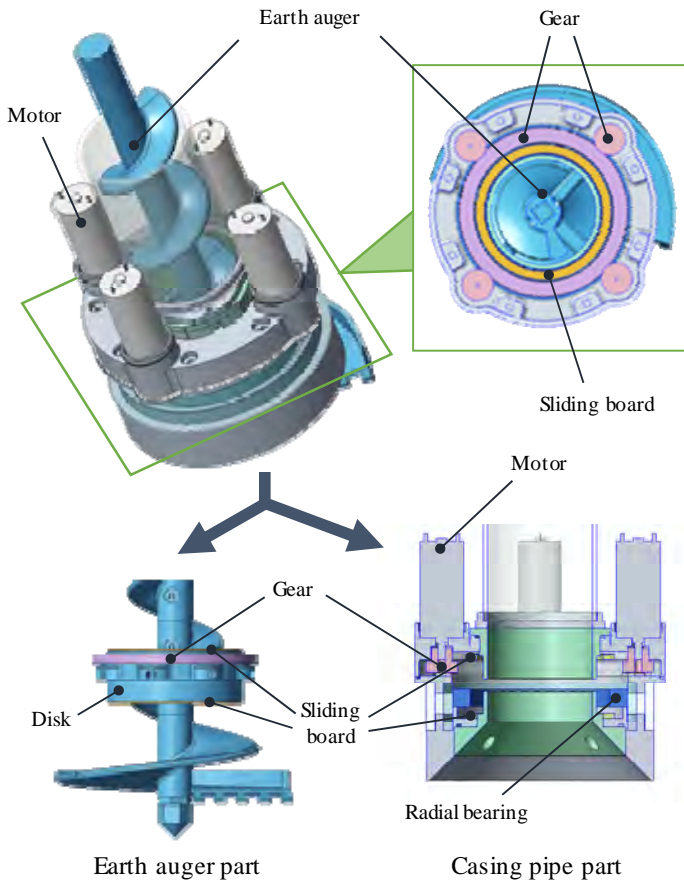
Figure 6. Prototype of the distributed driving system.

Table 1. Specifications of the prototype of the distributed driving system

Subject	Value	Condition
Output torque [N m]	27.5	Stall torque
Revolution per minutes [r/m]	5	Free run

4.3. *Design of Dustproofing for the Distributed Driving System*

In the distributed driving system, soil easily invaded the system. This led to the flexible auger becoming inoperable because of clogged gears. Therefore, dustproofing was necessary. Figure 7 shows the design of the dustproofing system. As this figure indicates, two O-rings are arranged on the circumference of a disk. Because of this arrangement, the O-rings are not excessively deformed by the pushing force of the excavation. Moreover, although the O-rings have a high coefficient of friction, this arrangement can keep any increase of the driving torque to a minimum.
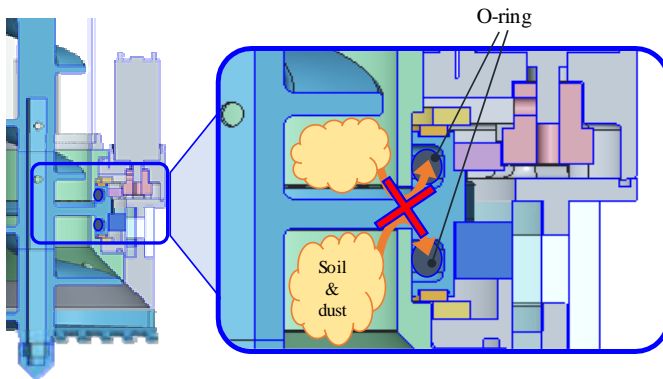
Figure 7. Overview of dustproofing system.

5. Maximum Output Torque Check of the Distributed Driving-Type Excavation Unit

In this section, as the distributed driving system's operational check, the maximum output torque was measured.

5.1. *Power check method*

Figure 8 shows the prototype of the distributed driving system, and Fig. 9 shows the environment of the operational check. As Fig. 9 indicates, in this check, a pulley (diameter $= \phi 160$ mm) was attached to the output shaft. Also, a wire was

connected to the pulley. This wire's maximum string force in the driving state was measured by a force gauge, and the maximum output torque calculated from this value. Also, the maximum output torque was taken from the average of five measurements.
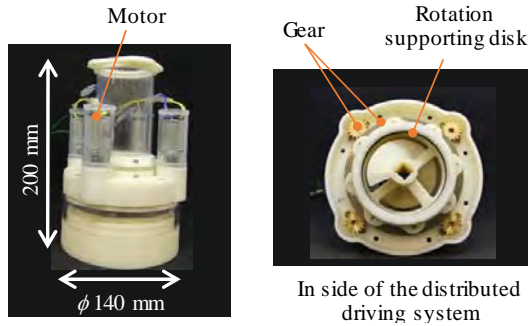

Figure 8. Appearance of the distributed driving system prototype.

5.2. *Result of the power check*

Table 2 shows the maximum output torque and the LEAVO's maximum excavation torque (this value is referenced from a previous study). From this result, the maximum output torque was sufficiently larger than the LEAVO's maximum excavation torque, and the excavation capacity of the distributed driving system was confirmed. The reason the maximum output torque was smaller than its designed value was assumed to be the friction force occurred in the dustproofing part.

Table 2. Results of the experiment

Distributed driving system's output torque [N m]	18.1
Excavation torque [N m]	13
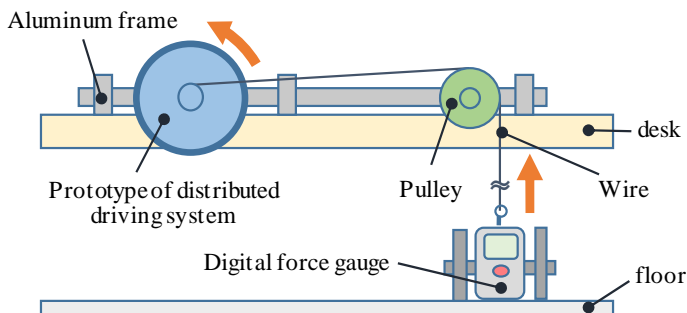
Figure 9. Overview of the power check experiment.

6. Conclusion

In this paper, a distributed driving system was proposed to efficiently transmit the motor power. Moreover, a prototype of the distributed driving system was developed, and its excavation capacity was confirmed by an operational check.

In future works, the authors will look at the excavation efficiency by performing a test on the excavation unit with the distributed driving system.

References

1. K. Nagaoka, T. Kubota and M. Otsuki, Experimental study on autonomous burrowing screw robot for subsurface exploration on the Moon, in *Proc. IEEE Int. Conf. on Intelligent Robots and Systems (IROS'08)*, (Nice, France, 2008).
2. K. Watanabe, S. Shimoda, T. Kubota and I. Nakatani, A mole-type drilling robot for lunar sub-surface exploration, *in Proc. Int. Symp. on Artificial Intelligence, Robotics and Automation in Space (i-SAIRAS'03)*, (Nara, Japan, 2003).
3. K. Nagaoka, T. Kubota, M. Otsuki and S. Tanaka, Robotic screw explorer for lunar subsurface investigation: Dynamics modeling and experimental validation, *Proc. IEEE Int. Conf. on robotics and Automation (ICRA'09)*,(Kobe, Japan, 2009)
4. H. Omori, T. Murakami, H. Nagai, T. Nakamura and T. Kubota, Planetary Subsurface Explorer Robot with Propulsion Units for Peristaltic Crawling, *Proc. IEEE Int. Conf. Robotics and Automation (ICRA'11)*, (Shanghai, China, 2011).
5. T. Nakatake, M. Konno, A. Mizushina, Y. Yamada, T. Nakamura and T. Kubota, Soil Circulating System for a Lunar Subsurface Explorer Robot Using a Peristaltic Crawling Mechanism, *Proc. IEEE Int. Conf. on Advanced Intelligent Mechatronics (AIM'16)*, (Banff, Canada, 2016).
6. M. Nagai, C. Hirabayashi, Y. Yamada, T Nakamura and H. Yoshida, Development of a Flexible Excavation Unit for a Peristaltic Crawling Seabed Excavation Robot, *Int. Conf. on Climbing and Walking Robots and Support Technologies for Mobile Machines (CLAWAR'16)*, (London, UK, 2016).
7. A. Fujiwara, T. Nakatake, M. Nagai, N. Tadami, Y. Yamada, T. Nakamura, H. Sawada and T. Kubota, Both-ends supported earth auger for a bending excavation of peristaltic-type lunar excavation robot, *Int. Conf. on Climbing and Walking Robots and Support Technologies for Mobile Machines (CLAWAR'17)*, (Porto, PT., 2017).

PROPOSAL OF PROPULSION UNIT BASED ON EARTHWORM SETAE FOR UNDERWATER EXCAVATION ROBOT

NAOAKI TADAMI, KEITA ISAKA,
TOYOHARU NAKATAKE, AMI FUJIWARA
YASUYUKI YAMADA, TARO NAKAMURA

Faculty of Science and Engineering, Chuo University,
1-13-27 Kasuga, Bunkyo-ku, Tokyo, 112-8551, Japan

MAKOTO SUGESAWA, HIROSHI YOSHIDA

Japan Agency for Marine-Earth Science and Technology, Yokosuka, Kanagawa, Japan

In this paper, we developed a propulsion unit with bristles imitating the setae of earthworm. This propulsion unit is installed in SEAVO: sub-seafloor excavation robot. To realize underwater excavation by SEAVO, it is necessary to move the soft and fluid sedimentary layer of seafloor surface. As a solution, we focused on the setae of earthworm which live in mud and soft soil. Then, we developed the propulsion unit with bristles imitating the earthworm's setae and measured the performance of the bristles-attached propulsion unit. Comparing the measurement result of the bristles-attached propulsion unit with the previous propulsion unit, we confirmed the usefulness of the bristles-attached propulsion unit.

Keywords: Excavation robot, earth auger, Seabed exploration

1. Introduction

The ocean occupies about 70 % of the earth's surface area. Recent studies have confirmed the existence of various mineral resources on this vast seabed.[1] To elucidate the reserves and generation process of these resources, it is necessary to explore the detail of seabed in a wide area. One of the seabed exploration has sampling.[2] In the current exploration, descending equipment such as drill string from the research vessel to collect soil at the seabed.[3] However, as the water depth gets deeper, exploration equipment and vessels become larger the size and increase the operation cost. In addition, since the area of these exploration is limited to one spot, it is not suitable for investigation of wide area. This problem can be improved by the cost reduction and the high efficiency exploration. Therefore, we will develop the robot that explore freely under seabed. Then, we realize low-cost and highly effective exploration by multiple robots.

In the previous research, we developed a flexible earth auger and propulsion unit for bending excavation.[4-5] We have developed the robot "SEAVO" which can be excavated and bent and confirmed its usefulness in some experiments.[6]

As the next stage of research, we propose excavation experiment underwater by SEAVO. To achieve underwater excavation, it is necessary to propel and excavate underwater ground rich in fluidity. In this paper, we propose the bristles-attached propulsion unit which improves the SEAVO's propulsion ability developed. First, we perform underwater excavation experiment with only the excavation unit and measure the torque generated by excavation. The propulsion unit must support this torque. Next, we develop the bristles-attached propulsion unit and measure the performance of this propulsion unit. Finally, we compare these results of experiments and evaluate whether propulsion unit can support the excavation torque of the target value: 4.79 N m.

2. Concept of SEAVO

Figure 1 shows the future vision of SEAVO. SEAVO is dropped from the ship to the seabed with the launcher. The launcher is a support rack of a robot and equipped with robot power and communication equipment. The exploration operation by SEAVO is divided into the five stages.

Phase 1. After arriving at the seabed, SEAVO start excavation from the launcher.
Phase 2. SEAVO excavates horizontally and performs the wide area exploration.
Phase 3. Transporting the seabed's sample, collecting the sample to the launcher.
Phase 4. After sampling, SEAVO moves backward and returns to the launcher.
Phase 5. The launcher floats up to the sea surface and is collected by vessels.

In this paper, we focus on Phase 1 and discuss the prototype of robot which can excavate in the linear direction underwater.
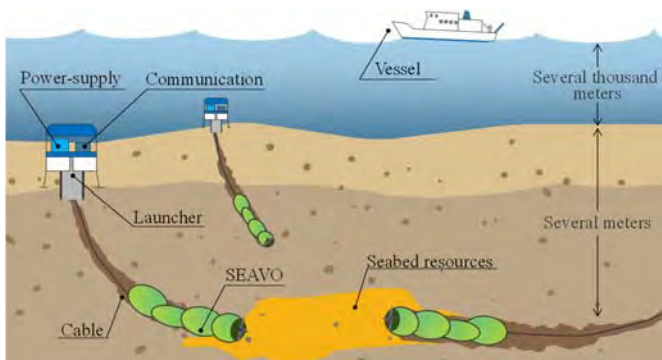
Figure 1.　Concept of sub seafloor excavation robot(SEAVO).

The overview of SEAVO is shown in Fig. 2 (a). This robot consists of an excavation unit and a propulsion unit. The overview of the excavation unit and the propulsion unit are shown in Fig. 2 (b) and Fig. 2 (c). The excavation unit has a role of securing a space for propelling. The propulsion unit has a role of the propulsion operation and the support of excavation reaction force.
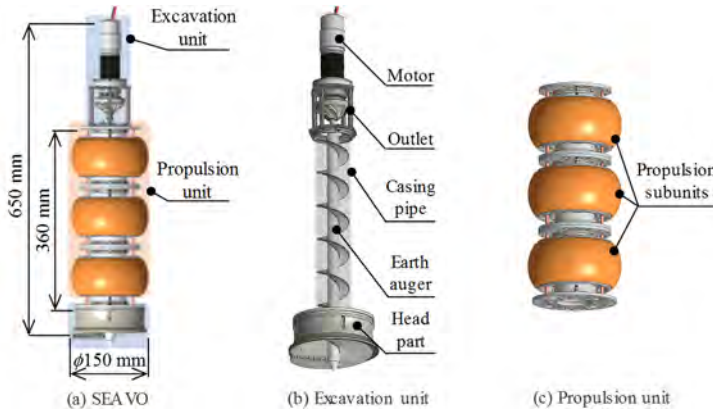

Figure 2.　Overview of the excavation robot.

3.　Hurdle of underwater excavation

In previous study, we confirmed the excavation and propulsion operation of SEAVO in land experiments. To realize underwater excavation by SEAVO, we will discuss the hurdle underwater environment and their countermeasures.

There is the problem that conventional propulsion units will not function in underwater. Unlike the onshore test, the ground is fluid, so it is difficult for the propulsion unit to support the excavation. So, when large reaction force of excavation occurs, excavation and propulsion are impossible, such as rotation of the robot body. Therefore, the propulsion unit functions reliably in fluid ground is important. About this problem, we focus on important excavation torque among the excavation reaction force and discuss it. Therefore, experimentally improve the gripping torque by biomimetic utilizing the characteristics of organisms which living underground.

Several ideas can be cited as an improvement plan for the gripping torque of the propulsion unit that supports the excavation torque. However, depending on the countermeasure, the propulsion movement may be affected. Also, it was difficult to analyze like the simulation in underwater environment. Therefore,

we try to improve gripping torque by using the characteristics of living things in underground.

3.1. *Setae of Earthworm*

As a method of improving gripping torque, we focused on the characteristic of earthworm. The structure of the earthworm is shown in Fig. 3. On the body surface of earthworms, hard bristles called setae are existing. Earthworm can fix soil like this anchor with these setae. As a result, earthworms can move in soft mud. We install the mechanism imitating this setae in the propulsion unit and improve the gripping torque without hindering the propulsion movement.

3.2. *Setae attached propulsion unit*

In this section, we explain the setae attached propulsion unit. Fig. 4 shows the appearance and gripping of setae attached propulsion unit. Like the setae of earthworm, when the propulsion unit contracts, there is little influence on the surroundings of the unit, and at the time of expansion, the setae widen, the frictional force increases, and the gripping torque improves. For the evaluation of the propulsion unit, it is necessary to decide the excavation torque generated by underwater excavation. However, the behavior of the soil in the underwater environment is very complicated, so it is extremely difficult to elucidate theoretically. Therefore, experimentally underwater excavation experiment of the excavation unit is performed, and the excavation torque is obtained. Then, we confirm from the comparison of experimental results whether the proposed propulsion unit can support excavation of SEAVO.
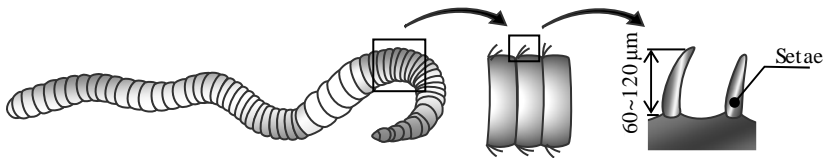

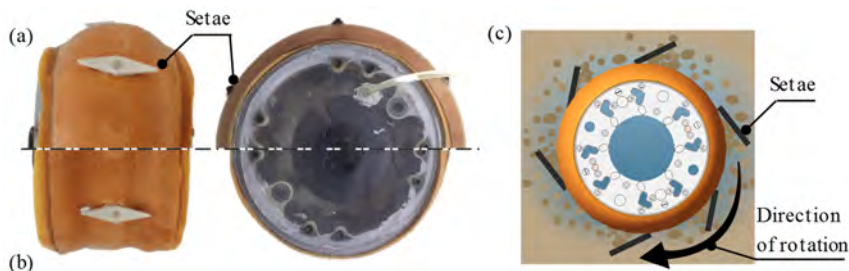Figure 3. Setae of earthworm.

Figure 4. Appearance and gripping of setae attached propulsion unit. a) Pressurized propulsion subunit at 0.03MPa. b) Unpressurized propulsion subunit. c) Gripping of propulsion subunit with setae.

4. Underwater excavation of the excavation unit

In this section, we carry out underwater excavation experiment of an excavation unit to measure excavation torque during excavation. Then, the excavation torque measured by the experiment is set as the target gripping torque of the propulsion unit.

4.1. *Experiment setup of excavation torque*

The experiment equipment of excavation unit is shown in Fig. 5. This equipment consists of excavation unit, slide rail, aluminum frame, and simulated sedimentary soil tank. In addition, Toyoura Silicone Sand (Toyoura Silicone Industry) was used as simulated sediment. Various things such as sand, mud and plankton carcasses are sediment on seafloor. However, reproducing this is difficult due to the diversity and non-uniformity of the marine sediment. Therefore, we experimentally selected silica sand which is one main component of the marine sediment and whose granularity is uniform from the viewpoint of reproducibility of the experiment.

The excavation unit is fixed to the aluminum frame so as not to rotate, and lows in the vertical direction by the slide rail. In the experiment. Also, the earth auger is rotated at 10 rpm, the pressing force is the mass of the excavating unit, and the mass of the excavating unit is 2.1 kg. Then, the excavation torque is calculated from the current flowing in the motor (RS - 775 GM 504, Suzaku Giken).
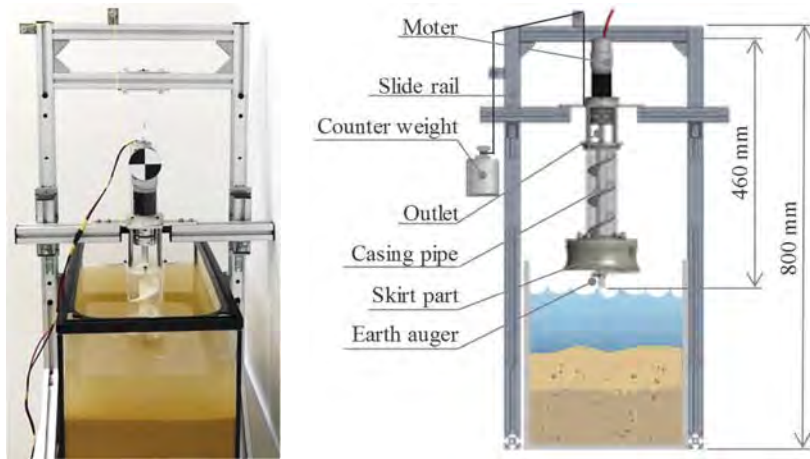
Figure 5.   Experiment setup of excavation unit.

4.2. *Experimental result and discuss*

The excavation process and the result of the excavation torque are shown in Fig. 6. After 67 s, excavation unit discharged soil from the outlet part, and it reached the lowest end of the movable range, we ended the experiment in 186 s. Next, the results of the torque are shown in Fig. 6. From this figure, the maximum excavation torque was 9.58 N m at 85 s. Because the propulsion unit always holds with two subunits, it needs gripping torque than 4.79 N m per one subunit. Therefore, the target gripping torque is set to 4.79 N m.

In addition, focusing on the result of the torque in Fig. 6, Torque is rising from around 50 s. we considered the influence of soil density as a factor that the Increase in torque. The surface layer of the sedimentary soil contains a lot of water, and it is soft. Because of that, we considered that the soil entry speed of the unit is faster, and a large torque has occurred. On the other hand, the soil became hard with the depth, and soil entry velocity declined by earth pressure and friction. As a result, the excavation time became longer, and the torque decreased. From these facts, we think that there is a relationship between excavation speed and torque.
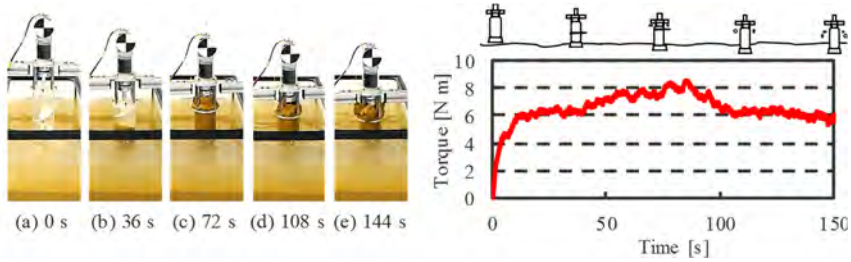
Figure 6.   Excavation process and result of excavation torque.

5. Experiment of propulsion unit

In this section, to confirm the usefulness of the setae attached propulsion unit proposed in section III, gripping torque is measured and compared with conventional propulsion unit.

5.1. *Experiment setup of gripping torque*

The experiment equipment is shown in Fig. 7. This equipment consists of propulsion subunit, aluminum frame, and simulated sedimentary soil tank. In the experiment, the propulsion subunit was buried in the sedimentary soil tank, and the pressure of the subunit applied to hold the inner wall. Then, a force was applied in the rotating direction to measure the magnitude of the force at the time of movement, using a force gauge, and the grip torque was calculated.
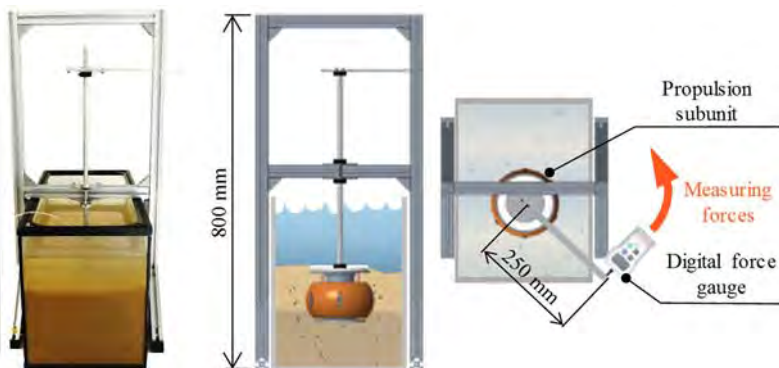
Figure 7.   Experiment setup of propulsion unit.

5.2. *Experimental result and discuss*

Measurement environment and the result of gripping torque are shown in Fig. 8. From the experimental result, it was confirmed that the gripping torque of the

propulsion subunit can be improved by attaching the setae. The maximum gripping torque of the conventional propulsion subunit was 3.5 N m when 30 kPa was applied. Therefore, it was insufficient for the 4.79 N m required to support excavation. In the experimental result, the maximum gripping torque of the propulsion subunit with the six setae attached was 5.8 N m for 30 kPa. From this result, it was confirmed that the propulsion subunit with setae-attached achieved the target value of 4.79 N m by applying 30 kPa.
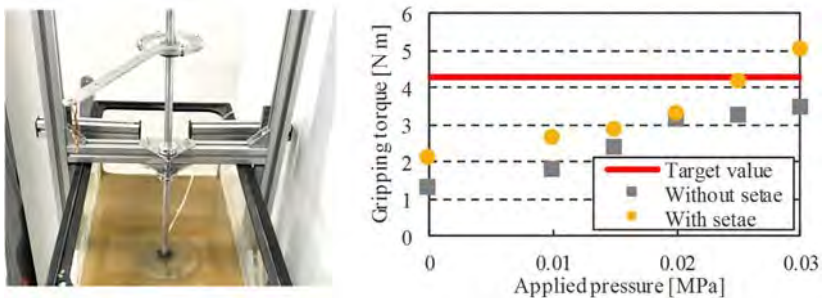
Figure 8.   Measurement environment and result of gripping torque.

6. Conclusion

In this paper, we presented a setae-attached propulsion subunit based on earthworm setae that realizes underwater excavation. The conclusions reached in this paper are presented below: Setae attached propulsion subunit inspired by the earthworm setae was presented.   The following future work is being considered.

- Setae attached propulsion subunit inspired by the earthworm setae was presented.
- The performance of the setae-attached propulsion subunit was confirmed via characteristic experiments.
- Experimental results confirmed that the setae-attached propulsion unit exceeds the target grip torque and showed usability.

7. Future works

The following future work is being considered.

- We will examine a new underwater excavation unit so that the unit can excavate a lower torque.
- We will confirm whether we can excavate excavation robot underwater equipped with the new propulsion unit proposed.

Reference

1. S. Scott, "Marine Minerals: Their Occurrences, Exploration and Exploitation", Oceans2011, IEEE, pp. 1-8, 2011.

2. H. Yoshida, T. Aoki, H. Osawa, S. Ishibashi, Y. Watanabe, J. Tahara, T. Miyazaki and K. Itoh, "A Deepest Depth ROV for Sediment Sampling and Its Sea Trial Result", Underwater Technology and Workshop on Scientific Use of Submarine Cables and Related Technologies, 2007.

3. Wada. K, "Coring Technology to be applied in IODP NAnTroSEIZE," OCEANS2008-MTS/IEEE Kobe Techno-Oceans, 1 (2008).

4. M. Nagai, C. Hirabayashi, Y. Yamada, T. Nakamura, and H. Yoshida, "Development of a flexible excavation unit for a peristaltic crawling seabed excavation robot," Proc. Int. Conf. on CLAWAR, pp.4950-4955, 2016.

5. N. Tadami, A. Fujiwara, T. Nakatake, M. Nagai, Y. Yamada, T. Nakamura, H.Yoshida, H. Sawada, and T.Kubota, "DEVELOPMENT OF A FLEXIBLE PROPULSION UNIT FOR A SEABED EXCAVATION ROBOT" Proc. Int. Conf. on CLAWAR, pp.4950-4955, 2017.

6. N. Tadami, M. Nagai, T. Nakatake, A. Fujiwara, Y. Yamada, T. Nakamura, H. Yoshida, H. Sawada and T. Kubota, "Curved Excavation by a Sub-safloor Excavation Robot", Proc. Int Conf on IROS, pp.4950-4955, 2017.

DEVELOPMENT THE ELECTRONIC SYSTEM OF CONTINUES MODULAR SNAKE-LIKE-ROBOT

DANIEL ARMANDO GÓMEZ, JAVIER CAMILO TORRES VERA

El Bosque University, Electronics Engineering Department
Av. Cra 9 No. 131 A – 02 Bogota, Colombia

HERNANDO LEÓN-RODRÍGUEZ

El Bosque University, Electronics Engineering and Bioengineering Department
Av. Cra 9 No. 131 A – 02 Bogota, Colombia

This project consists of the development of an electronic system to manipulate a snake like robot in a modular way. The electronic cards were implemented in a master-slave relationship for joint control of each mechanical module. These cards are composed of a DSPic30F4011, microchip 16-bit microcontroller that incorporates the CAN module, essential protocol for communication between cards, PWM outputs for motor control, analogue and digital ports; as well as a socket to connect to an external device through the UART. The firmware has been written in MikroC Pro. Each microcontroller implements the characteristic equation from the Hirose curves to generate a serpentine movement. These moves were simulated using ROS (Robotic Operating System in Rviz).

1. Introduction

The structural design of a snake is based on the repetition of its spine along its entire body, where only 3 types of bones make it up: the skull, the vertebrae and the ribs. The vertebral column is composed of between 100 and 400 vertebrae and each vertebra allows small movements in vertical and lateral direction, but the composition of so many vertebrae allows the snake a great flexibility and curvature with dramatically large forces.

The anatomy of the snake is composed of the same type of union and structure where each vertebra allows a rotation in the horizontal plane of 10-20 degrees and a rotation between 2-3 degrees in the vertical plane. [1] The locomotion system of the snake is very stable and the body is in constant contact with the ground at different points, allowing a low centre of mass and great traction which is easy to perceive its great ability with low energy consumption.

Snake-inspired robots were introduced in the 1970s by Shigeo Hirose. [2] Since then, several numbers of bio-inspired designs about snake like robots have been conceived and constructed. Although, the numerous designs of robots follow the kinematics and locomotion imitating the snake, they can change enormously in their physical configuration and purpose. For example, some robots are redundant; others are hyper-redundant while others may not have redundancy at all. [3] The first designs of snake-robots used traction wheels or tracks, while at present they can use passive wheels or without wheels at all. [4] Some designs are amphibious and can move effortlessly between terrestrial environments and water. [1] [6] [8] However, the demand for new types of

robots is still present for rescue and inspection applications, where they do not require a robot capable of negotiating such conditions and difficulties in sewer lines, water networks and swamps. Robots based on thin and flexible snakes meet some of these needs. [5][7][9][15]

Commercially, robots for exploration of pipes are of many kinds, where each one of them fulfils different functions, mainly visual inspection of pipelines of drinking water and hydro-sanitary lines through video capture. [16][17][18] However, these robots have a very large disadvantage, the most of them require a very expensive and heavy transport logistics and for inspection services where the cost of using this equipment makes its frequent application difficult.

Figure 1: Conceptual design and module of snake like robot.

Figure 1 shows the conceptual design of the modular snake scalable robot; it is composed by 7 modules each one adapted by 2 degrees of freedom, generated by two servomotors. In this sense, the electronic design is focused in a modular way so that each mechanical joint carries its electronic backup and battery.

2. Serpentine Locomotion

There are different types of locomotion in snakes based on the condition of the terrain and the type of environment. In the development of the project the cards and control can reproduce any of the 4 types of snake locomotion; however, the applications of the control system and the communications of the cards focused the serpentine locomotion, as verification of control system. [10]

3. Design of the electronic system

The conditions of the electronic design are based on the components necessary to generate the movement of the robot based on its locomotion, environment, size, current and application.

3.1. *Power requirement and voltage regulation*

The selected batteries are based on the power delivered, charging time and the space gap within of the modules. The selected batteries are lithium-polymer 72x34x14 mm 1000 mA, composed of two cells of 7.4 volts.

Due to the high efficiency of buck step-down type regulators, table 1 is showing the characteristics of the following devices that have been selected to satisfy current requirements of approximately 2.5 Amps, efficiency of 85% to 95%, capable to inverse voltage, and smaller as possible.

3.2. *Microcontroller and communication protocol*

The microcontroller that has been chosen mainly based on its 16-bit architecture; additionally, it has CAN communication protocol incorporated as a final purpose of control and position of the servomotors. Its parameters are: architecture:16-bits, CPU speed 30 MPS, type of minority: flash, memory: 48 KB, ram: 2 KB, temperature range 40 to 125 C, operating voltage 2.5 to 5.5 V, Number of I/O ports: 40, digital communication peripherals: 2-UART, 1-SPI; 1-I2C, analogue peripherals: 1-A/D, 9x10-bits; 1000 kps, communication protocol: CAN, PWM channels: 6 and parallel port: GPIO.

The proposed network protocol for internal communication between the electronic systems is a master-slave connexion. At the beginner, was considered to be performed through RS485, however, the CAN Bus was chosen, used in the automotive industry due to its robust protocol, which corrects transmission errors and It is invulnerable to electromagnetic disturbances, thanks to its physical layer requirements that are a shielded in a differential pair.

4. Mathematical analysis

Based on the cinematic analysis of Professor Hirose; [2] the behaviour and locomotion of a snake expresses the serpenoid curves and their joint trajectories as follow: [1] [2] [10] [14]

4.1. Serpenoidal Curves -Hirose

The following equations express the serpenoid curves proposed by Hirose. The length of the segment along the serpent is represented; a, b and c are parameters that determine the shape of the curve.

$$X(s) = \int_0^s \cos(a \, \cos b\sigma + c\sigma) \, d\sigma \qquad (1)$$

$$Y(s) = \int_0^s \sin(a \, \cos b\sigma + c\sigma) \, d\sigma \qquad (2)$$

4.2. Articular trajectories

The joint trajectories determine the angles that the joints must develop over time to generate a serpenoid curve; these equations are those which are executed by the microcontrollers on each electronic card in order to control the angles of the servomotors. The equation (3) contains a new component ω, which is determined by 2πf, where f is the frequency with the curve generated by equations (1) and (2).

$$\emptyset_i(t) = 2\alpha \ \sin(\omega t + (i-1)\beta) + \gamma \tag{3}$$

Where: (4), (5) and (6) come from the same parameters a, b and c of the serpenoid curve, [11]

$$\beta = \frac{b}{n} \tag{4}$$

$$\gamma = \frac{-c}{n} \tag{5}$$

$$\alpha = 2a \left|\sin\left(\frac{\beta}{2}\right)\right| \tag{6}$$

As a result: i, is the number of the joint, that is, the first joint will have an equation with $i = 1$, the second with $i = 2$ and so on.

5. Analysis and results

5.1. *Electronics card*

The figure 2 showing the electronic card implemented in each mechanical module of the robot structure. This card execute the master or slave control condition; the result is been done with a single card design allows to be configured as a master or slave according to the needs. Each card is identified with an internal code that permits to know its location on the robotic structure.
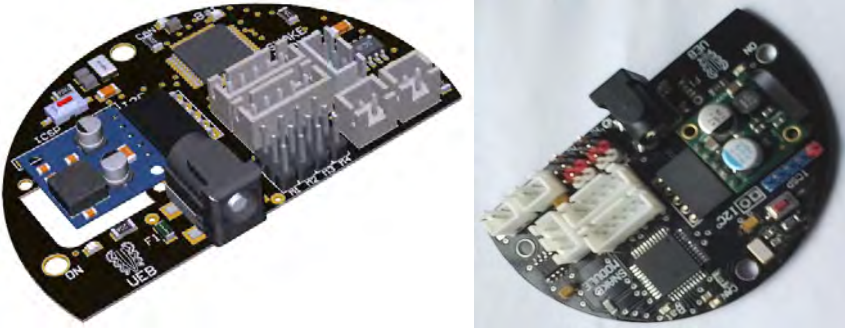
Figure 2: photorealistic image and picture of the developed control card.

The control and communication system of the developed card is presented in figure 3; this shows the diagram of any device with 5V supply voltage and logic, such as RF, Bluetooth, wifi modules that support the TTL/UART

interface. The diagram also showing the following the communication protocols: CAN; Uart, I2C that allow controlling any device such as sensors, servomotors, LEDs, etc. all them that support at the same time by the interface.
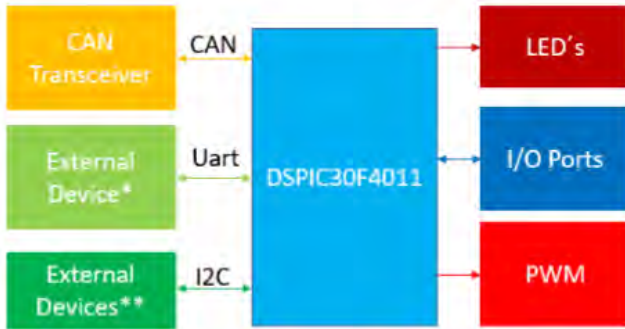

Figure 3: Block diagram of the electronic card.

5.2. *Mathematical analysis*

Figure 4-left is showing multiple serpenoid curves generated by the modification of different parameters in control, such as: frequency, amplitude and phase shifting.
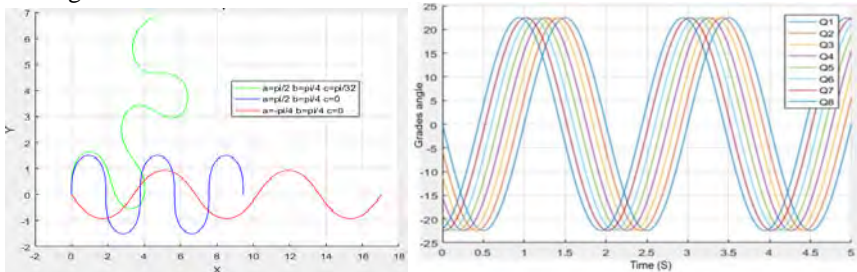

Figure 4: left: Simulation of trajectory behaviour and locomotion of the modular snake-robot; right: Articular angles with respect to time: left: a=-pi/4, c=pi/2, w=2pi*(0.5).

Figures 4-right is showing the simulations of each joint of the robotic system covering the joint angles (Q1 to Q8) with respect to time with different parameters *a, b* and *c*, based on equations 1 and 2.

Figure 4-right also showing the path of each of the joint modules to complete the serpenoid curve; it should be notice that if these graphs were developed with n=7, (number of joints) the results are similar.

6. Simulation of robot kinematics

The simulation includes the implementation of the joint trajectories in the mechanical modules of the robot. As a result, the robot design has been taken to

the URDF format compatible by the RVIZ simulator and through the publisher and subscriber of ROS. The described angles previously and the equations produce the simulated trajectories on RVIZ [12] [13].

Figure 5: Result of robot simulation developing serpenoid curve in RVIZ-ROS.

The figure 5 is showing the executed simulation in RVIZ, in addition is validating that the robot could move in a serpentine way. However, in this first implementation, aspects such as the weight of the robot, friction and floor uniformity were not considered.

a	*b*	*c*

d	*e*	*f*
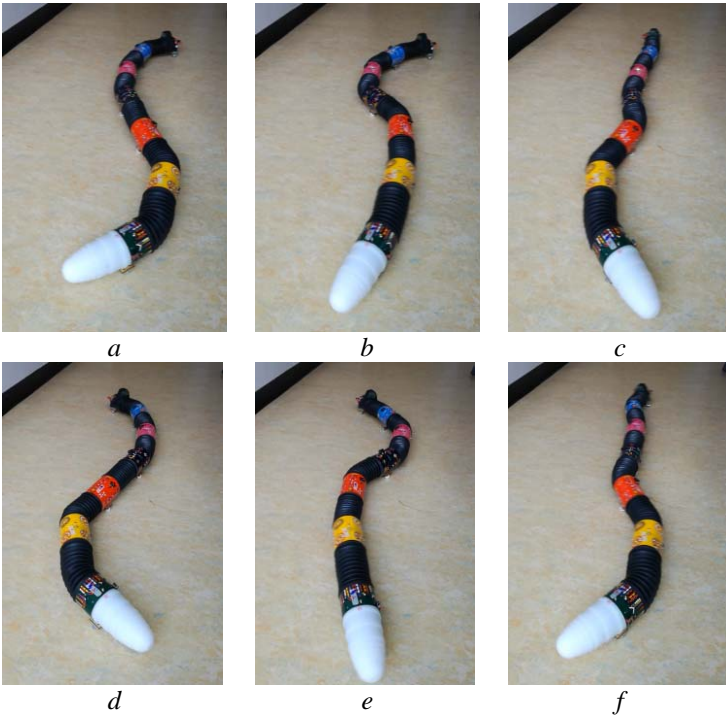
Figure 6: Motion sequence of the implemented robot like snake.

Figures 6 are showing the final implementation of the locomotion by the snake like robot based on the serpentine movements. Further research and word need

to be done in other to improve and produce soft-motion and better performance. Nevertheless, the control cards with CAN communications were well executed by the controllers, which were the aim of this preliminary research.

Conclusions

This project presents in a superficial way the design criteria for a particular electronic system to control a robot, these must cover its processing unit such as the microcontroller, its power supply and regulation, the peripherals that must be contemplated, either that you want to use sensors. Follow the rules as those established in IPC-2221 to develop PCBs with high quality standards.

The project presents the importance of a mathematical analysis in terms of robotics and its respective simulation to check its effectiveness. However, there is a huge gap between the simulation and the real, since some physical variables did not contemplated precisely.

Acknowledgment

This project openly thanks the contributions for the development of the control cards by the researchers: Michael Canu, Cecilia Murrugara; and especially to the Researcher Juan David Hernández of the University of Girona for his valuable contribution and knowledge in the management and control of ROS.

References

1. J. K. Hopkins, B.W. Spranklin, and S.K. Gupta, A survey of snake-inspired robot designs. Bioinspiration and Biomimetics, 4(2):021001, 2009.
2. S. Hirose and H. Yamada, Snake-Like Robots, Machine Design of Biologically Inspired Robots, IEEE Robotics & Automation Magazine, March 2009
3. K. J. Dowling, Limbless Locomotion: Learning to Crawl with a Snake Robot, The Robotics Institute Carnegie Mellon University and NASA Graduate Fellowships, December 1997.
4. S. Sugita, K. Ogami, G. Michele, S. Hirose, and K. Takita, A Study on the Mechanism and Locomotion Strategy for New Snake-Like Robot Active Cord Mechanism–Slime model 1 ACM-S1, Journal of Robotics andMechatronicsVol.20 No.2, 2008.
5. C. Wright, A. Buchan, B. Brown, J. Geist, M. Schwerin, D. Rollinson, M. Tesch, and H. Choset, Design and Architecture of the Unified Modular Snake Robot, 2012 IEEE International Conference.

6. S. Yu, S. Ma, B. Li, Y. Wang, An Amphibious Snake-like Robot: Design and Motion Experiments on Ground and in Water, Proceedings of the 2009 IEEE International Conference on Information and Automation, June 22 - 25, 2009, Zhuhai/Macau, China.

7. A. A. Transeth, R. I. Leine, C. Glocker and K. Y. Pettersen, 3D Snake Robot Motion: Nonsmooth Modeling, Simulations, and Experiments, IEEE transactions on robotics, vol. 24, no. 2, April 2008.

8. H. Yamada and S. Hirose, Study of a 2-DOF Joint for the Small Active Cord Mechanism, 2009 IEEE International Conference on Robotics and Automation Kobe International Conference Center, Kobe, Japan, May 12-17, 2009.

9. A.J. Ijspeert and A. Crespi; Online trajectory generation in an amphibious snake robot using a lamprey-like central pattern generator model, Proceedings of the 2007 IEEE International Conference on Robotics and Automation (ICRA 2007), pages 262-268,

10. David Rollinson; Control and Design of Snake Robots; School of Computer Science Carnegie Mellon University, 2014.

11. C. Gong, M. J. Travers, H.C. Astley, L. Li, J. R. Mendelson, D. I. Goldman and H. Choset; Kinematic gait synthesis for snake robots; The International Journal of Robotics Research 1–14, 2015

12. Filippo Sanfilippo, Øyvind Stavdahl and Pal Liljeback; SnakeSIM: A Snake Robot Simulation Framework for Perception-Driven Obstacle-Aided Locomotion; Proceeding of the 2nd International Symposium on Swarm Behavior and Bio-Inspired Robotics (SWARM), Kyoto, Japan, 2017.

13. F. Sanfilippo, Ø. Stavdahl and P. Liljeback; SnakeSIM: a ROS-based Rapid-Prototyping Framework for Perception-Driven Obstacle-Aided Locomotion of Snake Robots; Proceeding of the IEEE International Conference on Robotics and Biomimetics (ROBIO 2017).

14. S. G. Danielsen; Perception-Driven Obstacle-Aided Locomotion for snake robots, linking virtual to real prototypes; Norwegian University of Science and Technology, 2017

15. Biorobotics laboratory; (2018, May 16). Retrieved from: http://biorobotics.ri.cmu.edu/projects/modsnake/

16. Rausch Electronics USA; (2018, May 20). Retrieved from: http://rauschusa.com/

17. Aries Industries; (2018, June 13). Retrieved from: http://www.ariesindustries.com/

18. Ibak; (2018, June 10). Retrieved from: http://www.ibak.de

BIO-INSPIRED QUADRUPED ROBOT FOR DETECTION CARBON DIOXIDE IN THE AIR

MARIA CAMILA ROJAS SUÁREZ, SANTIAGO NORIEGA ÁLVAREZ

El Bosque University, Electronics Engineering Department
Av. Cra 9 No. 131 A – 02 Bogota, Colombia

HERNANDO LEÓN-RODRÍGUEZ

El Bosque University, Electronics Engineering and Bioengineering Department
Av. Cra 9 No. 131 A – 02 Bogota, Colombia

Quadruped in comparison with the majority of others animals, it has the ability to access to any kind of environment where others living creatures or even humans can't access. Those bio-inspired attributes are taken into this project in order to design and develop a quadruped robot with the abilities to move in all kind of directions like ascend or descend, avoid obstacles, etc. Combining these skills of the quadruped animals with the ability of continuously monitoring the carbon dioxide, the results can be determinants. This paper presents the dynamic and kinematics model in addition with the measurement scheme of the carbon dioxide index, with the purpose of establish a mechanical sturdy device, which can be monitoring an important variable. As a result, we studied the movement of real animals, so we can define a suitable bio-mimetic model for our robot.

1. Introduction

Recently, human has wanted to replicate all kind of movement of animal. This effort on doing it allowed humans to reproduce robots for certain task instead of risk their lives. This kind of biomimetic replication can be employed in land mines task and exploration task [1]. Another important application of these robots is the incursion in dangerous environments, like contaminated places, or hostile landmarks. In this order of ideas, we decided that the applicative background of the robot is the measurement of the concentration of carbon dioxide, which is an important variable that can generate negative impacts if no measurement (and regulation) control is applied. Besides, the human beings can be, easily, exposed to these gases without notice it, with mortal consequences.

Since 90's researches begin to innovate the whole world with bio-inspired robot [2]. In 2008 bio-inspired robots became in an important instrument, with several ability of walking and climbing in all kind of surfaces [3] [4].

Nowadays, the majority of quadruped robots have exceptional abilities and advanced material to be developed. Other approaches have been employed in their developed of quadruped robots as example parallel mechanism [5], soft materials [6] self-folding [7], Origami [7], printable robots and so on.

Nevertheless, this paper presents a device based on quadruped robots with some basic features and different attributes and applications. See figure 1.
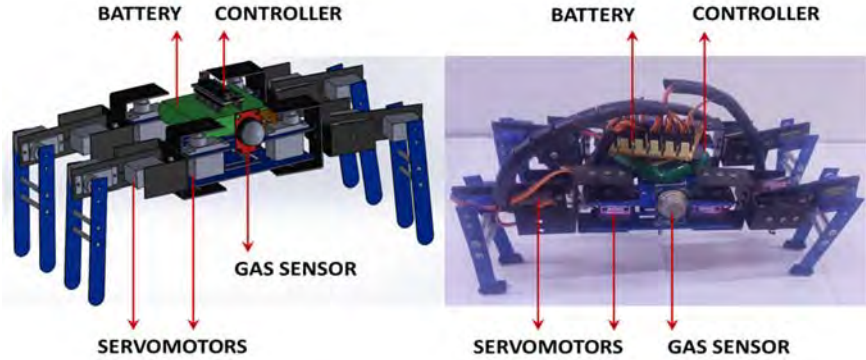

Figure 1: Quadruped robot design and prototype.

2. The Bio inspired quadruped and motion analysis

In order to accomplish this robot, we stablished how quadruped move and the algorithm behind this process. The majority of the quadrupeds move in a mammalian form, like a dog or a horse. Besides this, the spider has 8 limbs, so we couldn´t use them as a direct source of inspiration. To solve this problem, we used a mixture of sources of inspiration; we had the quadrupedal animals (their movement and behavior). On the other hand, we had the anatomy of the spider. As a result, the anatomy or physic shape of the spider, and the movement of the quadruped animals in an arachnid way was used.
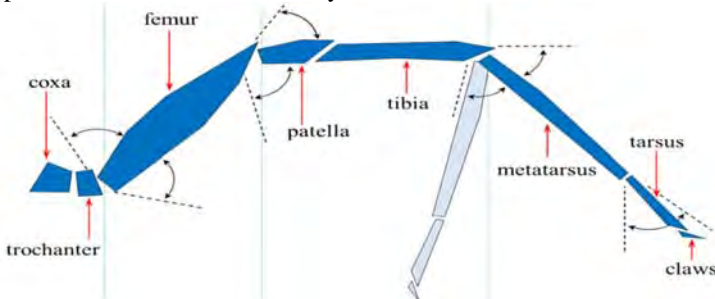
Figure 2: Spider's leg biomechanics

Initially, it's important to know that the spider has 7 parts by leg (figure 2). From the original anatomy of the spider, we suppress some components that we didn't need. The reason of this is that we wanted to simplify the whole system. Having said this, instead of using the Patella part, we linked the femur and the tibia by a direct joint. The metatarsus and the tibia were united as a single link or part. Similarly, we dismiss the tarsus. All of these changes were executed in the robot, but for the kinematics analysis we took into account the entirely system for a realistic approach.

One important aspect is the amplitude that has every part of the spider's leg. This means, for example, that the coxa has amplitude of 35 degrees while tibia has a mobility of 70 degrees. Also, every of the seven components of the limb, has a different axis of movement; for example, the trochanter has a movement in X-Y axis, meanwhile the femur in X-Z axis. This kind of association and motion is explained graphically in the figure 2.

3. Mathematical development

As we mentioned previously, there are some constraints that we applied in the anatomic development. We applied these modifications in the mathematical development and we decided to involve all the possible variables, based on the following table to produces the most faithful model and prototype.

Table 1. Degrees and planes of work of each part of the quadruped robot.

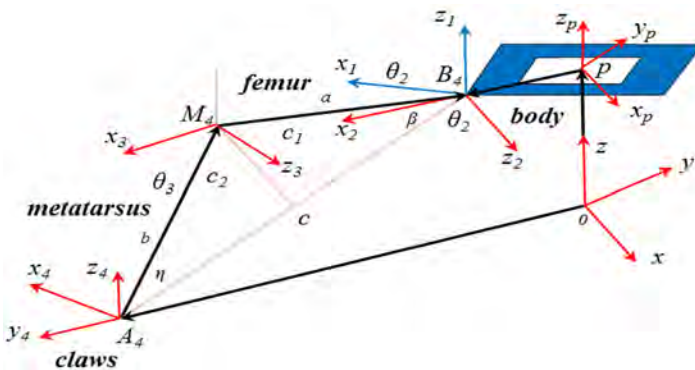| Parts	Movements (degrees)	Plane
Coxa	75	Transversal
Femur	140	Sagittal
Tibia	40	Sagittal

3.1. *Direct Kinematics*

Figure 3: Parameters of the system and coordinate frames of the robot.

In order to study the direct kinematics of the robot was necessary, at the beginning; use the joint's variables of contact limbs and the position and orientation of the platform. All of this, based on fixed frame represented in figure 3. Is important to establish that the Ai vectors denote the end points of contact legs and the Bi vectors represent the connection points of the legs of the robot to the platform. Taking into account the figure 3 and knowing Ai vectors, which are the end points of contact legs, we can establish the next expression:

$$rBi = rAi + \frac{rMi}{Ai} + \frac{rBi}{Mi} \tag{1}$$

In this expression, rBi and rAi represent the position vector of Bi. In the same way, we needed to determinate all the parameters of the system in a graphically mean. In the figure 3 these parameters can be observed.

One highly important aspect in our robot was the motion and the sequence that a quadruped robot must follow in order to walk correctly. This item is the quadruped walking system, which is illustrated in the figure 4.
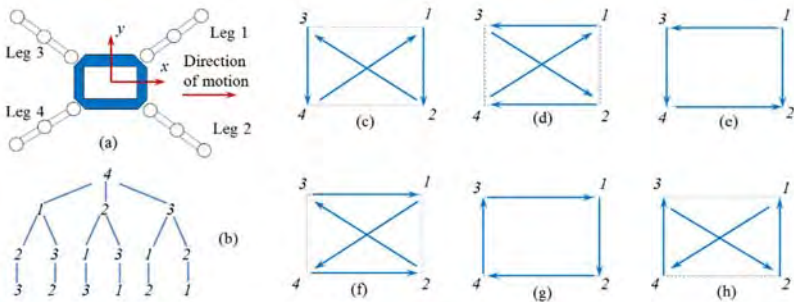
Figure 4: Sequence of quadruped walk

Suppose that the leg 1, 2 and 3 are standing on the ground. According to relation (1) the location of points Bi versus the fixed coordinate system are determined and, as direction of x axis of P-coordinate system is direct to $B3B1$ vector, is possible determine the direction of x-axis unit vector:

$$Ex = \frac{B3B1}{⟦B3B1⟧} \tag{2}$$

In the same way, we can determinate the vector $B3B2$

$$Em = \frac{B3B2}{⟦B3B2⟧} \tag{3}$$

By having this information, we can determinate the direction of unit vector, normal to the platform plane. To do this, we first need to implement the cross product of the two previous vectors:

$$Ez = EmxEx \tag{4}$$

In the same way, having the vectors *Ex* and *Ez*, is possible to determine the *Ey* vector using the same method:

$$Ey = Ex \ x \ Ez \tag{5}$$

These three vectors are necessary because we can establish the matrix of the platform versus the fixed coordinate system with the next expression:

$$^P_B R = [Ex \ Ey \ Ez] \tag{6}$$

In order to specify the origin of coordinate system, we can use the equation of the circle in this way:

$$(Xb1 - Xp)^2 + (Yb1 - Yp)^2 + (Zb1 - Zp)^2 = r^2 \tag{7}$$
$$(Xb2 - Xp)^2 + (Yb2 - Yp)^2 + (Zb2 - Zp)^2 = r^2 \tag{8}$$
$$(Xb3 - Xp)^2 + (Yb3 - Yp)^2 + (Zb3 - Zp)^2 = r^2 \tag{9}$$

If we solve the previously established equations system, we can determine the position of the body in the coordinate system.

3.2. Platform velocity

In order to establish the velocity of the robot's platform is necessary to determine the velocity and angular velocity of robot platform by using the position and velocity of the joint's variables. In order to specify the direct kinematics of platform velocity can use (10):

$$\overrightarrow{OA_i} + \overrightarrow{A_iM_i} + \overrightarrow{M_iB_i} + \overrightarrow{B_iP} = \overrightarrow{OP} \tag{10}$$

In the previous expression, *OAi* represents a vector that was drawn from the fix coordinate origin to point "A" from leg No. i. It's possible to determinate the relation between velocity of the joint's variables and platform velocity by differentiating from (10). The result is (11):

$$\overrightarrow{Vp} = {}^{B \to Tib}\overrightarrow{\omega_i} \times \overrightarrow{A_iM_i} + {}^{B \to Fem}\overrightarrow{\omega_i} \times \overrightarrow{M_iB_i} + {}^{B \to P}\overrightarrow{\omega} \times \overrightarrow{B_iP} \tag{11}$$

In (11), the first and third element of the equality represents the absolute angular velocity of femur and tibia, of limb No. i respectively. If we take into account the symmetry of our robot, (11) this process can be used for the other three contact legs. By using the fifth element of (11), is possible to establish *Vp*. Based on figure 3:

$$^{1 \to Tib}\overrightarrow{\omega_i} = \dot{\theta_1}\,{}^i\overrightarrow{K_1} + \dot{\zeta}\,{}^i\overrightarrow{K_2} \tag{12}$$

$$^{1 \to Fem}\overrightarrow{\omega_i} = \dot{\theta_1}\,{}^i\overrightarrow{K_1} + \dot{\zeta}\,{}^i\overrightarrow{K_3} \tag{13}$$

Regarding to the figure 3:

$$\zeta = \frac{\pi}{2} - \theta_2 - \theta_3 \rightarrow \dot{\zeta} = (\dot{\theta_2} + \dot{\theta_3}) \tag{14}$$

$$\gamma = \frac{\pi}{2} - \theta_2 \rightarrow \dot{\gamma} = -\dot{\theta_2} \tag{15}$$

In expressions (12) and (13), the first factor in both of them, indicates the unit vector direct to z-axis of first coordinate frame of limb No. i. The relation between the unit vectors of different coordinate frames of each leg is determined in function of the figure 3 as follow:

$$\overrightarrow{\imath_{K_3}} = \overrightarrow{\imath_{K_2}} \tag{16}$$

$$\overrightarrow{\imath_{K_2}} = -\sin(\theta_1)\overrightarrow{\imath_{I_1}} + \cos(\theta_1)\overrightarrow{\imath_{J_1}} \tag{17}$$

$$\overrightarrow{\imath_{J_4}} = -\overrightarrow{\imath_{K_3}} \tag{18}$$

Using the expressions from (12) to (18), we can determine the values of ωi as follows:

$$^{1\to Tib}\omega_i = \dot{\theta_1}{}^i\overrightarrow{K_1} - (\dot{\theta_2} + \dot{\theta_3})(-S(\theta_1){}^i\overrightarrow{\imath_1} + C(\theta_1){}^i\overrightarrow{\jmath_1}) \tag{19}$$

$$^{1\to Fem}\omega_i = \dot{\theta_1}{}^i\overrightarrow{K_1} - \dot{\theta_2}(-S(\theta_1){}^i\overrightarrow{\imath_1} + C(\theta_1){}^i\overrightarrow{\jmath_1}) \tag{20}$$

In (19) and (20) the S's and the C's, means cosines and sines. In this case, for mathematical simplicity, we can express all the previous equations as rotational matrices as follows:

$$^{B\to Fem}\omega_i = {}^P_B R \; {}^1_P R_i \; {}^{1\to Fem}\omega_i \tag{21}$$

$$^{B\to Fem}\omega_i = {}^1_B R_i \; {}^{1\to Fem}\omega_i \tag{22}$$

$$^{B\to Tib}\omega_i = {}^1_B R_i \; {}^{1\to Tib}\omega_i \tag{23}$$

As we mentioned previously, R represents the rotational matrix of platform relative to the fix coordinate frame. In this order $R1p$ is the rotation matrix of the first coordinate frame of limb No.i relative to P-coordinate frame system. This last rotational matrix is defined as follow:

$$R = \begin{bmatrix} \cos\left[(i-1)\frac{\Pi}{3} + \frac{\Pi}{6}\right] & -\sin\left[(i-1)\frac{\Pi}{3} + \frac{\Pi}{6}\right] & 0 \\ \sin\left[(i-1)\frac{\Pi}{3} + \frac{\Pi}{6}\right] & \cos\left[(i-1)\frac{\Pi}{3} + \frac{\Pi}{6}\right] & 0 \\ 0 & 0 & 1 \end{bmatrix} \tag{24}$$

3.3. Direct kinematics of non-contact leg

Direct kinematics of position for a non-contact limb is similar to the direct kinematics for a serial robot. As shown in Figure 3 can write:

$$OAi = OP + PBi + BiMi + MiAi \tag{25}$$

$$PBi = {}^P_B R \; PBi \tag{26}$$

$$BiMi = {}^P_B R \; {}^1_P R \; BiMi \tag{27}$$

$$MiAi = {}^P_B R \; {}^1_P R \; MiAi \tag{28}$$

Based on the previous expressions, PBi can be establishing as follows:

$$PBi = \begin{bmatrix} r\cos(\frac{\Pi}{6} + (i-1)\frac{\Pi}{6}) \\ r\sin(\frac{\Pi}{6} + (i-1)\frac{\Pi}{6}) \\ 0 \end{bmatrix} \qquad (29)$$

As we did with the contact legs, we wanted to determine the velocity of the non-contact limbs, so the procedure is similar. We first need to differentiate (25) as follows:

$$\vec{V}_{Ai} = \vec{Vp} + {}^{B\to P}\vec{\omega} \times B_iP + {}^{B\to Fem}\vec{\omega}_i \times B_i\vec{M}_i + {}^{B\to Tib}\vec{\omega}_i \times M_i\vec{A}_i \qquad (30)$$

Using Vp and ω, that were derived from (11):

$$ {}^{B\to Fem}\vec{\omega}_i = \dot{\theta}_1{}^i\vec{K}_1 + \dot{\theta}_2{}^i\vec{K}_2 + {}^{B\to P}\vec{\omega} \qquad (31)$$

$$ {}^{B\to Tib}\vec{\omega} = \dot{\theta}_3{}^i\vec{K}_3 + \dot{\theta}_1{}^i\vec{K}_1 + \dot{\theta}_2{}^i\vec{K}_2 + {}^{B\to P}\vec{\omega} \qquad (32)$$

From (30) to (32) we can determine the velocity of end points of non-contact legs; as a result, these values can be specified.

4. Software and Carbon Dioxide Reading Sensor

The robot control was based in arduino controller and Bluetooth communication system, sending and receiving routine commands from mobile device. We used an Arduino-Nano as the controller for the full platform control and communication system. For motion, 12 servo-actuators were set, 3 for each leg with a torque of 2.2 kg.cm. These servo-motors are attached directly as a joint of each link-leg. The supply voltage and current for the robot was a battery package of 4.8 V and 3000 mA with around power of 7.5 W approx.

Regarding to the reading of the carbon dioxide index, an embedded circuit capable of monitoring various types of gases was implemented.
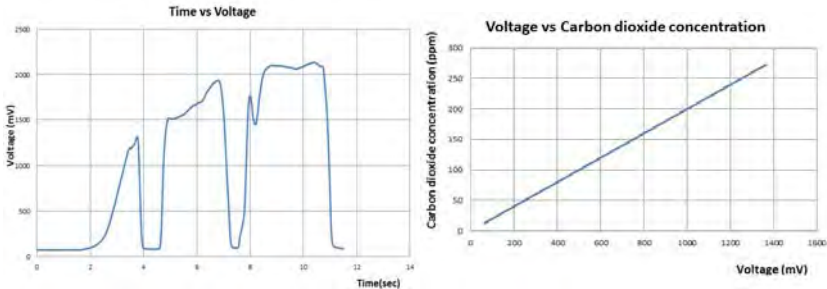
Figure 5: left: Response profile MQ4, time vs voltage; right: Voltage vs Carbon dioxide.

The figure 5-left shows the output voltage of the sensor depending of the gas concentration reading by itself. The result was obtained by adapting the gas

source next to the sensor; meanwhile the gas concentration was increasing.

Figure 5-right shows the relation of output voltage with the carbon dioxide concentration; in this way, the characterization of the sensor was adapted through a linear regression model, obtaining accurate results. An extremely important aspect to mention is the fact that this issue is still being evaluated and treated, with the purpose of implementing the sensor that best shapes to the context and conditioning with the purpose of achieving the best results.

5. Conclusions

The project has achieved systematically the design, development and control of a quadruped walking robot. The mathematical model helped out the modeling of the motion´s behavior of the robot. The robot has 12 DOF in total, 3 DOF for each leg, controlled by an Arduino Nano via a remote mobile device. The movement has been analyzed with biomimetic inspirations take from the spiders. The gas sensor MQ4 was an excellent first approach to the gas sensing technology because it allowed characterizing the behavior of the gas. Additionally, these results will serve us as a foundation in future research.

References

1. Z. Tang, P. Qi, J. Dai. (2017) "Mechanism design of a biomimetic quadruped robot", Industrial Robot: An Intl. Journal, Vol. 44 Issue: 4.
2. S. Shoval, E. Rimon and A. Shapiro, "Design of a spider-like robot for motion with quasi-static force constraints," Proc. 1999 IEEE Intl Conf on Robotics and Automation, Detroit, MI, 1999, pp. 1377-1383 vol.2.
3. Yi Lu, Keke Zhou, Nijia Ye, Design and kinemics/dynamics analysis of a novel climbing robot with tri-planar limbs for remanufacturing, J. Mech., Science and Tech., March 2017, Vol. 31, Iss. 3, pp 1427–1436
4. C. Semini, HyQ - Design and Development of a Hydraulically Actuated Quadruped Robot. PhD Thesis. April 2010.
5. H. Wang, Z. Qi, G. Xu, F. Xi, G. Hu and Z. Huang, Kinematics Analysis and Motion Simulation of a Quadruped Walking Robot with Parallel Leg Mechanism, The Open Mechanical Engineering Journal, 2010, 4, 77-85
6. M. Garabini, C.D. Santina, M. Bianchi, M. Catalano, G. Grioli, A. Bicchi (2017) Soft Robots that Mimic the Neuromusculoskeletal System. In: Converging Clinical and Engineering Research on Neurorehabilitation II. Biosystems & Biorobotics, vol 15. Springer, Cham.
7. C. D. Onal, M. T. Tolley, R. J. Wood, and D. Rus. Origami-Inspired Printed Robots; IEEE/ASME Trans. on Mech., Vol. 20, no. 5, Oct. 2015

SECTION 9

DESIGNS FOR BIOMEDICAL APPLICATIONS

PROPOSAL OF A REMOTE MONITORING SYSTEM OF VITAL SIGNS FOR HEART FAILURE PATIENTS

HECTOR MONTES[1, 2], ELIA CANO[3], CARLOS ROVETTO[3], JUAN SALDAÑA[3], SALVADOR VARGAS[1]

[1]Faculty of Electrical Engineering, Universidad Tecnológica de Panamá, Panama;
[2]Field and Service Robotics Group, Centre for Automation and Robotics (CSIC-UPM);
[3]Faculty of Systems Engineering and Computer Science, Universidad Tecnológica de Panamá, Panama, hector.montes1@utp.ac.pa

The heart failure patients care is increasing, in order to provide the specialized assistance at the right time. Therefore, some researchers have been developed some systems regarding the remote monitoring of the signals of these patients. In this work, it is described a proposal of a remote monitoring system of vital signs, acquired by means of non-invasive biosensors, for heart failure patients. The objective is for monitoring in real-time the vital signs of these patients in order to the specialist doctor to receive the processed data with other added signals and alarms for facilitating his/her diagnosis. This proposal will be developed in Panama, since there is not this kind of system in this country. It will be considered the intrinsic characteristics of the region for this development and also it will be considered the implementation of robotics unit in order to carry out some tasks as patient surveillance, mobile healthcare assistant in rural/remote areas, interface unit between communication systems, etc. However, after to develop this project, it would be extended to other regions of Latin America, since it is very necessary according to statistical data provided by the WHO.

Keywords: Heart failure patients; remote monitoring system; vital signs; bio-sensors; wireless data acquisition system.

1. Introduction

Cardiovascular diseases (CVD) are the leading cause of death in the world, which caused 15 million deaths in 2015 and have been the leading causes of death during the last 15 years, according to the World Health Organization (WHO) [1]. It is also where the most resources are invested from the public and private sectors worldwide, which in Latin America exceeded 30 billion dollars (in 2015), according to the available information from the WHO offered at the Congress of World Cardiology and Cardiovascular Health (WCC 2016) in Mexico [2].

In the statistical results presented by the WHO in WCC 2016 were indicated some Latin American countries have high rates of death from CVD, including

Panama. It was pointed out that heart diseases in Panama affect 29% of the population at a cost of $ 300 million dollars per year [2], which is a very high fee for this country. This is alarming. The Panamanian state must carry out policies for health care in a more forceful way since the percentage destined to deal with this type of diseases is very low, 2% of the annual budget according to the Social Security Department of Panama (CSS, Spanish language acronym) [3].

Some research works have been developed regarding the remote monitoring systems of patients' vital signs in the last decade, generating positive results. However, these works have been carried out in Europe, USA, Japan, etc., but in Latin America has no reference to any important work in this field. Nevertheless, according to [4] the implementation of patient remote monitoring is an issue that must be further developed in the USA and Europe. Therefore, it is obvious this kind of work must be developed in developing countries, such as Panama.

There are interesting projects regarding to telemedicine, e.g., the Health 2.0 project of the Recover Foundation, which is a non-synchronized telemedicine project through clinical platforms and scientific social networks that is a very effective tool for international cooperation projects in the health development. However, remote monitoring in real time did not used to verify patient variables [5]. On the other hand, there is other system named WANDA (Weight and Activity with Blood Pressure Monitoring System) that uses smartphones to collect data of remote way of heart failure patients [6]. Other related system uses the combination microcontroller-GSM-GPS to collect vital signs of these patients at their homes and send them to the hospital database [7]. Other researchers propose develop cost-effective, easy-to-use remote monitoring systems (using modern technology) for the sake of elderly healthcare and well-being [8], which it can be extended to other patients or people. In addition, currently, it is realized studies to understand challenges and design considerations for a personalized mHealth system that could effectively support heart failure patients after they transition into the home environment. To this end, experiences from users, nurses and physicians are collected [9]. This strengthens our proposal related with remote monitoring system of vital signs for heart failure patients.

In this paper, it is described the proposal of a remote monitoring system of vital signs for heart failure patients that comprises several non-invasive biosensors, data acquisition system, wireless connection, data processing, computers, and higher level addressing-communication capabilities. The rest of the article is organised as follow: in Section 2 a summary of patients' care with heart failure in Panama, making use of the technology is described. Afterward, Section 3 presents the proposal of the remote monitoring system. Finally, conclusions and future works are given in Section 4.

2. Overview of patients care with heart failure in Panama using the technology

There are several systems developed and in developing related to the patients care with heart failure in the world, using the telemedicine concepts, remote monitoring systems, etc., in order to improve the quality of life of them. This section focuses on Panama since the proposed project, presented in this work, will be carried out in this country. However, the authors consider the results of this research will have an international scope.

In Panama, according to a study presented by the WHO in [2], it is the fourth with the number of people with some type of CVD in Latin America with 29%, behind Chile, Venezuela, and Brazil. There is a wide difference between the number of people with CVD presented by the CSS with the presented by the WHO, which are 80 thousand people [3] and about one million people [2] with CVD, respectively. Therefore, in this project, these numbers will be reviewed, so that a map or a mathematical model of the affected population can be made.

The CSS has launched the Cardiac Failure Clinic (CFC) in 2017 with the aim of reducing mortality due to this type of condition, reducing hospitalizations, optimizing treatment, improving adherence to treatment, educating the patient and reducing the cost of health [3]. The CFC uses the face-to-face attention to the patients and by means of the videoconference. However, most of the patients cannot receive the specialised attention with only one clinic and with this protocol.

Telemedicine programs have been created in some hospital centres, which contain a communication network at voice and data levels, for the care of patients with specialists and general practitioners [10-12]. In the last 10 years, some tele-radiology works have been carried out and, occasionally, some electrocardiograms have been sent out, in order to be observed and evaluated by the doctor [11]. This is done from a remote hospital centre to another specialized hospital centre, where both have this program. This makes the speed of attention or monitoring of patients is very low, since these works are clearly face-to-face and the evaluation is deferred.

Telemedicine is the application of ICT to the area of health, wherein this project will be developed, which is the remote monitoring of vital signs of people with CVD risks. However, according to [4] the implementation of remote patient monitoring is an issue that must be further developed in the US and Europe. Therefore, it is obvious to know this kind of project must be carried out in developing countries; such is the case of Panama.

3. Proposal of the REMIT system

REMIT is the acronym of the remote monitoring system of vital signs for heart failure patients. This system consists of non-invasive biosensors, data acquisition system, wireless connection, data processing, computers, and higher-level addressing-communication capabilities. Figure 1 shows the architecture conceptualization architecture of this system.
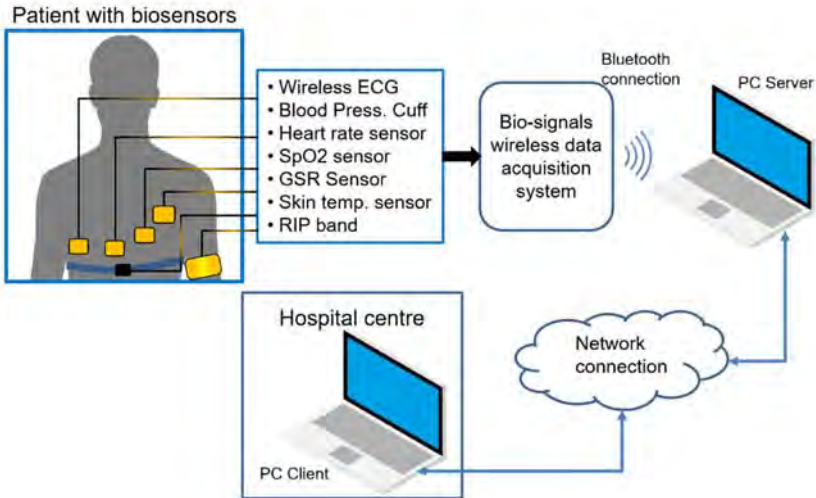

Figure 1. Conceptual Architecture of the REMIT system.

Some non-invasive biosensors are considered for the REMIT system, such as wireless ECG sensor, blood pressure sensor and heart rate sensor as main sensors of the system, but also other sensors can be used such as, pulse oximeter finger clip sensor (SpO2), GSR sensor, respiratory inductance plethysmography (RIP) band, others. Acquiring and processing the signals of these sensors can be obtained from several combinations of human physiological signals. In this case, for monitoring vital signs for heart failure patients.

ECG data and other sensor signals can be seen in real-time on PC server. This collected data is transmitted to this PC through the Bluetooth connection. Therefore, a data analysis after its processing can be carried out, in order to send to the PC client other important data or results together with the real data. After that, at hospital centre, the medical specialist will realize the diagnosis of the patient.

On the other hand, regarding the monitoring of the vital signs of the patient, in real-time, the doctor will be able an earlier diagnosis of heart failure in him/her. Because some alarms can appear depending on the measure threshold of the bio-signals established for each patient, previously settled in the database. With this concept, sudden cardiac arrests can be reduced, since the patient care protocol is activated. It is clear that this methodology must be designed meticulously.

The concepts described above are based when the patient in his/her home. However, the patient can be in any part, e.g., on the street, driving the car, a rural/remote area, etc. In this case, the bio-sensors and the data acquisition system must be connected to other devices, e.g., a smartphone, which replace the PC server in Figure 1. In addition, it is possible to consider an extreme case, where the bio-sensors wireless acquisition system must be connected to another communication mobile system, which can be versatile as a robotics unit for healthcare assistance. Thus, the network connection between the server-client will be Wi-Fi or 3G/4G mobile network. Besides, suppose several patients are being monitored at the same time with different and variable sampling times, depending on the variability their vital signs. Therefore, a server must be connected between the devices worn by the patients (motes) and the PC client, which must be controlled in order to carry out a successful traffic of data. For this, it is essential to have a mathematical model of the patients' distribution, including the main characteristics of their heart diseases, with the aim to have the better decision in the control system. Figure 2 shows the conceptual architecture of the several patients monitored at the same time located in any place, and by different communication systems, depending on their position.

The conceptual architecture summarized in Figure 2 is a complex technical and logistical infrastructure for the patients monitoring with heart failure (obviously, among other kinds of diseases). Therefore, a mathematical model according to the variability of the system must be developed. In this work, the mathematical model proposed will be designed using the Coloured Petri Nets (CPN) [13], since the CPN consist of a graphical representation of an explicit description of states and actions. The model carried out using CPN is useful to work with traffic problems in data networks, since it is necessary to consider the number of data packets transferred and received, the possible loss and overtaking of them, the acknowledgment data, the retransmissions [14], etc.

Initially, a simple CPN model will be designed for the proposed REMIT system presented in this paper, where will be omitted certain parts of the system or will make simplifying assumptions, as shown in the conceptual architecture in Figure 1. Afterward, the CPN model will be gradually modified and extended,

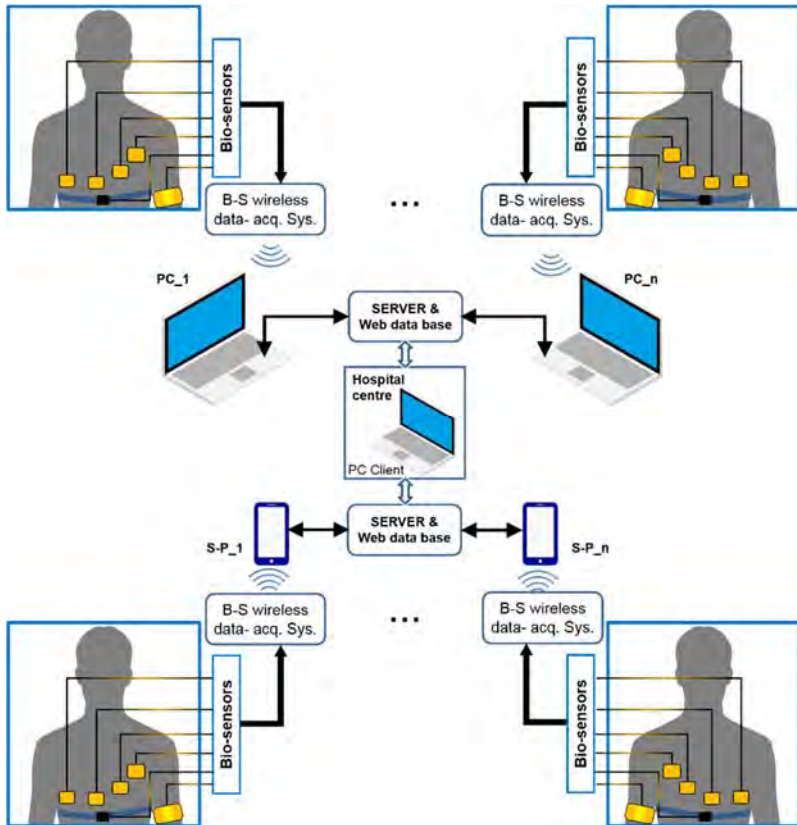adding the other omitted parts of the system and updating the first assumptions realized.

Figure 2. Conceptual Architecture of the REMIT system with several monitored patients.

In Figure 2 the robotics unit can be added in order to detect bio-sensory data through the wireless connection, and other signals of the environment where the patients are. First, the robotics unit can be considered to be installed in rural/remote areas as a mobile healthcare assistant and, in second, as patient surveillance assistant in some hospital that requires data from the patients in real time. Some studies related with the abovementioned can be revised in [15, 16]. However, in Panama case, a rigorous study must be carried out in order to adapt efficiently all mentioned concepts in this paper, for the patient health care and other related issues.

4. Conclusions

In this paper has been described a proposal of a remote monitoring system of vital signs for heart failure patients with the objective to be implemented in Panama. However, this proposal can be extended outside this country border, where this technology not has been developed nowadays.

With the described in this paper, it is evident the need to develop this kind of system in Panama and other countries of Latin America. With the implementation of the REMIT system, the probability of reduction of cardiac arrests will be possible. However, the patient care protocol must be designed and established painstakingly.

The work that will be carried out is extensive and will be divided into several stages since the first experimental tests with the biosensors and the wireless data acquisition system up to the first connection of two or more patients (can be healthy individuals) within a controlled environment. Afterward, the new stages will be added, with more patients in different positions in several places of the city or the country.

References

1. *WHO*, The top 10 causes of death. Media centre, WHO. (January 2017.) Available in: http://www.who.int/mediacentre/factsheets/fs310/es/
2. World Heart Federation, El costo de las enfermedades cardiacas en América Latina. *Congreso Mundial de Cardiología y Salud Cardiovascular (WCC 2016)*, México (2016).
3. CSS, Clínica de falla cardiaca inicia atención en el complejo metropolitano. *Nota de Prensa de la CSS*, (February 2017). Available in: http://www.css.gob.pa/web/8-febrero-2017car.html
4. R. Alvez, Aplicación de Telemedicina para la mejora de los sistemas de emergencias y diagnósticos clínicos. *Memoria de trabajos de difusión científica y técnica* **9**, 91 (2011).
5. D. Pérez-Machón, Telemedicina, una red social médica de ayuda humanitaria entre España y Camerún. *Gaceta Sanitaria* **29**(1), 59 (2015).

6. M. Lan, L. Samy, N. Alshurafa, M-K Suh, H. Ghasemzadeh, A. Macabasco, M. Sarrafzadeh, WANDA: An End-to-End Remote Health Monitoring and Analytics System for Heart Failure Patients. *Proc. of the Conf. on Wireless Health WH'12*, 9:1 (2012)

7. M. Arunkumar, Remote Monitoring of Vital Signs in Chronic Heart Failure Patients. *Intl. J. of Innovative Research in Computer and Comm. Eng.* **2**(1) (2014).

8. S. Majumder, T. Mondal, and M. J. Deen, Wearable Sensors for Remote Health Monitoring. *Sensors 2017* **17**, 130 (2017).

9. N. Alnosayan, S. Chatterjee, A. Alluhaidan, E. Lee, L. Houston, Design and Usability of a Heart Failure mHealth System:A Pilot Study. *JMIR Human Factors* **4**(1), e9 (2017).

10. CSS, Implementación del proyecto de telemedicina en Policlínica de Santiago. *Nota de Prensa de la CSS*. (April 2016) Available in: http://www.css.gob.pa/web/5-abril-2016santiago.html

11. F. Arias, Pasos que ha dado Panamá en el tema de telemedicina. *Avance Tecnológico en Salud, La Prensa*. (June 2016) Available in: https://www.prensa.com/salud_y_ciencia/Pasos-dado-Panama-telemedicina_0_4513048767.html

12. Estrella de Panamá, CSS refuerza la telemedicina. *Noticias, La Estrella de Panamá*. (December 2016). Available in: http://laestrella.com.pa/panama/nacional/refuerza-telemedicina/23977136

13. K. Jensen, Coloured Petri nets. *IEE Colloquium on Discrete Event Systems: A New Challenge for Intelligent Control Systems*, London, 1993, pp. 5/1-5/3.

14. K. Jensen and L.M. Kristensen, *Coulored Petri Nets, Modelling and Validation of Concurrent System*, (2009)

15. K. Boman, M. Olofsson, P. Berggren, P. Sengupta and J. Narula, Robot-Assisted Remote Echocardiographic Examination and Teleconsultation. *JACC: Cardiovascular Imaging* **7**(8), (2014).

16. E. Wicklund, Telemedicine robots: Out of science fiction and into the mainstream. *mHealth Intelligence*. (October 2017) Available in: https://mhealthintelligence.com/features/can-telemedicine-robots-move-from-fantasy-to-fact

COLOURED PETRI NET MODEL FOR REMOTE MONITORING OF CARDIOVASCULAR DYSFUNCTION [*]

CARLOS ROVETTO, ELIA CANO, KARINA OJO, MODALDO TUÑÓN

Department of Computer Science, Universidad Tecnológica de Panamá, Panamá.

HECTOR MONTES

Faculty of Electrical Engineering, Universidad Tecnológica de Panamá, Panama; Field and Service Robotics Group, Centre for Automation and Robotics (CSIC-UPM), Spain

Cardiovascular dysfunction is the main cause of death in the world and several of these incidents have not been detected in time for diverse reasons. Consequently, some research groups, in ICT area, have been developing remote monitoring systems to detect the bio-signals of cardiovascular dysfunction patients in the recent years. In this paper, a Coloured Petri Net (CPN) model for the remote healthcare process is presented. This CPN model uses the patient data formalization by means of set theory, providing a simplified perspective of the data transmission among all elements of the system. Using the CPN model, it will be investigated the behavior the system formed by the patients and their bio-signals, located in different city zones (e.g., Panama), by means of simulation processes, in a first stage. With obtained simulation results, a remote monitoring system of bio-signals using non-invasive sensors will be developed.

Keywords: Coloured Petri Net; Cardiovascular dysfunction; Remote monitoring system; Vital signs; Non-invasive sensors.

1. Introduction

The telemedicine field is changing very fast in different directions with the aim of offer healthcare to different kind of patients remotely located. As technology advances at exponential levels, so does the widespread affordability and accessibility to basic telemedicine tools. Nowadays, it is an advantage, in terms of time and resources, monitoring in remotely way to patients with any disease, especially people who present cardiovascular diseases (CVD) [1].

According to WHO [2], CVDs are the number 1 cause of death globally. An estimated 17.7 million people died from CVDs in 2015, representing 31% of all global deaths. Of these deaths, an estimated 7.4 million were due to coronary heart disease and 6.7 million were due to stroke. Over three-quarters of CVD deaths take place in low- and middle-income countries. People with CVD need early

---

detection and management using counseling and medicines, as appropriate. Considering the two last assertions, in a particular case, it indicates in Panama is necessary to develop a project related to the remote monitoring of CVDs, with the objective to reduce the risk of premature death caused for this disease.

CVD is also the most invested economic resources of the public and private sector worldwide, which in Latin America exceeded, in 2015, 30 billion dollars, according to the data of the WHO offered in the World Congress of Cardiology and Cardiovascular Health (WCC 2016) in Mexico [3]. Additionally, in studies presented to the WHO [3], Panama has the fourth position, with people that suffer any CVD in Latin America, turning into a priority the improvement and the inclusion of monitoring techniques for these patients.

On the other hand, systems modeling is essential in the management of complex and variable systems (as the remote monitoring of CVD) due to allows understanding the different process that can occur through previous simulations, before the implementation of the system. In this case, a system model using Coloured Petri Nets (CPN) can be appropriate of the proposed system in this work. Because it has a graphical representation for an explicit description of states and actions. Moreover, offering hierarchical descriptions, formal analysis, and simulations [4]. These strengths will allow a detailed analysis of remote healthcare process using the proposed CPN model.

A Coloured Petri Net (CPN) model for a system that analyses the cardiovascular dysfunction patients, which they will be remotely monitored, is presented in this paper. This CPN model uses the patient data formalization by means of set theory, providing a simplified perspective of the data transmission among all elements of the system [5] (signals type, signals variability, location, alarms, etc.). Using the CPN model, it will be investigated the behavior the system formed by the patients and their bio-signals, located in different city zones, by means of simulation processes.

This work will be developed in Panama and it is part of the remote monitoring system for heart failure patients project presented in [6]. The rest of this paper is organised as follow: in Section 2 a general description of the proposed system is presented. In the next section, a proposed model using CPN is described. Finally, conclusions and future works are given in Section 4.

2. Description of the system

The main vital signs that will be measured, for carrying out this work, are cardiac frequency, respiratory frequency, arterial pressure, temperature, pulse oximetry

and ECG. All used sensors are non-invasive and their data will be acquired by means of a wireless system.

The conceptualization of the full system is related to a perception of vital signs of a large number of cardiovascular dysfunction patients, located in several areas, e.g., at the hospital, at the city, at the home, at the workplace, and in rural zones. Figure 1 shows the conceived remote monitoring concept, which is divided into three levels, which are: Patient-level, Control centre level, and Healthcare service level.

Patients with non-invasive sensors can be in any place as mentioned above, and the sensors joined to them are connected to a wireless data acquisition system, which it sends the data to any data collector station established for this function, e.g., PC, smartphones, tablets, etc. However, depending on patient localization area, of the characteristic of the place, of the patient numbers, etc, a robotic system can be considered, in order to contribute to re-send the recollected data, to the patient surveillance, as a mobile healthcare assistant, etc. This robotic system would be included within the patient-level. Some researchers have considered the robotic systems into the automatic healthcare functions [7, 8]. Therefore the robotic system for this work will be very useful for the accomplishment of several tasks.
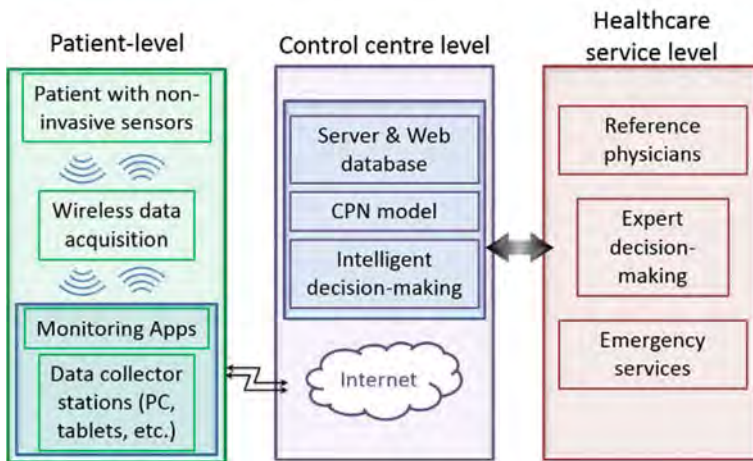
Figure 1. General overview remote monitoring system.

Control-centre level is compound by the network connection, specifically, the Internet, where is a server with a database, established previously with the first data received from the hospital centre. CPN model will be implemented into the server, which has been previously validated by means of several simulation

processes. Intelligent decision-making will be carried out using the designed CPN model in order to provide to the next healthcare-service level relevant information in order to the experts take the final decisions.

3. Proposed model using CPN

The proposed CPN model shown in Figure 2 represents a basic structure and processes related to the Health Care Service. The circles represent states, the rectangles represent processes and the arcs indicate information flows.

This abstraction process catches basics elements using simplified way, due to limited space. Moreover, the control flow decisions are represented using basic data. However, the structure remains functional for other data. Uppercase variables represent colored tokens, and the lower case represents variables used during the data flows. Values enclosed in parentheses represent data entries provide by the sensors and established medical information.
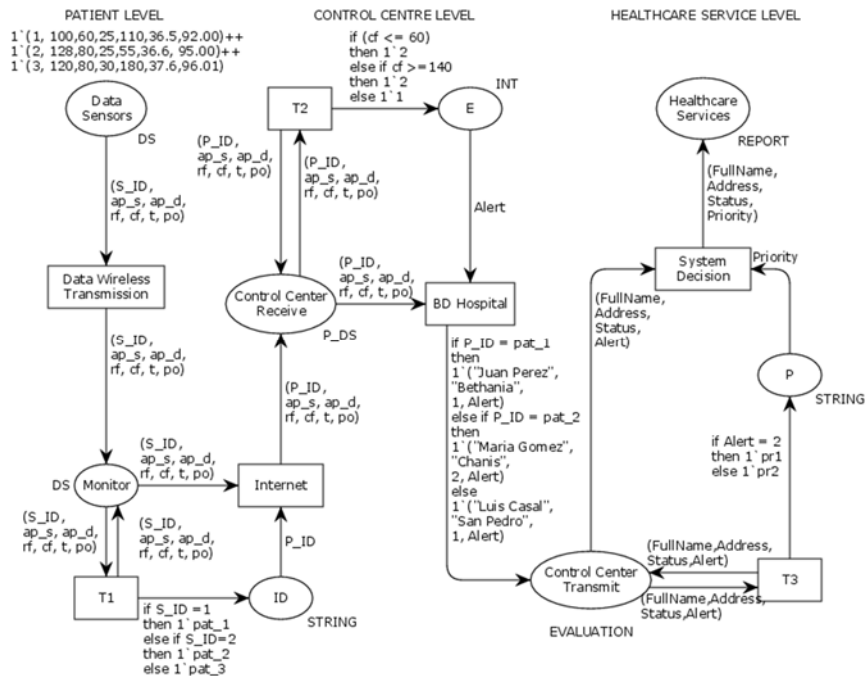
Figure 2. Coloured Petri Net Model.

Inputs parameters of the CPN net, shown in Figure 2, correspond to vital signs' measurements, i.e., systolic pressure (ap_s), diastolic pressure (ap_d),

respiratory frequency (rf); cardiac frequency (cf); temperature (t) and oxygen saturation (po). These values are chosen in an aleatory way for simulation purposes with the CPN model.

The CPN model conserves the proposed stages or levels in Figure 1, whereby the process starts with data collection by non-invasive sensors (see "Data Sensors" in Figure 2). For simulation purposes, it is considered an identification number for each sensor (S_ID), which will be used to identify the patient (in the proposed CPN model in Fig. 2 has been considered three patients as an example). The monitor device that receives the data from the sensor carries out the patient identification process. The next step is to send this information by the Internet to the server of the Control Centre level (see "Internet" in Fig. 2).

In the server (see "Control Centre Receive" in Fig. 2), the received information is evaluated by taking into consideration the criteria charged and given previously by reference physicians, to ensure the highest accuracy in the decision-making. The CPN model shown in Figure 2 presents a specific example related to the evaluation for one of the vital signs of the patient, which is the cardiac frequency (cf). In this case, depending on the cf values received, the CPN model assigns an alert level, where the highest value represents a more critical situation of the patient.

Data's verification processes are represented in the CPN model using auxiliary places and transitions. For the patient identification (P_ID), the variables in the CPN model representing the following:

- T1 and ID verify the sensor's identification number.
- T2 and E check the sensor's data and generate an alert (Alert) if necessary.
- T3 and P assign a priority (Priority) of being attended, based on clinical history and current patient status.

The final step consists of the intelligent decision-making by the proposed CPN model. The system generates a final report that is sent to Healthcare-Service level, which specifies the severity of the patients' conditions to physicians and experts in order to allow them taking action as fastest as possible. The proposed system could take other automatic decisions, based on intelligent decision-making such as (1) to send an ambulance toward the patient location, with independence if the patient is a different city where the system is installed; (2) to send a notification to a physician close to the patient with the collected data of him; (3) to send a notification to relatives if the patient is alone, etc.

CPN offers clear advantages for systems modeling, specifically for those systems where data transmission is critical for decision-making, as described above. This is because the CPN model has considerable strengths in visual

representation and simulation processes, which allow understanding abstract processes, as data management in real time, in a simple way, where common datatypes can be used during simulations.

Using a CPN model foresees to raise the efficiency level for the remote monitoring of CVD within the system proposed in this work. Even more when it is considered to have a robotic system within the first level of the proposed system, which it will make the system more versatile because several automatic actions will be included in future works.

4. Conclusions

In this paper, a system for the remote monitoring of cardiovascular dysfunctions has been described, which will be implemented in Panama, due to the high rate of CVD in Panama and the Latin-American region. The main idea is to contribute to increasing the medical attention to a large number of patients and in that way reduce the risk of premature death. Therefore, the health specialist, using the proposed system, will be able to take the right decisions after the early diagnostics for the patients' disease.

This system includes a CPN model, which has not been used for this application type according to the literature reviewed. Several discrete events will be considered into the CPN model and will be simulated using several possible cases acquired by medical personnel. In this work, it has been presented a simple simulation using three patients, and it has been evaluated the cardiac frequency vital sign, as an example. It is expected the CPN model will provide good results when it has been applicated to several patients located in different places.

Acknowledgments

References

1. WHO, "A Health Telematics Policy," *Report- WHO Group Consultation on Health Telematics - A Health Telematics Policy*. pp. 1–39, 1998.
2. *WHO*, Cardiovascular diseases (CVDs). Media centre, WHO. (May 2017).
3. "El costo de las enfermedades cardíacas en América Latina.," Congr. Mund. Cardiol. y Salud Cardiovasc. (WCC 2016), 2016.
4. K. Jensen, *A Brief Introduction to Coloured Petri Nets*, (2005)

5. K. Jensen and L.M. Kristensen, *Coulored Petri Nets, Modelling and Validation of Concurrent System*, (2009).
6. H. Montes, E. Cano, C. Rovetto, J. Saldaña, S. Vargas, Prop. of a rem. monit. sys. of vital sings heart failure patients, In *Proc. CLAWAR 2018*, (2018).
7. K. Boman, M. Olofsson, P. Berggren, P. Sengupta and J. Narula. *JACC: Cardiovascular Imaging* **7**(8), (2014).
8. E. Wicklund, Telemedicine robots: Out of science fiction and into the mainstream. *mHealth Intelligence*, (October 2017).

DESIGN OF A GRIPPING MOVEMENT CONTROL SYSTEM FOR A ROBOTIC HAND PROSTHESIS

RUTTY CEDEÑO ARANA[1], LISBETH MENA[1], HECTOR MONTES[2,3], RICARDO CAJO[1]

[1]*ESPOL Polytechnic University, Escuela Superior Politécnica del Litoral, ESPOL. (Facultad de Ingeniería en Electricidad y Computación), Campus Gustavo Galindo Km. 30.5 Via Perimetral, P.O. Box 09-01-5863, Guayaquil, Ecuador.*

[2]*Field and Service Robotics Group, Centre for Automation and Robotics-CAR (CSIC-UPM), Spain.*

[3]*Faculty of Electrical Engineering, Universidad Tecnológica de Panamá, Panama.*

rutacede@espol.edu.ec, lismena@espol.edu.ec, hector.montes@csic.es, rcajo@espol.edu.ec

In this paper, a description of a control system for basic grip movements for a low-cost hand prosthesis is presented. The idea is to provide movements to those people who do not have fingers due to congenital malformations, considering that the movements of their wrists are complete. The wrist movements are acquired by means of the Myo bracelet, which has wireless communication. The Myo bracelet has eight myoelectric sensors and an IMU, i.e., non-invasive sensors that are positioned around the forearm. The gestures read by means of the Myo bracelet are processed by the control system to send the commands to the small electric actuators installed in the prototype hand prosthesis.

Keywords: Robotic hand prosthesis; gripping movements; control system; non-invasive sensors; Myo bracelet.

1. Introduction

There are several causes why a person can have a physical disability, ranging from congenital malformations to degenerative diseases or accidents. The loss or absence of upper limbs of the human body is a limiting factor for the development of activities of daily life. The hand is one of the most useful parts of the body and the most used in daily activities, so the loss of it or lack of fingers is a drawback that greatly diminishes the functionality of the body. Some of the contributions that help improve the quality of life in people who have this condition, are robotic hand prostheses [1], [2].

The hand prosthesis that is proposed in this work will be controlled using myoelectric signals acquired from the forearm muscles and the use of IMU data

(inertial measurement unit). In this work, the device used is the Myo bracelet, developed by Thalmic Labs, which has an inertial measurement unit of nine axes and EMG (electromyography) muscle activity sensors. This bracelet is placed on the upper part of the forearm. In addition, it has a wireless communication interface, with low power consumption Bluetooth 4.0, which provides access to the raw data corresponding to IMU and EMG sensors [3]. The acquired data will be sent to a nano Arduino controller card in which the libraries and the corresponding program will be loaded to carry out an individual control of five servomotors in charge of the movements of flexion and extension of each finger of the prosthesis.

This project emerged with the motivation to develop a low-cost prosthesis to allow carry out gripping basic movements for Ecuador citizens that have this kind of problem. However, it has been considered a specific case of a person who has a birth defect in one hand. It has been diagnosed as metacarpal agenesis, which refers to the absence of partial or total of an organ or a tissue of the organism. In this case, the absence of fingers. However, the movements of the wrist are complete [4].

2. System Description

2.1. *Description of the elements of the prototype*

The Myo bracelet used in this project has its own processor called ARM Cortex M4Processor [5], to process the data of the 8 EMG sensors arranged as a bracelet, which thanks to its expandable band adapt to the shape of the forearm. It also has a gyroscope, an accelerometer and a magnetometer.

The standard communication and data acquisition of the Myo bracelet is realized by connecting it to a computer, through its USB Bluetooth adapter. This concept avoids the possibility of developing a portable prototype and the direct connection with other electronic platforms. Therefore, it is necessary to design and develop another route of data transmission. Consequently, for this project, an integrated Bluetooth 4.0 device with low power consumption has been employed [6].

The general structure of the software is composed by means of two libraries called MyoBridge and MyoIMUGestureController. The first library allows bidirectional communication with the Myo bracelet, and the second is responsible for reading and recognizing gestures. Besides, the second library contains the main program, where the control parameters are established and conditions for the generation of movements of the prosthesis.

2.2. *Control system architecture*

The control of the hand prosthesis shown in Figure 1 is based on the acquisition of IMU and EMG data captured by the Myo bracelet, which is positioned on the upper part of the forearm. It communicates wirelessly to a nano-Arduino controller card. This controller uses a Bluetooth module with low power consumption as an intermediary. The controller card is responsible for processing the signals captured by the Myo bracelet and transfers them into patterns of grip movements for a 3D printed prosthesis [7], by activating the servomotors.

The control for grip movements for the hand-held robotic prosthesis described in this work is based on the programming of an Arduino Nano board. This decision has been taken with the objective to develop a low-cost usable prototype and the simple programming language that provides the Arduino system. However, the knowledge that will be acquired in this work can be extrapolated using other types of electronic devices.

In addition, it is also considered the suitable motions of the prosthesis for the user comfort. The Myo bracelet has pre-established gesture recognition, movement tracking and measurement of muscle activity. As has been mentioned above, this system uses a Bluetooth 4.0 module in order to transmit and receive data in wireless mode. Because most low-power Bluetooth models have a very limited feature set, none of these is capable, under its factory state, of directly connecting to the Myo bracelet. This problem has been solved by loading a custom firmware MyoBridge, with CCLoader program and making the respective hardware connections.
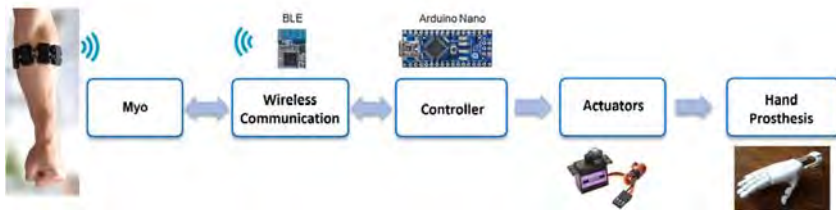
Fig. 1. Block diagram with the main components of the system.

3. Results

3.1. *Reading status*

The prosthesis has three LED indicators, a red-LED to show low battery level, an RGB-LED shows the gesture and a blue-LED shows reading state.

The state of data reading begins with a signal of muscular activity or a movement that produce force signals. The reading period it is programmed to be active for a lapse of 6 seconds, approximately. It may end or be blocked by the same muscle activity signal that was initially performed. For visualization, a blue LED is used, which will remain on only in the time of data acquisition.

3.2. *Gesture recognition*

Although the Arduino serial monitor is a useful tool for visualizing the gesture interpreted by the program, it only can use during the simulations. Therefore, another way of knowing the gesture that was recognized or not recognized is through the RGB-LED indicator, as shown in Figure 2.
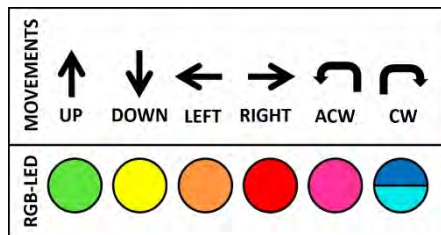
Fig. 2. Movement patterns and gesture indicators.

3.3. *Movements of the prosthesis*

Currently, the prosthesis movements are established in response to the registered gestures. In this case, it has been registered four movements of signs and five movements of grip, as shown in Table 1.

Table 1. List of movements of the prosthesis

Movement	Description
Grip 1	Hold hands
Grip 2	Hold bottle
Grip 3	Hold a cup
Grip 4	Hold mouse (Principal and secondary buttons)
Grip 5	Hold with index and middle fingers
Sign 1	Number 1, Point with the index finger
Sign 2	Number 2, Extension only the index and the middle fingers
Sign 3	Number 3, Flexion of the thumb and the index finger
Sign 4	Open hand, extension of the 5 fingers

Next, each one of the established grip movements will be described:

- Hold hands: This position is shown in Figure 3(a). It is achieved when the little, middle and index fingers are contracted, in order to be able to give greetings with a handshake.
- Hold bottle: This position is shown in Figure 3(b) and is achieved when all fingers except the thumb are contracted, in order to hold cylindrical objects.
- Holding mouse: This position is shown in Figure 3(c) and is achieved by contracting the little finger, ring finger, and thumb. These fingers in conjunction with the support of the palm control the sliding of a mouse on a surface flat. In addition, once the person is in this position, two more movements are unlocked, i.e., right click with the middle finger and left click with the index finger. This grip movement pretends to convert the prosthesis into a tool.
- Hold cup: This position is shown in Figure 3(d) and is achieved by contracting the little and ring fingers, so that the middle and index fingers are placed in the ear of a cup, then they contract and hold.
- Hold with index and middle fingers: This position is shown in Figure 3(e) and is achieved when the index and middle finger are closed to hold small objects such as tennis balls, keychains, etc.

The Figure 3(f) shows the prosthesis prototype used by the person with congenital malformation.
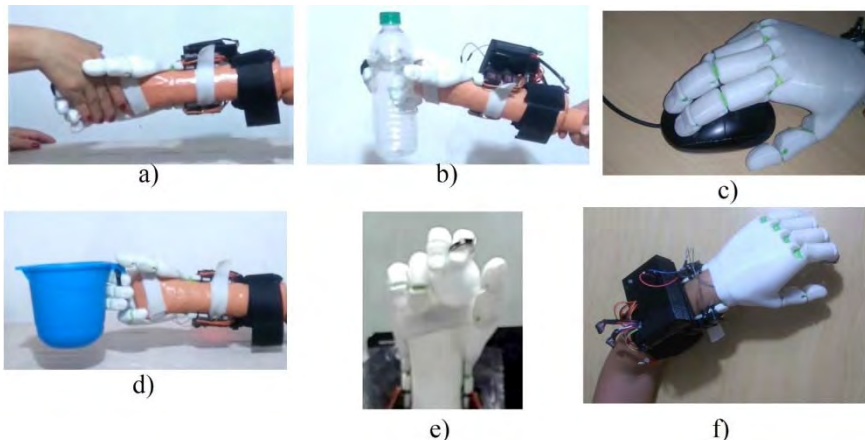
Fig. 3. Movement patterns and gesture indicators.

For gripping movements, a force resistive sensor (FSR) was installed in the fingerprint position of the index finger. Its functionality is to allow feedback

control loop when the grip has been carried out. As a future work, FSR will be installed on all fingers to have new control conditions.

4. Conclusions

The control of the hand prosthesis was made by means of Bluetooth 4.0 communication between the Myo Bracelet and the Arduino Nano card, with this the use of cables for the capture of the signals coming from the Myo bracelet sensors was eliminated. The reading patterns that the Myo bracelet should read are generated from movements of the forearm that are achieved with complete naturalness, which represents a great advantage since it facilitates the handling of the prosthesis.

The use of 3D printing technology can easily the manufacture of custom prostheses, since most people do not have the same deformation patterns in their extremities. In this work, a custom prosthesis has been designed and implemented to be used by the person that collaborates with the project.

The current prototype can perform nine movements, of which four are of sign making and five are grip movements. While the printed prosthesis allowed to validate the grip movements defined in the control system, this presented any drawbacks due to the material used in its printing. The rigid plastic generated slippages in most of the textures during the experimental tests using the prosthesis.

For future works, it will be acquired servomotors with torques higher than the current servomotors in order to exert sufficient force on the tendons of the hand to move and lift objects with considerable weight. Additionally, the 3D printed hand will be cover with special material in order to avoid the slippages.

Acknowledgements

References

1. J. Zuniga, D. Katsavelis, J. Peck, J. Stollberg, M. Petrykowski, A. Carson, and C. Fernandez. Cyborg beast: a low-cost 3d-printed prosthetic hand for children with upper-limb differences. *BMC Res Notes* **8**, No. 1, p. 10. (2015)

2. M. D. R. Ahsan, M. I. Ibrahimy, and O. O. Khalifa. Advances in electromyogram signal classification to improve the quality of life for the disabled and aged people. *Journal of Computer Science* **6**(7), 706. (2010)

3. Thalmic Labs, (Nov. 2015). Meet the Man With a Myo-Controlled Robotic Arm. [online] The Lab. Available in: http://developerblog.myo.com/meet-the-man- with-a-myo-controlled-robotic-arm/

4. M.A. Tonkin, S. K. Tolerton, T. J. Quick, I. Harvey, R. D. Lawson, N.C. Smith, and K. C. Oberg. Classification of congenital anomalies of the hand and upper limb: development and assessment of a new system. *Journal of Hand Surgery* **38**(9), 1845-1853, (2013).

5. Myo Gesture Control Armband, Myo.com, (2014), [Online]. Available in: https://www.myo.com/techspecs.

6. JNHuaMao Technology Company. Bluetooth 4.0 BLE module, Datasheet. (2014).

7. Flexy-Hand2. Thingiverse.com, (2014), [Online]. Available in: https://www.thingiverse.com/thing:380665.

8. C. Setiawan. Tangan Robot Bionik dengan Kendali Otot Berbasis EMG. *Journal Tahun*, (2015).

9. F. V. Tenore, A. Ramos, A. Fahmy, S. Acharya, R. Etienne-Cummings and N. V. Thakor. Decoding of Individuated Finger Movements Using Surface Electromyography. IEEE Trans Biomed Eng. **56**(5), 1427, (2009).

ROBOTICS FOR FACIAL RECONSTRUCTION USING MEDICAL IMAGES

JOSÉ SERRACÍN, IVETH MORENO, RONY CABALLERO

Faculty of Electrical Engineering, Universidad Tecnológica de Panamá, Chiriqui, Panama

HECTOR MONTES

Faculty of Electrical Engineering, Universidad Tecnológica de Panamá, Panama; Robotics of Exteriors and Services Group, Center of Automatics and Robotics, CSIC-UPM, Spain

The presented study in this paper deals with the development of a cranio-maxillofacial reconstruction system in three dimensions, which will interact with a haptic tool. In turn, a specific robot will be controlled using this tool, which it has installed applications associated with surgery. The proposed system will help physicians gain pre-operative experience, based on reconstructions of three-dimensional images taken from real patients. Good results have been obtained, which validate the proposed system.

1. Introduction

This article deals with the topic of cranio-maxillofacial reconstruction using medical images in two dimensions (2D) for its reconstruction in three dimensions (3D) within a virtual scenario, and the integration of a tele-operated robot by means of a haptic joystick. Specifically, it will refer to tests performed with the robot in bone machining tasks. In addition, in this work, the results obtained on the study and validation of the tele-operated system to perform simulated cranio-maxillofacial surgeries are presented.

The main objective of using a robot in maxillofacial reconstruction is to propose the use of a system that allows the doctor to obtain hours of effective preoperative practices for surgeries.

The article is structured as follows: in Section 1, introduction. Section 2, a brief state-of-the-art has been introduced. In Section 3, the description of the system will be presented. Section4, presents some experimental results. Finally, conclusions and future work are presented in Section 5.

2. Background

Among the most presented cases in the emergency rooms of hospitals in Latin America and worldwide, are the traumatic brain injuries (TBI), which are any structural or functional injury of the skull and / or its secondary content due to an abrupt exchange of energy mechanical [1]. This is a problem with a high incidence of mortality and morbidity in patients of productive age, affecting mainly the population between 15 to 45 years [2]. The main and most common cause of this problem is traffic accidents, with a 75%, approximately. A large percentage of survivors of this situation will have disabling sequelae [3], if they have not an early diagnosis and an adequate therapeutic strategy.

In order to help in this type of problem, training programs have been implemented to perform laparoscopic procedures, thus acquiring a fundamental role in surgical training. This training is intended for either resident doctors or surgeons, who wish to practice in new minimally invasive techniques, previously to surgery in patients [4]. In these surgical procedures, it has been required to change the model of surgical teaching that they had for more than a century of use, giving rise to the development and application of new simulation techniques, and bringing with them a tutored and optimized teaching, with more dexterity and fewer mistakes. In this way, better skills of the trained subject have been developed and the risk of subjecting patients to surgical errors and their potential subsequent damage is diminished, compared with the classic teaching model [5].

The presented study deals with the development of a cranio-maxillofacial reconstruction system in three dimensions, which will interact with a haptic tool that will also control a robot, with applications associated with surgery, also allowing tests with pig bones. The proposed system will allow the surgeon to perform preoperative tests in a simulated environment, with images of real patients. It should be noted that the surgeon can acquire some certain skills through the use of the robot to make more precise and reliable cuts and/or perforations.

3. Description of the system

The system that was developed consists of a user interface, which has an application which is fed by a stack of real cranio-maxillofacial images in two dimensions (2D), for reconstruction to a virtual solid in three dimensions (3D). The user interface was developed from the QT4 libraries, which is a cross-platform application development kit. The interface has a user-friendly environment. Through it, imagery files can be imported and, besides, they can be configured with the imagery acquired parameters.

The images are reconstructed generating a solid in three dimensions (3D), using the VTK libraries and visualized in a graphic environment within the interface created with QT4. At this point, the virtual representation of the proxy (final effector) of the Phantom Omni haptic joystick is added to the rendered image. The haptic joystick allows having a force feedback, which helps the operator in the control of the end-effector.

The joystick is in charge of controlling the end-effector of the robot that will perform the machining tasks in the bone, such as drilling, roughing, etc. In addition, the joystick will give the surgeon a feeling that he is in a real environment, guaranteeing the possibilities of a better performance during the surgery.

The robot used in this system was designed and assembled exclusively for this purpose. The robot is a two-bar parallel type, with two modular degrees of freedom [6], and with all the characteristics of a robot with a parallel structure: speed, precision, and small workspace, among others.
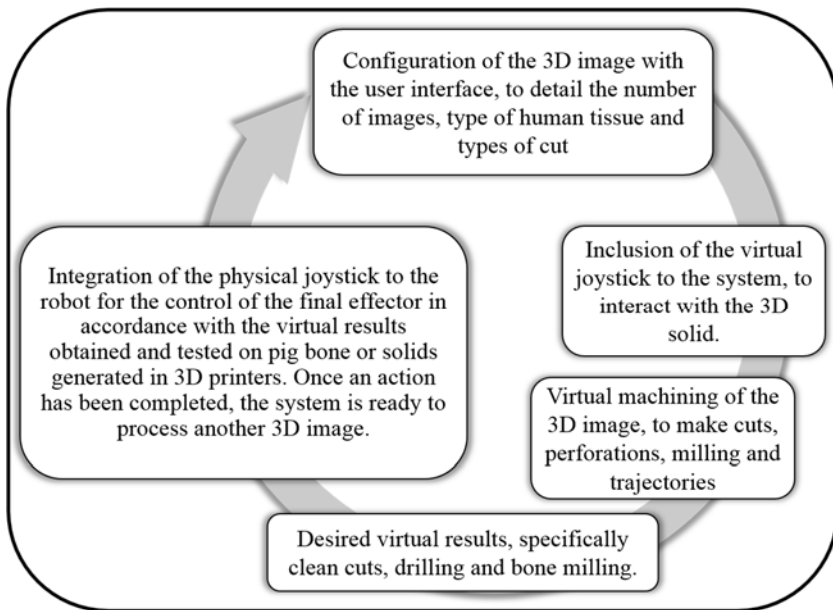
Figure 1. Description of the functioning of the facial reconstruction system using robotics.

The operation of the system can be considered in two phases: a first phase in which all virtual tests will be performed with the 3D reconstruction of skull-

maxillofacial images and the haptic joystick, until obtaining the desired results; and a second phase in which the joystick controls the end effector of the robot to perform tests on solids such as skulls printed with 3D printers or on the bones of animals such as pigs. The description of the system is summarized in Figure 1, and the interaction between each of the elements that comprise it is shown in Figure 2.
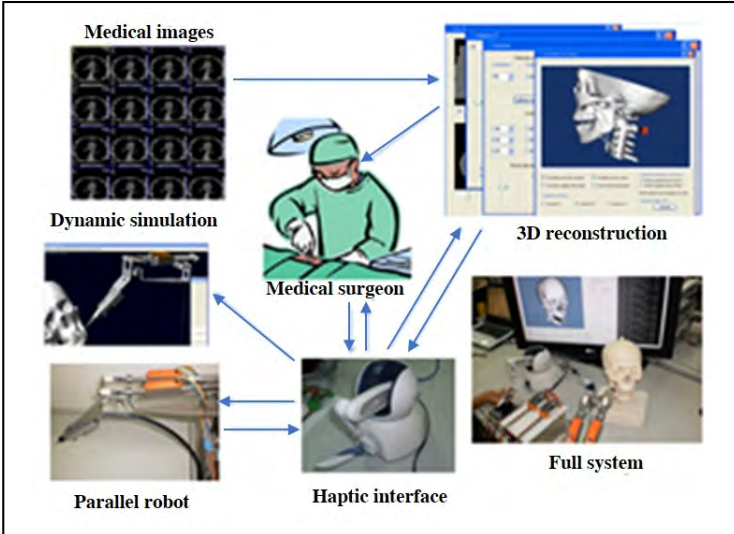
Figure 2. Interaction between the elements that make up the complete system.

4. Experimental results

The experimental tests of the proposed system were carried out with pig bones (see Figure 3), since this type of bone is very similar to the bone tissues of the human being, but stronger. To perform the machining tests on the bones, a drill bit placed in the end effector of the robot is approached at a constant speed of 8 millimeters per second (mm/s), approximately. Once the bone is reached and it is touched with the drill, the approach speed decreases to 0.25 mm/s, so that when the bone is drilled, no pressure is exerted that could splinter or break the bone during the drilling task.
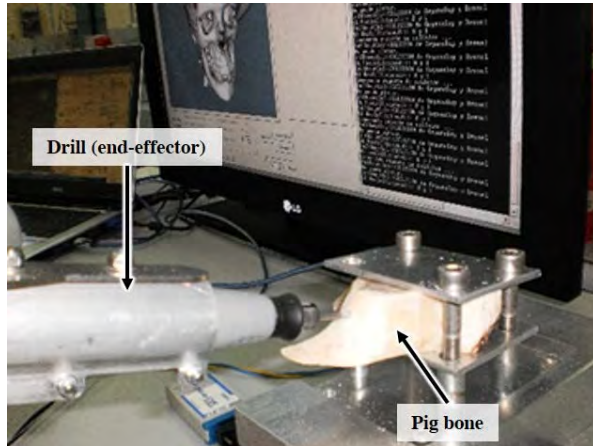
Figure 3. Final effector drilling a pig bone

The force exerted by the end effector on the bone is controlled taking into account the feedback obtained from the values of working current measurements made to each motor (see Figure 4). The approach speed control system is constantly being updated. So, if the currents increase above the maximum working current of the motors (around 450 mA), then the approach speed will be immediately reduced until the current consumption is maintained within the stipulated ranges (see Figure 5). Preventing the bone from fracturing or splintering.
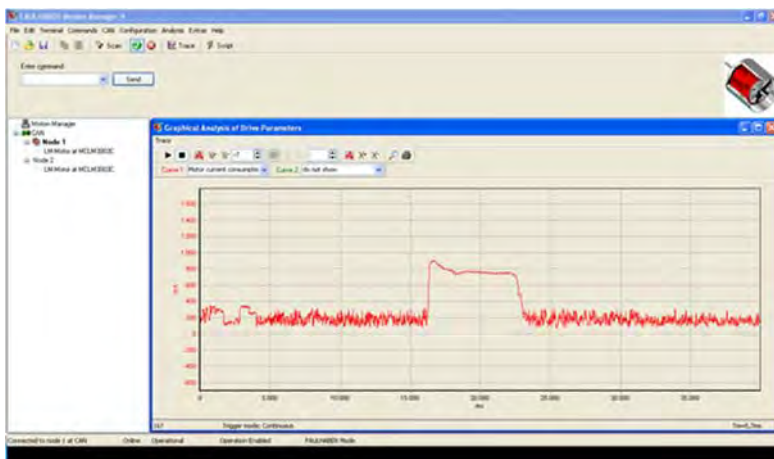
Figure 4. Measurement of the working current in motor 1 (without speed control).
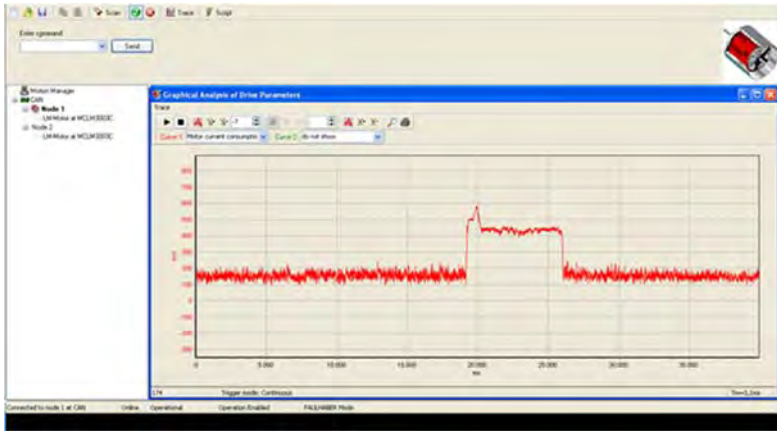
Figure 5. Measurement of the working current in motor 1 (with speed control).

The end-effector speed has been controlled by means of a PID controller. This controller has been implemented in LabVIEW, and in the user interface some values capture boxes have been placed in order to set the PID control parameters in any moment. The objective of this is to correct the approaching speed of the end-effector to the bone during the experimental tests. It is clear this manual control is only during the firsts experimental tests.

5. Conclusions and future work

The graphics interface presents all the options for an adequate treatment of 3D imagery, such as the movements of the solid generated in any direction, approaching and moving away from the solid, the making cuts, etc.

The full system (integrated by the robot with a parallel structure and by the haptic tool that in turn serves to control and guide the end-effector of the robot, product of the interaction of the haptic tool with the solid generated in 3D reconstruction) has given results satisfactory in terms of replication of guided trajectories, keeping consonance with the positions and orientations required.

It is expected as a product of future work the robot meets the requirements necessary to perform preoperative exercises of cranio-maxillofacial interventions. Besides, it will be created an algorithm, which automatically will generate the trajectories that the robot must perform. This will allow integrating surgical navigation with a robotic tool in the same application.

Acknowledgements

References

1. M. A. Hernández, A. J. Felipe, A. D. Mazariegos and M. L. Campos, Caracterización epidemiológica y clínica del trauma craneoencefálico producido por accidentes de tránsito, Guatemala, p. 87 (2017).
2. R. Carrillo and J. M. Meza, Trauma craneoencefálico, *Revista Mexicana de Anestesiología*, **38**, nº 3, pp. S433-S434 (2015).
3. A. Cabrera, O. Martínez, A. Ibarra, R. Morales, G. Laguna and M. Sánchez, Traumatismo Craneoencefálico Severo, *Revista de la Asociación Mexicana de Medicina Crítica y Terapia Intensiva*, **XXIII**, nº 2, pp. 94-101 (2009).
4. F. León, J. Varas, E. Buckel, F. Crovari, F. Pimentel, J. Martínez, N. Jarufe and C. Boza, Simulación en cirugía laparoscópica, *Cirugía Española*, **93**, nº 1, pp. 4-11 (2015).
5. N. Kerrigan, Simulación, ¿una necesidad en el entrenamiento para la cirugía laparoscópica colorrectal?, *Revista Chilena de Cirugía*, **69**, nº 6, pp. 508-512 (2017).
6. J.R. Serracín, L.J. Puglisi, R. Saltaren, G. Ejarque, J.M. Sabater-Navarro and R. Aracil, Kinematic analysis of a novel 2-d.o.f. orientation device, *Robotics and Autonomous Systems* **60**, 852-861 (2012).

SECTION 10

MULTIROBOTS AND COOPERATIVE SYSTEMS

NAVIGATION OF QUADRUPED MULTIROBOTS BY GESTURE RECOGNITION USING RESTRICTED BOLTZMANN MACHINES

ARATA A. SARAIVA[1]

UTAD University,Coimbra, Portugal
ORCID: 0000-0002-3960-697X [1] E-mail: aratasaraiva@gmail.com

SANTOS, D. B. S[2] and MARQUES JUNIOR, F.C.F [3]

State University of Piaui,
Piripiri, Piaui, Bazil
[2] ORCID: 0000-0003-4018-242X [2] E-mail: domingosbruno@prp.uespi.br
ORCID: 0000-0002-2751-0137 [3] E-mail: dev.jrmax@prp.uespi.br

JOSE VIGNO M SOUSA[3]

State University of Piaui, Piripiri,Brazil
University Brazil, Sao Paulo, Brazil
ORCID: 0000-0002-5164-360X [3] E-mail: vigno@prp.uespi.br

N. M. FONSECA FERREIRA[5]

Department of Electrical Engineering, Institute of Engineering of Coimbra,
Coimbra, Polytechnic Institute
Rua Pedro Nunes, 3031-601 Coimbra, Portugal
Knowledge Engineering and Decision-Support Research Center (GECAD) of the
Institute of Engineering, Polytechnic Institute of Porto
INESC-TEC Technology and Science, Campus da FEUP, Rua Dr. Roberto Frias, 378,
4200 - 465 Porto, Portugal
ORCID: 0000-0002-2204-6339 [5] E-mail: nunomig@isec.pt

ANTONIO VALENTE[6]

INESC-TEC Technology and Science
Campus da FEUP, Rua Dr. Roberto Frias, 378, 4200 - 465 Porto, Portugal
School of Science and Technology, University of Trás-os-Montes and Alto Douro,
Vila Real, Portugal
ORCID: 0000-0002-5798-1298 [6] E-mail: avalente@utad.pt

This article discusses a method that performs gesture recognition, with the objective of extracting characteristics of the segmented hand, from dynamic

images captured from a webcam and identifying signal patterns. With this method it is possible to manipulate simulated multirobots that perform specific movements. The method consists of the Continuously Adaptive Mean-SHIFT algorithm, followed by the Threshold segmentation algorithm and Deep Learning through Boltzmann restricted machines. As a result, an accuracy of 82.2%.

1. Introduction

A line of research and development in robotics that has received attention in recent years is the development of bio-inspired walking robots[1].[2]

Systems with artificial intelligence are applied in pattern recognition and can be coupled to manipulable robots, being used in industrial automation, patrols and territorial surveillance,[3] have resulted in systems that can operate on structured and unstructured media,[4] through the use of advanced sensorial feedback mechanisms, making decisions based on learning algorithms and reasoning.

Based on this has inspired the design of manipulation of 4 legs spider multirobots Figure 4, quadruped simulated, by means of manual gestures. The Objects of interest that need to be detected and reviewed are coordinated as being processed in real time. The method chosen and implemented is the capture and detection of regions of interest in the scene. With a preprocessing for noises reduction in the image acquisition process, the Threshold segmentation algorithm was used. And in the last step is performed the real-time classification by an artificial intelligence, which consists of a deep learning known as Restricted Boltzmann Machines (RBM).

The method covered ensures robust coverage in image recognition,[5] under certain assumptions that will be clarified throughout the text in robotic simulation. The developed structure allows the robots to maintain or alter the formation of the specified trajectories.

The document is divided into 6 sections, in which section 2 is characterized by the model of simulated robots used, section 3 consists of kinematics, follows the formulation of the central algorithm applied in section 4 and the statistical method to verify the reliability of the used system . The results after application of the proposal are presented in section 5 and the conclusion in section 6.

2. Quadruped Robot

Locomotion of legs on natural terrain presents complex problems such as foot placement, avoiding obstacles, load distribution, general stability[6].[7]

One way to deal with these problems is to use models that describe mathematically the different situations.[8] The model adopted has 4 identical legs, as can be seen in the Figure1.

Figure 1.   Quadruped Model

3. Kinematic

Kinematics is the branch of mechanics that studies the movement of a body or a system of bodies without considering its mass or the forces acting on it.[9]Kinematics has two types, direct and inverse kinematics. In the direct kinematics it is desired to obtain the position and orientation of the actuator in the Cartesian space of the base, from the positions of the joints[10] .

The inverse kinematics consists of the process of determining the angles in terms of the coordinates for the desired position of the leg in the Cartesian system.[9]

The procedure for obtaining the equations is strongly dependent on the configuration of the robot.[11] The kinematics chosen by the present work is the inverse, in this case, is obtained through geometric definitions based on the shape of the leg Figure2, the equations obtained are 1, 2, 3.
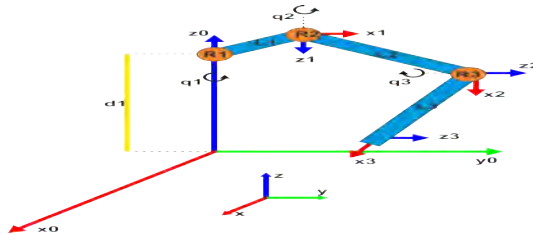
Figure 2.   Kinematic model of the legs.

$$\theta_1 = \arccos\left(\frac{y_1}{x_1}\right) \tag{1}$$

$$\theta_2 = \arccos\left(\frac{L_2^2 + x_3^2 + y_3^2 - L_3^2}{2.L_2.\sqrt{x_2^3 + y_3^2}}\right) + \arctan\left(\frac{y_3}{y_3}\right) \tag{2}$$

$$\theta_3 = \pi - \arccos\left(\frac{L_2^2 + L_3^2 - \left(x_3^2 + y_3^2\right)}{2.L_2.L_3}\right) \tag{3}$$

Each leg of the Quadruped Robots is composed of a chain of three links of freedom Figure 2.The assignment model of the link frame of the links is based on Denavit-Hartenberg direct geometric modeling algorithm.

The Figure 2 illustrates the leg used for the Robots, in which it has three joints R1, R2 and R3 respectively. R1 is the point at which the leg is attached to the body of the robot, L1 represents the "thigh", L2 is called the "femur" and L3 is the "tibia".

The Table 1 represents the parameters obtained through the application of the Danavit-Hartenberg method.

Table 1. Denavit-Hartenberg parameters.

Link	ai	αi	di	θi
1	$L1$	$\pi/2$	0	$\theta 1$
2	$L1$	0	0	$\theta 2$
3	$L1$	0	0	$\theta 3$

4. Methodology

In this section we will discuss the structure of the adopted system, the manual gestures chosen, the structure of the algorithm and finally the method of the classifier analysis.

The structure of the system corresponds to a sequence of steps that will allow the tracking of gestures in real time. Each step of recognition begins with algorithms to establish a region of interest, segmenter to reduce noise and improve classifier processing and lastly the use of the classifier. From the recognized gesture the robots will execute a certain movement. The operation of the used algorithm can be analyzed in the Figure 3.
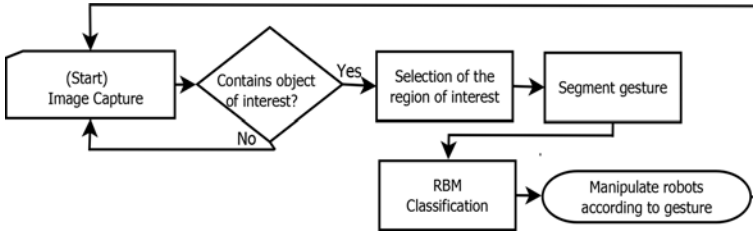
Figure 3.   Flowchart of the proposed method

For the real-time tracking of the object of interest was used the continuously adaptive algorithm CamShift which is an adaptation of the algorithm of MeanShift. For each captured frame, the original image is converted to a probabilistic color distribution of the image, which using a histogram model of the color to be traced.[12] In this case, the characteristic color to be tracked is that of the hand, after having recognized this pattern, the desired location is made in the scene, and then the segmentation of this as shown in Figure 4.b.
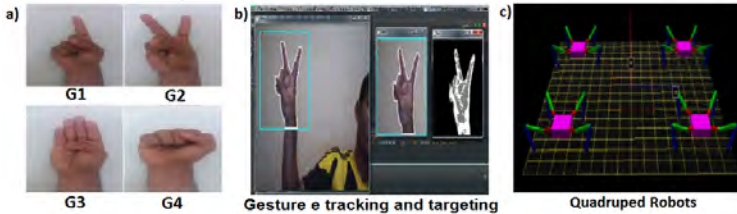
Figure 4.   a) Gestures used. b) Tracking and segmentation the object of interest. c)Used robots.

Four gestures were used to control the robots Figure 4.a, each gesture transmits an action to the robots being able to be of two categories, collective or individual. The gesture "G1" conveys a collective action for the robots which consists of the same ones executing a forward movement movement, "G2" just like the previous gesture transmits a collective action causing the robots to return to the initial position, "G3" by its Instead it consists of an individual action that causes the robot from the lower right corner to move to the center, "G4" transmits an individual action that causes the robot from the upper left corner to move up to the scepter.

The next step is segmentation. The algorithm chosen to perform this

stage of the system is Theshold algorithm, in order to reduce the noises in the image to obtain a greater precision in the classifier. This type of algorithm is based on the principle that an object of interest in the scene has distinct quantifiable characteristics, such characteristics as intensity or magnitude of the gradient.[13]

This segmentation process is based on the search for pixels whose values are within the ranges defined as thresholds. From a threshold established with the characteristics of the objects you want to isolate, the image can be segmented into two groups: the group of pixels with gray levels below the threshold and the group of pixels with gray levels above the threshold. If the value of the pixel is greater than a value stipulated as a limit, it is assigned a value, in this case it is white, however otherwise, another value is assigned that is black, the relevance of this method can be seen in Figure 4.b.

The last step is to start the classifier training that will be responsible for performing the signal recognition. The RBM algorithm was used. In addition, RBMs can be used as non-linear classifiers and can achieve better performance compared to conventional neural networks and SVMs.[14]

A RBM is a stochastic neural network composed of two layers,[14] visible and hidden. The visible units layer represents the observed data and is connected to the hidden layer, which in turn must learn to extract characteristics of this data. In a RBM neurons of the same layer are not connected between themselves. Therefore, there is only a connection between neurons of different layers, so the machine is restricted.

For the RBM classifier, 5685 images were used, which are an adaptation of the datasets provided by,[15] 3411 used for training consisting of 60 % of the total and 2274 images for testing consisting of 40 %. As a statistical tool we have the confusion matrix,[16] which provides the basis for describing the accuracy of the classification and characterizing the errors, helping to refine the classification.[17]

5. Results

Satisfactory results were obtained for each gesture evaluated, worst case, "G1", with 61% as shown in Table 2. The overall accuracy of the approach is 82.2%

Table 2.   Confusion matrix

Known	G1	G2	G3	G4
G1	61%	-	-	-
G2	-	95%	-	-
G3	-	-	76%	-
G4	-	-	-	92%

Note: Predicted %
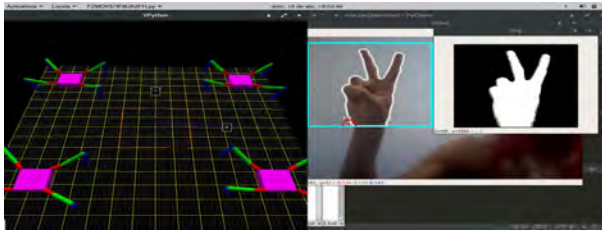
Figure 5.   Manipulating the robots.

In the Figure 5 is displayed to the real-time evaluation of the method used in the project, it can be observed that the gesture used is the "G4", that means that the command is transmitting a collective action, causing the robots to return to their initial position.

6. Conclusion

This article presents a real-time multirobot control system from robust and reliable hand signals. In addition, a good accuracy was obtained in the application of the algorithm chosen to classify the gestures Table 2.

The system presented satisfactory results with regard to real-time video processing, obtaining analysis and classification of the gestures, in order to transmit information to the robots, and with this to be performed actions instantly.

As future work it is suggested to increase the number of gestures, to test with other classifiers and to implement in real robots.

Acknowledgments

Bibliography

1. M. F. Silva, J. A. T. Machado and A. M. Lopes, *Robotica* **23**, p. 595–606 (2005).
2. N. M. Fonseca Ferreira, F. Moita, V. Santos, J. Ferreira, J. Santos, F. Santos and M. Silva, Education with robots inspired in biological systems(04 2018).
3. Y. Girdhar and G. Dudek, *Autonomous Robots* **40**, 1267 (2016).
4. M. Li, M. Su, R. Xie, Y. Zhang, H. Zhu, T. Zhang and Y. Guan, Development of a bio-inspired soft gripper with claws, in *Robotics and Biomimetics (ROBIO), 2017 IEEE International Conference on*, 2017.
5. *transações IEEE em imagens médicas* **35**, 1262.
6. M. Luneckas, T. Luneckas, D. Udris and N. M. Fonseca Ferreira, *Elektronika ir Elektrotechnika* **20**, 7(09 2014).
7. X. Xiong, F. Wörgötter and P. Manoonpong, *IEEE transactions on cybernetics* **46**, 2521 (2016).
8. H. Yu, H. Gao, L. Ding, M. Li, Z. Deng and G. Liu, *IEEE Transactions on Industrial Electronics* **63**, 5488 (2016).
9. P. Corke, *Robotics, Vision and Control: Fundamental Algorithms In MATLAB® Second, Completely Revised* (Springer, 2017).
10. A. Zeiaee, R. Soltani-Zarrin, R. Langari and R. Tafreshi, Design and kinematic analysis of a novel upper limb exoskeleton for rehabilitation of stroke patients, in *Rehabilitation Robotics (ICORR), 2017 International Conference on*, 2017.
11. M. S. Couceiro, N. M. Fonseca Ferreira and J. A. T. M. Dainius, *Journal of Communications in Nonlinear Science and Numerical Simulation* **17**, 893(02 2012).
12. C.-H. Hsia, Y.-J. Liou and J.-S. Chiang, *Journal of Real-Time Image Processing* **12**, 183 (2016).
13. M. Yazdi and M. Fani, Shot boundary detection with effective prediction of transitions' positions and spans by use of classifiers and adaptive thresholds, in *Electrical Engineering (ICEE), 2016 24th Iranian Conference on*, 2016.
14. C. Gou, K. Wang, Y. Yao and Z. Li, *IEEE Transactions on Intelligent Transportation Systems* **17**, 1096 (2016).
15. P. K. Pisharady, P. Vadakkepat and A. P. Loh, *International Journal of Computer Vision* **101**, 403 (2013).
16. X. Deng, Q. Liu, Y. Deng and S. Mahadevan, *Information Sciences* **340**, 250 (2016).
17. A. Saraiva, R. T. Melo, V. Filipe, J. V. M. Sousa, N. M. Fonseca Ferreira and A. Valente, *international journal of systems applications, engineering and development* **12**, 63 (2018).

Scalable Task Cleanup Assignment for Multi-agents

Arata A. Saraiva[1]

UTAD University,Coimbra, Portugal
ORCID 0000-0002-3960-697X [1] E-mail: aratasaraiva@gmail.com

Costa. NJC[2]

State University of Piaui,
Piripiri, Piaui, Bazil
ORCID 0000-0001-5636-424X [2] E-mail: trisna@prp.uespi.br

Jose Vigno M Sousa[3]

State University of Piaui, Piripiri,Brazil
University Brazil, Sao Paulo, Brazil
ORCID: 0000-0002-5164-360X [3] E-mail: vigno@prp.uespi.br

Thelmo Pontes De Araújo[4]

Ceara state University, Fortaleza, Ceara, Brazil
[4] E-mail: thelmo.dearaujo@gmail.com

N. M. Fonseca Ferreira[5]

INESC-TEC Technology and Science, Campus da FEUP, Rua Dr. Roberto Frias, 378,
4200 - 465 Porto, Portugal,
Knowledge Engineering and Decision-Support Research Center (GECAD) of the
Institute of Engineering, Polytechnic Institute of Porto
Department of Electrical Engineering, Institute of Engineering of Coimbra,
Coimbra, Polytechnic Institute
Rua Pedro Nunes, 3031-601 Coimbra, Portugal
ORCID: 0000-0002-2204-6339 [5] E-mail: nunomig@isec.pt

Antonio Valente[6]

INESC-TEC Technology and Science
Campus da FEUP, Rua Dr. Roberto Frias, 378, 4200 - 465 Porto, Portugal
School of Science and Technology, University of Trás-os-Montes and Alto Douro,
Vila Real, Portugal
ORCID: 0000-0002-5798-1298 [6] E-mail: avalente@utad.pt

This paper describes a group of robots for cleaning a simulated environment and proposes an efficient algorithm for navigation based on Pathfinding A *. No need for vision sensors. As a result it was observed that the robots can work cooperatively to clear the ground and that the navigation algorithm is effective in cleaning. In order to test its efficiency it was compared the combination of the Pathfinding A* algorithm and the decision algorithm proposed in this paper with Pathfinding A* and Euclidean distance, resulted in an improvement in time and distance traveled.

Keywords: Multi robots; Cleaning; Cooperative work; Navigation.

1. Introduction

The issue of protecting the environment from pollution is necessary and especially by the fact that natural resources are under threat. The human impact on the environment is undeniable and can be altered by the use of autonomous robotics.

Utility companies can benefit by reducing routine work, reaching hard-to-reach regions, and can perform service at scheduled times.[1] During harvesting, the robot moves independently on the given surface, removing garbage from it. Having found an obstacle in the way, the robot decides a method to overcome it based on special algorithms.[2]

The type of autonomous system to be developed takes into account the possibility of combining several simple yet functional techniques that are already known in the literature to solve the problem of having mobile agents identify and follow to soar, dirty target.

In the project it is proposed to use Breadth First Search (BFS) to do the mapping using the target pattern. This target will be arranged in a plane position and orientation environment, so the Euclidean distance is used to plot the route. Based on these readings the positioning control would be applied so that it can follow the target within the environment. A comparison was made by merging the navigation algorithm Pathfinding A *, Euclidean distance and the algorithm proposed in this work with Pathfinding A *, Euclidean distance.

The document is divided into 5 sections, in which section 2 is characterized by the contextualization of the work. It follows the methodology applied in section 3. The results after the application of the proposal are presented in section 4 and the conclusion in section 5.

2. Contextualization of work

Surface cleaning robots are environmental protection equipment used primarily to collect garbage. According to the task requirements, they can be

used to monitor the environment of parks, orchards, squares and accumulating information through sensors and performing dangerous operations such as search and rescue. They are also important tools in assessing environmental pollution, providing warnings and disaster prevention, which provides enormous economic and social benefits in addition to possible potential applications[34].[5]

One of the potential applications is in the work of[6] that a vacuum cleaning system is proposed integrated with a fuzzy inference system to improve the accuracy of the system. In[7] a system of automatic control of a room cleaning robot with cellular control capability using DTMF with the ability to avoid self-controlled obstacles, together with a system of cleaning of residues and dust is developed.

In[8] proposes an improvement in cleaning efficiency not because of obstacles and route planning. To solve this problem it develops a localization algorithm with the use of stereoscopic vision and wireless network. The use of multirobots for optimization of activities has been expanding[9] and in[10] a multi-area cooperative cover is applied to develop complex tasks where multiple robots are required to cover together in several areas. Practical operations such as garbage removal, demining and area scanning for information acquisition.[11]

Based on this information a work was developed with the objective of constructing a group of robots in which the agents are able to share cleaning workloads automatically and in an intelligent way. In addition, it is programmed to detect obstacles around it and control the robot to avoid collisions. The metology adopted is detailed in the following section.

3. Methodology

In this article, the game engine, Unity 3D, was used as the simulation environment for natively presenting robust features for the development of the[12] simulation environment, as shown in figure 1.

The figure 1 (b) represents the area of action and division of the mapping, in quadrants of 50 x 50 meters and each agent is circled in blue. At this stage they are responsible for traversing the quadrant, analyzing and storing the location where it contains dirt particles. The mapping route of an agent in the lower left quadrant, in red color, is also demonstrated.

Communication between the robots was done through sockets.[13] As a search algorithm for mapping, BFS[14] was chosen to go through the quadrant, we can check the route in the 1 (b) figure. Next, a navigation mesh will be generated, figure 1 (a), and routes to the dirt points. At each frame the

(a)   (b)
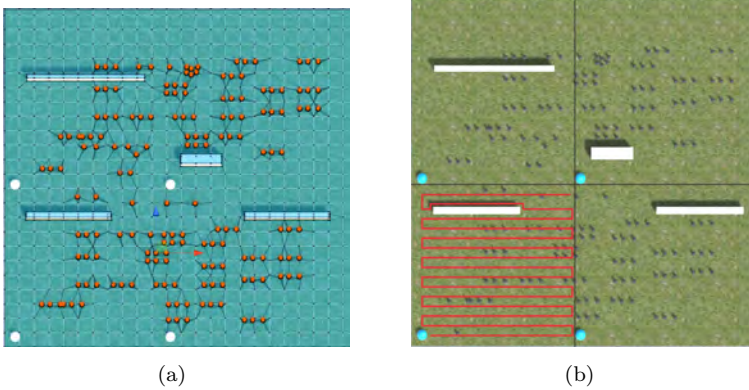
Figure 1.

agents calculate (algorithm 3.1) the closest point, this point must belong to only one agent.

A navigation mesh (NavMesh) has been created that consists of several two-dimensional convex polygons and defines which areas of an environment are likely to be traversed by agents. In other words, an agent can move within these unobstructed areas of the environment and Agents in a NavMesh can avoid collision detection checks with obstacles in the environment.[15]

NavMesh allows a large number of algorithms to search for graphics, and the algorithm discussed in this work was Pathfinding A* in each of the agents.[16] In the figure 1 (a) in blue, represents the finished mesh.

The algorithm Pathfinding A* is an algorithm capable of finding the shortest path,[17] it uses a function to determine which squares to traverse, according to equation 1.

$$f(n) = g(n) + h(n) \tag{1}$$

Where g is the cost of moving from a starting point to a given square,[17] oh (n) is the cost estimate of the ideal path from node n to destination.[17]

3.1. *Control Algorithm*

A priori is divided into two parts, mapping and cleaning. The BFS is the algorithm responsible for guiding the next point that the agent must follow in the mapping phase. The points were divided in the quadrant area and allowed to travel in a larger area. In order to perform the cleaning, two

algorithms were used, one for navigation Pathfinding A* and the other, algorithm 3.1, for point selection. A test without the algorithm 3.1 was also performed to evaluate the performance of the algorithm.

In conjunction with the algorithms, a decision method was proposed, which evaluates the most advantageous point that the agent should move, to carry out the cleaning. It calculates the distance of all mapped points and takes the closest one. Subsequently, the distance of the other agents is calculated to the chosen point, if only the agent in question is the shortest distance, is moved to the point, otherwise it picks up another nearby point and remakes the calculation. The method described is represented in the 3.1 algorithm.

The actions are shown in the flowchart, Figure 2, demonstrates the operation of the two steps described, mapping and cleaning, it is possible to verify that the agent always checks if there are still points that need cleaning, the algorithm 3.1.

Algorithm 3.1 Method of decision

1: **procedure** $\mathrm{NEXTPOINT}(agent, point)$
2:     $a \leftarrow ShorterDistanceThisAgent$
3:     $b \leftarrow ShorterDistanceOthesAgents$
4:     **if** $a < b$ **then return** nextPoint   ▷ Check if it's the closest
5:     **else return** nextInitial   ▷ Return to starting point

---

4. Results

In this section we present the performance of the algorithms, mapping and control. In the tables 1 and 2, the time each agent finished cleaning, the amount of dirt points collected and the distance traveled are represented.

Based on the results obtained, represented in the tables 1 e 2, the algorithm 3.1 presents a gain in time and distance, representing a differential of 91.46 seconds faster and a saving of 482.77 meters.

The use of the BFS mapping algorithm in conjunction with Pathfinding A* has been shown to be efficient, since the function of BFS is to ensure that the search is linear, but since the scenario has the presence of obstacles it was necessary to integrate the two for better efficiency. In the tests performed the agents were able to map the area and find all points.
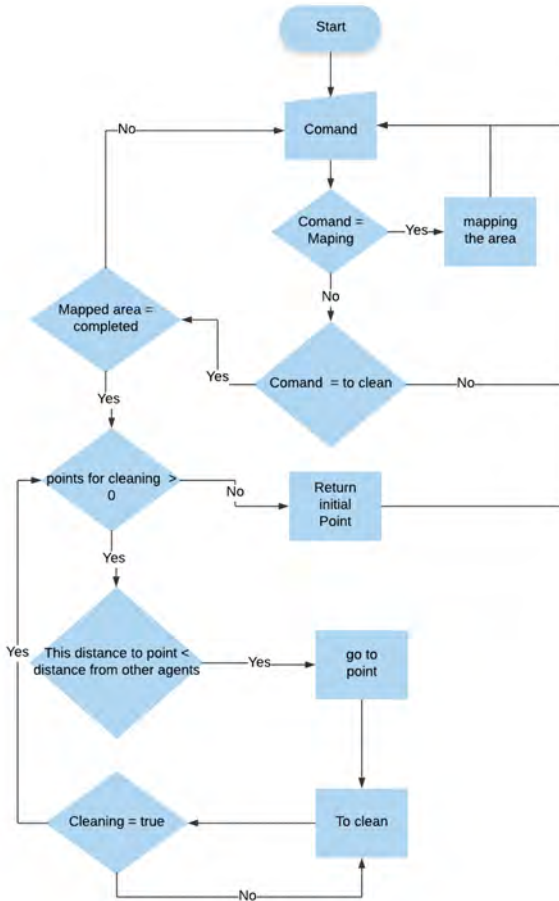
Figure 2.   Control software flowchart

Table 1.

Agent	Time	Collected dirt	Travelled distance
5000	29.24 s	42	241.45 m
5001	35.45 s	49	295.57 m
5002	34.48 s	37	319.65 m
5003	27.16 s	40	242.17 m
Total	126.33 s	167	1098.84 m

Note: Pathfinding A*, algorithm 1

Table 2.

Agent	Time	Collected dirt	Travelled distance
5000	54.61 s	36	367.47 m
5001	54.52 s	39	438.39 m
5002	53.97 s	36	393.44 m
5003	54.69 s	56	382.31 m
Total	217.79 s	167	1581.61 m

Note: Pathfinding A*, Euclidian Distance

5. Conclusion

In this article we have demonstrated the use of algorithms already known in the literature in the aid of autonomous robotics, the agents were able to clean, map, route routes and avoid obstacles. Because it is more than one agent, a combination was proposed in the algorithm of navigation Pathfinding A * with algorithm of decision based on Euclidean distance, as a result obtained an improvement in the time performance and distance traveled.

Acknowledgments

Bibliography

1. M. S. Couceiro, N. M. Fonseca Ferreira and R. Rocha, Multi-robot exploration based on swarm optimization algorithms, in *7th European Nonlinear Dynamics Conference ENOC*, 2011.
2. M. S. Couceiro, R. P. Rocha and N. M. Fonseca Ferreira, A novel multi-robot exploration approach based on particle swarm optimization algorithms, in *2011 IEEE International Symposium on Safety, Security, and Rescue Robotics*, Nov 2011.
3. K. R. Muske, H. Ashrafiuon, G. Haas, R. McCloskey and T. Flynn, Identification of a control oriented nonlinear dynamic usv model, in *American Control Conference, 2008*, 2008.
4. F. Y. Lee, B. H. Jun, P. M. Lee and K. Kim, Implementation and test of isimi100 auv for a member of auvs fleet, in *OCEANS 2008*, 2008.
5. J. Wang, W. Gu, J. Zhu and J. Zhang, An unmanned surface vehicle for multi-mission applications, in *Electronic Computer Technology, 2009 International Conference on*, 2009.

6. W. H. C. Wickramaarachchi, M. A. P. Chamikara and R. A. C. H. Rat-nayake, Towards implementing efficient autonomous vacuum cleaning systems, in *2017 IEEE International Conference on Industrial and Information Systems (ICIIS)*, Dec 2017.

7. H. Rashid, A. Mahmood, S. Shekha, M. Rasheduzzaman and S. Reza, Design and development of a dtmf controlled room cleaner robot with two path-following method(12 2016).

8. K. R. Muske, H. Ashrafiuon, G. Haas, R. McCloskey and T. Flynn, Identification of a control oriented nonlinear dynamic usv model, in *American Control Conference, 2008*, 2008.

9. A. Saraiva, R. Melo, V. Filipe, J. Sousa, N. M Fonseca Ferreira and A. Valente, Mobile multirobot manipulation by image recognition, in *International Journal of Systems Aplications, Engineering and Development*, 2018.

10. B. Xin, G.-Q. Gao, Y.-L. Ding, Y.-G. Zhu and H. Fang, Distributed multi-robot motion planning for cooperative multi-area coverage, in *Control & Automation (ICCA), 2017 13th IEEE International Conference on*, 2017.

11. M. Couceiro, C. Figueiredo, R. P. Rocha and N. M. Fonseca Ferreira, Initial deployment of a robotic team - a hierarchical approach under communication constraints verified on low-cost platforms, in *2012 IEEE/RSJ International Conference on Intelligent Robots and Systems*, Oct 2012.

12. C. Bartneck, M. Soucy, K. Fleuret and E. B. Sandoval, The robot engine—making the unity 3d game engine work for hri, in *2015 24th IEEE International Symposium on Robot and Human Interactive Communication (RO-MAN)*, Aug 2015.

13. M. Xue and C. Zhu, The socket programming and software design for communication based on client/server, in *2009 Pacific-Asia Conference on Circuits, Communications and Systems*, May 2009.

14. S. Beamer, K. Asanovic and D. Patterson, Direction-optimizing breadth-first search, in *High Performance Computing, Networking, Storage and Analysis (SC), 2012 International Conference for*, Nov 2012.

15. M. S. Couceiro, F. M. Martins, R. P. Rocha and N. M. Fonseca Ferreira, *Journal of Intelligent & Robotic Systems* **76**, 353 (2014).

16. W. van Toll, A. F. Cook and R. Geraerts, Navigation meshes for realistic multi-layered environments, in *2011 IEEE/RSJ International Conference on Intelligent Robots and Systems*, Sept 2011.

17. J. Hu, W. gen Wan and X. Yu, A pathfinding algorithm in real-time strategy game based on unity3d, in *2012 International Conference on Audio, Language and Image Processing*, July 2012.

COORDINATED CONTROL FOR VEHICLES COOPEARATIVE MANEUVERS USING DISTRIBUTED MODEL PREDICTIVE CONTROL

ANDONI URUTEGUI

Industry & Transportation, TECNALIA Research & Innovation
Derio, Spain

RAY LATTARULO

Industry & Transportation, TECNALIA Research & Innovation
Derio, Spain

GERARDO FERNÁNDEZ-LÓPEZ

Mechatronic Group, Simón Bolívar University
Sartenejas, Venezuela

The research and development focused towards autonomous vehicles has grown quickly and progressively, in search of a more efficient, safe and clean future. Thus, is necessary to consider: cooperation between multiple (2 or more) vehicles, security measures, priorities, among others. Under this framework we present a design of predictive controller for the management of cooperative maneuvers, considering safety, efficiency and comfort in driving, as well as a series of physical limitations of the vehicle, all this to obtain a speed profile that guarantees the optimal execution (locally) of the maneuver.

1. Introduction

Recent research suggest that Intelligent Transportation Systems aim to be the standard mode of transportation in the future, and for that to be possible we need to focus the investigation on real world scenarios, taking into consideration the complexity of multi-vehicle transit and its multiple variables. Within that framework we propose a solution to the problem where the vehicles must execute cooperative maneuvers. Several lines of research consider predictive control strategies for the resolution of this type of problems, because of the advantages that it presents in terms of handling constraints. Li *et al* [1] propose a trajectory tracking of mobile robots. [2] shows how MPC handles the steering of mobile robots in conjunction with visual processing. Recent works like the ones of Riegger *et al* [3] and Nordell [4] present centralized solutions for vehicle intersections and overtaking maneuvers. In this work a predictive control system is used in a distributed manner, similar to [5], where each agent has an MPC that contributes to the generation of a speed profile that allows the successful execution of the maneuver. The methodology of modeling the maneuvers inside

the predictive controller is introduced as a novelty, meaning that is the maneuver state as a whole what is calculated at each instant.

2. Modeling

For simplicity reasons, the following considerations are taken: (1) scenarios are design with two autonomous vehicles, (2) the vehicle trajectories are defined, (3) fully working vehicle to vehicle communication is present, (4) the information shared at time t is available to the other vehicle at time t + k. The point-mass model in Eq. (1) will be used.

$$\dot{x} = v$$
$$\dot{v} = a \qquad (1)$$
$$\dot{a} = Jr$$

2.1. *Intersection maneuver*

The aforementioned model is manipulated to generate a system of differential equations that describe the maneuver, first, the X distance between vehicles through the point of the intersection (collision point) is calculated.

$$X = d_1 + d_2 \qquad (2)$$

Expanding the point-mass model, a system of relative states is found in Eq. (3), where X is the distance between vehicles, V is the relative velocity and A is the relative acceleration. This model is used for the state predictions, treating the maneuver state as a whole.

$$\dot{X} = v_1 + v_2$$
$$\dot{V} = a_1 + a_2 \qquad (3)$$
$$\dot{A} = Jr_1 + Jr_2$$

2.2. *Obstacle avoidance.*

The vehicles are in opposite lanes of the road and one of them must occupy the lane against-flow momentarily to continue on its way. The X distance is calculated considering a safety barrier, as proposed in [6], placed at a distance that depends on the maneuver speeds, initially at 3L of the, where L is the length of vehicle 1.

2.3. *Maneuver parameters*

The parameters represent the MPCs variable constraints; First of all, we must ensure that the vehicles do not collide, maintaining at least a minimum safety distance between them:

$$X_{(t + k|t)} > X_{safe\,(t + k|t)} \qquad (4)$$

$(t + k / t)$ being the predicted instant $t + k$ calculated in t by the MPC using Eq.3 and previous values as inputs. Additionally, for efficiency reasons we want this to happen as close as possible to a reference speed:

$$0 < v_{1 (t + k|t)} \leq v_{ref(t + k|t)} \tag{5}$$

Velocity constraint written in terms of V:

$$v_{2(t + k|t)} < V_{(t + k|t)} < v_{ref (t + k|t)} + v_{2 (t + k|t)} \tag{6}$$
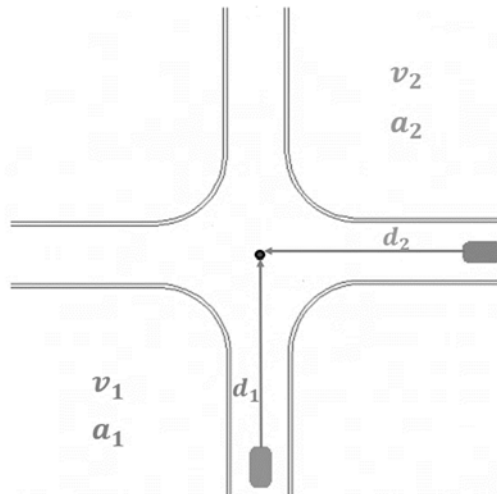
Figure 1. Intersection maneuver
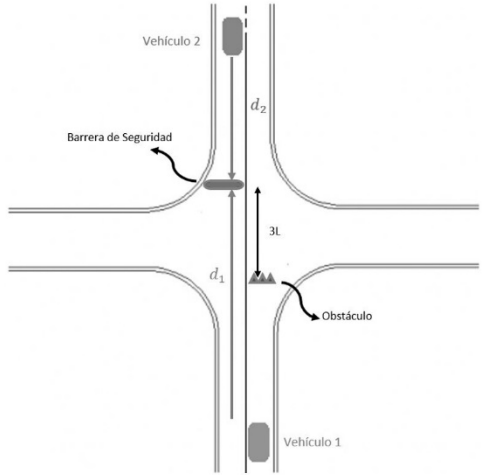
Figure 2. Obstacle Avoidance maneuver

Finally, considering driving comfort, violent accelerations and decelerations are limited, resulting in the following constraint:

$$a_{\min(t + k|t)} + a_2 < A_{(t + k|t)} < a_{m\acute{a}x(t + k|t)} + a_2 \qquad (7)$$

3. Predictive controller

The function of the MPC is to obtain a control signal, ensuring that all the conditions are satisfied and that the system variables remain within their limits. It is proposed: (1) the MPC Prediction Horizon, (2) the cost function for optimization, and (3) the control input $u_{(t)}$ of the system.

At the top speed of 20Km/h the test vehicle, a Renault Twizy, takes 14 meters to stop, a horizon of 10 samples at 300ms is chosen, thus, making predictions for the next 17 meters of travel, enough for an emergency stop. The cost function has the objective of minimizing the mean square error of the current speed with its reference:

$$J = \sum_{t=0}^{10} \left(v_{ref(t + k|t)} - v_{(t + k|t)} \right)^2 \qquad (8)$$

The jerk is chosen as control variable, with the only purpose of taking comfort into consideration, forcing the system to make its predictions within comfortable jerk values. This system is proposed as a high-level controller and its output is not used for further stages, the MPC predictions are instead, they guarantee that the

predicted values of V comply with the maneuver requirements, so they are used as a reference for the lower level controllers as a maneuver speed profile. Generally, this type of MPC is applied as a centralized maneuver solving unit, where every agent sends its information and then receive the speed profile. In this case each vehicle has an MPC, at each timestep every vehicle shares it information to the other so that the optimization problem can be solved locally, reducing the computational load on the computer and making the system more robust in case one vehicle malfunctions. Additionally, if each vehicle is programmed to meet the condition of safety distance, it is necessary to implement priorities. This decision system is based on the calculations of reaction distance and breaking distance proposed in [7] [8], reducing it to the point of granting a higher priority (the value of zero) to the vehicle that has less reaction time.

4. Results

The vehicles are set to collide, giving priority to vehicle 1, which results in the lifting of its MPC constraints. The MPC on vehicle 2 predicts that a safety violation will occur and generates a speed profile that reduces velocity as shown by the blue curve in Figure 3.
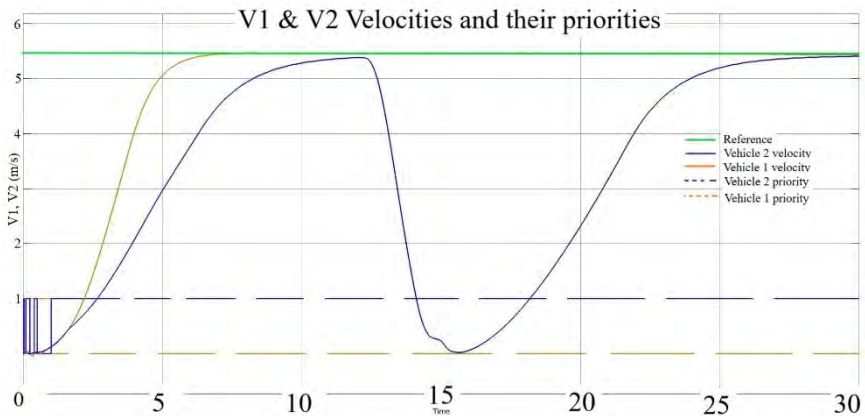
Figure 3. Speed curves. Vehicle 1 has priority.

Safety distance was modified to values of 10m, 20m and 40m, the curves shown in Figure 4 demonstrate how the controller executes the corrective actions earlier in time while the safety distance is increased. Both curves stabilize at 5.5 m/s which corresponds to the reference value, meaning that the optimization of the cost function is done correctly. Also, is shown in both figures that the variables

are within their bounds at all times, meaning that the constraints are being respected by the MPC calculations.
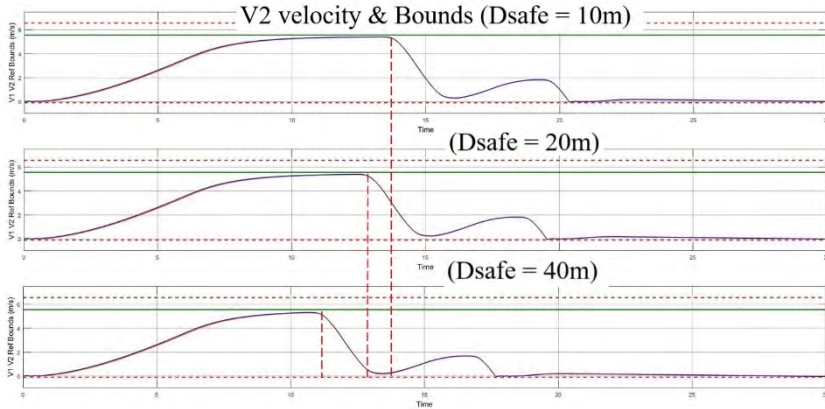
Figure 4. Speed curves at different safety distance values.

5. Conclusions and future works

Predictive controllers, together with the other modern control strategies, present promising results in terms of control systems, showing the advantage they have over other strategies. Its relative ease of modeling in MIMO systems, the robustness of applying corrections to future errors and the distributed approach are essential characteristics for a real-time application such as autonomous vehicles. Regarding future work, an extension of its scope is considered, that is, the design of a controller that involves maneuvers of more than two vehicles, the inclusion of external agents in the cost function and, in general terms, search for the application of this strategy in all maneuvers that the vehicle can perform.

6. References

1. Z. Li, J. Deng, R. Lu, Y. Xu, J. Bai and C. Su, "Trajectory-Tracking Control of Mobile Robot Systems Incorporating Neural-Dynamic Optimized Model Predictive Approach," in *IEEE Transactions on Systems, Man, and Cybernetics: Systems*, vol. 46, no. 6, pp. 740-749, June 2016.
2. Z. Li, C. Yang, C. Su, J. Deng and W. Zhang, "Vision-Based Model Predictive Control for Steering of a Nonholonomic Mobile Robot," in *IEEE Transactions on Control Systems Technology*, vol. 24, no. 2, pp. 553-564, March 2016.

3. L. Riegger, M. Carlander, N. Lidander, N. Murgovski, & J. Sjöberg. (2016, November). Centralized mpc for autonomous intersection crossing. In Intelligent Transportation Systems (ITSC), 2016 IEEE 19th International Conference on (pp. 1372-1377). IEEE.

4. B. Nordell. (2016). Trajectory Planning for Autonomous Vehicles and Cooperative Driving. TRITA EE, KTH Royal Institute of Technology, Sweden.

5. A. Katriniok, P. Kleibaum, and M. Joˇsevski. (2017). Distributed model predictive control for intersection automation using a parallelized optimization approach. IFAC-PapersOnLine, 50(1):5940–5946.

6. J. Pérez Rastelli. (2012). Agents control for autonomous vehicles in urban and highways environments. PhD thesis, Complutense University of Madrid, Spain.

7. P. Delaigue and A. Eskandarian. (2014) A comprehensive vehicle braking model for predictions of stopping distances. Proceedings of the Institution of Mechanical Engineers, Part D: Journal of Automobile Engineering, 218(12):1409–1417.

8. Y-L Chen and C-A Wang. (2017) Vehicle safety distance warning system: A novel algorithm for vehicle safety distance calculating between moving cars. In Vehicular Technology Conference, 2007. VTC2007-Spring. IEEE 65th, pages 2570–2574. IEEE.

INDOOR LOCALIZATION OF MOBILE ROBOTS WITH WIRELESS SENSOR NETWORK BASED ON ULTRA WIDEBAND USING EXPERIMENTAL MEASUREMENTS OF TIME DIFFERENCE OF ARRIVAL

OUSMANE ABDOULAYE OUMAR

School of Engineering, London South Bank University, 103 Borough Road, London, SE1 0AA, UK

TARIQ P. SATTAR

School of Engineering, London South Bank University, 103 Borough Road, London, SE1 0AA, UK

MOHAMMAD OSMAN TOKHI

School of Engineering, London South Bank University, 103 Borough Road, London, SE1 0AA, UK

This paper presents investigations into wireless localization techniques for mobile robots operat-ing in indoor environments. Localization systems can guide robots to perform different tasks such as monitoring children or elderly people, aid mobility of the visually impaired and localize mobile objects or packages in warehouses. They are essential for localization of robots operating in re-mote places that are inaccessible or hazardous to humans. Currently, ultra wide band (UWB) in indoor environments provides an accuracy of 24 mm under line of sight (LOS) or non-line of sight (NLOS) conditions in a working range of 160 m indoors. The work presented in this paper carries out experimental validation of localization algorithms using mobile robots and UWB signals. These are measured in LOS and NLOS environments. The measurements are performed with the UWB radio PulsON 410 (P410) and mobile robots (AmigoBot) with maximum travel-ling speed of 1 m/s and equipped with an on-board computer, sonar, odometer, camera and iner-tial navigation system. Experimental results obtained for the system show positioning errors of less than 55 mm.

1. Introduction

In recent years, ultra wide band (UWB) technologies have drawn significant interest in the wireless community [1]. The UWB is a generic term used to identify a radio technique that has been tested under different names since the mid-twentieth century such as impulse radio, carrier-free radio, baseband radio, time

domain radio, non-sinusoid radio and wide bandwidth on the radio. It was not until 1990 that the U.S. Department of Defense introduced the term UWB. UWB localization is superior in terms of accuracy and power consumption compared with general positioning system (GPS) and wireless local area network (WLAN) localization. It is thus more suitable for indoor location-based applications [2].

Currently, the great flexibility of UWB technology (variable bit rates, multiple modulations, low power consumption, low cost, etc) provides the opportunity for the emergence of new types of network that are pervasive and reconfigurable. Typically, sensor networks and distributed networks that require no infrastructure or limited infrastructure could eventually be made up of a large number of low cost UWB devices that understand an environment, that can adapt to it and operate autonomously. New requirements for localization have emerged in recent years. These requirements, which relate mainly to indoor environments (inside buildings), require precision and a quality of unmatched service (availability, reliability, sustainability, independence, continuity, etc). Many applications and services have emerged whose effectiveness depends mainly on localization performance. Representative examples include localization and monitoring of goods and people in buildings and / or areas at risk, institutional or opportunist looking for victims on the scene of disasters (fires, earthquakes, avalanches, etc), identification, operational monitoring of military urban guerrilla, supervision of prisoners etc., applications in industry telecommunications transport, and the medical sector.

A position location technique involves two steps: the measurement of relative distances (ranging) and positioning based on the measured ranges. The received signal strength (RSS), time difference of arrival (TDOA), angle of arrival (AOA) and time of arrival (TOA) are the four commonly used ranging techniques. Among these RSS and TDOA are of more interest with UWB.

Earlier studies have indicated that TDOA and RSS techniques are the best choices for indoor and outdoor localization. RSS localization techniques have been widely studied as an inexpensive solution for wireless indoor positioning systems in recent years. The RSS technique is, however, not always reliable, because the estimate of the distance depends on several factors such as the absence of a direct signal path, fading due to multipath, the channel characteristics and the distance between reference points. The TDOA technique is suitable for indoor and outdoor systems due to its high accuracy and low computational complexity.

To achieve the objective, the accuracy of indoor localization with UWB using TDOA experimental measurements was analysed with experiments using AmigoBot mobile robots and Time Domain PulsOn 410 radio transmitter/receivers. The experiments were conducted using UWB signals

measured in line of sight (LOS) and non-line of sight (NLOS) environments and for location estimation the TDOA algorithm was used. The measurements were made with the UWB radio PulsON 410 systems tracking mobile robots (AmigoBot's) that were equipped with an on-board computer, sonar, odometer, encoder, camera and an inertial navigation system. These tests were done in an indoor environment with the AmigoBot robot programmed for different motion trajectories e.g. in a straight line, curved line, rotation, and return to the starting point (the coordinates of the reference point (0, 0)). The tests were repeated several times and UWB localization compared with measurements made by the AmigoBot robot's own localization system.

The experimental tests conducted many times showed that the UWB accuracy is very good with the positioning error between 24 and 55 mm with the error never exceeding 55 mm with a working range of 160 m. The difficulty of obtaining a very accurate positioning system is due to NLOS propagation conditions. The localization error increased with longer robot travel distance. Results indicate that a system that uses UWB gives much more accurate position measurement in indoor environments than other localization techniques (which are mostly applied in outdoor environments). UWB TDOA measurement should be used to locate devices because of low cost, low power consumption and little computational complexity and precise positioning capability. Hence, UWB TDOA systems are suitable for applications such as monitoring children or elderly people, visitor management, enforcing restricted zones, security and asset tracking.

2. Materials

The TDOA algorithm is validated by using UWB signals measured in LOS and NLOS. These are measured by using the PulsON 410 system, which is formed by tags (transmitters / receivers) supplied by the Time Domain corporation. The localization techniques used by the Amigo robots (AmigoBot) are used to compare the position measurement with UWB for accuracy.

The AmigoBot contains all of the basic components for autonomous sensing and navigation in a real-world environment, including battery power, drive motors and wheels, position/speed encoders, sonar range-finding sensors, and integrated accessories, all managed via an on-board micro controller and mobile-robot server software. In this study, UWB sensors are used to find and track multiple moving robots in an indoor environment. Four P410 sensors are employed each fitted with a UWB transmitter and a UWB receiver. The sensors use different code channels to prevent interference and to reduce the effects of multipath signals at the receiver. An environment scanning phase of thirty minutes duration is employed

as a reference to determine signals reflected from non-stationary targets. UWB pulses are transmitted from the sensors at every millisecond by the transmitter and all reflected signals picked up by the receiver. UWB signals are characterized by the transmission of a few nanosecond duration pulses [3, 4, 5]. They have very high time resolution and localization precision, which make UWB sensors an ideal equipment for short-range radar sensor network applications [6, 7]. In this study, UWB sensors are employed for detecting and tracking multiple moving objects in an indoor environment in the context of passive localization [8, 9].

In the experiments, there are four sensors (fixed nodes), which are constantly transmitting signals, and the reflected signals from a robot moving in an indoor environment are collected by each of these sensors and four different experiments are performed.

TDOA needs to have a direct path, time synchronization is required between pairs of base stations and this needs high temporal resolution at the receiver and the technique is accurate.

The frequency band allocated by the FCC to UWB ranges from 3.1 GHz to 10.6 GHz in single band or multiband, except for the strip of 5 to 6 GHz, which is the UNI band (Figure 2) and is reserved for industrial testing, scientific and medical applications.
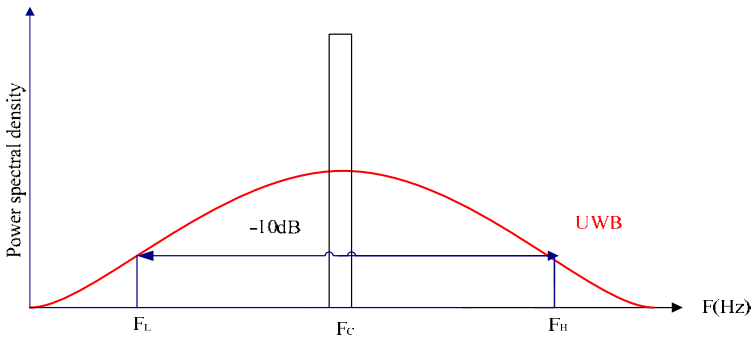
Figure 1. Illustration of the spectrum of UWB signal versus narrowband signal.
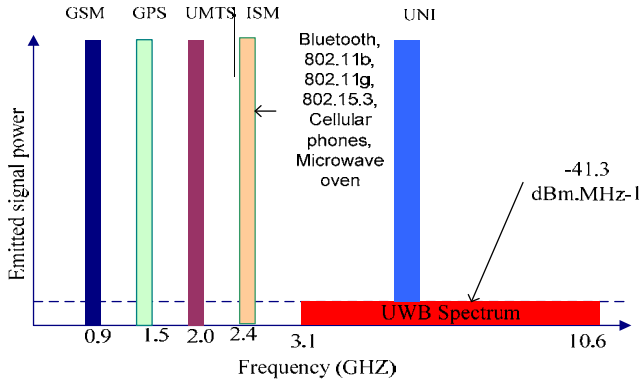
Figure 2. The different systems in ultra-high and super high frequency band.

The PulsON 410 transmitters and receivers equipment used for the experiment is the time domain P410 module, which is a small, low power UWB sensor device, and provides a very good accuracy, high rate range measurements and superior operational performance when compared to conventional radio frequency identification (RFID) and real-time locating systems (RTLS). P410 system consists of tags (transmitters / receivers) of the American firm Time Domain as shown in Figure 3.

Figure 3. Three PulsOn 410 UWB sensors (each PulsOn 410 is in an enclosure).

The AmigoBots shown in Figure 4 are small robots developed by Adept Mobile Robots for research and education purposes. Each AmigoBot has a two-wheel differential drive system with a rear-stabilizing wheel. It senses the environment through an array of eight sonar sensors [10]: six at the front and two at the rear, all of which detect the robot's proximity to its environment. The sonar sensors detect objects in their path at distances between approximately 15 mm to

6 metres. Extremely close objects, less than 15 mm, are seen by the sensors as being equivalent to over 6 metres away. An omnidirectional vision system allows the robot a 360-degree field of vision [11]. The sonar-firing rate of AmigoBot sensors is 25 Hz with distance measurement data sent wirelessly to other devices. The AmigoBot is also fitted with an internal coordinate system. It has two encoders, one fitted to each motor shaft and these are used as odometer to estimate the robot's position and orientation relative to its starting position. This gives a precise localization in a mapped space using robot odometry combined with laser rangefinder data implemented by the Advanced Robotics Navigation and Localisation (ARNL) laser localization library, and navigation software program along with mapping software tools and a laser rangefinder.

Figure 4. Two Amigo robots mounted with P410 in a testing environment.

3. Estimation of TDOA and measurement environment

To estimate TDOA with UWB, the signal is measured in both LOS and NLOS environments. Four antennas are connected to each channel of a laptop using wireless communication. The method of measuring the TDOA is equivalent to the measurement of TOA but without requiring knowledge of the initial time t_0. The exact position of each node is known. Figure 5 shows the measurement system used in the experiments. The measurement system displays the time stamp (consecutive measurements updated every second), range and velocity information. Nodes 100, 104, 105 and 106 are fixed nodes while 107 is a mobile node and node 100 is regarded as node of reference.

The measured signals indicate that there are signals coming from the relative time of arrival multipath between received pulses as shown in Figure 6. It can be found from Figure 6 that the first arriving pulse is the first waveform (between points 180 and 249) and the two later arriving waveforms (between points 250 and 299) and (between points 300 and 350) are multipath reflections. Examining the received signal in Figure 6 shows that the shape of a Gaussian signal is derived twice as a modulating sinusoid, which in turn shows the effect of the derivative of transmitting and receiving sensors.

Figure 6 illustrates an example of a bandpass signal at sixty picosecond increments relative to the initial point. For each measurement set and for each sensor, the filter is applied to the bandpass signal, and the motion-filtered signal is brought forth. The points of the motion-filtered signal correspond to possible target distances as can be noted in Figure 6. This clearly shows that the first arriving pulse is the first waveform (between points 180 and 249) and the two later arriving waveforms (between points 250 and 299) and (between points 300 and 350) are multipath reflections.
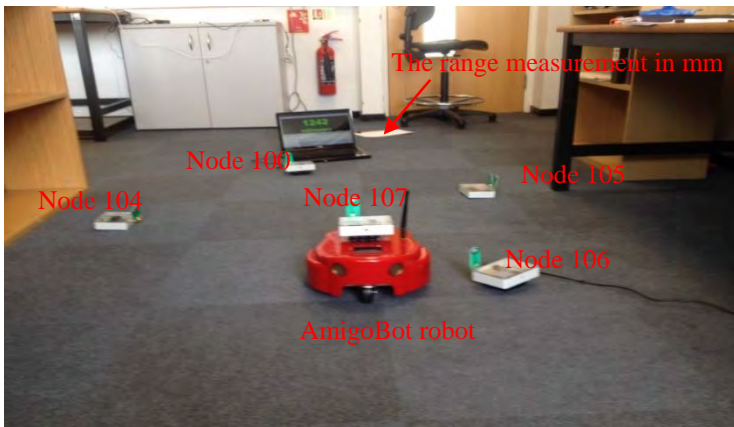
Figure 5. Mechanism of localization with the device descriptions.
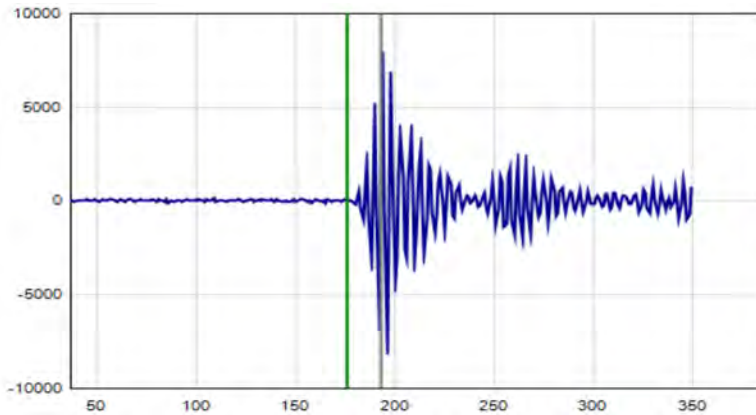
Figure 6. Bandpass signal.

4. Mechanism of localization

The mobile robot is localised using the setup and equipment shown in Figure 5. This comprises fives PulsON 410 (four fix nodes and one moving node (robot)), the AmigoBot robot, a laptop and laser rangefinder. The mobile PulsOn 410 is mounted on an AmigoBot robot and four receiver antennas are fixed nodes. Furthermore, the receiving antennas are connected to the receiver wirelessly. In addition, the receiver is connected to the laptop through the Ethernet connection to transfer the received signals for processing.

5. Experimental results

The measurements taken were recorded on a laptop and processed. The processed data contain the time stamp, range and velocity information, although the only important information is the fact that these are consecutive measurements with an update rate of every millisecond. Several 2D tests were performed using nodes 100, 104, 105, 106 as fix nodes and a mobile node 107 (here the node 107 is carried on the back of the Amigobot is a programmable robot) in all experiments. Figure 7 illustrates the initial geometry measurement with just two fix nodes and a mobile positioned at (0, 0). The figure shows comparison with the extracted x and y results from the AmigoBot robot system, so the UWB based localization results can be identified. Figures 8 and 9 show the two signals received by two different nodes (nodes 105 and 106).

For the node 105, the antennas were very close to the transmitter and for the second node 106, the antennas were distant from the transmitter. Figure 9 shows

that PulsON 410 had high resolution than in Figure 8 and the signals were sampled at sampling period of 1.4073 nanoseconds.

To evaluate the performance of the TDOA estimation algorithm and the localization algorithm, the mobile node 107 was selected and AmigoBot robot containing thousand positions. Ten measurements of the received signal for each position were performed, having thirty TDOA position values. The measurements were conducted in an indoor environment of dimensions 15 m × 8 m × 3 m, with block walls, large glass windows, two doors, tables, concrete floors, ceiling, wooden and metallic furniture. The estimation results achieved in the tests of UWB and AmigoBot robot are shown in Figures 10, 11, 12 and 13. During the experiments, the robot drove from a point A to point B, and in the last test, the robot drove from A to B, returned to A, and for safety reasons all experiments were conducted inside the lab. Table 1 shows positions of UWB nodes with corresponding estimated errors.
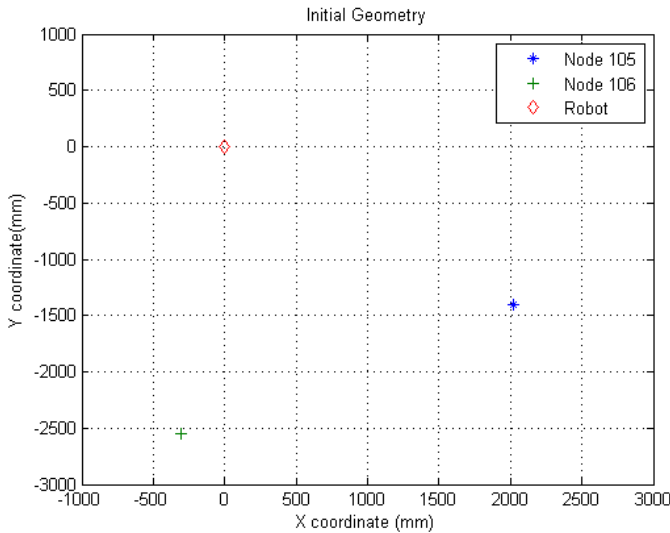
Figure 7. Initial geometry in a testing environment.
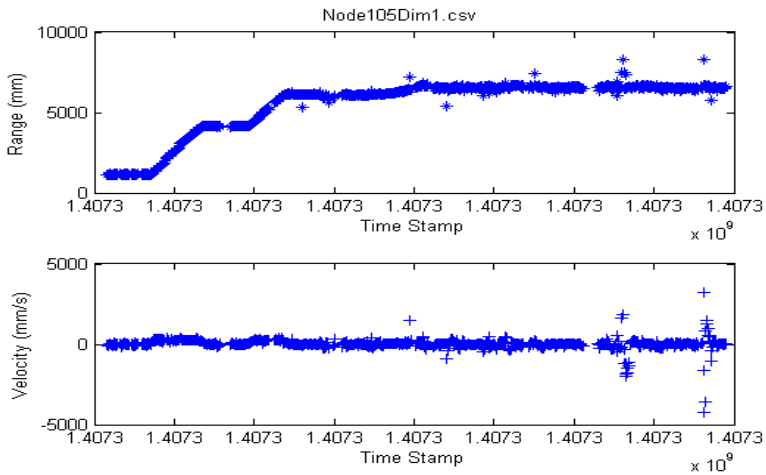
Figure 8. Received signals from node 105 and a bit close to the transmitter.
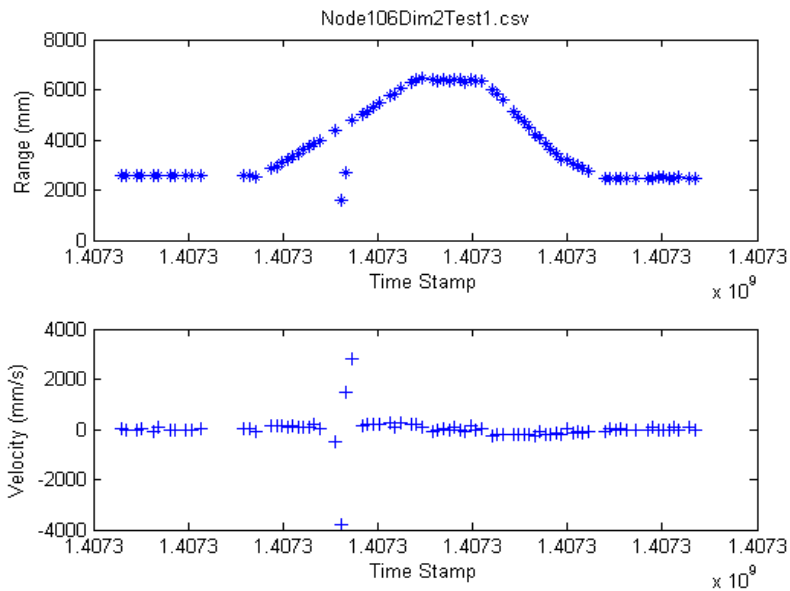
Figure 9. Received signals from node 106 and a bit far from the transmitter.
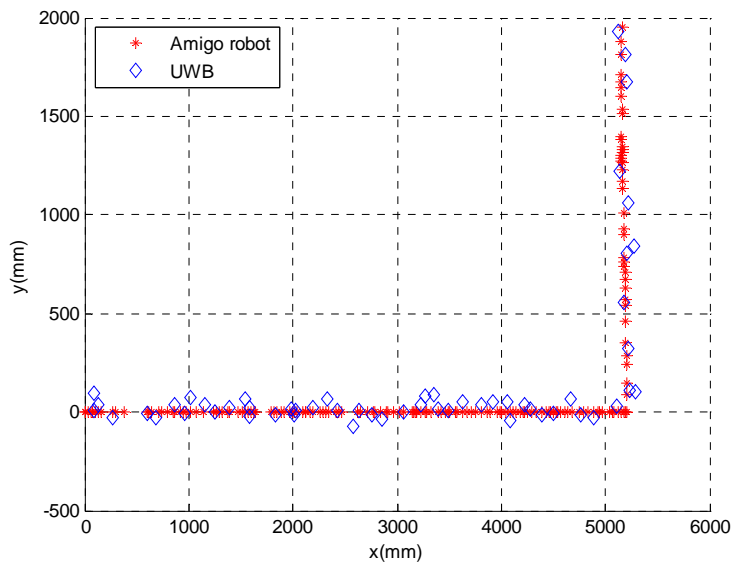
Figure 10. Test 1- positioning of the mobile robot using Odometry & orientation sensors and UWB from point A to B.
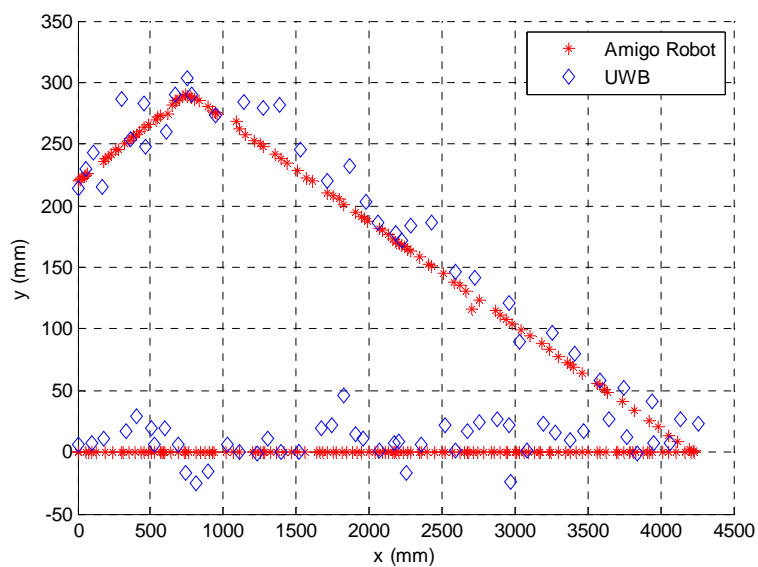
Figure 11. Test 2- positioning of the mobile robot using Odometry & orientation sensors and UWB from point A to B.
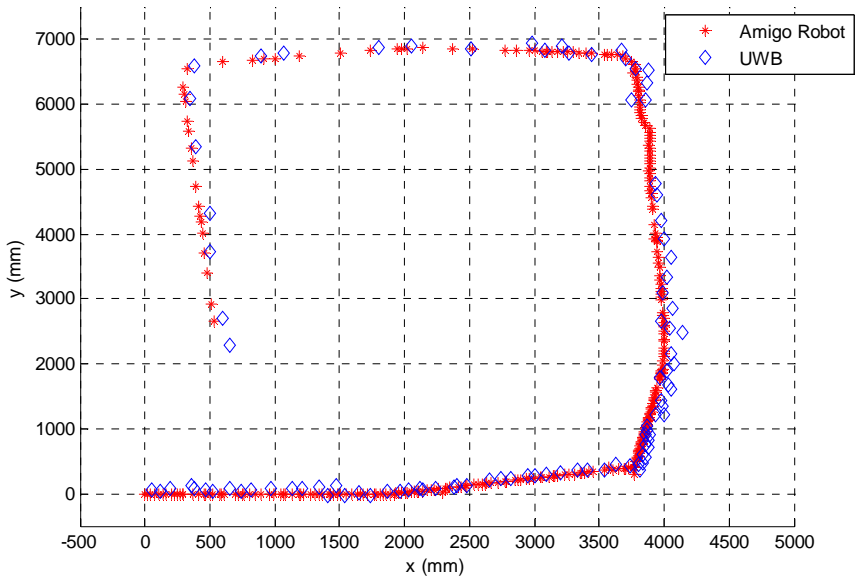
Figure 12. Test 3- positioning of the mobile robot using Odometry & orientation sensors and UWB from point A to B.
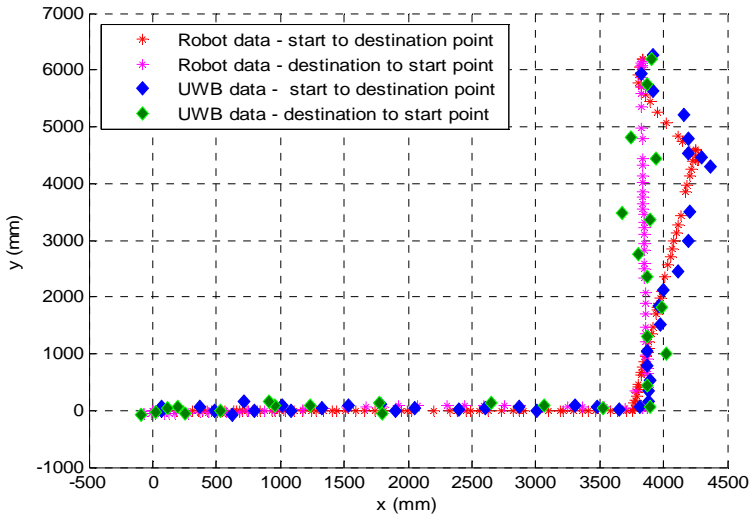
Figure 13. Test 4- positioning of the mobile robot using Odometry & orientation sensors and UWB from point A to B and from B to A.

Table 1. Position of UWB nodes with the estimated error in mm accuracy.

Connected Node	Distance from Node 107 in mm	Estimated error in mm
100	4739	55
100	8247	55
100	3023	55
100	1884	24

6. Conclusion

Experimental investigations have been conducted using UWB signals measured in LOS and NLOS environments for location estimation using the TDOA algorithm. A new measurement scheme has been proposed for improved localization through performance assessment and validation of the use of UWB signals measured in LOS and NLOS indoor environments. The experimental tests have shown that the UWB accuracy is very good with the positioning error between 24 and 55 mm, and the error not exceeding 55 mm. The localization error increases with longer robot travel. Results indicate that a system that uses UWB gives much more accurate position measurement in indoor environments than other localization techniques. UWB provides an accuracy indoors of less than 55 mm error with a working range of 160 m. The difficulty of obtaining a very accurate positioning system is due to NLOS propagation conditions. The use of UWB TDOA measurement is thus recommended for localisation because of it low cost, low power consumption and low computational complexity and precise positioning capability.

To improve the UWB localization technique in wireless sensor networks in indoor environments, its performance should be evaluated with the objective of proposing new measurement schemes that improve localization and use this information to perform simultaneous localization and mapping (SLAM) to navigate robots to perform cooperative tasks in inspection and non-destructive testing of large safety critical infrastructures. More sophisticated state estimation algorithms such as particle filters using Monte Carlo methods may give more accurate tracking of mobile robots.

References

1. M. diBenedetto, T. Kaiser, A. Molisch, I. Oppermann, C. Politano, and D. Porcino, Eds., "UWB Communications Systems: A Comprehensive Overview," Darmstadt, Germany: EURASIP, 2005.
2. M. Guizani, R.C. Qiu, and T. Le-Ngoc, "Ultra-Wideband wireless communications and networks," John Wiley and Sons Ltd, 2006.
3. Z. Sahinoglu, S. Gezici, and I. Guvenc, "Ultra-Wideband Positioning Systems: Theoretical Limits, Ranging Algorithms, and Protocols". Cambridge, Dec 2008.
4. S. Gezici, Z. Tian, G. Giannakis, H. Kobayashi, A. Molisch, H. Poor, and Z. Sahinoglu, "Localization via ultra-wideband radios: a look at positioning aspects for future sensor networks," IEEE Signal Processing Magazine, vol. 22, page 70-84, July 2005.
5. S. Gezici, Z. Tian, G. Giannakis, H. Kobayashi, A. Molisch, H. Poor, and Z. Sahinoglu, "Localization via ultra-wideband radios: a look at positioning aspects for future sensor networks," IEEE Signal Processing Magazine, vol. 22, page 70-84, July 2005.
6. B. Sobhani, M. Mazzotti, E. Paolini, A. Giorgetti, and M. Chiani, "Effect of state space partitioning on bayesian tracking for UWB radar sensor networks," in IEEE International Conference on Ultra-Wideband, page 120 - 125, Sep. 2013.
7. B. Sobhani, E. Paolini, A. Giorgetti, M. Mazzotti, and M. Chiani, "Bayesian tracking in UWB radar sensor networks," in IEEE International Conference on Communications Workshops (ICC), page 47-51, June 2013
8. S. Bartoletti, A. Conti, and A. Giorgetti, "Analysis of UWB radar sensor networks", in IEEE International Conference on Communications (ICC), page 1-6, May 2010.
9. H. Ding, C. Chen, S. Peng, X. Li, and L. Zheng, "Multistatic ultra-wideband localization for NLOS environments", in Second International Conference on Intelligent System Design and Engineering Application (ISDEA), page 380-384, Jan 2012.
10. Activemedia. Amigobot technical manual. Activemedia Robotics, Nov 2000.
11. J. Gwatkin, "Robo-CAMAL:Anchoring in a Cognitive Robot," PhD thesis in the University of Hull, December 2009.

AUTHOR INDEX

ROBOTICS TRANSFORMING THE FUTURE

This book provides state-of-the-art scientific and engineering research findings and developments in the area of service robotics and associated support technologies around the theme of robotics transforming the future. The book contains peer reviewed articles presented at the CLAWAR 2018 conference. The book contains a strong stream of papers on robotic locomotion strategies and robotics for assistance and rehabilitation. There is also a strong collection of papers on no-destructive inspection robots, robotics in education and education in robotics to meet the growing emerging needs in various sectors of society. Robot designs based on biological inspirations and for biomedical applications are also strongly featured.